

The Faint Extragalactic Radio Sky

by

Tessa Vernstrom

B.Sc., The University of Minnesota, 2008

M.Sc., The University of British Columbia, 2011

A THESIS SUBMITTED IN PARTIAL FULFILLMENT
OF THE REQUIREMENTS FOR THE DEGREE OF

Doctor of Philosophy

in

THE FACULTY OF GRADUATE AND POSTDOCTORAL
STUDIES
(Astronomy)

The University of British Columbia
(Vancouver)

August 2015

© Tessa Vernstrom, 2015

Abstract

The radio sky covers a large range of sources, from small single galaxies to large clusters of galaxies and the space between them. These sources consist of some of the most powerful objects in the Universe, as well as diffuse weak emitters. Understanding the radio sky tells us about how galaxies have evolved over time, the different kinds of galaxy populations, the star formation history of the Universe, and the role of magnetism, as well as details of large-scale structure and clustering. Advancements in radio telescopes now allow us to push observational limits to new depths, probing fainter galaxies and farther back in cosmic time.

We use a multi-pronged approach to examine several aspects of the faint extragalactic radio sky. Using new deep data from the Karl G. Jansky Very Large Array telescope, combined with the confusion analysis technique of $P(D)$, we obtain the deepest estimates of the source count of individual radio galaxies and their contribution to the cosmic radio background temperature. Additionally, these data are used to catalogue the individual galaxies in order to study characteristics such as source size, spectral dependence, galaxy type, and redshift. We then examine the contribution from extended large-scale diffuse emission to the radio sky using data from the Australia Telescope Compact Array. This yields constraints on the total emission from such sources, including galactic halos, galaxy cluster halos and relics, and the inter- and intra-cluster medium. Finally, we investigate the radio angular power spectrum using interferometric data. These measurements show the fluctuations coming from the unresolved radio background as a function of angular scale.

Together these studies present the deepest constraints available for the faint radio sky across a range of statistical areas. The measurements obtained here provide

constraints on the evolving population of galaxies through their radio emission in order to further our knowledge of galaxy evolution in general.

Preface

The text of this dissertation includes modified reprints of previously published material as listed below. Per publishing convention, throughout this thesis the word “we” is used when discussing the work performed. However, the breakdown of my contribution to the work is as follows¹.

Chapter 1 (published):

- T. Vernstrom, D. Scott, J. V. Wall, *Contribution to the Diffuse Radio Background from Extragalactic Radio Sources*, MNRAS, **415**, 3641 (2011) [182]

The work for this paper was performed as part of, and is also published in, my Masters Thesis. This paper presents an analysis of radio source counts, and their contribution to the radio background temperature, across a range of frequencies from a compilation of previously published data. I wrote the entire text and performed all of the analysis. D. Scott and J.V. Wall provided support for the work, including the initial idea, along with comments on the writing.

Chapter 2.2 (published):

- J.J. Condon, W.D. Cotton, E.B. Fomalont, K.I. Kellermann, N. Miller, R.A. Perley, D. Scott, T. Vernstrom, J.V. Wall. *Resolving the Radio Source Background: Deeper Understanding through Confusion*, ApJ, **758**, 23 (2012) [37]

This paper presents the initial data reduction methods and analysis of new data from the Karl G. Jansky Very Large Array. This work was a collaboration between

¹ Chapters 6 and 7 describe work not yet published. I have performed the entirety of the analysis for those chapters, with commentary contributions from D. Scott and J.V. Wall.

myself and advisors (D. Scott and J.V. Wall) at the University of British Columbia and collaborators at the National Radio Astrophysical Observatory (NRAO). The work presented was carried out, and written up, predominately by W.D. Cotton and J.J Condon, who was the PI for the genesis of this project. I assisted in the taking of the observations, and provided considerable input in the writing of the paper. The work presented in Chapter 2.2 presents a portion of the work from the published paper.

Chapter 3.2, Chapter 4 (published):

- T. Vernstrom, D. Scott, J.V. Wall, J.J. Condon, W.D. Cotton, E.B. Fomalont, K.I. Kellermann, N. Miller, R.A. Perley. *Deep 3 GHz Number Counts from a P(D) fluctuation analysis*, MNRAS, **440**, 2791 (2014) [183]

This paper was a follow-up to the previously mentioned paper and presents my analysis of the data described in that work. The initial data calibration and imaging was performed by W.D. Cotton. However, I carried out the entirety of the analysis and wrote the text of the paper. Important feedback on the work and text was provided by all of the co-authors.

Chapter 2.1, Chapter 5 (published):

- T. Vernstrom, R.P. Norris, D. Scott, J.V. Wall. *The Deep Diffuse Extragalactic Radio Sky at 1.75 GHz*, MNRAS, **447**, 2243 (2015) [184]

This work was a collaboration between myself and advisors at UBC and R.P. Norris at the Australia Telescope National Facility/Commonwealth Scientific and Industrial Research Organization (ATNF/CSIRO). The idea for the project and initial telescope proposal were the responsibility of R.P. Norris. I assisted with the telescope observations at the Australia Telescope Compact Array in Australia and performed all data calibration and imaging. I carried out the analysis and wrote the text of the paper, with helpful commentary from my co-authors on the analysis and writing.

Table of Contents

Abstract	ii
Preface	iv
Table of Contents	vi
List of Tables	x
List of Figures	xii
List of Acronyms and Abbreviations	xvi
List of Symbols	xviii
Acknowledgments	xx
1 Introduction	1
1.1 Thesis Outline	5
1.2 Source Counts	6
1.3 The Radio Background	12
1.3.1 Source Count Contribution to Temperature	14
1.3.2 ARCADE 2	16
2 Data	20
2.1 Australia Telescope Compact Array	24
2.1.1 Calibration	25

2.1.2	Imaging	26
2.1.3	Image Noise	27
2.2	Karl G. Jansky Very Large Array	31
2.2.1	Calibration	33
2.2.2	Imaging	34
2.2.3	Image Noise	37
2.2.4	The SNR-Optimized Wideband Sky Image	39
2.3	SKADS Simulation	40
3	Confusion and $P(D)$	42
3.1	Confusion	42
3.2	Probability of Deflection	46
3.2.1	$P(D)$ Simulation Tests	47
3.2.2	Clustering and Source Sizes	50
4	Discrete-Source Count	53
4.1	Introduction	53
4.2	$P(D)$ and Image Noise	55
4.3	Model Fitting	59
4.4	Choice of Model	66
4.4.1	Modified Power Law	66
4.4.2	Node Model	67
4.5	Discrete Source Count Fitting Results	71
4.5.1	Estimated Number Counts	71
4.5.2	Parameter Degeneracies	74
4.5.3	Background Temperature	79
4.6	Discrete Emission Discussion	81
4.6.1	Image Artefacts	81
4.6.2	Weighting	85
4.6.3	Comparison to Other Estimates	86
4.7	Conclusions	90

5	Extended-Source Count	96
5.1	Introduction	96
5.2	$P(D)$ and Beams	98
5.3	Discrete Sources	99
5.3.1	Source Subtraction	101
5.3.2	Counts and Confusion	102
5.4	Extended Sources	105
5.4.1	High Resolution Extended Emission	105
5.4.2	Source Size Sensitivity	107
5.5	Extended Source Count Models	107
5.5.1	Shifted Discrete Count Model	110
5.5.2	Parabola Model	111
5.5.3	Node Model	111
5.6	Background Temperature	113
5.7	Extended Emission Source Count Fitting Results	113
5.7.1	Summary of Fits	113
5.7.2	Model Uncertainties	114
5.7.3	ARCADE 2 Fits	119
5.8	Extended Emission Discussion	120
5.8.1	Sources of Diffuse Emission	120
5.8.2	Cluster Emission	122
5.8.3	Dark Matter Constraints	125
5.9	Integral Counts	127
5.10	Conclusions	130
6	Discrete-Source Catalogue	132
6.1	Simulations	133
6.1.1	Uncertainties	134
6.1.2	Completeness, False Detections, and Blending	141
6.2	Catalogue	144
6.2.1	Angular Size Distribution	147
6.2.2	Extended Sources	151
6.3	Source Count	153

6.4	Spectral Indices	160
6.5	Cross-Identifications	164
6.5.1	Optical and IR	164
6.5.2	Radio	167
6.6	Conclusions and Future Work	167
7	The Radio Angular Power Spectrum	173
7.1	Introduction	173
7.2	Visibility Data	175
7.2.1	Primary Beam	175
7.2.2	Frequency Weighting	178
7.2.3	Mosaicking	179
7.3	Bare Estimator	181
7.4	Simulations	184
7.5	Model Fitting	188
7.6	Simulation Results	191
7.7	ATCA Results	194
7.8	Conclusions	199
8	Impact and Conclusions	202
8.1	Summary	202
8.2	Future Work	205
8.2.1	High Resolution	205
8.2.2	Low Frequencies	206
8.2.3	The Far Infrared to Radio Correlation	207
8.2.4	Polarisation	208
8.3	Conclusion	209
Bibliography	210	
A C Catalogue	232	
B CB Catalogue	252	

List of Tables

Table 1.1	References for the extragalactic radio count data compilation	11
Table 1.2	Best-fit parameter and χ^2 values for source count polynomial fits	11
Table 1.3	Background temperatures from fitting of compiled source counts	18
Table 2.1	ATLAS ELAIS-S1 pointings centres	24
Table 2.2	VLA observing Runs Summary	32
Table 2.3	Frequency and noise properties of the 16 VLA subband images	36
Table 2.4	Image properties for the wide-band VLA 3 GHz data	40
Table 4.1	Best-fitting parameters for VLa 3 GHz modified power-law model	74
Table 4.2	Best-fitting parameters from VLA 3 GHz node model	75
Table 4.3	Slopes and normalizations from best-fitting VLA 3 GHz node model	75
Table 4.4	Correlation matrix for best-fitting VLA 3 GHz parameters	79
Table 4.5	Radio background temperatures from best-fitting source count VLA 3 GHz models	81
Table 4.6	VLA 3 GHz best-fitting model parameters	90
Table 5.1	Angular and physical source sizes at different redshifts	109
Table 5.2	Best-fitting results for extended emission Model 1.	114
Table 5.3	Best-fitting results for extended emission Model 2.	118
Table 5.4	Best-fitting results for extended emission Model 3.	118
Table 5.5	Luminosity and redshift estimates for Model 2.	120
Table 5.6	Integrated source count values of the different models scaled to 1.4 GHz.	129

Table 6.1	Differential Euclidean normalized source count	160
Table A.1	Discrete VLA C Catalogue	233
Table B.1	Discrete VLA CB Catalogue	253

List of Figures

Figure 1.1	Differential and integral source counts with different normalizations	8
Figure 1.2	Compilation of published survey source counts and fits at multiple radio frequencies	10
Figure 1.3	The Cosmic Backgrounds	13
Figure 1.4	Background temperature distributions from fitting published source counts	15
Figure 1.5	Extragalactic background temperature values from ARCADE 2 and source counts	17
Figure 2.1	Example Interferometer <i>uv</i> Coverage	22
Figure 2.2	ELAIS-S1 1.75 GHz mosaic images	28
Figure 2.3	Instrumental noise from ATCA 1.75 GHz images	29
Figure 2.4	Frequency dependence of ATCA 1.75 GHz wide-band mosaic image	30
Figure 2.5	Lockman Hole 3 GHz images	38
Figure 3.1	Confusion of simulated noiseless images with different beam sizes	44
Figure 3.2	Confusion of simulated images with different noise values	45
Figure 3.3	Euclidean-normalised source count from SKADS simulation	49
Figure 3.4	Comparison of pixel histograms from 1.4 GHz simulation	50
Figure 4.1	Change in VLA image noise as a function of distance	56

Figure 4.2	Differences in PDFs of purely Gaussian noise and weighted varying noise.	57
Figure 4.3	VLA 3-GHz contour images of the Lockman hole.	60
Figure 4.4	$P(D)$ Bin correlations and uncertainties	61
Figure 4.5	Comparison of Monte Carlo fitting output for 3 GHz source count with different model settings	72
Figure 4.6	MCMC source count fitting results of VLA 3 GHz data using modified power-law model	73
Figure 4.7	$P(D)$ s of best-fitting source counts at 3 GHz from modified power-law model	76
Figure 4.8	MCMC source count fitting results of VLA 3 GHz data using node model	77
Figure 4.9	$P(D)$ s of best-fitting source counts at 3 GHz from node model	78
Figure 4.10	One and two dimensional likelihood distributions for the six VLA 3 GHz nodes	80
Figure 4.11	Histogram of CRB temperatures at 3 GHz from modified power-law model	82
Figure 4.12	Histogram of CRB temperatures at 3 GHz from node model .	83
Figure 4.13	Negative flux-density region of the VLA 3 GHz $P(D)$ distribution	84
Figure 4.14	Comparison of $P(D)$ fitting for wide-band images with different spectral indices in the weighting	87
Figure 4.15	Best-fit modified power-law model of VLA source count compared with other models and observed counts	91
Figure 4.16	Best-fit node model of VLA source count compared with other models and observed counts	92
Figure 4.17	Source count bump models for ARCADE 2 temperature . . .	93
Figure 5.1	Images of the synthesized beams for the 1.75 GHz data . . .	99
Figure 5.2	$P(D)$ distributions for the ATCA 1.75 GHZ mosaic central regions	100
Figure 5.3	Discrete source $P(D)$ distribution at 1.75 GHz	103
Figure 5.4	Simulated point source and extended emission images at 9 arcsec resolution	108

Figure 5.5	Fitted $P(D)$ s of simulated images with different source sizes	109
Figure 5.6	Discrete source counts of AGN and starburst at 1.75 GHz with flux density shift	112
Figure 5.7	$P(D)$ distributions from fitting for extended emission source count models	115
Figure 5.8	Temperature histograms from MCMC fitting of the three extended emission source count models	116
Figure 5.9	S^2 normalized source counts at 1.75 GHz of best-fitting models	117
Figure 5.10	Comparison of the radio cluster halo model from Zandanel et al. [198] with ATCA 1.75 GHz data	124
Figure 5.11	Comparison of one dark matter modelling approach with ATCA 1.75 GHz data	126
Figure 5.12	Integrated source counts at 1.4 GHz and 1.75 GHz	128
Figure 6.1	Catalogue Simulation Uncertainties	135
Figure 6.2	Catalogue Simulation 2D Size Ratio Distribution	137
Figure 6.3	Catalogue Simulation 2D Size Ratio Uncertainty Distribution	138
Figure 6.4	Catalogue Simulation Corrected Uncertainties	139
Figure 6.5	Catalogue Simulation Completeness	142
Figure 6.6	Catalogue Simulation False Detections	143
Figure 6.7	Catalogue Flux Distribution	145
Figure 6.8	Catalogue Resolution Comparison	148
Figure 6.9	CB Catalogue Angular Size Distribution	149
Figure 6.10	C Catalogue Angular Size Distribution	150
Figure 6.11	Catalogue Mean Sizes vs Flux	152
Figure 6.12	Images for extended source at J2000 161°.6051, 59°.090913 .	154
Figure 6.13	Images for extended source at J2000 161°.41572, 58°.955855	155
Figure 6.14	Images for extended source at J2000 161°.45361, 58°.90226 .	156
Figure 6.15	Images for extended source at J2000 161°.6575, 58°.906266 .	157
Figure 6.16	3GHz Catalogue Source Count	159
Figure 6.17	Catalogue Spectral Index Histograms	162
Figure 6.18	Catalogue Mean Spectral Indices vs Flux Density	163
Figure 6.19	Details of Catalogue Cross Matching	165

Figure 6.20	Colour-Colour plots of optical and NIR CB catalogue matches	168
Figure 6.21	Colour-Colour plots of optical and NIR C catalogue matches .	169
Figure 6.22	1.4 GHz to 3 GHz Spectral Indices and Fluxes	170
Figure 7.1	ATCA Spatial Scale Responsivity	177
Figure 7.2	2D Log Power with ATCA <i>uv</i> coverage	180
Figure 7.3	Power vs <i>uv</i> Distance Simulated Visibilities	183
Figure 7.4	Simulation models for power spectrum	184
Figure 7.5	Simulated Clustered Point Sources	186
Figure 7.6	Bootstrap Power Spectrum Scatter Random Positions	189
Figure 7.7	Bootstrap Power Spectrum Scatter Clustered Positions	190
Figure 7.8	Power Spectra from Simulations–Clustered	192
Figure 7.9	Power Spectra from Simulations–Extended	193
Figure 7.10	Power Spectra from Simulations–Mosaic	195
Figure 7.11	Parameter Distributions from fitting Simulated 1D random power spectrum	196
Figure 7.12	Parameter Distributions from fitting Simulated 1D clustered power spectrum	197
Figure 7.13	Power Spectra from ATCA data	198
Figure 7.14	$C_\ell \Delta T/T$ Limits	200

List of Acronyms and Abbreviations

AGN	active galactic nuclei
ATCA	Australia Telescope Compact Array
ATLAS	Australia Telescope Large Area Survey
BAO	baryon acoustic oscillations
CFHT	Canada France Hawaii Telescope
CHIME	Canadian Hydrogen Intensity Mapping Experiment
CMB	cosmic microwave background
CRB	cosmic radio background
Dec	Declination
GMRT	Giant Metrewave Radio Telescope
EMU	Evolutionary Map of the Universe survey
FIR	far infrared
FOV	field of view
FR	Fanaroff-Riley
FWHM	full width at half maximum

ICM	intracluster medium
IGM	intergalactic medium
IF	intermediate frequency
LIRG	luminous infrared galaxy
MCMC	Monte Carlo Markov Chain
QSO	Quasar
PSF	point spread function
PDF	probability distribution function
RA	Right Ascension
RFI	radio frequency interference
SKA	Square Kilometre Array
ASKAP	Australian Square Kilometre Array Pathfinder
SDSS	Sloan Digital Sky Survey
SED	spectral energy distribution
SERVS	<i>Spitzer</i> Extragalactic Representative Volume Survey
SKADS	Square Kilometre Array Design Studies
SNR	signal-to-noise ratio
SWIRE	<i>Spitzer</i> Wide-Area Infrared Extragalactic Survey
UKIDSS	UKIRT Infrared Deep Sky Survey
ULIRG	ultra-luminous infrared galaxy
VLA	Karl G. Jansky Very Large Array
VCLASS	VLA Sky Survey

List of Symbols

S	flux density
N_{dof}	Number of degrees of freedom
D_L	luminosity distance
H_0	Hubble constant
ϕ_L	luminosity function; number density as a function of luminosity
Ω_m	matter density
Ω_λ	vacuum energy density; cosmological constant
D_a	antenna diameter
b	(maximum) baseline length
\mathcal{C}_T	flux to temperature conversion factor
α	spectral index
Ω_B	beam solid angle
Ω_S	source solid angle
T_b	background temperature
k_B	Boltzmann constant
E_l	left hand complex electric field amplitude

E_r	right hand complex electric field amplitude
ρ	angular offset from the pointing centre
dN/dS	differential source count
$N(> S)$	integral source count
D	deflection (observed brightness)
$P(D)$	Probability of deflection
$B(\theta, \phi)$	beam or point spread function
$R(x)$	mean number of pixel values per steradian with observed intensities between x and $x + dx$
σ_c	confusion noise
σ_n	instrumental noise
σ_n^*	weighted instrumental noise
ς	histogram bin uncertainty
θ_M	major axis FWHM
θ_{DM}	deconvolved major axis
θ_m	minor axis FWHM
θ_{Dm}	deconvolved minor axis
θ_B	beam FWHM
ϕ	position angle
S_P	peak flux density
S_T	total integrated flux density
$w(\theta)$	2-point angular correlation function

Acknowledgments

I acknowledge the financial support of the Natural Sciences and Engineering Research Council (NSERC) of Canada. I thank the staff of the VLA , which is operated by the National Radio Astronomy Observatory (NRAO). The National Radio Astronomy Observatory is a facility of the National Science Foundation operated under cooperative agreement by Associated Universities, Inc. I thank the ATCA and CSIRO staff. The Australia Telescope Compact Array is part of the Australia Telescope National Facility which is funded by the Commonwealth of Australia for operation as a National Facility managed by CSIRO.

I would like to personally thank my advisors Douglas Scott and Jasper Wall for all their help. And thank my parents, sister, and husband for all their support.

Chapter 1

Introduction

The radio sky can be broken up into three main components. There is the contribution from our Galaxy the Milky Way (and all the sources within it), the contribution from the cosmic microwave background (CMB) radiation, and a contribution from all extragalactic sources. The Milky Way contribution is by far the dominant source at radio wavelengths (10's of Kelvin in temperature), whereas the other two components contribute less (roughly milliKelvins in Temperature), though it depends on the exact frequency to say which of the CMB or extragalactic is a stronger contributor. This work focus on the the extragalactic component. We break this category down into two parts: discrete sources and extended sources.

Discrete sources are point sources, or small angular scale sources (typically below a few arcsec). This is emission from individual galaxies, which at radio frequencies are predominantly active galactic nuclei (AGN) and star forming, or starburst, galaxies. AGN were first discovered by Bolton et al. [14] and Ryle et al. [153]. These are galaxies which host a supermassive black hole at the centre which is actively accreting material yielding a much higher luminosity than normal at some, if not all, wavelengths. AGN are some of the most luminous persistent sources of radiation in the Universe. At 1.4 GHz the flux densities range from mJy to 10s or hundreds of Jy's (with Jy being the conventional unit of flux density and $1 \text{ Jy} = 1 \times 10^{-26} \text{ W m}^{-2} \text{ sr}^{-1} \text{ Hz}^{-1}$). The accreting black holes generate strong magnetic fields resulting in powerful synchrotron emission. At radio frequencies AGN can have several features such as relativistic jets, lobes, or hotspots.

There are several classifications of AGN, although with the current unified model it is thought these are all the same type of galaxy with the differences a result of our particular viewing angle (Barthel [6], Orr and Browne [132], Scheuer and Readhead [158], Urry and Padovani [179]). These can be classified as low-radio-power edge-dimmed Fanaroff-Riley (FR) type 1 ([48]) which have broad emission lines (optically featureless continua), and powerful FR type 2 (edge-brightened) with narrow lines in the optical/UV spectra sometimes known as radio quasars (FSRQs). It is generally accepted that type 2 sources are obscured versions of type 1. These can be broken down into flat and steep-spectrum sources. The emission from the core (stellar-like) tends to have a flat spectrum and these are known as BL Lacs or Quasars (sometimes referred to as Blazars). Whereas the emission dominated by the extended optically thin components (the jets, lobes, or hot-spots) has a steep spectrum. In general each source has both a compact flat-spectrum core and extended steep-spectrum lobes, it just depends on our viewing angle with respect to the source.

There are radio-loud and radio-quiet AGN, which refers to the type of accretion happening, hot-mode and cold-mode, respectively. Radio-loud objects are the brighter sources which produce the large scale radio jets and lobes, with the kinetic power of the jets being a significant fraction of the total bolometric luminosity; whereas, the weak ejecta of the radio-quiet objects are energetically insignificant. Radio-loud objects tend to be associated with elliptical galaxies which have undergone recent mergers, while radio-quies generally have spiral hosts. The thermal emissions from the AGN (continua and lines from X-ray to infrared wavelengths) are quite similar in the two classes (Sanders et al. [154]), which has been argued to mean the black hole masses and mass accretion rates are not greatly different and that the difference is associated with the spin of the black hole [192]. There has been much work looking into the different AGN classes, the emission mechanisms, and more and for a reviews of such topics see e.g. Antonucci [3], Wilson and Colbert [192].

In terms of non-AGN radio galaxies the main kinds are star-forming and starburst galaxies. Star-forming galaxies are considered “normal” spiral-type galaxies (sometimes referred to as main sequence galaxies). Starburst galaxies are undergoing a large burst of star formation and are usually classified as luminous infrared

galaxies (LIRG) or ultra luminous infrared galaxies (ULIRG). The primary emission is synchrotron emission from the star formation in the disk of the galaxies. These both tend to be less luminous than AGN (or at least than radio-loud AGN) with flux densities \leq mJy's.

The counts (or number of objects per sr as a function of flux density) of discrete radio sources and their contribution to the cosmic radio background (CRB) can be used to constrain galaxy evolution. The history of radio source counts goes back to Mills [119] who discussed the cumulative count or ‘ogive’, giving one of the first published source counts, followed by Ryle and Scheuer [152], with the discovery that the slope of the source count was steeper than expected from a static Euclidean universe, which implied that sources must be evolving in space density or luminosity. Since then many more surveys have been carried out to measure the source counts at various radio frequencies, both whole-sky and limited area surveys, which confirmed the importance of evolution [see 42, for a recent review]. These counts can now be broken down into different source populations.

With advancements in radio telescope capabilities we have been able to probe the source count to ever increasing depth, so that estimating the count in the μ Jy and sub- μ Jy regions is now possible. Investigating the count at these faint flux densities is important for understanding the evolution of sources at lower luminosities and/or higher redshifts ($z \geq 2$). How the count below 10μ Jy behaves has been unknown until now: what the slope is in this region, whether the Euclidean-normalised count declines or begins to rise again (possibly indicating a new population), and whether the sources continue to obey the well-known far infrared (FIR) to radio correlation [35, 41, 95] out to higher redshifts.

The brightest radio sources are known to be radio-loud AGN. However, it was not until the 1980s that the radio source counts at the sub-mJy level revealed a new radio population (Mitchell and Condon [120], Windhorst et al. [193]). It is now known from various studies (e.g. Seymour et al. [161], Simpson et al. [164], Smolčić et al. [167]) that the bulk of discrete radio sources in the sub-mJy range, for frequencies near 1.4 GHz, are star-forming galaxies (starbursts, spirals, or irregulars) and low luminosity radio AGNs (faint FR I radio galaxies, Seyfert galaxies, radio-quiet Quasar (QSO), see e.g Mignano et al. [117], Padovani et al. [136]). Using optical/IR cross-match identifications and redshift data, their space

distributions have been modelled via their luminosity functions to determine how they evolve with redshift. The number counts dN/dS , or the differential number of sources per steradian per flux density interval, have now been measured well into the sub-mJy region [37, 134], as well as the contribution from these sources to the isotropic diffuse radio background.

However, what is less well characterized is extended large-angular-scale diffuse low-surface brightness sources (sizes of 10s of arcseconds to arcminutes) . There have been few surveys carried out for diffuse arcminute-scale extragalactic emission, and very few that also have high sensitivity at that scale. The most sensitive lower resolution survey yet published was by Subrahmanyan et al. [172], which reached an rms of $85 \mu\text{Jy beam}^{-1}$ with a 50 arcsec beam. This angular scale encompasses emission from individual galaxy haloes, emission from galaxy clusters and groups (e.g. Cassano et al. [23], Fabian et al. [47], Liang et al. [109], Peterson and Fabian [140], Venturi et al. [180, 181]), or emission from large-scale structure (the cosmic web), such as the intergalactic medium (IGM) or inter-cluster medium (e.g. Bagchi et al. [4], Kronberg et al. [101]).

Clusters of galaxies are the largest gravitationally bound systems in the Universe. They are formed by hierarchical structure formation processes, or mergers of smaller systems. It is believed the underlying dark matter in the Universe consists of filaments and voids. Denser regions form a filament and clusters are formed within the filaments. Major cluster mergers are some of the most energetic events in the Universe. During mergers, shocks are driven into the intracluster medium (ICM) , following with the injection of turbulence. Eventually, clusters can reach a relaxed state with a giant galaxy and hot gas in the centre. In recent years there has been growing evidence of cluster large-scale diffuse radio sources of synchrotron origin associated with the ICM ([e.g. 54, 71]). Diffuse features demonstrate that the thermal ICM plasma is mixed with the non-thermal components of large-scale magnetic fields with relativistic electrons in the cluster volume. These magnetic fields have been observed through studies of the Faraday rotation of polarized radio galaxies in the background or within the magnetized ICM.

The diffuse sources are usually grouped into three categories: haloes, mini haloes, and relics. Haloes are hosted in clusters showing merging processes (Feretti [51]) and are located near the cluster centre. Relics are located in the cluster

peripheral regions of both merging and relaxed clusters. Mini haloes are hosted in relaxed cool-core clusters and are usually centrally located near a powerful radio galaxy. These objects all tend to have steep spectrums ($\geq 1.$), however, the relics, at the peripherals, tend to be more strongly polarized (Feretti [51]). For a detailed review of these objects see Feretti et al. [53].

1.1 Thesis Outline

Rather than looking at a small number of radio sources in detail, this work focuses on characterizing the population of sources by looking at large numbers of them. Statistical surveys complement studies of individual sources, thereby yielding information on the flux densities, numbers, and source sizes, the source count (i.e. the 1-point statistics) and the 2-point statistics (e.g power spectrum or two-point correlation function). The goal of this work is to use these methods to examine the faint radio sky and faint radio sources at both large and small angular scales. We first give an introduction to source counts and the cosmic radio background in the remainder of this Chapter.

In Chapter 2 we discuss the data that are used in the analysis, including the observation, data calibration, and imaging details based on Condon et al. [37] and Vernstrom et al. [183, 184], as well as the details of the main simulation data from Wilman et al. [191] that are used throughout this thesis. In Chapter 3 the main method used (at least in Chapters 4 and 5) is explained. This includes example tests of the method using the realistic simulations described in Chapter 2.

Chapter 4 details the work carried out to investigate the faint discrete source count using new deep radio observations, based on Vernstrom et al. [183]. Chapter 5 is based on the work of Vernstrom et al. [184] investigating extended radio emission. In Chapter 6 a preliminary version of the discrete-source catalogue is constructed and described, using the data from Condon et al. [37] and Vernstrom et al. [183]. Chapter 7 presents a first measurement of the radio angular power spectrum at faint intensities. Finally, Chapter 8 gathers together the conclusions from the previous chapters and considers their broader impacts, as well as discussing some avenues for future work to continue these investigations.

1.2 Source Counts

Source counts, namely the surface density of sources as a function of flux density (S), can be directly compiled from any complete sample, without any additional data. Because flux density is primarily a function of both redshift and luminosity, source counts are the first probes into the behaviour of galaxy evolution. Studying source counts is important for a number of reasons. They tell us the number and density of galaxies in the Universe. Source counts can, in principle, also tell us about the cosmology of the Universe, particularly the faint counts. Source counts come from the luminosity function, ϕ_L , which is the number of galaxies as a function of luminosity in some volume. The volume depends on cosmological parameters such that

$$\frac{dV}{dz} = \frac{c}{H_0} \frac{D_L^2}{(1+z)^2(1+\Omega_m z) - z(2+z)\Omega_\Lambda}. \quad (1.1)$$

Here D_L is the luminosity distance, H_0 is the Hubble constant, Ω_m is the matter density, and Ω_Λ is the energy density. The luminosity distance is dependent is also a function of the cosmological parameters,

$$D_L = \frac{c}{H_0} \int_0^{z(L,S)} \frac{(1+z)dz}{\sqrt{(1+z)^2(1+\Omega_m z) - z(2+z)\Omega_\Lambda}}. \quad (1.2)$$

The flux density depends on the luminosity distance, where

$$S = \frac{L}{4\pi D_L^2}. \quad (1.3)$$

Thus, if $\Omega_\Lambda \neq 0$, there is faster expansion, a larger volume, and more galaxies (though evolution of source populations is the dominant factor in the form of the source counts, and distinguishing cosmological parameters in practice is complicated by issues such as survey systematics).

Source counts enable us to investigate the evolution of galaxies, comparing galaxies today with galaxies in the past. Additionally, we can quantify and constrain the evolution in galaxy populations and discriminate the nature of the evolution.

Source counts can reveal the contribution of different galaxy populations to the overall population of galaxies. The counts at different wavelengths are dominated by different types of galaxies, for example X-ray are predominantly AGN, radio counts are AGN (bright flux densities) and star-forming galaxies (dominate at $S \leq 1$ mJy), whereas infrared is mainly spiral star forming galaxies. Comparing data from the different wavelengths can reveal information about the underlying physical processes. For example comparing radio data to X-ray data can tell us about the connection between synchrotron emission and Inverse Compton scattering ([9, 50, 83, 92]). The radio and infrared can both be tracers of star formation; thus combining data from those two wavebands can help to map the star formation history of the Universe.

Source counts can be presented in different forms, the most basic being the cumulative integral source count ($N(> S)$) (Fig. 1.1, top left panel), describing the expected number of sources per unit area above a given flux density. Because of its cumulative nature, consecutive data points are not statistically independent, which can be problematic, especially in the corresponding error analysis. The differential form of the source count dN/dS (Fig. 1.1, top right panel), describes the number of sources per unit area in a given flux density bin and avoids the problem of dependence of consecutive values.

Because the differential source count is generally very steep, possibly hiding some important features, it is customary to represent it relative to the count of uniformly distributed sources in a flat, non-evolving Euclidean Universe, where the flux $S \propto 1/D^2$ and the number density $N \propto D^3$. Thus the integral count has the form

$$N(> S)_{\text{Euc}} = K S^{-3/2}. \quad (1.4)$$

Here the arbitrary constant K is usually taken from the number density of sources with flux-densities above 1 Jy. In the differential form the Euclidean count becomes $S^{-5/2}$. Normalizing the source count by this factor provides the relative Euclidean-normalized differential source count, $\frac{dN}{dS} S^{5/2}$ (Fig. 1.1, bottom left panel), which is the third form of count usually considered. The fourth form of the count shown in Fig. 1.1 (bottom right panel) is weighting the differential counts by S^2 . This alternate weighting of $S^2 dN/dS$ is proportional to the source count contribution

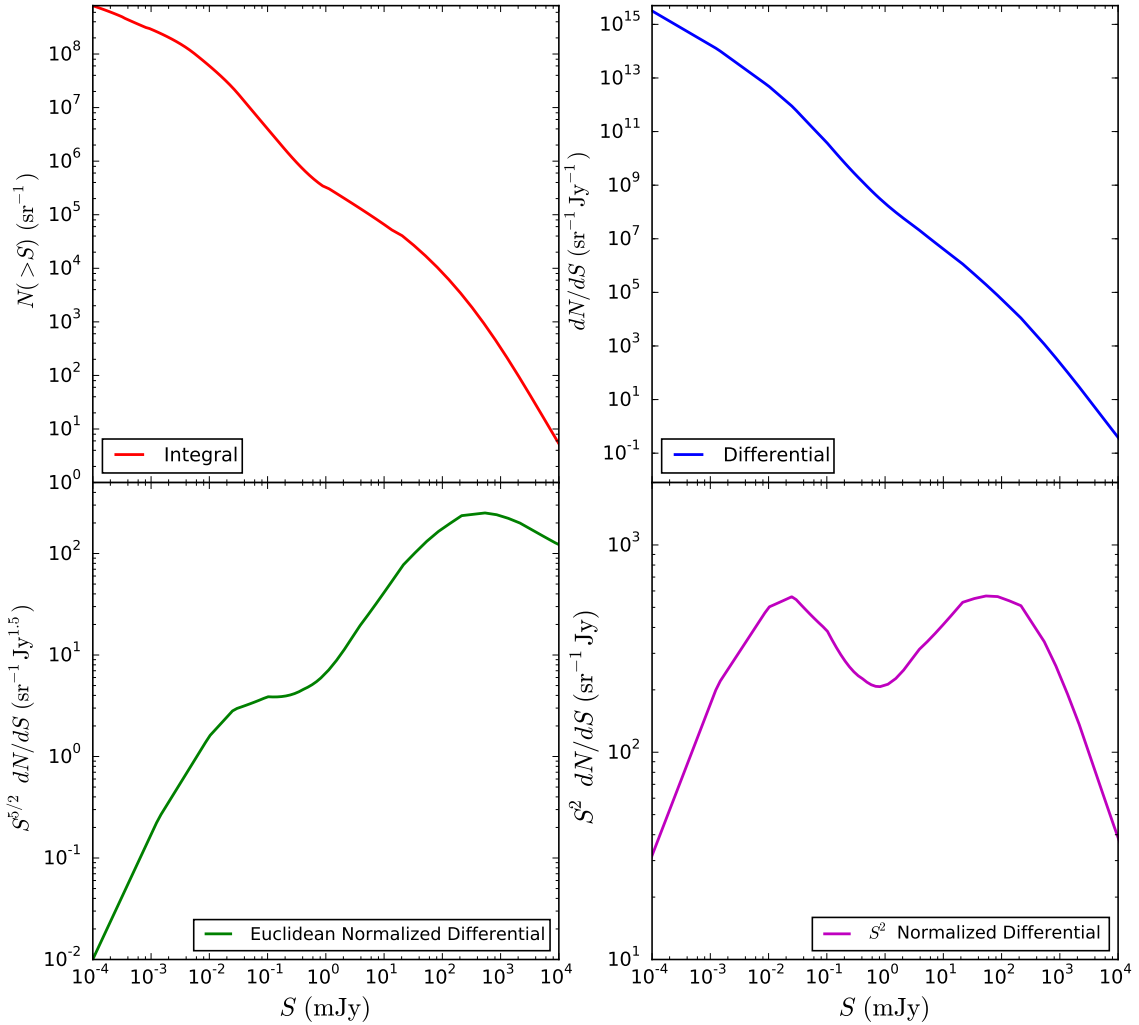


Figure 1.1: Example source count (taken from Condon and Mitchell [34] and Vernstrom et al. [183]) showing the differential and integral source counts with different normalizations. The top left panel shows the integral source count, $N(> S)$, the number of sources brighter than flux density S per steradian. The top right panel is dN/dS , or the number of sources per steradian with flux densities between S and $S + dS$. The bottom left panel is the differential source count normalized by the Euclidean (static universe) count of $S^{-5/2}$ and the bottom right panel is the differential source count normalized by S^2 (as appropriate for estimating the contribution to the radio background).

to the background temperature per logarithmic interval of flux density.

Gervasi et al. [69] obtained fits to the source count data for different radio-emitting galaxy populations across a range of frequencies from $\nu = 150$ to 8440 MHz. From their fits, which ranged from $1 \mu\text{Jy}$ to 100 Jy, they were able to integrate the source counts to obtain an estimate of the sky brightness temperature contribution at each of the frequencies. They determined a power-law sky brightness temperature dependency on frequency, with a spectral index (α) of -2.7 , which is in agreement with the frequency dependence of the flux density emitted by synchrotron-dominated steep-spectrum radio sources [31]. These estimates were used to interpret absolute measurements of the radio sky brightness by the TRIS experiment [199].

As part of my Masters thesis, I performed similar work using published source count data at $\nu = 150$ MHz, 325 MHz, 408 MHz, 610 MHz, 1.4 GHz, 4.8 GHz, and 8.4 GHz. The survey data were compiled in de Zotti et al. [42], with all the individual surveys listed in Table 1.1. For each frequency I fit a 5th order polynomial of the form

$$F(S) = A_0 + A_1 S + A_2 S^2 + A_3 S^3 + A_4 S^4 + A_5 S^5. \quad (1.5)$$

The fitting was initially performed using a χ^2 minimization routine. The coefficients given by the χ^2 minima were then used as starting points in a Monte Carlo Markov Chain (MCMC) approach [107], which was used to refine the fits and obtain estimates of uncertainty. The best-fit values for all the parameters at each of the frequency bands can be found in Table 1.2, along with χ^2 values for each fit. The data and the best-fit lines are plotted in Fig. 1.2, which shows the Euclidean-normalized data.

Table 1.2 shows that the χ^2 values of the fits are generally reasonable (given the different choices made for calibration and other corrections for synthetic effects among the data sets), with all but one of the reduced χ^2 values being below 2. The exception is for the 1.4 GHz data set, with a χ^2 of over 20 per degree of freedom. To obtain anything like a reasonable χ^2 we would have to increase the errors by a factor of four. It is worrisome that the 1.4 GHz compilation is the one with the most available data. As can be seen in the plot, there are many data points that are

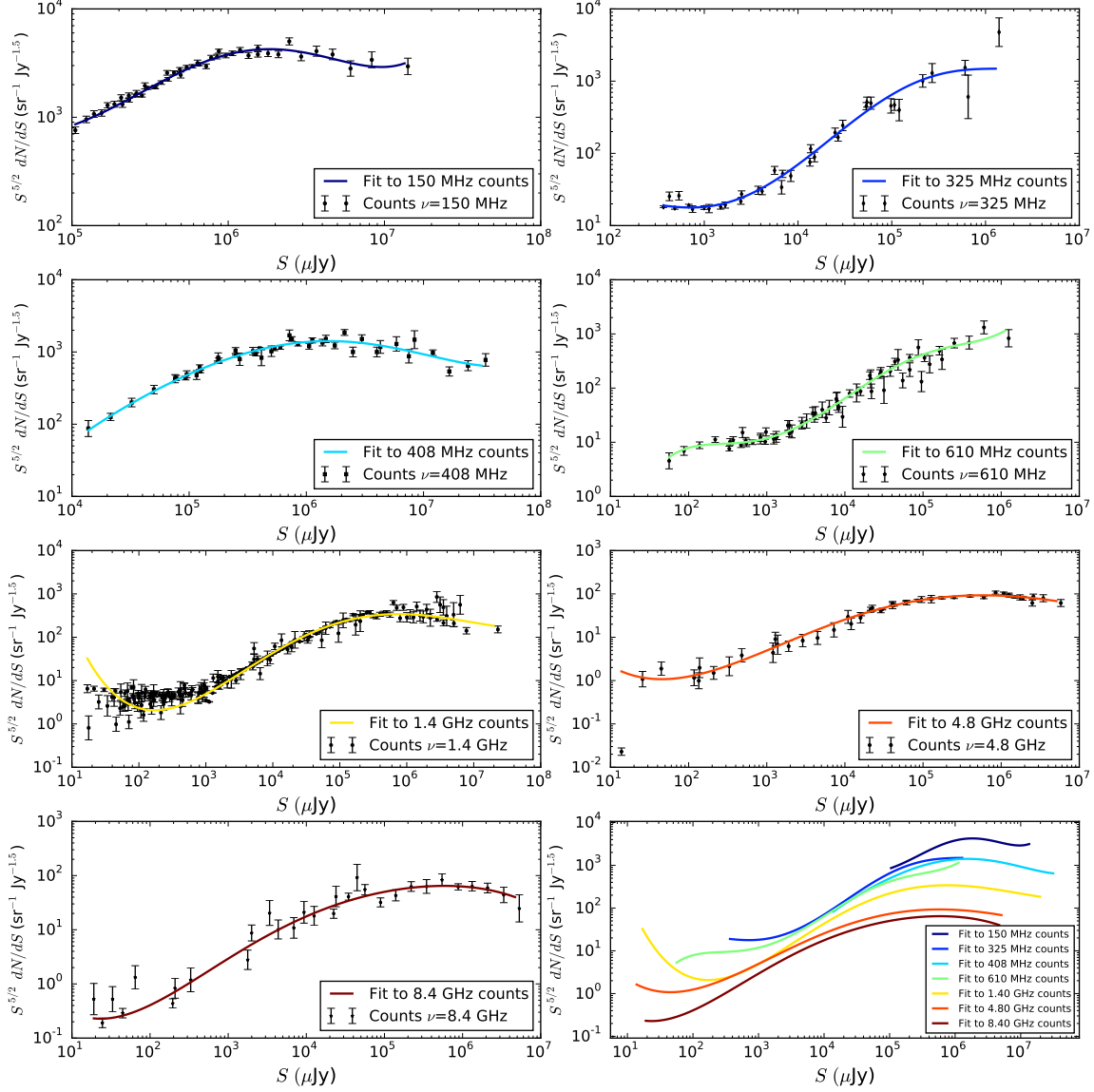


Figure 1.2: Compilation of published survey source counts and fits at multiple radio frequencies. The published data (black points) were compiled from de Zotti et al. [42] and the models (solid colored lines) are fits to the data using eq. 1.5. The references for the surveys used at each frequency are listed in Table 1.1 and the best-fit parameter values are given in Table 1.2. The bottom right panel shows the models from all the frequencies on the same axes for comparison.

Table 1.1: References for the extragalactic radio count data compilation

Frequency	References
150 MHz	Hales et al. [81], McGilchrist et al. [115].
325 MHz	Oort et al. [131], Owen and Morrison [134], Sirothia et al. [166].
408 MHz	Benn et al. [8], Grueff [77], Robertson [150].
610 MHz	Bondi et al. [15], Garn et al. [67], Ibar et al. [94].
	Katgert [99], Moss et al. [123].
1.4 GHz	Bondi et al. [16], Bridle et al. [17], Ciliegi et al. [29], Fomalont et al. [62], Gruppioni et al. [78], Hopkins et al. [91], Ibar et al. [94], Miller et al. [118]; Mitchell and Condon [120], Owen and Morrison [134], Richards [148], Seymour et al. [161], White et al. [190].
4.8 GHz	Altschuler [2], Donnelly et al. [44], Fomalont et al. [59], Gregory et al. [76], Kuehr et al. [102], Pauliny-Toth et al. [139], Wrobel and Krause [195].
8.4 GHz	Fomalont et al. [61], Henkel and Partridge [85], Windhorst et al. [194].

Table 1.2: Best fit parameter and χ^2 values for source count polynomial fits

ν MHz	χ^2	N_{dof}	A_0	A_1	A_2	A_3	A_4	A_5
150	68	45	6.58	0.36	-0.65	-0.19	0.26	0.099
325	59	34	5.17	0.029	-0.11	0.36	0.17	0.20
408	66	44	4.13	0.13	-0.34	-0.003	0.035	0.01
610	75	59	3.02	0.71	0.97	0.91	0.28	0.028
1400	4230	196	2.53	-0.052	-0.020	0.051	0.010	-0.0013
4800	32	47	1.95	-0.076	-0.15	0.020	0.0029	-0.00079
8400	41	29	0.79	-0.10	-0.23	-0.051	-0.019	-0.0029

inconsistent with each other, even with the relatively “large” error bars.

There are systematic differences between different surveys at 1.4 GHz, thus particularly at the faint end (see Condon [33] for further discussion). In the μJy range it is difficult to obtain reliable counts, since this range is close to the confusion limit of most radio surveys ([34, 193], though this depends on survey resolution) and hence the level of incompleteness may be incorrectly estimated in some surveys. Moreover, at the bright end there are significant and systematic sources of error introduced when attempting to correct for source extension and surface brightness limitations (see discussion in Singal et al. [165] and Subrahmanyan et al.

[172]). In addition to these effects, the total variance is enhanced by source clustering. We know cosmic variance can lead to differences in counts for small fields, but an order of magnitude less than the observed scatter.

1.3 The Radio Background

The sum of all emission at different wavelengths yields a measure of the background, with different sources contributing at the different wavelengths. Measurements of the backgrounds as a function of wavelength is shown in Fig. 1.3. Most of the electromagnetic energy of the Universe is in the cosmic microwave background radiation left over from the hot big bang. It has a nearly perfect 2.73 K blackbody spectrum peaking at $\lambda \sim 1$ mm (300 GHz) [55]. The strong UV/optical peak is primarily thermal emission from stars, supplemented by a smaller contribution of thermal and nonthermal emission from the active galactic nuclei (AGN) in Seyfert galaxies and quasars. Most of the comparably strong cosmic infrared background is thermal re-emission from interstellar dust heated by absorbing that UV/optical radiation. The cosmic X-ray and gamma-ray backgrounds are mixtures of non-thermal emission (e.g., synchrotron radiation or inverse-Compton scattering) from high-energy particles accelerated by AGN and thermal emission from very hot gas (e.g., gas in clusters of galaxies).

By comparison, the cosmic radio-source background is extremely weak. Although the overall contribution from these sources is small there are some extremely powerful radio sources; they are just so rare that the build up of integrated radiation is small. These powerful sources are now known to play an important role in the formation and evolution of galaxies. Radio sources do trace most phenomena that are detectable in other portions of the electromagnetic spectrum, and modern radio telescopes are sensitive enough to detect extremely faint radio emission. The cosmic radio background is a combination of emission from these extragalactic sources, a component from the CMB blackbody, and Milky Way emission. It depends on the frequency as to how the contributions from these components compare. However, at radio frequencies the Galaxy emission is dominant. In order to study the extragalactic component it is therefore necessary to observe areas far from the Galactic plane. Since the CMB blackbody radiation is well measured, it

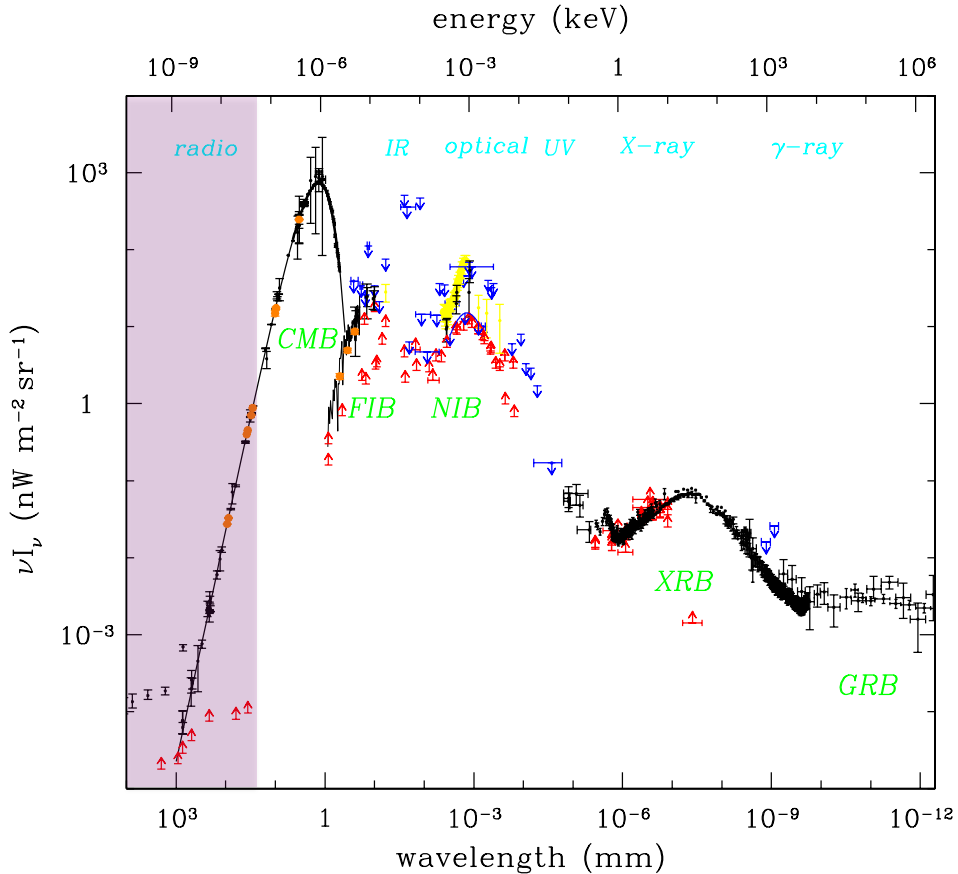


Figure 1.3: The Cosmic Backgrounds: the electromagnetic spectrum of the universe [figure 1 from 159]. The brightness per logarithmic frequency (or wavelength) interval is shown as a function of the logarithm of the wavelength, so the highest peaks correspond to the most energetic spectral ranges. These data are based on a compilation from Ressell and Turner [147], with data from Smoot [168] (CMB); Hauser et al. [84], Lagache et al. [103] (FIB); Leinert et al. [106] (NIR, UV); Dwek and Arendt [45] (NIR); Pozzetti et al. [144] (optical); Gendreau et al. [68], Miyaji et al. [121] (X-ray); Kappadath et al. [98], Sreekumar et al. [169], Weidenspointner et al. [187] (γ -ray). The purple shaded region shows the radio wavelengths which we are interested in here.

can be effectively removed, leaving the component from extragalactic radio sources to be studied further.

1.3.1 Source Count Contribution to Temperature

We can easily obtain an estimate of the contribution from sources to the radio background temperature (T_b). The source count and the sky temperature at a frequency ν are related by the Rayleigh-Jeans approximation,

$$\int_{S_{\min}}^{\infty} S \frac{dN}{dS} dS = \frac{T_b 2 k_B \nu^2}{c^2}. \quad (1.6)$$

In the above equation k_B is the Boltzmann constant (k_B), and T_b is the sky temperature from all the sources brighter than S_{\min} . Equation (1.6) is also equivalent to

$$\int_{S_{\min}}^{\infty} S^2 \frac{dN}{dS} d[\ln(S)] = \frac{T_b 2 k_B \nu^2}{c^2}. \quad (1.7)$$

It is for this reason that it is convenient to show the source count weighted not by the Euclidean $S^{5/2}$ but by S^2 . With such a plot the source count must fall off at both ends to avoid over-predicting the background (i.e. violating Olber's paradox¹); hence the higher end must turn over at flux densities above those we have plotted.

The fitting of the compiled source count data can be used to obtain estimates of the background temperature contribution by extragalactic sources at each frequency. The results from integrating the best-fit models of Table 1.2 yields the background temperatures shown in Table 1.3. To investigate the uncertainties thoroughly, we carried out our fits using MCMC analysis, by adopting CosmoMC [107] as a generic MCMC sampler. The χ^2 function was sampled for each set using the polynomial in eq. 1.5, which was then fed to the sampler to locate the χ^2 minimum. Each of the six parameters of the polynomials was varied for each step of the chain and the chains were run with 500,000 steps. CosmoMC generates statistics for the chains, including the minimum χ^2 , the best fit values for each of the parameters, and their uncertainties.

¹Olber's paradox states that a static, infinitely old universe with an infinite number of stars and galaxies would yield a bright rather dark night sky. Thus to avoid violating this paradox the number of galaxies must at some point turn over and stop increasing.

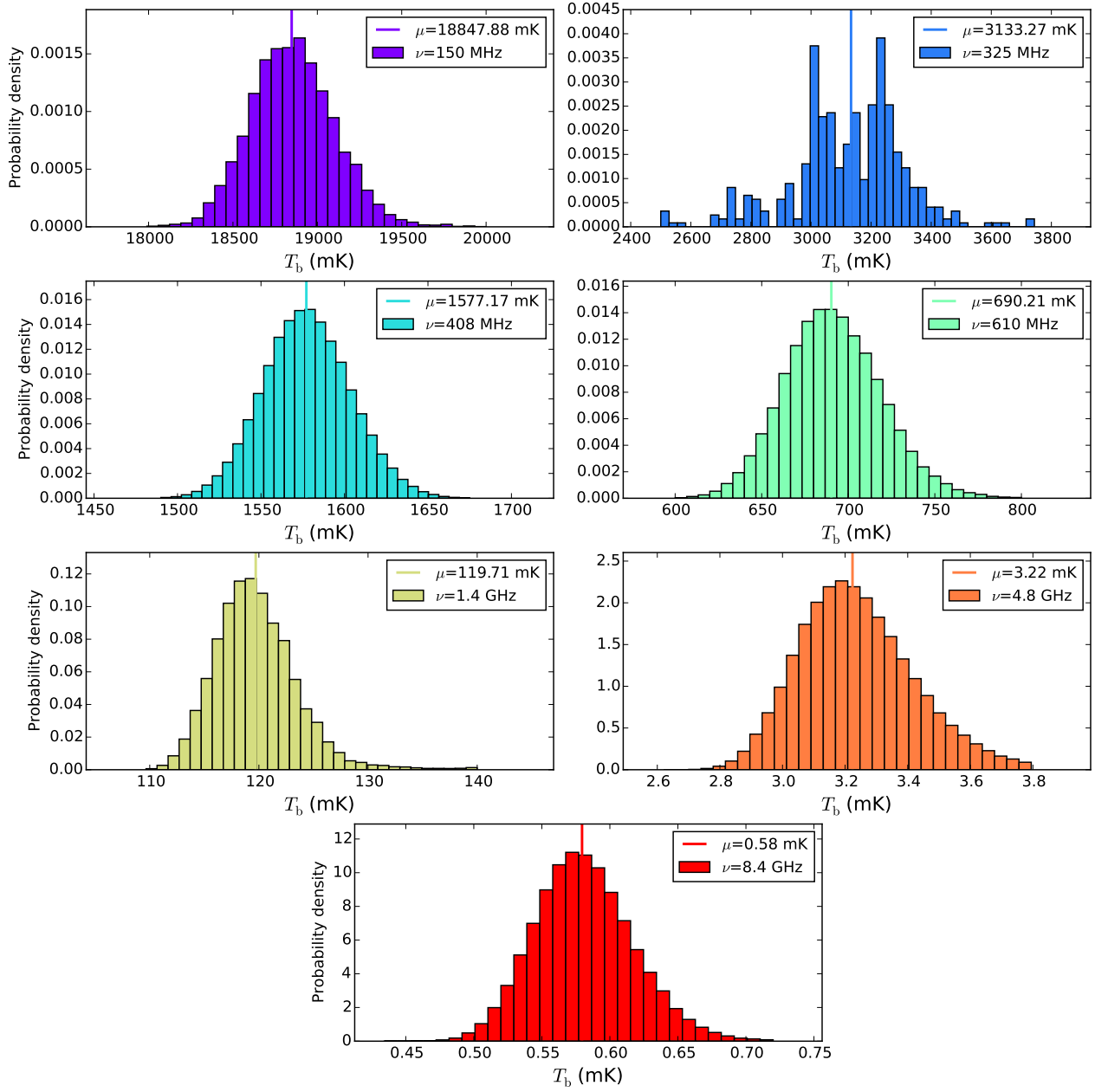


Figure 1.4: Background temperature distributions from fitting published source counts. Using Monte Carlo Markov Chains we fit the source counts in Fig. 1.2 with eq. (1.5), then each step in the chain is used to compute a background temperature using eq. (1.6).

Histograms of the chain values for the background temperature are shown in Fig. 1.4. From the width of these histograms we are able to measure the uncertainty in our estimates for the background temperature, taken here as the 68 percent area values, fully accounting for the correlations among the parameters in the polynomial fits. The 1σ uncertainties are listed in Table 1.3.

Most of the histograms are fairly Gaussian, which is a reflection of the quality of the data. Source counts at frequencies with well-sampled data around the peak contribution tend to have well-constrained background temperature values, e.g. at 408 MHz. However, there is a noticeable irregularity with the 325 MHz histogram. Because of the limited data available at 325 MHz, and with the peak area of contribution having little to no data, the histogram at this frequency does not have a well defined shape, and the uncertainty is far from Gaussian.

Over the years there have not been many estimates of the CRB made using source count data [52, 69, 110, 143, 185]. And within this list, the frequencies covered were rather limited and uncertainties not always quoted. It is important to see how our estimates compare with these previous estimates. Longair [110] gives a value for $T_{178} = 23 \pm 5$ K. Wall [185] lists estimates of $T_{408} = 2.6$ K, $T_{1.4} = 0.09$ K, and $T_{2.5} = 0.02$ K. Our results are in agreement with these earlier estimates to within $\pm 2\sigma$. The values for source contributions from Gervasi et al. [69] tend to be a little higher than the values found here, the differences being traceable to choices made for the limits of integration and for the parameterized form for the fits.

1.3.2 ARCADE 2

Results from the Absolute Radiometer for Cosmology, Astrophysics, and Diffuse Emission, or ARCADE 2 [56, 160], revived interest in the CRB and how it may be related to the faint² counts. The results of the ARCADE 2 experiment have had a significant impact on the study of the radio background. This instrument provided absolute measurements of the sky temperature at 3, 8, 10, 30, and 90 GHz. These results showed measured temperatures of the radio background about 5 times greater than that currently determined from radio source counts, with the most no-

²In this work the terms “faint” and “bright” refer to the flux density of the source or sources and not to intrinsic brightness or luminosity.

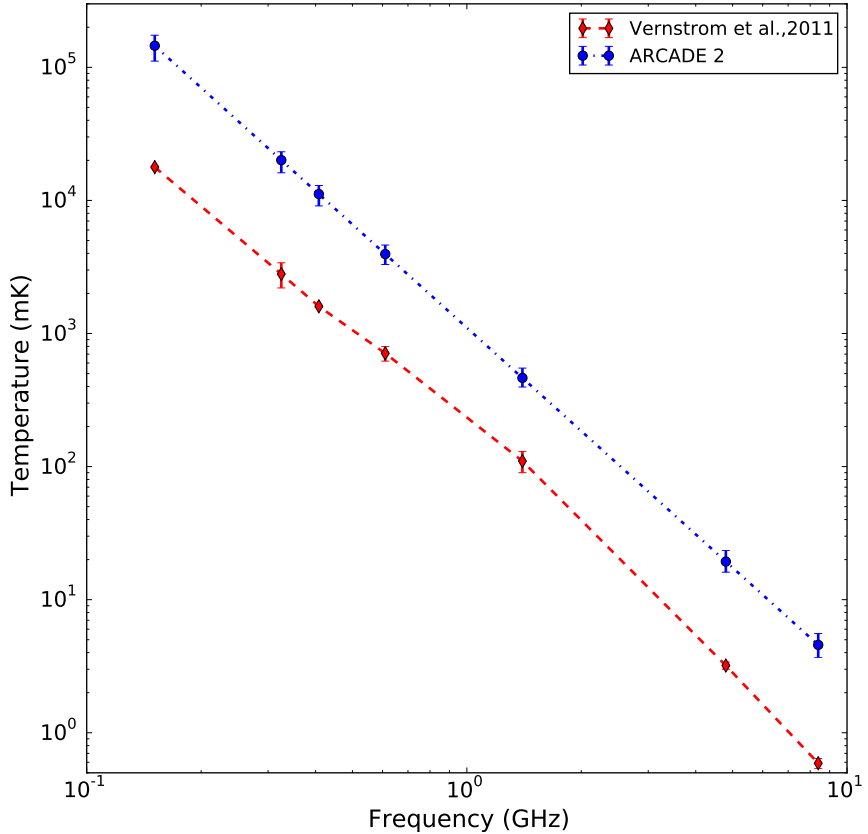


Figure 1.5: Extragalactic background temperatures from ARCADE 2 and source counts at multiple frequencies. The blue points and dot-dashed line is an extrapolation to the frequencies used in Vernstrom et al. [182] using the best-fit power-laws (eq. (1.8) and eq. (1.9)) from the ARCADE 2 experiment. The red points and dashed line are from the fitting of published source counts as discussed in Sections 1.2 and 1.3.1.

Table 1.3: Values of the integrated sky brightness and temperature contribution from radio source counts for different frequency bands. The uncertainties are 1σ limits determined from Markov chain polynomial fits to the data.

ν MHz	νI_ν $\text{W m}^{-2} \text{sr}^{-1}$	T mK	δT mK
150	1.8×10^{-14}	17800	300
325	2.1×10^{-14}	2800	600
408	2.9×10^{-14}	1600	30
610	4.2×10^{-14}	710	90
1400	7.5×10^{-14}	110	20
4800	8.0×10^{-14}	3.2	0.2
8400	9.6×10^{-14}	0.59	0.05

table excess of emission being detected at 3 GHz. Since most systematic effects explaining this emission were ruled out, we are left with the question of whether it could be caused by some previously unknown source of extragalactic emission (or observational error).

The ARCADE 2 experiment measured a background temperature of (54 ± 6) mK at 3.3 GHz. Several fits are provided to these data, which allow for scaling of the result to different frequencies. The initial fit provided in Seiffert et al. [160] is

$$T_b = (1.06 \pm 0.11 \text{K}) \left(\frac{\nu}{1 \text{GHz}} \right)^{-2.56 \pm 0.04}. \quad (1.8)$$

There is another fit, incorporating data from lower frequencies, given in Fixsen et al. [57] as

$$T_b = (24.1 \pm 2.1 \text{K}) \left(\frac{\nu}{310 \text{MHz}} \right)^{-2.599 \pm 0.036}. \quad (1.9)$$

The quantities extrapolated from the ARCADE 2 data fits and our current estimates from source counts are shown in Fig. 1.5. Here it can be seen that the ARCADE 2 absolute measurements lie far above source estimates, particularly at lower frequencies. Clearly, the excess detected around 3 GHz would correspond to a large excess at lower frequencies if the power-law behaviour continued (which was the main result from Vernstrom et al. [182], the outcome of my Masters thesis work).

Singal et al. [165] suggested some possible explanations for this excess as a new population of radio sources below current detection limits; or diffuse large scale emission from galaxies or clusters, or the cosmic web (either from conventional synchrotron emission from cosmic ray electrons or electrons from dark matter particle annihilation or decay causing synchrotron emission). All possibilities we set out to examine with the work in this thesis.

Chapter 2

Data

The work presented in this thesis relies on data from radio interferometric telescopes. Before describing the data used I will provide a brief overview of radio telescopes, interferometers, and the data calibration and imaging process (full details can be found in e.g. Christiansen and Hogbom [27] and Rohlfs and Wilson [151]).

Electromagnetic wave electric field oscillations can induce voltage oscillations in a conductor. In a radio telescope this process happens at the antenna focus in a device called the feed; the simplest sort of feed is a linear dipole. The output of a feed is a voltage representing power from the radio source. This power is measured in kelvins and is referred to as the antenna temperature (the antenna temperature is not the physical temperature of the antenna but the temperature a matched resistor whose thermally generated power per unit frequency equals that produced by the antenna) .

In a single dish telescope the angular resolution is given by

$$\theta = \frac{1.22\lambda}{D_a}, \quad (2.1)$$

with λ the wavelength of the radiation received and D_a is the diameter of the telescope. In the optical, a 6-m dish provides approximately 0.025 arcsec resolution, however at radio wavelengths a single dish can achieve at best only a few arcminute resolution. For example, the Effelsberg telescope is one of the largest

steerable single dish radio telescopes with a diameter of 100 m and has a resolution of ~ 9 arcminutes at 1.4 GHz. It is too difficult and costly to build a single dish with a large enough diameter to achieve arcsecond or sub-arcsecond resolution and thus we rely on interferometers.

The key concept behind an interferometer is that one can link many single dish telescopes together, combining the signal received at each, and effectively simulating a large single radio telescope dish with a diameter equivalent to the largest distance between the smaller dishes. The distance between two dishes is known as a baseline. The angular resolution achievable by an interferometer is $1.22\lambda/b$, where b is the longest baseline distance. For comparison, an interferometer with a longest baseline of 30 km can have a resolution of 1.5 arcseconds at 1.4 GHz. The field of view (FOV) is limited by the size of the individual antennas.

Each antenna measures different phases of the electric field wavefront arriving from the source. The signals from each antenna are cross-correlated, the result depending on the path taken and the distance between the antennas; the interferometer output will thus either be constructive or destructive. Adding in the Earth's rotation, one can imagine a source moving through the interferometer beam, giving positive and negative output, and producing a fringe pattern. The measurements then become the complex visibilities from each baseline. Chapter 7 has more details on this method, and for a full discussion and derivations of the mathematics of interferometry see e.g. Burke and Graham-Smith [22] and Goldsmith [74].

The beam pattern from an instantaneous sample from one pair of antennas represents one point in the Fourier plane, or uv coordinates. As the source is observed for more time the antenna pair traces out a track in uv space. The exact shapes of the tracks depends on the the number of baselines, antennae configuration, amount of observing time, source declination, and local hour angle. Figure 2.1 shows two examples of the uv coverage from a 12 hour observation with the Karl G. Jansky Very Large Array (VLA) in its most compact configuration at $+60^\circ$ Declination (Dec) and the Australia Telescope Compact Array (ATCA) in a compact configuration at -40° Dec both at $\nu = 3$ GHz. The uv coordinates are the Fourier conjugate of Right Ascension (RA) and Dec, with units of inverse radians (sometimes written as $k\lambda$). The outer boundary shows the limit of the resolution, or rather the boundary of the beam for a single dish with $D_a = b$. It is important to have this uv

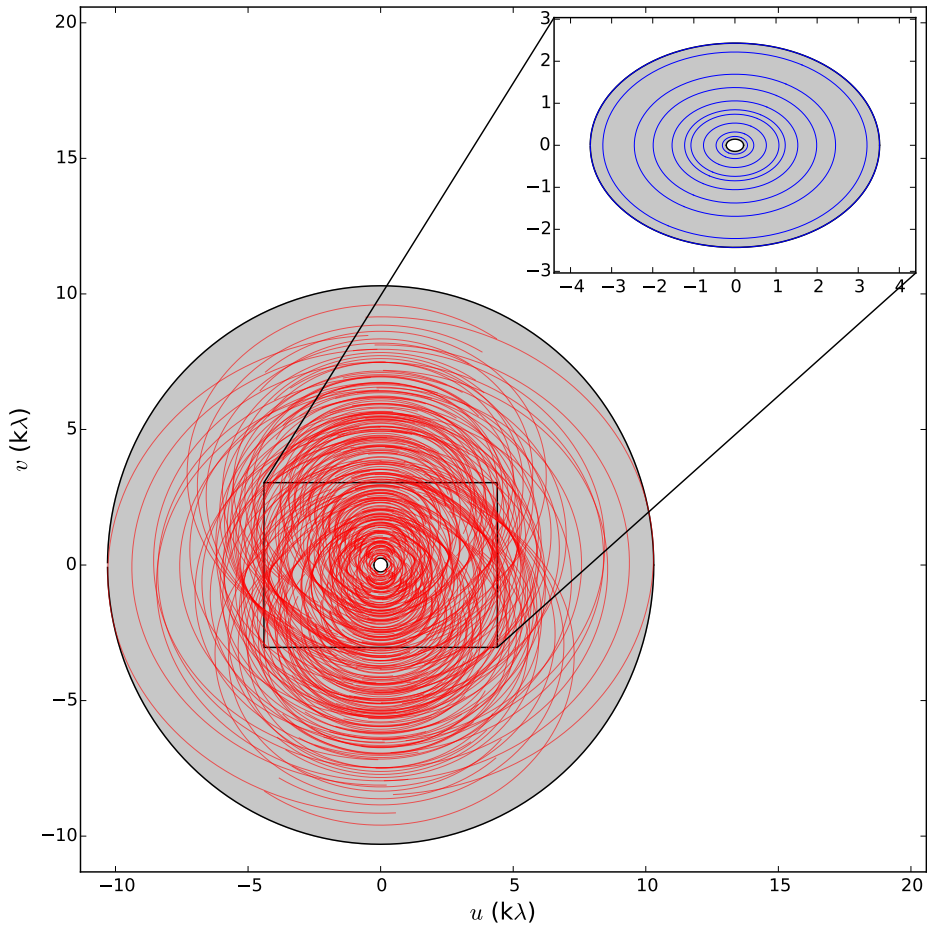


Figure 2.1: Example interferometer uv coverage from two arrays. The main panel shows the coverage for a 12 hour observation of the Very Large Array in its most compact configuration (27 antennas, maximum baseline 1 km) at $+60^\circ$ Dec. The inset shows the coverage for a 12 hour observation with the Australia Telescope Compact Array (5 antennas, maximum baseline 352 m) at -40° Dec. The coloured lines show the baseline tracks. The grey regions show the coverage of a single dish telescope with an antenna diameter equal to the maximum baseline length.

plane as filled as possible, which requires longer observations and telescopes with a large number of baselines; note how much more filled in the VLA array is with its 27 antennas compared to the ATCA with only five antennas. The more baselines (and thus more coverage) increases the sensitivity and increases the accuracy when transforming to the image plane.

The basic calibration steps include, deleting or flagging bad points, e.g. those corrupted due to radio frequency interference (RFI) such as from satellites. In addition to observing the source of interest it is usually necessary to observe a strong source with a well known brightness and spectrum in order to calibrate the data amplitude and spectrum, and possibly a second source (usually more frequently through out the observations) with well known phases, in order to calibrate the target phases as a function of time. Sometimes other corrections are necessary for antenna positions offsets, delays, or the atmosphere.

In terms of imaging, the individual visibilities are gridded (with chosen weights) and then Fourier transformed to make an image. In radio interferometry images the point spread function (PSF) resulting from the Fourier transform of the *uv* coverage and weighting functions is known as the “dirty” synthesized beam. The dirty beam generally contains positive and negative sidelobes. A “dirty” image is the Fourier transform of the *uv* data with all pixels convolved by the “dirty” beam. The image then goes through a process known as cleaning. The cleaning process finds bright peaks, stores them in a model as pixel flux densities known as the “clean” model, and subtracts them from the dirty image. These model components are then convolved with the central Gaussian distribution of the dirty beam (which is known as the “clean” synthesized beam) and added back to the residual image, with the final image known as the “clean image”. This clean beam is free of sidelobes (though the cleaned image still contains contamination from the dirty beam and its sidelobes for fainter sources).

The remainder of this chapter will describe the observations specifically made for use in this thesis, as well as the details of the calibration and imaging processes.

Table 2.1: ATLAS ELAIS-S1 pointings.

ATLAS Pointing	RA (HH:MM:SS.ss)	Dec (HH:MM:SS.ss)	σ_n ($\mu\text{Jy beam}^{-1}$)
e11_1	00 : 32 : 03.55	-43 : 44 : 51.24	53.7 ± 4.64
e11_5	00 : 32 : 57.67	-43 : 28 : 09.00	52.3 ± 2.66
e11_6	00 : 33 : 50.79	-43 : 44 : 57.36	57.0 ± 5.31
e11_7	00 : 35 : 38.02	-43 : 44 : 57.36	57.8 ± 3.18
e11_8	00 : 34 : 44.40	-43 : 28 : 11.88	58.1 ± 7.28
e11_16	00 : 34 : 44.40	-44 : 01 : 42.84	59.2 ± 6.51
e11_17	00 : 32 : 57.67	-44 : 01 : 42.84	50.8 ± 3.61

2.1 Australia Telescope Compact Array

In order to study extended emission we were granted 12 hours of time with the ATCA, which has good short baseline coverage needed for lower resolution imaging.

We targeted a portion of the European Large Area *Infrared Space Observatory* Survey – South 1 field [ELAIS-S1, 129], an extragalactic region originally selected for *ISO* observations. This field was chosen because it has previously been surveyed with higher resolution for the Australia Telescope Large Area Survey (ATLAS) [80, 116, 126, Franzen et. al, 2014 in preparation, Banfield et. al, 2014 in preparation]. Our new observations were made with the ATCA EW352 array configuration, which has a maximum baseline of 352 m and a minimum baseline of 30.6 m. A total of 12 hours of observation time was obtained in a single session on November, 28 2013. We observed using the ATCA band which is centred on 2.1 GHz, with 2 GHz of bandwidth. The bandwidth is separated into 2048 channels of 1 MHz width. The resolution with this configuration ranges from 1 to 2 arcmin, depending on the image frequency. We observed seven pointings in the ELAIS-S1 field, chosen from the 20 pointings used by the ATLAS survey. The pointing centres are listed in Table 2.1 and are shown in Fig. 2.2.

2.1.1 Calibration

The calibration, editing, and imaging were performed using the MIRIAD¹ software package [155]. Following several rounds of RFI flagging, the source J1934+638 was used for bandpass and flux density calibration. The source PKS 0022–423 (PMN J0024–4202) was observed for 2-minute intervals every 10 minutes and used to correct the gain phases. The task GPCAL was utilized to derive frequency-dependent gain solutions, solving for the gains of the upper and lower parts of the band separately.

Observations at this frequency are highly affected by RFI, most notably at the lowest frequencies. The task MIRFLAG was used for automated RFI flagging on the phase calibrator source and the target fields. This allowed us to flag the majority of interference, so that only a small amount of manual flagging was required. Each of the seven pointings was flagged individually for *uv* points above an amplitude threshold. The data were then split into two frequency bands (1.1 to 2.1 GHz and 2.1 to 3.1 GHz), and separated into individual data sets for each pointing. The last hour of time was not usable, since the source was setting, and for the final four hours Antenna 1 was lost due to shadowing. In the end about 55 per cent of the data was flagged (i.e. not used) in the 1.1 to 2.1 GHz frequency band, and about 30 per cent in the 2.1 to 3.1 GHz band.

The following analysis is only carried out for the lower part of the band (1.1 to 2.1 GHz), which, after flagging, ranged from 1.38 to 2.1 GHz, with a centre frequency of 1.75 GHz. This decision was made because it more closely matches the image frequency of the ATLAS survey. We planned to use the ATLAS point-source models to subtract discrete emission from our data. The change in size of the primary beam going from the lower band to the upper band (2.1 to 3.1 GHz) is large, which makes accurate scaling of the point source models difficult and the output of the subtraction at the higher frequency less reliable. For this reason we do not believe the addition of the upper band would contribute additional meaningful information for our analysis.

¹<http://www.atnf.csiro.au/computing/software/miriad/>

2.1.2 Imaging

Imaging was first performed on the full uv data sets, primarily for the purposes of self-calibration of the data. However, the ultimate goal was to perform subtraction of the known point sources in the fields and re-image the source-subtracted data for further analysis. The subtraction process is discussed in more detail in Section 5.3.1.

The MIRIAD tasks INVERT, MFCLEAN, and RESTOR were used to create and clean the images. Due to the large frequency range covered, we used multi-frequency synthesis and deconvolution, or cleaning (MFCLEAN). MFCLEAN attempts to solve for a frequency dependent intensity, $I(\nu)$. Here

$$I(\nu) = I(\nu_0) \left(\frac{\nu}{\nu_0} \right)^\alpha, \quad (2.2)$$

and solving for the partial derivative of the intensity with frequency gives the spectral index,

$$I(\nu_0)\alpha = \nu_0 \frac{\partial I}{\partial \nu} \Big|_{\nu_0}. \quad (2.3)$$

Thus by using MFCLEAN the resulting image has two planes, the intensity at the reference frequency and the intensity times the spectral index. This allows us to take advantage of the large bandwidth and solve for the frequency dependence of sources (though a high signal-to-noise ratio is usually required in order to produce an accurate measurement). Note that this process can be complicated by the changing primary beam size at the different frequencies. There should therefore be an additional term representing the spectral dependence of the primary beam; however, currently MFCLEAN only allows for fitting of one additional spectral term. Instead the primary beam frequency dependence was accounted for during the mosaicing process.

Each pointing was cleaned separately, initially down to a level of $600 \mu\text{Jy beam}^{-1}$. At this stage we performed two rounds of phase-only self-calibration and one of amplitude and phase. The final images were cleaned down to $250 \mu\text{Jy beam}^{-1}$. The resulting PSF, or synthesized clean beam, size is $150 \text{ arcsec} \times 60 \text{ arcsec}$, with a position angle of 6° , using Briggs² weighting [18] and a robustness factor of

²Uniform weighting of the uv data usually results in a better-behaved synthesized beam, and

0.5. A mosaic of the seven pointings was made using LINMOS, with each pointing having a primary beam full width at half maximum (FWHM) of roughly 27 arcmin; the final mosaic (Fig. 2.2) has a total area of approximately 2.46 deg².

Regarding the brightness units, radio images are often generated with brightness units of Jy beam⁻¹. However, it can be useful (particularly with this type of discussion) to convert these units to that of brightness temperature in K (or mK). Conversion between these units can be computed using a factor

$$\mathcal{C}_T = \frac{\lambda^2 10^{-26} \text{Wm}^{-2}}{2k_B\Omega_B}, \quad (2.4)$$

such that $T = \mathcal{C}_T S$ in Kelvin, with S the flux density in units of Jy beam⁻¹, and where Ω_B is the beam solid angle in steradians, and k_B is the Boltzmann constant. Thus for our case of a Gaussian elliptical beam with FWHM sizes of 150 arcsec \times 60 arcsec and frequency of 1.75 GHz, $\mathcal{C}_T = 44.54$. Throughout the discussion of the ATCA data, for convenience, we present results in both units.

2.1.3 Image Noise

Obtaining a precise measure of the instrumental noise (σ_n) is difficult, because with the large beam size the confusion rms σ_c is expected to dominate over the instrumental noise. However, for our analysis goals an accurate measurement and characterization of the noise is required. We employed two different techniques in order to estimate the instrumental image noise. First we made measurements of the noise using the “jackknife” method. This involves taking two (approximately) equal halves of the data and creating separate images. Each of these images should have noise equal $\sqrt{2}\sigma_{\text{total}}$. By taking the difference between the images and dividing by two, the result is noise of the combined image, with all the signal subtracted out. Since the noise in each half adds in quadrature, then after the subtraction,

$$\sigma = \frac{\sqrt{\sigma_1^2 + \sigma_2^2}}{2} = \frac{\sqrt{(\sqrt{2}\sigma_{\text{total}})^2 + (\sqrt{2}\sigma_{\text{total}})^2}}{2} = \sigma_{\text{total}}. \quad (2.5)$$

smaller side lobes, but usually with higher noise. Natural weighting generally gives the best signal-to-noise ratio (though not in the confusion-limited case), but at the expense of an increased beam size. Briggs, or “robust”, weighting allows for weighting between the two options, doing so in an optimal sense (similar to Wiener optimization).

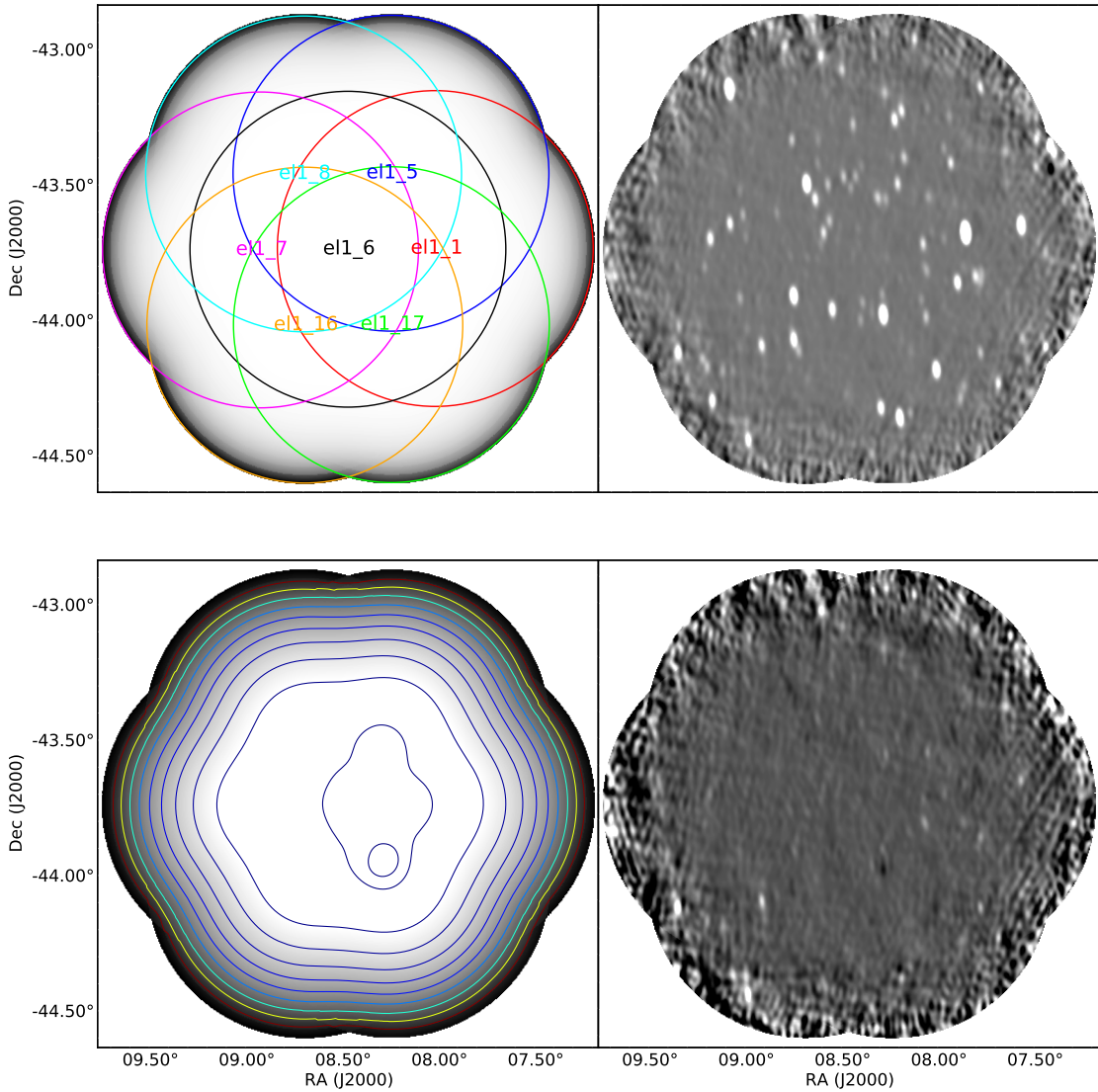


Figure 2.2: ELAIS-S1 mosaics. The top left panel shows the full area, with the seven pointings outlined and labelled at their centres. The top right panel is the final 1.75 GHz mosaic image. The bottom left panel shows the noise across the mosaic field, with contour levels at 46, 48, 78, 120, 190, 305, 480, 760, 1200, 1900, and $3000 \mu\text{Jy beam}^{-1}$. The bottom right panel shows the image after subtraction of the ATLAS point sources.

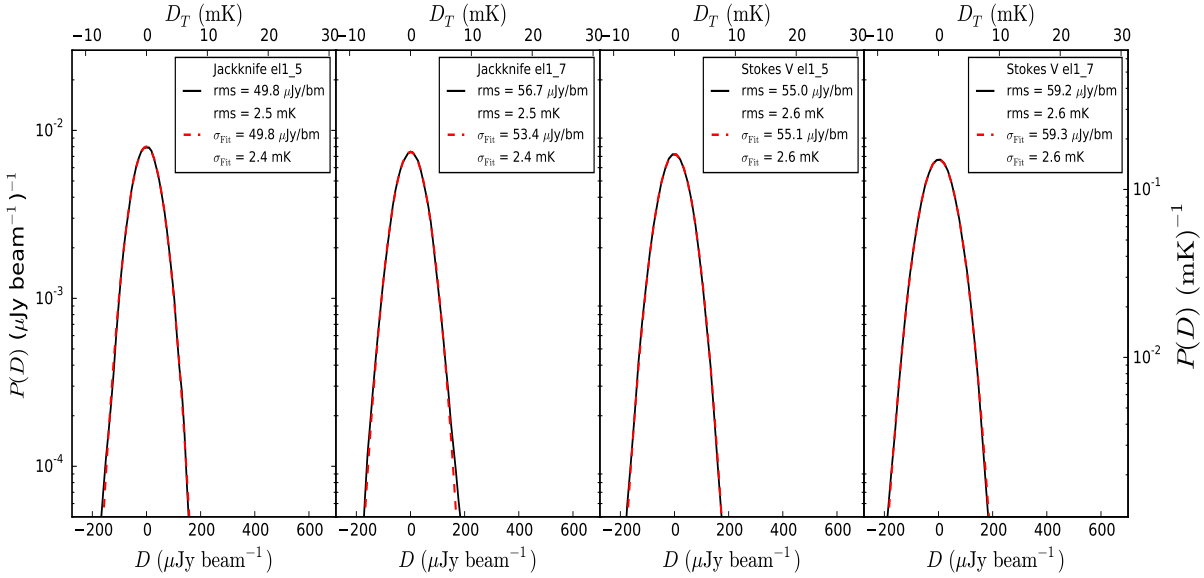


Figure 2.3: Measurements and estimates of the instrumental noise using the jackknife method (first two panels) and Stokes V method (second two panels) for two of the pointings. The black solid lines are from the pixel histograms of the images and the red dashed lines are fitted Gaussian distributions. The quoted values are the measured rms from the image pixel values, while σ_{Fit} is the width of the fitted Gaussian distributions.

It can be challenging with interferometry to create images with equal halves of the data. Choosing two equal time chunks can introduce issues with different uv coverage between the two data sets. We therefore chose to create two images using the even and odd numbered spectral channels, which should give approximately half in each set with most of the obvious types of systematic effects common to both. The images were cleaned in the same manner and then subtracted for each pointing. We measured the rms in the cleaned portion of the image, as well as fitting the pixel distribution with a Gaussian to obtain a fitted rms noise σ_n . This can be seen for two of the pointings in Fig. 2.3. The jackknife procedure yielded measurements of the instrumental noise of the individual pointings of $50\text{--}65 \mu\text{Jy beam}^{-1}$, or $2.2\text{--}2.9 \text{mK}$.

We used a second approach as a check on this procedure. The Stokes V pa-

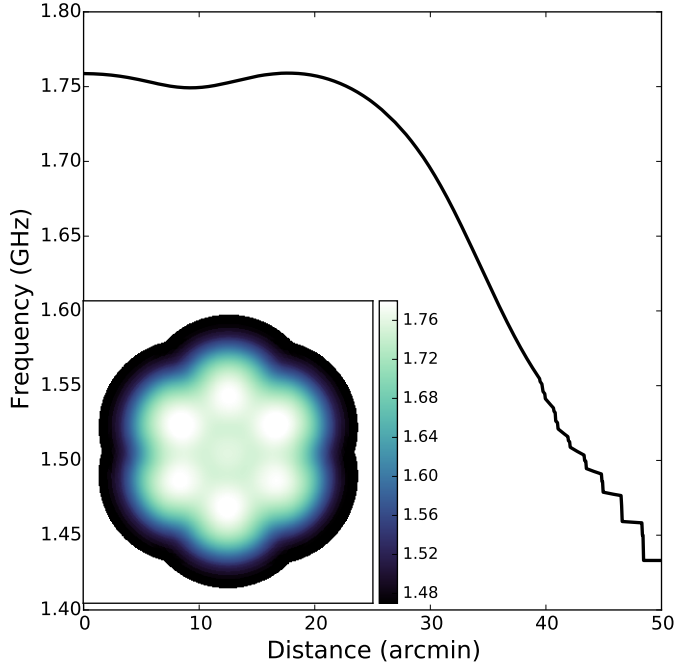


Figure 2.4: Frequency dependence of the final mosaic image due to the wide-band primary beam correction. The solid black line shows the effective frequency $\langle \nu \rangle$ from the centre to the edge of the image, as a function of radius. The inset is the full mosaic image, with the colour scale showing the change in effective frequency.

parameter measures circular polarization and is defined as

$$V = \langle E_l^2 \rangle - \langle E_r^2 \rangle, \quad (2.6)$$

where E_l and E_r are, respectively, the left and right hand complex electric field amplitudes in the circular basis as measured by the antennas. The total intensity, or the Stokes I parameter, is defined as

$$I = \langle E_l^2 \rangle + \langle E_r^2 \rangle. \quad (2.7)$$

Extragalactic radio sources generally have low levels of circular polarisation [146] and so a Stokes V image should have subtracted out all the signal, leaving only

instrumental noise (similar to the jackknife, but performed in the uv plane rather than the image plane). We therefore made Stokes V images of all the pointings and again measured the rms and fit Gaussian distributions to the pixel probability distributions to obtain a fitted rms σ_n . This yielded similar estimates of $55\text{--}65 \mu\text{Jy beam}^{-1}$ ($2.4\text{--}2.9 \text{mK}$), as can also be seen in Fig. 2.3. For final values of σ_n we averaged the measured and fitted values from the jackknife and Stokes V for each pointing, and have listed them in Table 2.1. These values only account for instrument noise and do not include any additional noise contributions from the imaging process, such as uncleaned dirty beam sidelobes, artefacts from bright sources, or from sources out in the lobes of the primary beam (of which there are several).

For the final mosaic, each pointing had a primary beam correction applied to it, raising the noise radially. LINMOS takes in the values of σ_n for each pointing and combines pixels by weighting as

$$S(x, y) = \sum_i \frac{S_i(x, y)}{(\sigma_{n,i}/p_i(x, y))^2}, \quad (2.8)$$

where $S(x, y)$ is the final flux density of the pixel, $S_i(x, y)$ is the flux density in pointing i , $\sigma_{n,i}$ is the noise in pointing i and $p_i(x, y)$ is the primary beam correction of pointing i at position (x, y) . This results in non-uniform noise across the field. The resulting instrumental noise for the full mosaic is shown with contours in Fig. 2.2. The actual procedure used to combine the pointings is more complicated than eq. (2.8), since, due to the wide bandwidth, the primary beam correction becomes frequency dependent. LINMOS takes into account the bandwidth used, as well as the spectral index information found from MFCLEAN, to correct for the frequency effects. This results in an effective frequency $\langle\nu\rangle$ in the field that varies with distance from the centre, going from 1.75 to 1.4 GHz, as shown in Fig. 2.4.

2.2 Karl G. Jansky Very Large Array

The VLA has four main antenna configurations: A, B, C, and D. These configurations range from most to least extended, respectively, and have average resolutions at 1.4 GHz of $1.3'', 4.3'', 14'',$ and $46''$. There are also three hybrid configurations:

Table 2.2: Observing Runs Summary. The B^* data were taken during BnA configuration and transition period to A configuration, although images were made at B configuration resolution

Configuration	Start Date	End Date	Hours
C	2012 Feb 21	2012 Mar 18	57.0
B^*	2014 Feb 02	2014 Feb 17	24.0

DnC, CnB, BnA. These hybrid configurations have the antennas on the east and west arms moved out for the next configuration, and have resolutions similar to the smaller configuration of the hybrid.

Another set of observations was made with the VLA in *S*-band, which ranges from 2 to 4 GHz. There were two main observing sessions: one with the C configuration (maximum baseline 3.4 km), with an average of 21 antennas; and one with higher resolution in the BnA configuration (maximum baseline \sim 11.1 km). The BnA configuration’s resolution is comparable to that of the smaller, or B, configuration. The observing dates and time spent in each configuration are listed in Table 2.2.

The 3-GHz VLA pointing was selected explicitly to overlap the region Owen & Morrison (2008) observed in the Lockman Hole at 1.4 GHz. The field is centred on RA= $10^{\text{h}}46^{\text{m}}00^{\text{s}}$, Dec= $+59^{\circ}01'00''$ (J2000), and was originally chosen as it is known to be a “random” (i.e. for our purposes quite crowded) field, with few bright sources (the brightest source being 7 mJy), and no very bright radio sources nearby. It is also covered in many other wavebands (*Spitzer*, *Chandra*, *Herschel*, GMRT, and more) allowing for source cross-identification, investigation of AGN contribution, and study of the far-IR/radio correlation. The 3 GHz (centre frequency) S-band was chosen rather than the 1.4 GHz L-Band, because the contamination from interference is less, the requirements on dynamic range are lower, the confusion is lower, and additionally S-Band has greater available bandwidth (2 GHz), all resulting in overall better sensitivity on average. This is in addition to S-band being closer to the frequency of the largest ARCADE 2 observed excess that we wanted to investigate.

2.2.1 Calibration

This section describes the steps and details of calibrating the VLA data. The procedure below describes the work on the C-configuration data; however, the steps were the same for the B-configuration data, which were added to the C-configuration data once they were calibrated.

Our 57 hours of observing time was spread over six observing nights between 2012 February 21 and March 18, and 50 hours of this time was spent on the target field. The phase calibrator J1035+564 was monitored for 30 seconds every 30 minutes. The flux density and bandpass calibrators 3C 147 and 3C 286 were each observed once per night.

The 2–4 GHz frequency range was divided into 16 sub-bands (subband also known as intermediate frequency (IF)), each with 64 channels of width 2 MHz. The primary beam attenuation pattern is very nearly that of a uniformly illuminated circular aperture [36]:

$$A(\rho/\theta_p) \approx \left[\frac{2J_1(3.233\rho/\theta)}{(3.233\rho/\theta)} \right]^2, \quad (2.9)$$

where J_1 is the Bessel function of the first kind and order, ρ is the angular offset from the pointing centre, and

$$\theta_p = (43.3' \pm 0.4') \left(\frac{\nu}{\text{GHz}} \right)^{-1} \quad (2.10)$$

is the measured FWHM of the S-band primary beam at frequency ν . The primary FWHM ranges from 21.7' at $\nu = 2$ GHz to 10.8' at $\nu = 4$ GHz.

We used the OBIT package [39]³ to edit and calibrate the uv data; with the six observing sessions calibrated and edited separately. Two of the 16 subbands contained satellite RFI strong enough to cause serious Gibbs ringing in the raw data (sidelobes in the data at the location of a discontinuity or change in the subbands due to the finite number of correlator lags). Hanning smoothing (combining adjacent spectral channels with weights 1/4, 1/2, and 1/4) suppressed this ringing and cut the number of channels per IF to 32. Spectral channels still containing

³<http://www.cv.nrao.edu/~bcotton/Obit.html>

strong interfering signals were flagged and removed from the data, as were a few edge channels in each subband. Prior to calibration, the remaining data samples containing strong interfering signals were identified by their large deviations from running medians in time and frequency, and they were flagged.

Subsequent calibration and editing consisted of the following steps:

1. Instrumental group delay offsets were determined from observations of all calibrators and applied to all of the data.
2. Residual variations of gain and phase with frequency were corrected by bandpass calibration based on 3C 286.
3. Amplitude calibration was based on the VLA standard spectrum of 3C 286 and was used to calibrate J1035+564. The more frequent observations of J1035+564 were then used to calibrate the amplitudes and phases of the target *uv* data. Data from some antennas, time intervals, and frequency ranges were still degraded by interference that had evaded earlier editing, corrupted a small fraction of our amplitude and phase solutions, and were thus flagged.
4. The calibrated data were then subjected to further editing in which data with excessive Stokes *I* or *V* amplitudes were deleted, as well as another pass at removing narrowband interference.

After this calibration and editing, the initial calibration was reset and the whole process was repeated using only the data that had survived the editing process. Finally, we were able to flag the small amount of the data having amplitudes significantly above the noise. About 53% of the *uv* data survived all of the editing steps. The calibrated and edited *uv* data from all six observing sessions were then combined for imaging. Before imaging, the data were averaged over baseline-dependent time intervals subject to the constraints that (1) the averaging should not cause time smearing within our central image and (2) the averaging time should never exceed the 20 second phase self-calibration interval.

2.2.2 Imaging

Again this section details the work on the C-configuration data, with the process for imaging the combined C+B-configurations being the same except for the subband

weighting used.

Observations spanning the frequency range between the low frequency limit ν_l and the high frequency limit ν_h have centre frequency $\nu_c = (\nu_l + \nu_h)/2$, bandwidth $\Delta\nu = (\nu_h - \nu_l)$, and fractional bandwidth $\Delta\nu/\nu_c$. The fractional bandwidth covered by our 2–4 GHz *uv* data is large: $\Delta\nu/\nu_c = 2/3$. Using such data to make an image suitable for measuring confusion encounters three problems, namely that the field of view, the PSF, and the flux densities of most sources can vary significantly with frequency. To deal with these problems, we separated the *uv* data into 16 subbands, each having a small fractional bandwidth, $\Delta\nu/\nu_c \ll 1$. The *uv* data were tapered heavily in the higher-frequency subbands, and each subband was imaged with an independent “robustness” [18] to force nearly identical PSFs in all subbands. We weighted and recombined the narrowband images to produce a sensitive wideband image characterized by an “effective frequency” $\langle\nu\rangle$, where $\langle\nu\rangle$ at any position in a wideband image is defined as the frequency at which the flux density of a point source with a typical spectral index $\langle\alpha\rangle \equiv d\ln S/d\ln\nu = -0.7$ equals its flux density in the wideband sky image. The effective frequency declines with angular distance ρ from the pointing centre because the primary beam width is inversely proportional to frequency.

Table 2.3 lists the centre frequencies ν_c of the 16 subbands and the rms noise values σ_n of the 16 subband images. The fractional bandwidths of these subbands range from 3% to 6%, so each subband image is a narrowband image. We used the OBIT task MFIMAGE (also a multi-frequency clean algorithm) to form separate dirty and residual images in each subband. We assigned each subband image a weight inversely proportional to its rms noise, generated a combined wideband image from their weighted average, and used this sensitive combined image to locate clean components for a joint deconvolution. The clean operation used flux densities from the individual subband images, but at locations selected from the combined image. At the end of each major clean cycle, the clean components with flux densities from the individual subband images were used to create residual subband *uv* data and then new residual images.

In order to obtain nearly identical PSFs in all subbands, we tapered the *uv* data in each subband differently and assigned individual robust weighting factors, adjusted to ensure that each synthesized dirty beam was nearly circular with major

Table 2.3: Frequency and noise properties of the 16 VLA subband images.

Subband number	Frequency (GHz)	σ_n C (Jy)	σ_n CB ($\mu\text{Jy beam}^{-1}$)
01	2.0500	9.22	8.46
02	2.1780	13.19	26.14
03	2.3060	18.17	1000.9
04	2.4340	4.48	5.09
05	2.5620	4.24	5.00
06	2.6900	4.31	4.42
07	2.8180	4.04	4.26
08	2.9460	3.72	4.75
09	3.0500	4.48	4.01
10	3.1780	3.14	3.49
11	3.3060	3.07	3.56
12	3.4340	2.97	3.19
13	3.5620	2.88	3.47
14	3.6900	3.47	4.04
15	3.8180	4.45	5.66
16	3.9460	4.40	117.38

and minor axes between 7'' and 8''. After CLEANing, each residual image was smoothed by convolution with its own elliptical Gaussian distribution, tailored to yield a circular and nearly Gaussian PSF with a precisely 8 arcsec FWHM. Finally, all CLEAN components were restored with an 8'' FWHM circular Gaussian beam (for the CB-combined data the clean beam is a circular Gaussian with FWHM 2.75'').

Two iterations of phase-only self calibration were used to remove residual phase errors. Fluctuations, indistinguishable from confusion, are produced by any dirty-beam sidelobes remaining in our combined image. Fortunately, they are small, because the combination of long observing tracks and bandwidth synthesis over our wide fractional bandwidth ensures excellent *uv*-plane coverage and keeps the dirty-beam sidelobe levels well below 1% of the peak. Consequently the highest dirty-beam sidelobes from sources in the residual image are $< 0.01 \times 10 \mu\text{Jy beam}^{-1} \approx 0.1 \mu\text{Jy beam}^{-1}$, so their contribution to the image variance is more than two orders of magnitude below the $(1 \mu\text{Jy beam}^{-1})^2$ contri-

butions of noise and confusion.

2.2.3 Image Noise

We used the AIPS task IMEAN to calculate the rms noise values σ_n of the CLEANed subband images in several large areas that are well outside the main lobe of the primary beam and contain no visible ($S_{\text{peak}} \geq 6 \mu\text{Jy beam}^{-1}$) sources. This ensures that the contribution from source signals in these regions is negligible. The σ_n values are listed in Table 2.3. Next we assigned to each subband image a weight inversely proportional to its noise variance σ_n^2 , generated a wideband image from the weighted average of the subband images, and measured the noise distribution in four large regions well outside the primary main beam and free of visible sources. The best-fit to the logarithmic noise histogram indicates a Gaussian distribution with an rms $\sigma_n \approx 1.02 \mu\text{Jy beam}^{-1}$.

The B-configuration data had several subbands that were more severely affected by interference issues that were not resolved through the flagging and editing process; this is evident in the σ_n values shown in Table 2.3. For imaging and analysis these subbands were given very small weights when combining the images to make a centre image.

We also wanted to know the rms statistical uncertainty $\Delta\sigma_n$ in our estimate of σ_n . The image PSF is a Gaussian, and the effective noise area for a Gaussian PSF is that of the Gaussian PSF squared [32, 36]. Squaring a Gaussian PSF of width θ yields a narrower Gaussian of width $\theta/\sqrt{2}$ and solid angle $\Omega_b/2$. Consequently there are actually $2N$ statistically independent noise samples in $\Omega = N\Omega_b$ beam solid angles, and the rms fractional uncertainty in σ_n is

$$\frac{\Delta\sigma_n}{\sigma_n} = \left(\frac{1}{2N} \right)^{1/2}, \quad (2.11)$$

not the commonly believed $(1/N)^{1/2}$; for further discussion on this see Appendix A of Condon et al. [37].

The final result is $\sigma_n = 1.012 \pm 0.007 \mu\text{Jy beam}^{-1}$. In theory the rms noise is uniform across the image prior to correction for primary-beam attenuation, so we used this value to estimate the noise in confusion-limited regions near the pointing

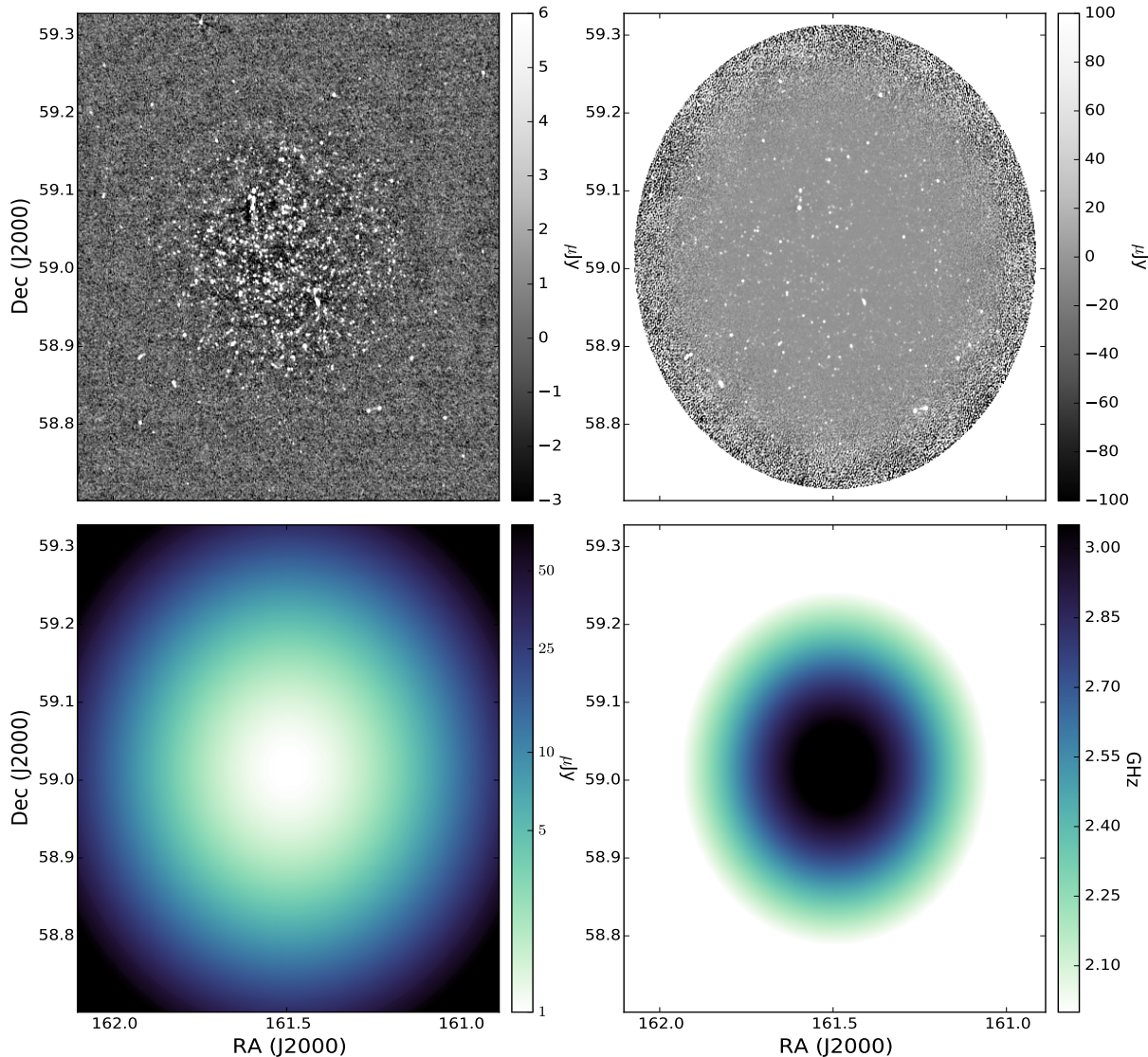


Figure 2.5: Lockman Hole VLA 3 GHz images. The top left shows the C-configuration field before correction for the primary beam. The top right panel is the field after wide-band primary beam correction. The bottom left panel shows the noise change across the field after wide-band primary beam correction. The bottom right panel shows the effective frequency after the wide-band combination.

centre. The total intensity-proportional error arising from uncertainties in the flux-density calibration and primary beamwidth is not more than 3% inside the primary beam half-power circle. For more details on the imaging process and noise measurements see section 2.4 of Condon et al. [37]. The noise for the combined CB data is $\sigma_n = 1.15 \pm 0.007 \mu\text{Jy beam}^{-1}$.

2.2.4 The SNR-Optimized Wideband Sky Image

Our final wideband image of the sky was made with weights designed to correct for primary-beam attenuation and simultaneously maximize the signal-to-noise ratio (SNR) for sources having spectral indices near $\langle \alpha \rangle = -0.7$, the mean spectral index of faint sources found at frequencies around 3 GHz [31]. This differs from the traditional weighting designed to minimize noise, which maximizes the SNR in a narrowband image, but in a wideband image only if $\langle \alpha \rangle \approx 0$. The brightness $b_i(\rho)$ of each pixel in each of the $i = 1, 16$ subband images was assigned a weight

$$W_i(\rho, \nu_c) \propto \left[\frac{\nu_c^{\langle \alpha \rangle}}{\sigma_n A(\rho, \nu_c)} \right]^2, \quad (2.12)$$

where the rms noise σ_n and centre frequency ν_c of each subband image is listed in Table 2.3. Each pixel in the weighted wideband sky image was generated from the ratio

$$b(\rho) = \sum_{i=1}^{16} [b_i(\rho) W_i(\rho)] \Bigg/ \sum_{i=1}^{16} W_i(\rho). \quad (2.13)$$

The final C-configuration images, before and after primary beam correction, are shown in the top panels of Fig. 2.5.

Even at the pointing centre, weighting to optimize the SNR for $\langle \alpha \rangle = -0.7$ increases the sky image noise slightly from $\sigma_n = 1.012 \pm 0.007 \mu\text{Jy beam}^{-1}$ to $\sigma_n = 1.080 \pm 0.007 \mu\text{Jy beam}^{-1}$. Away from the pointing centre, the frequency-dependent primary-beam attenuation correction causes the rms noise on the sky image to grow with the radial offset ρ . Weighting also affects how the effective frequency $\langle \nu \rangle$ at each point in the wideband sky image decreases with the offset ρ from the pointing centre. Also, $\langle \nu \rangle$ in our sky image declines monotonically from 3.06 GHz at the pointing centre to 2.96 GHz at $\rho = 5$ arcmin. The radial changes in

Table 2.4: Image properties for the wide-band VLA data. The reported noise values are all after correction for the primary beam and frequency weighting effects, with ρ being the distance from the pointing centre. The clean beam size, θ_B , is the FWHM, and the synthesized beam solid angle, Ω_B , is $(\theta_B^2 \pi)/(4 \ln 2)$.

Quantity	Value C-data	Value CB-data	Unit
$\langle \nu \rangle$ in centre	3.06	3.036	GHz
$\langle \nu \rangle$ at 5 arcmin	2.96	2.96	GHz
$\langle \nu \rangle$ inside 5 arcmin Ring	3.02	3.02	GHz
Pixel size	1.252	0.5	arcsec
Clean beam FWHM, θ_B	8.00	2.75	arcsec
Beam solid angle, Ω_B	72.32	8.55	arcsec ²
$\sigma_n(\rho=0)$	1.08	1.15	$\mu\text{Jy beam}^{-1}$
$\sigma_n(\rho = 5')$	1.447	1.54	$\mu\text{Jy beam}^{-1}$
$\sigma_n(\rho \leq 5')$	1.255	1.33	$\mu\text{Jy beam}^{-1}$

noise and frequency are shown in the bottom panels of Fig. 2.5. The final image is confusion limited in the sense that the rms fluctuations are everywhere larger than the noise levels. Table 2.4 provides a summary of the image properties.

2.3 SKADS Simulation

Throughout this work we rely on using realistic simulated radio data from the Square Kilometre Array (SKA) Simulated Skies (S^3) simulation⁴. This is a computer simulation of the radio and submm Universe, dedicated to the preparation of the Square Kilometre Array and its pathfinders. This simulation was led by the University of Oxford as part of the Square Kilometre Array Design Studies (SKADS). While several simulations were done, we used only data from S^3 -SEX, which is a semi-empirical simulation of extragalactic radio continuum sources in a sky area of $20^\circ \times 20^\circ$, out to a cosmological redshift of $z = 20$.

The simulation is based on a realisation of the linear matter power spectrum produced by CAMB [108]. The cosmological model used is: $\Omega_m = 0.3$, $\Omega_k = 0.0$, $w = -1.0$, $h = 0.0$, $f_{\text{baryon}} = 0.16$, $\sigma_8 = 0.74$, $b = 1.0$, and $f_{\text{NL}} = 0$. This density field realisation is gridded in cells of size $5 h^{-1} \text{ Mpc}$, from which galaxies are

⁴<http://s-cubed.physics.ox.ac.uk/>

sampled. The galaxy bias function $b(z)$ follows the description of Mo and White [122] with a cut-off redshift for different galaxy types. Thus cut-off is chosen so that the bias is held constant above a given redshift to prevent exponential blow-up of the clustering. Galaxy clusters are identified by looking for regions with densities larger than the critical density with the use of the Press-Schechter [145] and Sheth-Tormen formulations [163]. The simulated sources were drawn from four types of calculated luminosity functions (radio-loud AGN of high and low luminosities, radio-quiet AGN, star-forming galaxies, and starburst galaxies). These galaxies were inserted into the evolving dark matter density field. This simulation, therefore, has realistic approximations of the known source counts and contains both small and large-scale clustering. Full details of the simulation are described in Wilman et al. [191].

Chapter 3

Confusion and $P(D)$

3.1 Confusion

The traditional way of doing a source count, as discussed in Section 1.2, is to fit for and count all the sources in an image above some threshold, generally $> 5\sigma$. The problem with this is the uncertainties in the peak finding and fitting, as well as corrections for sizes, flux boosting, and clean bias (see Chapter 6 for more discussion on these corrections) all create a lot of uncertainty in the source count. Another way to obtain a statistical estimate of the source count is to take advantage of something known as confusion. Confusion is a term which refers to the blending of faint sources due to the telescope beam or PSF. There is such a thing as natural confusion, which is the blending of faint sources due solely to their number density causing overlap on the sky. However, here we focus on the confusion resulting from the finite resolution of the telescope.

In a noiseless image with just point sources convolved with a telescope beam the shape of the normalized histogram of the pixels, or 1D probability distribution function (PDF), is dictated by the source count in the image and the shape of the beam. To illustrate this we made a simulated image of point sources with no noise and a realistic source count. We then convolved it with several different sized Gaussian beams and looked at the pixel histograms, which is shown in Fig. 3.1. The top row shows the simulated image convolved with four different Gaussian beams. The middle row shows the beams, while the bottom row shows the PDFs. This

figure shows that as the beam size gets larger more sources are blended together, thus widening the PDF.

The confusion noise (σ_c) is the width of the PDF due to confusion. The noiseless distribution will generally have an extended bright tail such that the method of finding σ of a Gaussian shaped curve does not give an accurate estimate of the width. Instead, to find σ_c we find the median and D_1 and D_2 such that

$$\sum_{D_1}^{\text{median}} P(D) = \sum_{\text{median}}^{D_2} P(D) = 0.34 \quad (3.1)$$

when normalised such that the sum of the PDF= 1 (with D being the observed brightness or pixel value), since in the Gaussian case 68 per cent of the area is between $\pm 1\sigma$. The confusion noise is then $\sigma_c = (D_2 - D_1)/2$ (thus yielding an estimate of something resembling the σ of a Gaussian distribution).

However, in the real world we have instrument noise from our telescope added to the confusion noise, such that the total noise is $\sigma_t = \sqrt{\sigma_n^2 + \sigma_c^2}$. In terms of the PDF the instrument noise adds more width and becomes degenerate with the contribution from faint sources. For this reason, to attempt to measure faint counts using confusion, it is best to have $\sigma_n \leq \sigma_c$. We illustrate this by taking one of the noiseless images from before, at a set beam size of 8 arcsec, and add Gaussian random beam-convolved noise to the image while varying the σ_n of the noise. This is shown in Fig. 3.2, where the top row is the sources plus noise, the middle row is just noise, and the bottom row shows the histograms from the noise, noiseless sources, and noisy sources. This shows that as the instrumental noise decreases, and drops below the confusion noise, the combined histogram's shape approaches that of the noiseless histogram, which is what is to be estimated.

For data where the confusion noise is larger than the instrumental noise, which can be achieved by choosing the beam size and exposure times, the method of Probability of deflection ($P(D)$) can be used in order to model the source count below the current cut-offs. This method, which forward models the source count by fitting the image histogram, is described in detail in the next section.

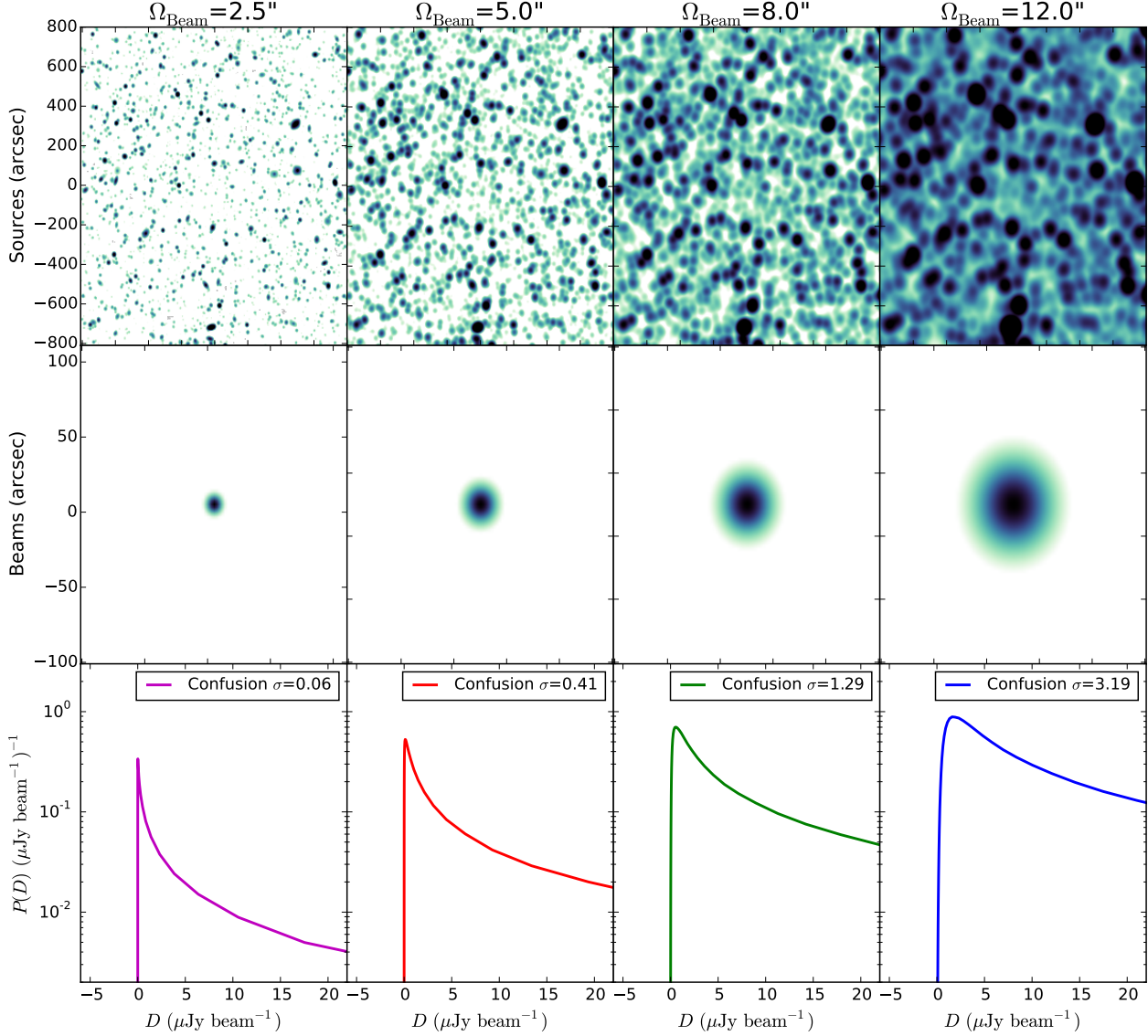


Figure 3.1: The top row shows a region of simulated noiseless images each convolved with beams with FWHM=2.5, 5.0, 8.0, and 12 arcsec; all images have the same colour scale. The middle row shows the peak normalized beams. The bottom row shows the image pixel histograms and the confusion widths as measured by eq. 5.1.

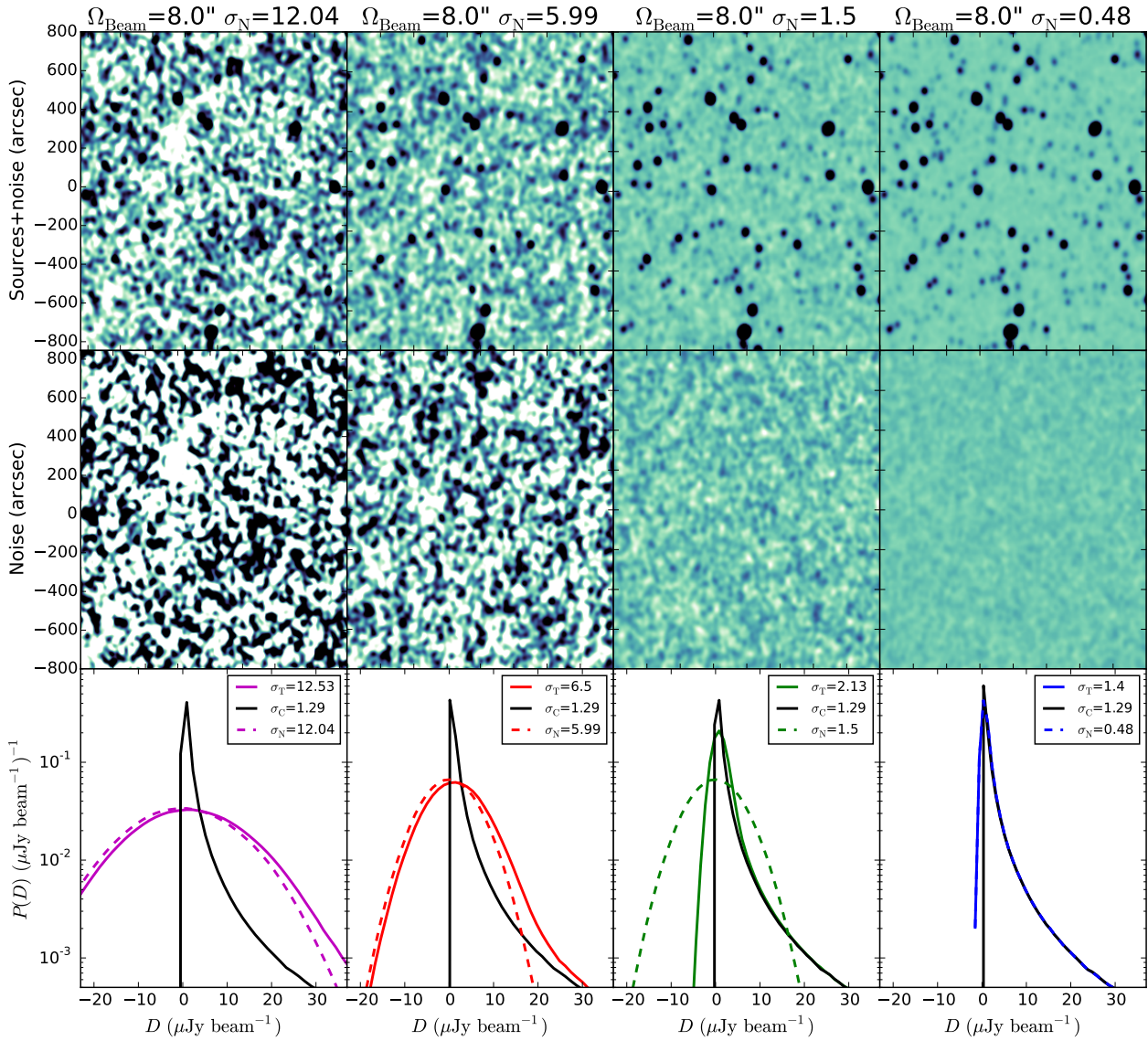


Figure 3.2: The top row shows simulated images with sources and noise each convolved with a beam of FWHM = 8.0 arcsec; all images have the same colour scale. The middle row shows the same regions with just noise; all images have the same colour scale. The bottom row shows the image pixel histograms for the noiseless case (solid black lines), just noise (dashed lines), and sources plus noise (solid coloured lines). The σ values listed are σ_t = total combined width, σ_c = noiseless confusion, and σ_n = instrumental noise as measured by eq. 5.1.

3.2 Probability of Deflection

The method of $P(D)$ was introduced by Scheuer [156] as the probability of pen deflections on a chart-recorder from a single baseline of a two-element radio interferometer. The $P(D)$ distribution of an image is the PDF of pixel intensities, or the “1-point statistics”. Condon [30] and Scheuer [157] gave analytical derivations of $P(D)$ for a single power-law model of a source count. The method which has been most often applied is to count the objects in the map brighter than some cut-off (usually about $5\sigma_n$) and use $P(D)$ analysis for the faint end of the count, constraining an amplitude and a slope. A similar approach with the VLA data described here was carried out in Condon et al. [37], where a simple power law was fit to the count below $10 \mu\text{Jy}$. In this paper we follow the more computationally intensive approach of Patanchon et al. [138] to apply a histogram-fitting procedure for the full range of image source brightnesses. This approach does not require that the source count model be a power law, allowing for more flexibility in accurately modelling the true source count. For completeness we give here a brief summary of the statistics of $P(D)$, providing some specific details on how we applied this to the 3 GHz VLA data. For more detailed derivations see Condon [30], Takeuchi et al. [176], and Patanchon et al. [138].

The deflection, D , at any point (pixel) is an image intensity (in units such as Jy per beam solid angle) at that point. $P(D)$ is then the probability distribution of those deflections in some finite region of the image. The differential number count $dN(S)/dS$ is the number of sources per steradian with flux densities between S and $S+dS$ per unit flux-density interval. The relative point spread function $B(\theta, \phi)$ is the relative gain of the peak-normalised CLEAN beam at the offset of a pixel from the source¹. The image response to a point source of flux density S at a point in the PSF where the relative gain is $B(\theta, \phi)$ is $x = SB(\theta, \phi)$. The mean number of source responses (e.g. pixel values) per steradian with observed intensities between

¹An assumption with the $P(D)$ method is that the PSF is constant across the image. With single dish observations or those done at other wavelengths, such as sub-mm or infrared, this may not always be the case. However, with our interferometric image the synthesized beam is set before transformation from the Fourier plane to the image plane. Thus, with our VLA data the PSF is a constant size and shape across the entire image

x and $x + dx$ is $R(x)dx$ [see 30, for example], with

$$R(x) dx = \int_{\Omega} \frac{dN}{dS} \left(\frac{x}{B(\theta, \phi)} \right) B(\theta, \phi)^{-1} d\Omega dx. \quad (3.2)$$

The PDF for the observed flux density in each sky area unit (in this case an image pixel) is the convolution of the PDFs for each flux density interval over all flux densities – this is $P(D)$. The convolution in the image plane is just multiplication in the Fourier plane of the individual characteristic functions. In this case D is the total flux density from all sources with the observed flux density x . Thus, $p(\omega)$ is

$$p(\omega) = \exp \left[\int_0^{\infty} R(x) \exp(i\omega x) dx - \int_0^{\infty} R(x) dx \right], \quad (3.3)$$

and $P(D)$ is the inverse Fourier transform of this,

$$P(D) = \mathcal{F}^{-1}[p(\omega)]. \quad (3.4)$$

The $P(D)$ distribution in a noisy image is the convolution of the noiseless $P(D)$ distribution with the noise intensity distribution. Convolution is equivalent to multiplication in the Fourier transform plane, and the Fourier transform of a Gaussian is a Gaussian, so for Gaussian noise with rms σ_n ,²

$$P(D) = \mathcal{F}^{-1} \left[p(\omega) \exp \left(\frac{-\sigma_n^2 \omega^2}{2} \right) \right]. \quad (3.5)$$

The task then boils down to using the measured $P(D)$ to constrain a model for dN/dS , via $R(x)$, for a given noise and beam.

3.2.1 $P(D)$ Simulation Tests

To test our model and statistical approach we used data from the SKADS S³ simulation (see Section 2.3 for details). Using these data allowed us to test not only

²In the case of single dish observations, or steep-slope counts ($\gamma > 2$), the mean deflection above absolute zero μ should also be subtracted off, such that D would then represent the deflection about μ rather than zero. The mean deflection can be found from $\mu = \int x R(x) dx$. The zero point of the $P(D)$ distribution is lost in an interferometer image, which has no “DC” response to isotropic emission, so the zero point must be a free parameter when fitting our VLA data to model $P(D)$ distributions.

the functionality and accuracy of our code, but also any effects that small-scale (beam-sized) clustering might have on the output, by comparing the fitted model to the known input.

We used the simulated data at 1.4 GHz, the closest frequency in the simulation to our VLA data. The full size of the simulation is 400 deg^2 , from which we extracted the central 1 deg^2 . The simulated image was constructed to have the same beam and pixel size as our VLA data. Random (beam-convolved) Gaussian noise was added to the simulated image, with $\sigma_n = 2.14 \mu\text{Jy beam}^{-1}$ rms. This noise value is slightly larger than that of our VLA image central 5 arcmin due to the simulation being at 1.4 GHz instead of 3 GHz. The model count was set up as described in Section 4.4, with six variable nodes and two fixed ones. The faintest node was set at 10 nJy, as this was the faintest flux density simulated in the data. The second node was set at $0.1\sigma_n$.

The output from the MCMC fitting to the simulated data can be seen in the top panel of Fig. 3.3 and the $P(D)$ distributions are shown in Fig. 3.4. The plot shows the marginalised mean amplitudes from each parameter's likelihood distribution for all six nodes. The values for the six nodes and the χ^2 values at each point in the chain can be used to compute 68 per cent confidence intervals (useful for examining the full likelihood surface, since there are shape changes due to the parameter degeneracies, as discussed in Section 4.5.2). The results from this simulated image indicate that our fitting procedure is unbiased; the input source count model is always within the relevant confidence regions. There is some slight deviation from the input count for the faintest three nodes. This is perhaps not unexpected, since this region is well below the instrumental noise. However, while the error bars on the faintest node are large, it is important to note that that the count is still constrained; even the 95 per cent limits for this node do not reach the high and low limits given to the MCMC routine. The marginalised mean for the faintest node is within 1 per cent of the input value, even though this is two orders of magnitude below the noise limit. This test shows that the method and model are not only capable of fitting the underlying source count of an image, but that there is still information about the count well below the instrumental noise, as long as that noise value is known well.

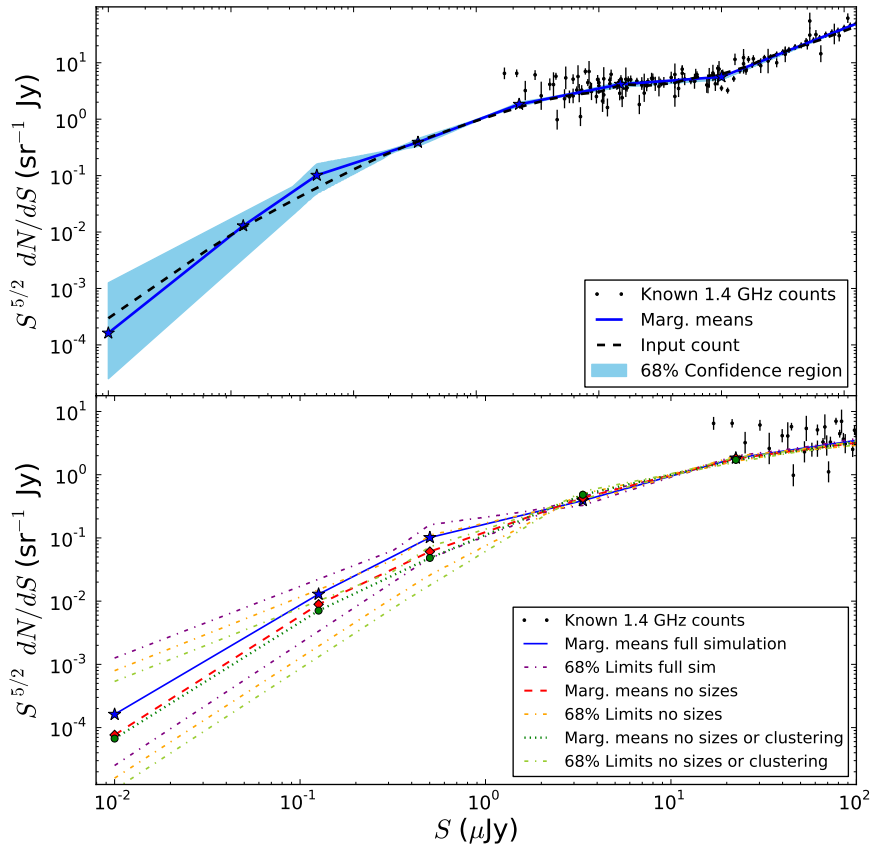


Figure 3.3: Euclidean-normalised source count from SKADS simulation.

The black points are real data counts from the de Zotti et al. [42] compilation. Top: MCMC marginalised mean (blue line and points) node positions. The black dashed line is the input source count model from Wilman et al. [191]. The shaded area is the 68 per cent confidence region. Bottom: The marginalised mean node positions from the simulated image, zoomed in on the region $S \leq 2 \mu\text{Jy}$, taking into account source sizes and clustering (blue solid line), but with sources all unresolved (red dashed line), and for unresolved sizes and random positions (green dotted line), with 68 per cent confidence regions as the dot-dashed purple, orange, and green lines.

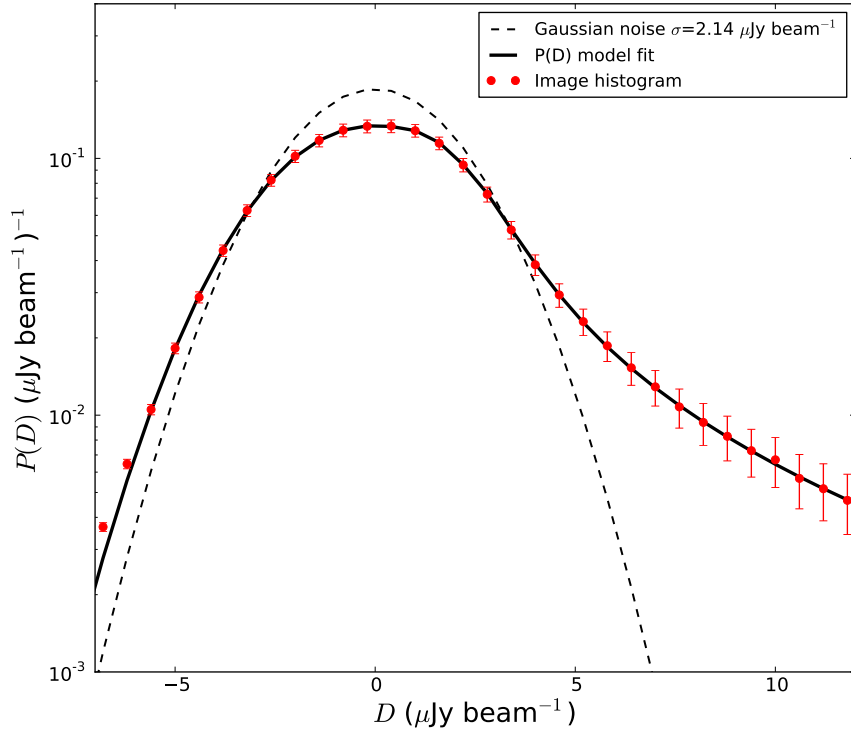


Figure 3.4: Comparison of pixel histograms from 1.4 GHz simulation (red dots) with the output of the marginalised means model $P(D)$ using as input six variable nodes (solid line) and a fixed $\sigma_n = 2.14 \mu\text{Jy beam}^{-1}$ noise level (dashed line).

3.2.2 Clustering and Source Sizes

The simulated image included sources with varying sizes, sources with multiple components, and the underlying clustering information. In Wilman et al. [191] the angular two-point correlation function, $w(\theta)$, is shown for the full simulation; this is a little higher than measurements made by Blake et al. [13] at a somewhat brighter flux density limit. We computed $w(\theta)$ for the specific 1 deg^2 simulated sample. The function $w(\theta)$ is usually approximated by a power law of the form $w(\theta) = A\theta^{-\gamma}$ (or sometimes written as $w(\theta) = (\theta/\theta_\phi)^{-\gamma}$). Blake and Wall [11, 12] found $A = 1.0 \times 10^{-3}$ and $\gamma = 0.8$, using data from the the NRAO VLA Sky Survey [NVSS; 36]. We assumed $\gamma = 0.8$ and calculated θ_ϕ for the subset of

simulated data we used. Using all the sources down to the limit of 10 nJy we found $\theta_\phi = 1.6 \times 10^{-5}$ deg or 0.06 arcsec. The sources are certainly clustered on the scale of our beam ($\simeq 8$ arcsec), but very weakly, because θ_0 (the angular scale for non-linear clustering) is so small compared with our synthesized beam size. Our $P(D)$ calculation does not take into account any clustering correction. It also does not account for source sizes, but assumes that all the sources are unresolved. While in the case of both the VLA data and the simulated data, many of the sources are smaller than the beam, we know that this is not the case for all of them. In the simulated data there are roughly 700,000 sources, with a mean major axis size of 1.4 arcsec and mean minor axis of 0.8 arcsec, giving a mean source solid angle of $\Omega_S \simeq 1.27$ arcsec 2 (before convolution with the beam). This is much smaller than our beam solid angle of 72.3 arcsec 2 .

To test what kind of effect source sizes and clustering have on the model fitting, two other images were made. The first kept the source position information, so that any clustering would be preserved, but all source size information was neglected. Every source, single and multi-component, was set to a single delta function with flux density equal to the total source flux density, and then this was convolved with the beam. The second image also had all the sources as delta functions, but in this case the positions were randomised as well, so that the sources were unclustered. The MCMC fitting was rerun on histograms from these two simulated images with all other factors being the same. The results from fitting each of the three images are compared in the bottom panel of Fig. 3.3.

The amplitudes and error regions of the three brighter S nodes are the same in each case. The only differences are for the faintest nodes, which are more difficult to constrain. Comparing the full image with the case where no size information is present, we see that the full image case is higher; as anticipated given that with the larger source sizes one might expect more blending, more bright pixels, and a slightly wider histogram. When comparing the case with randomised positions and unresolved sources, again the results are the same down to about the noise level, although fainter than this does give lower values. This again is expected, due to the lack of both source sizes and clustering. Clustering within the beam will tend to boost the pixel values after beam convolution, producing a slight widening of the distribution [see 175]. We would expect these fainter nodes to be of lower

amplitude without clustering, as seen. When not accounting for source sizes or clustering, the largest fractional change in node amplitude from the full image is 2.3 per cent at the first node, 2.2 per cent for the second node, with the others all 1 per cent or less; all of the values lie within the 68 per cent confidence limits of the full simulation. These results make us confident that neglecting the effects of clustering and source size when fitting our real data results in no significant bias.

Regarding the issue of source sizes, it is important to note that $P(D)$ counts are much more robust than comparably deep individual source counts. This is because $P(D)$ counts use a much bigger beam. For example, the 8 arcsec VLA beam corresponds to about one source per beam. Individual sources can be counted reliably only if there are at least 25 beams per source. This means the beam width for individual counts can not be much bigger than $8./\sqrt{25} \sim 1.6$ arcsec, which is quite close to the mean source size in the SKADS simulation and would require large corrections for partial resolution of the sources. The mean source size from the SKADS simulation is small enough compared to our beam that source size should not impact the $P(D)$. It should be noted, however, that the SKADS sizes are larger than estimates from high-resolution studies of faint radio sources. For example, Muxlow et al. [124] finds the average source size for weak radio sources to be closer to 0.7 arcseconds.

Chapter 4

Discrete-Source Count

4.1 Introduction

There has been considerable discussion recently about possible different types of radio sources contributing to the source count at flux densities fainter than the limits of the current source counts. Measurements from ARCADE 2 indicate the presence of an excess of radio emission over previous measurements or estimates using source count data. Vernstrom et al. [182], motivated by the ARCADE 2 results, presented new estimates of lower limits to the background from a compilation of source counts at eight frequencies and found an expected value for the background temperature almost five times lower than that of ARCADE 2 at 1.4 GHz.

The ARCADE2 results suggested that this excess emission might be coming from a previously unrecognized population of discrete radio sources below the flux density limit of existing surveys, and that this new population might be seen in radio source counts extending to lower flux density levels. This issue was further examined by Singal et al. [165], who concluded that this emission could primarily be coming from ordinary star forming galaxies at $z > 1$ *only if* the far-IR/radio ratio decreases with redshift. In other words we can only explain the background results with sources if they break the far-IR/radio correlation [79].

Vernstrom et al. [182] (Chapter 1) also showed that the known radio source counts cannot on their own account for the ARCADE 2 excess, although the source counts, at least at 1.4 GHz, are not inconsistent with a possible upturn below about

$10\,\mu\text{Jy}$. Such a possible upturn is mainly driven by the faintest count available at 1.4 GHz, from Owen and Morrison [134]. Owen & Morrison found that their (Euclidean-normalised) count, which extends down to $15\,\mu\text{Jy}$, did not decrease with decreasing flux density (compared to static Euclidean counts), but seemed to level off or even show signs of increasing. It is important to note that the Euclidean-normalised count ($S^{5/2}dN/dS$) does not need to level off or turn up to explain the high ARCADE 2 background temperature; it is sufficient that S^2dN/dS levels off or turns up.

New 3-GHz data from the VLA, reach down to μJy levels [37] and the resulting map is the deepest currently available. In this previous paper we estimated the source count from 1 to $10\,\mu\text{Jy}$ using a technique known for historical reasons as $P(D)$ analysis [30, 156]. This approach allows a statistical estimate of the count from a confusion-limited survey, extending down to flux densities below the confusion limit. $P(D)$ is the probability distribution of peak flux densities in an image. This approach results in statistical estimates of the source count that are much fainter than the faintest sources that can be counted individually (about 5 times the rms noise). The count model used in Condon et al. [37] was a single power law over a limited flux density range. However, there appeared to be evidence for a break in the slope somewhere in this region and certainly the results did not support any upturn in the count. While this previous result puts strong limits on the μJy count, it is possible that more comprehensive analysis of the $P(D)$ distribution, with a more general count model, could reveal additional information about the true shape of the count, as well as constraining the count fainter than $1\,\mu\text{Jy}$.

Here we present a more sophisticated modelling approach to the $P(D)$ fitting process, motivated by Patanchon et al. [138], using a model based on multiple joined power laws. The statistical uncertainties here are evaluated using Markov chains. We test this technique with a large-scale simulation incorporating realistic source sizes, multi-component sources, and clustering. This method allows for exploration of the flux density limit of the $P(D)$ approach, and the count below the confusion noise, as well as a thorough non-parametric error analysis.

Sections 4.2 and 4.3 describe the process adopted for model fitting and error analysis. In Section 4.4 we discuss the models used in the fitting and the details of their application to the VLA data. In Section 4.5 we present the results of the

fitting from two different models, a discussion of the parameter degeneracies, and the derived radio background temperature. Section 4.6 gives a discussion of the systematics and comparisons with previous results.

For all the work in this Chapter only the VLA C-configuration data were used, as described in Section 2.2.

4.2 $P(D)$ and Image Noise

It is important to have an accurate measure of the instrumental noise in the image for analysis. As mentioned in Section 2.2 we created 16 images from the different S-band frequency sub-bands. The images created from the UV data should have constant instrumental noise across the images, before any primary beam corrections and neglecting any deconvolution artifacts or contamination from dirty-beam sidelobes (which in our case were small with the largest dirty-beam sidelobe contamination being $\simeq 0.1 \mu\text{Jy beam}^{-1}$). We used the AIPS task IMEAN to calculate the rms noise values of the CLEANed sub-band images in four large areas well outside the primary beam of each. This ensures that the contribution from source signals in these regions is negligible. The 16 images were combined with weights inversely proportional to the sub-band noise to create the 3 GHz centre image. The noise was then measured again in several large areas outside the 3 GHz primary beam area of the centre image. From these measurements we obtained our noise estimate of $\sigma_n = 1.012 \pm 0.007 \mu\text{Jy beam}^{-1}$, constant across the image, before the primary beam correction. For more details on the imaging process and noise measurements see section 2.4 of Condon et al. [37].

For the basic $P(D)$ calculation using eq. (3.5), it is assumed that the noise, σ_n , is constant across the image. However, for our VLA data this is not the case. While the true instrumental noise does not change, because of the primary beam correction and frequency weighting effects, the noise measured in $\mu\text{Jy beam}^{-1}$ increases radially with distance, ρ , from the pointing centre. The noise for the ring of pixels at a radius of 5 arcmin has already increased from $1.08 \mu\text{Jy beam}^{-1}$ to $1.447 \mu\text{Jy beam}^{-1}$. However, the actual noise contributing to the $P(D)$ is a weighted combination of the variance of the rings inside some set radius. Thus, for a circle of radius 5 arcmin the weighted effective noise from all the rings inside

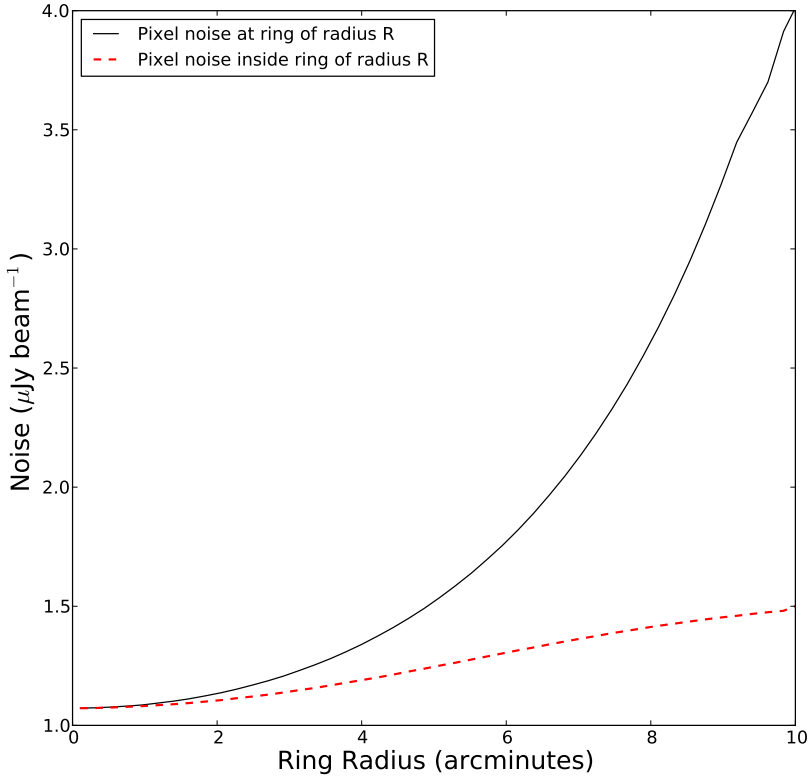


Figure 4.1: Change in image noise as a function of ring radius. The lines show how the noise at each ring changes with distance from the centre (black solid line) and the weighted noise within a ring of that radius (red dashed line).

is $1.255 \mu\text{Jy beam}^{-1}$, as seen as the red dashed line in Fig. 4.1. We have to choose an area where the variation in the noise is not too large, since for a $P(D)$ analysis we want σ_n to be roughly constant. For highest accuracy we would also like $\sigma_n \leq \sigma_c$, where σ_c is the confusion noise; and yet we want the area to be as large as possible to provide the most samples. We chose to carry out the main $P(D)$ calculation within the central 5 arcmin, where the fractional change in the noise has a broad minimum and the effective noise is $\leq \sigma_c$.

When binning the pixels for the histogram, weighting must be applied for the histogram to reflect the effective width of $\sigma_n^* = 1.255 \mu\text{Jy beam}^{-1}$. To accomplish

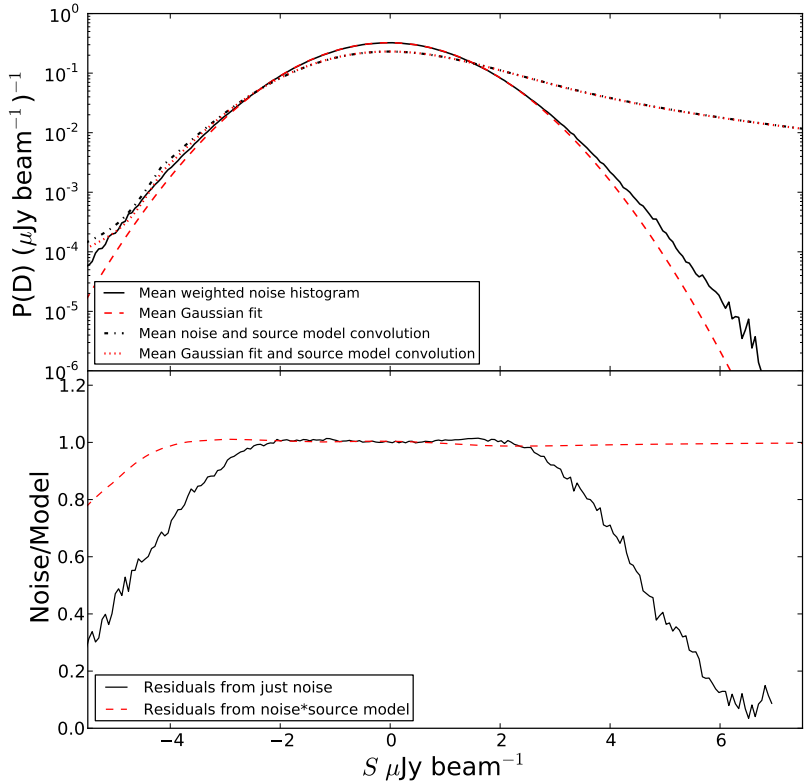


Figure 4.2: Differences in PDFs of purely Gaussian noise and weighted varying noise. The top panel shows the mean results from 100 simulated noise generations. The solid black line is the mean from the weighted noise image histograms, and the red dashed line is the mean from Gaussian distributions fitted to those histograms. The dot-dashed black line is the mean from convolving the noise image histograms with a noiseless source count $P(D)$ and the red dotted line is the mean from convolving the same source count $P(D)$ with the fitted Gaussian distributions. The bottom panel shows the ratios of the means. The black line is the mean from the fitted Gaussian distributions divided by noise image histograms and the red dashed line is the mean from the fitted Gaussian distribution convolution divided by the mean from image convolution. This shows how the noise weighting we apply to our data causes it to deviate from purely Gaussian noise.

this the area is split into sub-rings with radii (as measured from the mid-point radius of the ring) increasing by 0.11 arcmin. A histogram is made for each ring and a value equal to

$$w_k = \frac{1}{\sigma_{n_k}^4}, \quad (4.1)$$

gives the pixel weight in the k th ring. The σ_{n_k} is the value of the noise, after the primary beam correction, in the k th ring (the black line of Fig. 4.1). The weights, w_k , go as $\sigma_{n_k}^{-4}$ because in this case the estimator is a variance, and thus the weights go as the square of the variance, or the variance of the variance [see section 3 of 37, for a more detailed discussion of the noise, weighting, and choice of area]. These weights are applied to each ring histogram and the histograms are combined. The rings used for the central 5 arcmin can be seen in Fig. 4.3. This weighting scheme takes into account the areas of the rings but also favours the more sensitive (lower noise) rings.

The weighting also affects the uncertainties on the bins for the combined histogram. There are 23 rings in the central area and thus 23 histograms; each of those histogram's bins has Poisson uncertainties of $\varsigma_{i,k} = \sqrt{n_{i,k}}$, for the i th bin of the k th histogram (or k th ring). The uncertainties of the combined histogram are then a weighted combination of these such that,

$$\varsigma_i^2 = \sum_k n_{i,k} w_k^2, \quad (4.2)$$

which can be seen compared with the standard $\sqrt{n_i}$ Poisson value in the bottom panel of Fig. 4.4. It is these bin uncertainties that are used when model fitting.

Additionally, to increase the amount of data used to constrain the count we ran the fitting in two other zones. The first extends from 5 to 7.5 arcmin, and the second covers from 7.5 to 10 arcmin. The effective noise inside this second zone is $2.005 \mu\text{Jy beam}^{-1}$ and the effective noise inside the third zone is $3.550 \mu\text{Jy beam}^{-1}$. With just the 0 to 5 arcmin zone we are sampling about 8 per cent of the available pixels. The use of all three zones brings that up to around 32 per cent of the image pixels. While this still leaves a large fraction of the total image unused for constraining the count, outside a 10 arcmin radius the instrumental noise overwhelms the confusion noise.

The frequency-dependent primary beam correction, and our weighting scheme, does mean that our image noise is not purely Gaussian, as is assumed in the $P(D)$ calculation. We ran a simulation to see by how much our noise might be deviating from Gaussian and whether this could impact our fitting. We created images of random Gaussian noise, of the same size as our central 5 arcmin and convolved them with a Gaussian distribution the same shape and size as our beam. We then applied the same corrections as to our actual data and created a weighted histogram of each using the process described above. A Gaussian distribution was fit and calculated for each sample noise image, and then the noise image $P(D)$ and that of the fitted Gaussian distributions were both convolved with a noiseless $P(D)$ from a source count model (the specific source PDF used can be seen in Fig. 4.9). After 100 trials we calculated the mean $P(D)$ from the noise histograms, fitted Gaussian distributions, noise histograms convolved with the source model PDF, and fitted Gaussian distributions convolved with the source model PDF. These four means can be seen in the top panel of Fig. 4.2, with the ratio of the fitted Gaussian distributions to the noise images shown in the bottom panel. We can see that for the noise alone the true weighted histograms do deviate from Gaussian distributions starting at around 3σ , with the largest deviations being about a factor of 2.5 in the 5σ region. However, once convolved with the source count $P(D)$ the deviation is much smaller. There is then no discernible difference in the two distributions on the positive side. On the negative side the maximum deviation from the Gaussian model is only about a factor of 1.25, and this is only in the $4-5\sigma$ range, where in the images there are likely only 0–3 pixels/bin. Thus, with our current data this should not present any bias in the fitting.

4.3 Model Fitting

When calculating the $P(D)$ distribution we use very fine binning in flux density: 2^{18} bins with bin size = $0.04 \mu\text{Jy beam}^{-1}$. The output PDF is then interpolated onto the bins used for the image histogram to perform the fit. We calculate and fit $P(D)$ over the entire range of pixel values in the given image. For the image histogram we use a bin size of $0.3 \mu\text{Jy beam}^{-1}$ below $D = 10 \mu\text{Jy beam}^{-1}$. However, for pixels with flux densities above $10 \mu\text{Jy beam}^{-1}$ there would be very few pixels per

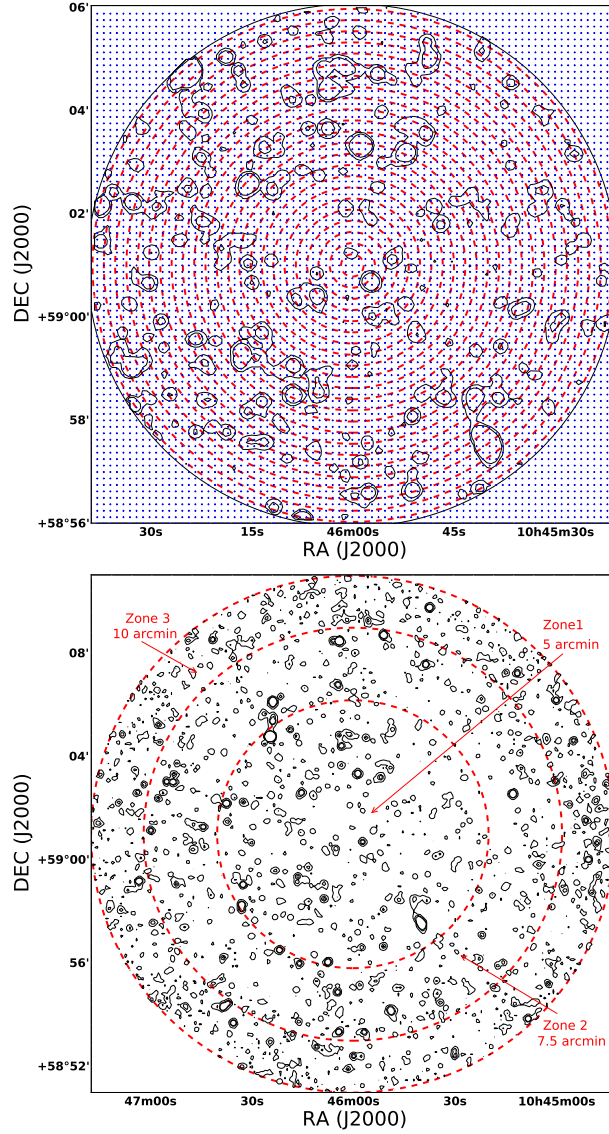


Figure 4.3: VLA 3-GHz contour images of the Lockman hole. The upper panel shows the central 5 arcmin, where the red dashed lines are rings used for weighting the histogram for the primary beam and the blue crosses are the pixel locations from one of the grids, with spacing between the points equal to the beam FWHM. The lower panel is the same image out to 10 arcmin, with the red dashed lines now showing the separation of the three noise zones discussed in Section 2.2.3.

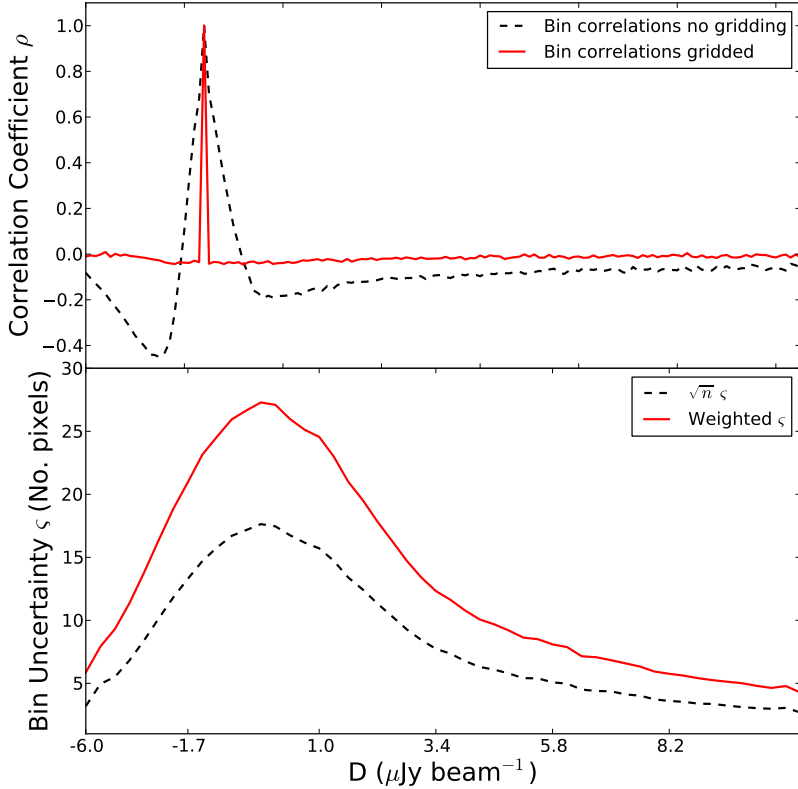


Figure 4.4: Bin correlations and uncertainties. The top panel shows the bin-to-bin correlation coefficients for one row of the correlation matrix at the peak, computed using eq. (4.5). The black dashed line shows the correlation values computed from full pixel histograms of 20,000 simulated images. The red solid line indicates the correlation values for the same bin computed from 20,000 simulated images but with the histograms made from pixels separated by one beam FWHM. The bottom panel shows the uncertainties for each bin. The black dashed line is $\xi = \sqrt{n_i}$ and the red solid line is the uncertainty ξ due to weighting calculated from eq. (4.2).

bin, because of the small bin size as well as the lack of bright sources in the image; thus a majority would have value 0 or 1. To ensure a large enough number of pixels per bin (to use a Gaussian approximation for fitting) we used expanded bin sizes in the tails. The bin size above $10 \mu\text{Jy}$ increases to ensure a minimum of 10 pixels in all bins. A total of 65 bins were used for the central 5 arcmin region, spanning the range $-7 \mu\text{Jy beam}^{-1}$ to $6900 \mu\text{Jy beam}^{-1}$.

We have developed a code to fit $P(D)$ based on a set of input model parameters. The input model need not be a simple power law, and may take on various forms, as long as it is continuous over the chosen flux density range. To fit the parameters we forward-model and use Markov chain Monte Carlo (MCMC) sampling methods. We make use of the publicly available MCMC package COSMOMC [107]¹, which, while developed for use in cosmological modelling, may be used as a generic sampler, if one provides data, model, and likelihood function. The MCMC code varies the input parameters in order to minimize the chosen fit statistic. Once the chain has past the “burn-in” phase it converges near the minimum and will then sample the parameter space, drawing from the parameter’s proposal density to decide on the next step in the chain. A well chosen proposal density can improve the efficiency of the fitting procedure. For all of our chains we first ran sample chains, with about an order of magnitude fewer steps than the final chains, and used these to compute the covariance matrix of the parameters, which we then supplied to the MCMC code to use for the proposal density.

There has been discussion about the optimal choice of statistic to use for $P(D)$ fitting. One possibility is to use the classical χ^2 , as done by Friedmann and Bouchet [65] and Maloney et al. [112]. However, the weighting of $1/n_i$, with n_i being the number of pixels in the i th bin, will tend to over-weight the bins when n_i is small, giving more weight to the tails of the distribution. Since for small numbers the uncertainty is not well modelled by $\sqrt{n_i}$, this option is not ideal. Another choice is to minimize the more correctly calculated negative log likelihood, as done by Patanchon et al. [138] and Glenn and e.a. [73]. While this method gives proper weighting, the problems come when trying to interpret the goodness of the fit. For

¹<http://cosmologist.info/cosmomc/>

the $P(D)$ model with Poisson statistics the log likelihood is defined as

$$\log \mathcal{L} = - \sum_i n_i \log(p_i) - \log(N!) + \sum_i \log(n_i!). \quad (4.3)$$

Here N is the total number of pixels in the image, p_i is the probability in the i th bin when the PDF is normalised to sum to one, and n_i is the the number of image pixels in the i th bin. In the limit that $n_i \gg 1$ this approximates a χ^2 distribution:

$$\frac{\chi^2}{2} \simeq \frac{1}{2} \sum_i \frac{(n_i - Np_i)^2}{Np_i} + K, \quad (4.4)$$

where K is a normalisation factor usually taken to be $K = (1/2) \sum_i (Np_i)$. However, when the log likelihood of eq. (4.3) does not equal the left hand side of eq. (4.4) it can be difficult to determine K and therefore difficult to interpret the log likelihood.

Neither of these two methods takes into account the fact that the pixels in the map (and hence bins in the histogram) are correlated. Due to the sources and noise being convolved with the beam, values in one location will affect neighbouring pixel values within an area roughly equal to the size of the beam [or the size of the beam area divided by 2 in the case of the noise; for further explanation see 37]. Furthermore, one source, when convolved with the beam, will contribute pixels to multiple bins. Ignoring these issues will underestimate the uncertainties of the bins and correspondingly the uncertainties of the fit parameters.²

When dealing with correlated variables the ideal solution is to use the gener-

²Both Patanchon et al. [138] and Glenn and e.a. [73] discuss the related issue of the optimal smoothing kernel for obtaining maximum signal-to-noise ratio for using $P(D)$ to constrain counts. However, it is important to realise that the situation in interferometry is fundamentally different than for single dish data. In direct imaging observations the instrumental noise is (ideally) independent at the map level, and hence it makes sense to further smooth this by a kernel of approximately the beam size [as shown in figure 3 of 138]. However, for interferometric imaging, the noise is independent in the Fourier plane, and when going to the image plane has *already* been convolved by the synthesized (dirty) beam. Chapin et al. [25] found from simulations of sub-mm data that in the very confused regime the optimal filter is the inverse of the PSF in Fourier space, i.e., the map is de-convolved by the beam; and in the regime dominated by instrument noise the optimal filter is the PSF. In our case, with $\sigma_n \simeq \sigma_c$ our current weighting scheme may not be optimal for $P(D)$, but is likely close. To determine the ideal weighting and filtering scheme for our type of data would require a more thorough analysis, starting in the Fourier plane and looking at ways to optimize before transformation to the image plane, rather than applying filters post transformation. This is beyond the scope of this investigation.

alised form of χ^2 , which includes the covariance matrix of the data. However, tests run using simulated images show this correlation matrix to be highly dependent on the underlying source count model. As we do not know in advance the true source count for our data, we want to avoid biasing the results by using a covariance matrix calculated from simulations performed with only an approximated source count. Additionally, using the MCMC method the covariance matrix should be that of the model being tested. This would entail making many simulated images to obtain a covariance matrix from each source count model in the MCMC chain, which is much more computationally expensive.

In order to remove the bin-to-bin correlations we instead sampled the image using a grid of positions with spacings of one beam FWHM. This should ensure that the pixels are approximately independent and correspondingly that the histogram bins are also independent. Of course the optimal sampling will be a compromise between reducing the correlations, and not losing too much fine-scale information, so it is certainly necessary to test that sampling with $1 \times \text{FWHM}$ spacing is close to the best choice.

We tested the effectiveness of this method using simulations. We used a simple broken power-law source count of slope -1.7 for flux densities less than $10 \mu\text{Jy}$ and -2.3 for sources brighter than $10 \mu\text{Jy}$, to generate sources that were randomly placed in an image with the same number of pixels as our data image. We convolved these sources with a beam of the same size as ours, and added them to beam-convolved Gaussian noise with $\sigma = 1.255 \times 10^{-6}$. We simulated 20,000 realisations in this way, made full histograms of each and also created histograms using pixels sampled from a grid with spacings of $\text{FWHM}/\sqrt{2}$, $1 \times \text{FWHM}$, and $\sqrt{2} \times \text{FWHM}$. We computed the mean number of pixels per bin from these and then computed the corresponding correlation matrix. Each entry in the correlation matrix was computed such that,

$$\rho_{i,j} = \frac{1}{20000} \sum_k \frac{(n_{i,k} - \mu_i)(n_{j,k} - \mu_j)}{\varsigma_i \varsigma_j}, \quad (4.5)$$

the diagonals of which are equal to 1. The correlation coefficient, $\rho_{i,j}$, is equal to $C_{i,j}/\varsigma_i \varsigma_j$, where $C_{i,j}$ is the covariance of the i th and j th bin. One row from this

matrix, near the peak of the histogram, is plotted in the top panel of Fig. 4.4. This shows that by taking FWHM-separated samples from the grid we remove nearly all of the correlation between the bins; the off-diagonals of the gridded simulation are all zero within statistical error. The samples with grid spacings of $\text{FWHM}/\sqrt{2}$ showed higher off-diagonal correlations. The $\sqrt{2} \times \text{FWHM}$ samples have roughly the same correlations as using $1 \times \text{FWHM}$, but with lower resolution. Thus we chose to use grids with the FWHM spacing.

The images we use have a beam width of approximately six pixels. Hence the FWHM grid which samples the image could be shifted in RA and Dec, with 36 different choices possible without repeating any pixels. An example of the grids can be seen in the top panel of Fig. 4.3, where the blue mini-crosses represent the positions of the image pixels selected for binning that grid. From the 36 histograms we are able to compute the scatter for each bin, which can be used as a check on the calculated bin uncertainties described in eq. (4.2).

We chose to carry out the MCMC fitting by minimising

$$\chi^2 = \frac{1}{2} \sum_i \frac{(n_i - N p_i)^2}{\varsigma_i^2}, \quad (4.6)$$

where the uncertainties used were not the usual Poisson $\sqrt{n_i}$ error bars, but rather (due to weighting effects from the primary beam) those from eq. (4.2). We performed MCMC trials on our VLA data using both eq. (4.6) and eq. (4.3) (both using the gridded image histograms). Comparisons of the output fit parameters for the different methods can be seen in Fig. 4.5. Although the outputs from the two methods are consistent, because the value of the log likelihood does not equal the $\chi^2/2$ it is difficult to interpret the goodness of the fit.

Also in Fig. 4.5 we show the gridded method against the results of a trial using all of the image pixels. The output is not significantly different for the parameters; however, as mentioned, the full resolution method underestimates the limits, the 68 per cent error region being roughly a factor of 1.5 to 3 times smaller in $\log_{10} dN/dS$. We know that the fits performed with the gridded data use approximately independent samples. Even though we do lose some resolution we believe this method to be more statistically robust and to model more accurately the vari-

ance and correlations.

4.4 Choice of Model

In Condon et al. [37] a single power-law model was fit to the data in this field. The best fitting single power law in the range $1 < S < 10 \mu\text{Jy}$ was $dN/dS = 9000S^{-1.7} \text{ Jy}^{-1} \text{ sr}^{-1}$. It was noted that power law models from Condon [31], $dN/dS = 9.17 \times 10^4 S^{-1.5} \text{ Jy}^{-1} \text{ sr}^{-1}$, and Wilman et al. [191] simulations, $dN/dS = 2.5 \times 10^4 S^{-1.6} \text{ Jy}^{-1} \text{ sr}^{-1}$, were both reasonably good approximations to the data in this range (assuming $\langle \alpha \rangle = -0.7$ to convert from 1.4 GHz to 3 GHz). However, it is the case that no single power law fits well across the whole μJy region³.

4.4.1 Modified Power Law

Since the single power-law model had already been explored, we first decided to try fitting a modified power law of the form

$$\frac{dN}{dS} = \kappa S^{\alpha + \beta \log_{10} S + \gamma (\log_{10} S)^2}, \quad (4.7)$$

in the range $0.01 < S < 60 \mu\text{Jy}$. For $S > 60 \mu\text{Jy}$ we connected the modified power law to the model from Condon [31] (scaled to 3 GHz using $\langle \alpha \rangle = -0.7$), where this model is in good agreement with known counts. We chose the cut-off at $60 \mu\text{Jy}$ so that we would fit the data not just in the μJy region but also in the slightly brighter area where the count from Owen and Morrison [134] was found to be higher than expected at 1.4 GHz. We fit for α , β , and γ , while κ was calculated as a normalisation constant to ensure continuity at $S = 60 \mu\text{Jy}$. The results are presented in Section 4.5.

The modified power law is a better fit than a simple power law (with a significant change in χ^2 for the change in degrees of freedom). One might say that this is an obvious result as the modified power-law model has more free parameters.

³With this method of $P(D)$ a physical model such as a luminosity function may be used. We opted to use a non-physical model because we intend to investigate a region where no prior data exist. Using a luminosity function would assume something about the type and number of different populations in that region, which could bias the results. Thus using a non-physical model allows us to more freely sample the shape of the counts and then, in the future, determine what type(s) of physical models and populations could result in a similar shape.

However, if the underlying region were simply a power-law with a nearly constant power-law index in that region, than a model which allowed for more departure from that would not necessarily result in a significant improvement in the fitting simply due to the addition of the extra parameters.

One would still like to be able to constrain the shape of the count in more detail over different intervals of flux density. With the modified power law, the fit parameters are not very sensitive to the region $S \leq \sigma_n$, even though there is still information in the image at these faint flux densities. This model also does not allow us to investigate the faintest limits for which constraints are still possible. Therefore, we have followed the approach of Patanchon et al. [138] and Glenn and e.a. [73] and fit a phenomenological parametric model of multiple joined power laws, allowing for more variation in the shape of the count. In this approach we fix the position in $\log_{10}(S)$ of a fixed number of nodes, and fit for the node amplitude of $\log_{10} dN/dS$. Between the nodes the count is interpolated in log space to ensure a continuous function, with the count outside the highest and lowest nodes set to zero. The node amplitudes do not actually represent the value of dN/dS at the positions of the nodes, but rather represent an integral constraint on some region surrounding the node. Therefore, the best-fit position of any given node depends not only on the underlying source count but also on the number, or spacing, of the nodes, and also the type of interpolation used between the nodes.

4.4.2 Node Model

The choice of the number and position of the nodes is somewhat subjective. There need to be enough nodes across the flux-density range to be able to account for changes in the underlying count, and the choice is also influenced by the resulting uncertainties on the parameters. The fits of the node positions are degenerate; neighbouring nodes will be most strongly correlated, and so, adding too many nodes will increase the correlations and parameter degeneracies. We examined trials using five, six, and eight nodes. We found that there was no significant change in the $\Delta\chi^2$ with the total of eight nodes, and with six the results were most consistent over repeated trials. Comparison of the results with different number of nodes can be seen in Fig. 4.5; based on this, we decided to fit six nodes, spaced roughly

evenly in $\log_{10} S$. The value of the faintest node is to be considered only as an upper limit, since the code cannot distinguish between low amplitude values and zero. Therefore, the situation is effectively that we fit five well constrained nodes and one upper limit. In the $P(D)$ calculation we also considered two additional brighter nodes at fixed dN/dS values. The highest node is far above any source in our field, and it was found that changing its value during $P(D)$ calculation had no effect on the output. The second highest is also in a very sparsely populated flux density area for our image (only one source brighter). These two node positions are in a well-constrained range of the 1.4 GHz source count, so rather than fitting for these nodes their values were estimated from existing 1.4 GHz source counts, scaled to 3 GHz using $\langle \alpha \rangle = -0.7$. Adding these extra nodes is essentially the same as adopting a prior on the brightest count region considered.

The positions for the six nodes were chosen through trial and error. We found that the results were not sensitive to a faintest node below -7.3 , in $\log_{10}(S)$, and thus this position was chosen for the lowest node. For the second faintest node, we found that any nodes placed in the region between the faintest and $\sim 0.25\sigma_n$ were difficult to constrain and very degenerate for more than one in that region. We therefore chose to place the second node at about a quarter of the instrumental noise, which produces reasonably robust constraints. As far as the spacing between the second and sixth nodes, the requirements are to have fairly evenly spaced nodes in $\log_{10}(S)$, while still having at least one node in the μJy region, one near the Owen & Morrison (2008) flux density limit, and one between that and the fixed node near our brightest flux density. We ended up with four nodes (three power laws) encompassing the region from 0.2 to $17.2\,\mu\text{Jy}$, fully covering the region fit in Condon et al. [37] and the Owen & Morrison (2008) sources. Although the node placement was fixed, to make sure that the precise positions did not bias the results we also ran chains at ± 0.1 in $\log_{10} S$ of the centre nodes, the results of which can also be seen in Fig. 4.5. Since no discernible difference was observed when varying the positions, for the rest of the analysis the centre positions were adopted.

Since the source count comes from a redshift integral over luminosities, the count must be continuous between S_{\min} and S_{\max} . S_{\max} is set by the flux density of the brightest node, 0.0126 Jy, which, as above, was chosen to be brighter than any source in our image, but not so bright as to greatly increase the range (so

that our bin size could be kept as small as possible). S_{\min} in our case is set by the number of bins, and is thus $0.0126/2^{18} = 0.04 \mu\text{Jy}$. Since we are fitting for nodes at only a few positions, it is necessary to interpolate the count between the nodes. As well as using linear interpolation (multiple power laws), we considered a cubic spline model, with the cubic spline interpolation done in $\log_{10} dN/dS$ and $\log_{10} S$. We ran chains using both models while keeping other variables fixed, and compared the output, which can be seen in Fig. 4.5. The comparison is not straightforward, since the values at each node do not have exactly the same meaning, being effectively integral constraints over different flux density regions. However, the two methods produce very similar results: the marginalised means are almost exactly the same, but the uncertainties in the fainter regions are larger for the cubic spline model. For simplicity we decided to use the power-law model for the rest of the analysis.

Some additional constraints on the fitting parameters were applied to ensure physically reasonable results. A prior on the background temperature from the integrated count was used. It was set as a cut-off, such that any count model yielding a temperature greater than 95 mK at 3 GHz was not considered. This was imposed to allow the count to produce (but not overproduce) the background temperature seen by ARCADE 2 of around 70 mK. This is a very weak prior, and hence very reasonable to impose, as it not only exceeds the ARCADE 2 value but also greatly exceeds previous source count temperature estimates of 13 mK. It is important to set some limit on the amplitude of the faintest nodes, where the data constraints are weakest. For the brighter nodes, a starting estimate of the count was given by approximating known source counts around the node at 1.4 GHz scaled to 3 GHz. High and low cut-offs were placed on the nodes, limiting the region to be sampled. These were chosen based on the observed high and low count values in the region around the node measured using the compilation of 1.4 GHz source counts from de Zotti et al. [42], scaled to 3 GHz. For the nodes fainter than the current cut-off as set by Owen and Morrison [134], starting estimates were based on the scaled Condon (1984) model at 1.4 GHz. Limits were placed on the sampling space by extrapolating two lines (in log-log space) from the current cut-off, one with a positive slope and one a negative slope. The extreme allowed values for the last node, at $\sim 0.05 \mu\text{Jy}$, were 20 and 14 (in $\log_{10}[dN/dS]$). This yielded a wide area to be

sampled in a region where no previous information existed.

It is very important to have an accurate value for the instrumental noise in this calculation, because it convolves the noise-free $P(D)$ distribution. Unless $\sigma_n \ll \sigma_c$, then small changes in σ_n can have a significant effect on the output, particularly in the faint flux density regime. Our estimate for the confusion noise is roughly the same as our estimate of the effective instrumental noise inside the 5 arcmin ring, $\sigma_c = 1.2 \simeq \sigma_n^* = 1.255$. Since our noise estimate comes from a weighted average of the instrumental noise of the 16 frequency sub-band images, and then a weighted average of the noise after primary beam correction, any errors in the measurement or calculation of those would affect our calculated noise value. To allow for the possibility of uncertainty in our noise value we performed the MCMC $P(D)$ fitting with: (1) the noise fixed at the calculated values for σ_n^* for each model; and (2) allowing the noise to be a free parameter. In this latter case the calculated noise value was given as a starting estimate for the fitting and we allowed a sampling range of $(1.255 \pm 0.05) \mu\text{Jy beam}^{-1}$.

In the modified power-law case the marginalised mean for the noise is $\sigma_n^* = 1.268 \pm 0.005$, while the node-based model gives a marginalised value of $\sigma_n^* = 1.250 \pm 0.006$. These are consistent with the original estimate of $1.255 \mu\text{Jy beam}^{-1}$. The results of fitting with the noise being variable versus fixed can be seen in the bottom left panel of Fig. 4.5. The noise parameter is strongly degenerate with the faintest two node amplitudes. These nodes do not contribute much to the bright tail of the $P(D)$, but mainly affect its width. This explains why, for the variable noise case, the faintest two nodes are slightly higher than in the fixed noise case, since the fitted σ_n^* is smaller. For both models the fixed and variable noise results are consistent within uncertainties. For the rest of the analysis only the fixed noise results are used.

In terms of the multiple noise zones, the three zones were all fit independently; the results are shown in Fig. 4.5. We also fit all three zones simultaneously, such that the fit χ^2 was a sum of the individual χ^2 's. So in this case we minimized

$$\chi_{\text{total}}^2 = \sum_i \chi_i^2, \quad (4.8)$$

where χ_i^2 is the χ^2 of eq. (4.6) from each zone for a given set of input model

parameters. The results presented in Section 4.5 report the fitting of just the first zone (with the lowest noise) and the three zones together ,for both the modified power-law model and the node-based model.

4.5 Discrete Source Count Fitting Results

4.5.1 Estimated Number Counts

For all the models investigated here we report the means from the marginalised parameter likelihood distributions for the variable parameters and any derived parameters. This is done both for fitting just the first noise zone and for fitting all three zones simultaneously. The limits listed are 68 per cent (upper and lower) confidence limits for the marginalised means, except for the first node which is only an upper limit. We can also compare these results with the single power-law best-fit from Condon et al. [37] and with a compilation of known source counts from de Zotti et al. [42]. The confusion noise is measured from the noiseless $P(D)$ distribution (eq. (3.4) with the noise term set to zero). Calculating the standard deviation is not an accurate way of finding σ_c , since it is such a skewed distribution. Instead we found the median and D_1 and D_2 such that

$$\sum_{D_1}^{\text{median}} P(D) = \sum_{\text{median}}^{D_2} P(D) = 0.34 \quad (4.9)$$

when normalised such that the sum of the $P(D) = 1$, since in the Gaussian case 68 per cent of the area is between $\pm 1\sigma$. Then we took $\sigma_c = (D_2 - D_1)/2$. The confusion noise values for the different models are listed in Tables 4.1 and 4.2. The value estimated from the single power-law fit in Condon et al. [37] is $1.2 \mu\text{Jy beam}^{-1}$, in the middle of our range of $1.05 \leq \sigma_c^* \leq 1.37 \mu\text{Jy beam}^{-1}$.

The MCMC fitting was first run with the modified power-law model. The results from these runs are listed in Table 4.1, with the fits scaled to 1.4 GHz plotted in Fig. 4.6. The data and model $P(D)$ distributions can be seen in Fig. 4.7, along with the noise distributions and model noiseless $P(D)$ distributions. Above about $3 \mu\text{Jy}$ all the fits are consistent. Below this the results from fitting the three noise zones simultaneously fall off faster than the fits from the first noise zone alone.

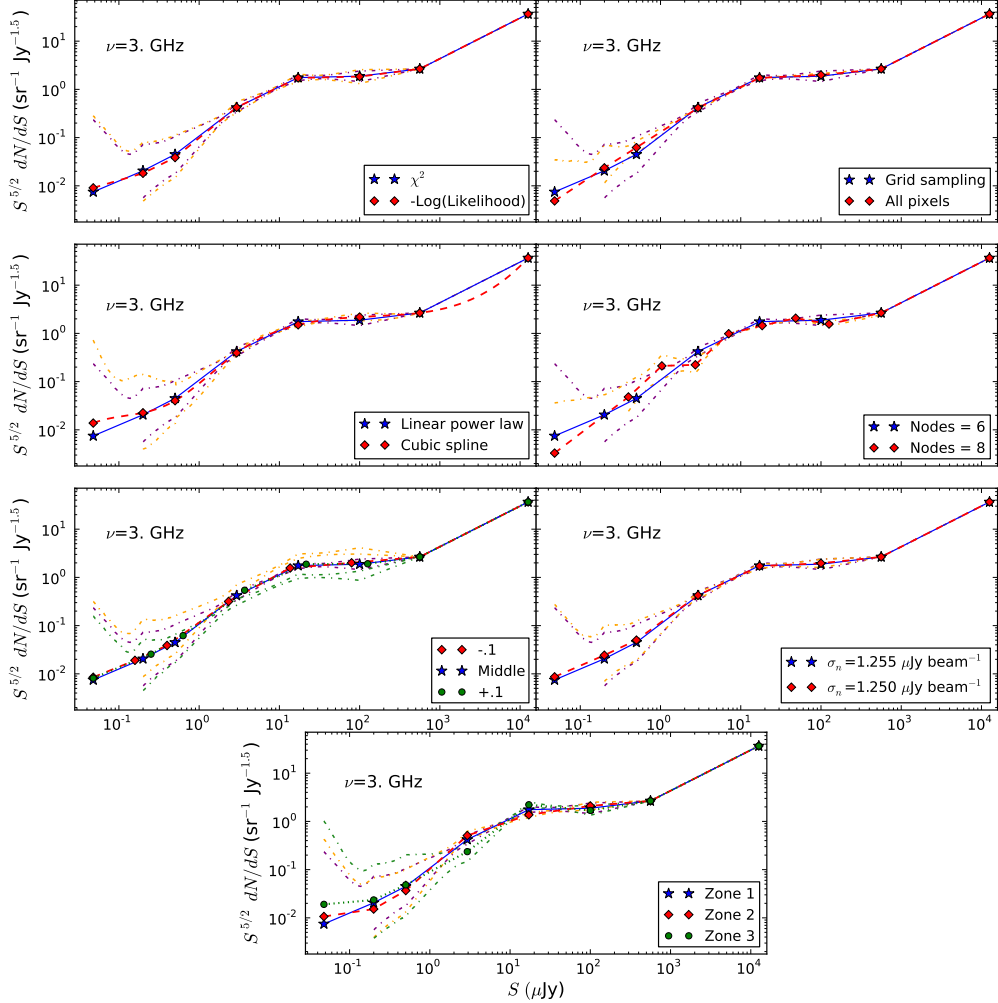


Figure 4.5: Comparison of MCMC output for source counts with different settings. Points are best-fitting amplitudes and dot-dashed lines represent the 68% confidence regions. The blue solid line is the same in all plots and is the best-fit for zone 1 reported in Section 4.5 (Model 1), the red-dashed and green dotted lines are comparisons (Model 2 and Model 3). Top left: Model 1 is fit with $\chi^2/2$, Model 2 is fit with the $\log\mathcal{L}$. Top right: Model 1 is the gridded pixel histograms, and Model 2 is all pixels. 2nd row left: Model 1 uses linear interpolation in $\log_{10}(S)$, while Model 2 uses cubic spline. 2nd row right: Model 1 has six nodes and Model 2 has eight. 3rd row left: Model 1 is run with initial positions S_{centre} , Model 2 has positions $\log_{10}(S_{\text{centre}}) - 0.1$ and Model 3 has $\log_{10}(S_{\text{centre}}) + 0.1$. 3rd row right: Model 1 is fixed noise of $1.255 \mu\text{Jy beam}^{-1}$ and Model 2 allows the noise to float. Bottom: Model 1 is noise zone 1, Model 2 is noise zone 2, and Model 3 is noise zone 3.

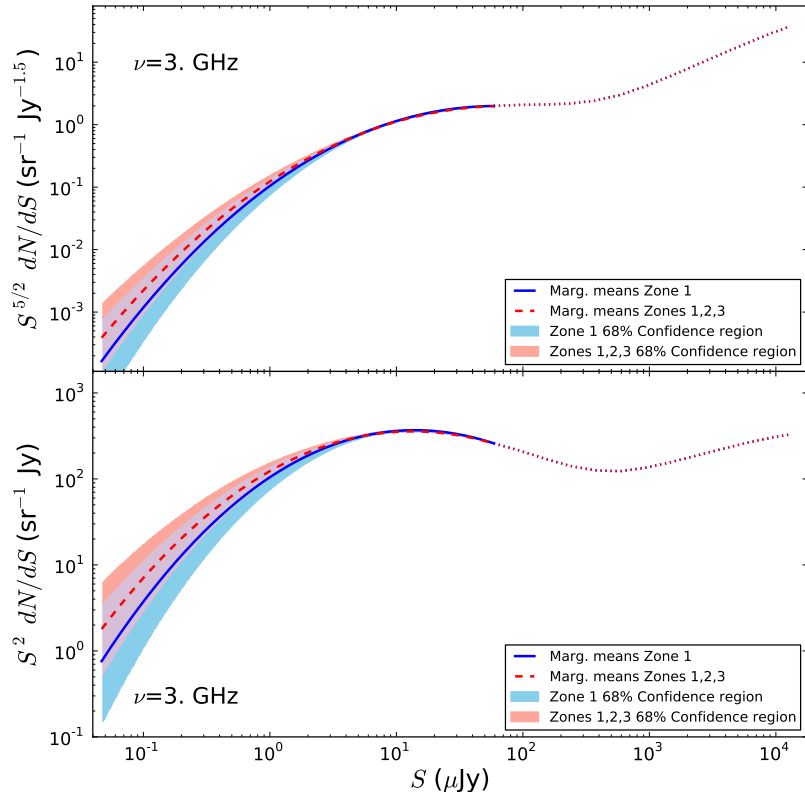


Figure 4.6: Source count at 3 GHz from MCMC fitting of the modified power-law model from eq. (4.7). Lines are from the marginalised means of the parameters of eq. (4.7) (red dashed is from all three zones, i.e. out to 10 arcmin, while blue solid is from zone 1, i.e. 5 arcmin). The dotted lines is where the model was fixed to the values of the Condon (1984) model. The shaded areas are 68 per cent confidence regions. The top panel uses the Euclidean normalisation, while the bottom panel has the S^2 normalisation.

Table 4.1: Marginalised fits for the modified power law in eq. (4.7) at 3 GHz.

The quoted uncertainties are 68 per cent confidence intervals. For the combined fit we treat each zone separately, and hence the number of degrees of freedom is approximately 3 times higher.

Noise zones	1	1, 2, 3
Parameter	Marginalised means	Marginalised means
α	$-4.5^{+1.3}_{-1.3}$	$-4.7^{+1.2}_{-1.2}$
β	$-0.17^{+0.25}_{-0.25}$	$-0.16^{+0.25}_{-0.25}$
γ	$0.012^{+0.017}_{-0.017}$	$0.016^{+0.016}_{-0.016}$
$\log_{10}(\kappa)$	$-4.34^{+1.3}_{-1.3}$	$-5.01^{+1.2}_{-1.1}$
$\sigma_c (\mu\text{Jy beam}^{-1})$	$1.122^{+0.009}_{-0.009}$	$1.068^{+0.008}_{-0.008}$
χ^2	87.3	160.3
N_{dof}	59	149

The results for the node-based model are listed in Table 4.2. The slopes and normalisation constants for the interpolated power laws between the nodes, of the form $dN/dS = kS^\gamma$, are listed in Table 4.3. The source counts from these models are plotted in Fig. 4.8 and the $P(D)$ distributions are shown in Fig. 4.9. The χ^2 values are lower than in the modified power-law model, though the χ^2 values for all four model fits are reasonably consistent with N_{dof} the number of bins minus the number of fit parameters. The models are consistent with each other, except for $S \leq 1 \mu\text{Jy}$, where the node-based model falls off more slowly. The modified power law has the advantage of being a single continuous function, as well as having less fit parameters. However, the node-based model allows for a larger range of possibilities than the modified power law and is much more sensitive to the count below the noise level, as it is able to fit that region with little to no effect on the brighter values. With this model, the count for the one-zone case is above those from the three-zone case in the faint region, although the marginalised means are almost identical.

4.5.2 Parameter Degeneracies

The values of the parameters are highly correlated, particularly between adjacent nodes where the correlation is negative. This means that the errors on the number count parameters will also be correlated, giving non-Gaussian shapes to some of

Table 4.2: Marginalised mean amplitudes for the six fit nodes and two fixed nodes at 3 GHz, given separately for the deepest noise zone and for all three noise zones fit simultaneously. The brightest two nodes were fixed to values estimated from known counts at 1.4 GHz and scaled to 3 GHz using $\langle \alpha \rangle = -0.7$.

Noise Zones	1	1, 2, 3
Node μJy	Marginalised means $\log_{10}[\text{sr}^{-1} \text{ Jy}^{-1}]$	Marginalised means $\log_{10}[\text{sr}^{-1} \text{ Jy}^{-1}]$
0.05	$16.17^{+1.69}$	$15.79^{+1.20}$
0.20	$15.06^{+0.56}_{-0.56}$	$15.05^{+0.45}_{-0.43}$
0.50	$14.43^{+0.38}_{-0.40}$	$14.43^{+0.20}_{-0.20}$
2.93	$13.45^{+0.09}_{-0.09}$	$13.48^{+0.03}_{-0.03}$
17.2	$12.16^{+0.06}_{-0.06}$	$12.11^{+0.02}_{-0.02}$
100	$10.27^{+0.11}_{-0.11}$	$10.35^{+0.02}_{-0.02}$
572	8.55	8.55
12600	6.32	6.32
$\sigma_c (\mu\text{Jy beam}^{-1})$	$1.283^{+0.006}_{-0.007}$	$1.266^{+0.003}_{-0.003}$
χ^2	54.8	153.05
N_{dof}	59	149

Table 4.3: Slopes and normalisation constants for the interpolated power laws between the nodes, of the form $\frac{dN}{dS} = kS^\gamma$ at 3 GHz.

Noise Zones	1		1, 2, 3	
Between Nodes (μJy)	γ	$\log_{10} k_{3\text{GHz}}$	γ	$\log_{10} k_{3\text{GHz}}$
0.05–0.20	-1.79	3.05	-1.19	7.06
0.20–0.50	-1.65	4.01	-1.55	4.69
0.50–2.90	-1.23	6.63	-1.25	6.57
2.93–17.2	-1.69	4.09	-1.78	3.63
17.2–100	-2.46	0.43	-2.30	1.15
100–560	-2.29	1.08	-2.40	0.75
572–12600	-1.66	3.16	-1.66	3.16

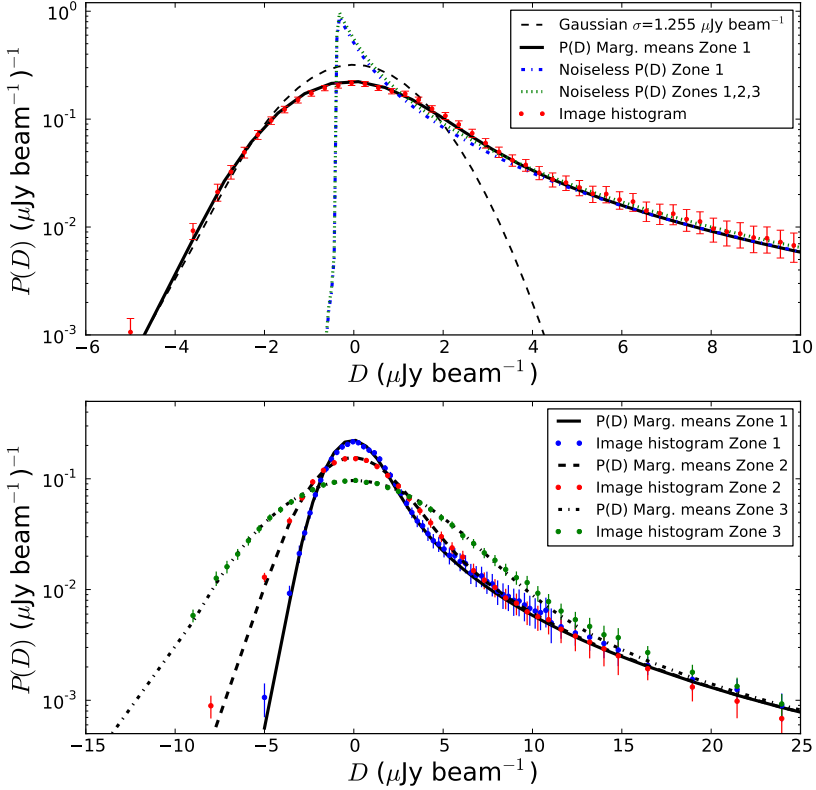


Figure 4.7: Comparison of 3 GHz pixel histograms (red dots) with the marginalised means model $P(D)$ for zone 1 only (top panel) and models for all three zones (bottom panel) using a modified power-law input model. The dashed line is Gaussian noise of $\sigma = 1.255 \mu\text{Jy beam}^{-1}$. The noiseless $P(D)$ for each model is shown by the blue dot-dashed line for the one zone fit and the green dotted line for the three zone fit.

the joint likelihoods of the two parameter distributions. Sources at a given flux density contribute to many different $P(D)$ pixel values when convolved with the beam. This means that some sources could be effectively moved from one flux density bin to another, still retaining the same shape for the resulting histogram. This is illustrated in the confidence regions plotted with the source counts (see Fig. 4.5). Instead of being straight power laws from one parameter's upper limit to the next, the confidence regions tends to “bow” inwards between the two nodes; as

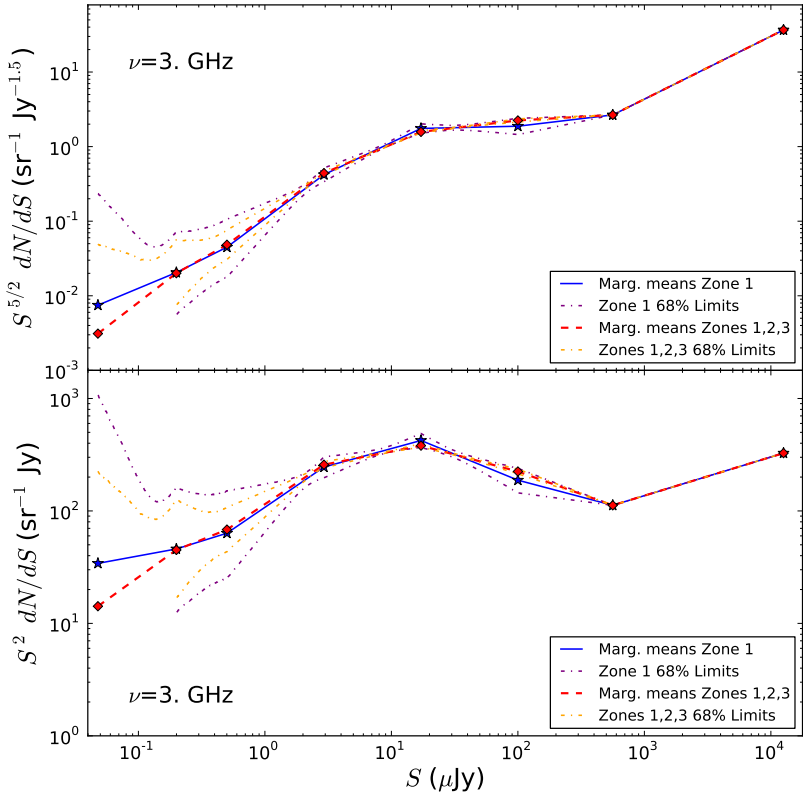


Figure 4.8: Source count at 3 GHz from MCMC fitting of the node-based model using six free nodes and two fixed nodes. Points and corresponding lines are the node marginalised means, with the red dashed line being from all three noise zones (out to 10 arcmin), while the blue solid line is from one zone (5 arcmin). The dot-dashed lines are 68 per cent confidence regions (purple for Zone 1, orange for all three zones). The top panel uses the Euclidean normalisation, while the bottom panel has the S^2 normalisation indicative of contribution to the background temperature.

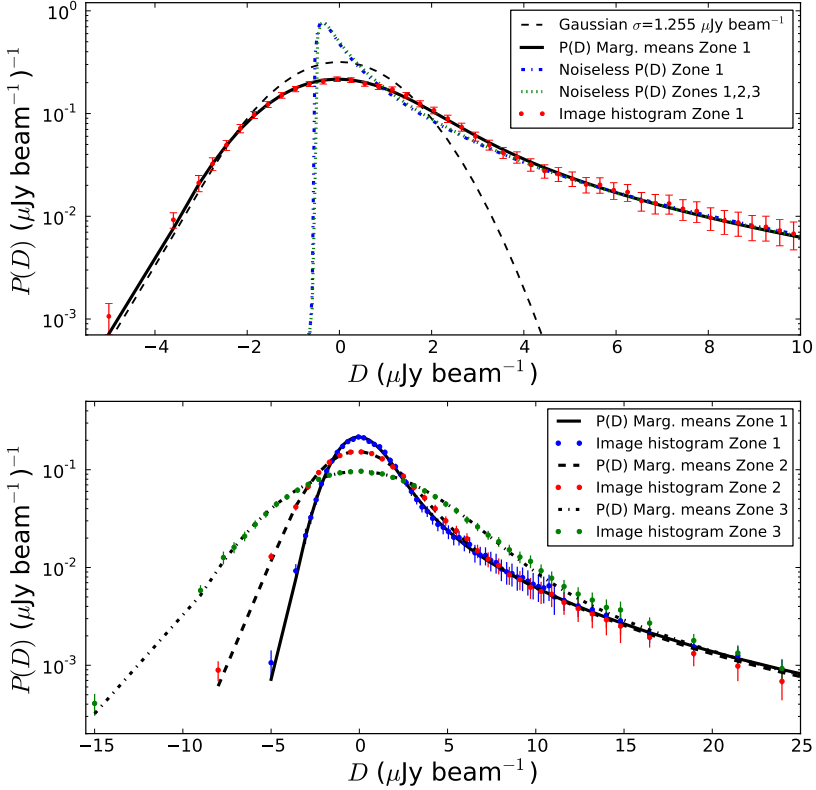


Figure 4.9: Comparison of 3 GHz pixel histograms (red dots) with the marginalised means model $P(D)$ for Zone 1 only (top panel) and models for all three zones (bottom panel) for the node-based input model. The dashed line is Gaussian noise of $\sigma = 1.255 \mu\text{Jy beam}^{-1}$. The noiseless $P(D)$ for each model is shown by the blue dot-dashed line for the one zone fit and the green dotted line for the three zone fit.

one node amplitude is raised the amplitude of the neighbours must decrease. This degeneracy is strongest for the fainter flux densities, as they are not only degenerate with neighbouring nodes, but also with the instrumental noise.

The Pearson correlation matrix for the two cases is listed in Table 4.4, and the 2D likelihood distributions are shown in Fig. 4.10. The degeneracy means that adding more nodes in the fainter regions does not improve the fit. We would require lower instrumental noise, as well as increased resolution, to benefit from

Table 4.4: Correlation matrix for parameters. Coefficients are computed for fitting all three zones (upper triangle) and just zone one (lower triangle), following the definition $C_{ij} = \sum_r p_i p_j / \sqrt{\sum_r p_i^2 \sum_r p_j^2}$, where p_i and p_j are parameter numbers i and j , and r is the realization number.

Node (μJy)	0.05	0.20	0.50	2.90	17.2	100
0.05	1.00	-0.16	-0.17	0.02	0.03	0.01
0.20	-0.23	1.00	0.35	-0.28	0.15	-0.11
0.50	-0.26	0.66	1.00	-0.64	0.33	-0.19
2.93	0.01	-0.44	-0.61	1.00	-0.78	0.44
17.2	0.03	0.25	0.31	-0.79	1.00	-0.72
100	0.01	-0.11	-0.14	0.37	-0.68	1.00

extra nodes.

4.5.3 Background Temperature

Using eq. (1.6) we are able to obtain estimates for the discrete-source contribution to the background temperature from our results. Integrating the MCMC output at each step in the chains allows us to look at the distribution of temperatures. Fig. 4.11 shows the histograms obtained from the modified power-law fitting for both noise zone cases at 3 GHz, as well as scaled to 1.4 GHz; the same is shown in Fig. 4.12 for the node-based model. For the modified power-law fits we integrated over the flux density range $0.05 \leq S (\mu\text{Jy}) \leq 60$ and used the values from the Condon (1984) model for $60 < S (\mu\text{Jy}) < 10^9$. For the node-based model the fit results were used in the range $0.05 < S (\mu\text{Jy}) < 1.26 \times 10^4$ and the Condon (1984) model for $1.26 \times 10^4 < S (\mu\text{Jy}) < 10^9$.

The outputs obtained from the MCMC fitting allow us to compute 68 per cent confidence intervals for each distribution, as well as the means, medians, peaks, and values from the source counts from the marginalised means from each parameter. These values are listed in Table 4.5. The values from the different models and noise settings are all consistent. These yield a background temperature of around 14.5 mK at 3 GHz, corresponding to 115 mK at 1.4 GHz. The distributions from the node-based models tend toward higher values and have more elongated tails. Because of this skewness, the 68 per cent confidence limits for these two distribu-

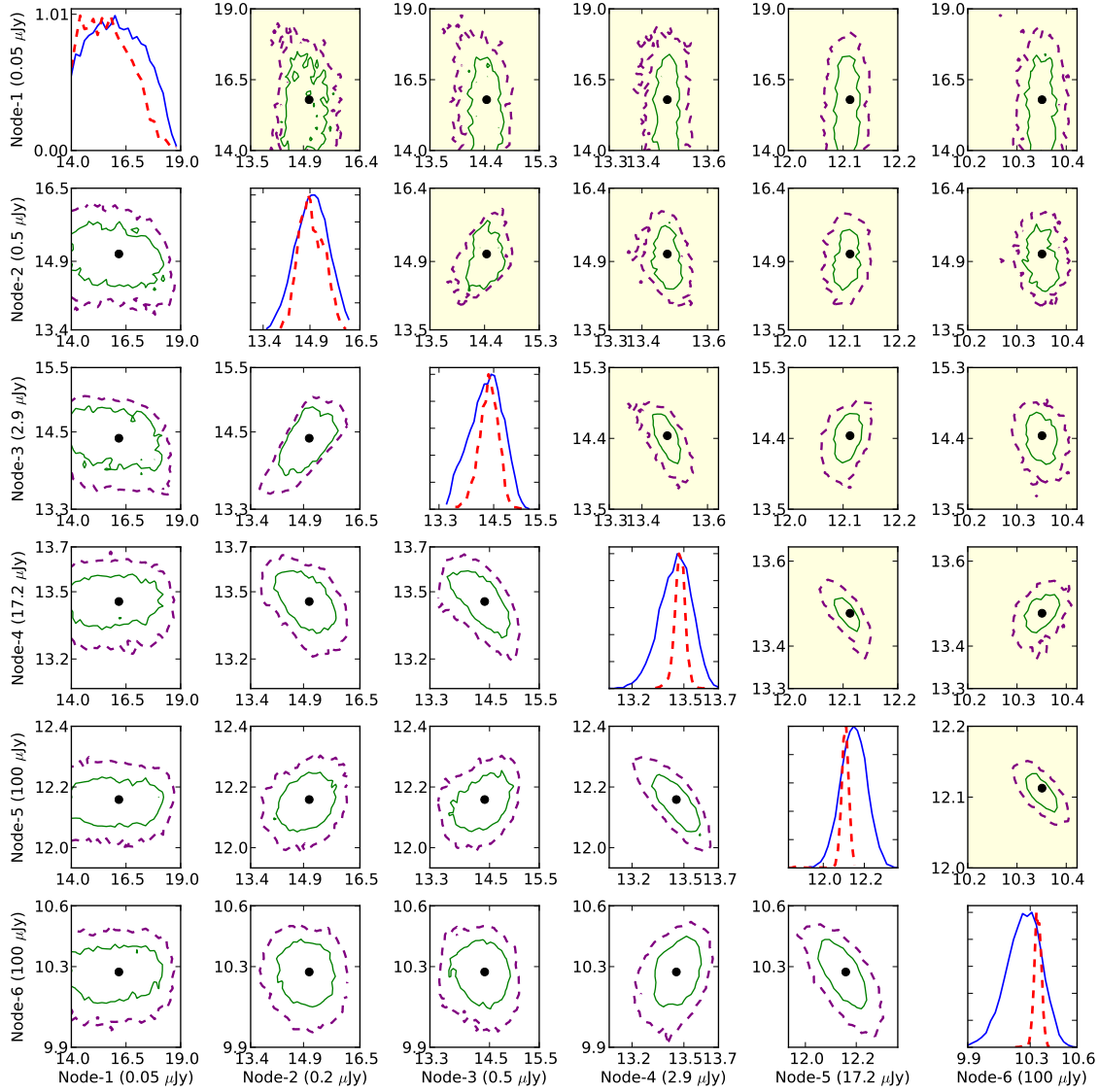


Figure 4.10: One and two dimensional likelihood distributions for the six fit nodes. The upper triangle 2D plots (yellow background) are for the three noise zone fits and the lower triangle 2D plots are the one noise zone fits. The 1D plots show the marginalised likelihood distributions for those nodes with three noise zones (red dashed line) and one noise zone (blue solid line). For the 2D plots the contours are 68 (green solid) and 95 per cent (purple dashed) confidence limits. The black dots show the positions of the marginalised means. Parameter units for each plot are $\log_{10}[\text{sr}^{-1}\text{Jy}^{-1}]$.

Table 4.5: Radio background temperatures from integration of the source counts using eq. (1.6).

Model	Node model				Modified power-law model			
	3.0	3.0	1.4	1.4	3.0	3.0	1.4	1.4
Frequency (GHz)	3.0	3.0	1.4	1.4	3.0	3.0	1.4	1.4
Zones	1	1, 2, 3	1	1, 2, 3	1	1, 2, 3	1	1, 2, 3
Peak (mK)	14.6	14.6	115.8	116.3	13.1	13.4	104.7	106.1
Median (mK)	14.9	14.7	118.7	117.3	13.3	13.4	106.4	106.9
68% Lower Limit (mK)	14.4	14.4	115.5	115.5	13.1	13.2	103.9	104.9
68% Upper Limit (mK)	16.4	15.3	127.7	121.5	13.9	13.8	110.4	109.9
marginalised Fit (mK)	14.9	14.8	109.2	111.7	13.5	13.4	107.7	106.8

tions are computed from the median instead of the mean. This skewness is simply due to the fact that this model allows for more possible values in the faintest region, letting the faintest node rise to higher amplitudes, thus affecting the integrated temperature.

4.6 Discrete Emission Discussion

4.6.1 Image Artefacts

This $P(D)$ fitting technique assumes that the instrumental noise is Gaussian distributed and well characterised. In practice our image noise is very nearly Gaussian, with the highest contamination from dirty beam sidelobes being only about $0.1 \mu\text{Jy beam}^{-1}$. There is, however, another effect that contributes to the shape of the histogram: it appears to have a tail of excess negative flux density pixels and thus does not drop off in a purely Gaussian way on the negative side. Visual inspection of the image reveals that the pixels responsible (with values $> 5\sigma$, even considering the primary beam correction) are all clustered around the brightest two sources, with almost all of them around the brightest source in the image which is about 7 mJy, right at the edge of the 5 arcmin ring.

It is clear that this is an artefact caused by the imaging and cleaning process, or by asymmetry in the antenna pattern. The VLA antennas use alt-az mounts which cause the antenna pattern to rotate on the sky with parallactic angle. The support legs for the secondary introduce asymmetries in the antenna pattern, which, when

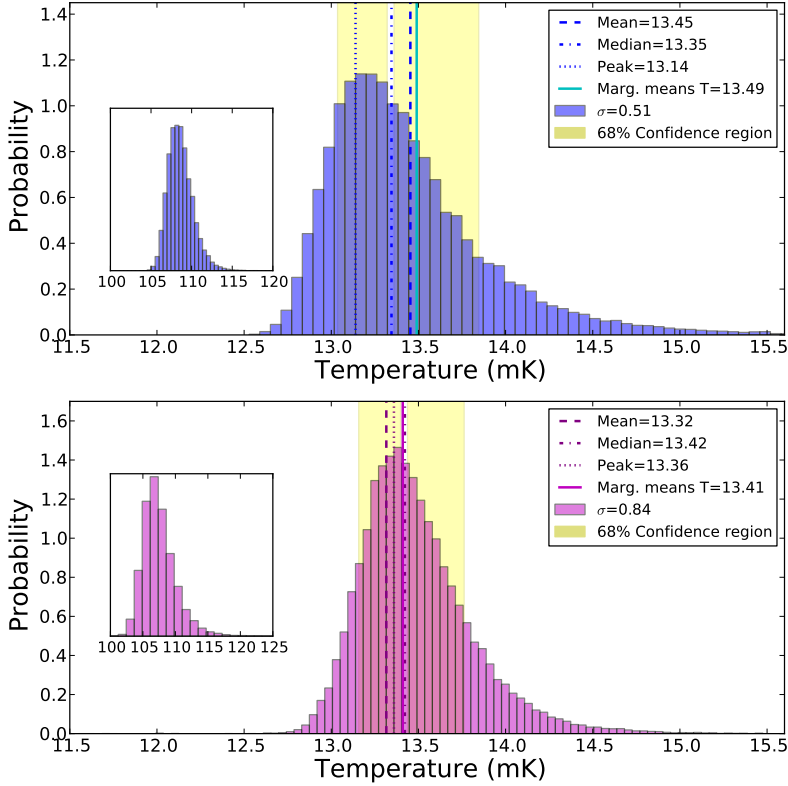


Figure 4.11: Normalised histogram of radio background temperatures at 3 GHz from integrating each step in the MCMC according to eq. (1.6) using the *modified power-law model*. The top panel comes from just fitting noise Zone 1, while the bottom panel is from fitting for all three noise zones. Insets are temperature histograms at 1.4 GHz made by scaling the 3 GHz chains with $\langle \alpha \rangle = -0.7$.

combined with the rotation with parallactic angle, cause sources away from the pointing centre to appear variable. This in turn causes areas of negative excess pixels around brighter sources. The effect gets stronger with distance from the field centre, with increasing frequency, and source brightness. When examining the 16 sub-band images it does seem that this effect increases in strength with frequency. However, it is difficult to say if this is truly the cause, as beyond 5 arcmin there are very few bright sources. To be able to remove this effect we would need detailed

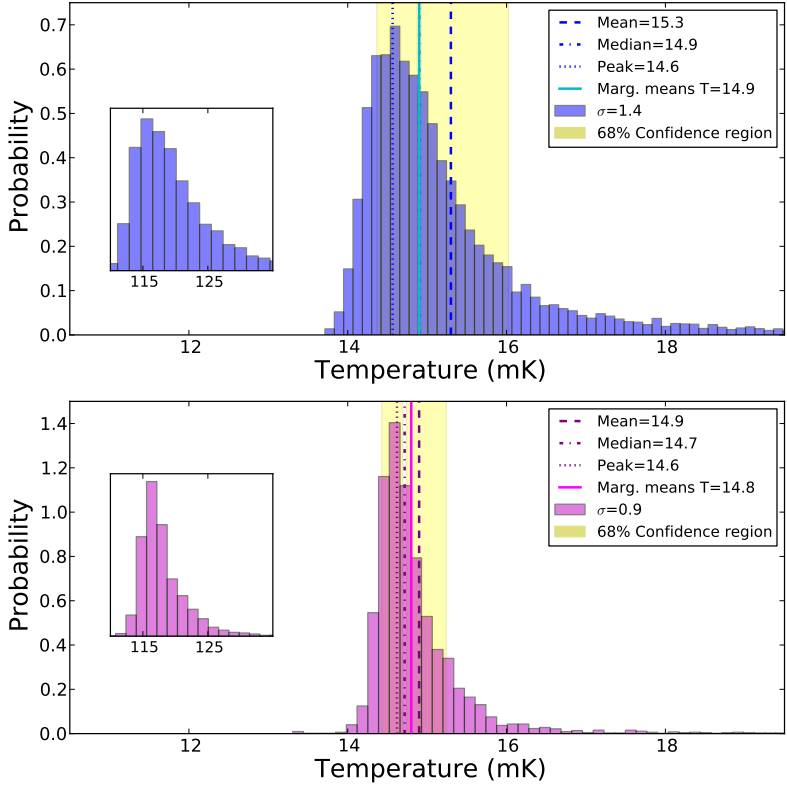


Figure 4.12: Normalised histogram of radio background temperatures at 3 GHz from integrating each step in the MCMC according to eq. (1.6) using the *node-based model*. The top panel comes from just fitting noise Zone 1, while the bottom panel is from fitting for all three noise zones. Insets are temperature histograms at 1.4 GHz made by scaling the 3 GHz chains with $\langle \alpha \rangle = -0.7$.

measurements of the antenna beam pattern at S-band. Such measurements have not yet been made; we hope that future imaging will be able to correct for artefacts of this type.

With the current data the presence of this negative tail seriously affects the MCMC fitting. Since there is a large deviation from the predicted $P(D)$ calculation with Gaussian noise, attempting to fit the entire histogram gives too broad a distribution, and too low a peak. The fitting procedure inflates the faintest (and

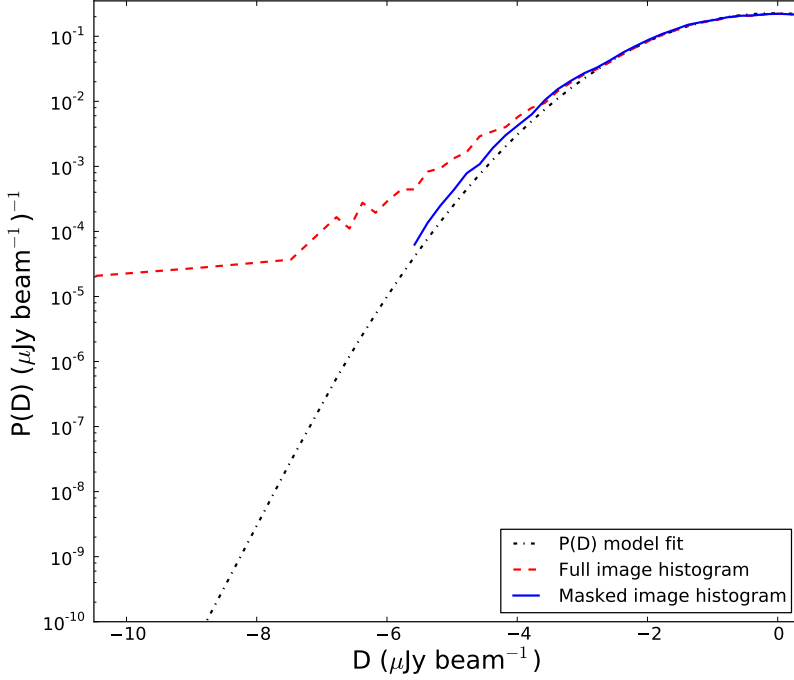


Figure 4.13: Negative flux-density region of the $P(D)$ distribution. The red dashed line is from the full histogram of the data. The black dot-dashed line is from the marginalised mean node parameters from the MCMC fitting. The blue solid line shows the image histogram after masking.

possibly second faintest) node to higher amplitudes to achieve this. Without being able to correct or model the antenna pattern we simply masked out the negative pixels around the 7 mJy source and a smaller region near a second (1 mJy) source. This decreased the total number of pixels used by about 0.2 per cent. We also masked the negative pixels in the second noise zone around this source, decreasing its number of pixels by 0.07 per cent.

The negative side of the image $P(D)$ can be seen in Fig. 4.13. Red points indicate the image values, while the black line is the $P(D)$ model using the node values from the first noise zone fitting. The blue line shows the image values after masking out the negative regions. Tests run on the masked and unmasked versions clearly show that the masking has no effect on any nodes other than the first two,

which become artificially inflated in the unmasked fitting. Thus we feel justified in performing the masking. All of the results presented in Section 4.5 were fit using the masked images.

4.6.2 Weighting

New data reduction and imaging challenges arise from the 2 GHz bandwidth of the VLA at S band. Across this bandwidth there are substantial changes in the synthesised beam size and the primary beam, as well as source flux-density changes due to the spectral dependence. In our particular case each sub-band was imaged independently (although cleaned simultaneously), with weighting and taper factors applied during cleaning to force the synthesized beams to be the same size. In the narrow-band case changes due to the frequency bandwidth are usually small and thus weighting to produce an image at the centre frequency of the band does not usually need to include any spectral dependence. With wide-band data this type of weighting scheme would maximize signal to noise only for sources with $\langle \alpha \rangle = 0$. Instead one could perform a weighted fit of the spectral dependence in each pixel of the 16 sub-band images, correct for the primary beam spectral dependence at the distance of each pixel from the centre, and use that value to calculate the flux density at the centre frequency. However, this requires having enough signal-to-noise in each pixel to obtain an accurate fit. The weighting scheme we used was

$$W_i(\rho, \nu_i) \propto \left[\frac{\nu_c^{\langle \alpha \rangle}}{\sigma_{ni} A(\rho, \nu_c)} \right]^2, \quad (4.10)$$

where i labels the sub-bands, σ_{ni} is the noise in each sub-band image, and $A(\rho, \nu_c)$ is the primary beam value at pixel distance ρ and sub-band frequency ν_i . Using these weights the 3-GHz pixel values were given by

$$b_{\text{3GHz}}(\rho) = \sum_{i=1}^{16} [b_i(\rho) W_i(\rho)] \Bigg/ \sum_{i=1}^{16} W_i(\rho), \quad (4.11)$$

with b_i being the pixel brightness in the i th sub-band. This combination is designed to maximize the signal-to-noise ratio for sources with $\langle \alpha \rangle = -0.7$, the average spectral index for faint sources in this frequency range [e.g. 31].

However, it is possible that this choice of weighting scheme might have affected our $P(D)$ results. To test this we created two new wide-band images with different weightings applied. One image was made using $\langle \alpha \rangle = -0.45$ and one with $\langle \alpha \rangle = -0.95$. The MCMC fitting was rerun on both of these images, leaving the noise as a free parameter, since changing the weighting could have also affected the noise level. The marginalised mean values for the noise are $\sigma_n^* = 1.259 \mu\text{Jy beam}^{-1}$ for $\langle \alpha \rangle = -0.45$ and $\sigma_n^* = 1.245 \mu\text{Jy beam}^{-1}$ for $\langle \alpha \rangle = -0.95$. The results of the MCMC fitting can be seen in Fig. 4.14, compared with the $\langle \alpha \rangle = -0.7$ case with variable noise. There is very little difference in the fits. The largest fractional difference between the marginalised fits is still only 0.6 per cent for the third node between the -0.7 and the -0.95 cases. Therefore, it does not appear that the spectral dependence of the weighting has a significant effect on the output.

4.6.3 Comparison to Other Estimates

Condon et al. [37] found that the best-fit slope for a single power-law in the μJy region was $\gamma = -1.7$. It was noted that at the fainter end a shallower slope of $\gamma = -1.5$ or -1.6 might be better. Looking at the slopes between our fit nodes and the earlier result, we have three power-law sections that cover this region: between the second and third nodes corresponds to the region $0.2 \leq S(\mu\text{Jy}) \leq 0.5$; between the third and fourth nodes is the region $0.5 \leq S(\mu\text{Jy}) \leq 2.9$; and between the fourth and fifth nodes is the region $2.9 \leq S(\mu\text{Jy}) \leq 17.2$. The slopes for these regions can be seen in Table 4.3. For the faint part of the region our slopes range from -1.23 to -1.65 , while for the brighter part they range from -1.69 to -1.78 . The new results therefore agree well with a -1.7 slope for the brighter part of the μJy region and do seem to suggest a shift to a shallower slope in the μJy regime. Our χ^2 value of 153.0 for $N_{\text{dof}} = 149$ over the full 10 arcmin is lower than those we obtain with a single-slope model of slope -1.7 , where $\chi^2 = 249.1$ for $N_{\text{dof}} = 153$ (or a slope of -1.6 , which gives $\chi^2 = 292.3$). By using the node-based model instead of the single power-law model the improvement in the fit yields $\Delta\chi^2 = 96.1$, which is a highly significant improvement for 149 degrees of freedom.

Condon [31] used the local luminosity function to constrain the epoch-dependent

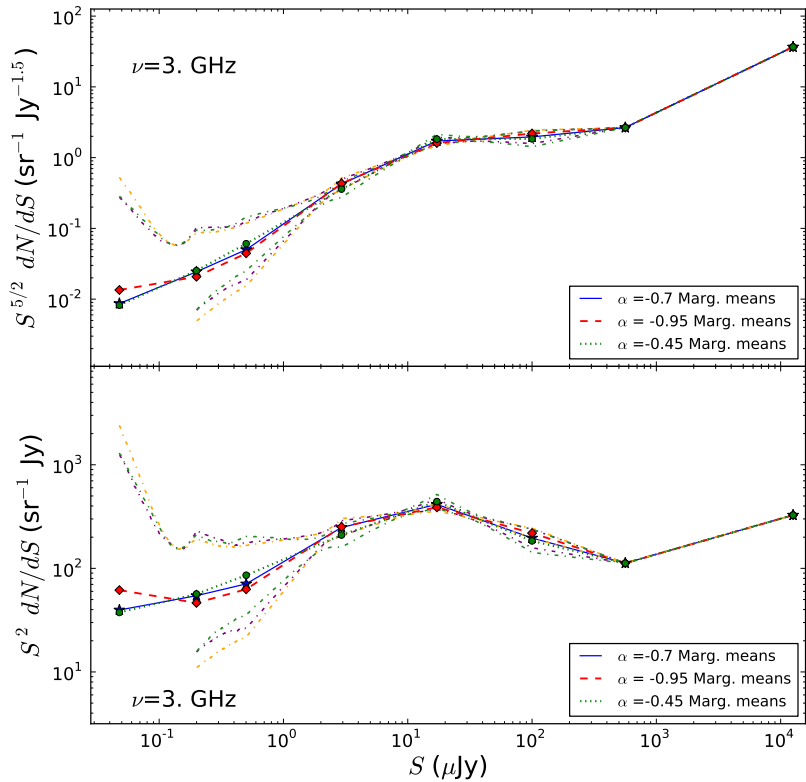


Figure 4.14: Comparison of MCMC $P(D)$ fitting for wide-band images made with different spectral indices in the weighting scaled to 3 GHz. The top panel is with the Euclidean normalisation, while the bottom panel is S^2 normalised. Lines and points are the parameter marginalised means. The red dashed line is for $\langle \alpha \rangle = -0.95$, the green dotted line is for $\langle \alpha \rangle = -0.45$, and the blue solid line is $\langle \alpha \rangle = -0.7$. The dot-dashed lines are the 68 per cent confidence limits.

spectral luminosity function of extragalactic radio sources, finding a simple model based on luminosity, redshift, and frequency that accurately predicted the source count at 1.4 GHz at that time. This model shows two peaks in the $S^2 dN/dS$ source count, one dominated by starburst-powered galaxies peaking at $50 \mu\text{Jy}$, and the other dominated by AGN-powered galaxies peaking near 0.1 Jy . In the brighter flux density range, where there is a large amount of observational data, this model describes the source count well. We have plotted this Condon (1984) model against our fits for comparison in Fig. 4.15 and Fig. 4.16 . At the brighter end of the count, $S \geq 90 \mu\text{Jy}$, there is good agreement between this model and all of our fits. In the region $S \leq 3 \mu\text{Jy}$ the model is also within the uncertainties for all the node-based fits, and lines up quite closely with the marginalised mean fits. However, in the region $3 \leq S (\mu\text{Jy}) \leq 90$ the Condon model is consistently below our fits, both from the node-based model and the modified power law. In this region the dominant component of the Condon model is star-forming galaxies. The discrepancy between the model and our source count results suggests the contribution from these galaxies is greater than previously thought. If the star-forming component from Condon’s model is increased by roughly a factor of 2 it would match quite closely. It is clear that any successful models should not deviate too strongly from the Condon (1984) model, but may need a slightly different treatment of star-forming galaxies.

We have also compared our results with the empirical model from Béthermin et al. [10]. This model is derived from the infrared luminosity functions of star forming galaxies, broken into two groups: ‘main sequence’ galaxies and ‘starburst galaxies’, combined with new spectral energy distributions from the *Herschel* observatory as well as source counts from a range of IR and submm wavelengths. The Béthermin model was scaled to 1.4 GHz assuming a non-evolving IR-radio correlation of $q_{\text{TIR}} \equiv \log \left(\frac{L_{\text{IR}}}{3.75 \times 10^{12} \text{W}} \times \frac{\text{WHz}^{-1}}{L_{1.4}} \right) = 2.64$ out to high redshift and a spectral index of $\alpha = 0.8$. This model is plotted in Fig. 4.15 and Fig. 4.16, with our best fit results, as well as the Condon (1984) model and Condon et al. [37] power law. In contrast to the Condon (1984) model, the Béthermin model matches our results quite closely in the region $1 \leq S (\mu\text{Jy}) \leq 50$, where the star-forming contribution is dominant. However, for $50 \leq S (\mu\text{Jy}) \leq 1000$ the model drops below our best fits, as well as the Condon (1984) model, and is clearly under-

predicting the observed counts. From figure 3 of Béthermin et al. [10] this is the region where the main sequence contribution starts to decline and where the starburst contribution peaks. If the starburst contribution is increased by a factor of around 3 then the model in this region more closely approximates the other estimates.

All of our model fits, even allowing liberal uncertainties, lie below the source-count values from Owen and Morrison [134]. These points are highlighted in red in Fig. 4.17; they seem to level off, or rise, toward fainter flux densities. We do not see any such indication for our results, all of our model fits declining in amplitude within this region and beyond. As discussed in Condon et al. [37] we believe this discrepancy to be mainly due to incorrect source size corrections in constructing the earlier source count estimates. Higher resolution VLA observations at 3 GHz would resolve the size issues definitively.

As to the matter of the ARCADE 2 excess emission, it seems unlikely from these results that it could be coming from discrete sources. All of our model fits, both node-based and modified power law, as well as the single power-law from Condon et al. [37], imply a background temperature at 3 GHz of around 13 mK. Using the fit provided in Fixsen et al. [56] to scale the ARCADE 2 result from 3.2 GHz to 3 GHz yields a temperature of 62 mK, far outside the uncertainties in our results.

There is no indication in our results of any new population of sources. Fig. 4.17 shows two possible bumps (representing new possible populations) that would integrate up to the extra temperature necessary to account for the ARCADE 2 result. These were modelled as simple parabolas in the $\log_{10}[S] - \log_{10}[S^{5/2}dN/dS]$ plane, with fixed peak position. The bump peaking at around 2 μ Jy is clearly much higher in amplitude than any of our fits. Any kind of new population peaking above about 50 nJy can be ruled out. Of course there is still the possibility that a new population could exist that is even fainter than our current limits, peaking somewhere below 50 nJy. The fainter bump shown in Fig. 4.17 is one such example. However, the source density required for such sources to contribute significantly to the background is extreme.

Between the faintest two nodes, 0.05 μ Jy and 0.20 μ Jy, and particularly near the faintest node, the count is not well constrained and the uncertainties do allow

Table 4.6: Marginalised parameter means for the best fit (three-zone) node model and modified power law model scaled to 1.4 GHz using $\langle \alpha \rangle = -0.7$. The form for the modified power law is given in eq. (4.7)

Node 1.4 GHz μJy	Marginalised means $\log_{10}[\text{sr}^{-1} \text{ Jy}^{-1}]$
0.08	$15.55^{+1.20}_{-1.20}$
0.34	$14.82^{+0.45}_{-0.43}$
0.86	$14.20^{+0.20}_{-0.20}$
5.02	$13.24^{+0.03}_{-0.03}$
29.3	$11.87^{+0.02}_{-0.02}$
171.	$10.11^{+0.02}_{-0.02}$
963	8.31
21600	6.08
Parameter 1.4 GHz $0.08 \leq S (\mu\text{Jy}) \leq 100.$	Marginalised means
α	$-4.7^{+1.2}_{-1.2}$
β	$-0.16^{+0.25}_{-0.25}$
γ	$0.016^{+0.016}_{-0.016}$
$\log_{10}(\kappa)$	$-4.68^{+1.2}_{-1.1}$

for a rise in the count. We therefore cannot rule out bumps with peaks fainter than 10 nJy. However, as the peak goes to fainter flux densities the bump needs to increase in width or height to produce the required background temperature. Note that any such population would far exceed the total number of known galaxies, as well as requiring a complete departure from the radio/far-IR correlation (assuming the sources are not AGN and are star-forming or starburst galaxies).

4.7 Conclusions

Our VLA image [CO12] is the deepest currently available, with an instrumental noise of $1 \mu\text{Jy beam}^{-1}$. To do justice to these data we have developed a novel and thorough $P(D)$ analysis that has revealed the structure of the 3-GHz source count down to $0.1 \mu\text{Jy}$.

The novel features are the following.

1. We have modelled the source count by a series of nodes joined by short

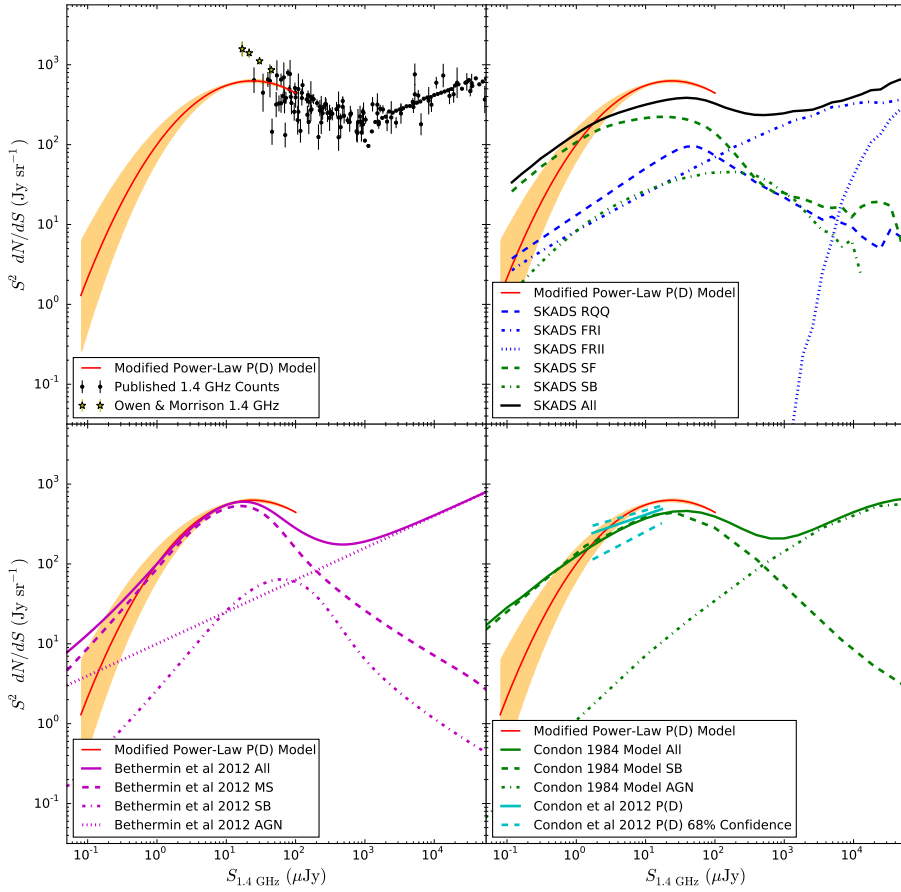


Figure 4.15: Source counts at 1.4 GHz of models and observed counts. In all four plots the solid red line is the modified power-law model from fitting of the 3 noise zones scaled to 1.4 GHz using $\alpha = -0.7$. The orange regions are the 68 per cent confidence regions. Top left: Black points are known counts compiled from de Zotti et al. [42], with the yellow stars showing the Owen & Morrison 2008 counts. Top Right: The solid black line is the source count from the SKADS simulation. The green dashed and dot-dashed lines are the star-forming and starburst populations, respectively. The blue dot-dashed, dotted, and dashed lines are FRI AGN, FRII AGN, and radio quiet AGN, respectively. Bottom left: The purple solid line is the evolutionary model from Béthermin et al. [10], with the dashed, dot-dashed, and dotted lines being main sequence, starburst, and AGN galaxies. Bottom right: The green solid line is the evolutionary model from Condon [31], with the dashed and dot-dashed lines being the starburst and AGN populations. The solid light blue line is the P(D) result from Condon et al. [37], with surrounding error box.

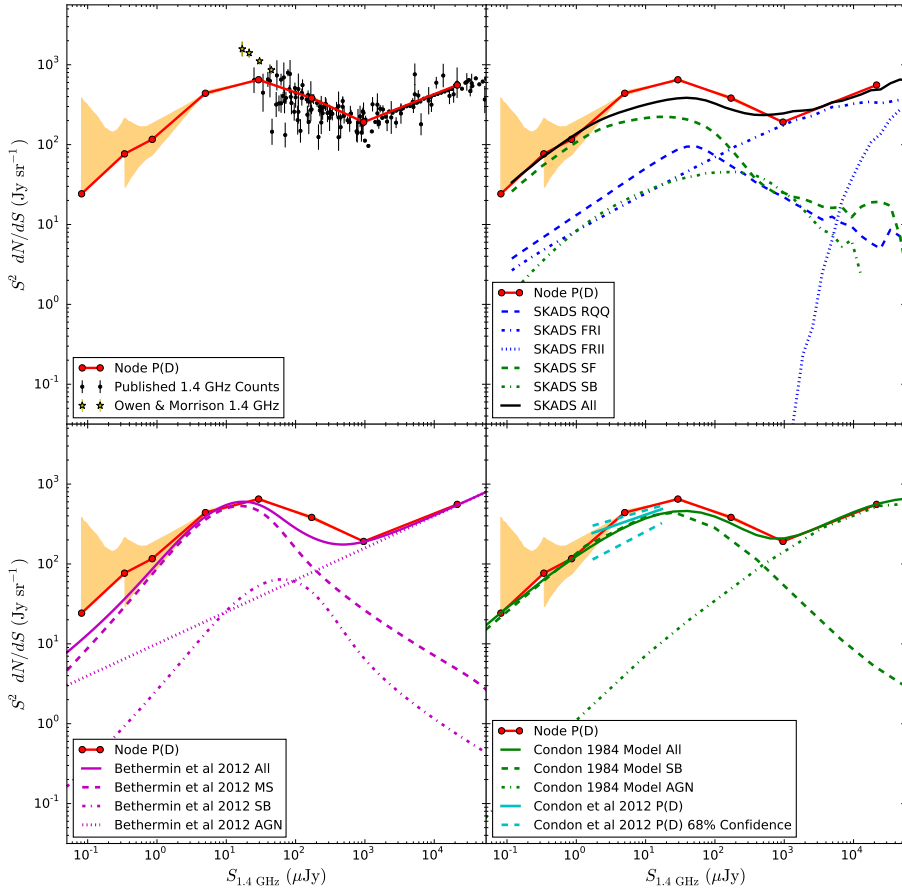


Figure 4.16: Source counts at 1.4 GHz of models and observed counts. In all four plots the solid red line is the node model from fitting of the 3 noise zones scaled to 1.4 GHz using $\alpha = -0.7$. The orange regions are the 68 per cent confidence regions. Top left: Black points are known counts compiled from de Zotti et al. [42], with the yellow stars showing the Owen & Morrison 2008 counts. Top Right: The solid black line is the source count from the SKADS simulation. The green dashed and dot-dashed lines are the star-forming and starburst populations, respectively. The blue dot-dashed, dotted, and dashed lines are FRI AGN, FRII AGN, and radio quiet AGN, respectively. Bottom left: The purple solid line is the evolutionary model from Béthermin et al. [10], with the dashed, dot-dashed, and dotted lines being main sequence, starburst, and AGN galaxies. Bottom right: The green solid line is the evolutionary model from Condon [31], with the dashed and dot-dashed lines being the starburst and AGN populations. The solid light blue line is the P(D) result from Condon et al. [37], with surrounding error box.

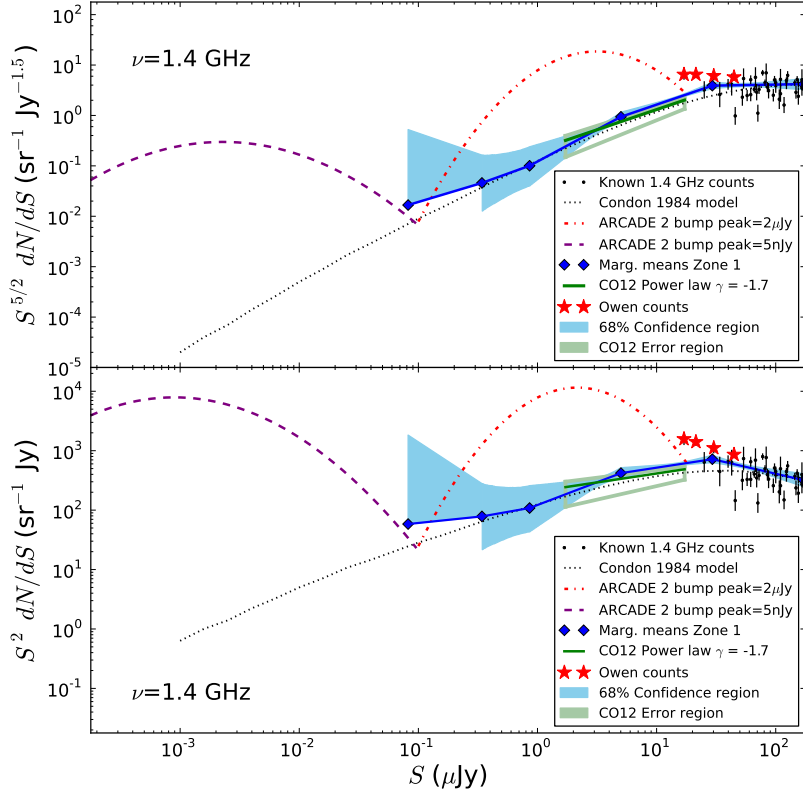


Figure 4.17: Faint end of the 1.4 GHz source count. The top panel is with the Euclidean normalisation, while the bottom panel is S^2 normalised. The bumps are two examples of counts that, when integrated, produce the extra background temperature necessary to match the ARCADE 2 emission, with the red dot-dashed line peaking at $2 \mu\text{Jy}$ and the purple dashed bump peaking at 5nJy . The red star points show the source count of Owen and Morrison [134].

sections of power-law form [138]. In this way, there is no prescription, assumption or constraint on the form the count might follow. The parameters in our model then simply become the node values.

2. We have used Markov chain Monte Carlo sampling throughout to provide unbiased determinations of the parameters and accurate estimates of parameter uncertainties. This demonstrates with clarity the dependence on flux density, how the inter-parameter dependencies increase with decreasing flux density, and the faintest limits to which $P(D)$ is sensitive.

From the use of these novel techniques we have drawn the following conclusions.

1. The MCMC approach shows that the uncertainties are dominated by sample variance rather than systematic effects, at least at the high end of the count. Hence a wider image *at the same depth* would lead to an improved estimate of the source count.
2. Our results are broadly consistent with the single power-law slope of -1.7 found by CO12, although differing slightly in detail. They show that the error estimate of CO12 is somewhat generous. They also show with greater conviction the change to a shallower slope below $3 \mu\text{Jy}$ suggested by CO12.
3. The consistency with previous estimates persists even when we take into account changes in the instrumental noise with frequency and position within the primary beam, different weightings of the wide-band bandpass data, and non-Gaussian features in the noise.
4. We have shown that the method allows extraction of count information from these data to flux densities an order of magnitude below the limit traditionally set by noise plus confusion, and far below the 5σ noise limit of around $5 \mu\text{Jy}$ set by direct source-counting.
5. Using a realistic large-scale simulation from Wilman et al. [191], we have verified our approach and shown that it is unbiased. This simulation enabled us to quantify the effects of clustering and source sizes on the $P(D)$ distribution, both of which we found to be insignificant. While simulated $P(D)$

from a model sky is not new [e.g. 186], never before has a comprehensive simulation been combined with a comprehensive count-fitting technique.

6. Our source count estimates rule out any new populations that could be invoked to account for the ARCADE 2 excess temperature, down to a level of about 50 nJy. The count is closely represented by existing models of evolving luminosity functions, including the contributions of star-forming and starburst galaxies and radio-quiet AGN at the faintest flux densities observed; this suggests that we have a substantially robust accounting of the galaxies that contribute to the radio sky.

Here we presented a brief summary of the conclusions from this chapter. For a discussion of these results in a broader context see Chapter 8.

Chapter 5

Extended-Source Count

5.1 Introduction

Extended low-surface-brightness radio emission can be difficult to survey. Galactic- and cluster-scale emission can extend up to several arcminutes. Single-dish telescopes at radio frequencies have beams on much larger scales and are limited in their continuum sensitivity by systematic errors, while most interferometers are not ideal for measuring low-surface-brightness extended objects. The surface brightness sensitivity of an interferometer is limited by its spatial frequency coverage in the image domain, which is the Fourier transform of its coverage of the aperture plane, often referred to as its ‘*uv* coverage’. For example, if an interferometer consists of antennas of diameter D_a , and the length of the shortest baseline is b , then the interferometer is generally insensitive to objects in the sky with angular size greater than $\lambda/(b - D_a)$ radians. An interferometer with $D_a = 25\text{ m}$ and $b = 1000\text{ m}$ observing at 20 cm is therefore insensitive to astronomical objects with scale sizes greater than 0.7 arcmin. Mosaicing can recover spatial information $> \lambda/D_a$ in size but nothing can recover information between $> \lambda/D_a$ and $< \lambda/(b - D_a)$, as that has not been measured by the interferometer. Thus, not many deep extended emission surveys have been carried out at radio frequencies.

It is unknown how much this large-scale emission may contribute to the cosmic radio background (CRB) temperature. This background at radio frequencies (T_b) is composed of emission from the cosmic microwave background (CMB, T_{CMB}),

the contribution from the Milky Way (T_{Gal}), and the contribution from extragalactic sources (T_{source}); thus $T_b = T_{\text{CMB}} + T_{\text{Gal}} + T_{\text{source}}$. The CMB contribution has been measured to high accuracy and corresponds to a blackbody with $T = 2.7255 \text{ K}$ [55]. Recent estimates from the deep survey by Condon et al. [37] and Vernstrom et al. [183, hereafter V14] were made of the contribution from extragalactic sources using the Karl G. Jansky Very Large Array (VLA) at 3 GHz. They found the contribution from compact sources to be $T_{\text{source}} = 14 \text{ mK}$ at 3 GHz and 120 mK when scaling this result to 1.4 GHz. However, the synthesized beam size from the VLA at 3 GHz was 8 arcsec and the image was constructed from uv weighting that filtered out scales much larger than the beam. Thus that survey would not have been sensitive to emission on larger scales.

The issue of large-scale emission and the CRB has been of greater interest in the last few years, following the results of ARCADE 2. This balloon-borne experiment observed the sky at several radio frequencies, ranging from 3.3 to 100 GHz. It measured a background temperature at 3.3 GHz that is much higher than current estimates from extragalactic sources, $(54 \pm 6) \text{ mK}$ compared with the $T_{\text{source}} \simeq 14 \text{ mK}$ of Chapter 4. Singal et al. [165] proposed that the excess could be due to a new population of faint distant star-forming galaxies. Chapter 4 ruled out any new populations of discrete compact sources having peaks in the source count above 50 nJy.

For compact sources to be causing the excess emission seen by ARCADE 2, the additional sources would need to have number-count peaks at very faint flux densities. This *could* raise a problem with the far-IR to radio correlation if the sources are not some form of AGN (unless this correlation evolves with redshift), and conflict with limits on the overall number of galaxies.

However, the cause of the ARCADE 2 excess *could* be larger-scale emission (scales ranging from around 0.5 arcmin up to the 12° primary beam size of the ARCADE 2 experiment). It has been proposed that the emission could be caused by dark matter annihilation [63, 64, 89, 196], in which case it would trace the dark matter distribution of clusters of galaxies, with a characteristic scale size of arcmin. Other emission processes could include those normally seen from clusters, such as radio relics and haloes, or with diffuse synchrotron emission from the cosmic web [20]. Such emission processes do not directly correlate with star formation and

therefore could evade constraints from the far-IR radio correlation.

In this chapter we use deep low-resolution radio observations from the Australia Telescope Compact Array (ATCA) to investigate the emission that might be present at larger angular scales and constrain how it might contribute to the CRB. Section 5.2 describes the technique used to examine the data. In Section 5.3 we discuss our treatment of discrete point sources, our subtraction method, and the contribution from faint un-subtracted sources. We discuss issues of detecting extended emission at both high and low resolutions in Section 5.4. Section 5.5 details the models we use for investigating the extended or diffuse emission. Section 5.6 discusses the conversion from source count to background temperature, as well as the predicted background temperatures from ARCADE 2 at our image frequency. Section 5.7.1 presents the results of fitting our extended emission source count models to our new data and their contribution to the CRB, and discusses models fit to the ARCADE 2 results. In Section 5.8 we discuss our findings, in particular what the results might mean in terms of astrophysical sources. We examine models of cluster halo emission as well as a source count models from dark matter. Finally, in Section 5.9 we present our current estimates of integral source counts for both discrete and extended source count models.

5.2 $P(D)$ and Beams

The technique described in Section 3.2 was used in this analysis as well.

In order to fit an accurate $P(D)$ with a source-count model in this way, the shape of the beam and the image noise must be well understood. Ordinarily one would use a Gaussian model of the synthesized clean beam in the calculation of the model $P(D)$, under the assumption that it is not significantly different from the dirty synthesized beam. However, in our case, the dirty beam has fairly large sidelobes, and is not well approximated by the clean beam. This is shown in Fig. 5.1, with the full-sized beams and with a close-up of the regions near the peaks. The peak sidelobes are at about the ± 0.1 level. However, there are pronounced streaks in the outer regions, of amplitude around ± 0.02 , which, when convolved with a source of $S \approx 100 \mu\text{Jy}$, would create many pixel values in the μJy region. If only the clean beam were used in the calculation then a source count model with a large number

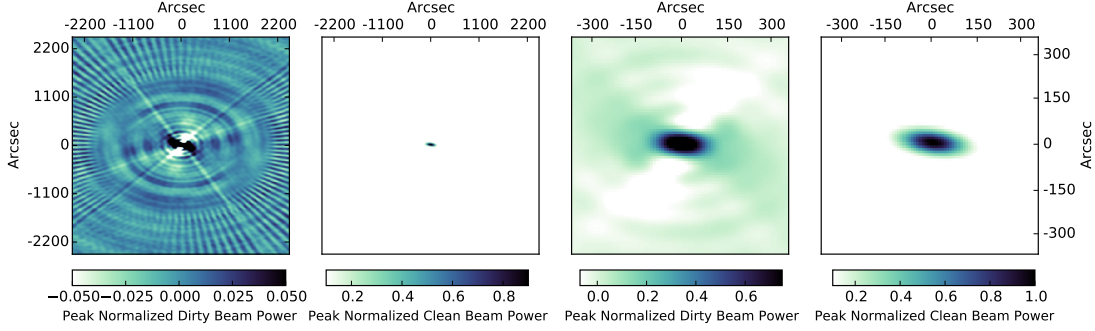


Figure 5.1: Images of the synthesized beams for the 1.75 GHz data. The first two panels are the full ‘dirty’ and ‘clean’ synthesized beams. The third and fourth panels show close ups of the region around the peaks of the beams (dirty and then clean). All beams have been peak-normalized to unity.

of μJy sources would be required to achieve a decent fit, even if no such population of sources truly existed. Thus in all following $P(D)$ calculations we used the dirty beam for all sources below our cleaning limit of $S < 150 \mu\text{Jy}$, while for sources with $S > 150 \mu\text{Jy}$ the clean beam values were used.

5.3 Discrete Sources

The discrete source count is now known quite well, and has been shown to provide a very much lower background temperature than the one seen by ARCADE 2, down to at least 50 nJy Chapter 4. In this paper we are therefore interested in more diffuse extended emission, which would be resolved out at higher resolution. By discrete sources we are referring to sources which are point sources in our $150 \text{ arcsec} \times 60 \text{ arcsec}$ beam, or sources with $\Omega_{\text{source}} \ll \Omega_{\text{beam}}$. In order to focus on this emission we first need to subtract out the known contribution from point source emission. We are only able to subtract out sources down to a certain flux density; therefore we must also consider any discrete emission that was not subtracted out.

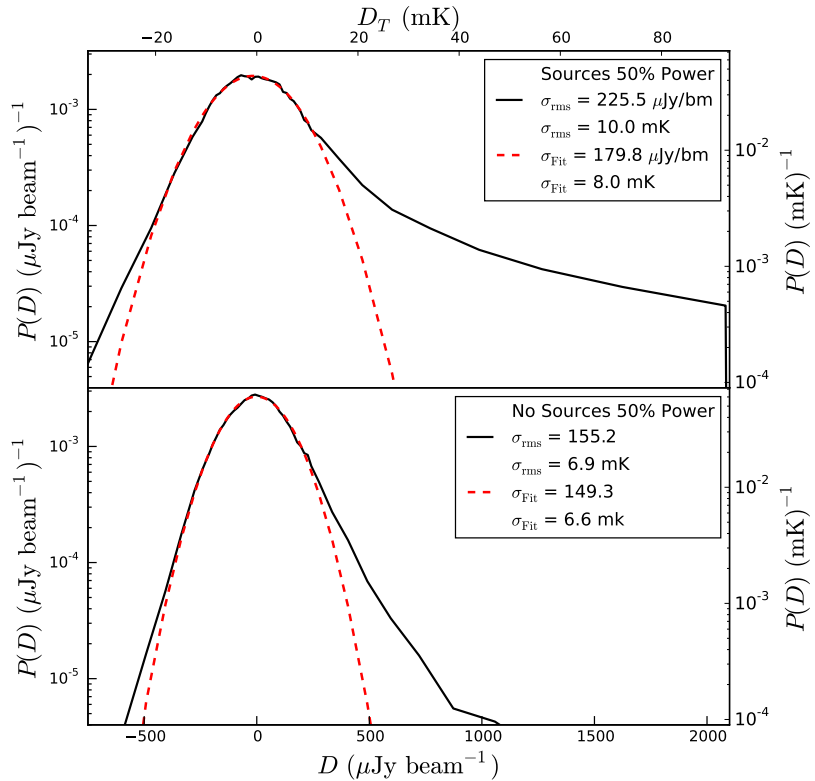


Figure 5.2: $P(D)$ distributions for the mosaic image central regions, where the increase in noise due to the primary beam is 1.5 times the minimum noise or lower, an area of roughly 0.61 deg^2 . The top panel shows the pixel histogram for the mosaic before point source subtraction. The bottom panel shows the distribution for the mosaic after subtraction of the ATLAS point sources. The solid black lines are the image distributions, while the red dashed lines are fitted Gaussians.

5.3.1 Source Subtraction

We used the clean component models from the ATLAS survey third data release (Franzen et. al, 2014 in preparation, Banfield et. al, 2014 in preparation) as point source models for subtraction, since the ATLAS resolution is significantly higher than our data, at around 10 arcsec. It is not entirely clear what the median source size might be and how it changes with flux density, but we expect a value between 1 and 3 arcsec for typical galaxies in evolutionary models [e.g. 191]. Thus the ATLAS resolution should be sufficient to measure all of the discrete or point source emission. The ATLAS point source models were split into two frequency bands: the lower frequencies from 1.30 to 1.48 GHz; and the higher frequencies from 1.63 to 1.80 GHz. For the subtraction we split our seven *uv*-data sets (for each pointing) into two equal frequency bands as well: 1.30 to 1.70 GHz; and 1.70 to 2.10 GHz. The ATLAS images were made using multi-frequency deconvolution and thus contain estimates of the spectral indices of the clean components, which can be used to scale the flux density to different frequencies during subtraction. The task UVMODEL was used to subtract the appropriate pointing and frequency coverage clean model from each corresponding *uv*-data set; then the *uv*-data for each pointing were concatenated using the task UVGLUE (combining the lower and upper frequency parts for each pointing). An independent image was constructed from each pointing with a mosaic constructed subsequently.

The ATLAS survey has an rms sensitivity of 15 to 25 μJy beam $^{-1}$ (depending on the individual pointing) and the models were cleaned down to a level of 150 μJy beam $^{-1}$. Thus all point sources with $S > 150 \mu\text{Jy}$ should have some fraction of their discrete emission subtracted out. There is some residual emission apparent around the brightest sources, which is visible in the bottom right panel of Fig. 2.2. We cannot say if this is due to some slight calibration or subtraction error, possible time variability of AGN sources, or if this represents a portion of the sources' diffuse emission. Looking at the peak positions of the well defined objects in each of the images, the average residual is only 5 per cent of the peaks. The $P(D)$ s for the central region of the mosaic images before and after source subtraction are presented in Fig. 5.2; this shows a clear decrease in the size of the positive source tail for the subtracted image.

When comparing our data to $P(D)$ predictions from source-count models we use the $P(D)$ of the source-subtracted mosaic image, including only pixels from regions where the noise due to the primary beam correction is not more than 1.5 times the lowest noise value. This is because the $P(D)$ calculation from a source-count model assumes a constant value for image noise. The noise is certainly inhomogeneous in our data. However, simulations have shown that the effect on the $P(D)$ calculation is small if we limit ourselves to a region where the change in the noise is small and create a noise-weighted histogram. Using a weighting scheme described in Chapter 4, we calculate a mean noise in this area (approximately 0.61 deg^2) of $\sigma_n = (52 \pm 5) \mu\text{Jy beam}^{-1}$, or $(2.3 \pm 0.2 \text{ mK})$.

5.3.2 Counts and Confusion

It is necessary to estimate the contribution of discrete emission from sources that were not subtracted out. For sources below the clean threshold of the ATLAS models we took the discrete source count of Chapter 4, including sources up to $S = 150 \mu\text{Jy}$, which is measured via confusion analysis down to $S \simeq 0.05 \mu\text{Jy}$ at 3 GHz. We scaled this to 1.75 GHz according to $S \propto \nu^\alpha$, with $\alpha = -0.70 \pm 0.05$ being the mean spectral index of star-forming galaxies [31]. We found that slight variation in this spectral index produces no significant effect on the output.

For the bright residuals left over from the subtraction process the issue is not as straightforward. Even neglecting any errors in calibration or subtraction, the clean process which generated the models is highly non-linear. The clean components may only represent a fraction of the true flux density, which can vary by peak flux density and from pointing to pointing. We do not believe there to be extended emission brighter than approximately $150 \mu\text{Jy beam}^{-1}$ (as discussed in more detail in Section 5.4.1). To account for unresolved residuals brighter than this we counted all the peaks in the source-subtracted image brighter than $150 \mu\text{Jy beam}^{-1}$ that are associated with point sources in the image with no subtraction, and calculated a power law index for their differential source count of -2.50 .

Our model for the unsubtracted point-source contribution is then the scaled Chapter 4 source count up to $150 \mu\text{Jy}$ with a power law of slope -2.50 attached for sources with $150 \mu\text{Jy} < S < 3 \text{ mJy}$ (3 mJy being the brightest residual in the

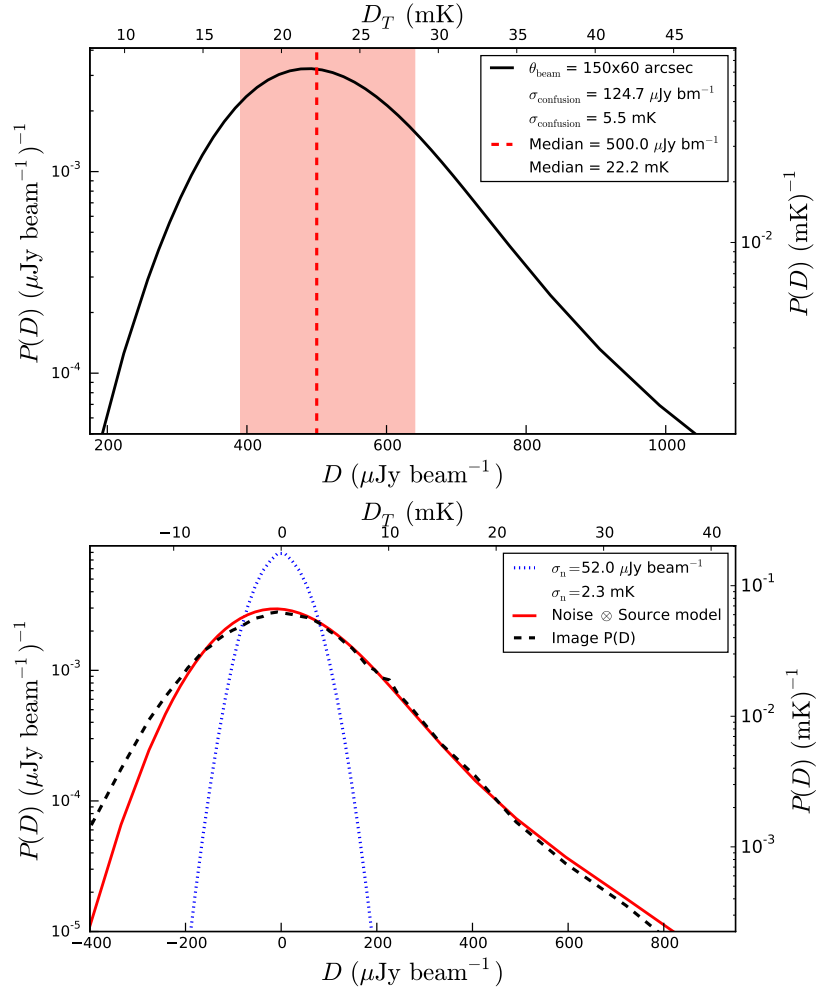


Figure 5.3: Source confusion distribution for discrete sources (point sources in our $150 \text{ arcsec} \times 60 \text{ arcsec}$ beam). The top panel shows the noiseless $P(D)$ from the source count of Chapter 4, scaled from 3 GHz to 1.75 GHz using $\alpha = -0.7$, including only sources up to a flux density of $S = 150 \mu\text{Jy}$, with a differential source count logarithmic slope of -2.5 for $150 \leq S \leq 3000 \mu\text{Jy}$. The measured confusion rms from this distribution is $\sigma_c = (125 \pm 10) \mu\text{Jy beam}^{-1}$, or $(5.5 \pm 0.44) \text{ mK}$, with the dashed lines showing the median and the shaded region showing the $\pm 1\sigma$ values. The bottom panel shows this distribution convolved with a Gaussian of width $\sigma_n = 52 \mu\text{Jy beam}^{-1}$. The Gaussian is the blue dotted line, the convolution is the red solid line, and the $P(D)$ from the inner region of the source-subtracted mosaic image is shown as the black dashed line.

fitting area). We computed the $P(D)$ from this count and convolved this $P(D)$ with a Gaussian noise distribution of width $\sigma_n = (52 \pm 5) \mu\text{Jy beam}^{-1}$, or $(2.3 \pm 0.2) \text{ mK}$. The noiseless and convolved $P(D)$ distributions are shown in Fig. 5.3. We measured the confusion noise σ_c , or width of the distribution, by first finding D_1 and D_2 ,

$$\sum_{D_1}^{\text{median}} P(D) = \sum_{\text{median}}^{D_2} P(D) = 0.34, \quad (5.1)$$

when normalised such that the sum over the $P(D)$ is 1. Then we take $\sigma_c = (D_2 - D_1)/2$. We do this since, in the Gaussian case, 68 per cent of the area is between $\pm 1\sigma$, and since, in the more realistic case, the long positive tail makes the variance of the full distribution a poor estimate of the width of the peak. The estimated width of the source-subtracted image $P(D)$ is $\sigma = 155 \mu\text{Jy beam}^{-1}$ (6.9 mK) with an uncertainty of $\pm 5 \mu\text{Jy beam}^{-1}$ ($\pm 0.22 \text{ mK}$) measured from bootstrap resampling. For the discrete source model $P(D)$ we find a value of $\sigma_c = 125 \mu\text{Jy beam}^{-1}$ (5.5 mK). The $P(D)$ of this model convolved with Gaussian noise thus has an rms of $\sigma_{c \otimes n} = 135 \mu\text{Jy beam}^{-1}$ (6.0 mK).

This discrete model estimate should be treated with some caution. The result is dependent on the exact value of the noise used in the calculation and the exact shape of the unsubtracted discrete count contribution. The unsubtracted discrete count is based on a model which is dependent on the maximum flux density value for the point sources with no subtraction, as well as the power law used for the brighter sources. Taking these points into consideration we adopt an uncertainty of $\pm 10 \mu\text{Jy beam}^{-1}$, or $\pm 0.44 \text{ mK}$, on the measure of $\sigma_c = 125 \mu\text{Jy beam}^{-1} = 5.5 \text{ mK}$, yielding a measurement and uncertainty for the width of the noise convolved distribution of $\sigma_{c \otimes n} = (135 \pm 12) \mu\text{Jy beam}^{-1}$, or $(6.0 \pm 0.53) \text{ mK}$.

We want to know how different the model of unsubtracted discrete source emission is from the data. To do this we performed a bootstrap significance test. We randomly selected a subset of half the image pixels, generated random numbers from the noiseless model distribution and added varying amounts of Gaussian noise (to account for the uncertainty in the model). We then combined the real and model data into one set and drew two new subsets at random from the combined distribution. We compared the binned real data to the binned model data, and the binned

combined random sets to each other. We repeated this procedure 5000 times. This yields a distribution of the test statistic from the combined random samples of the null hypothesis (that the observed and model data come from the same population) and a distribution of the test statistic when comparing the ordered sets (the observed and model sets not combined). We computed three different test statistics: the Euclidean distance (the root-mean-square distance between the histograms); the Jeffries-Matusita distance (similar to the Euclidean distance but more sensitive to differences in small number bins); and a simple χ^2 .

The results of the bootstrap test show an average excess width of $(76 \pm 23) \mu\text{Jy beam}^{-1}$, $(3.4 \pm 1.0) \text{ mK}$, with the value of 76 coming from $\sqrt{\sigma^2 - \sigma_{c\otimes n}^2}$, which with the measured values is $\sqrt{155^2 - 135^2}$. The exact significance of this excess depends on the test statistic . However, regardless of which test statistic is used the data and model are statistically different, with a minimum of 99.5 per cent confidence. This excess cannot be converted directly into a background temperature since the conversion depends on the underlying source-count model responsible for the width (see Section 5.6 for more discussion on the temperature conversion).

Based on these tests, we conclude that there is more emission present than that from compact galaxies alone at the roughly 3σ level. However, due to the uncertainty in the source subtraction process, this excess and any resulting extended emission models are here considered as upper limits on the extended emission present.

5.4 Extended Sources

5.4.1 High Resolution Extended Emission

Before attempting to model any extended emission in the ATCA data we consider how extended emission is detected at higher resolutions, comparing the VLA data used by Chapter 4 and the ATLAS ATCA high resolution images. The VLA 3-GHz beam used in Chapter 4 had a FWHM of 8 arcsec, while the ATLAS beam was roughly 10 arcsec. We would like to know how emission on arcmin scales appears with these types of observations, since we know that some emission will be resolved out at higher resolution.

This was tested using sources from 1 deg^2 of the SKADS simulation [191] at 1.4 GHz. This simulation was shown in Chapter 4 to be a close approximation to observed source counts. Using the flux densities provided, we made one image containing only point sources. Then assuming each point source has an extended halo with total flux set to $S_{\text{dis}}/10$, with S_{dis} being the point source (discrete) flux, we made two images, assuming all the haloes were Gaussians with FWHM of 30 or 60 arcsec. We added the point sources to these and convolved the images with a 9 arcsec beam (the average size of the VLA and ATCA resolutions).

The confusion noise of each of the noiseless images are 1.53 , 1.95 , and $1.78 \mu\text{Jy beam}^{-1}$ for the discrete, discrete+30 arcsec, and discrete+60 arcsec data sets at 1.4 GHz. The 30 arcsec haloes add a width of $\sigma_{30} = \sqrt{1.95^2 - 1.53^2} = 1.21 \mu\text{Jy beam}^{-1}$, and the 60 arcsec haloes add $\sigma_{60} = \sqrt{1.78^2 - 1.53^2} = 0.91 \mu\text{Jy beam}^{-1}$. The $P(D)$ s for the images with point sources plus extended emission are shown in the bottom panel of Fig. 5.4. The smaller the extended objects the greater the increase in the width of the distribution. For images with the same total flux density the distribution for the larger sources would have its DC level shifted to higher flux densities; however interferometers are not sensitive to the DC level (or lowest spatial frequency) and thus do not measure total flux densities.

The measured confusion rms from the 3 GHz VLA data is approximately $(1.2 \pm 0.07) \mu\text{Jy beam}^{-1}$ (depending on the source-count model). Scaling the simulated values to 3 GHz, the addition of the 30 arcsec extended emission to the VLA point source model would yield a width of $1.38 \mu\text{Jy beam}^{-1}$, with the 60 arcsec haloes yielding $1.31 \mu\text{Jy beam}^{-1}$. Although in this case these exceed the estimated uncertainty, the simulated confusion widths depend on the exact source count used and the assumption of how the extended emission depends on the point-source flux density. Thus these particular extended emission models produce excess widths in the $P(D)$ distributions that are large enough to have been detected in deep high resolution images. However, these simulations show that there likely exist models with either fainter or larger-scale extended emission that would have been undetected in the VLA $P(D)$ experiment of Chapter 4.

From the simulated extended-size images we see that sources with total halo flux densities greater than approximately $150 \mu\text{Jy}$ would be visible in the VLA or ATLAS images. The top panel of Fig. 5.4 shows a cut-out of the simulated images;

when the point-source flux density is faint ($\leq 200 \mu\text{Jy}$), the extended emission is not visible in the image. However, for brighter point sources (with brighter halo emission), the extended haloes are visible in both the 30 and 60 arcsec images. Since nothing of this nature is seen in either the VLA or ATLAS images, we conclude that any extended emission in the current low resolution ATCA data should also have total flux density less than about $150 \mu\text{Jy}$, or else has to be very rare.

5.4.2 Source Size Sensitivity

The $P(D)$ calculation does not use any size information and assumes only unresolved sources. Therefore, it is important to understand how resolution affects the $P(D)$ fitting. To test this we used the simulated halo flux densities for the extended emission described in Section 5.4.1 and made four separate images for sources treated simply as point sources and as Gaussians with FWHM of 60, 90, and 300 arcsec. These give a range of sizes in relation to the ATCA beam. We then ran each image through the fitting routine for source-count amplitudes at specific flux densities, i.e. a set of connected power laws [e.g. 138, 183].

The results show that there is no significant change in the fitting results between the point source and 60 arcsec size images. However, the count amplitudes for the 90 arcsec sizes are lower than the true count at both the faintest and brightest flux densities, while the 300 arcsec size results are significantly lower at all flux densities. The results of this test are presented in Fig. 5.5. This shows that the $P(D)$ fitting procedure is reliable for sources on the order of the beam size or smaller; Table 5.1 shows the linear sizes for the angular scales to which we are sensitive given a range of redshifts, assuming standard ΛCDM cosmology with $H_0 = 67.8 \text{ km s}^{-1} \text{ Mpc}^{-1}$, $\Omega_m = 0.308$, and $\Omega_\Lambda = 0.692$ [141].

5.5 Extended Source Count Models

We have shown that there is a significant excess in the width of the observed distribution over that estimated from noise and discrete point sources, suggesting the presence of diffuse or extended sources. This emission could be low surface brightness diffuse emission around individual galaxies, diffuse cluster emission, or something more exotic, such as emission from dark matter annihilation in haloes. We

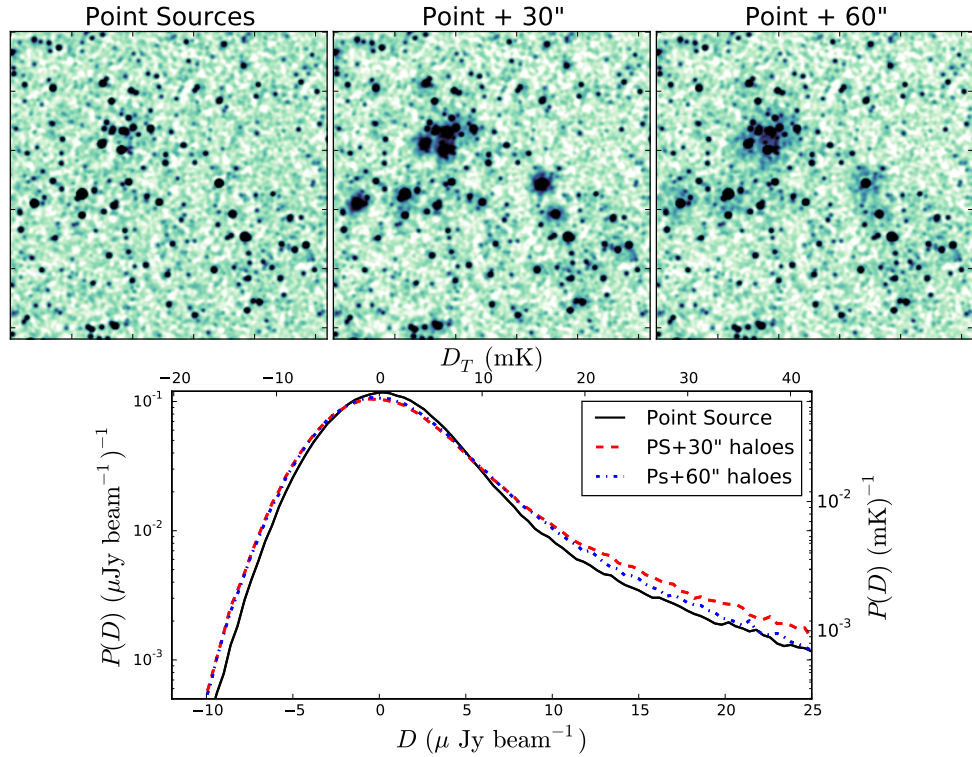


Figure 5.4: Simulation showing point source and extended emission at higher resolution. The top panels show cut-outs of the simulation with just point source emission (left), point sources plus haloes of 30 arcsec diameter (middle), and point sources plus haloes of 60 arcsec diameter (right), all convolved with a 9 arcsec beam and with Gaussian noise of $2 \mu\text{Jy beam}^{-1}$. The total flux density of each halo is taken as the point source flux density divided by 10. The bottom panel shows the $P(D)$ distributions from the three images, with the solid black line being for point sources only, the red dashed line point sources plus 30 arcsec haloes, and the blue dot-dashed line point sources plus 60 arcsec haloes.

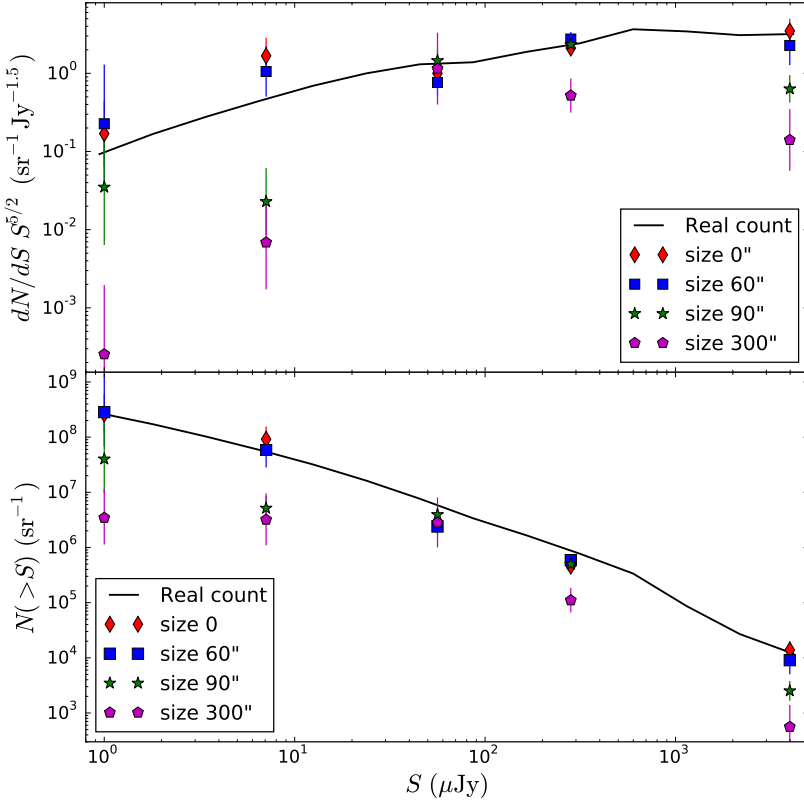


Figure 5.5: Results of $P(D)$ fitting of simulated images with different source sizes. The top panel shows the Euclidean-normalized differential source count of the input count (solid black line) and best-fitting results of the point source image (red diamonds), the 60 arcsec size image (blue squares), the 90 arcsec size image (green stars), and the 300 arcsec size image (magenta pentagons). The bottom panel shows the same information, but plotted as integrated source counts.

Table 5.1: Angular and physical source sizes at different redshifts.

Angular Size (arcsec)	Physical Size			
	$z = 0.25$ (Mpc)	$z = 0.5$ (Mpc)	$z = 1$ (Mpc)	$z = 2$ (Mpc)
30	0.12	0.19	0.25	0.26
60	0.24	0.38	0.49	0.51
100	0.40	0.63	0.82	0.86
150	0.60	0.94	1.23	1.29

then used three source count models to investigate the possible excess (extended) emission. We follow the fitting procedure described in detail in Chapter 4. We use Monte Carlo Markov Chains (MCMC), employing the software package CosmOMC [107]¹, to minimize χ^2 for each model. The three most negative bins ($-500 \leq D(\mu\text{Jy beam}^{-1}) \leq -250$) from the image histogram were neglected in the calculation of χ^2 . This is because the data have a clearly non-Gaussian negative tail, due in part to the non-constant noise but also due to the areas of over-subtraction, which produce an excess of negative points (see the bottom panel of Fig. 5.2). Tests on subsets of the data, and using different detailed approaches for subtracting bright sources, showed that these effects were restricted to the most negative bins, with the rest of the histogram being quite stable.

5.5.1 Shifted Discrete Count Model

Using evolutionary models [e.g. 31, 90] the source count can be broken into contributions from two populations, namely AGN and star-forming galaxies, as shown in Fig. 5.6. The simplest extended-emission model assumes that each of these populations has a radio-emitting halo on arcmin scales, proportional to some fraction of the discrete flux density (or $S_{\text{discrete}} \times C$), separately for the two populations. The origin of these haloes would be either cosmic ray electrons (or dark matter annihilation products in the haloes) interacting with the galaxy's magnetic fields. These would have to be quite faint, or diffuse, to have not already been observed, and is not believed to be a likely source of much emission, though still a possibility. The counts associated with this extended emission must then retain the shape of the discrete counts for each population, but can be shifted in flux density. To estimate the extended counts that are consistent with our data we took the discrete counts for each population and simply applied a shift in $\log_{10}[S]$ separately. Thus,

$$\begin{aligned}\frac{dN(S_{\text{ext}})_{\text{AGN}}}{dS_{\text{ext}}} &= \frac{dN([S_{\text{dis}}C_1])_{\text{AGN}}}{d[S_{\text{dis}}C_1]}, \\ \frac{dN(S_{\text{ext}})_{\text{SB}}}{dS_{\text{ext}}} &= \frac{dN([S_{\text{dis}}C_2])_{\text{SB}}}{d[S_{\text{dis}}C_2]},\end{aligned}\tag{5.2}$$

¹<http://cosmologist.info/cosmomc/>

where C_1 and C_2 are constants that are varied to fit the counts. When combined with the unsubtracted discrete count and Gaussian noise, we can find the values that best fit the observed $P(D)$ distribution of our source-subtracted image. Figure 5.6 shows an example of this model with the two populations of discrete counts, each with shifts applied. We plot the results with the usual S^2 normalization and with no normalization (so that the horizontal shifts can be seen). This model will be referred to as Model 1.

5.5.2 Parabola Model

We also wished to investigate the possibility of the extra emission being fit by a single new population. To do this we introduce a new population as a parabola in $\log_{10}[S^2 dN/dS]$ of the form

$$S^2 \frac{dN(S)_{\text{ext}}}{dS} = A(x - h)^2 + k. \quad (5.3)$$

Here $x = \log_{10}[S]$ and A , h , and k are all free parameters. The parameter h is the peak position in $\log_{10}[S]$, k is the amplitude or height of the peak, and A (along with k) controls the width. We chose this model because it allows for a smooth curve, and since the discrete count populations are themselves crudely approximated by parabolas in $\log_{10}[S^2 dN/dS]$. This model will be referred to as Model 2.

5.5.3 Node Model

There may be several types of sources or populations contributing to the extended emission counts, including individual galaxies, clusters, dark matter, intra-cluster medium, etc. Without having physical models for these different populations, we would require too many parameters to fit separate models for each. Therefore, we have chosen also to fit a model of connected power laws. This model allows for the shape of the source count to vary over a particular flux density range, rather than having a fixed shape based on a few parameters. It therefore has the potential to be sensitive to contributions from different populations at different flux densities.

The model consists of fitting for the amplitude of $\log_{10}[dN/dS]$ at specific flux

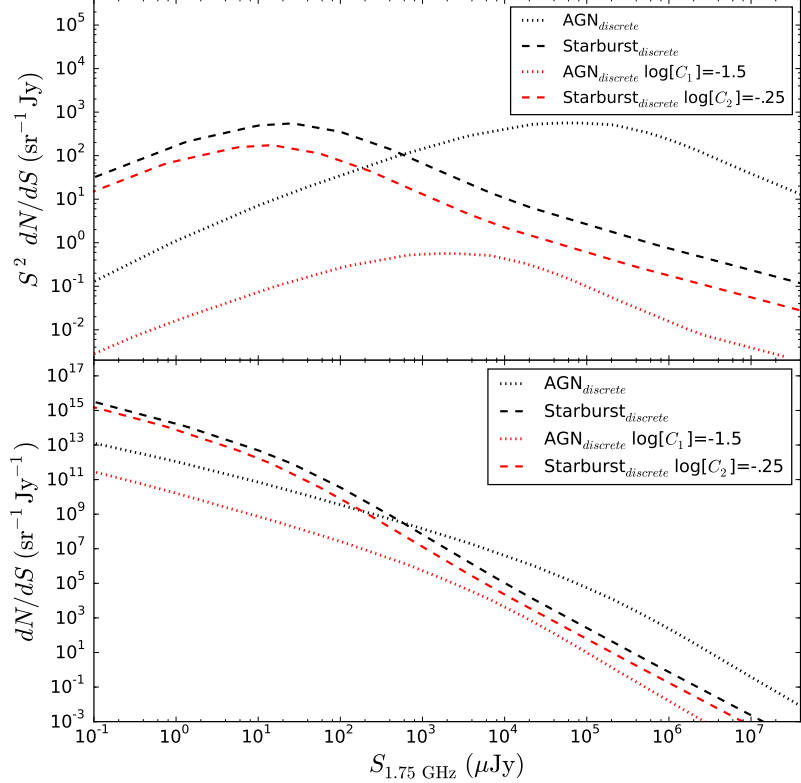


Figure 5.6: Discrete and shifted source counts of AGN and starburst. The top panel shows the discrete AGN and starburst source counts (black dotted line and black dashed line) using S^2 normalization. The red lines are example of the shifting model described in Section 5.5.1, where S for the AGN count has been shifted by $\log_{10}[C_1] = -1.5$ and the starburst count is shifted by $\log_{10}[C_2] = -0.25$. The bottom panel shows the same lines with *no* normalization on the source counts. This demonstrates how applying only a horizontal shift in $\log_{10}[S]$ will appear as a combination of vertical or amplitude shift when the S^2 normalization is applied.

densities, or nodes, and interpolating linearly (in log space) between the nodes – for more details on this model see Chapter 4. We specifically use five nodes spaced evenly in $\log_{10}[S]$, covering the range of $0.5 \leq S \leq 1000 \mu\text{Jy}$. This model will be referred to as Model 3.

5.6 Background Temperature

The discrete source count used by Chapter 4 integrates (up to $S = 900 \text{ Jy}$) to a background temperature at 1.75 GHz of $T_{\text{dis}}(1.75 \text{ GHz}) = 63 \text{ mK}$, where T_{dis} is the temperature from the discrete source contribution, using eq. 1.6.

The ARCADE 2 experiment measured a background temperature of $(54 \pm 6) \text{ mK}$ at 3.3 GHz. Using both of the fits from eq. 1.8 and eq. 1.9 we calculated the estimated background temperature at 1.75 GHz by taking the average from the two equations, and an uncertainty using the highest and lowest values from the uncertainties in the equation parameters. This yields $T_{\text{ARC2}}(1.75 \text{ GHz}) = (265 \pm 45) \text{ mK}$, which corresponds to a total flux density, given our beam size, of $5600 \mu\text{Jy beam}^{-1}$.

In addition to fitting the data with no constraints, we also fit the models to see what kind of count shapes would be necessary to achieve the ARCADE 2 temperature. We fit the models as described above, only this time adding a prior requiring that the integrated temperature be in the range of 150 to 300 mK. This should show if there is any such source count model consistent with both ARCADE 2 and our data.

These models are referred to as Model 1A (shifts), Model 2A (parabola), and Model 3A (nodes).

5.7 Extended Emission Source Count Fitting Results

5.7.1 Summary of Fits

Using the three models from Section 5.5 we (a) examined what model parameters best fit our new ATCA data, (b) calculated the resulting contribution to the background brightness temperature, and (c) modelled what would be necessary to achieve a background temperature consistent with ARCADE 2.

Table 5.2: Best-fitting results for Model 1. The temperature, T_{ext} , is the contribution to the background (using eq. 1.6), for the extended source count contribution only.

	Model 1 (unconstrained)	Model 1A (constrained)
$\log_{10}[C_1]$	-1.91 ± 0.11	-2.0 ± 0.15
$\log_{10}[C_2]$	-0.61 ± 0.16	0.39 ± 0.03
T_{ext} (mK)	$1.65^{+1.85}_{-0.75}$	201.2 ± 40
σ_c ($\mu\text{Jy beam}^{-1}$)	62.63	480.1
σ_c (mK)	2.78	21.36
χ^2 ($N_{\text{dof}} = 42$)	109.6	45200

The results from Model 1 and Model 1A are in Table 5.2, results from fitting Model 2 and 2A are in Table 5.3, and results from Model 3 and Model 3A are listed in Table 5.4. Each of these extended counts was added to the unsubtracted discrete count model (discrete source count fainter than the subtraction limit plus a power law for subtraction residuals, as discussed in Section 5.3.2) to compute the $P(D)$ for each model. The $P(D)$ models, convolved with Gaussian noise of $52 \mu\text{Jy beam}^{-1}$, are shown in Fig. 5.7, along with the $P(D)$ for the central region of our source-subtracted mosaic image.

Each step in the MCMC chains is another source count model. For each model we used the MCMC results and calculated the background temperature distributions, using eq. (1.6), which are plotted in Fig. 5.8. The temperature distributions imply a mean temperature of (10 ± 7) mK. The resulting source count models are presented in Fig. 5.9, broken down by population and shown along with the discrete counts at 1.75 GHz.

5.7.2 Model Uncertainties

We tried variations in the fitting method by first changing the fit statistic used (χ^2 vs. log likelihood), which produced little change in the output; and second by trying different models. Instead of the parabola we tried a Gaussian in $S^2 dN/dS$. The Gaussian model produces a peak in roughly the same spot as the parabola, though the parameters are not as well constrained. All models tried resulted in

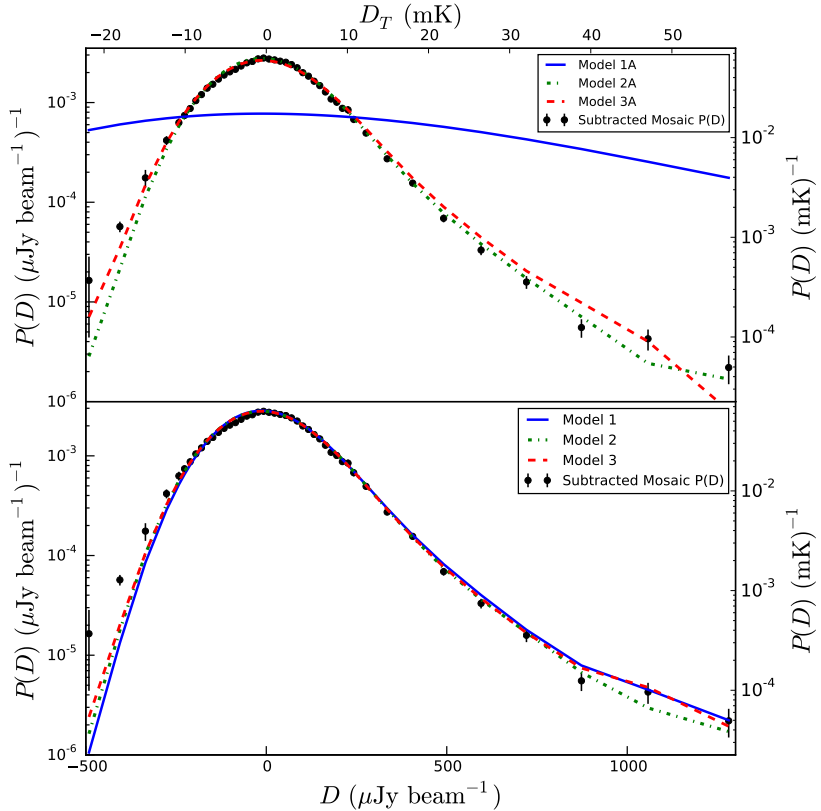


Figure 5.7: $P(D)$ distributions for various extended-emission source counts.

The top panel shows the $P(D)$ distributions for the best-fitting models of extended-emission counts with a prior for the ARCADE 2 temperature for Model 1A (blue solid line), Model 2A (green dot-dashed line), and Model 3A (red dashed line). The bottom panel shows the results of fitting the same models, but without the temperature requirement. All models have been convolved with Gaussian noise of $\sigma_n = 52 \mu\text{Jy beam}^{-1}$ and the unsubtracted discrete source count contribution. The black points are the source-subtracted mosaic histogram (as seen in the bottom of Fig. 5.2).

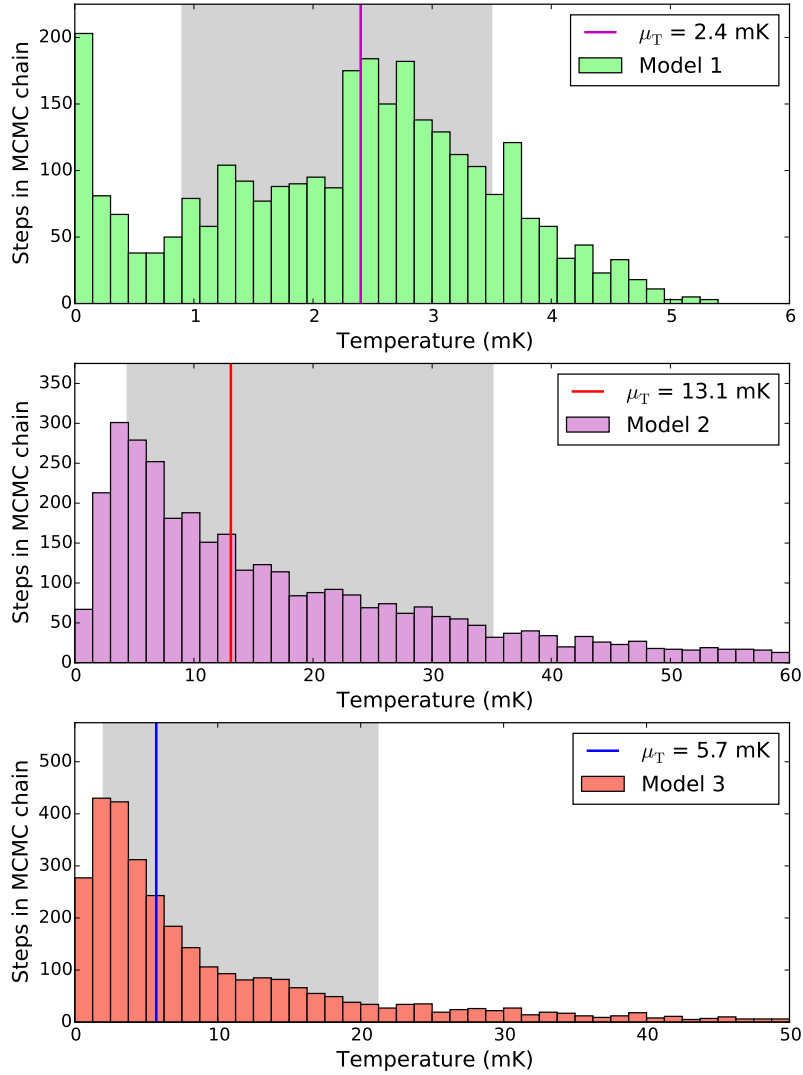


Figure 5.8: Histograms of the contribution to the background temperature from MCMC fitting of the three source count models. Temperatures are for extended emission counts only, with the discrete source count being $T_{\text{dis}} = 63 \text{ mK}$. The top panel shows the background temperatures from fitting Model 1, the middle panel is the histogram from Model 2, and the bottom panel from Model 3. The solid vertical lines are the medians for each distribution, with the grey shaded regions showing the 68 per cent confidence regions.

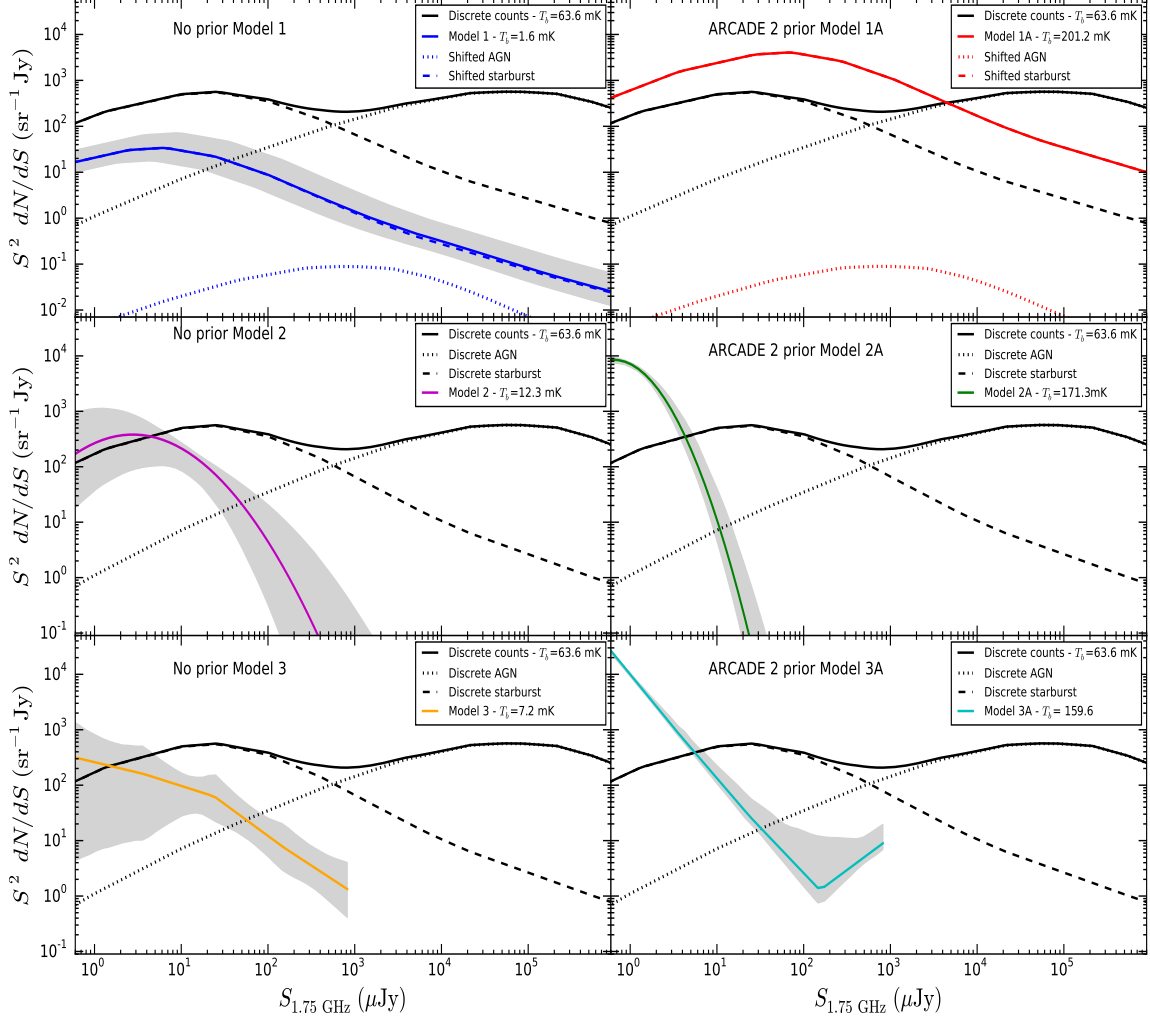


Figure 5.9: S^2 normalized source counts at 1.75 GHz. The black lines are the same in all plots and are counts of discrete sources from the estimates in Chapter 4 at 3 GHz, scaled to 1.75 GHz using $\alpha = -0.7$, while the coloured lines are the extended-emission counts from models. The discrete count is broken into two populations, AGN and starbursts, based on evolutionary models, shown as the dotted and dashed lines, respectively, with the solid lines being the sum of both components. The left panels show the models with no priors and the right panels show models with ARCADE2 priors. The top panels are Model 1 and 1A (blue and red lines). The middle panels show Model 2 and 2A (magenta and green lines). The bottom panels show Model 3 and 3A (orange and cyan lines). The grey regions are the 68 per cent confidence intervals.

Table 5.3: Best-fitting parameter results for Model 2 and Model 2A. The temperature, T_{ext} , is the contribution to the background (using eq. 1.6), for the extended source count contribution only.

Parameter	Model 2 (unconstrained)	Model 2A (constrained)
A	-0.79 ± 0.29	-2.04 ± 0.22
h	-5.55 ± 0.40	-6.19 ± 0.04
k	2.58 ± 0.49	3.93 ± 0.05
T_{ext} (mK)	$12.3^{+22.8}_{-7.90}$	$171.3^{+16.2}_{-13.3}$
σ_c ($\mu\text{Jy beam}^{-1}$)	62.81	63.10
σ_c (mK)	2.79	2.81
χ^2 ($N_{\text{dof}} = 41$)	76.1	111.1

Table 5.4: Best-fitting parameter results for Model 3 and Model 3A. The temperature, T_{ext} , is the contribution to the background (using eq. 1.6), for the extended source count contribution only.

Parameter	Model 3 (unconstrained)	Model 3A (constrained)
$\log_{10}[\frac{S}{\text{Jy}}]$	$\log_{10}[\frac{dN/dS}{\text{sr}^{-1} \text{Jy}^{-1}}]$	$\log_{10}[\frac{dN/dS}{\text{sr}^{-1} \text{Jy}^{-1}}]$
-6.25	15.01 ± 1.26	16.97 ± 0.04
-5.43	13.06 ± 0.74	13.77 ± 0.07
-4.62	11.04 ± 0.62	10.67 ± 0.13
-3.81	8.50 ± 0.76	7.73 ± 0.55
-3.00	6.04 ± 0.92	7.05 ± 0.17
T_{ext} (mK)	$7.2^{+14.0}_{-5.20}$	$159.6^{+9.50}_{-12.6}$
σ_c ($\mu\text{Jy beam}^{-1}$)	62.73	78.12
σ_c (mK)	2.79	3.47
χ^2 ($N_{\text{dof}} = 39$)	75.3	251.6

best-fit parameters that yielded background temperature estimates for the extended emission in the range of (10 ± 7) mK.

We tested whether an incorrect estimate of the instrumental noise of (52 ± 5) $\mu\text{Jy beam}^{-1}$ could affect the results by re-fitting the models while allowing the noise to vary between 40 and $70 \mu\text{Jy beam}^{-1}$. This has little effect, except in Model 3, where the faintest node is degenerate with the noise. Thus a higher noise would decrease the amplitude of the faintest node. Nevertheless, we conclude that our noise estimate cannot be far enough off to explain the excess $P(D)$ width.

5.7.3 ARCADE 2 Fits

We refitted the models to explore what source counts would be necessary to yield background temperatures in the range predicted by ARCADE 2, and to assess how well those source counts fit our data. It is clear from Fig. 5.7 that shifting the two populations with the ARCADE 2 prior (Model 1A) is strongly inconsistent with our data. With Model 2A or Model 3A it is possible to obtain source count temperatures in the ARCADE 2 range and find a reasonable fit to our data. Figure 5.9 shows that in doing so, such a population would need to be extremely faint and numerous. The typical flux density of the peak of the parabola is three orders of magnitude below our instrumental and confusion noise limits. That region of the source count is nearly impossible to constrain with existing data. With Model 3A, the fitting routine makes the faintest node higher in amplitude, since changes to the counts that far below the noise result in very little change in the predicted $P(D)$ shape.

The two models are also difficult to interpret in terms of physical objects. Since these extended, faint, numerous objects would completely overlap on the sky, modelling them as discrete objects fails. Future work will examine whether a faint diffuse cosmic web structure could produce this emission.

We conclude that there are no source count models, to a depth of $1 \mu\text{Jy}$, that are consistent with both our data and the ARCADE 2 background temperature. Scaling our best-fitting discrete and extended source-count temperature (70 mK) to the ARCADE 2 frequency of 3.3 GHz via a spectral index of -0.7 gives only 13 mK, compared with the nearly 55 mK result from ARCADE 2.

Table 5.5: Luminosity and redshift estimates for Model 2.

S_{peak}	$S_{-50\%}$	$S_{+50\%}$	$z_{\text{pk}} = 0.25$	$z_{\text{pk}} = 0.5$	$z_{\text{pk}} = 1$	$z_{\text{pk}} = 2$		
(μJy)	(μJy)	(μJy)	$\log[L_{1.4}]$	Δz	$\log[L_{1.4}]$	Δz	$\log[L_{1.4}]$	Δz
2.8	0.7	11.0	19.8	0.39	20.6	0.84	21.5	1.83
							22.5	4.08

Chapter 4 ruled out a new discrete population peaking brighter than 50 nJy. Combining that with our constraint on an extended population peaking above 1 μJy indicates that the ARCADE 2 result is highly unlikely to be due to extragalactic emission. Residual emission from subtraction of the Galactic component thus seems a more likely explanation for the excess seen by the ARCADE 2 experiment. The contribution from extragalactic sources from ARCADE 2 depends on the model used for the contribution of the Galactic component. Subrahmanyan and Cowsik [170] showed that using a more realistic model of the Galaxy, as opposed to the plane parallel slab used by ARCADE 2 [100], obviates the need for any further contribution from the extragalactic sources beyond that predicted from the counts.

5.8 Extended Emission Discussion

When unconstrained by the ARCADE results, we find that Model 2 and Model 3 fit our data significantly better than Model 1 (an improved $\Delta\chi^2$ per degree of freedom of around 34). Though the χ^2 's for Model 2 and Model 3 are still somewhat high, either model is a reasonable approximation to the data, at least when compared with the unsubtracted discrete model on its own, which has a $\chi^2 = 335$ for 44 degrees of freedom. We now consider potential astrophysical sources of this emission.

5.8.1 Sources of Diffuse Emission

Model 1, consisting of only shifts in the discrete counts, is considered here as an approximate representation of individual galaxy haloes. The best-fit results from this model should be considered only as upper limits for galactic haloes. This model on its own does not optimally fit the data. If there are other sources contributing to the measured $P(D)$, the fitting process would push the shifts artificially high in an attempt to make the model as consistent with the data as possible. Also,

this model falls apart when considering nearby galaxies that have been observed with single dish telescopes. According to the model, a 1Jy nearby galaxy would have an extended halo of 250 mJy. This type of emission has not been seen around such sources. This implies that if all galaxies have some form of diffuse halo then the flux density of that halo cannot simply be a fraction of the discrete flux density. Models using the luminosity functions of the separate populations, where the halos may be a fraction of the point source luminosity, and or may have different evolution with redshift, would likely produce more consistent results.

For any of the models, in order to be consistent with known constraints on the cosmic infrared background (CIB) the emission process(es) must not be linked directly to star formation rates. Moreover, as noted in Section 5.4.2, this technique can only constrain sources that are roughly 2 arcmin or smaller. Thus, these models are valid only for objects in that size range.

Additionally, since we assume the sources in these models are powered by synchrotron emission, we must also consider the associated X-ray emission and how that compares with the known cosmic X-ray background (CXB). The electrons that generate the synchrotron emission can inverse-Compton (IC) scatter off of CMB photons to generate X-ray emission (e.g. [9, 50, 83]), the brightness of which we can estimate as follows.

The synchrotron and IC power are related by,

$$\frac{L_{\text{IC}}}{L_{\text{sync}}} = \frac{U_0(1+z)^4}{U_B} \quad (5.4)$$

[see e.g. 125]. Here L_{sync} and L_{IC} are the synchrotron and IC luminosities, U_B is the magnetic field energy density, and $U_0 = 4.2 \times 10^{-14} \text{ J m}^{-3}$ is the CMB energy density at $z = 0$. Using the simplification that all of the sources are at the same redshift, we can calculate the IC flux density for a range of redshift and magnetic field values. We used redshifts of $0.01 \leq z \leq 4$ and magnetic field values in the range of $0.01 \mu\text{G} \leq B \leq 10 \mu\text{G}$ [based on B values for nearby clusters being around $1 \mu\text{G}$, 53].

When integrating the new source count (dN/dS_{IC}) we obtain a range of values of the CXB for energies of 100s of keV. Churazov et al. [28] presented observations of the CXB spectrum measured by INTEGRAL of $E^2 dN/dE \leq 15 \text{ keV}^2 \text{ s}^{-1}$

$\text{cm}^{-2} \text{ keV}^{-1} \text{ sr}^{-1}$ for $E \geq 100 \text{ keV}$. In these units our models yield values of 10^{-13} to 5 for $E^2 dN/dE$, depending on the assumed redshift and magnetic field strength (larger values for lower B and higher z). This shows that such models should not have a large impact on the X-ray background.

5.8.2 Cluster Emission

If we are to assume that Model 2 (middle right panel of Fig. 5.9) represents astrophysical sources, we need to determine how they compare to known objects. Making some simple assumptions, we can calculate possible luminosities and redshifts. We chose several redshifts for the peak of the parabola and calculated the K -corrected 1.4-GHz luminosity, assuming a spectral index of $\alpha = -1.1$. Then, assuming the objects all have the same intrinsic luminosity, we calculated the redshifts at which the counts have fallen to 50 per-cent of the peak. We did this for peak redshifts of $z = 0.25, 0.5, 1$, and 2; the results are listed in Table 5.5.

It seems unlikely that this population could represent cluster emission from radio haloes or relics. The luminosity values for such objects, given in Feretti et al. [53], are in the range of $23 \leq \log_{10}[L_{1.4}] \leq 26$, several orders of magnitude larger than seen here. To date, we know of less than 100 clusters that host giant or mini radio haloes [53]. Extended radio emission in clusters has only been observed in high mass clusters ($\geq 10^{14} M_\odot$) at low redshift, and all with total 1.4 GHz flux densities in the 10s to 100s of mJy.

There could of course be similar objects (relics, haloes, etc.) in smaller mass groups at higher redshifts that are contributing. Nurmi et al. [128], using data from the SDSS survey, found that the majority of galaxies reside in intermediate mass groups, as opposed to large clusters. Stacking of subsamples of luminous X-ray clusters by Brown et al. [19] found a signal of diffuse radio emission below the radio upper limits on individual clusters. It is possible that there are clusters or groups that are more ‘radio quiet’, below current detection thresholds [e.g. 21, 24].

Zandanel et al. [198] used a cosmological mock galaxy cluster catalogue, built from the MultiDark simulation [197], to investigate radio loud and radio quiet halo populations. Their model, which assumes 10 per cent of clusters to have radio loud haloes, is a good fit [see figure 5 of 198] to the observed radio cluster

data from the NVSS survey [72]. The luminosity limit for the observed NVSS data is $\log_{10}[L_{1.4} (\text{W Hz}^{-1})] \simeq 23.5$, while the simulation continues to a limit of $\log_{10}[L_{1.4} (\text{W Hz}^{-1})] \simeq 20$.

It is instructive to compare these simulated haloes with our ATCA data. Using the online database to access the simulation [149]², we used the 1.4-GHz halo simulation snapshots for $z = 0, 0.1, 0.5$, and 1 , scaling the luminosities for each redshift snapshot to give the flux density that would be observed at 1.75 GHz. We computed a source count from these data, combined it with the unsubtracted discrete emission model and Gaussian noise to obtain a predicted $P(D)$. The source count and $P(D)$ are shown in Fig. 5.10. The source count from this model only adds an additional 1.5 mK to the radio background temperature.

The fit to the image $P(D)$ is not unreasonable, with this model adding only a modest excess width to the distribution compared with the unsubtracted discrete model on its own. The source count would likely not decrease as significantly in the sub-mJy region if the simulation included data from redshifts higher than $z = 1$, and this would likely improve the fit. The χ^2 is high mainly due to this model having a slightly higher number of bright objects and thus over-predicting the tail of the distribution. However, some of these brighter haloes would be relatively nearby, hence larger on the sky and so potentially resolved out in our data (see Table 5.1).

The halo model has similar count amplitude to our best-fit for Model 3 around 1 mJy. This halo model then begins to fall off, whereas the node model rises; this again could be due to the lack of high redshift objects. This type of halo model is therefore not necessarily inconsistent with our phenomenological model. Assuming the model from Zandanel et al. [198] is a realistic extension of radio haloes to fainter luminosities, then it is possible for such haloes to exist given our data. However, more deep observations of clusters are necessary to test the accuracy of this model.

One thing to keep in mind is that the model from Zandanel et al. [198] deals with the issue of the origin of radio haloes, i.e. haloes being generated from re-acceleration or hadronic-induced emission. This model assumes a fraction of the

²<http://www.cosmosim.org>

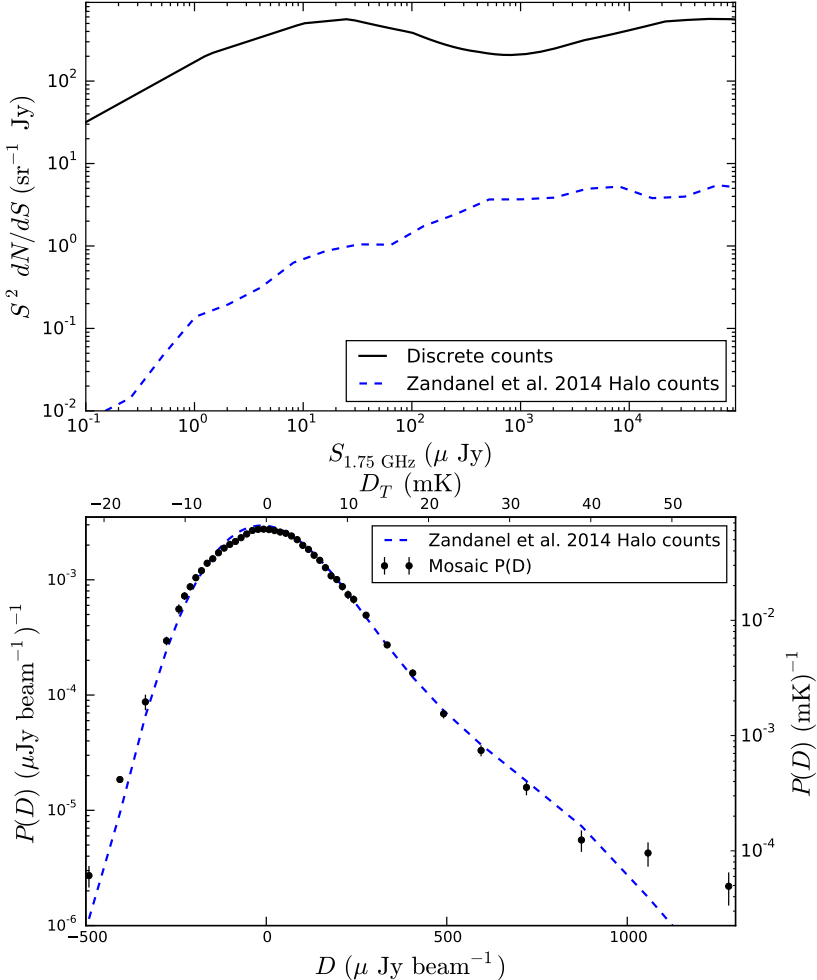


Figure 5.10: Comparison of the radio cluster halo model from Zandanel et al. [198] with current data. The top panel shows the S^2 normalized source count derived from taking the halo radio luminosity values at redshift snapshots $z = 0, 0.1, 0.5$, and 1 , and converting to 1.75 GHz (blue dashed line), compared with the discrete radio source count (black solid line). The bottom panel shows the output $P(D)$ for the halo model plus the unsubtracted point source contribution, convolved with Gaussian noise of $52 \mu\text{Jy beam}^{-1}$ (black points).

observed radio emission is of hadronic origin. However, if the hadronic contribution is negligible, acting only at radio-quiet levels, the predicted counts would be dramatically lower at all masses.

5.8.3 Dark Matter Constraints

It has been proposed that radio emission may originate from WIMP dark matter particles. Dark-matter particle annihilation in haloes releases energy as charged particles, which emit synchrotron radiation due to the magnetic field of the surrounding galaxy or galaxies. The predicted emission depends on the mass of the dark matter particle and halo mass or density profile, as well as the strength of the magnetic field.

Fornengo et al. [63] presented one dark matter model with two source-count predictions, the first assuming all the halo substructures are resolved and the second assuming all the substructures are unresolved. The predicted source counts, shifted to 1.75 GHz, is shown in the top panel of Fig. 5.11 along with the discrete radio source count. Their best-fit model has a dark matter mass of 10 GeV, assuming annihilation or decay into leptons. We computed the predicted $P(D)$ for both models, plus the unsubtracted discrete source contribution convolved with Gaussian noise of $52 \mu\text{Jy beam}^{-1}$. The model $P(D)$ s are shown in the bottom panel of Fig. 5.11 along with our radio image $P(D)$.

Clearly these particular models are not consistent with our current radio data. Any other dark matter models would need reduced amplitude of the counts for flux densities greater than about $10 \mu\text{Jy}$. Models with the dark matter count amplitude as high as or higher than that from known radio sources for these brighter flux densities would overproduce the emission seen and are therefore ruled out. Dark matter models consistent with our data and responsible for the ARCADE 2 emission would need to produce a large portion of the emission from the sub- μJy region, a region not constrained by our data. However, the required number counts would render such predictions unrelated to galactic haloes (i.e. the number sources that faint required to account for that amount of emission would be too very large compared with the number if individual galaxy count models/predictions).

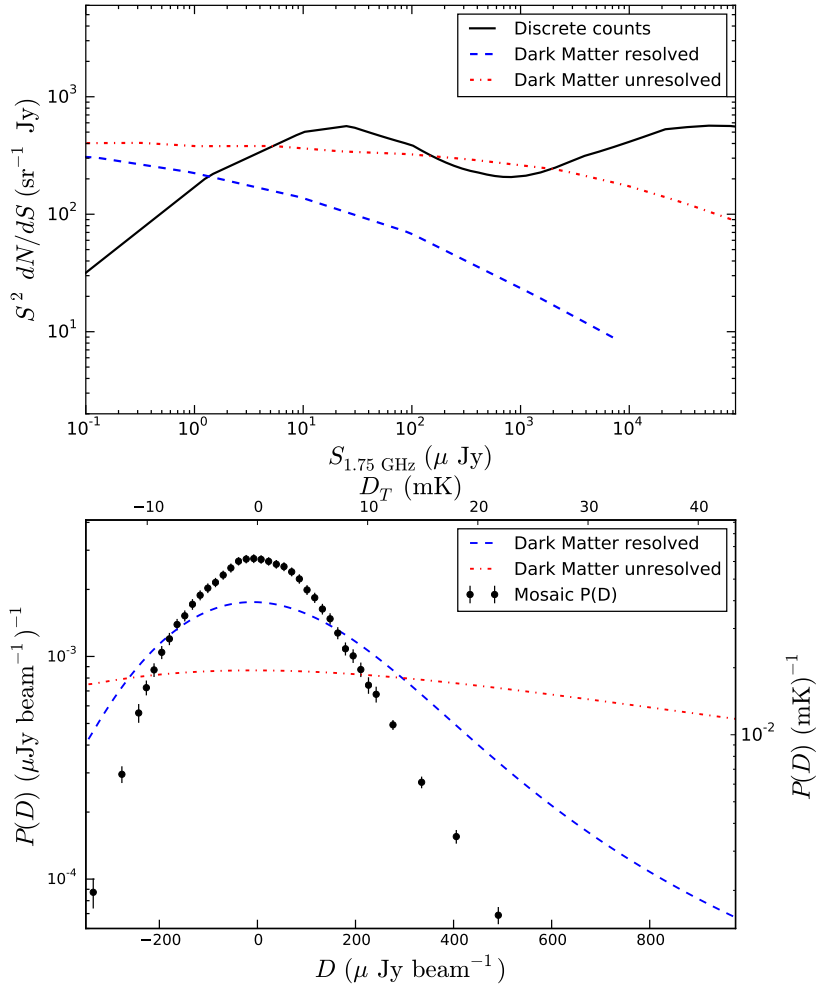


Figure 5.11: Comparison of one particular dark matter model with current radio data. The top panel shows the two predicted source count models [see figure 3 in 63], shifted to 1.75 GHz, for a 10 GeV dark matter particle mass, assuming all the structures are resolved (blue dashed line) and unresolved (red dot-dashed line), together with the discrete radio source count (black solid line), with S^2 normalization. The bottom panel shows the output $P(D)$ s for the two models plus the unsubtracted point source contribution, convolved with Gaussian noise of $52 \mu\text{Jy beam}^{-1}$ (black points).

5.9 Integral Counts

Now that we have closed the loophole of extended emission, we can revisit source count constraints in general. It is important for future deep survey designs to have an accurate estimate of the expected number of source detections. To estimate this we can derive the integral source counts $N(> S)$, or the total number of sources with flux density greater than S per unit area. Deep and accurate estimates of $N(> S)$ can provide useful information for surveys at a range of frequencies, with proper scaling; in the synchrotron-dominated regime we should be able to extrapolate by a factor of a $\sim \pm 2$ in frequency.

This is of particular relevance to the SKA, and its pathfinders, Australian Square Kilometre Array Pathfinder (ASKAP) and MeerKAT, as well as the new planned deep VLA survey. The VLA Sky Survey (VLASS) is aiming to map an area 10 deg^2 to a depth of $1.5 \mu\text{Jy}$ at 1.4 GHz with a resolution of roughly 1 arcsec [97]. The Evolutionary Map of the Universe survey (EMU) continuum survey [127] planned for ASKAP will cover the entire sky south of Dec $+30^\circ$ with a resolution of 10 arcsec at 1.4 GHz , and will also be sensitive to diffuse emission with a sensitivity at 1 arcmin scale similar to that reached in this paper. The deep survey with MeerKAT [MIGHTEE, 96], will reach an rms of $1 \mu\text{Jy}$ over 35 deg^2 with arcsec resolution. In the following decade, the SKA will conduct an all-sky survey to an rms of $1 \mu\text{Jy}$, and a smaller survey to an rms of 100 nJy . It would be helpful in planning to know what source densities are expected in these surveys.

We can obtain the integral source counts from

$$N(> S) = \int_S^\infty \frac{dN}{dS} dS. \quad (5.5)$$

We have derived the integrated source counts from the discrete model in Chapter 4, as well as that discrete model plus the best-fits from the extended emission models. These are shown in Fig. 5.12, with values listed in Table 5.6. Also shown on the plot are the expected SKA and SKA Pathfinder survey limits.

The SKA and Pathfinders should not be limited by any natural source confusion for discrete sources. The natural confusion limit is the confusion caused by the finite source sizes, as opposed to confusion caused by the telescope beam size.

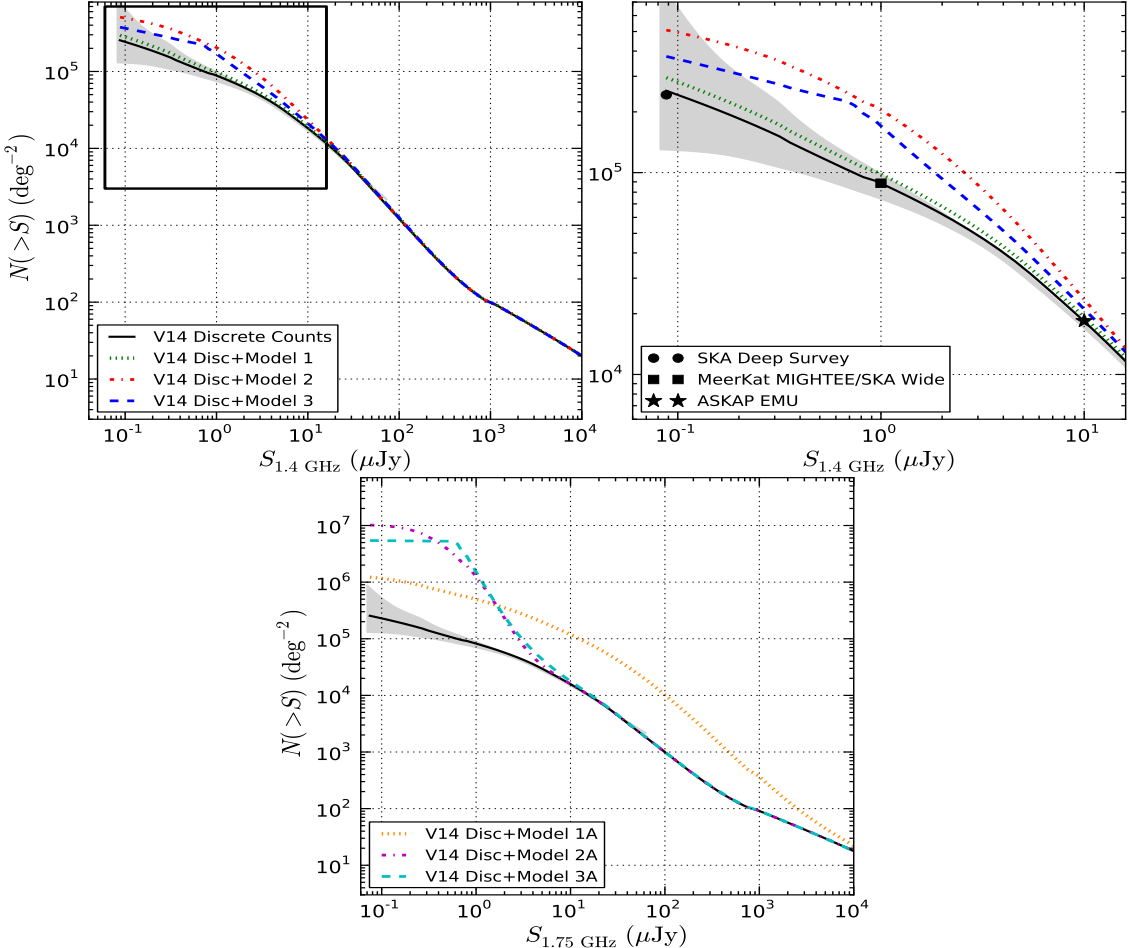


Figure 5.12: Integrated source counts at 1.4 GHz (top) and 1.75 GHz (bottom). The solid black lines are the discrete source count (DS) from Chapter 4, scaled from 3 GHz using $\alpha = -0.7$. The green dotted lines are DS + Model 1, the red dot-dashed lines are DS + Model 2, and the blue dashed lines are DS+ Model 3. The shaded grey areas represent 68 per cent confidence regions of the discrete count derived from Chapter 4. The upper right-hand panel shows a close up of the region marked by the solid rectangle in the upper left panel. The three points show the expected number of sources per square degree for the upcoming SKA and SKA Pathfinder surveys based on their expected depths (the circle is SKA, the square is MIGHTEE and the all sky SKA, and the star is the EMU survey). The bottom panel (1.75 GHz) shows Model 1A, Model 2A, and Model 3A as orange dotted, magenta dot-dashed, and cyan dashed lines, respectively (models fit with the ARCADE 2 prior).

Table 5.6: Integrated source count values of the different models scaled to 1.4 GHz.

$\log_{10}[\frac{S}{\text{Jy}}]$	Discrete (No. deg $^{-2}$)	Dis+Mod1 (No. deg $^{-2}$)	Dis+Mod 2 (No. deg $^{-2}$)	Dis+Mod 3 No. deg $^{-2}$)
-7.0	2.4×10^5	2.8×10^5	4.9×10^5	3.6×10^5
-6.5	1.5×10^5	1.7×10^5	3.5×10^5	2.7×10^5
-6.0	8.8×10^4	9.8×10^4	2.1×10^5	1.7×10^5
-5.5	4.7×10^4	5.1×10^4	8.3×10^4	6.3×10^4
-5.0	1.8×10^4	1.9×10^4	2.3×10^4	2.1×10^4
-4.5	5.4×10^3	5.6×10^3	5.7×10^3	5.8×10^3
-4.0	1.2×10^3	1.2×10^3	1.2×10^3	1.2×10^3
-3.5	2.9×10^2	2.9×10^2	2.9×10^2	2.9×10^2

For discrete sources with an average source size of approximately 1 arcsec 2 for faint sources, the natural confusion limit would be less than 10 nJy. However, extended objects of 2 arcmin diameter, for example, would begin to heavily overlap above 1000 sources per deg 2 which corresponds to a flux density at 1.4 GHz of approximately 100 μ Jy.

To highlight some numbers (ignoring extended emission now) the discrete model predicts 1×10^9 sources over the whole sky brighter than 23 μ Jy, and 10 sources per arcmin 2 brighter than 4.6 μ Jy. At a limit of 1 μ Jy we estimate 88,500 sources per square degree at 1.4 GHz. For relatively modest extrapolations in flux density and frequency, the cumulative counts for $0.1 \leq S \leq 5 \mu\text{Jy}$ can be well described by

$$N(> S) \simeq 84,800 \left(\frac{S}{1\mu\text{Jy}} \right)^{-0.48} \left(\frac{\nu}{1.4\text{GHz}} \right)^{-0.33} \text{deg}^{-2}, \quad (5.6)$$

and for $5 < S \leq 500 \mu\text{Jy}$

$$N(> S) \simeq 296,700 \left(\frac{S}{1\mu\text{Jy}} \right)^{-1.20} \left(\frac{\nu}{1.4\text{GHz}} \right)^{-0.33} \text{deg}^{-2}. \quad (5.7)$$

5.10 Conclusions

Our ATCA image is the deepest available with a mean frequency of 1.75 GHz and a FWHM resolution of $150 \text{ arcsec} \times 60 \text{ arcsec}$. The image is confusion-limited with an rms of $(155 \pm 5) \mu\text{Jy beam}^{-1} = (6.9 \pm 0.2) \text{ mK}$ and average instrumental noise $\sigma_n = (52 \pm 5) \mu\text{Jy beam}^{-1} = (2.3 \pm 0.2) \text{ mK}$. Using this data we were able to test techniques and constrain models.

The novel techniques are the following.

1. We have used wide-band high resolution data to perform source subtraction in our low resolution data while accounting for frequency change and un-subtracted sources.
2. We tested simulations at both low and high angular resolution in order to determine the how large scale emission appears on small scales.
3. With this data we have performed a $P(D)$ analysis and bootstrap tests to confirm a excess emission over that from point sources at the 3σ level.
4. We have used Markov chain Monte Carlo sampling with $P(D)$ analysis to test a variety of source count models for this excess extended emission.

Using these techniques we have drawn the following conclusions.

1. The $P(D)$ approach is a viable test for data of this larger resolution as long as sources are still not much larger than the beam size.
2. It is possible for there to be a large amount of emission from extended sources that would be missed, or resolved out, with higher resolution images.
3. Our extended source count models rule out emission or populations that could account for the ARCADE 2 emission down to the $1 \mu\text{Jy}$ level.
4. Cluster emission and dark matter annihilation emission source count model can be constrained by this technique, with the tightest constraints for flux densities $\geq 0.5 \text{ mJy}$.

5. Faint large scale emission may only be detectable by such techniques as the confusion level at large angular scales is too great to allow for imaging of individual sources.

Here we presented a brief summary of the conclusions from this chapter. For a discussion of these results in a broader context see Chapter 8.

Chapter 6

Discrete-Source Catalogue

There is far more to be gleamed from a radio survey than just the source count. In order to fully explore the sources and their properties a catalogue is necessary. Catalogues yield information on source sizes, spectral dependence, and when combined with catalogues from surveys at other wavebands, information on galaxy population types, redshifts, the star formation rates, evolution and more.

We decided to catalogue both the C-configuration data and the CB-configuration data separately (with the C data being the data from just the VLA C antenna configuration and CB being the data from the C-configuration and the B-configuration together, see Chapter 2.2). The CB data have a higher resolution, which should provide more positional accuracy in the fitting. However, it also has higher noise for the resolution. This is because, even though it is a combination of the C and B data, and thus should have lower noise given more data, the majority of the data is from the lower resolution and so to achieve higher resolution, weighting is applied to the data before transforming to an image. This down-weights the lower resolution and up-weights the high resolution samples where there are fewer data, essentially decreasing the total amount of data and increasing the image noise.

We also want to catalogue both resolution data sets in order to see how they compare for future surveys. The proposed VLASS survey [97] would have a resolution closer to our CB data (or higher) whereas SKA Pathfinder surveys, such as EMU [127], will have lower resolution similar to the C data. Cataloguing the two resolutions of the same field, calibrated and transformed to images in the same

way, should inform us about what kind of differences can be expected between the surveys.

This work has not yet been published and the catalogue presented here may not be the published version. In Section 6.1 we describe the general process of source finding and fitting and how we used simulations to test for uncertainties as well as other effects such as completeness. Section 6.2 details the catalogues from the actual VLA data, including a comparison between the two resolutions and our investigation of extended sources. Section 6.3 presents the source counts from the two catalogue versions. Section 6.4 discusses how we can use the wide VLA bandwidth to look at the spectral dependence of the catalogue sources. Finally, in Section 6.5, we present preliminary cross-matches of our catalogues with others from the optical, IR, and radio.

6.1 Simulations

For source fitting we used the OBIT task FNDsou. The images are searched for peaks down to the 3σ level. Each peak area is then fit with a 2D elliptical Gaussian with the fit parameters being the peak flux density (S_P), the centre RA and centre Dec positions, the major axis FWHM (θ_M) and minor axis FWHM (θ_m) and the position angle (ϕ). The fitting was constrained such that the major and minor axes could not be less than the image beam FWHM (θ_B). The total integrated flux density (S_T) is computed as

$$S_T = S_{\text{peak}} \frac{\theta_M \theta_m}{\theta_B^2}. \quad (6.1)$$

To understand the fit uncertainties associated with our images, noise properties, and fitting software, we generated simulated images and run them through our fitting procedure. We are then able to compare the fit output with the known input. We performed several sets of simulations.

First we ran the simplest case of inserting point sources with set flux densities of 3, 4, 5, 8, 12, and 100 μJy . These were inserted at points chosen from a grid over the image, such that the distance between the sources was $\gg \theta_B$. These

point sources were convolved with the beams from our C and CB images, then added to backgrounds of random Gaussian beam-convolved noise with $\sigma = 1.05$ and $1.15 \mu\text{Jy beam}^{-1}$ for the two resolutions. This initial case was meant simply to determine the uncertainties of fitting in the presence of correlated noise. We created four simulated images (each made at both the high and low resolutions), each image having 400 sources in it. These images were then fit using FNDSOU. The output of FNDSOU was cross-matched with the true positions to within a 5 arcsec radius. Then the data from all four cases were collated to look at the results.

However, the real world case is more complicated. We next wanted to carry out tests with as realistic a setup as possible. We used the source catalogues from eight separate $0.5^\circ \times 0.5^\circ$ areas of the SKADS S³ simulation. We know already that the source count from the simulation matches fairly closely to published source counts, and it includes some clustering as well as a fairly realistic source size distribution. We scaled the flux densities from 1.4 GHz to 3 GHz using $\alpha = -0.7$. We then cut out any sources with $S > 1 \text{ mJy}$ to more closely approximate our field, where the brightest source is around 3 mJy. We also cut out AGN objects with extended lobes or jets, because in real images the few such sources would not be fit with Gaussians and we are solely concerned here with single component sources. The images were generated and the 3 GHz VLA primary beam was applied to each simulated image. Then the images were convolved with the CB and C beams to create high and low resolution versions of each. Finally, beam-convolved noise was added to each image. These eight images were then fit using FNDSOU, with the output of FNDSOU cross-matched with the known positions to within a 5 arcsec radius. Finally the data from all cases were collated.

6.1.1 Uncertainties

In Condon [32] the errors for 2D elliptical Gaussian fits are discussed. The square of the overall signal-to-noise ratio p^2 is

$$p^2 = \frac{\pi}{8 \ln 2} \frac{\theta_M \theta_m S_P^2}{h^2 \mu^2}, \quad (6.2)$$

where h is the pixel size, and μ is the image noise. The errors on each of the fit parameters as related to p^2 (from Condon [32]) are

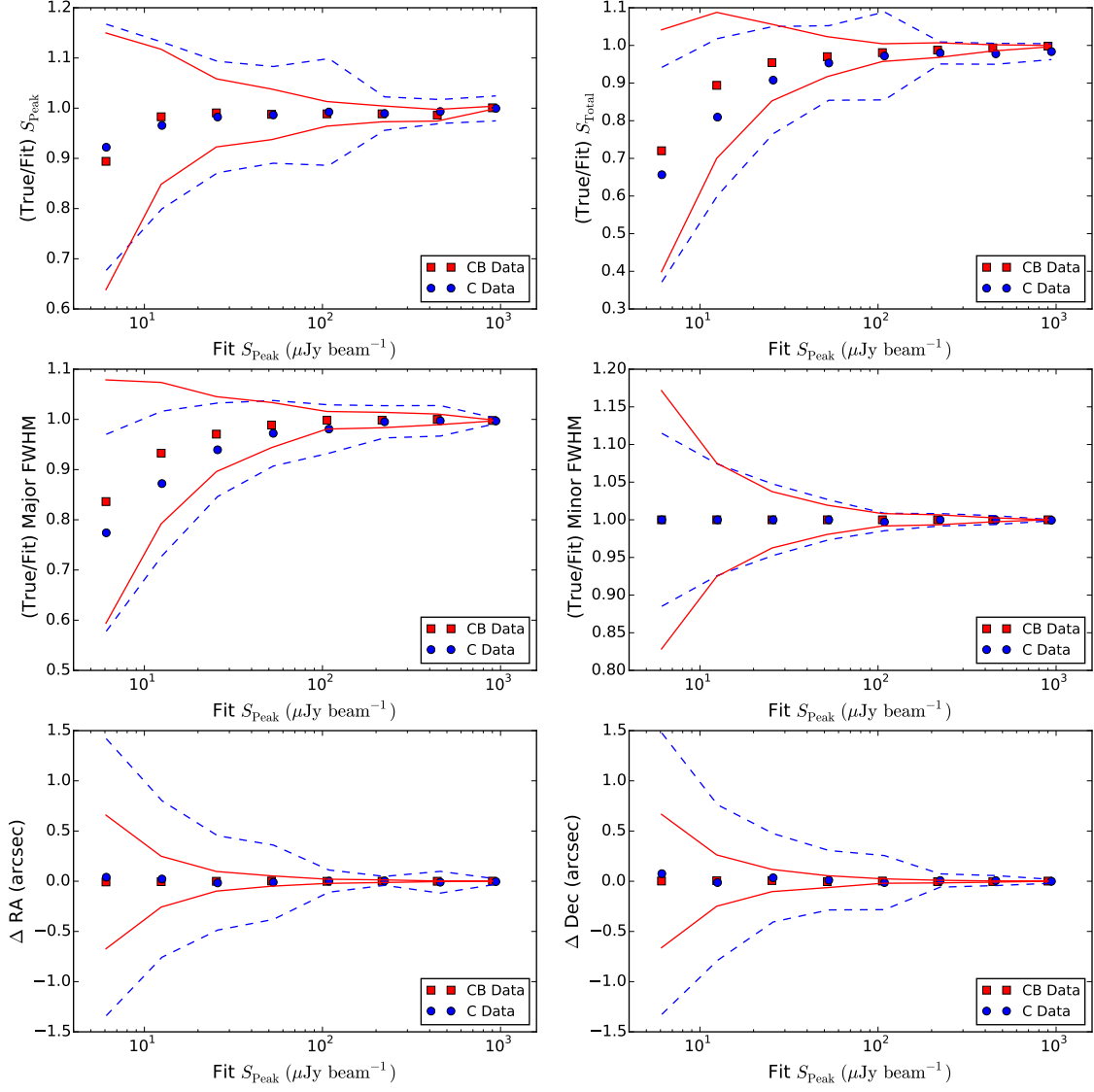


Figure 6.1: The mean of either the ratio of the true to fitted values or difference from the realistic simulations in bins of peak flux density. The C values (blue circles) were made with C data image resolution and CB values (red squares) made with CB data image resolution. The lines show the 1σ uncertainties (red solid lines for CB data and blue dashed lines for C data). From left to right and top to bottom the panels are S_{peak} ratios, S_{total} ratios, major axis size ratios, minor axis size ratios, ΔRA , and ΔDec .

$$\begin{aligned}
\frac{2}{p^2} &\simeq \frac{\mu^2(S_P)}{S_P^2} = \frac{\mu^2(S_T)}{S_T^2} = \\
8 \ln 2 \frac{\mu^2(x_0)}{\theta_M^2} &= 8 \ln 2 \frac{\mu^2(y_0)}{\theta_m^2} = \\
\frac{\mu^2(\theta_M)}{\theta_M^2} &= \frac{\mu^2(\theta_m)}{\theta_m^2} = \\
\frac{\mu^2(\phi)}{2} \left(\frac{\theta_M^2 - \theta_m^2}{\theta_M \theta_m} \right).
\end{aligned} \tag{6.3}$$

Here x_0 , and y_0 are the centre coordinates.

However, these equations do not factor in the presence of correlated noise. The simple simulation case should then test whether these equations hold up when the noise has also been convolved with the beam. Taking the fitted and matched data and binning by true flux density we computed the mean and standard deviation for the fitted peak flux density, total flux density, positions, axis sizes, and position angle, and observe that the resulting parameter uncertainties are consistent with those predicted by eq. 6.3.

We took all the sources from the realistic simulations that were found from the fitting routine and cross-matched that catalogue with the true, or input, source catalogue. Using the matches, we computed the ratios of the true to fitted values for the peaks, major axis size, minor axis size, total flux density, and the difference in RA and Dec positions and binned them in bins of peak flux density. Figure 6.1 shows the mean ratios and standard deviations for these bins for both image resolutions. We can see from this that the error bars decrease as expected with peak flux density. Also noticeable here is that the fitting overestimates the major axis size and peak flux density for faint flux density sources. This is a known complication with most fitting routines when dealing with low signal to noise sources.

The goal of the realistic simulations was to use the results in order to estimate uncertainties on the fit results for the real data. To do this we took all the matched simulated sources and binned them by fitted peak flux density and fitted deconvolved major axis size, where the deconvolved major axis (θ_{DM}) and deconvolved minor axis (θ_{Dm}) were computed as $\theta_{DM} = \sqrt{\theta_M^2 - \theta_B^2}$ and $\theta_{Dm} = \sqrt{\theta_m^2 - \theta_B^2}$.

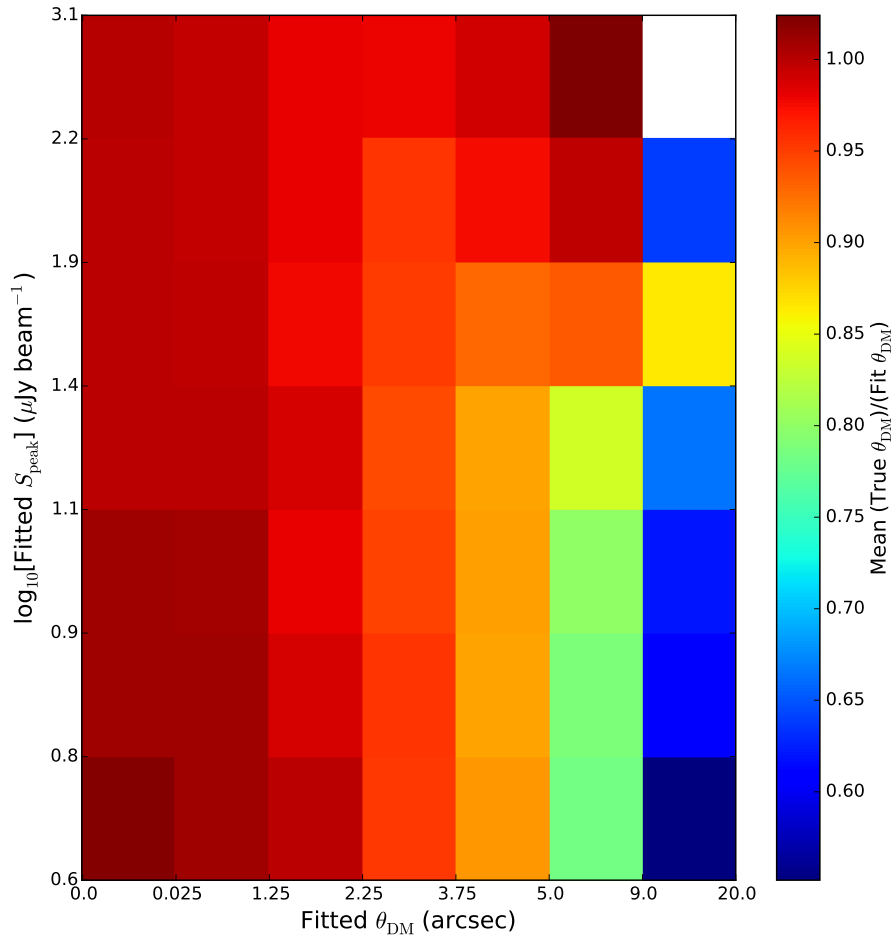


Figure 6.2: Mean ratio of true deconvolved major axis size to fitted deconvolved major axis size of sources from the realistic simulation in bins of peak fitted flux density and fitted major axis FWHM. The white bins mean there are no sources within those size and peak ranges. The left-most bins are unresolved sources ($\theta_M = \theta_B$).

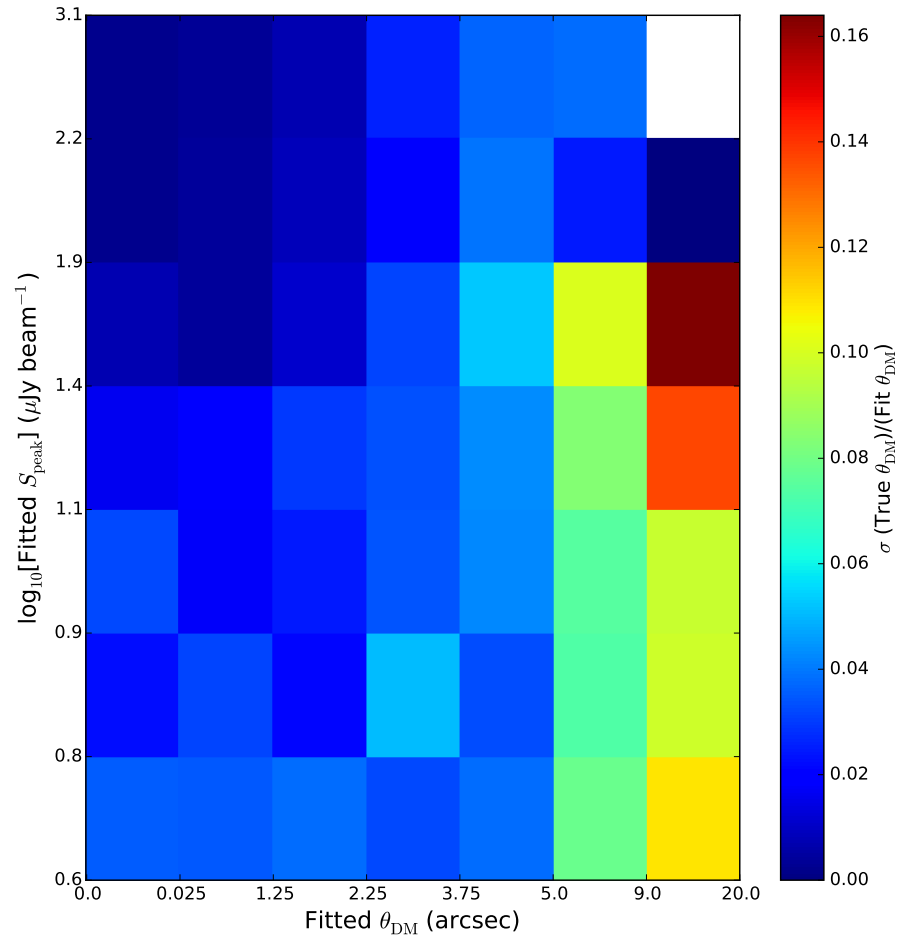


Figure 6.3: Standard deviation of the ratio of true deconvolved major axis size to fitted deconvolved major axis size of sources from the realistic simulation in bins of peak fitted flux density and fitted major axis FWHM. The white bins mean there are no sources within those size and peak ranges. The leftmost bins are unresolved sources ($\theta_M = \theta_B$).

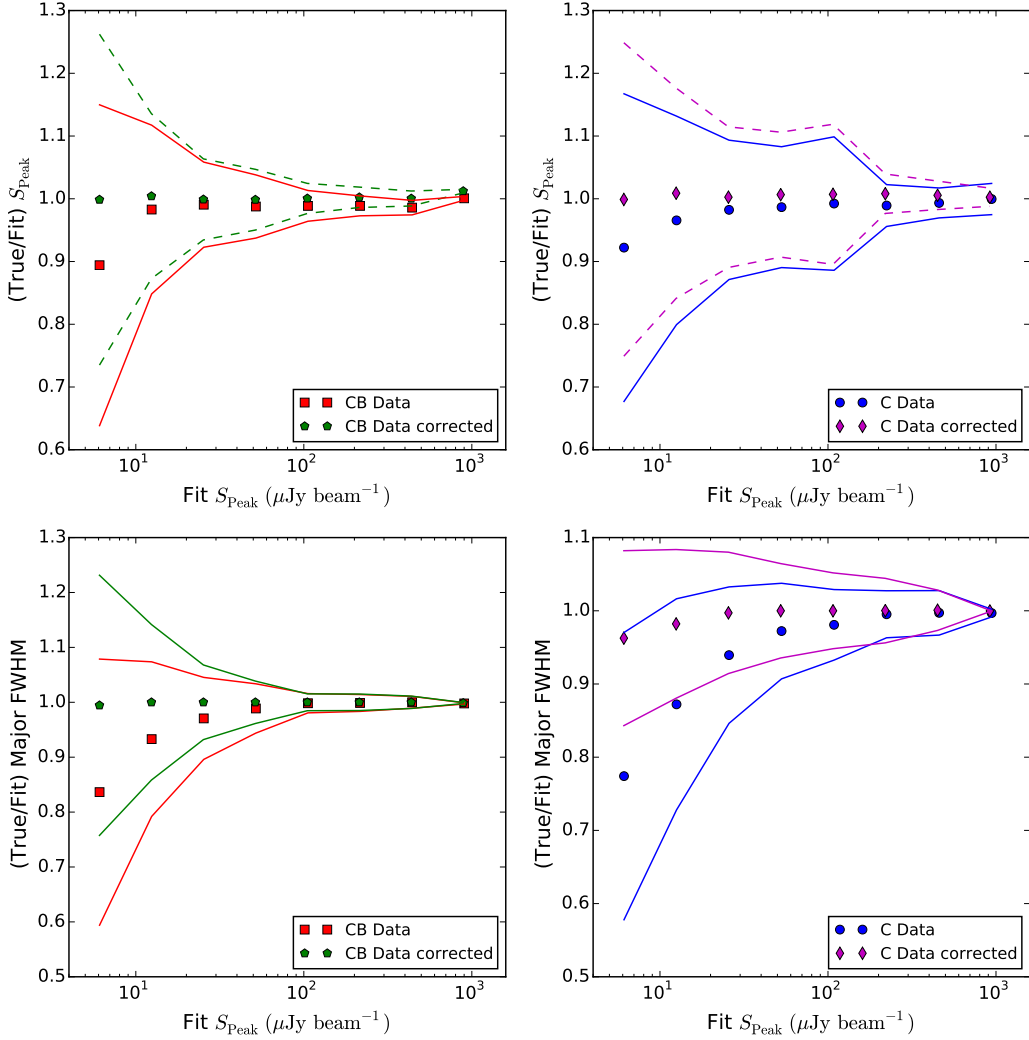


Figure 6.4: Mean of the ratio of the true to fitted values for peaks (top row) and major axis size (bottom row) from the realistic simulations in bins of peak flux density. The C values were made with C data image resolution (left column) and CB values made with CB data image resolution (right column). The corrected values are obtained after using the method of 2D binning and interpolation to get correction factors and uncertainties for individual sources.

We computed the mean and standard deviations of the ratios of the true values to the fitted values, i.e. $\text{Peak}^{\text{True}}/\text{Peak}^{\text{Fit}}$ in two dimensional bins; an example of the mean ratios is shown in Fig. 6.2 and the standard deviation ratios in Fig. 6.3 for major axis size. These show similar trends as fig. 6.1, however, the addition of binning by size as well shows that the effect of over estimation in a parameter is largest for those not just with the faintest peaks but also with the largest sizes. These figures show the 2D arrays for correction of the major axis size, however, corresponding arrays and corrections were computed for the fitted peaks and minor axis size, as well as uncertainties for the RA and Dec.

The bin setups were chosen to ensure a minimum of 20 sources in a bin (or when genuinely zero). We then interpolated the values of ratios and ratio standard deviations for peak flux density, total flux density, major and minor axes deconvolved sizes, and mean and standard deviation for ΔRA and ΔDec , for all of the sources fit. We tested this correction method on the simulated sources. Figure 6.4 shows how the mean ratios and uncertainties change after interpolating new values for the simulated fit values.

This method should enable us to account for the effect of flux boosting in our catalogue. This well known effect means that, particularly for sources near the noise limit, the fitted fluxes densities are more likely to be overestimated than underestimated, due to both instrumental and confusion noise. There are many papers that discuss correcting for flux boosting using Bayesian methods [e.g. 25]. However, many of those deal with submm or infrared data, where $\theta_B \gg \theta_S$ and therefore are only fitting for a total flux density rather than a peak together with size and shape. Submm and infrared images are also not affected by the primary beam, which complicates the Bayesian method used to compute probabilities directly from source counts. Therefore, considering our more complicated case, we chose to use the realistic simulations and this 2D interpolation to account for this effect by computing the corrections for the both size axes and the peak flux densities.

6.1.2 Completeness, False Detections, and Blending

The simulation catalogues can also be used to examine how well the fitting software does at finding all of the known sources, how often it includes a false detection, and how often it mistakes multiple sources for one source.

For each simulation realisation there are approximately 1000 sources within the primary beam area that are “detectable” by the limits set. Among those 1000 for the low resolution images, there are on the order of 50 to 100 sources that are fit as one source when there are in fact multiple (fainter) sources in or around the fitted source position. In these “blended” cases the fitting software tends to fit large (12 to 20 arcsec convolved) sizes for one or both of the axes and the total flux density for the one source is on average larger than the sum of the totals of the individuals it encompasses. This will have an impact on the source count of a catalogue, obviously lowering the count of fainter sources and increasing the count of the brighter sources. One possible way to improve this, or at least investigate it, would be to fit the same image multiple times, starting with the sizes being fixed to the beam size and then increasing the maximum allowed axis sizes. Comparing the results and residuals from this could help shed light on whether there is some fitting constraint process that would minimize blending or else some limits on the parameter space to identify blended objects. This issue is under active investigation.

The issues of completeness and false detections are somewhat complicated by whether one is interested in uncorrected or primary beam-corrected peak or total fluxes and whether we look at the fitted values or the true values of the matched sources. Examples of this for completeness are shown in Fig. 6.5. These plots show the number of sources, in bins of flux density, that were found by the fitting routine and had a known match within 5 arcsec, divided by the total number of known inserted objects in that flux density bin. This shows us that the completeness levels are lower if we consider the total flux density values rather than the peak flux densities. Also, the fitted flux densities values, both peaks and totals, seem to overestimate the number of bright sources. The figure also shows the difference that the primary beam and source size makes. For example the CB image for total flux densities at the faintest fluxes, when considering those that could have been detected (i.e. peaks $> 4\sigma$, bottom middle panel) is roughly 85%, whereas it drops

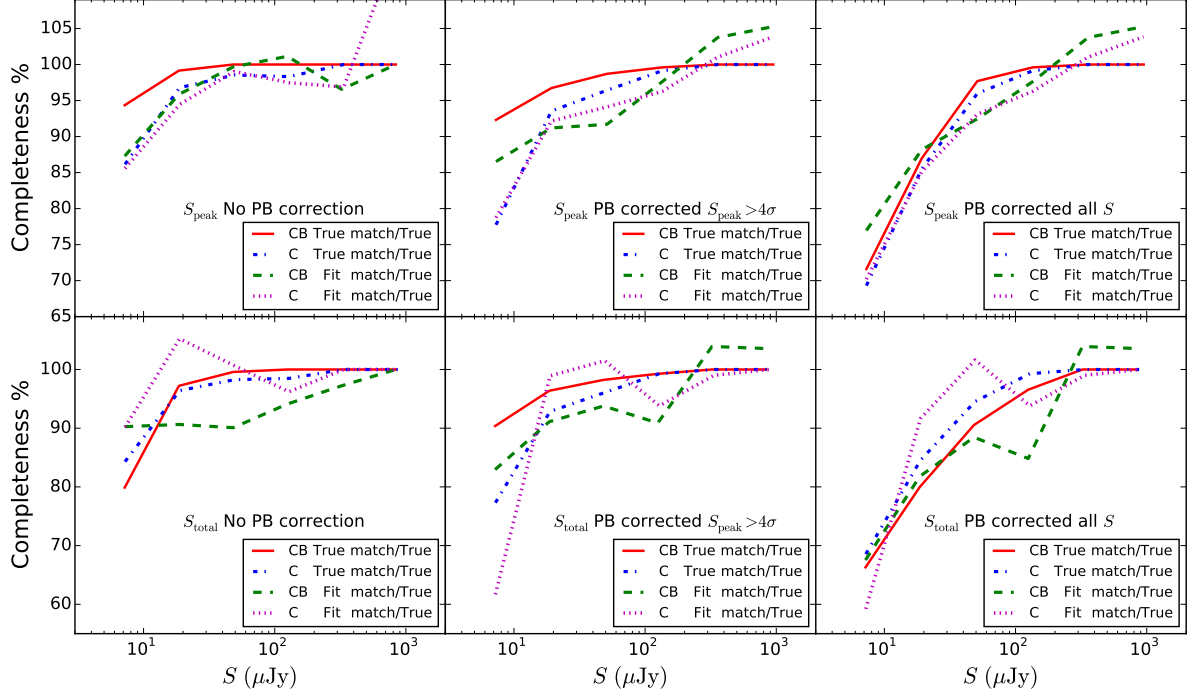


Figure 6.5: Completeness of sources from simulation. The plots show the number of sources binned by flux density of the sources with matches divided by the true total number of inserted sources. The top row shows the sources binned by peak flux density while the bottom row shows binned by total flux density. The left most plots show the sources binned by flux density uncorrected for the primary beam. The middle column is primary beam corrected flux densities but only those sources whose uncorrected peaks are $> 4\sigma$, or those that could have been detected. The right column is the primary beam corrected flux density for all sources. The red solid and green dashed lines are for the CB images true matched values and fitted matched values respectively. The blue dot-dashed line and magenta dotted lines are for the C images true matched values and fitted matched values.

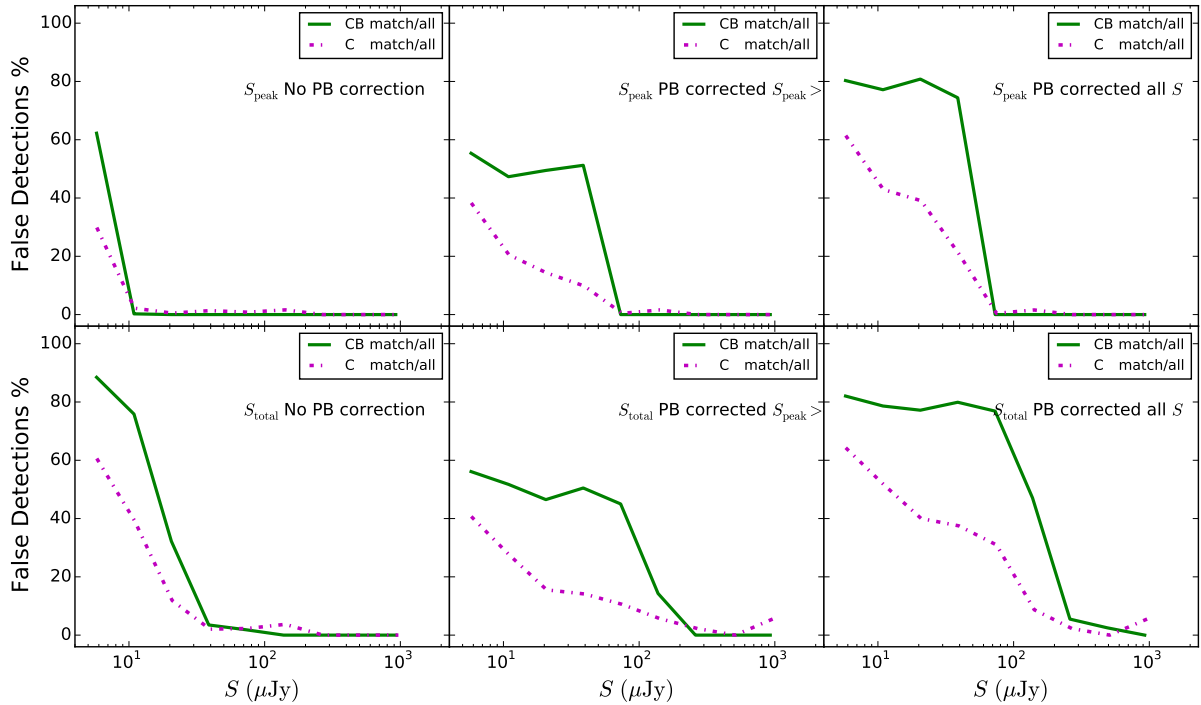


Figure 6.6: Percentage of false detections of sources from simulations. The plots show one minus the ratio of matched to all fit sources binned by flux density. The top row shows the sources binned by peak flux density while the bottom row shows them binned by total flux density. The leftmost plots show the sources binned by flux density uncorrected for the primary beam. The middle column is primary beam-corrected flux densities, but only those sources whose uncorrected peaks are $> 4\sigma$, or those that could have been detected. The right column shows the primary beam-corrected flux density for all sources. The green solid lines are for the CB images matched values, while the magenta dotted lines are for the C images matched values.

closer to 65% when considering all of the known sources whose total flux density is above 4σ (including ones whose peak is below 4σ , bottom right panel).

Examples of the false detection rate in the simulations are shown in Fig. 6.6. The plots show (1 minus) the number of sources binned by flux density for the sources with matches divided by the total number of sources detected. Again we can see how the false detection rate drops quickly to zero when considering non-primary beam-corrected flux densities, but levels off much more when looking at the corrected fluxes. There is an overall lower number of false detections with the C images, likely due to its lower noise.

When considering the completeness and false detection rate together there should be some flux density level which balances the number of possible false detections with a high completeness percent that can be used to set some kind of detection threshold. These constraints are usually dependent on the type of science to be carried out with the catalogue. Such results from these simulations for corrections to our catalogues is still under active investigation.

6.2 Catalogue

The catalogues were made in the same manner as described for the simulations. We fit the C and CB images separately before any primary beam corrections. Any sources with peaks $< 4\sigma$ were removed, with the CB data having $\sigma = 1.15 \mu\text{Jy beam}^{-1}$ and the C data having $\sigma = 1.02 \mu\text{Jy beam}^{-1}$. Fitted Gaussians for sources with structure were also cut from the initial catalogue and were treated separately (see below). The total flux densities were computed according to eq. 6.1. The flux densities are corrected for the primary beam based on the primary beam value at the fitted location. Full versions of the catalogues are given in Appendix A and B.

The method of 2D interpolation from simulated data (described in Sec. 6.1.1) was used for each catalogue and yielded uncertainty estimates for each source parameter. Residual images were made using the original fitted parameter values and the corrected parameter values. Where the χ^2 inside a box with size $2\theta_B \times 2\theta_B$ was smaller with the corrected values, those values were adopted as the new values in the catalogue. Spectral index estimates for each source are included, with the method described further in Sec. 6.4. The flux density distributions for each cata-

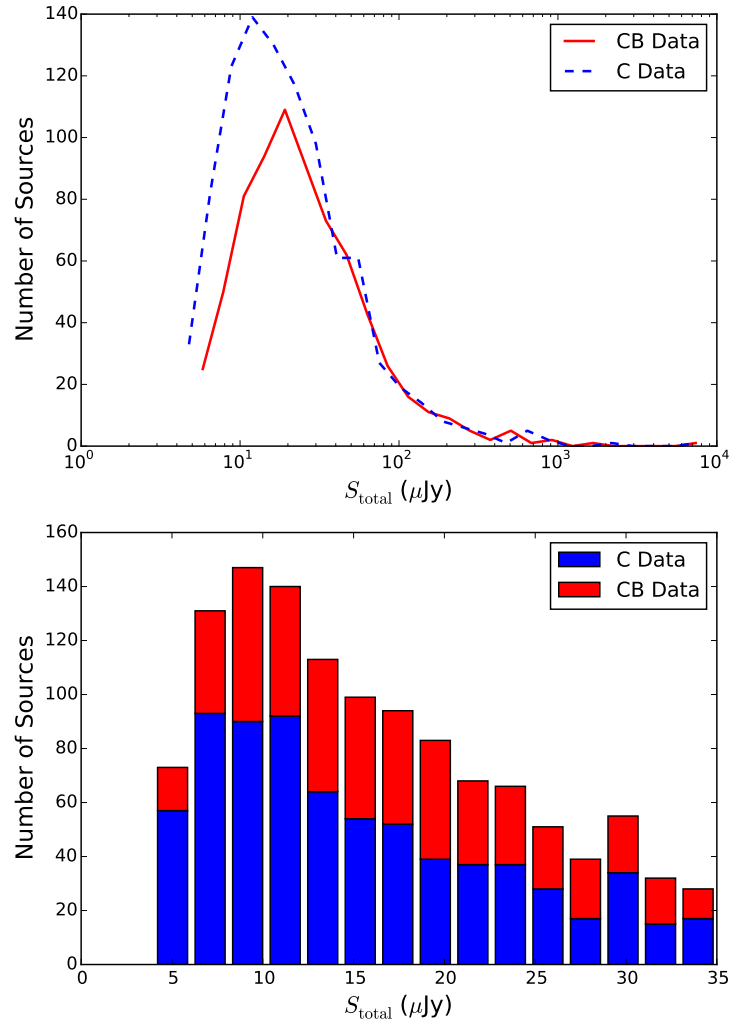


Figure 6.7: Histograms of total flux densities from both the CB and C catalogues. The top panel shows the full flux density distributions for the CB data (red solid line) and C data (blue dashed line). The bottom panel shows the distribution for just the fainter flux densities, with the CB data being red and the C data being blue.

logue are shown in Fig. 6.7, which shows that the catalogues are roughly complete down to 10 to 20 μ Jy.

We cross-matched the two resolution catalogues with each other, using a matching radius of 5 arcsec. Roughly 80 per-cent of the sources in the CB catalogue were found in the C catalogue, with about 60 percent of the C sources matched. One reason for only 80 per-cent of the CB sources being matched (besides possible false detections or faint sources near the detection limit), even though the C data has higher sensitivity, is source blending in the C catalogue. There are a number of sources where two (or possibly more) individual sources were fit in the CB image where only one blended source was fit in the C image. Thus during the cross-matching only the CB source closest to the C blended source was included. The non-blended sources without a counterpart (in either catalogue) are all near the noise threshold. This means they are either false detections or, due to the local noise distribution, the source is above the noise threshold in one image and below in the other. For the final version of the catalogue a source-by-source comparison will be necessary to accurately match the two resolution catalogues.

The C catalogue has about 1.3 times as many sources, mainly due to the lower noise threshold. Figure 6.8 shows a comparison of some of the parameters for the matched sources. The top left panel of this figure shows the total fluxes from each source from each catalogue. There is little scatter from a one-to-one relation for sources with $S \geq 100 \mu$ Jy. As well for these brighter sources the separation in centre positions is small (bottom left panel). There is certainly much more scatter between the two catalogues for fainter sources, which is not surprising. There is very little correlation in the major axis sizes (top right panel), which could be due to the poorer size sensitivity of the C data, incorrect matches, or source blending in the C data.

In some cases it is necessary to correct for the effects of time and bandwidth smearing. Bandwidth smearing is an effect of the limited spectral resolution and will radially broaden the synthesized beam by convolving it with a rectangle of angular width $\Delta\theta\Delta\nu/\nu$, where $\Delta\theta$ is the radial offset from the pointing centre. With our VLA data, even after the spectral averaging that was done, at the FWHM of the primary beam the bandwidth smearing is roughly 1.0 arcsec at 3 GHz, and hence is not a large concern for us. Similarly, time averaging can also produce

a radial smearing. The amount of smearing due to the time resolution goes as $\Delta\theta\Delta t/f$, where f is the Earth's sidereal rotation period of $86164\text{ s}/2\pi = 1.37 \times 10^4\text{ s}$. With our VLA data, after the time averaging for imaging, the maximum smearing from this effect at is only $\sim 0.4\text{ arcsec}$ at the FWHM of the primary beam.

6.2.1 Angular Size Distribution

There are several conventions when it comes to dealing with source sizes. If it is clear that a source has extended structure and is not well fit by a Gaussian we consider it to be extended. If both fitted axes have their lower limits larger than the beam these objects are fully resolved. If $\theta_M = \theta_m = \theta_B$ then these objects are unresolved. If for the major or minor axis $\theta_{M,m} - \Delta\theta_{M,m} < \theta_B < \theta_{M,m}$ then the axis is partially resolved. For some previous catalogues the procedure has been that when an axis is partially resolved than it is just set to the beam size [e.g. 118]. We have chosen not to do this when we report sizes and use sizes to calculate total flux densities. Instead we leave the axes at the fitted values and report a size flag to indicate the status. These flags are: (0) extended; (1) resolved; (2) major axis resolved minor partially resolved; (3) major axis resolved minor axis unresolved; (4) both major and minor axes partially resolved; (5) major axis partially resolved and minor axis unresolved; and (6) both axes unresolved.

The issue of the source angular size distribution as a function of flux density is very important (e.g. for $P(D)$ studies and source counts) yet the distribution is still not well known. It is not known how the size distribution changes with flux density at faint flux densities, and how if it varies by galaxy type, at least not with great accuracy. The source size distribution has an effect on the source count as well, and it is believed that differences in corrections regarding source sizes are likely to blame for the large amount of scatter in the counts from different surveys in the sub-mJy region. A deep survey with high resolution will miss larger sources near the survey limit, and this has sometimes been ignored, but at other times over-corrected.

The C image resolution is not ideal for investigating this, since the larger beam decreases the accuracy when measuring deconvolved source sizes. Because of

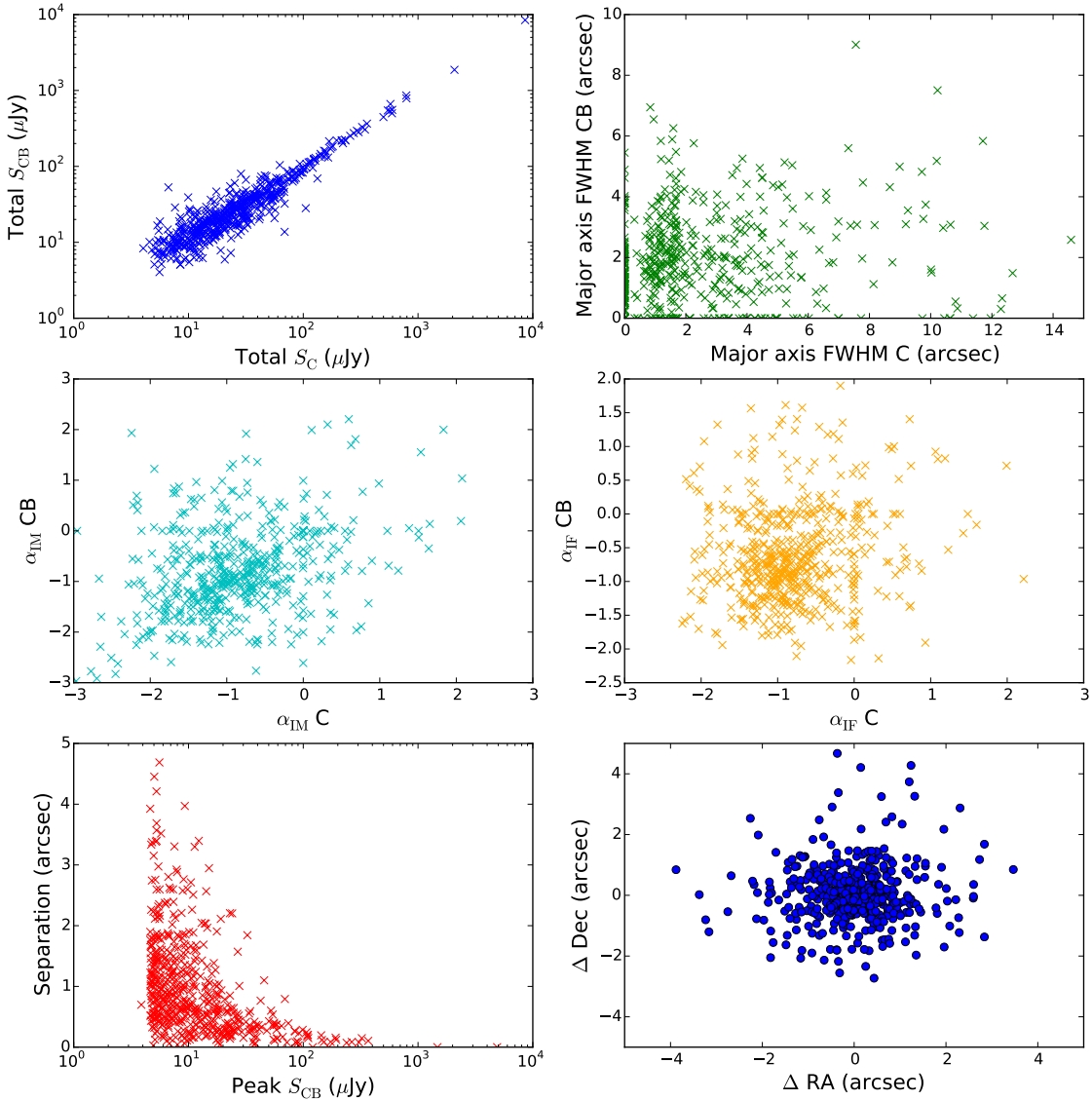


Figure 6.8: Comparison of matched sources from the C and CB catalogues.

The top left panel is the total flux density of the sources from each catalogue. The top right panel is the deconvolved major axis sizes for the matched sources. The middle panels show the spectral indices for α_{IM} (left) and α_{IF} (right). The bottom left panel is the matched separation vs. the fitted CB peak flux density. The bottom right panel is the difference in RA vs the difference in Dec.

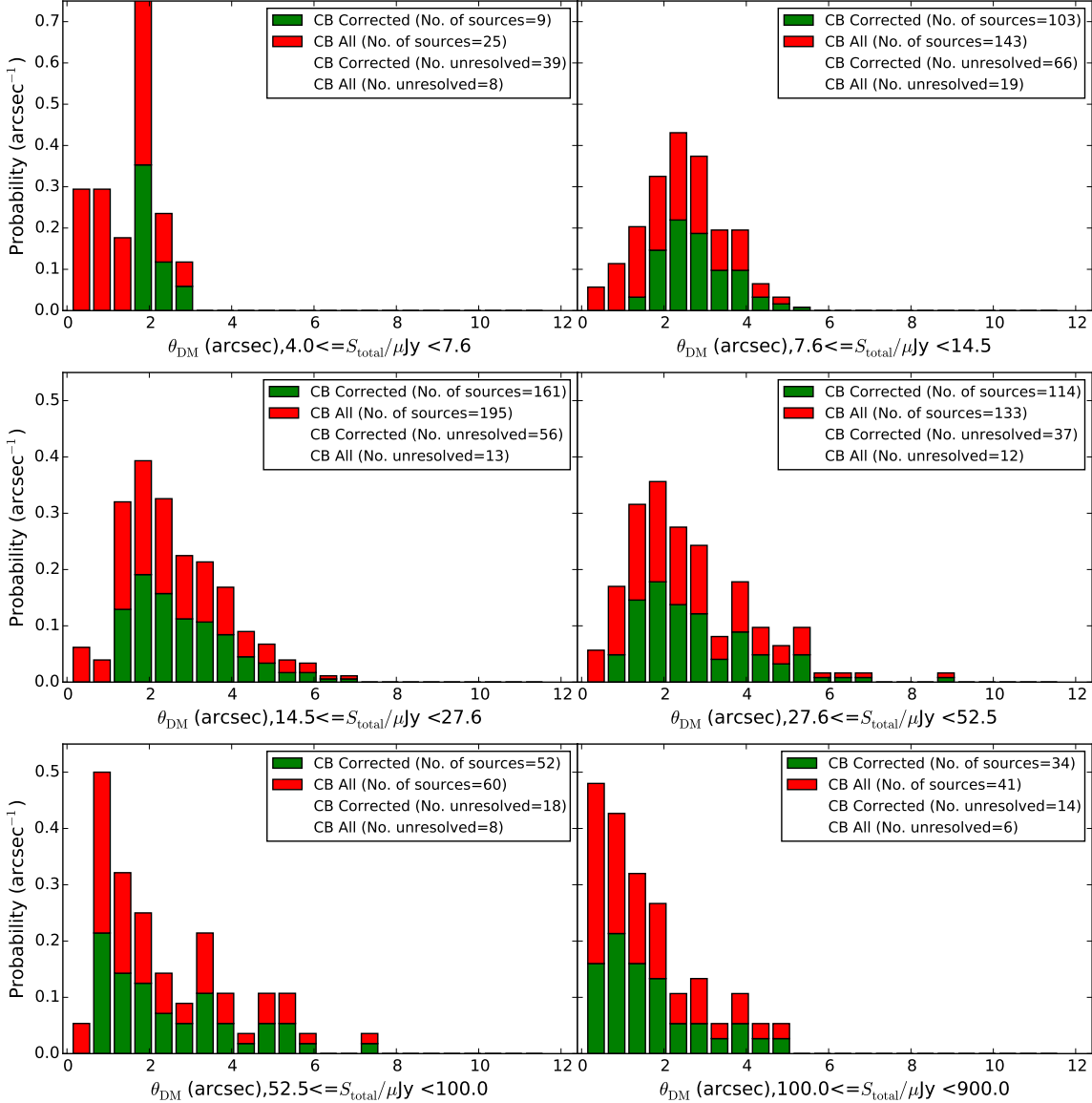


Figure 6.9: Deconvolved major axis size distributions from the CB catalogue in bins of total flux density. The sizes have been “corrected” if the partially resolved sources are set to the beam size.

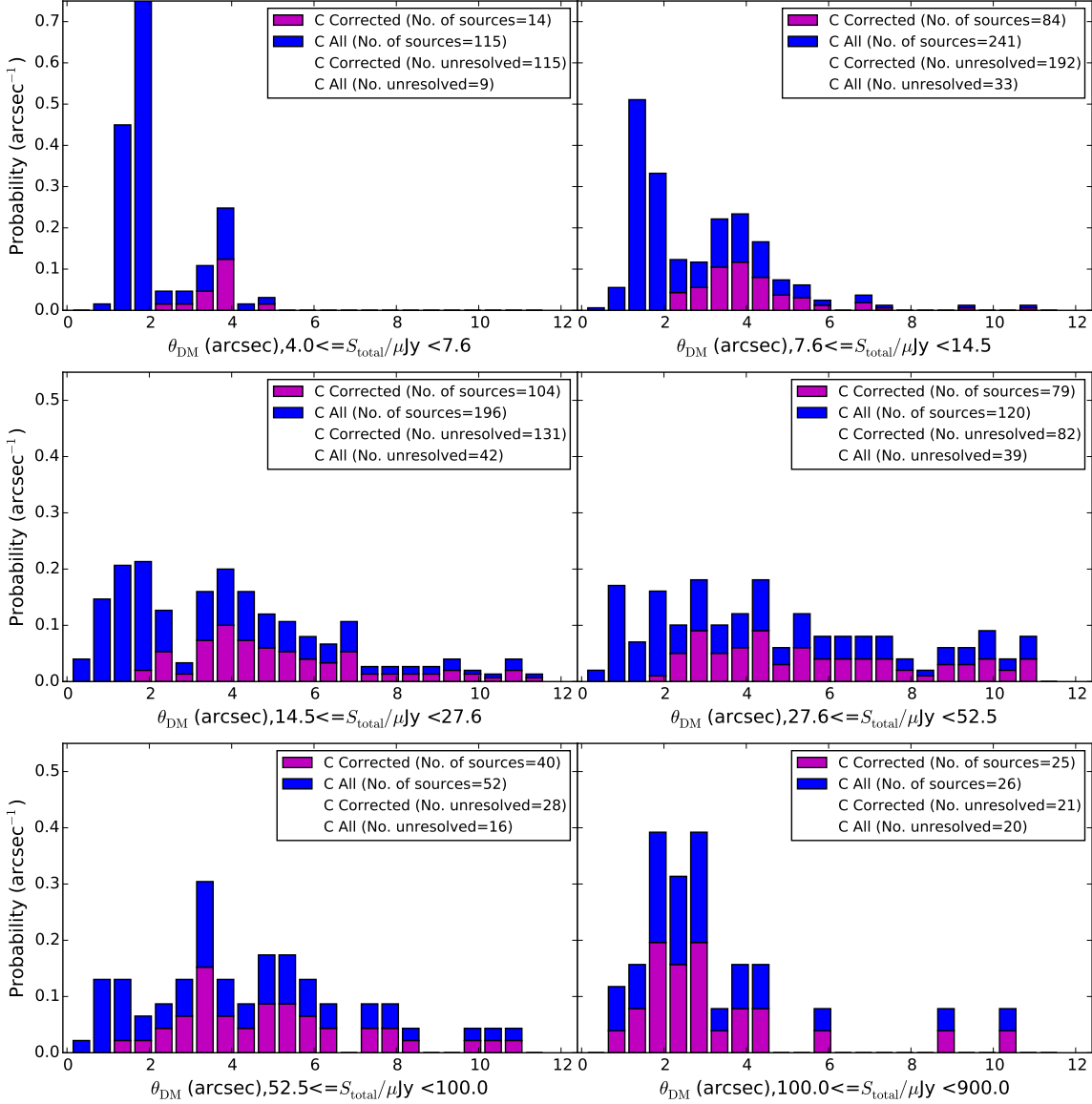


Figure 6.10: Deconvolved major axis size distributions from the C catalogue in bins of total flux density. The sizes have been “corrected” if the partially resolved sources have been set to the beam size.

this we expect the C catalogue to be missing smaller sources at the faintest flux densities. However, the CB catalogue will likely be missing larger sources at the faintest flux densities, since their sizes will make it such that their peaks are below detection. This is indeed what we see, as is shown in Figs. 6.9 and 6.10. These plots show the size distributions in bins of total flux density for the two catalogues. The values labelled “Corrected” have the sizes set to the beam size if the axis is partially resolved. There is a lack of large sources ($\theta_{\text{DM}} > 8 \text{ arcsec}$ for the CB data regardless of flux density. This may mean there are no sources of this size in our data; however, it is more likely that these sources are missed in the CB data as the large size makes the peak flux below detection. The CB plot also shows there to be a peak in the size distributions around $\theta_{\text{DM}} \simeq 2 \text{ arcsec}$ in all of the flux density bins. In the C data distributions, however, the distributions are much more evenly spread out with no discernible (common) peaks.

Figure 6.11 shows the mean sizes from these distributions in bins of flux density. It appears from this plot that the mean source sizes are much larger than the $\sim 0.7''$, estimated from high-resolution imaging (Muxlow et al. [124]). However, the means shown here do not take into account sources that are unresolved or partially resolved, which, particularly at the $8''$ resolution, will be the majority of sources. Many of the sizes $1''$ or less cannot be measured with the fit uncertainties. This plot indicates a trend in the average source size as a function of flux density regardless of catalogue resolution or corrections. But it is unclear how this might be biased by incompleteness, which is something that is still under investigation.

6.2.2 Extended Sources

There are four sources that by our examination (as well as in the catalogue from Owen and Morrison [134]) are not well fit by Gaussians and are categorized as extended, or having extended structure. For each of these four sources the total flux densities were found by summing the flux density values inside lines guided by the contours but edited to not include nearby sources. The reported positions are found by cross-matching with optical and infrared catalogues as well as the Owen and Morrison [134] catalogue. Figures 6.12, 6.13, 6.14, and 6.15 show these four sources for the C image contours against the CB image, along with the spectral

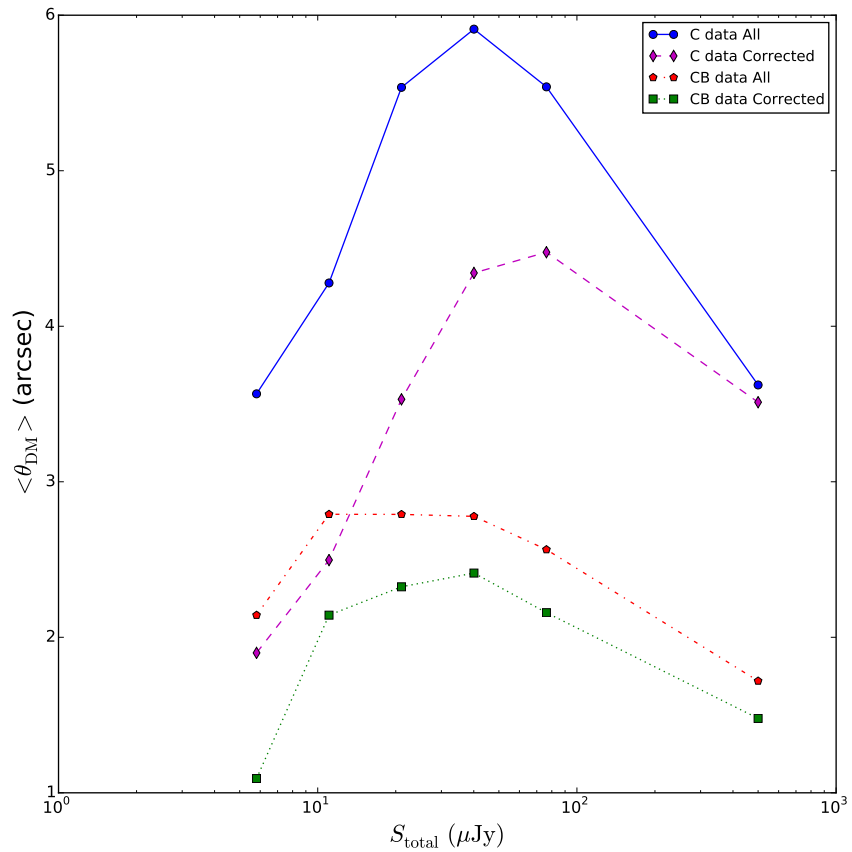


Figure 6.11: Mean deconvolved major axis size in bins of total flux density. The sizes have been “corrected” if the partially resolved sources have been set to the beam size. The blue solid line and purple dashed line are for the C data with original size values and corrected size values, respectively. The red dot-dashed line and green dotted line are the CB data with original size values and corrected size values.

index image, optical image from the Canada France Hawaii Telescope (CFHT), and infrared *Spitzer* IRAC image.

The source in Fig. 6.12 is a known Quasar classified as a double-lobed FR type II object [58]. It also has associated X-ray as seen with *Chandra* (X-ray ID CXOX J104623.9+590522). The spectral index image in Fig. 6.12 shows that the core has a flatter spectrum ($\alpha \simeq -0.6$), while the lobes have steeper spectrums ($\alpha \simeq -1.3$), as is commonly seen with AGN lobes. The other three extended objects did not cross match with any known AGN or QSO objects in catalogues.

It is clear looking at the optical and IR images that there could be emission from multiple sources contributing in the radio images. As stated above the source in Fig. 6.12 has a clear optical match near the centre that is responsible for the majority of the radio emission seen in the centre and the two lobes. The source in Fig. 6.13 has a bright optical/IR counter part near the centre. The extended trailing emission seen in the radio images is likely associated with that source, with possible contributions from some of the other nearby optical/IR sources seen, but again the radio emission of the two non-central parts of this source is quite bright (hundreds of μ Jys), making it likely to be mainly associated with the bright central source rather than solely from multiple smaller fainter nearby sources (also the trailing radio emission does not line up directly with any of the optical/IR sources).

The source in Fig. 6.14 again has multiple possible optical/IR counterparts. None of these line up well with the C image contours that show emission to the sides and below the source. Similarly for the source in Fig. 6.15, with multiple possible optical/ID counterparts for the emission seen to the left, but with no obvious counterparts with the emission on the right. For both of these sources, it is possible the radio emission is some combination of the multiple optical/IR sources, or also possible that none of the optical/IR sources are true counterparts. Either way, none of these sources are fit well by single or even multiple Gaussian models, therefore we classify them as extended.

6.3 Source Count

A source count was made of all the best-fit total primary-beam-corrected flux densities for both the C and CB catalogues. The differential source count, dN/dS , for

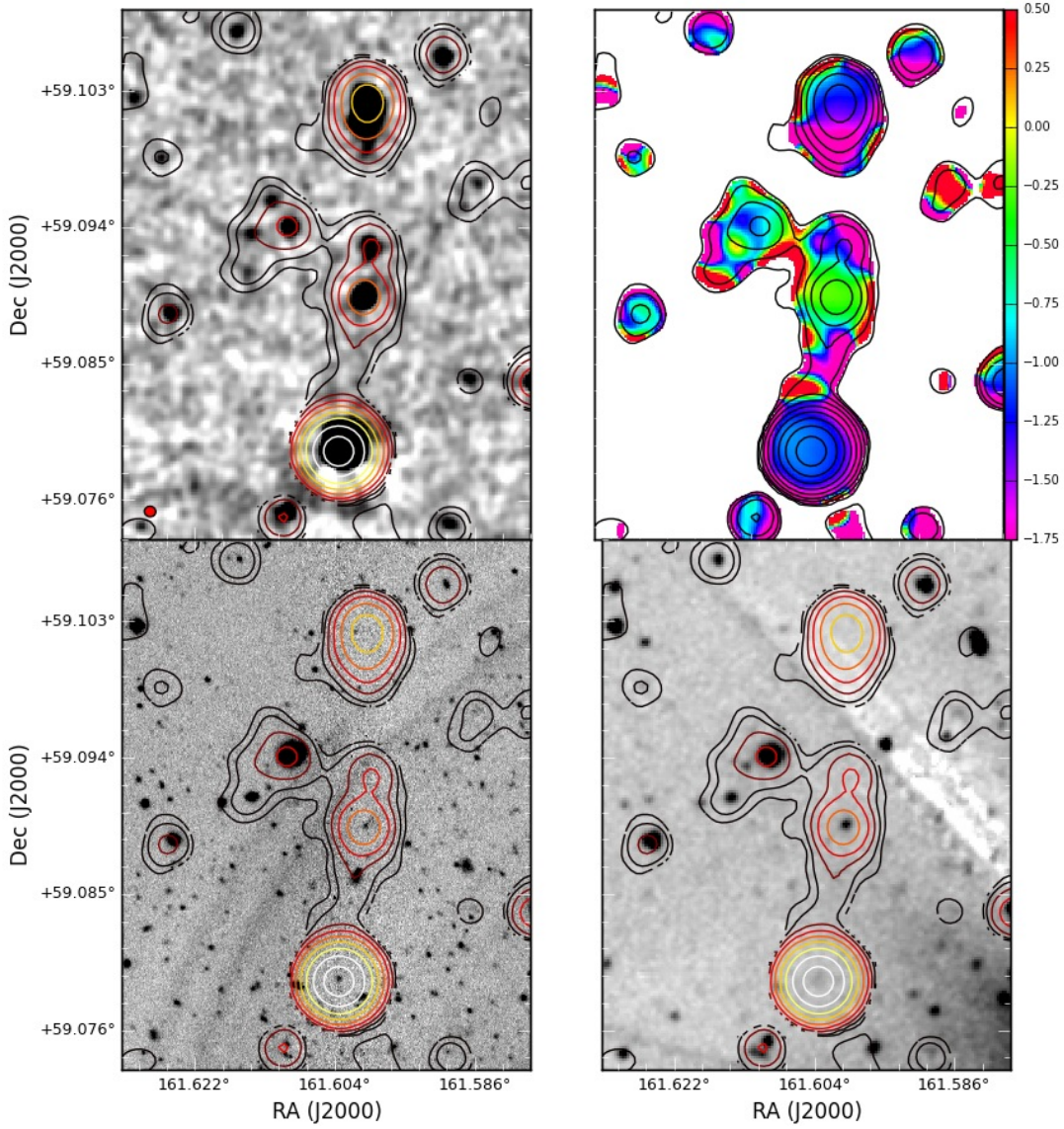


Figure 6.12: Extended source image for source position J2000 161°.6051, 59°.090913. The top left panel is the CB-data 3 GHz image. The top right is the C-data spectral index image. The bottom left image is the CFHT *g*-band image. The bottom right is the *Spitzer* 3.6 μm image. The overlaid contours are from the lower resolution C-data. The contours levels are 2, 5, 12, 30, 75, 200, 500, 1200, and 3000 μJy .

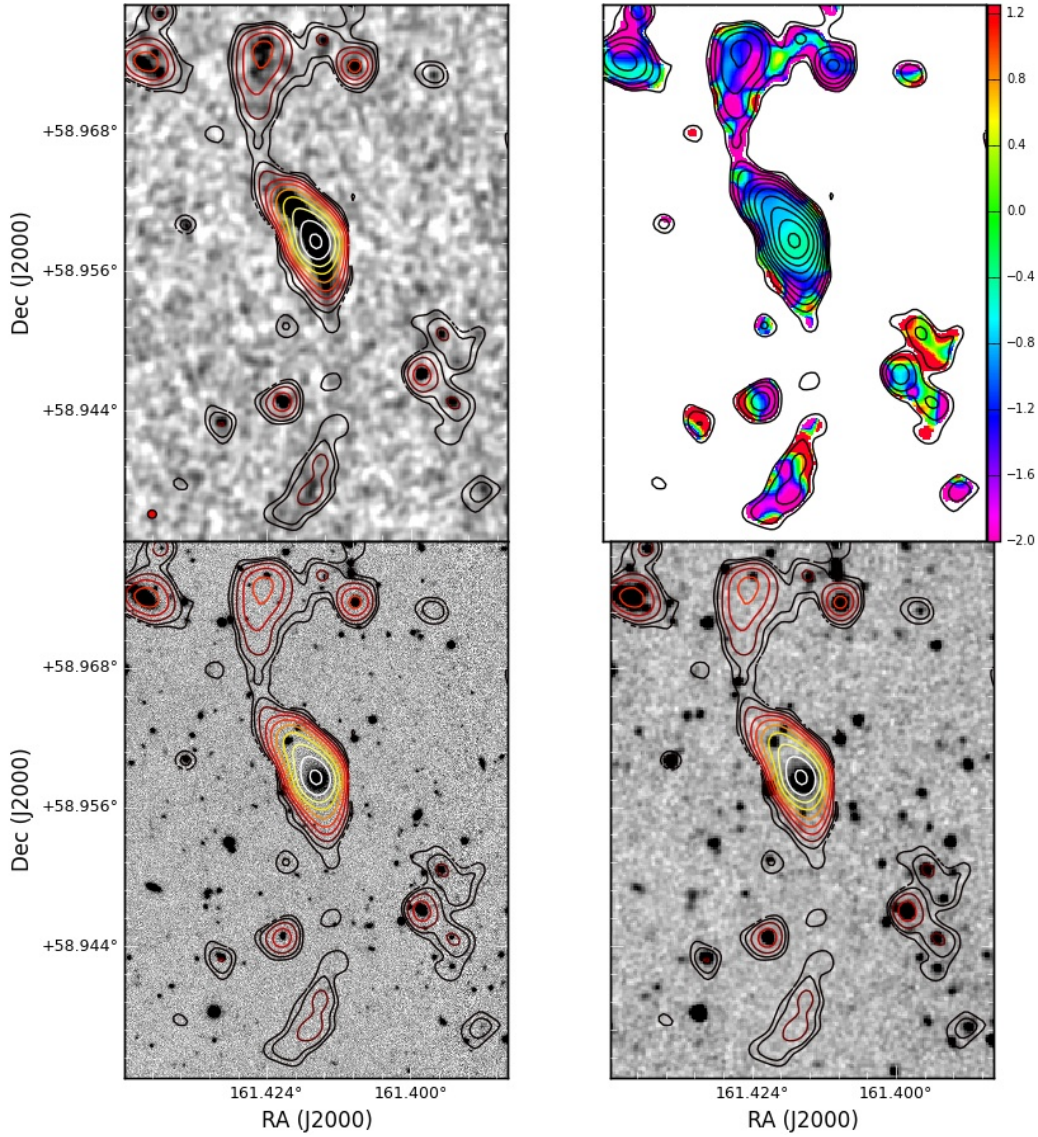


Figure 6.13: Extended source images for source position is J2000 $161^{\circ}.41572$, $58^{\circ}.955855$. The top left panel is the CB-data 3 GHz image. The top right is the C-data spectral index image. The bottom left image is the CFHT *g*-band image. The bottom right is the *Spitzer* $3.6 \mu\text{m}$ image. The overlaid contours are from the lower resolution C-data. The contours levels are 2, 4, 8, 15, 30, 50, 100, 200, and $700 \mu\text{Jy}$.

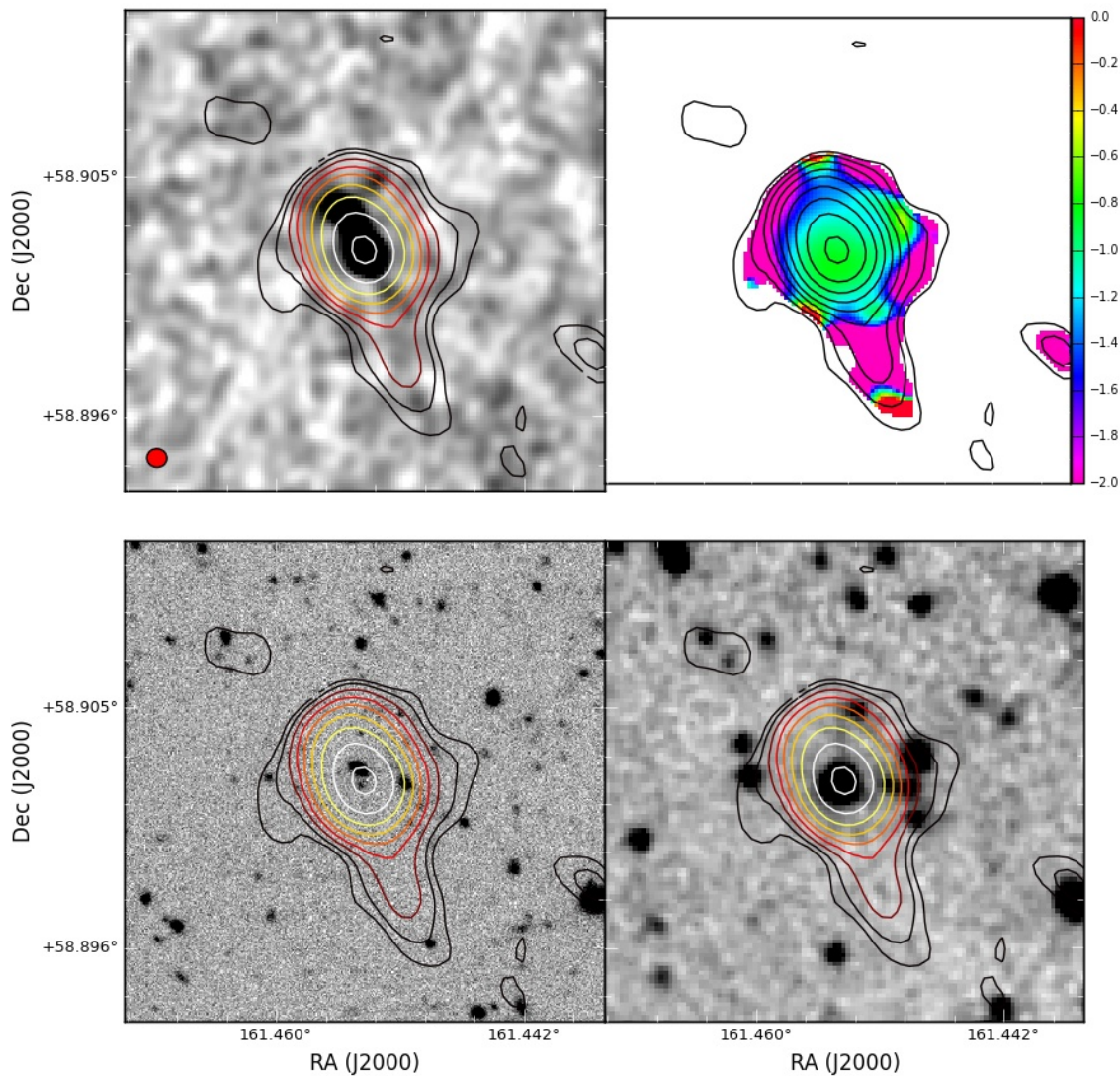


Figure 6.14: Extended source images for source position J2000 161°.45361, 58°.90226. The top left panel is the CB-data 3 GHz image. The top right is the C-data spectral index image. The bottom left image is the CFHT *g*-band image. The bottom right is the *Spitzer* 3.6 μm image. The overlaid contours are from the lower resolution C-data. The contours levels are 2, 3.5, 6, 10, 20, 30, 50, 90, and 150 μJy .

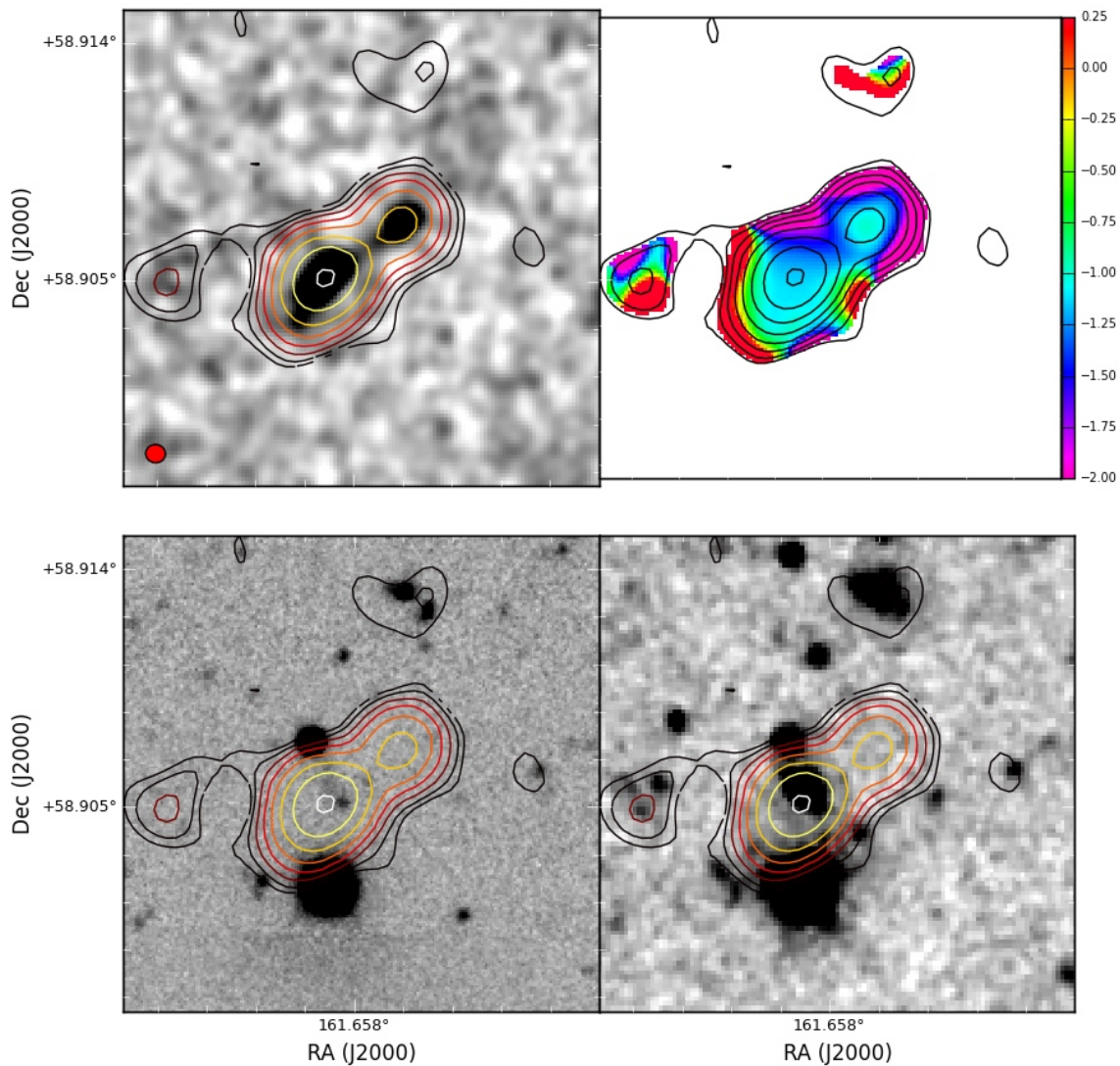


Figure 6.15: Extended source images for source position J2000 161°.6575, 58°.906266. The top left panel is the CB-data 3 GHz image. The top right is the C-data spectral index image. The bottom left image is the CFHT *g*-band image. The bottom right is the *Spitzer* 3.6 μm image. The overlaid contours are from the lower resolution C-data. The contours levels are 2, 4, 6, 12, 20, 35, 65, and 120 μJy .

bin a was computed as

$$\frac{dN}{dS_a} = \frac{N_a}{A_a \Delta S_a}. \quad (6.4)$$

Here N_a is the total number of sources in bin a , $\Delta S_a = S_{a,\text{high}} - S_{a,\text{low}}$, and A_a is the area over which the sources with mean flux $\langle S_a \rangle$ could be detected given the primary beam, noise, and detection limit. The angle over which a source can be detected is

$$\Theta_a = \sqrt{\frac{\ln P_a}{\ln 2}} \frac{\Omega_{\text{FWHM}}}{2}, \quad (6.5)$$

where Ω_{FWHM} is the FWHM of the primary beam in radians and $P_a = \langle S_a \rangle / (4\sigma)$, which is signal-to-detection limit ratio rather than just the signal-to-noise ratio.

Then the area (for small Θ_a) is

$$\Omega_a = \pi \Theta_a^2. \quad (6.6)$$

This is the area over which a point source could be detected with a 4σ peak detection cutoff. However, for non-point sources P_a changes to $P_a = \langle S_a \rangle / (4\sigma\mathcal{N})$, where \mathcal{N} is the size correction or $\mathcal{N} = (\theta_M \theta_m) / \theta_B^2$.

We computed the source count for our catalogues by computing \mathcal{N} for all the sources, binning the sources by \mathcal{N} , computing dN/dS for each \mathcal{N} bin and then summing over all the \mathcal{N} counts. The final source count is then

$$\frac{dN}{dS} = \sum_i \left(\frac{dN}{dS} \right)_{\mathcal{N}_i}. \quad (6.7)$$

The \mathcal{N} bins used are $\mathcal{N}=[1, 1.13, 1.375, 2, 4.25]$. The mean flux density for the summed source count is the average of the mean flux densities for each size bin in each flux density bin. This is shown in Fig. 6.16, along with the $P(D)$ fits from Vernstrom et al. [183] and Condon et al. [37]. Table 6.1 shows the counts from using all the sources. The counts from both catalogues are in good agreement with each other and with the $P(D)$ models, being slightly lower than the $P(D)$ model around 100 μJy .

The correction for flux boosting has been performed on the individual source flux densities via the 2D interpolation corrections, rather than a correction to the

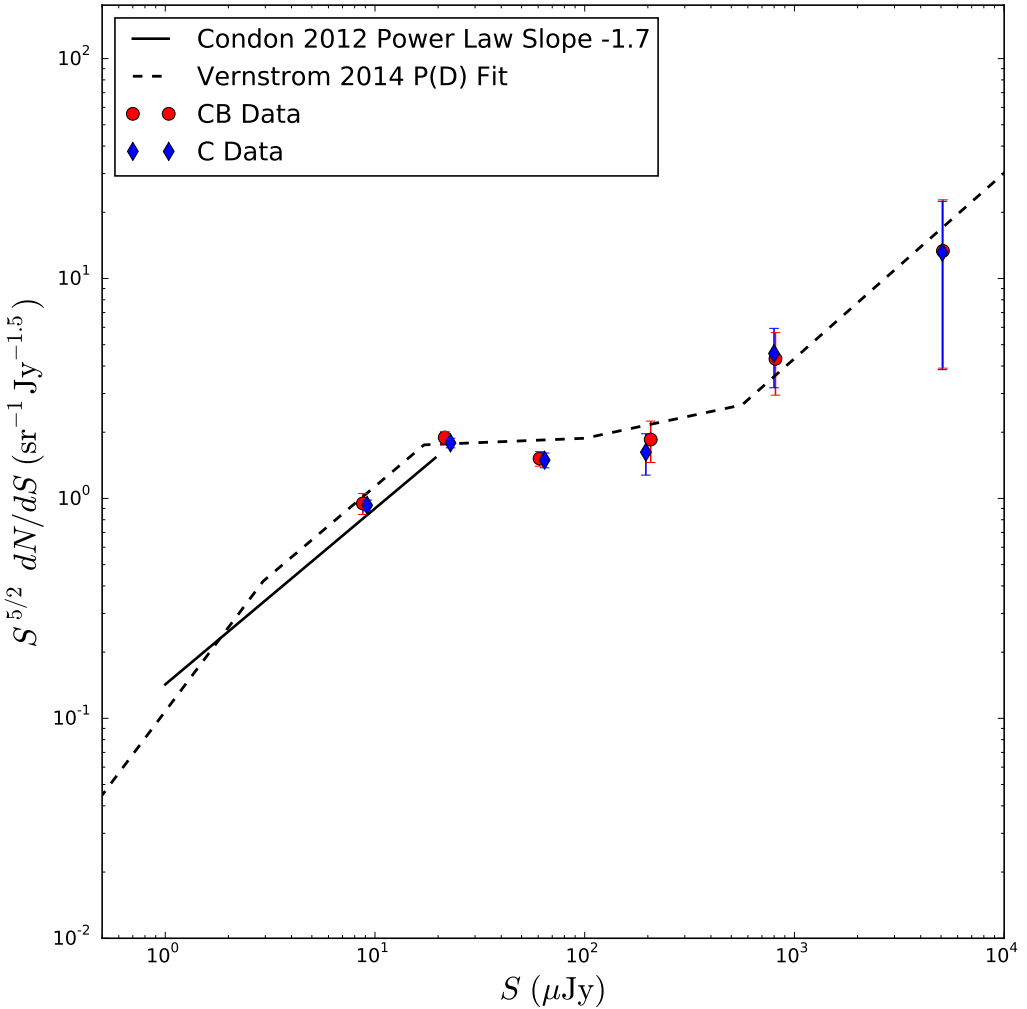


Figure 6.16: 3 GHz source count. The black dashed line is the $P(D)$ count from Vernstrom et al. [183]. The black solid line is the power-law $P(D)$ from Condon et al. [37]. The red circles are the count using the best-fit total flux densities from the CB image, with the blue diamonds being the count from the C image. The counts from the catalogues are binned counts (with the points plotted at the mean flux densities), whereas the $P(D)$ counts are for a power-law model (or multiple connected power laws).

Table 6.1: Differential Euclidean normalized source count

S_{low} (μJy)	S_{high} (μJy)	$\langle S_{\text{CB}} \rangle$ (μJy)	$\langle S_{\text{C}} \rangle$ (μJy)	dN/dS_{CB} ($\text{Jy}^{1.5} \text{ sr}^{-1}$)	$S^{5/2}$	dN/dS_{C} ($\text{Jy}^{1.5} \text{ sr}^{-1}$)	$S^{5/2}$
4	12	8.8	9.1	0.9 ± 0.1		0.9 ± 0.1	
12	36	22	23	1.9 ± 0.1		1.8 ± 0.1	
36	130	61	64	1.5 ± 0.1		1.5 ± 0.1	
130	320	210	200	1.9 ± 0.4		1.6 ± 0.4	
320	1500	810	800	4.3 ± 1.4		4.6 ± 1.4	
1500	8700	5100	5100	$13. \pm 9.5$		$13. \pm 9.3$	

source count. Corrections for completeness, false detections, and “clean bias” should all be looked at for these catalogues. The clean bias is a bias resulting from the cleaning process. This involves flux being removed from fainter sources, which are affected by the sidelobes of brighter sources. To correct for this, simulations are required, which entails inserting fake sources into the uv data and repeating the cleaning process as before and examining the flux of the simulated sources. We do not expect a large clean bias for our data as the sidelobes of our beams are not large and there are not many bright sources; however, this still needs to be examined. The completeness and false detections have been briefly examined using the simulation data. However, the corrections are not expected to be large at the flux density thresholds we selected (with the peak completeness from the simulations around 80% at the threshold and false detection rate around 30%), and hence a comprehensive analysis of those effects is postponed to a future study.

6.4 Spectral Indices

The 2-GHz bandwidth of the VLA correlator allows us to obtain information on the spectral dependence of the sources. We first retrieved the flux density values of each source at the positions of the fitted peaks in each of the 16 sub-band images. We applied a primary beam correction to each value, based on the primary beam for each sub-band frequency and source position. We then performed a least squares fit for the spectral index α_i and the corresponding fitted 3-GHz flux density, F , of

each source by minimizing

$$\chi^2 = \sum_{i=1}^{16} (S_i - ((\nu_i/3.0)^\alpha F))^2 w_i. \quad (6.8)$$

Here w_i is the normalized weight from the sub-band divided by the primary beam correction at the source position:

$$w_i = \frac{\frac{1}{\sigma_i^{*2}}}{\sum_i \frac{1}{\sigma_i^{*2}}}. \quad (6.9)$$

If the source is outside the 10 per cent power region for a particular sub-band's primary beam it was not included the fitting. This method works well for sources with large signal-to-noise, but for the fainter sources it is difficult to obtain a well-constrained fit, since each sub-band has noise that is 3 to 18 times the noise level in the combined 3-GHz image.

In an attempt to deal with the noisier sources we also performed a separate method to estimate spectral indices. We made two new images at 2.5, and 3.5 GHz, each using 1 GHz of bandwidth, resulting in noise values of 1.75 and $3.5 \mu\text{Jy beam}^{-1}$. These were again constructed to have nearly circular 8 arcsec beams. We took the primary beam-corrected images and made a spectral index image by taking \log_{10} of the images and dividing one image by the other. This yielded a spectral index image with $\alpha_{2.5-3.5}$. Some parts of this image can be seen in Figs. 6.12, 6.13, 6.14, and 6.15 for the extended sources. The spectral index for each catalogue source was then read off from this image at the pixel position of the fitted peak.

A separate spectral index image was made for both the CB and C data. The spectral indices are labelled as α_{IF} when fitting the 16 sub-bands and α_{IM} from the spectral index image. Values outside the range $-2.25 \leq \alpha \geq 2.25$ were set to zero in the catalogue. Histograms showing the different spectral indices are shown in Fig. 6.17 and plots of the mean α in bins of flux density are shown in Fig. 6.18.

All versions of the spectral index distribution have means near $\alpha = -0.7$, as would be expected if the majority of sources are star-forming galaxies; the only exception is α_{IF} for the CB data. This is likely due to several of the sub bands in the CB data being more severely affected by RFI than in the C data alone (note

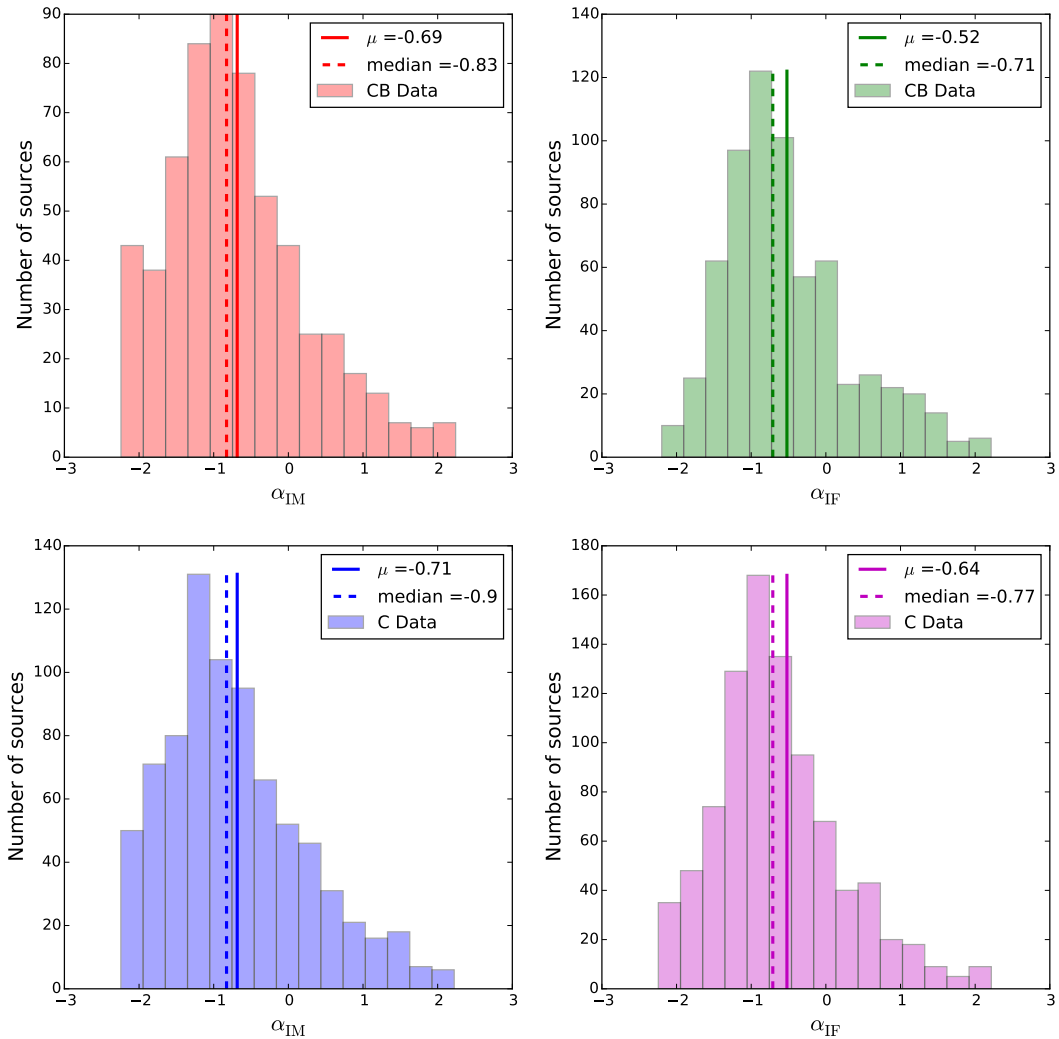


Figure 6.17: Catalogue spectral index histograms. The top panels show the spectral index distributions for the CB data and the bottom panels are for the C data. The left panels are indices obtained from the spectral index images, while the right panels show indices obtained from sub-band fitting.

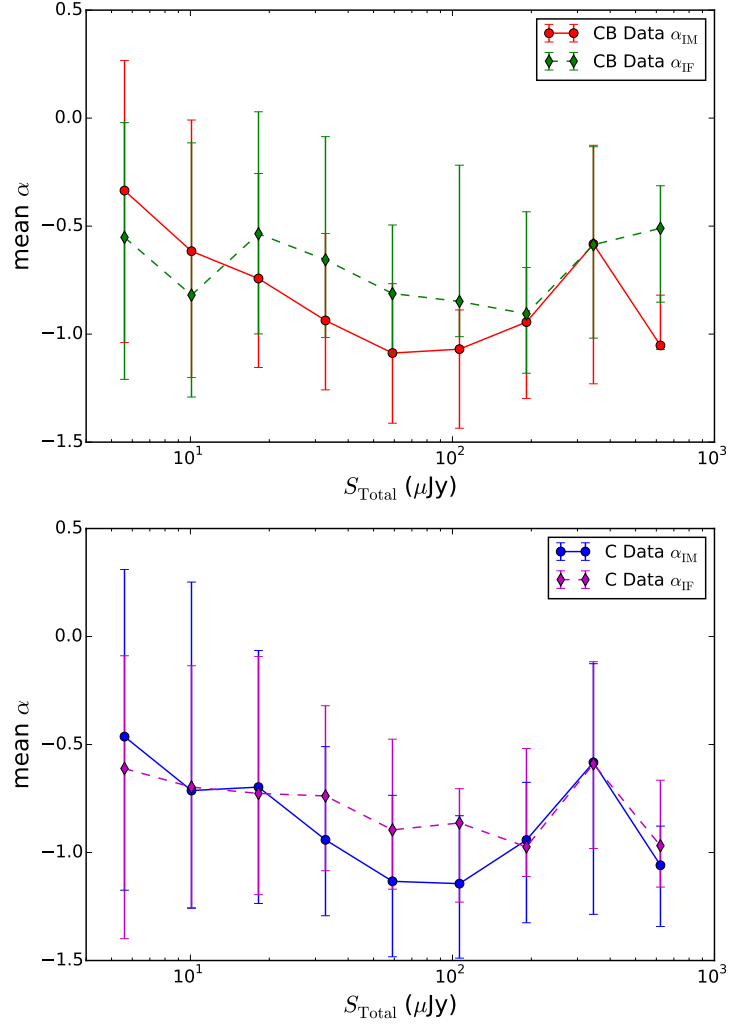


Figure 6.18: Catalogue mean spectral indices in bins of flux density. The top panel shows the mean α_{IM} (red solid line) and α_{IF} (green dashed line) for the CB data. The bottom panel shows the mean α_{IM} (blue solid line) and α_{IF} (purple dashed line) for the C data. The uncertainties show the inter-quantile range for each bin.

these sub bands were not used in the fitting at all). The image method is more consistent between the two catalogues, as seen by the tighter correlation in the middle left panel of Fig. 6.8, which is likely due to the higher SNR.

There has been some recent discussion of the mean spectral index for fainter sources being closer to -0.5 rather than -0.7 . Looking at Fig. 6.18, there does seem to be some indication for this. However, for any method of estimation it is more difficult to obtain an accurate estimate with a smaller SNR; thus we should treat the faintest flux density spectral index estimates with some caution.

The differences in spectral indices dependent on the type of source, as well as the redshift (and frequency). To say the mean spectral index expected is $\alpha = -0.7$ depends on observing frequency as synchrotron self absorption can lead to flattening of the spectrum if observed at lower frequencies or if the source is at a high redshift.

6.5 Cross-Identifications

The 3 GHz catalogue best fit positions were used to cross match the sources with 26 other catalogues, though some of those come from the same instrument or survey, but with different filters. The source positions were matched with a search radius of $2\sigma_B$, or 2.25 arcsec and 6.75 arcsec for the CB and C catalogues, respectively. Details of the matching can be seen in Fig. 6.19. A more detailed analysis is required to determine true counterparts from these catalogues. This will entail looking at the likelihood ratio of the matches using information on the positional offset uncertainties, and the counterpart distributions rather than just using the closest matches. This was deferred to a future study of the properties of the catalogue sources.

6.5.1 Optical and IR

For optical and near infrared data our catalogue was cross-matched with several catalogues. There is the Sloan Digital Sky Survey (SDSS) data release 9 [1], which includes u, g, i, r , and z bands. There is deeper optical data from CFHT, in the u, g, i, r , and z bands. There is *Spitzer*/IRAC data from the *Spitzer* Wide-Area Infrared Extragalactic Survey (SWIRE) survey at 3.6, 4.5, 5.8, and $8.5 \mu\text{m}$ [111,

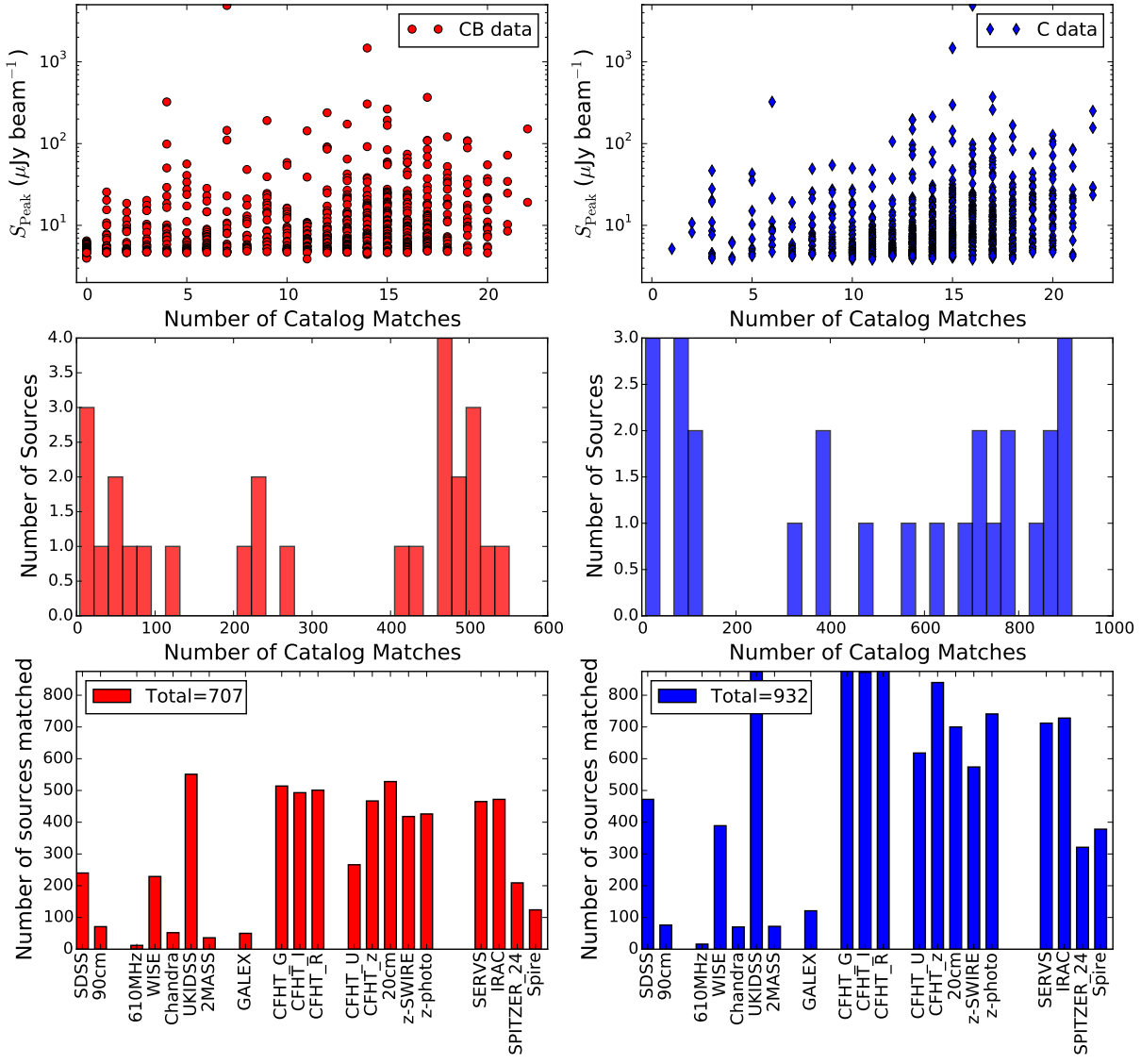


Figure 6.19: Details of catalogue cross-matching. The panels on the right are for the CB data catalogue, while the panels on the left are for the C data catalogue.

173], as well as “warm” *Spitzer* data from the *Spitzer* Extragalactic Representative Volume Survey (SERVS) at 3.6 and 4.5 μm . There are also data from the UKIRT Infrared Deep Sky Survey (UKIDSS) data release 9 survey [104, 105] in K and J bands. We computed colour cuts for each of our two catalogues using the cross-matched data, which can be seen in Figs. 6.20 and 6.21.

There are distinct features in the colour-colour plots. These can tell us about the redshifts of the sources, as well as the separate populations (i.e. AGN vs star-forming galaxies). We have highlighted some features. The bottom panel of the figures shows IRAC [5.8] – [8.0] μm vs [3.6] – [4.5] μm colours. The yellow region shows the divide between $z < 1.2$ and $z > 1.2$ from Marsden et al. [114], with the equation for the dividing line being

$$([3.6] - [4.5]) = 0.0682 \times ([5.8] - [8.0]) - 0.075. \quad (6.10)$$

Also on this panel the AGN selection criteria from Donley et al. [43] is shown as the grey shaded region. These criteria are define as follows, where \wedge is the logical “AND” operator:

$$x = \log_{10} \left(\frac{f_{5.8}}{f_{3.6}} \right), \quad y = \log_{10} \left(\frac{f_{8.0}}{f_{5.8}} \right) \quad (6.11)$$

$$\begin{aligned} x &\geq 0.08 \wedge y \geq 0.15 \\ \wedge y &\geq (1.21 \times x) - 0.27 \wedge y \leq (1.21 \times x) + 0.27 \\ \wedge f_{4.5} &> f_{3.6} \wedge f_{5.8} > f_{4.5} \wedge f_{8.0} > f_{5.8}. \end{aligned} \quad (6.12)$$

These criteria were then converted from this flux colour space to the magnitude colour space shown in the figure. Additionally, we have shown four galaxy redshift tracks (starting at $z = 0$ going to $z = 4$ and assuming no evolution) using rest-frame galaxy spectral energy distribution (SED) templates from Polletta et al. [142]. We chose one galaxy from each category of elliptical, spiral, starburst or ultra-luminous infrared galaxy (ULIRG), and quasar.

The optical and IR colours, combined with these tracks, show that the majority of sources are likely spiral or star-forming type at intermediate redshift. This is not unexpected. From the source count and luminosity functions, it is believed

that star-forming galaxies dominate in the sub-mJy regime. These criteria, when combined with firm optical matches, spectral indices and available redshifts, will allow us to categorize and investigate the properties of the different galaxy types in the catalogues.

6.5.2 Radio

We cross matched our VLA catalogue with the 1.4 GHz VLA catalogue from Owen and Morrison [134]. The majority of the 1.4 GHz sources that did not have matches in our catalogue were near the Owen signal-to-noise limit and a large majority were out near the edge of our cataloguing area, where the sensitivity is weak from the primary beam (the primary beam is smaller at 3 GHz than at 1.4 GHz). The 1.4 GHz catalogue reports the total flux density corrected for the primary beam, as well as bandwidth and time smearing effects.

We computed the spectral indices of the matched sources for both versions of our catalogues, with histograms and flux-flux plots shown in Fig. 6.22. The averages of the spectral indices range from -0.9 to -1.04 , which is clearly steeper than the expected -0.7 . The exact cause for this has not yet been determined. The average deconvolved size for the 1.4 GHz sources is smaller than the average deconvolved size at 3 GHz; thus to obtain a steep spectral index with our source sizes being larger would mean either we are underestimating our flux densities on average or Owen & Morrison over estimated the 1.4 GHz flux densities. We believe that it is more likely that the 1.4 GHz flux densities have been overestimated, since the source count produced by Owen & Morrison is higher than our source counts for the fainter flux densities (both the catalogue counts as well as the $P(D)$ count); this would not make the Owen & Morrison count less believable except that (as discussed in earlier Chapters) the counts are expected to show a downturn at fainter flux densities rather than the levelling off (or upturn, depending on the normalization) shown by Owen & Morrison .

6.6 Conclusions and Future Work

As has been mentioned, what is presented here are only the preliminary versions of these catalogues and a brief investigation of the source properties. We plan to

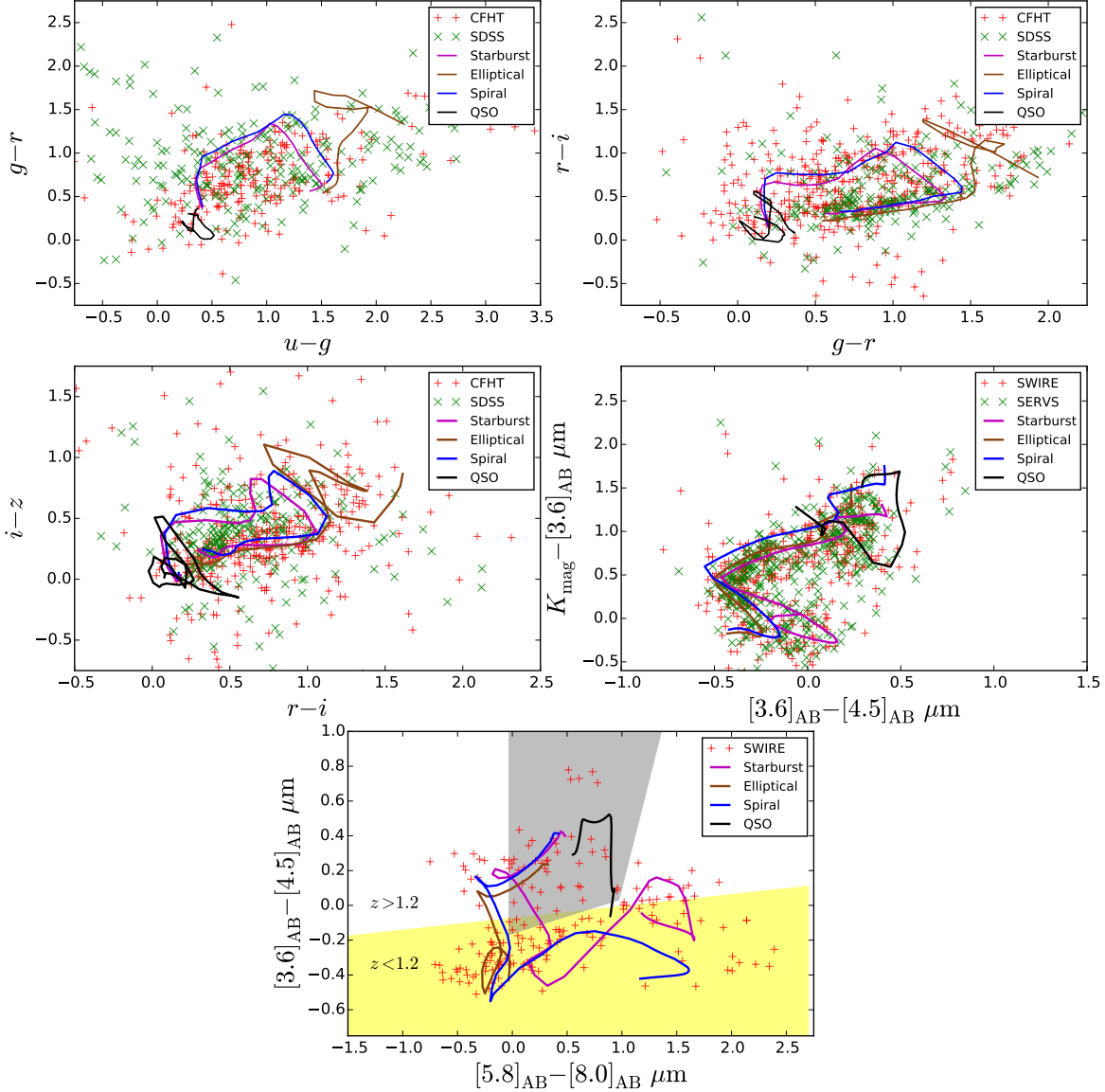


Figure 6.20: Colour-Colour plots of optical and NIR catalogue matches for the CB catalogue. The top and middle left panels include data from the SDSS DR9 and CFHT. The middle right panel is *Spitzer* IRAC and UKIDSS data, while the bottom panel is *Spitzer* IRAC. The coloured lines are redshift tracks (for $0 < z < 4$ and assuming no evolution) using galaxy templates from Polletta et al. [142]. The yellow shaded region in the bottom panel shows $z < 1.2$ from eq. 6.10 (Marsden et al. [114]). The grey shaded region is the AGN criteria from Donley et al. [43].

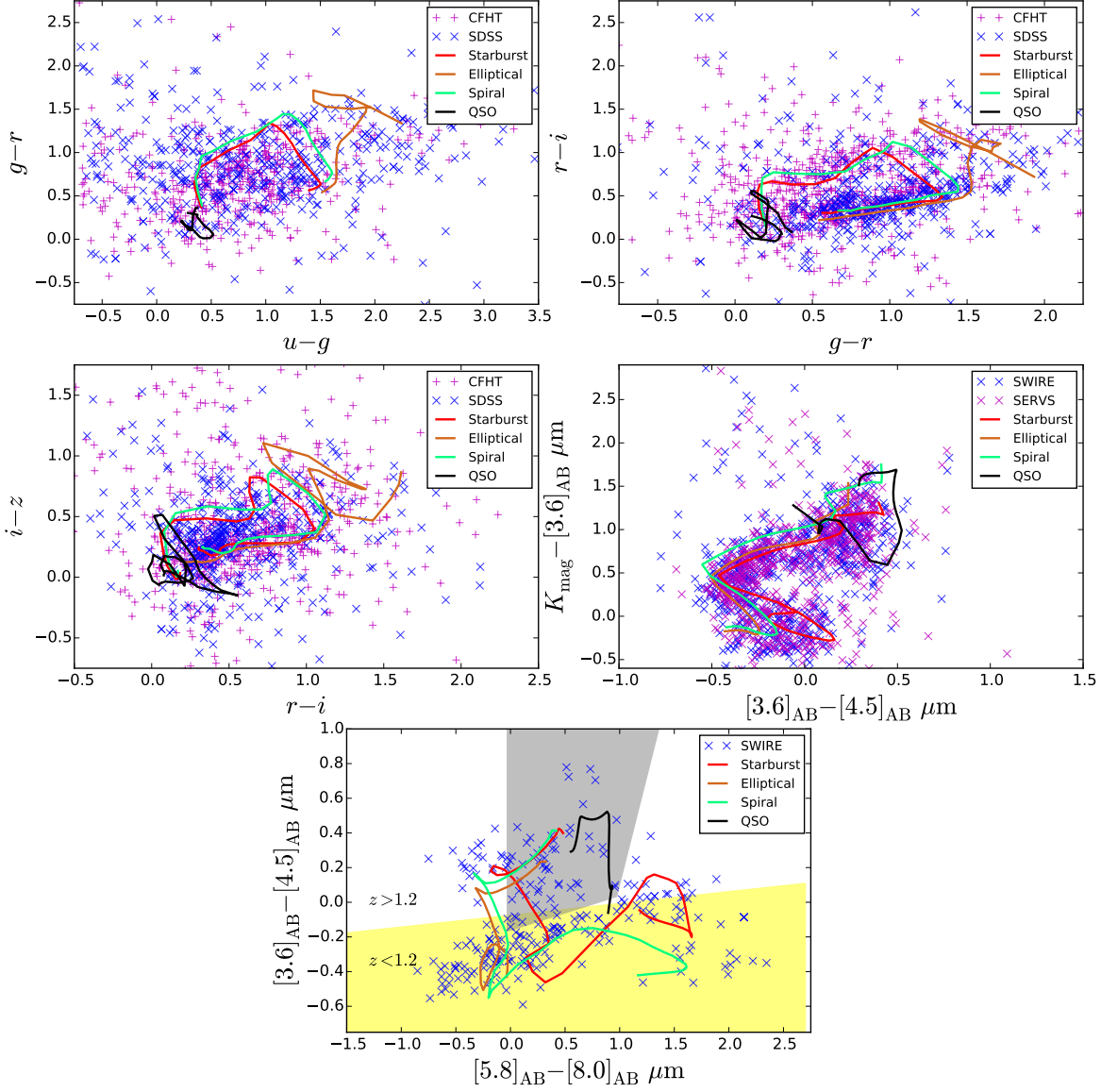


Figure 6.21: Colour-Colour plots of optical and NIR catalogue matches for the C catalogue. The top and middle left panels include data from the SDSS DR9 and CFHT. The middle right panel is *Spitzer* IRAC and UKIDSS data, while the bottom panel is *Spitzer* IRAC. The coloured lines are redshift tracks (for $0 < z < 4$ and assuming no evolution) using four galaxy templates from Polletta et al. [142]. The yellow shaded region in the bottom panel shows $z < 1.2$ from eq. 6.10 (Marsden et al. [114]). The grey shaded region is the AGN criteria from Donley et al. [43].

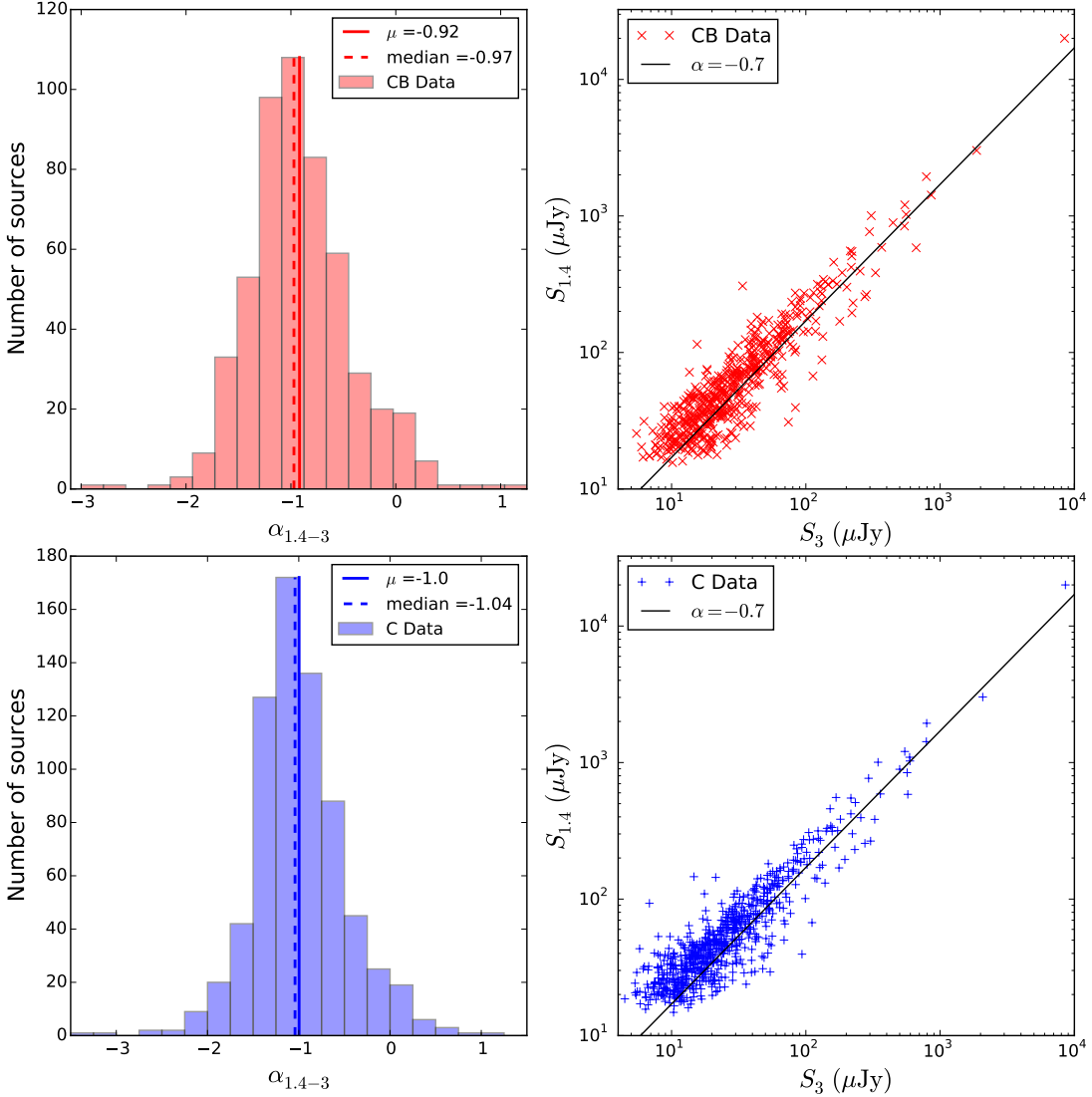


Figure 6.22: The left panels show the histograms of spectral indices from the cross-matched sources at 1.4 GHz of Owen and Morrison [134] with our 3 GHz catalogues. The right panels show the 1.4 GHz flux densities vs the 3 GHz flux densities for each cross-matches source. The top panels are the CB data while the bottom panels are the C data. The black diagonal lines show the predicted flux densities for an $\alpha = -0.7$.

build on this analysis by looking more deeply at the completeness and false detections, the clean bias, the redshift distribution, the source size distribution, the true counterparts and population investigation. This will include counterpart matching at the presented counterpart wavelengths, as well as those not discussed in detail here (infrared, submm, X-ray, and lower frequency radio). However, we have already made detailed simulations and used them for analysis of the uncertainties in our catalogues. These early catalogues are likely not very different from their final versions. We have shown that VLA wideband data can be used to obtain spectral index estimates and that these agree with previous estimates for the mean spectral index of $\langle \alpha \rangle = -0.7$, with the possibility of shallower spectral indices for fainter flux densities. We have shown there are many counterparts in other wavebands and that their distributions show distinct features. We were able to match a majority of our catalogue sources with those from the Owen and Morrison [134] catalogue, and have shown again that the previous flux densities seem to be overestimated (both from comparing source counts and spectral indices). Our source count from both catalogues agrees well with the $P(D)$ work from Vernstrom et al. [183] and Condon et al. [37], as well as being in line with most previous source counts from other surveys (with the exception of the low flux density counts of Owen and Morrison [134]).

When comparing the two catalogues of different resolution, they seem to perform comparably well when it comes to finding the same sources and their parameters. From our simulations, with the CB resolution 77% of the input sources had a match in the fit results. The mean $\Delta\text{RA}/\text{Dec}$ was 0.003 ± 0.75 , the mean ratio of true to fitted total flux density was 0.83 ± 0.3 and the mean ratio for the major axis was 0.87 ± 0.24 . For the C resolution, 81% of the input sources were matched in the fit results. The mean ΔRA and Dec was 0.03 ± 1.25 . The mean ratio for the total flux density was 0.078 ± 0.65 and the mean ratio for the major axis was 0.81 ± 0.19 . These numbers are for all sources, regardless of flux density.

When thinking in the context of future surveys, such as VLASS (higher resolution) vs EMU (lower resolution), we would suggest that the higher resolution data has the distinct advantage of providing more accurate positions and avoids the problem of blending. On the other hand, the low resolution data have the advantage of being able to find more of the extended sources near the noise cutoff. Both

resolution choices, as long as the noise is comparably deep, should find roughly the same number and the same sources and provide accurate estimates of their parameters.

Chapter 7

The Radio Angular Power Spectrum

7.1 Introduction

The clustering of radio emission on the sky is represented by the power spectrum which is the distribution of power C_ℓ in each mode as a function of angular scale or spherical mode ℓ . There currently exist measurements of the angular power spectrum of resolved radio sources (Blake et al. [13]) through the 2-point angular correlation function ($w(\theta)$) but there exist only a few upper limits on the fluctuations from the unresolved radio background. Given the nature of radio emission, produced from magnetic fields between galaxies and clusters, models predict that the radio power spectrum should trace large-scale clustering or the cosmic web. Whether or not this emission is strong enough to be currently detectable is unclear. However, most previous studies have focused on trying to detect specific structures, such as filaments between clusters. Detecting the overall structure in a statistical sense, as we attempt here, should be easier.

Searches for CMB anisotropies at low frequencies provide strong constraints on clustering of the radio background. Some previous studies providing upper limits on anisotropies have been performed, such as Fomalont et al. [60] using the VLA at 4.8 GHz, Partridge et al. [137] with the VLA at 8.4 GHz , and Subrahmanyan et al. [171] with the ATCA at 8.7 GHz (see figure 1 from Holder [88]).

These limits on CMB clustering can also be used to constrain CRB clustering. This is complicated by the fact that the value of the CRB temperature (i.e. the DC level of monopole of the sky) is unknown.

The study of the C_ℓ of the radio sky extends our 1-point statistical studies (Chapters 4 and 5) to 2-point statistics. This is another means by which we can study and constrain models of cluster emission, as well as dark matter particle models.

The power spectrum is a natural quantity to investigate here since the power spectrum is measured in Fourier space and radio interferometry data are also measured in Fourier space – this is in contrast to data which start in the image plane and must be transformed to the Fourier domain. Nevertheless, this is not a trivial process, since it requires a firm understanding of all the corrections that must be made, particularly uv -weighting, primary beam correction and calibration. Similar interferometric studies of CMB anisotropies have been carried out at higher frequencies (e.g. Hobson and Maisinger [86], Sutter et al. [174], White et al. [188, 189]). There has also been much related recent work using radio interferometer data and redshifted 21 cm emission to try to measure baryon acoustic oscillations (BAO) or the re-ionization signal. There are currently projects underway with the Giant Metrewave Radio Telescope (GMRT), the LOFAR telescope, the Canadian Hydrogen Intensity Mapping Experiment (CHIME), and others (e.g. Bandura et al. [5], Ghosh et al. [70], Harker et al. [82], Trott et al. [178]). This involves measuring the 3D power spectrum as a function of angular scale as well as redshift or frequency, rather than the 2D power as a function of multipole, but these works provide valuable references for the treatment of interferometric data.

In this Chapter we will discuss our (preliminary) attempt to measure the angular power spectrum using our existing ATCA data. Section 7.2 discusses the visibility data that are used, with subsections describing the telescope primary beam, the issues of wideband frequency coverage, and of mosaicked data. Section 7.3 goes over the current method used for estimating C_ℓ from visibility data. Section 7.4 details our simulations used to demonstrate and investigate these effects as well as the issues of clustering and extended emission, while Section 7.5 describes our model fitting procedures. Section 7.6 compares early results from these simulations and our real ATCA data, along with some discussion of the results.

7.2 Visibility Data

Here we discuss the relation between the visibility correlation and the angular power spectrum of the intensity $I(\vec{\theta}, \nu)$, or equivalently the brightness temperature $T(\vec{\theta}, \nu)$ distribution on the sky under the flat-sky approximation. The quantity $\vec{\theta}$ is the two dimensional vector on the plane of the sky with the origin at the pointing centre.

In radio interferometric observations, every pair of antennas in the interferometer measures a complex visibility $\mathcal{V}(\mathbf{u}, \nu)$ at a given point in the Fourier plane, where \mathbf{u} is the vector of u, v coordinates in the Fourier plane, with dimensions of inverse angle measured in wavelengths, and $\vec{\theta}$ is the variable conjugate to $\vec{\theta}$. Since interferometers are missing the zero-spacing they are insensitive to the DC level in any region mapped and are thus sensitive only to angular fluctuations on scales smaller than the primary beam and bigger than scales probed by the longest available baseline.

7.2.1 Primary Beam

The complex visibility is a measure of the sky signal plus instrument noise,

$$\mathcal{V}(\mathbf{u}_j, \nu) = \mathcal{S}(\mathbf{u}_j, \nu) + \mathcal{N}(\mathbf{u}_j, \nu). \quad (7.1)$$

where $\mathcal{S}(\mathbf{u}_j, \nu)$ is the contribution from the sky signal and $\mathcal{N}(\mathbf{u}_j)$ is the instrumental noise on the j th visibility (which we expected to be approximately uncorrelated and Gaussian). The visibility contribution from the sky signal is the Fourier transform of the product of the sky brightness $I(\vec{\theta}, \nu)$ and the antenna power pattern, or primary beam, $A(\vec{\theta}, \nu)$,

$$\mathcal{S}(\mathbf{u}_j, \nu) = \int d\vec{\theta} A(\vec{\theta}, \nu) I(\vec{\theta}, \nu) e^{2\pi i \mathbf{u} \cdot \vec{\theta}}. \quad (7.2)$$

The field of view is set by the primary beam size. The power pattern is very nearly a uniformly illuminated circular aperture [36]:

$$A(\vec{\theta}, \nu) = A(\rho, \nu) = \left[\frac{2\lambda}{\pi\rho D} J_1 \left(\frac{\pi\rho D}{\lambda} \right) \right]^2, \quad (7.3)$$

where D is the diameter of the antenna, $\rho = |\vec{\theta}|$ is the angular offset from the pointing centre, and J_1 is the Bessel function of the first kind and order. However, in practice the primary beam can be closely approximated by a Gaussian function with FWHM $\theta_F = 1.02\lambda/D$:

$$A(\rho, \nu)_G = e^{\frac{-\rho^2}{\theta_0^2}}. \quad (7.4)$$

In this case $\theta_0 = \theta_F\sqrt{2}/2.3548 \simeq 0.6\theta_F$. Each pair of antennas is separated by a baseline of length d metres projected on the plane perpendicular to the sky in units of the observing wavelength λ . Each antenna pair is sensitive to all baselines between $d - D$ and $d + D$, with the responsivity determined by the antenna primary beam. This means that the array is insensitive to any angular scales corresponding to baselines smaller than $d_{\min} - D$ or larger than $d_{\max} + D$. This is shown for the ATCA setup in Fig. 7.1, which has $D = 22$ m, shortest baseline of $d_{\min} = 30$ m, and longest baseline of $d_{\max} = 352$ m.

The visibilities are convolved by the Fourier transform of $A(\rho)$,

$$\mathcal{A}(k_\theta) = \int A(\rho, \nu) e^{2\pi i k_\theta \cdot \rho} d\rho, \quad (7.5)$$

where k_θ is the uv distance or $|\mathbf{u}|$ (k_θ has units of inverse radians, not to be confused with the spatial scale k with units of inverse Mpc) and in the small sky approximation $\ell = 2\pi k_\theta$. This can also be approximated by a Gaussian

$$\mathcal{A}(k_\theta)_G = \frac{1}{\pi U_0} e^{-k_\theta^2/U_0^2}, \quad (7.6)$$

where $U_0 = 1/\pi\theta_0 = 0.53\theta_F$.

The two dimensional power spectrum $P(\mathbf{u}, \nu)$ is

$$\langle \Delta \tilde{I}(\mathbf{u}, \nu) \Delta \tilde{I}^*(\mathbf{u}, \nu) \rangle = \delta^2(\mathbf{u} - \mathbf{u}') P(\mathbf{u}, \nu), \quad (7.7)$$

where $\Delta \tilde{I}(\mathbf{u}, \nu)$ is the Fourier transform of $\delta I(\vec{\theta}, \nu)$ and is $\mathcal{S}(\mathbf{u}_j, \nu)$ without a primary beam convolution, and $\delta^2(\mathbf{u} - \mathbf{u}')$ is a two dimensional Dirac delta function. The angular brackets denote an ensemble average over different realizations of the

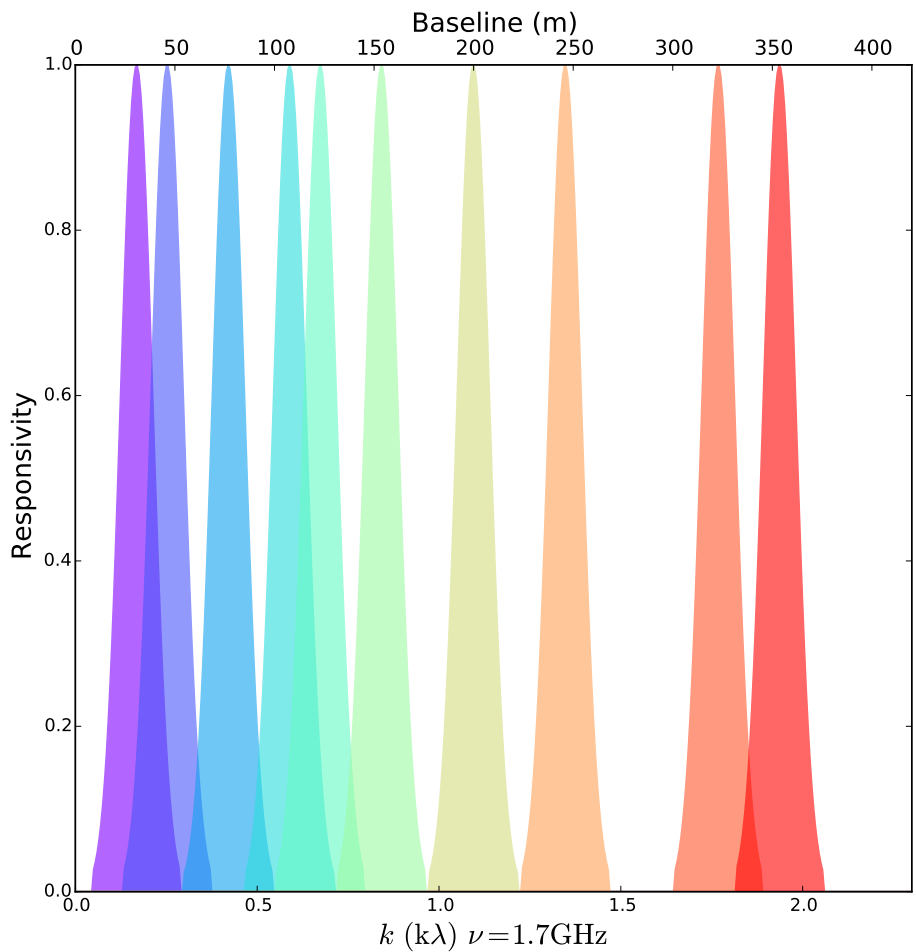


Figure 7.1: Responsivity of the ATCA interferometer setup as a function of the uv distance k_θ at a frequency of 1.75 GHz and baseline length (upper axis). The different colours represent the 10 different baselines, with the shape of each curve determined by the individual antenna power patterns, or primary beam.

sky intensity fluctuations. We know that $P(\mathbf{u}, \nu)$ is related to C_ℓ by

$$C_\ell(\nu) = \left(\frac{\partial B}{\partial T} \right)^{-2} P(\ell/2\pi, \nu). \quad (7.8)$$

In this $\left(\frac{\partial B}{\partial T} \right)^{-2} = \left(\frac{2k_B}{\lambda^2} \right)^{-2}$ is used to convert from Jy sr⁻¹ to temperature. From eq. 7.7 and eq. 7.1 we can see that the visibility correlation function is related to C_ℓ ,

$$\langle \mathcal{V}_i \mathcal{V}_j^* \rangle = V_0 e^{-|\Delta \mathbf{u}_{i,j}|^2/\sigma_0^2} C_{\ell_i} + \delta_{ij} 2\sigma_n^2, \quad (7.9)$$

where $\sigma_0 = \sqrt{2}U_0 = 0.76/\theta_F$. The factor V_0 is defined as

$$V_0 = \frac{\pi\theta_0^2}{2} \left(\frac{\partial B}{\partial T} \right)^2 = \frac{\pi\theta_0^2}{2} \left(\frac{2k_B}{\lambda^2} \right)^2. \quad (7.10)$$

The effect of the primary beam convolution on C_ℓ is to lower the mean amplitude by a factor f_{Pb} ,

$$f_{\text{Pb}} = \frac{1}{\int A(\rho)^2 d\rho}. \quad (7.11)$$

Equation 7.11 holds for the mean of many realisations, or if the flux distribution is fairly uniformly distributed in ρ . The exact value of f_{Pb} for an individual realisation of C_ℓ varies depending on the exact flux density distribution as a function of ρ . By this we mean that if there are outlier sources with $S \gg \langle S \rangle$ far out in the primary beam then f_{Pb} will be greater than eq. 7.11 predicts, and likewise if outlier sources were located near the pointing centre then f_{Pb} would be less than predicted. The value of f_{Pb} for our ATCA data, at the mean frequency, is $f_{\text{Pb}} = 8.05$.

7.2.2 Frequency Weighting

The upgraded correlator on the ATCA telescope provides for wide frequency bandwidth coverage. This allows for more data and thus higher signal-to-noise, as well as the possibility of measuring spectral changes across the band. It is less clear, however, what is the best way in which to handle the large frequency coverage for the power spectrum. The power spectrum could be measured individually at many different frequencies across the band. This decreases the data available for measurements and thus decreases the SNR, but this would be recovered by averag-

ing the estimates together. However, splitting into many frequencies also results in sparser coverage of the uv plane at each frequency. This is shown in Fig. 7.2, where the top panel gives the uv coverage of one ATCA pointing for all frequencies and the bottom panel gives the uv coverage at a single frequency.

There is also the option of measuring all of the visibilities together for a central or mean frequency. In this case the change in amplitude from the spectral index must be accounted for. If α is known, then the visibilities can be corrected by

$$\mathcal{V}(\mathbf{u}_j, \langle \nu \rangle) = \mathcal{V}(\mathbf{u}_j, \nu_i) \left(\frac{\langle \nu \rangle}{\nu_i} \right)^\alpha. \quad (7.12)$$

While the exact value of α may vary between sources, using simulations we have found that the mean expected α is a good approximation.

The spectral index of the primary beam $\alpha_{\text{Pb}}(\rho)$ is a function of distance from the pointing centre and is simply the derivative of eq. 7.3 with respect to frequency. When calculating C_ℓ at a single frequency using multi-frequency data, f_{Pb} becomes frequency dependent, such that

$$f_{\text{Pb}}(\nu_i) = f_{\text{Pb}}(\langle \nu \rangle) \frac{\theta_F(\langle \nu \rangle)}{\theta_F(\nu_i)}. \quad (7.13)$$

7.2.3 Mosaicking

The field of view, and correspondingly the uv resolution, are set by the size of the primary beam. To obtain high resolution in ℓ -space the Fourier transform of the primary beam needs to be narrow, implying small antennas. However, high sensitivity requires a large collecting area for each antenna. This problem can be somewhat circumvented by the technique of mosaicking [38, 46, 87]. Mosaicking entails observing overlapping fields on the sky, which increases the effective survey size and thus improves the ℓ -resolution. Mosaicking takes advantage of the fact that a telescope samples a whole superposition of visibilities along a baseline. Unfortunately, overlapping observations also require that we take into account the correlations between the fields. The fields, and their primary beams, are correlated

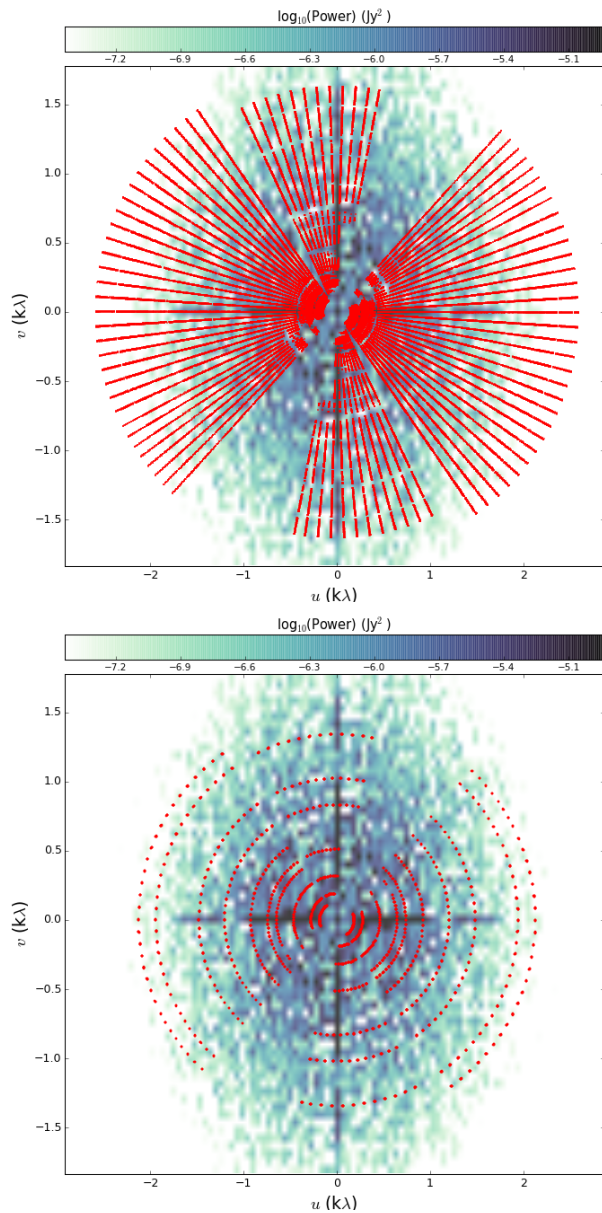


Figure 7.2: Logarithm of the 2D power of one simulated sky model with the ATCA uv coverage. The top panel shows the full uv coverage for one pointing with all frequencies. The bottom panel shows the same image with the uv coverage from one pointing at just one frequency.

by a phase shift relative to the global phase centre, such that

$$\mathcal{S}(\mathbf{u}_{j,l}, \nu) = \mathcal{S}(\mathbf{u}_{j,0}, \nu) e^{2\pi i \mathbf{u} \cdot \Delta \tilde{\theta}}. \quad (7.14)$$

Here $\mathcal{S}(\mathbf{u}_{j,l}, \nu)$ is the sky contribution to the complex visibilities from the l th pointing, $\mathcal{S}(\mathbf{u}_{j,0}, \nu)$ is the sky contribution at the phase centre, and $\Delta \tilde{\theta}$ is the distance of the l th pointing centre to the phase centre.

There are two routes to analyzing mosaicked data. The first is to treat the visibilities from each pointing as separate data, highly correlated in a calculable way, with apparently low resolution, but a lot of information in the correlations between visibilities. The other route is to statistically weight the visibilities from the different pointings to form a synthesized data set with fewer visibilities and correlations and intrinsically higher resolution. This is discussed in some detail for CMB interferometric measurements in White et al. [189] and Hobson and Maisinger [86].

7.3 Bare Estimator

We employ the Bare Estimator method as described in Choudhuri et al. [26]. This method uses the individual visibilities rather than gridding them into uv bins. Each visibility corresponds to a Fourier mode of the sky signal, and the visibility squared $|\mathcal{V}\mathcal{V}^*|$ gives the angular power spectrum. This simple estimator, however, has the severe drawback that the noise contribution $2\sigma_n^2$ is usually much larger than the sky signal. This can be mitigated by only including contributions where the noise is uncorrelated, or not including the correlations of any visibility with itself. The visibilities at two different baselines are correlated only if the separation between them is small, meaning $|\Delta \mathbf{u}_{ij}|^2 \leq \sigma_0$.

The Bare Estimator $\hat{E}_B(a)$ is defined as

$$\hat{E}_B(b) = \frac{\sum_{i,j} w_{ij} \mathcal{V}_i \mathcal{V}_j^*}{\sum_{i,j} w_{ij} e^{-|\Delta \mathbf{u}_{ij}|^2 / \sigma_0^2} V_0}, \quad (7.15)$$

for bin b , where all k_θ are in the range $k_\theta(b) - dk_\theta/2 \leq k_\theta \leq k_\theta(b) + dk_\theta/2$. The weights w_{ij} are chosen to: (1) maximize the SNR; and (2) go to zero when a visibility is correlated with itself, in order to avoid the correlated noise contribution.

The simplest case, ignoring any issues arising from calibration errors, is $w_{ij} = (1 - \delta_{ij})e^{-|\Delta\mathbf{u}_{ij}|^2/\sigma_0^2}$, which is proportional to its contribution to $\hat{E}_B(b)$.

The Bare Estimator is a measure of the average angular power spectrum \bar{C}_{ℓ_b} at the mean ℓ for bin b $\bar{\ell}_b$, i.e.

$$\langle \hat{E}_B(b) \rangle = \frac{\sum_{i,j} w_{ij} \langle \mathcal{V}_i \mathcal{V}_j^* \rangle}{\sum_{i,j} w_{ij} V_0, e^{-|\Delta\mathbf{u}_{ij}|^2/\sigma_0^2}} = \frac{\sum_{i,j} w_{ij} V_0, e^{-|\Delta\mathbf{u}_{ij}|^2/\sigma_0^2} C_{\ell_i}}{\sum_{i,j} w_{ij} V_0, e^{-|\Delta\mathbf{u}_{ij}|^2/\sigma_0^2}}. \quad (7.16)$$

If one is using multifrequency data to estimate the primary beam-corrected C_ℓ , then $\langle \mathcal{V}_i \mathcal{V}_j^* \rangle$ become the corrected visibilities

$$\langle \mathcal{V}_i^C \mathcal{V}_j^{*C} \rangle = \langle \mathcal{V}_i \mathcal{V}_j^* \rangle f_{\text{Pb}}(\nu_k) \left(\frac{\langle \nu \rangle}{\nu_k} \right)^\alpha. \quad (7.17)$$

Figure 7.3 shows the effect of these corrections on simulated noiseless visibilities of randomly distributed point sources. Because of the different sizes of the primary beams the different frequency visibilities are calculated separately for $\langle \hat{E}_B(b) \rangle$,

$$\langle \hat{E}_B(b)_C \rangle = \frac{\sum_{k,i,j} w_{kij} \langle \mathcal{V}_i^C(\nu_k) \mathcal{V}_j^{*C}(\nu_k) \rangle}{\sum_{k,i,j} w_{kij} V_0, e^{-|\Delta\mathbf{u}_{kij}|^2/\sigma_0(\nu_k)^2}}. \quad (7.18)$$

The variance of the Bare estimator for bin b , $\sigma_{E_b}^2$, is

$$\sigma_{E_b}^2 = \langle \hat{E}_B(b)^2 \rangle - \langle \hat{E}_B(b) \rangle^2, \quad (7.19)$$

assuming the visibilities are Gaussian random variables. Then the average angular multiple for bin b , $\bar{\ell}_b$, is

$$\bar{\ell}_b = \frac{\sum_{i,j} w_{ij} e^{-|\Delta\mathbf{u}_{ij}|^2/\sigma_0^2} \ell_i}{\sum_{i,j} w_{ij} e^{-|\Delta\mathbf{u}_{ij}|^2/\sigma_0^2}}. \quad (7.20)$$

The choice of the bin size $\Delta\ell$ is driven by the trade-off between the desired narrow widths for localizing features in the power spectrum and the correlations between bins introduced by the transform of the primary beam, where the minimum resolution is set by the size of the primary beam.

We note that this method can potentially be very computationally expensive,

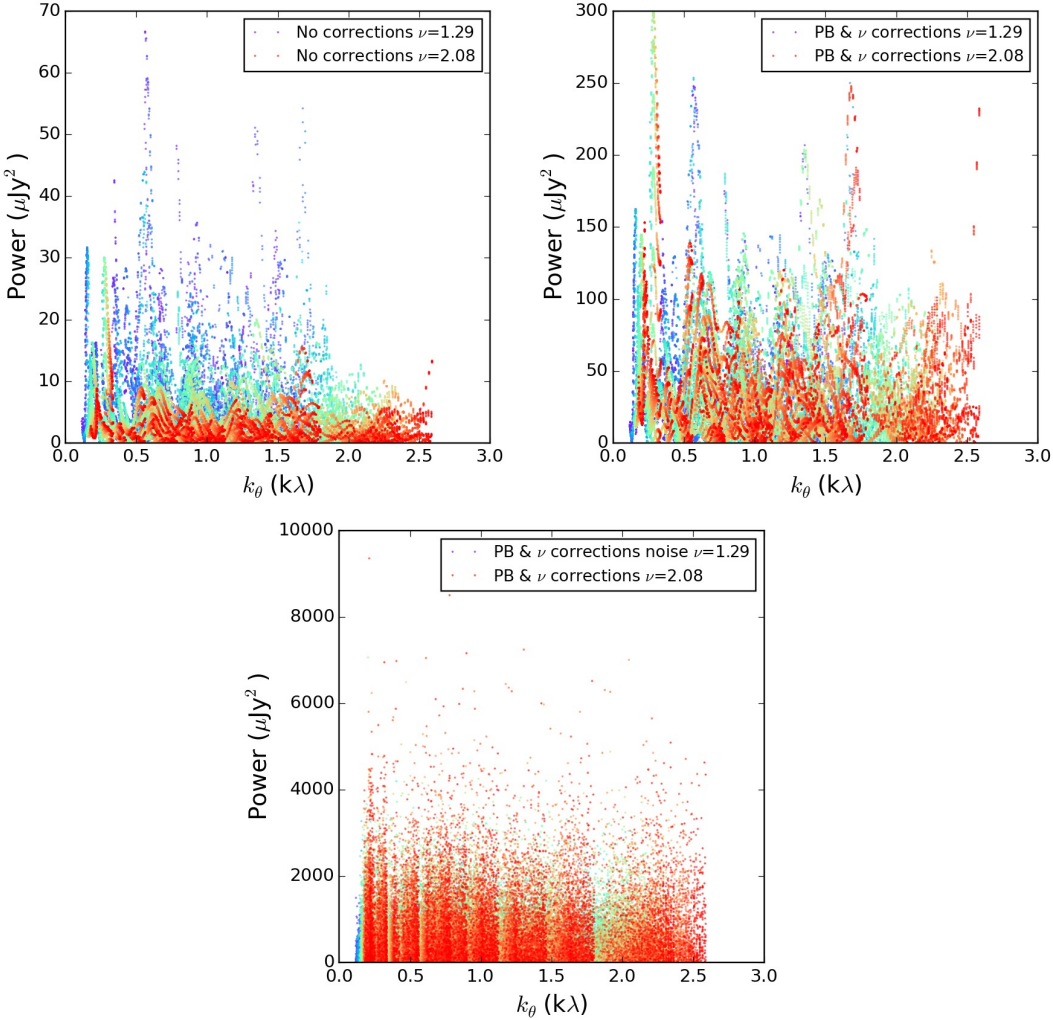


Figure 7.3: Power vs uv distance for the visibilities of one simulated data set (where the model includes no clustering or extended sources). The colours represent the different frequencies, ranging from blue at the low end to red at the high end. The top left panel shows the noiseless visibility power without any corrections. The top right panel shows the same visibilities with a correction for: (1) frequency scaling applied according to eq. 7.12; (2) the primary beam spectral scaling of eq. 7.13; and (3) the primary beam amplitude of eq. 7.11. The bottom panel shows the same as the top right, but with Gaussian noise of $\sigma = 0.1$ Jy added to the visibilities.

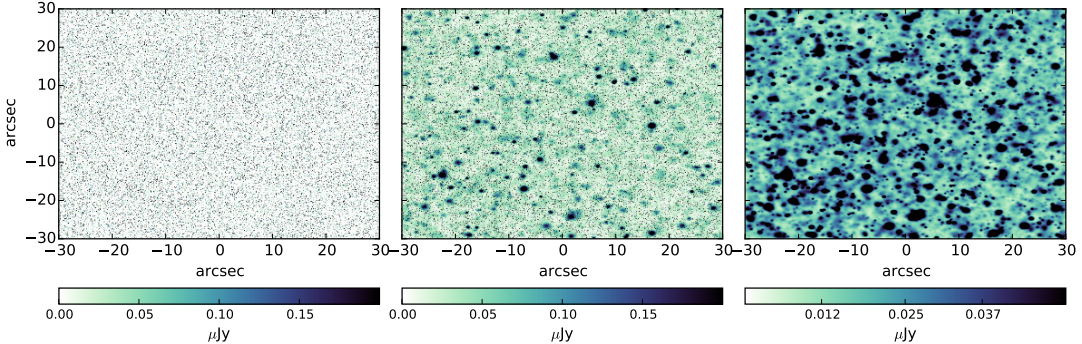


Figure 7.4: Images of simulated sources from the SKADS simulation used as models for simulated ATCA observations. The left panel shows the single frequency point sources, while the middle panel shows the point sources plus extended emission halos, and the right panel being only the extended halos.

depending on the size of the data set. It scales as N^2 , with N the total number of visibilities, which depends on the telescope setup (number of baselines, number of frequency channels, and integration time). For our ATCA data, which uses only 12 hours of total time, approximately 44 unique frequency channels (after flagging), and 10 baselines, there are on the order of 70,000 visibilities. However, for a setup like our VLA data the number of visibilities is over 1,000,000. A data set like that would likely require a method involving gridding of the visibilities (such as is done before imaging).

Finally, we note that the baseline visibilities contain two uv points considering the property $\mathcal{V}(\mathbf{u}) = \mathcal{V}^*(-\mathbf{u})$. Thus in data analysis only one half of the visibilities need be used, as long as this property is taken into consideration. This also means that even when performing a cross-correlation the imaginary part of the sum cancels out.

7.4 Simulations

We first examined simulated data sets in order to test many of the issues previously mentioned (visibility weighting, frequency scaling, primary beam correction, etc.). We used the source catalogue in 1 deg² of the SKADS simulation at 1.4 GHz. This

simulated area roughly matches the size of the ATCA primary beam. The catalogue includes positions, flux densities, and sizes for about 600,000 sources with $S > 1$ nJy. With $\alpha = -0.7$ we scaled all the fluxes to a frequency of 1.70 GHz to more closely match the ATCA data. We only included sources with $S \leq 5$ mJy, to more closely match the source-subtracted ATCA data, as well as to ensure the Poisson signal from a few bright sources does not overwhelm fainter signals. We did not include any source sizes here, setting all objects to point sources or delta functions in the image.

We created several cases to test different features. These test images include the following features:

1. Point sources; random positions.
2. Extended Gaussian halos; random positions .
3. Point sources + extended Gaussian halos; random positions.
4. Point sources; clustered positions.
5. Extended Gaussian halos; clustered positions.
6. Point sources + extended Gaussian halos; clustered positions.
7. Point sources; random positions: 7 pointing mosaic of 2 deg^2 .

These cases allow us to examine the power spectrum from point sources, or Poisson noise, from large-scale clustering, and from extended emission, as well as to test the effects of the frequency correction, mosaicking, the primary beam, and the particular *uv* coverage. The models with random position point sources, point sources plus halos, and just halos are shown in Fig. 7.4.

The extended halos were created as Gaussian distributions centred around point sources. The total halo flux was set to S_{ps} divided by some factor ranging from 3 to 8, with brighter sources having a smaller factor, and S_{ps} being the flux density of the point source. The size of the haloes ranged from 15 to 90 arcsec, scaled with S_{ps} such that the brightest point sources would have the largest haloes.

The SKADS catalogue positions were used for the point source only mosaic models, which should include some level of clustering. In Wilman et al. [191] it

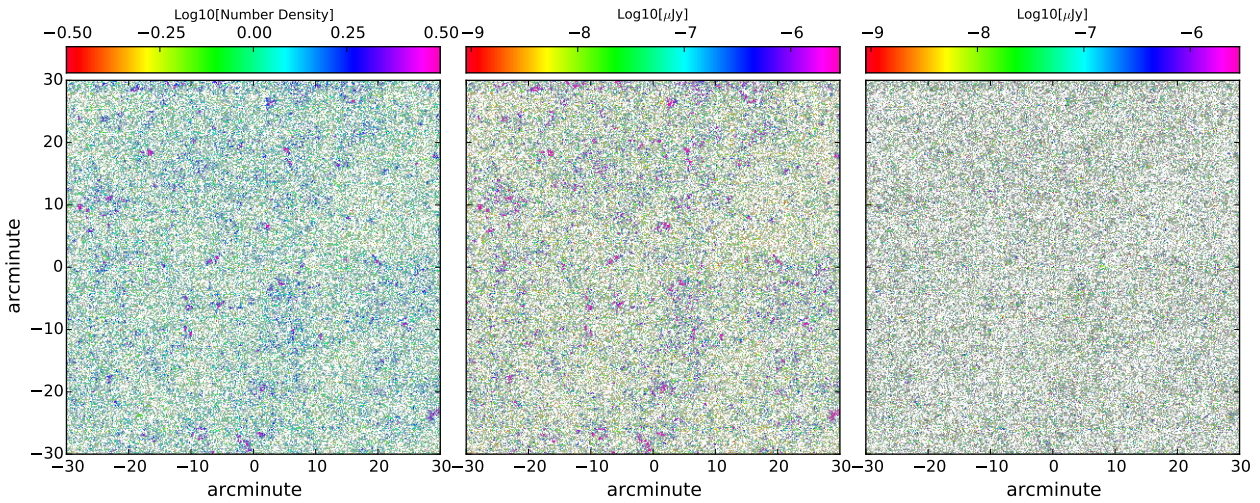


Figure 7.5: Simulated clustered and random skies. The left panel shows the density field (degree of over or under density). The middle panel shows the clustered positions with the brightest flux densities being set to the pixels with the highest over-densities, thus a strong clustering bias. The right panel shows the same clustered positions but with randomized flux densities.

is said the simulation has different clustering for (i) radio-quiet AGN, (ii) radio-loud AGN and (iii) star-forming galaxies. The radio-quiet AGN clustering was derived to match observations from the 2dFQZ survey ([40]); while the radio-loud clustering comes from the NVSS and FIRST surveys ([133]). The star-forming cluster was taken from Overzier et al. [133] and using IR data from Farrah et al. [49]. This is likely as good of an approximation to the actual clustering spectrum as may be possible with current data and simulations.

However, even though the SKADS catalogue positions should already have this clustering information encoded we do not know the exact shape of the clustering spectrum for those simulations and it appears to be quite weak compared to the Poisson level. For these simulations we would like to clearly test the method and possible effects on a clearly known and visible input clustering spectrum. Thus, we decided to take the catalogue fluxes (since we know that the source count is fairly realistic) and generate positions with a known clustering signal, relatively strong

compared to the Poisson level and with a distinguishable shape. The clustered positions were generated assuming a Gaussian source distribution in redshift $N(z)$ with mean=0 and standard deviation=0.5, between $z = 0.5$ and $z = 1.5$. Sources had 3D clustering $\xi(r) = (r_0/r)^\gamma$. We used r_0 of 5 Mpc h^{-1} and $\gamma = 1.8$. This produces an angular correlation function $w(\theta) = 0.0021\theta_{\text{deg}}^{-0.8}$, matching that measured by Blake et al. [13]. The clustered positions and this method were provided to us by Chris Blake.

This process resulted in realistically clustered positions; however, it is not so clear how to assign flux densities to those positions, since the brightness-dependence of clustering is more of a mystery. We certainly know there should be a Poisson component from the source distribution. The Poisson power term can be computed from the source count

$$P_{\text{shot}} = \int_0^{S_{\text{cut}}} S^2 \frac{dN}{dS} dS. \quad (7.21)$$

The fluxes can then either be randomly assigned or, to strengthen the clustering signal, higher fluxes can be assigned to the positions in higher over-densities. Figure 7.5 shows the over and under-densities of the clustered positions, as well as one case of assigning the fluxes with a bias and one with random assignment.

Thus we have simulated images with SKADS clustering (the point source mosaics) and the $w(\theta)$ of Blake et al. [13] (point sources and extended single pointings) along with single pointings with randomised positions. Thus we should have simulations that may more closely resemble that true radio source spectrum and others that allow for clearer testing of the method effects on a spectrum with clustering.

To create simulated radio interferometer observations from these sky models we used the MIRIAD task UVMODEL. UVMODEL allows you to use a model image and a real visibility data set and then replace the real visibilities with model visibilities. We used the central pointing of the ATCA observations as the input, except for the mosaic simulation, which used all seven ATCA pointings. This ensures that the simulated data have the same observational setup as our real data. Each of the simulated images was used as a model for this task, with primary beams applied (to mimic a clean component model image) and a second plane describing the spectral index of each source ($\alpha = -0.7$) plus the spectral index due to the primary

beam at each position. This allows the task to scale the single frequency image to all the observing frequencies. This created noiseless visibility sets. We averaged from the full 1024 spectral channels to 64, though only about 44 frequencies had non-zero amplitude visibilities, due to the flagging in the real data; this seemed a good compromise between having a large number of visibilities and still testing for the effects of wide-bandwidth.

The power spectrum was then computed using these noiseless visibilities via eq. 7.18, as well as a computation with Gaussian random noise of $\sigma = 0.03$ Jy added to the visibilities (consistent with the rms per visibility for our ATCA observations). These were then compared with the auto-power spectra from the input model images.

In order to investigate the effects of the binning, cosmic variance, and the primary beam, we performed a bootstrap analysis. First, we took the SKADS flux density catalogue and used it to generate 1000 realisations of the source count with random positions each time. We applied a primary beam to each realisation. We then computed the 1D power spectrum (using the auto-correlation) of each model image, with and without the primary beam, and using both linear and logarithmic binning in ℓ , with the number of bins ranging from 4 to 12 in the range of $600 < \ell < 16500$. We then repeated the procedure, except that this time we used clustered positions with randomized flux density assignment. The mean, uncertainties, and 100 realisations for 7 bins are shown in Fig. 7.6 and Fig. 7.7. From the unclustered power spectra we can see that we recover the input well, with perhaps a slight bias at the lowest ℓ s after performing the beam correction. Similarly, the clustered simulations show that we can recover approximately the correct power spectrum. These bootstraps can also be used to look at the correlations or covariance between the bins.

7.5 Model Fitting

When it comes to fitting a model, the most straightforward case is to perform a least squares fit to the 1D power spectrum. It may be worthwhile to use the full covariance matrix of the bins in the fitting rather than just the bin uncertainties. This covariance matrix can be obtained from a bootstrap analysis such as described

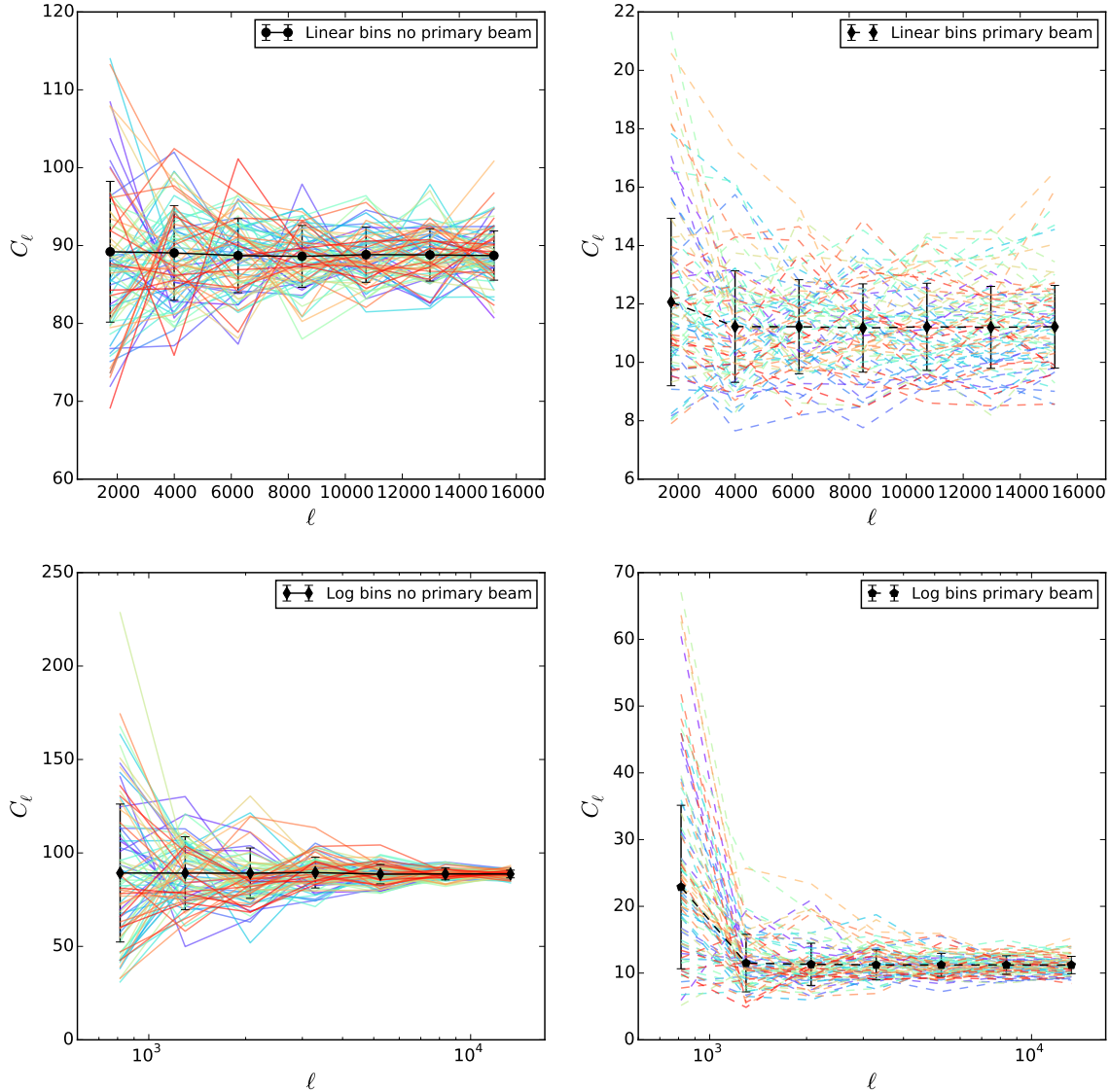


Figure 7.6: Results from bootstrap tests of random Poisson (i.e. uniformly-distributed) sources, using both linear and logarithmic bins (top and bottom rows) and with and without a primary beam correction (left and right columns) for 7 bins. The solid black line is the mean from 1000 realizations. The coloured lines are 100 different individual realizations. The results are clearly consistent with the Poisson (i.e. flat power) inputs.

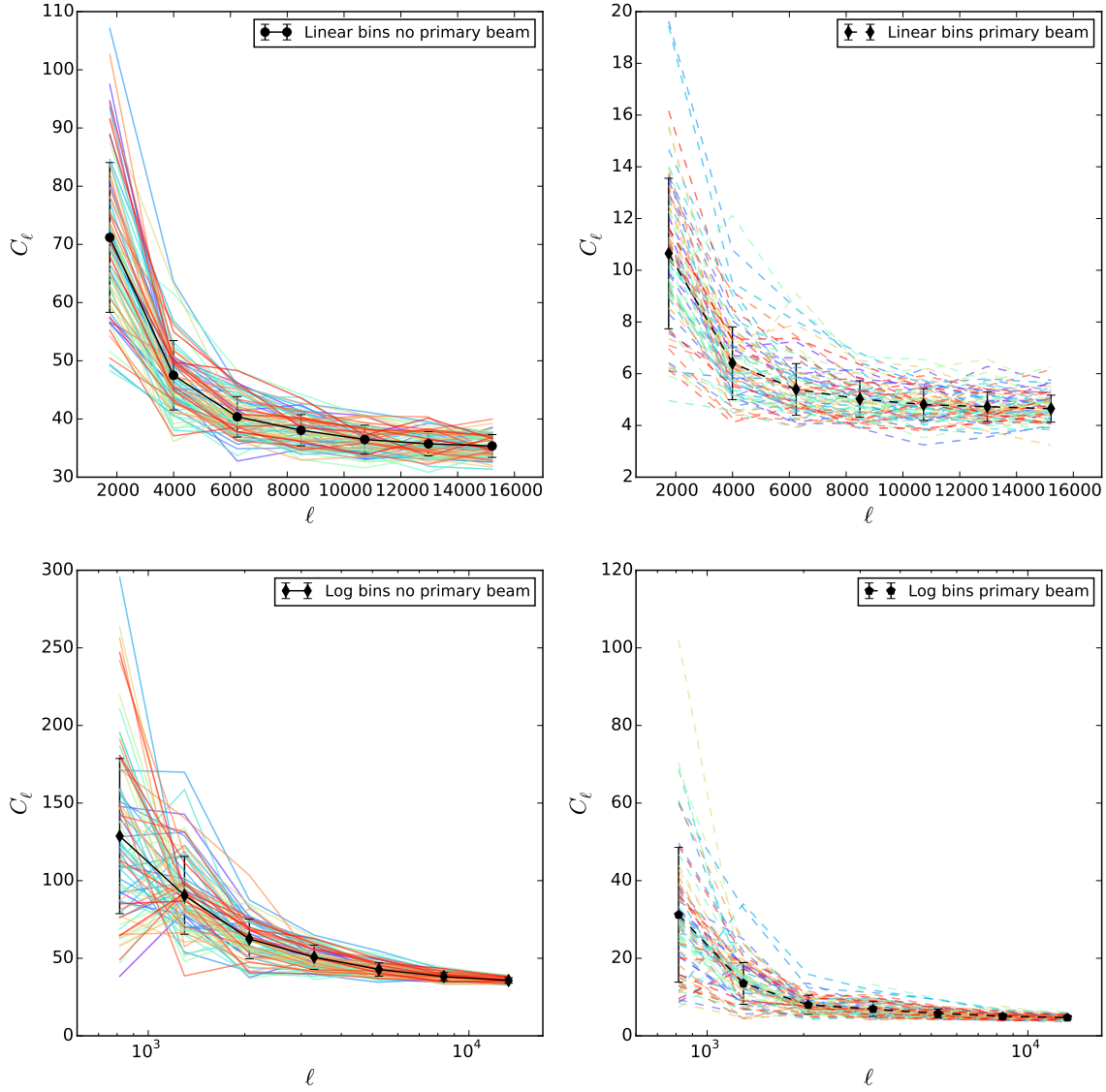


Figure 7.7: Results from bootstrap tests of clustered sources (with randomly distributed flux densities) using both linear and logarithmic bins (top and bottom rows) and with and without a primary beam correction (left and right columns) for 7 bins. The solid black line is the mean from 1000 realizations. The coloured lines are 100 different individual realizations.

above. However, it is unknown what effect (particularly any bias) the model used to generate the bootstrap may have on the output and thus we have not used this method here. There are many other possible ways of model fitting, some of which we plan to explore at a later date.

For the choice of model, the simplest approach is to simply fit for the Poisson level (Model 1),

$$C_\ell = \mathcal{P}. \quad (7.22)$$

If we assume there is some clustering which follows a power law, we can fit for the Poisson level plus the clustering power law (Model 2)

$$C_\ell = D \left(\frac{\ell}{\ell_0} \right)^\beta + \mathcal{P}, \quad (7.23)$$

after picking some value for ℓ_0 . Optionally, if no correction for the primary beam is applied during the power spectrum calculation, the value of $f_{\text{Pb}}(\langle \nu \rangle)$ can be fit as a free parameter, since it is not exact for an individual realisation of the sky. As for a model to include an extended emission component, this is more difficult. It is not known how much extended emission contributes to the power spectrum or what shape it will take. Models using Gaussian type halos could be fit by a simple model; however, it is unknown how realistic that type of model is. At this time we have therefore not fit any models for extended emission.

It is necessary to apply some priors on the parameters to constrain the fits. We have left these fairly relaxed at the moment, constraining the Poisson level and the clustering amplitude to be greater than zero and less than the maximum amplitude from the input. The β value for the clustering model is constrained to be less than zero and greater than -6 . When fitting the primary beam-correction amplitude as a free parameter, a Gaussian prior is set with a mean of the expected value from eq. 7.11.

The model fitting is performed using MCMC analysis.

7.6 Simulation Results

The C_ℓ s from all of the simulations are shown in Fig. 7.8 (clustering), Fig. 7.9 (extended emission), and Fig. 7.10 (mosaics). We have also run some early trials of

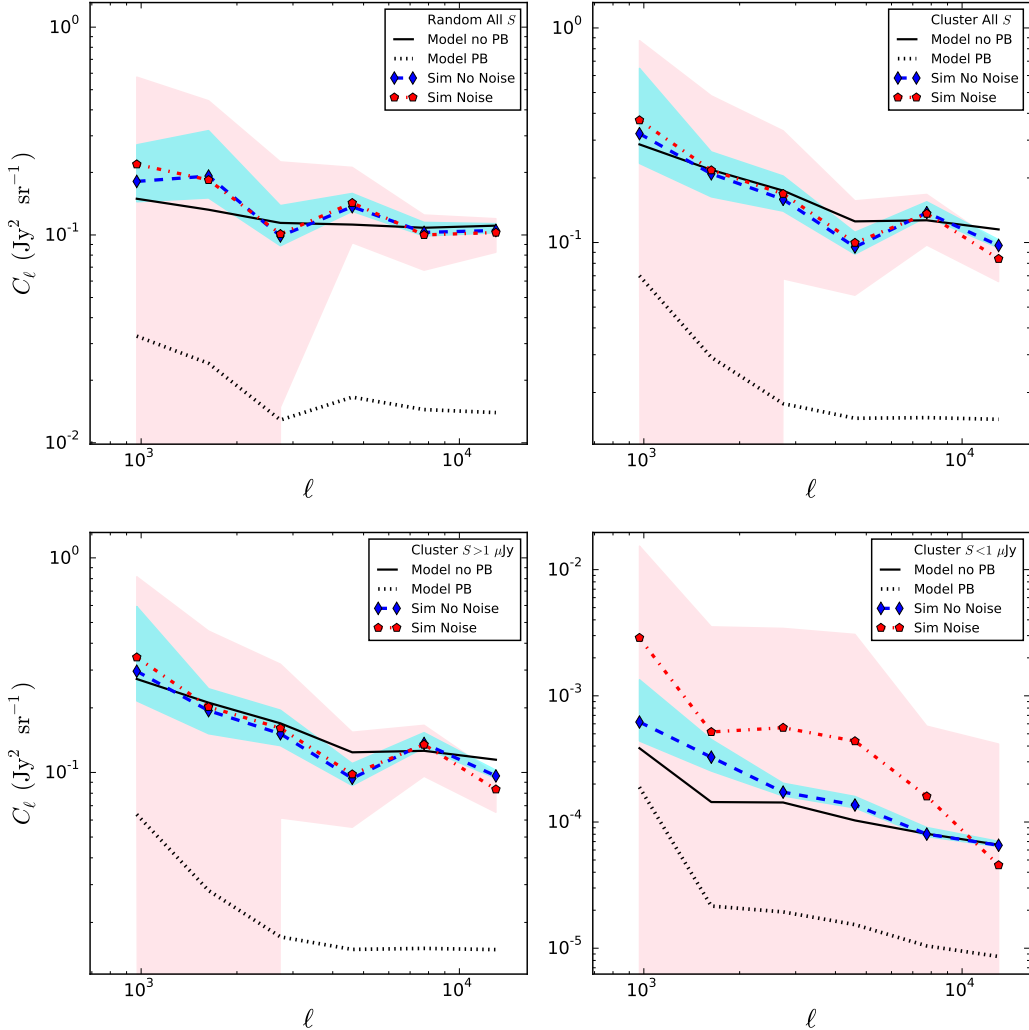


Figure 7.8: C_ℓ measurements from simulations that contain clustering. The black solid lines are the input noiseless model images, while the black dotted lines are the input models with a primary beam applied. The blue dashed and red dot-dashed lines are the simulated visibilities with no noise and with Gaussian random noise of $\sigma = 0.02$, respectively. All simulations here include only point sources. The top left panel has randomized positions for all S ($S_{\max} = 0.5$ mJy). The top right panel is clustered positions for all S . The bottom left panel is clustered, including only sources with $S > 1 \mu\text{Jy}$. The bottom right panel is clustered for sources with $S < 1 \mu\text{Jy}$. The shaded regions are the $\pm 1\sigma$ uncertainties from the visibilities.

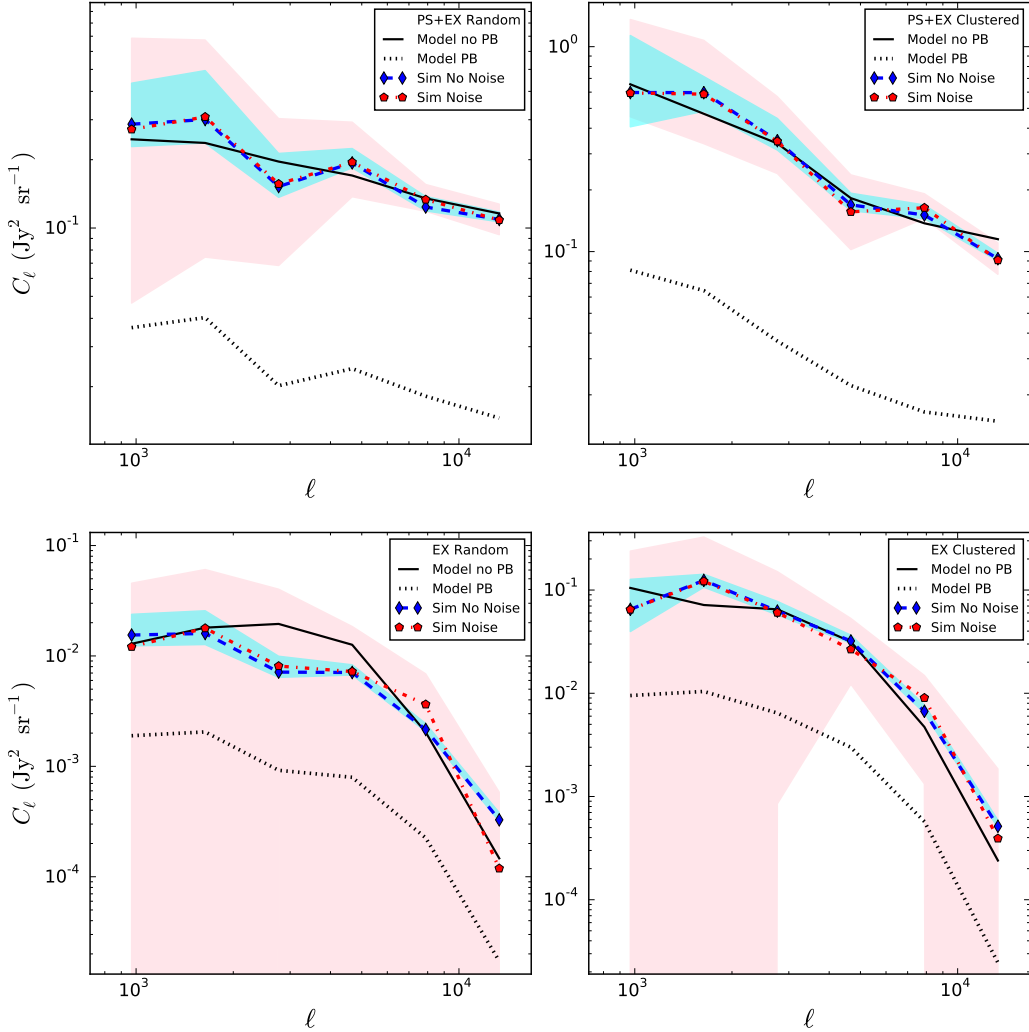


Figure 7.9: C_ℓ measurements from simulations with extended emission. The black solid lines are the input noiseless model images, while the black dotted lines are the input models with a primary beam applied. The blue dashed and red dot-dashed lines are the simulated visibilities with no noise and with Gaussian random noise of $\sigma = 0.02$, respectively. The top panels are point sources plus extended halos for randomized positions (left) and for clustered positions (right). The bottom panels are extended halos only, for random positions (left) and for clustered positions (right). The shaded regions are the $\pm 1\sigma$ uncertainties from the visibilities.

model fitting on the simulated data sets. Parameter distributions (1D and 2D) from fitting Model 2 (cluster power law plus Poisson) for the simulated noisy data are shown in Figs. 7.11 (random positions no clustering) and 7.12 (clustered positions). These were fit without any additional priors on the known or estimated Poisson level, which should be $0.1 \text{ Jy}^2 \text{ sr}^{-1}$. We can see that for the data with no clustering the fitted Poisson level is approximately right (median value of $0.097 \text{ Jy}^2 \text{ sr}^{-1}$), and that the routine had difficulty fitting the clustering level and index, as it should. On the other hand, when fitting the data that contains clustering, the true index should be $\beta \simeq -1.2$, and we can see that the peak of the distribution is near this value (the median is -1.08). The Poisson level is still close to the input value, although perhaps a bit low (median value of $0.07 \text{ Jy}^2 \text{ sr}^{-1}$).

We can see it is certainly possible to detect the Poisson level of an image even, with the existing noise level. The clustering level and index strongly depend on the amount of noise, amount of clustering, and the particular realisation of the sky. If the uncertainties from cosmic variance large compared to the clustering amplitude then the clustering is much harder to constrain. The particular clustering setup we have used in the simulations seems optimistic, at least for the clustering amplitude, compared to the Poisson amplitude. While the clustered positions are set up to match previous observations, the assignment of flux-density values is likely not as realistic. In reality the clustering amplitude is likely to be lower, since we have not seen something with such a distinctive power-law addition to the flat Poisson level in the real data. Perhaps with the higher multipole resolution from mosaicking, lower noise, or a better treatment of the primary beam effect the clustering levels could be fit with smaller uncertainty.

7.7 ATCA Results

The C_ℓ s from our real ATCA data individual pointings are shown in Fig. 7.13. These data have had the bright ($S \geq 150 \mu\text{Jy}$) point sources subtracted, as described in Section 5.3.1, using the ATLAS models. Using the source count from Chapter 4 scaled to 1.75 GHz and eq. 7.21 with $S_{\text{cut}} = 150 \mu\text{Jy}$, the expected Poisson level is $3.8 \text{ Jy}^2 \text{ sr}^{-1}$, with the mean from all seven pointings being $3.36 \text{ Jy}^2 \text{ sr}^{-1}$.

We have not yet attempted any model fitting on these data, since there are still

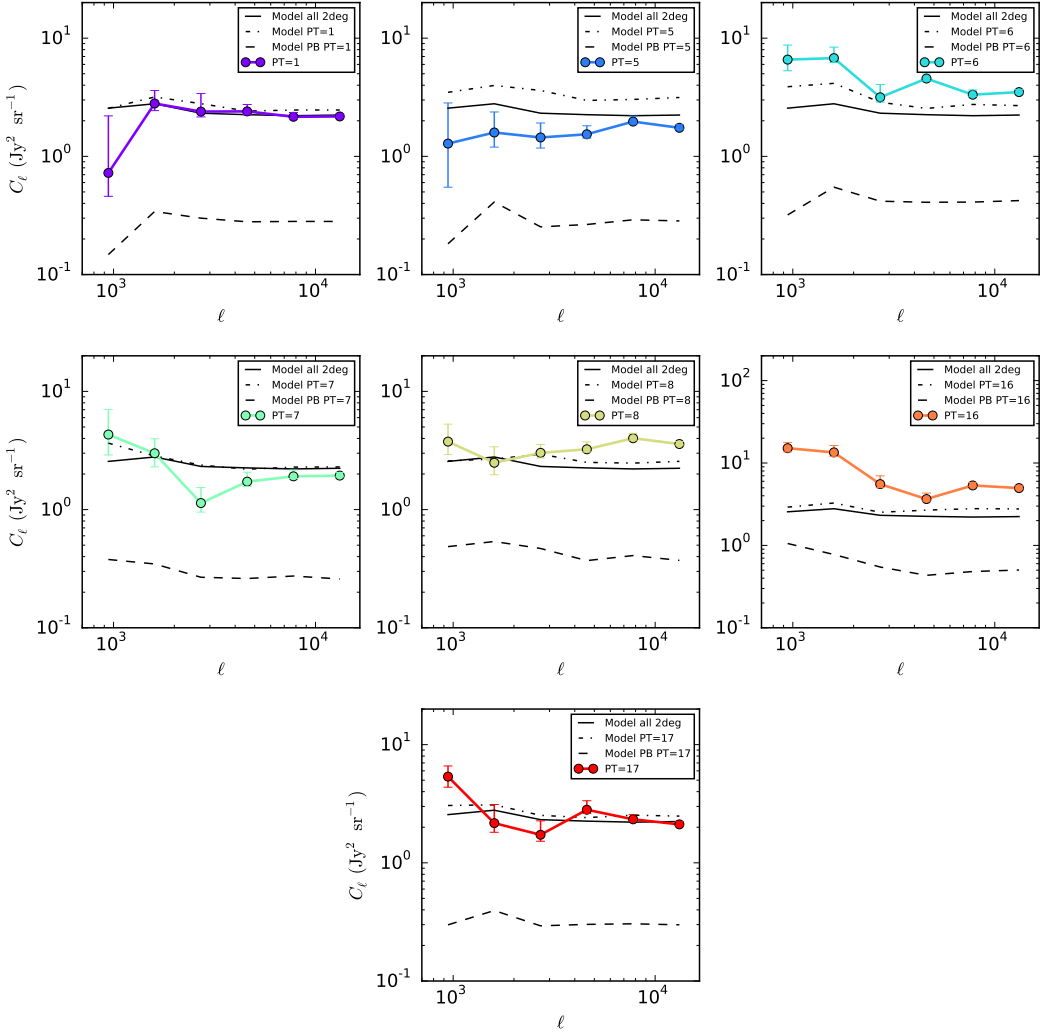


Figure 7.10: C_ℓ measurements from simulations with mosaicked data. The black solid lines are from the input noiseless model image of the whole field, the black dot-dashed lines are the input models for the individual pointings, and the black dashed lines are the individual input models with a primary beam applied. The solid coloured lines are the simulated noiseless visibilities from the individual pointings.

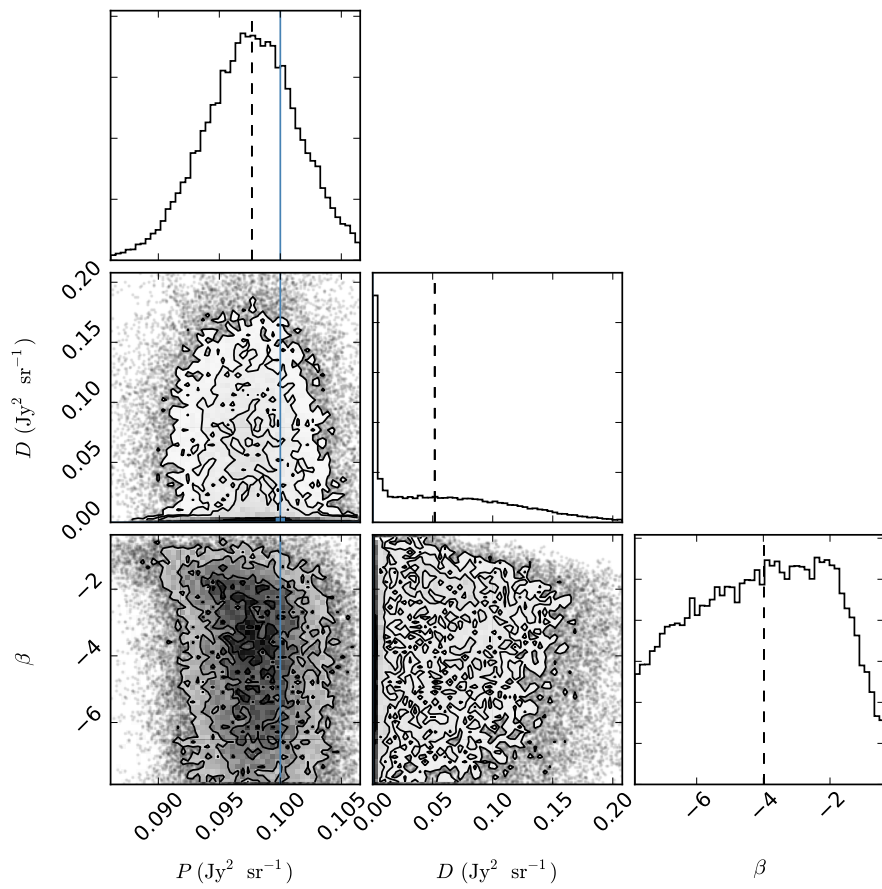


Figure 7.11: Parameter distribution (1D and 2D) results from MCMC fitting of Model 2 on the simulated noisy data with random positions and random flux assignment. The solid blue lines indicate the true input values for each parameter and and back dashed vertical lines show the medians for the each parameter distribution.

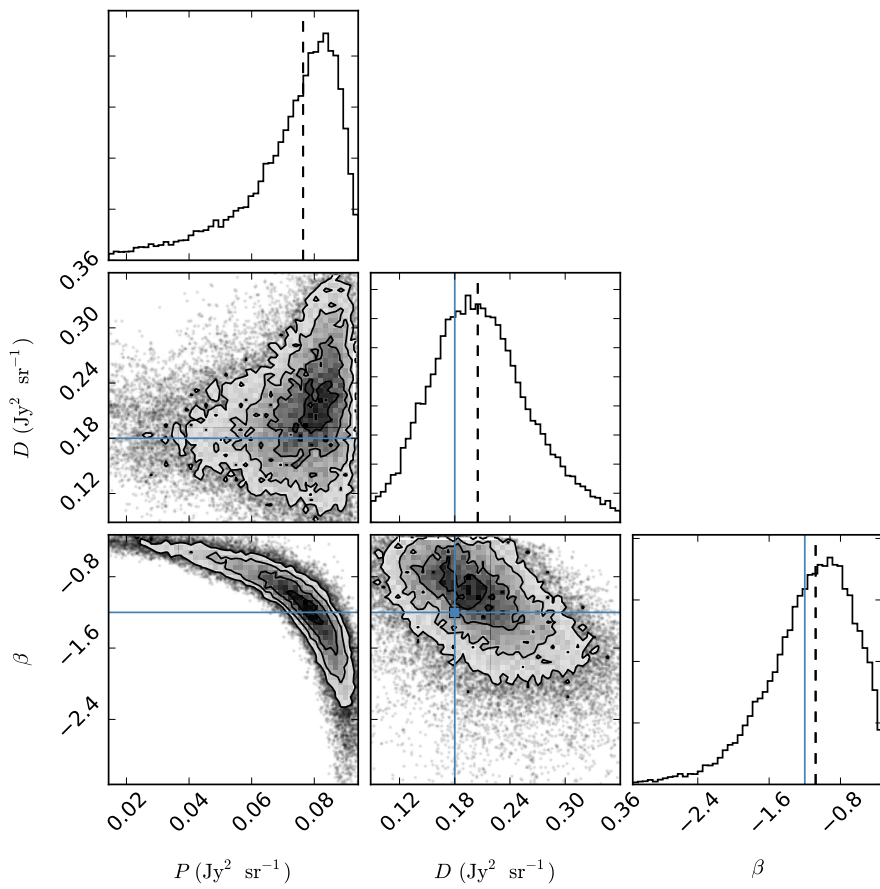


Figure 7.12: Parameter distribution (1D and 2D) results from MCMC fitting of Model 2 on the simulated noisy data, with clustered positions and random flux assignment. The solid blue lines indicate the true input values for each parameter and and back dashed vertical lines show the medians for the each parameter distribution.

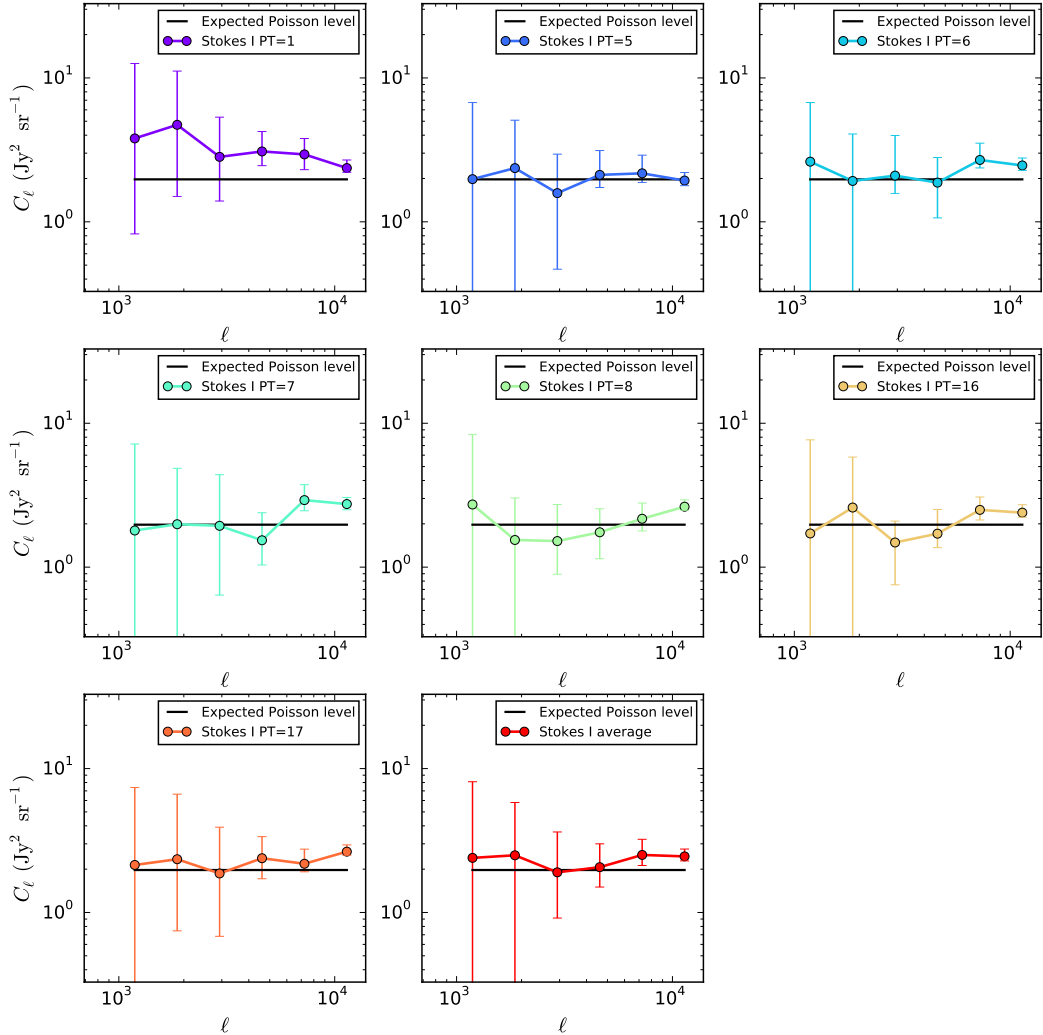


Figure 7.13: C_ℓ measurements from individual ATCA pointings with all corrections applied and with ATLAS point source models ($S \geq 150 \mu\text{Jy}$) subtracted. The black solid line represents the expected Poisson amplitude using the source count from Chapter 4 scaled to 1.75 GHz and eq. 7.21 with $S_{\text{cut}} = 150 \mu\text{Jy}$.

issues being resolved with the use of the simulations. The weighting for these data is likely different than that used in the simulations as the data include phase and calibration errors, as well as time dependent noise. The time dependent noise is a result of the source approaching the horizon during the final few hours of the 12 hour observation and some antennas being shadowed. This likely needs to be taken into account in the visibility weights; we are currently investigating the optimal weighting in this case.

It is clear from visual inspection that if there is clustering signal present, its amplitude is weaker than the Poisson amplitude, and weaker than that adopted in our simulations. This does not mean there is no clustering signal, simply that it could be entirely swamped by the Poisson contribution.

Previous upper limits on the contribution to the unresolved background come from Fomalont et al. [60], Partridge et al. [137] and Subrahmanyan et al. [171] at 4.86, 8.4, and 8.7 GHz, respectively. We can compare results by looking at the fractional rms or $\Delta T/T$, the question being what T to use (i.e. the temperature predicted by ARCADE 2, predicted from source counts, or something else). These limits are shown in Fig. 7.14, along with the ranges from the seven ATCA pointings. Work continues on the proper mosaicking treatment to make one measurement from the seven. We show three different cases. The first uses $T = T_{\text{CMB}} = 2.7255 \text{ K}$. The second normalizes the C_ℓ s by the ARCADE 2 temperature at each frequency T_{AR2} , computed using the fits from eq. 1.8 and eq. 1.9. The third shows the C_ℓ s normalized by the temperature predicted from integrating the source count at each frequency T_{count} .

7.8 Conclusions

Measuring the radio angular power spectrum is challenging using data from traditional interferometers, which are effectively optimized for the detection of compact sources. Using realistic physical assumptions we created simulated skies with a range of features. Using these we created simulated interferometric observations with the same setup as for our ATCA data. We have used these to investigate and determine the effects from (and corrections for) wide frequency coverage, uv sampling, the primary beam, mosaicking, and more. We have shown that by using the

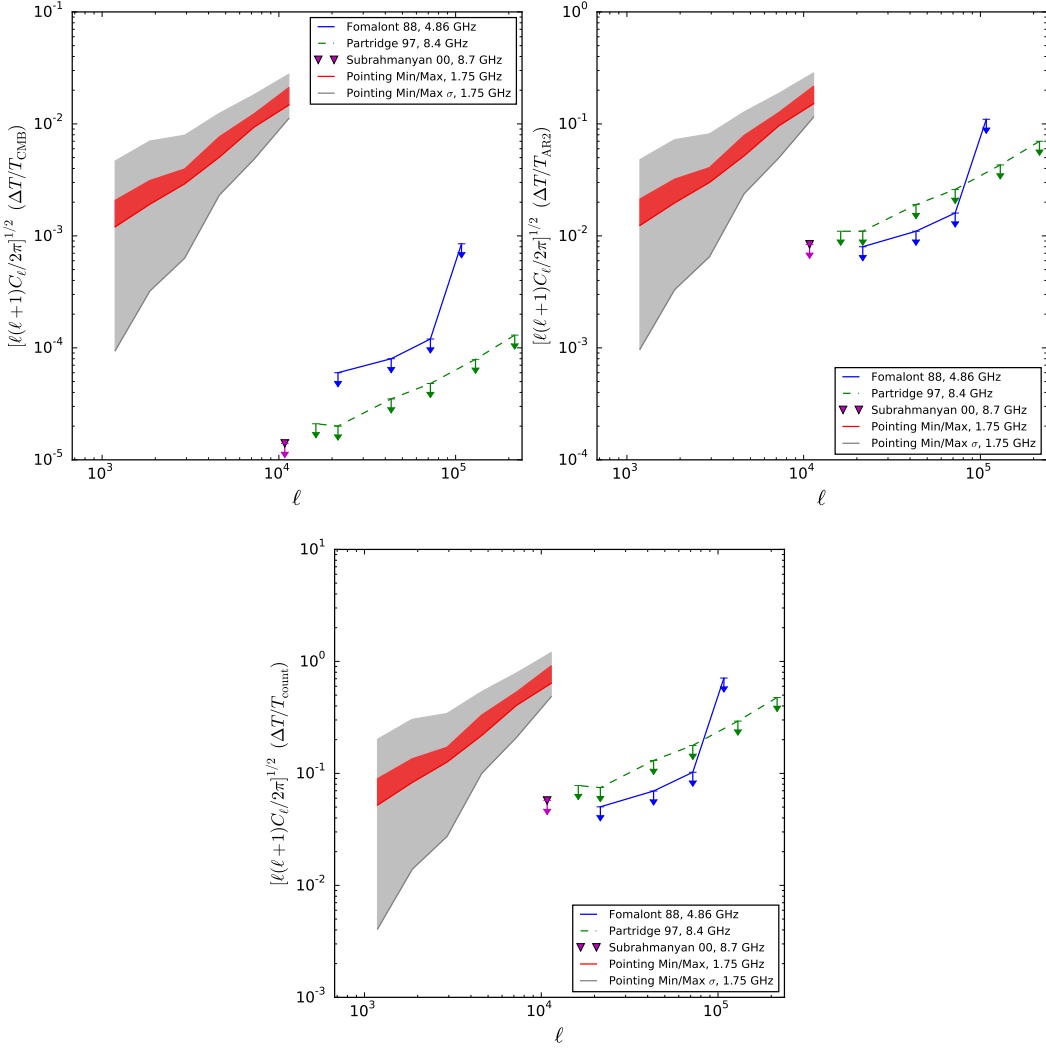


Figure 7.14: Normalized C_ℓ measurements to show $\Delta T/T$ from ATCA data with all corrections applied and ATLAS models subtracted ($S \geq 150 \mu\text{Jy}$), with upper limits from Fomalont et al. [60] (green dashed line), Partridge et al. [137] (purple solid line), and Subrahmanyan et al. [171] (blue triangle). The red regions are the maximum and minimum range from the 7 pointings, while the grey regions are the range of the 1σ uncertainties. The top left panel shows the C_ℓ s normalized by $T_{\text{CMB}} = 2.7255 \text{ K}$. The top right panel is normalized by the ARCADE 2 temperature at each frequency (T_{AR2}), while the bottom panel uses the temperature from the source count at each frequency, T_{count} .

Bare Estimator to calculate the average C_ℓ s from the visibilities, we are able to recover the input power spectrum. Early attempts at model fitting seem promising for fitting the Poisson level, which is something that has not been measured in this way at radio frequencies before. Moreover, there are indications that it may be possible to detect the clustering signal as well.

Work remaining on this project includes determining the optimal visibility weighting and the correct measure of the uncertainty, considering things like phases or calibration errors. We also need to understand how to properly combine and measure mosaicked data, the optimal fitting procedure, and how to fit for extended emission. Once these issues have been explored, applying this technique fully to actual ATCA data and model fitting will be possible.

It is clear that this type of experiment would benefit from a different observational strategy. Observations covering a larger sky area would be optimal, since we are interested in clustering and large angular scale emission. Plus, getting more short baseline data will increase sensitivity to large scales. Also, observations at a lower frequency would be beneficial, since the majority of the emission is produced via synchrotron processes, which become stronger at lower frequencies, thus increasing the signal to noise. However, determining the optimal observing strategy for future measurements of radio clustering will require further study with smaller-scale data sets, such as those we already have in hand.

Chapter 8

Impact and Conclusions

8.1 Summary

My research lies primarily in investigating the faint (μJy) extragalactic radio sky. In broad terms this work involves statistically characterizing faint radio galaxies: how many there are; what kind of galaxies they are; how large are these galaxies etc. Characterizing these rarely studied galaxies on both large and small angular scales can tell us much about galaxy evolution, dynamics in galaxy clusters, different types of galaxy populations, as well as the star formation history of the Universe. The radio-galaxy phase of galaxy evolution is a critical one because the feedback from AGN significantly effects galaxy star formation thereby governing the growth and evolution of the galaxies. Studying the characteristics of radio emission to new depths will help to better understand this crucial phase, and may also help to constrain models of dark matter particles. There are also more specific issues to study such as the contribution of faint galaxies to the cosmic radio background: how the size of radio galaxies scales with brightness; how the far-infrared to radio correlation evolves (or otherwise) with redshift; and what we can learn from the radio power spectrum. In this thesis I have detailed some of the ways in which I have already started to investigate these areas.

We have presented several different estimates of the radio source count extracted directly from $P(D)$ analysis at 3 GHz, and the count extrapolated to 1.4 GHz using new deep data from the VLA. These involve different assumptions about the

count shape, e.g. the number of nodes, and different choices of data, namely the various noise zones. We have provided an estimate of the extragalactic discrete source contribution to the CRB at 3 GHz of (15 ± 1) mK and (120 ± 3) mK at 1.4 GHz. We have also found an upper limit to the peak of any new discrete population of 50 nJy.

Comparing our source count to known luminosity function models shows a good match in some flux density ranges whilst a poor fit in other. There is certainly room for improvement in the physical models. The Béthermin et al. [10] model tuned by considering both infrared and radio counts comes up too low in the ~ 50 to several hundred μ Jy region. This could indicate some kind of evolution between the radio to infrared correlation (see below for more discussion on this). Further modelling of the luminosity function would be important for connecting the source count to galaxy population evolution.

Using the ATCA telescope we have found, after discrete source subtraction, a roughly 3σ excess in the 1.75 GHz image PDF, which could be caused by extended emission. After fitting several models we find an upper limit on the contribution to CRB at this frequency from extended emission to be (10 ± 7) mK. We found a limit to any possible extended population that could cause the ARCADE 2 excess of 1 μ Jy.

The models used represent upper limits on the extended emission, and are valid for sources with angular size of approximately 2 arcmin or less. Assuming the excess is truly from extended emission, rather than data artefacts, we discussed some possible sources for the extended emission. These include individual galaxy haloes from starburst or AGN galaxies, haloes from another population such as dwarf spheroidals (or something unknown), and some contribution from clusters (or smaller mass groups) through emission structures such as radio relics and haloes. We compared one model of cluster halo emission and found it is not ruled out by our data, although there is room for some additional emission besides that provided by the model. The amount of faint cluster emission is not well known and depends on many factors (e.g. origin of the halo, dissipation timescales). This type of technique will be important for studying this issue, since for sources of this size the confusion level is quite high, making imaging of individual faint objects difficult.

Modelling is required to see if any known objects could produce similar source count shapes, either by means of ‘normal’ emission, i.e. synchrotron emission from magnetic fields, or from something more exotic such as via dark matter annihilation. We showed an example of dark matter models from Fornengo et al. [63] and found them to be inconsistent with our data. It is clear that the resulting source count for any WIMP dark matter model, for source sizes up to 2 arcmin, must lie below the source count of current radio galaxies, at least for flux densities greater than around $10\,\mu\text{Jy}$.

Using the deep VLA data at two different resolutions, we presented discrete source catalogues from these data along with an analysis of the source fitting and uncertainties using simulations. We have shown that, as long as the data are comparably deep, the output from cataloguing the two resolutions finds roughly the same sources and source parameters. There are pros and cons for each resolution, which can be used when planning future deep surveys.

We found that the source counts from the discrete catalogues agree very well with the $P(D)$ result. Also, the spectral indices, measured using two different methods, yield a mean of approximately -0.7 , as would be expected if the galaxies are predominately star-forming. When cross-matched with catalogues from other wavelengths we are able to determine the optical and infrared colours. With the use of these colours, combined with radio spectral indices, the galaxy types and redshifts can be determined.

The final part of this thesis dealt with using radio interferometry data from the ATCA telescope to measure the angular power spectrum. We showed, through the use of realistic simulations, that corrections for the primary beam and wide frequency coverage can be determined and the visibilities combined to measure the binned mean power spectrum. With model fitting, it is clear that the Poisson level is detectable, with the possibility of the clustering level being detectable, depending on the strength of the clustering amplitude compared to that of the Poisson amplitude.

Throughout the thesis considerable time has been spent on fine tuning the methods and statistics. This is because many of these are new techniques (or at least new in these specific applications). These analyses now permit the physical interpretation of the data, largely left as further work, to be considered with confidence.

8.2 Future Work

The work presented here only scratches the surface when it comes to the faint radio sky. There is still much to do with currently available data and soon there will be large amount of data coming in from telescopes such as LOFAR and the SKA Pathfinders. In the immediate future the next steps are to finish the work on the discrete catalogues and angular power spectrum. Below we discuss some possible avenues for further investigation.

8.2.1 High Resolution

The SKA and its pathfinders all have plans for deep extragalactic surveys. Between these there will be varying levels of area, resolution, and depth, but the combination of them will allow for precise measurements of the radio luminosity function for AGN and star-forming galaxies over the full range in radio luminosity unmatched by previous surveys. Probably sooner than these is the VLA Sky Survey, which plans to map an area 10 deg^2 to a depth of $1.5 \mu\text{Jy}$ at 1.4 GHz , with roughly 1 arcsec resolution [VLASS, 97].

It will be important to determine the optimum resolution for these surveys to best achieve the corresponding science goals. To do this we need to have an accurate understanding of the angular sizes of radio sources, and how these sizes change with source brightness, particularly for faint sources. Previous attempts to measure the angular-size distribution of faint radio sources were based on images made at a single high resolution. As image resolution approaches the source size, more sources are resolved and can only be fit by Gaussian distributions having free axis sizes and orientations. These extra parameters increase fitting errors on individual sources.

Additionally, source counts must be corrected for sources that were missed because their peaks are below the survey limit but their total brightness levels are above the limit. These corrections are large and very uncertain, even for brighter sources, and such corrections are largely responsible for the disparity among published faint radio counts. Angular-size errors multiply in population statistics; a steep integral count intensifies any overestimation of flux density, driving the counts rapidly, and inaccurately, to higher numbers at fainter sources.

Neither the source count nor the angular-size distribution can be determined accurately from single high-resolution images with current telescopes and common imaging methods. It would be possible with a single high resolution image if the observations baseline distribution produced the optimal *uv* coverage. While this is not possible with the VLA the SKA may do much better. Additionally, the traditional CLEAN imaging algorithm is not optimized for multi-resolution imaging, but newer algorithms, such as compressive sensing, may perform much better at recovering information on all/more angular scales.

Determining the evolving radio-source luminosity function, the evolving star-formation rate, the sizes of distant obscured starbursts, planning for future surveys, and designing the next generation of radio arrays all depend on our understanding of the angular-size distribution of μ Jy sources. The only way to measure reliable sizes and flux densities, and avoid overestimating the number of missing extended sources, is to analyze sources and flux densities in comparably sensitive images having several different resolutions ranging from the beam sizes being much larger than the source size to beam sizes roughly equivalent to source sizes.

The logical next step is to use the deepest data currently available at multiple resolutions to obtain the most accurate source size distribution estimates for faint radio sources. Currently this means using the VLA data we already have at 8 arcsec and 2.75 arcsec and adding one more image at higher resolution (~ 0.7 arcsec). This encompasses a range of possible beam sizes for future surveys and therefore should give important estimates for determining the optimum resolution. We have already been granted this time on the VLA in its next A-configuration setup, with data to be taken in the summer of 2015.

8.2.2 Low Frequencies

The low frequency radio sky is an increasingly interesting region of study. With upgrades to current telescopes and new low frequency telescopes such as LOFAR, as well as new imaging and calibration methods, the sky at low frequencies is being explored to new depths. Studying the same sources at multiple frequencies is important for fully understanding the physical emission processes, as well as how different galaxy types evolve with redshift. The emission from synchrotron

gets stronger at lower frequencies, which also means the ARCADE 2 background is predicted to get stronger; thus, observing at these frequencies should add further constraints on the background. Moreover, as the low frequency sky can probe out to higher redshifts (depending on sensitivity and population of interest), it is vital to obtaining a better understanding of the faint low frequency sky. The low frequency source count (MHz range) is not nearly as well constrained as at 1.4 GHz, with the faintest measurements only hundreds of μ Jy at 325 MHz (thousands of μ Jy at 150 or 408 MHz), as is shown in Fig. 1.2.

Along with collaborators, I recently acquired time with the GMRT at 325 MHz in the same field as our 3 GHz VLA observations. I propose to use the $P(D)$ confusion technique to push the low frequency count to new limits, as well as tightening the constraints on the existing count. $P(D)$ analysis should be performed on this GMRT data (or the GMRT data combined with previous 325 MHz VLA data in this field[135]) to provide improved estimates of counts at this lower frequency.

With multi-frequency data of the same field, a two-dimensional $P(D)$ analysis could be performed, where an evolutionary model describing frequency dependence (as well as redshift evolution for different populations) is used to predict the source count at both frequencies. Rather than just the 1D histograms at each frequency this would involve fitting the 2D histogram, which includes information about source position as well as brightness (i.e. a bright sources should be bright in both images). This has never been done before and I believe could yield not just constraints on the source count, but information on the physics and evolution of the sources.

8.2.3 The Far Infrared to Radio Correlation

Another aspect to consider when discussing faint radio galaxies is the far-infrared-to-radio correlation. These faint (sub-mJy) radio galaxies are generally star-forming galaxies. As the radio emission from star formation is not affected by attenuation from dust, these sources are good tracers of star formation out to high redshifts. The infrared luminosity is also used to determine star-formation rates, and thus the FIR-to-radio flux density ratio has been useful when estimating the dust temperature of a distant starburst, when defining samples of AGN, or when probing

magnetic field strength. This ratio has been shown to be roughly constant out to $z \simeq 1$ [e.g. 93, 95, 162]. However, at higher redshifts there are less measurements and larger uncertainties, making it unclear if this ratio is evolving with time.

With radio survey limits being pushed fainter, new deep sub-mm and infrared data, as well as large scale redshift surveys, determining this ratio at higher redshifts with tighter constraints is now possible. The sub-mm data tends to have much larger beam sizes than the radio and thus confusion at sub-mm wavelengths can be a limiting factor. The main limitation, however, is having deep and accurate correspond redshift estimates for the sources. Our current deep VLA data could be used along with *Herschel*/SPIRE data from the Lockman Hole [part of the HERMES survey 130] to investigate the FIR-to-radio correlation, as there is also a large amount of other data available in this field to obtain redshift measurements. Since it is believed that the peak of star formation activity happened in the range $1 \leq z \leq 2$, it will be interesting to determine if or how the ratio is affected by this peak and what that might tell us about the evolution of the sources.

8.2.4 Polarisation

In addition to the source count at multiple frequencies, the source count of polarised radio sources is important. The emergence and evolution of magnetic fields in normal galaxies is of fundamental interest because of the strong role in star formation and other processes that drive galaxy evolution (e.g. Beck and Wielebinski [7], Gaensler et al. [66], Mao et al. [113]). Yet little is currently known about the faint polarized sky. The polarized radio source population at polarized flux densities near $10 \mu\text{Jy}$ will be determined by the fractional polarization of radio sources with total intensity flux density in the range 0.1 to 1 mJy, where star-forming galaxies become a significant population of the radio sources. Direct observation of polarized emission from high redshift galaxies thus requires sensitivity approaching $1 \mu\text{Jy}$. There are limited counts of polarized sources below a few mJy at 1.4 GHz and less at lower frequencies. However, observations show a strong excess over predictions based on the polarization properties of strong sources [75, 177]. There is clearly still a lot to be learned from the faint polarized sky.

8.3 Conclusion

We have provided new measurements and constraints on the faint extragalactic radio sky. We have also demonstrated the usefulness of applying new statistical techniques to these data. Studying both the 1-point and 2-point statistics will be increasingly powerful ways of investigating cosmological information in future radio surveys. The coming years will be an exciting time in radio astronomy with new instruments and new surveys probing a range of frequencies, angular scales, and redshifts. There will soon be a wealth of new data to analyze and new science to discover. It is our belief that the work presented here provides important tools and information from which to build on.

Bibliography

- [1] C. P. Ahn, R. Alexandroff, C. Allende Prieto, S. F. Anderson, T. Anderton, B. H. Andrews, É. Aubourg, S. Bailey, E. Balbinot, R. Barnes, and e.a. The Ninth Data Release of the Sloan Digital Sky Survey: First Spectroscopic Data from the SDSS-III Baryon Oscillation Spectroscopic Survey. *ApJl*, 203:21, Dec. 2012. doi:10.1088/0067-0049/203/2/21. → pages 164
- [2] D. R. Altschuler. A 5-GHz survey of radio sources. *A&AS*, 65:267–281, Aug. 1986. → pages 11
- [3] R. Antonucci. Unified models for active galactic nuclei and quasars. *ARA&A*, 31:473–521, 1993. doi:10.1146/annurev.aa.31.090193.002353. → pages 2
- [4] J. Bagchi, T. A. Enßlin, F. Miniati, C. S. Stalin, M. Singh, S. Raychaudhury, and N. B. Humeshkar. Evidence for shock acceleration and intergalactic magnetic fields in a large-scale filament of galaxies ZwCl 2341.1+0000. *New Astronomy*, 7:249–277, July 2002. doi:10.1016/S1384-1076(02)00137-9. → pages 4
- [5] K. Bandura, G. E. Addison, M. Amiri, J. R. Bond, D. Campbell-Wilson, L. Connor, and J.-F. e. a. Cliche. Canadian Hydrogen Intensity Mapping Experiment (CHIME) pathfinder. In *Society of Photo-Optical Instrumentation Engineers (SPIE) Conference Series*, volume 9145 of *Society of Photo-Optical Instrumentation Engineers (SPIE) Conference Series*, page 22, July 2014. doi:10.1117/12.2054950. → pages 174
- [6] P. D. Barthel. Is every quasar beamed? *ApJ*, 336:606–611, Jan. 1989. doi:10.1086/167038. → pages 2
- [7] R. Beck and R. Wielebinski. *Magnetic Fields in Galaxies*, page 641. 2013. doi:10.1007/978-94-007-5612-0_13. → pages 208

- [8] C. R. Benn, G. Grueff, M. Vigotti, and J. V. Wall. A deep radio/optical survey near the North Galactic Pole. I. The 5C12 catalogue. *MNRAS*, 200: 747–766, Aug. 1982. → pages 11
- [9] R. Bergamini, P. Londrillo, and G. Setti. The cosmic black-body radiation and the inverse compton effect in the radio galaxies: The X-ray background. *Nuovo Cimento B Serie*, 52:495–506, Dec. 1967.
doi:10.1007/BF02711093. → pages 7, 121
- [10] M. Béthermin, E. Daddi, G. Magdis, M. T. Sargent, Y. Hezaveh, D. Elbaz, D. Le Borgne, J. Mullaney, M. Pannella, V. Buat, V. Charmandaris, G. Lagache, and D. Scott. A Unified Empirical Model for Infrared Galaxy Counts Based on the Observed Physical Evolution of Distant Galaxies. *ApJl*, 757:L23, Oct. 2012. doi:10.1088/2041-8205/757/2/L23. → pages 88, 89, 91, 92, 203
- [11] C. Blake and J. Wall. Measurement of the angular correlation function of radio galaxies from the NRAO VLA Sky Survey. *MNRAS*, 329:L37–L41, Jan. 2002. doi:10.1046/j.1365-8711.2002.05163.x. → pages 50
- [12] C. Blake and J. Wall. Quantifying angular clustering in wide-area radio surveys. *MNRAS*, 337:993–1003, Dec. 2002.
doi:10.1046/j.1365-8711.2002.05979.x. → pages 50
- [13] C. Blake, T. Mauch, and E. M. Sadler. Angular clustering in the Sydney University Molonglo Sky Survey. *MNRAS*, 347:787–794, Jan. 2004.
doi:10.1111/j.1365-2966.2004.07240.x. → pages 50, 173, 187
- [14] J. G. Bolton, G. J. Stanley, and O. B. Slee. Positions of Three Discrete Sources of Galactic Radio-Frequency Radiation. *Nature*, 164:101–102, July 1949. doi:10.1038/164101b0. → pages 1
- [15] M. Bondi, P. Ciliegi, T. Venturi, D. Dallacasa, S. Bardelli, E. Zucca, R. M. Athreya, L. Gregorini, A. Zanichelli, O. Le Fèvre, T. Contini, B. Garilli, A. Iovino, S. Temporin, and D. Vergani. The VVDS-VLA deep field. III. GMRT observations at 610 MHz and the radio spectral index properties of the sub-mJy population. *A&A*, 463:519–527, Feb. 2007.
doi:10.1051/0004-6361:20066428. → pages 11
- [16] M. Bondi, P. Ciliegi, E. Schinnerer, V. Smolčić, K. Jahnke, C. Carilli, and G. Zamorani. The VLA-COSMOS Survey. III. Further Catalog Analysis and the Radio Source Counts. *ApJ*, 681:1129–1135, July 2008.
doi:10.1086/589324. → pages 11

- [17] A. H. Bridle, M. M. Davis, E. B. Fomalont, and J. Lequeux. Flux densities, positions, and structures for a complete sample of intense radio sources at 1400 MHz. *AJ*, 77:405–443, Aug. 1972. doi:10.1086/111301. → pages 11
- [18] D. S. Briggs. High Fidelity Deconvolution of Moderately Resolved Radio Sources. *Ph.D. thesis, New Mexico Inst. of Mining & Technology*, 1995. → pages 26, 35
- [19] S. Brown, A. Emerick, L. Rudnick, and G. Brunetti. Probing the Off-state of Cluster Giant Radio Halos. *ApJl*, 740:L28, Oct. 2011. doi:10.1088/2041-8205/740/1/L28. → pages 122
- [20] S. D. Brown. Synchrotron Emission on the Largest Scales: Radio Detection of the Cosmic-Web. *Journal of Astrophysics and Astronomy*, 32: 577–584, Dec. 2011. doi:10.1007/s12036-011-9114-4. → pages 97
- [21] G. Brunetti and A. Lazarian. Acceleration of primary and secondary particles in galaxy clusters by compressible MHD turbulence: from radio haloes to gamma-rays. *MNRAS*, 410:127–142, Jan. 2011. doi:10.1111/j.1365-2966.2010.17457.x. → pages 122
- [22] B. F. Burke and F. Graham-Smith. *An introduction to radio astronomy*. 1997. → pages 21
- [23] R. Cassano, G. Brunetti, and G. Setti. Statistics of giant radio haloes from electron reacceleration models. *MNRAS*, 369:1577–1595, July 2006. doi:10.1111/j.1365-2966.2006.10423.x. → pages 4
- [24] R. Cassano, G. Brunetti, R. P. Norris, H. J. A. Röttgering, M. Johnston-Hollitt, and M. Trasatti. Radio halos in future surveys in the radio continuum. *A&A*, 548:A100, Dec. 2012. doi:10.1051/0004-6361/201220018. → pages 122
- [25] E. L. Chapin, S. C. Chapman, and K. E. e. a. Coppin. A joint analysis of BLAST 250–500 μm and LABOCA 870 μm observations in the Extended Chandra Deep Field-South. *MNRAS*, 411:505–549, Feb. 2011. doi:10.1111/j.1365-2966.2010.17697.x. → pages 63, 140
- [26] S. Choudhuri, S. Bharadwaj, A. Ghosh, and S. S. Ali. Visibility-based angular power spectrum estimation in low-frequency radio interferometric observations. *MNRAS*, 445:4351–4365, Dec. 2014. doi:10.1093/mnras/stu2027. → pages 181

- [27] W. N. Christiansen and J. A. Hogbom. *Radiotelescopes /2nd edition/*. 1985. → pages 20
- [28] E. Churazov, R. Sunyaev, M. Revnivtsev, S. Sazonov, S. Molkov, S. Grebenev, and e.a. INTEGRAL observations of the cosmic X-ray background in the 5-100 keV range via occultation by the Earth. *A&A*, 467:529–540, May 2007. doi:10.1051/0004-6361:20066230. → pages 121
- [29] P. Ciliegi, R. G. McMahon, G. Miley, C. Gruppioni, M. Rowan-Robinson, C. Cesarsky, L. Danese, A. Franceschini, R. Genzel, A. Lawrence, D. Lemke, S. Oliver, J. Puget, and B. Rocca-Volmerange. A deep VLA survey at 20 CM of the ISO ELAIS survey regions. *MNRAS*, 302:222–244, Jan. 1999. doi:10.1046/j.1365-8711.1999.02103.x. → pages 11
- [30] J. J. Condon. Confusion and Flux-Density Error Distributions. *ApJ*, 188: 279–286, Mar. 1974. doi:10.1086/152714. → pages 46, 47, 54
- [31] J. J. Condon. Cosmological evolution of radio sources. *ApJ*, 287:461–474, Dec. 1984. doi:10.1086/162705. → pages 9, 39, 66, 85, 86, 91, 92, 102, 110
- [32] J. J. Condon. Errors in Elliptical Gaussian FITS. *PASP*, 109:166–172, Feb. 1997. doi:10.1086/133871. → pages 37, 134
- [33] J. J. Condon. Deep Radio Surveys. In J. Afonso, H. C. Ferguson, B. Mobasher, and R. Norris, editors, *Deepest Astronomical Surveys*, volume 380 of *Astronomical Society of the Pacific Conference Series*, page 189, Dec. 2007. → pages 11
- [34] J. J. Condon and K. J. Mitchell. A deeper VLA survey of the alpha = 08h52m15s, delta = +17 deg 16 arcmin field. *AJ*, 89:610–617, May 1984. doi:10.1086/113556. → pages 8, 11
- [35] J. J. Condon, M. L. Anderson, and G. Helou. Correlations between the far-infrared, radio, and blue luminosities of spiral galaxies. *ApJ*, 376: 95–103, July 1991. doi:10.1086/170258. → pages 3
- [36] J. J. Condon, W. D. Cotton, E. W. Greisen, Q. F. Yin, R. A. Perley, G. B. Taylor, and J. J. Broderick. The NRAO VLA Sky Survey. *AJ*, 115: 1693–1716, May 1998. doi:10.1086/300337. → pages 33, 37, 50, 175
- [37] J. J. Condon, W. D. Cotton, E. B. Fomalont, K. I. Kellermann, N. Miller, R. A. Perley, D. Scott, T. Vernstrom, and J. V. Wall. Resolving the Radio

- Source Background: Deeper Understanding through Confusion. *ApJ*, 758: 23, Oct. 2012. doi:10.1088/0004-637X/758/1/23. → pages iv, 4, 5, 37, 39, 46, 54, 55, 58, 63, 66, 68, 71, 86, 88, 89, 90, 91, 92, 94, 97, 158, 159, 171
- [38] T. J. Cornwell. Radio-interferometric imaging of very large objects. *A&A*, 202:316–321, Aug. 1988. → pages 179
 - [39] W. D. Cotton. Obit: A Development Environment for Astronomical Algorithms. *PASP*, 120:439–448, Apr. 2008. doi:10.1086/586754. → pages 33
 - [40] S. M. Croom, B. J. Boyle, T. Shanks, R. J. Smith, L. Miller, P. J. Outram, N. S. Loaring, F. Hoyle, and J. da Ângela. The 2dF QSO Redshift Survey - XIV. Structure and evolution from the two-point correlation function. *MNRAS*, 356:415–438, Jan. 2005. doi:10.1111/j.1365-2966.2004.08379.x. → pages 186
 - [41] T. de Jong, U. Klein, R. Wielebinski, and E. Wunderlich. Radio continuum and far-infrared emission from spiral galaxies - A close correlation. *A&A*, 147:L6–L9, June 1985. → pages 3
 - [42] G. de Zotti, M. Massardi, M. Negrello, and J. Wall. Radio and millimeter continuum surveys and their astrophysical implications. *A&A Rev.*, 18: 1–65, Feb. 2010. doi:10.1007/s00159-009-0026-0. → pages 3, 9, 10, 49, 69, 71, 91, 92
 - [43] J. L. Donley, A. M. Koekemoer, M. Brusa, P. Capak, C. N. Cardamone, F. Civano, O. Ilbert, C. D. Impey, J. S. Kartaltepe, T. Miyaji, M. Salvato, D. B. Sanders, J. R. Trump, and G. Zamorani. Identifying Luminous Active Galactic Nuclei in Deep Surveys: Revised IRAC Selection Criteria. *ApJ*, 748:142, Apr. 2012. doi:10.1088/0004-637X/748/2/142. → pages 166, 168, 169
 - [44] R. H. Donnelly, R. B. Partridge, and R. A. Windhorst. 6 centimeter radio source counts and spectral index studies down to 0.1 millijansky. *ApJ*, 321: 94–112, Oct. 1987. doi:10.1086/165618. → pages 11
 - [45] E. Dwek and R. G. Arendt. A Tentative Detection of the Cosmic Infrared Background at $3.5 \mu\text{m}$ from COBE/DIRBE Observations. *ApJL*, 508: L9–L12, Nov. 1998. doi:10.1086/311714. → pages 13
 - [46] R. D. Ekers and A. H. Rots. Short Spacing Synthesis from a Primary Beam Scanned Interferometer. In C. van Schooneveld, editor, *IAU Colloq. 49*:

Image Formation from Coherence Functions in Astronomy, volume 76 of *Astrophysics and Space Science Library*, page 61, 1979. → pages 179

- [47] A. C. Fabian, P. E. J. Nulsen, and C. R. Canizares. Cooling flows in clusters of galaxies. *A&A Rev.*, 2:191–226, Apr. 1991.
doi:10.1007/BF00872767. → pages 4
- [48] B. L. Fanaroff and J. M. Riley. The morphology of extragalactic radio sources of high and low luminosity. *MNRAS*, 167:31P–36P, May 1974. → pages 2
- [49] D. Farrah, C. J. Lonsdale, C. Borys, F. Fang, I. Waddington, S. Oliver, M. Rowan-Robinson, T. Babbedge, D. Shupe, M. Polletta, H. E. Smith, and J. Surace. The Spatial Clustering of Ultraluminous Infrared Galaxies over $1.5 \leq z \leq 3$. *ApJl*, 641:L17–L20, Apr. 2006. doi:10.1086/503769. → pages 186
- [50] E. D. Feigelson, S. A. Laurent-Muehleisen, R. I. Kollgaard, and E. B. Fomalont. Discovery of Inverse-Compton X-Rays in Radio Lobes. *ApJl*, 449:L149, Aug. 1995. doi:10.1086/309642. → pages 7, 121
- [51] L. Feretti. Observational Properties of Diffuse Halos in Clusters. In A. Pramesh Rao, G. Swarup, and Gopal-Krishna, editors, *The Universe at Low Radio Frequencies*, volume 199 of *IAU Symposium*, page 133, 2002. → pages 4, 5
- [52] L. Feretti, C. Burigana, and T. A. Enßlin. Diffuse radio emission from the intracluster medium. *New Astronomy Reviews*, 48:1137–1144, Dec. 2004.
doi:10.1016/j.newar.2004.09.025. → pages 16
- [53] L. Feretti, G. Giovannini, F. Govoni, and M. Murgia. Clusters of galaxies: observational properties of the diffuse radio emission. *A&A Rev.*, 20:54, May 2012. doi:10.1007/s00159-012-0054-z. → pages 5, 121, 122
- [54] C. Ferrari, F. Govoni, S. Schindler, A. M. Bykov, and Y. Rephaeli. Observations of Extended Radio Emission in Clusters. *Space Sci. Rev.*, 134:93–118, Feb. 2008. doi:10.1007/s11214-008-9311-x. → pages 4
- [55] D. J. Fixsen. The Temperature of the Cosmic Microwave Background. *ApJ*, 707:916–920, Dec. 2009. doi:10.1088/0004-637X/707/2/916. → pages 12, 97

- [56] D. J. Fixsen, A. Kogut, S. Levin, M. Limon, P. Lubin, P. Mirel, M. Seiffert, J. Singal, E. Wollack, T. Villela, and C. A. Wuensche. ARCADE 2 Measurement of the Extra-Galactic Sky Temperature at 3-90 GHz. *preprint (arXiv: 0901.0555)*, Jan. 2009. → pages 16, 89
- [57] D. J. Fixsen, A. Kogut, S. Levin, M. Limon, P. Lubin, P. Mirel, M. Seiffert, J. Singal, E. Wollack, T. Villela, and C. A. Wuensche. ARCADE 2 Measurement of the Absolute Sky Brightness at 3-90 GHz. *ApJ*, 734:5, June 2011. doi:10.1088/0004-637X/734/1/5. → pages 18
- [58] E. W. Flesch. The Half Million Quasars (HMQ) Catalogue. *PASA*, 32: e010, Mar. 2015. doi:10.1017/pasa.2015.10. → pages 153
- [59] E. B. Fomalont, K. I. Kellermann, J. V. Wall, and D. Weistrop. A deep 6-centimeter radio source survey. *Science*, 225:23–28, July 1984. doi:10.1126/science.225.4657.23. → pages 11
- [60] E. B. Fomalont, K. I. Kellermann, M. C. Anderson, D. Weistrop, J. V. Wall, R. A. Windhorst, and J. A. Kristian. New limits to fluctuations in the cosmic background radiation at 4.86 GHz between 12 and 60 arcsecond resolution. *AJ*, 96:1187–1191, Oct. 1988. doi:10.1086/114872. → pages 173, 199, 200
- [61] E. B. Fomalont, K. I. Kellermann, R. B. Partridge, R. A. Windhorst, and E. A. Richards. The Microjansky Sky at 8.4 GHz. *AJ*, 123:2402–2416, May 2002. doi:10.1086/339308. → pages 11
- [62] E. B. Fomalont, K. I. Kellermann, L. L. Cowie, P. Capak, A. J. Barger, R. B. Partridge, R. A. Windhorst, and E. A. Richards. The Radio/Optical Catalog of the SSA 13 Field. *ApJL*, 167:103–160, Dec. 2006. doi:10.1086/508169. → pages 11
- [63] N. Fornengo, R. Lineros, M. Regis, and M. Taoso. Possibility of a Dark Matter Interpretation for the Excess in Isotropic Radio Emission Reported by ARCADE. *Physical Review Letters*, 107(26):271302, Dec. 2011. doi:10.1103/PhysRevLett.107.271302. → pages 97, 125, 126, 204
- [64] N. Fornengo, R. A. Lineros, M. Regis, and M. Taoso. The isotropic radio background revisited. *preprint (arXiv:1402.2218)*, Feb. 2014. → pages 97
- [65] Y. Friedmann and F. Bouchet. Fluctuation analysis of the far-infrared background - information from the confusion. *MNRAS*, 348:737–744, Mar. 2004. doi:10.1111/j.1365-2966.2004.07323.x. → pages 62

- [66] B. M. Gaensler, M. Havercorn, L. Staveley-Smith, J. M. Dickey, N. M. McClure-Griffiths, J. R. Dickel, and M. Wolleben. The Magnetic Field of the Large Magellanic Cloud Revealed Through Faraday Rotation. *Science*, 307:1610–1612, Mar. 2005. doi:10.1126/science.1108832. → pages 208
- [67] T. Garn, D. A. Green, J. M. Riley, and P. Alexander. A 610-MHz survey of the Lockman Hole with the Giant Metrewave Radio Telescope - I. Observations, data reduction and source catalogue for the central 5 deg². *MNRAS*, 387:1037–1044, July 2008. doi:10.1111/j.1365-2966.2008.13335.x. → pages 11
- [68] K. C. Gendreau, R. Mushotzky, A. C. Fabian, S. S. Holt, T. Kii, and P. J. e. a. Serlemitsos. ASCA Observations of the Spectrum of the X-Ray Background. *PASJ*, 47:L5–L9, Apr. 1995. → pages 13
- [69] M. Gervasi, A. Tartari, M. Zannoni, G. Boella, and G. Sironi. The Contribution of the Unresolved Extragalactic Radio Sources to the Brightness Temperature of the Sky. *ApJ*, 682:223–230, July 2008. doi:10.1086/588628. → pages 9, 16
- [70] A. Ghosh, S. Bharadwaj, S. S. Ali, and J. N. Chengalur. GMRT observation towards detecting the post-reionization 21-cm signal. *MNRAS*, 411:2426–2438, Mar. 2011. doi:10.1111/j.1365-2966.2010.17853.x. → pages 174
- [71] G. Giovannini and L. Feretti. Diffuse Radio Sources and Cluster Mergers: Radio Halos and Relics. In L. Feretti, I. M. Gioia, and G. Giovannini, editors, *Merging Processes in Galaxy Clusters*, volume 272 of *Astrophysics and Space Science Library*, pages 197–227, June 2002. doi:10.1007/0-306-48096-4_7. → pages 4
- [72] G. Giovannini, M. Tordi, and L. Feretti. Radio halo and relic candidates from the NRAO VLA Sky Survey. *New Astronomy*, 4:141–155, Mar. 1999. doi:10.1016/S1384-1076(99)00018-4. → pages 123
- [73] J. Glenn and e.a. HerMES: deep galaxy number counts from a P(D) fluctuation analysis of SPIRE Science Demonstration Phase observations. *MNRAS*, 409:109–121, Nov. 2010. doi:10.1111/j.1365-2966.2010.17781.x. → pages 62, 63, 67
- [74] P. F. Goldsmith. *Instrumentation and techniques for radio astronomy*. 1988. → pages 21

- [75] J. K. Grant, A. R. Taylor, J. M. Stil, T. L. Landecker, R. Kothes, R. R. Ransom, and D. Scott. The DRAO Planck Deep Fields: The Polarization Properties of Radio Galaxies at 1.4 GHz. *ApJ*, 714:1689–1701, May 2010. doi:10.1088/0004-637X/714/2/1689. → pages 208
- [76] P. C. Gregory, W. K. Scott, K. Douglas, and J. J. Condon. The GB6 Catalog of Radio Sources. *ApJl*, 103:427–+, Apr. 1996. doi:10.1086/192282. → pages 11
- [77] G. Grueff. A Determination of the 408-MHZ Log N-Log from the b3 Radio Sources Catalogue. *A&A*, 193:40–+, Mar. 1988. → pages 11
- [78] C. Gruppioni, P. Ciliegi, M. Rowan-Robinson, L. Cram, A. Hopkins, C. Cesarsky, L. Danese, A. Franceschini, R. Genzel, A. Lawrence, D. Lemke, R. G. McMahon, G. Miley, S. Oliver, J. Puget, and B. Rocca-Volmerange. A 1.4-GHz survey of the southern European Large-Area ISO Survey region. *MNRAS*, 305:297–308, Apr. 1999. doi:10.1046/j.1365-8711.1999.02415.x. → pages 11
- [79] D. B. Haarsma and R. B. Partridge. Radio Wavelength Constraints on the Sources of the Far-Infrared Background. *ApJl*, 503:L5+, Aug. 1998. doi:10.1086/311528. → pages 53
- [80] C. A. Hales, R. P. Norris, B. M. Gaensler, E. Middelberg, K. E. Chow, A. M. Hopkins, M. T. Huynh, E. Lenc, and M. Y. Mao. ATLAS 1.4 GHz Data Release 2 – I. Observations of the CDF-S and ELAIS-S1 fields and methods for constructing differential number counts. *preprint (arXiv:1403.5307)*, Mar. 2014. → pages 24
- [81] S. E. G. Hales, J. E. Baldwin, and P. J. Warner. The 6C survey of radio sources. II - The zone delta = 30-51 deg, alpha = 08h30m-17h30m. *MNRAS*, 234:919–936, Oct. 1988. → pages 11
- [82] G. Harker, S. Zaroubi, G. Bernardi, M. A. Brentjens, A. G. de Bruyn, B. Ciardi, V. Jelić, L. V. E. Koopmans, P. Labropoulos, G. Mellema, A. Offringa, V. N. Pandey, A. H. Pawlik, J. Schaye, R. M. Thomas, and S. Yatawatta. Power spectrum extraction for redshifted 21-cm Epoch of Reionization experiments: the LOFAR case. *MNRAS*, 405:2492–2504, July 2010. doi:10.1111/j.1365-2966.2010.16628.x. → pages 174
- [83] D. E. Harris and J. E. Grindlay. The prospects for X-ray detection of inverse-Compton emission from radio source electrons and photons of the microwave background. *MNRAS*, 188:25–37, July 1979. → pages 7, 121

- [84] M. G. Hauser, R. G. Arendt, T. Kelsall, E. Dwek, N. Odegard, and J. L. e. a. Weiland. The COBE Diffuse Infrared Background Experiment Search for the Cosmic Infrared Background. I. Limits and Detections. *ApJ*, 508: 25–43, Nov. 1998. doi:10.1086/306379. → pages 13
- [85] B. Henkel and R. B. Partridge. Completing the Counts of Radio Sources at 8.5 GHz. *ApJ*, 635:950–958, Dec. 2005. doi:10.1086/497588. → pages 11
- [86] M. P. Hobson and K. Maisinger. Maximum-likelihood estimation of the cosmic microwave background power spectrum from interferometer observations. *MNRAS*, 334:569–588, Aug. 2002. doi:10.1046/j.1365-8711.2002.05524.x. → pages 174, 181
- [87] M. A. Holdaway. Mosaicing with Interferometric Arrays. In G. B. Taylor, C. L. Carilli, and R. A. Perley, editors, *Synthesis Imaging in Radio Astronomy II*, volume 180 of *Astronomical Society of the Pacific Conference Series*, page 401, 1999. → pages 179
- [88] G. P. Holder. The Unusual Smoothness of the Extragalactic Unresolved Radio Background. *ApJ*, 780:112, Jan. 2014. doi:10.1088/0004-637X/780/1/112. → pages 173
- [89] D. Hooper, A. V. Belikov, T. E. Jeltema, T. Linden, S. Profumo, and T. R. Slatyer. The isotropic radio background and annihilating dark matter. *Phys. Rev. D*, 86(10):103003, Nov. 2012. doi:10.1103/PhysRevD.86.103003. → pages 97
- [90] A. Hopkins, R. Windhorst, L. Cram, and R. Ekers. What Will the Next Generation Radio Telescope Detect at 1.4 GHz? *Experimental Astronomy*, 10:419–437, Nov. 2000. → pages 110
- [91] A. M. Hopkins, J. Afonso, B. Chan, L. E. Cram, A. Georgakakis, and B. Mobasher. The Phoenix Deep Survey: The 1.4 GHz Microjansky Catalog. *AJ*, 125:465–477, Feb. 2003. doi:10.1086/345974. → pages 11
- [92] F. Hoyle. Origin of Cosmic X Rays. *Physical Review Letters*, 15:131–132, July 1965. doi:10.1103/PhysRevLett.15.131. → pages 7
- [93] E. Ibar, M. Cirasuolo, R. Ivison, P. Best, I. Smail, A. Biggs, C. Simpson, J. Dunlop, O. Almaini, R. McLure, S. Foucaud, and S. Rawlings. Exploring the infrared/radio correlation at high redshift. *MNRAS*, 386:953–962, May 2008. doi:10.1111/j.1365-2966.2008.13077.x. → pages 208

- [94] E. Ibar, R. J. Ivison, A. D. Biggs, D. V. Lal, P. N. Best, and D. A. Green. Deep multi-frequency radio imaging in the Lockman Hole using the GMRT and VLA - I. The nature of the sub-mJy radio population. *MNRAS*, 397: 281–298, July 2009. doi:10.1111/j.1365-2966.2009.14866.x. → pages 11
- [95] R. J. Ivison, D. M. Alexander, A. D. Biggs, W. N. Brandt, E. L. Chapin, K. E. K. Coppin, M. J. Devlin, M. Dickinson, J. Dunlop, S. Dye, S. A. Eales, D. T. Frayer, M. Halpern, D. H. Hughes, E. Ibar, A. Kovács, and G. Marsden. BLAST: the far-infrared/radio correlation in distant galaxies. *MNRAS*, 402:245–258, Feb. 2010. doi:10.1111/j.1365-2966.2009.15918.x. → pages 3, 208
- [96] M. J. Jarvis. Multi-wavelength Extragalactic Surveys and the Role of MeerKAT and SALT. *African Skies*, 16:44, Mar. 2012. → pages 127
- [97] M. J. Jarvis, S. Bhatnagar, M. Bruggen, C. Ferrari, I. Heywood, M. Hardcastle, E. Murphy, R. Taylor, O. Smirnov, C. Simpson, V. Smolcic, J. Stil, and K. van der Heyden. A JVLA 10°degree^2 deep survey. *preprint (arXiv: 1401.4018)*, Jan. 2014. → pages 127, 132, 205
- [98] S. C. Kappadath, M. McConnell, J. Ryan, K. Bennett, C. Winkler, H. Bloemen, W. Hermsen, V. Schoenfelder, M. Varendorff, and G. Weidenspointner. COMPTEL Measurements of the Cosmic Diffuse Gamma-Ray Spectrum from 800 keV to 30 MeV. In *AAS/High Energy Astrophysics Division #4*, volume 31 of *Bulletin of the American Astronomical Society*, page 737, Apr. 1999. → pages 13
- [99] J. K. Katgert. A catalogue of sources found at 610 MHz with the Westerbork synthesis radio telescope - Source counts and spectral index distributions. *A&A*, 73:107–112, Mar. 1979. → pages 11
- [100] A. Kogut, D. J. Fixsen, S. M. Levin, M. Limon, P. M. Lubin, P. Mirel, M. Seiffert, J. Singal, T. Villela, E. Wollack, and C. A. Wuensche. ARCADE 2 Observations of Galactic Radio Emission. *ApJ*, 734:4, June 2011. doi:10.1088/0004-637X/734/1/4. → pages 120
- [101] P. P. Kronberg, R. Kothes, C. J. Salter, and P. Perillat. Discovery of New Faint Radio Emission on 8deg to 3' Scales in the Coma Field, and Some Galactic and Extragalactic Implications. *ApJ*, 659:267–274, Apr. 2007. doi:10.1086/511512. → pages 4

- [102] H. Kuehr, A. Witzel, I. I. K. Pauliny-Toth, and U. Nauber. A catalogue of extragalactic radio sources having flux densities greater than 1 Jy at 5 GHz. *A&AS*, 45:367–430, Sept. 1981. → pages 11
- [103] G. Lagache, A. Abergel, F. Boulanger, F. X. Désert, and J.-L. Puget. First detection of the warm ionised medium dust emission. Implication for the cosmic far-infrared background. *A&A*, 344:322–332, Apr. 1999. → pages 13
- [104] A. Lawrence, S. J. Warren, and O. Almaini. The UKIRT Infrared Deep Sky Survey (UKIDSS). *MNRAS*, 379:1599–1617, Aug. 2007.
doi:10.1111/j.1365-2966.2007.12040.x. → pages 166
- [105] A. Lawrence, S. J. Warren, O. Almaini, A. C. Edge, and N. C. Hambly. UKIDSS-DR8 LAS, GCS and DXS Surveys. *VizieR Online Data Catalog*, 2314:0, Mar. 2012. → pages 166
- [106] C. Leinert, S. Bowyer, L. K. Haikala, M. S. Hanner, M. G. Hauser, A.-C. Levasseur-Regourd, I. Mann, K. Mattila, W. T. Reach, W. Schlosser, H. J. Staude, G. N. Toller, J. L. Weiland, J. L. Weinberg, and A. N. Witt. The 1997 reference of diffuse night sky brightness. *A&AS*, 127:1–99, Jan. 1998. doi:10.1051/aas:1998105. → pages 13
- [107] A. Lewis and S. Bridle. Cosmological parameters from CMB and other data: A Monte Carlo approach. *Phys. Rev. D*, 66(10):103511–+, Nov. 2002. doi:10.1103/PhysRevD.66.103511. → pages 9, 14, 62, 110
- [108] A. Lewis, A. Challinor, and A. Lasenby. Efficient Computation of Cosmic Microwave Background Anisotropies in Closed Friedmann-Robertson-Walker Models. *ApJ*, 538:473–476, Aug. 2000.
doi:10.1086/309179. → pages 40
- [109] H. Liang, R. W. Hunstead, M. Birkinshaw, and P. Andreani. A Powerful Radio Halo in the Hottest Known Cluster of Galaxies 1E 0657-56. *ApJ*, 544:686–701, Dec. 2000. doi:10.1086/317223. → pages 4
- [110] M. S. Longair. On the interpretation of radio source counts. *MNRAS*, 133: 421–+, 1966. → pages 16
- [111] C. J. Lonsdale, H. E. Smith, and M. Rowan-Robinson. SWIRE: The SIRTF Wide-Area Infrared Extragalactic Survey. *PASP*, 115:897–927, Aug. 2003.
doi:10.1086/376850. → pages 164

- [112] P. R. Maloney, J. Glenn, J. E. Aguirre, S. R. Golwala, G. T. Laurent, P. A. R. Ade, J. J. Bock, S. F. Edgington, A. Goldin, D. Haig, A. E. Lange, P. D. Mauskopf, H. Nguyen, P. Rossinot, J. Sayers, and P. Stover. A Fluctuation Analysis of the Bolocam 1.1 mm Lockman Hole Survey. *ApJ*, 635:1044–1052, Dec. 2005. doi:10.1086/497585. → pages 62
- [113] S. A. Mao, B. M. Gaensler, S. Stanimirović, M. Havercorn, N. M. McClure-Griffiths, L. Staveley-Smith, and J. M. Dickey. A Radio and Optical Polarization Study of the Magnetic Field in the Small Magellanic Cloud. *ApJ*, 688:1029–1049, Dec. 2008. doi:10.1086/590546. → pages 208
- [114] G. Marsden, P. A. R. Ade, J. J. Bock, E. L. Chapin, and M. J. Devlin. BLAST: Resolving the Cosmic Submillimeter Background. *ApJ*, 707:1729–1739, Dec. 2009. doi:10.1088/0004-637X/707/2/1729. → pages 166, 168, 169
- [115] M. M. McGilchrist, J. E. Baldwin, J. M. Riley, D. J. Titterington, E. M. Waldram, and P. J. Warner. The 7c Survey of Radio Sources at 151-MHZ - Two Regions Centred at Ra: 10H28M Dec: 41DEG and Ra: 06H28M Dec: 45DEG. *MNRAS*, 246:110–+, Sept. 1990. → pages 11
- [116] E. Middelberg, R. P. Norris, T. J. Cornwell, M. A. Voronkov, B. D. Siana, B. J. Boyle, P. Ciliegi, C. A. Jackson, M. T. Huynh, S. Berta, S. Rubele, C. J. Lonsdale, R. J. Ivison, and I. Smail. Deep Australia Telescope Large Area Survey Radio Observations of the European Large Area ISO Survey S1/Spitzer Wide-Area Infrared Extragalactic Field. *AJ*, 135:1276–1290, Apr. 2008. doi:10.1088/0004-6256/135/4/1276. → pages 24
- [117] A. Mignano, I. Prandoni, L. Gregorini, P. Parma, H. R. de Ruiter, M. H. Wieringa, G. Vettolani, and R. D. Ekers. The ATESP 5 GHz radio survey. II. Physical properties of the faint radio population. *A&A*, 477:459–471, Jan. 2008. doi:10.1051/0004-6361:20078545. → pages 3
- [118] N. A. Miller, E. B. Fomalont, K. I. Kellermann, V. Mainieri, C. Norman, P. Padovani, P. Rosati, and P. Tozzi. The VLA 1.4 GHz Survey of the Extended Chandra Deep Field-South: First Data Release. *ApJl*, 179:114–123, Nov. 2008. doi:10.1086/591054. → pages 11, 147
- [119] B. Y. Mills. The Distribution of the Discrete Sources of Cosmic Radio Radiation. *Australian Journal of Scientific Research A Physical Sciences*, 5:266, June 1952. → pages 3

- [120] K. J. Mitchell and J. J. Condon. A confusion-limited 1.49-GHz VLA survey centered on alpha = 13 H 00 M 37 s, delta = + 30 deg 34 arcmin. *AJ*, 90:1957–1966, Oct. 1985. doi:10.1086/113899. → pages 3, 11
- [121] T. Miyaji, Y. Ishisaki, Y. Ogasaka, Y. Ueda, M. J. Freyberg, G. Hasinger, and Y. Tanaka. The cosmic X-ray background spectrum observed with ROSAT and ASCA. *A&A*, 334:L13–L16, June 1998. → pages 13
- [122] H. J. Mo and S. D. M. White. An analytic model for the spatial clustering of dark matter haloes. *MNRAS*, 282:347–361, Sept. 1996. → pages 41
- [123] D. Moss, N. Seymour, I. M. McHardy, T. Dwelly, M. J. Page, and N. S. Loaring. A deep Giant Metre-wave Radio Telescope 610-MHz survey of the 1^H XMM-Newton/Chandra survey field. *MNRAS*, 378:995–1006, July 2007. doi:10.1111/j.1365-2966.2007.11842.x. → pages 11
- [124] T. W. B. Muxlow, R. J. Beswick, H. Thrall, A. M. S. Richards, S. T. Garrington, and A. Pedlar. The Statistical Properties of the Very Weak Radio Source Population in the GOODS/ACS HDF-N Region. *ASPCS*, 380:199, Dec. 2007. → pages 52, 151
- [125] B. B. Nath. Extended X-ray emission from radio galaxy cocoons. *MNRAS*, 407:1998–2006, Sept. 2010. doi:10.1111/j.1365-2966.2010.17058.x. → pages 121
- [126] R. P. Norris, J. Afonso, P. N. Appleton, and B. J. Boyle. Deep ATLAS Radio Observations of the Chandra Deep Field-South/Spitzer Wide-Area Infrared Extragalactic Field. *AJ*, 132:2409–2423, Dec. 2006. doi:10.1086/508275. → pages 24
- [127] R. P. Norris, A. M. Hopkins, J. Afonso, and e.a. EMU: Evolutionary Map of the Universe. *PASA*, 28:215–248, Aug. 2011. doi:10.1071/AS11021. → pages 127, 132
- [128] P. Nurmi, P. Heinämäki, T. Sepp, E. Tago, E. Saar, M. Gramann, M. Einasto, E. Tempel, and J. Einasto. Groups in the Millennium Simulation and in SDSS DR7. *MNRAS*, 436:380–394, Nov. 2013. doi:10.1093/mnras/stt1571. → pages 122
- [129] S. Oliver, M. Rowan-Robinson, D. M. Alexander, O. Almaini, and e.a. The European Large Area ISO Survey - I. Goals, definition and observations. *MNRAS*, 316:749–767, Aug. 2000. doi:10.1046/j.1365-8711.2000.03550.x. → pages 24

- [130] S. J. Oliver, J. Bock, B. Altieri, A. Amblard, V. Arumugam, H. Aussel, T. Babbedge, and e. Beelen, A. The Herschel Multi-tiered Extragalactic Survey: HerMES. *MNRAS*, 424:1614–1635, Aug. 2012. doi:10.1111/j.1365-2966.2012.20912.x. → pages 208
- [131] M. J. A. Oort, W. J. G. Steemers, and R. A. Windhorst. A deep 92 CM survey of the Lynx area. *A&AS*, 73:103–123, Apr. 1988. → pages 11
- [132] M. J. L. Orr and I. W. A. Browne. Relativistic beaming and quasar statistics. *MNRAS*, 200:1067–1080, Sept. 1982. → pages 2
- [133] R. A. Overzier, H. J. A. Röttgering, R. B. Rengelink, and R. J. Wilman. The spatial clustering of radio sources in NVSS and FIRST; implications for galaxy clustering evolution. *A&A*, 405:53–72, July 2003. doi:10.1051/0004-6361:20030527. → pages 186
- [134] F. N. Owen and G. E. Morrison. The Deep Swire Field. I. 20 cm Continuum Radio Observations: A Crowded Sky. *AJ*, 136:1889–1900, Nov. 2008. doi:10.1088/0004-6256/136/5/1889. → pages 4, 11, 54, 66, 69, 89, 93, 151, 167, 170, 171
- [135] F. N. Owen, G. E. Morrison, M. D. Klimek, and E. W. Greisen. The Deep SWIRE Field. II. 90 cm Continuum Observations and 20 cm-90 cm Spectra. *AJ*, 137:4846–4853, June 2009. doi:10.1088/0004-6256/137/6/4846. → pages 207
- [136] P. Padovani, V. Mainieri, P. Tozzi, K. I. Kellermann, E. B. Fomalont, N. Miller, P. Rosati, and P. Shaver. The Very Large Array Survey of the Chandra Deep Field South. IV. Source Population. *ApJ*, 694:235–246, Mar. 2009. doi:10.1088/0004-637X/694/1/235. → pages 3
- [137] R. B. Partridge, E. A. Richards, E. B. Fomalont, K. I. Kellermann, and R. A. Windhorst. Small-Scale Cosmic Microwave Background Observations at 8.4 GHz. *ApJ*, 483:38, July 1997. doi:10.1086/304226. → pages 173, 199, 200
- [138] G. Patanchon, P. A. R. Ade, J. J. Bock, E. L. Chapin, M. J. Devlin, S. R. Dicker, M. Griffin, J. O. Gunderson, M. Halpern, and P. Hargrave. Submillimeter Number Counts from Statistical Analysis of BLAST Maps. *ApJ*, 707:1750–1765, Dec. 2009. doi:10.1088/0004-637X/707/2/1750. → pages 46, 54, 62, 63, 67, 94, 107

- [139] I. I. K. Pauliny-Toth, H. Steppe, and A. Witzel. A deep survey of selected regions for extragalactic sources at 4.85 GHz. *A&A*, 85:329–331, May 1980. → pages 11
- [140] J. R. Peterson and A. C. Fabian. X-ray spectroscopy of cooling clusters. *Phys. Rep.*, 427:1–39, Apr. 2006. doi:10.1016/j.physrep.2005.12.007. → pages 4
- [141] Planck Collaboration, P. A. R. Ade, N. Aghanim, M. I. R. Alves, C. Armitage-Caplan, M. Arnaud, M. Ashdown, F. Atrio-Barandela, J. Aumont, H. Aussel, and e.a. Planck 2013 results. I. Overview of products and scientific results. *preprint (arXiv:1303.5062)*, Mar. 2013. → pages 107
- [142] M. Polletta, M. Tajer, L. Maraschi, G. Trinchieri, C. J. Lonsdale, L. Chiappetti, and S. e. a. Andreon. Spectral Energy Distributions of Hard X-Ray Selected Active Galactic Nuclei in the XMM-Newton Medium Deep Survey. *ApJ*, 663:81–102, July 2007. doi:10.1086/518113. → pages 166, 168, 169
- [143] G. G. Pooley and M. Ryle. The extension of the number-flux density relation for radio sources to very small flux densities. *MNRAS*, 139:515–+, 1968. → pages 16
- [144] L. Pozzetti, P. Madau, G. Zamorani, H. C. Ferguson, and G. Bruzual A. High-redshift galaxies in the Hubble Deep Field - II. Colours and number counts. *MNRAS*, 298:1133–1144, Aug. 1998. doi:10.1046/j.1365-8711.1998.01724.x. → pages 13
- [145] W. H. Press and P. Schechter. Formation of Galaxies and Clusters of Galaxies by Self-Similar Gravitational Condensation. *ApJ*, 187:425–438, Feb. 1974. doi:10.1086/152650. → pages 41
- [146] D. P. Rayner, R. P. Norris, and R. J. Sault. Radio circular polarization of active galaxies. *MNRAS*, 319:484–496, Dec. 2000. doi:10.1046/j.1365-8711.2000.03854.x. → pages 30
- [147] M. T. Ressell and M. S. Turner. The Grand Unified Photon Spectrum: A Coherent View of the Diffuse Extragalactic Background Radiation. *Comments on Astrophysics*, 14:323–+, 1990. → pages 13
- [148] E. A. Richards. The Nature of Radio Emission from Distant Galaxies: The 1.4 GHZ Observations. *ApJ*, 533:611–630, Apr. 2000. doi:10.1086/308684. → pages 11

- [149] K. Riebe, A. M. Partl, H. Enke, J. Forero-Romero, S. Gottlöber, A. Klypin, G. Lemson, F. Prada, J. R. Primack, M. Steinmetz, and V. Turchaninov. The MultiDark Database: Release of the Bolshoi and MultiDark cosmological simulations. *Astronomische Nachrichten*, 334:691–708, Aug. 2013. doi:10.1002/asna.201211900. → pages 123
- [150] J. G. Robertson. An all-sky catalogue of strong radio sources at 408 MHz. *Australian Journal of Physics*, 26:403–+, June 1973. → pages 11
- [151] K. Rohlfs and T. L. Wilson. *Tools of radio astronomy*. 2000. → pages 20
- [152] M. Ryle and P. A. G. Scheuer. The Spatial Distribution and the Nature of Radio Stars. *Royal Society of London Proceedings Series A*, 230:448–462, July 1955. doi:10.1098/rspa.1955.0146. → pages 3
- [153] M. Ryle, F. G. Smith, and B. Elsmore. A preliminary survey of the radio stars in the Northern Hemisphere. *MNRAS*, 110:508, 1950. → pages 1
- [154] D. B. Sanders, E. S. Phinney, G. Neugebauer, B. T. Soifer, and K. Matthews. Continuum energy distribution of quasars - Shapes and origins. *ApJ*, 347:29–51, Dec. 1989. doi:10.1086/168094. → pages 2
- [155] R. J. Sault, P. J. Teuben, and M. C. H. Wright. A Retrospective View of MIRIAD. In R. A. Shaw, H. E. Payne, and J. J. E. Hayes, editors, *Astronomical Data Analysis Software and Systems IV*, volume 77 of *Astronomical Society of the Pacific Conference Series*, page 433, 1995. → pages 25
- [156] P. A. G. Scheuer. A statistical method for analysing observations of faint radio stars. *Proceedings of the Cambridge Philosophical Society*, 53: 764–773, 1957. doi:10.1017/S0305004100032825. → pages 46, 54
- [157] P. A. G. Scheuer. Fluctuations in the X-ray background. *MNRAS*, 166: 329–338, Feb. 1974. → pages 46
- [158] P. A. G. Scheuer and A. C. S. Readhead. Superluminally expanding radio sources and the radio-quiet QSOs. *Nature*, 277:182–185, Jan. 1979. doi:10.1038/277182a0. → pages 2
- [159] D. Scott. Cosmic Glows. *ArXiv Astrophysics e-prints*, Dec. 1999. → pages 13
- [160] M. Seiffert, D. J. Fixsen, A. Kogut, S. M. Levin, M. Limon, P. M. Lubin, P. Mirel, J. Singal, T. Villela, E. Wollack, and C. A. Wuensche.

Interpretation of the Extragalactic Radio Background. *preprint*
(*arXiv:0901.0559*), Jan. 2009. → pages 16, 18

- [161] N. Seymour, T. Dwelly, D. Moss, I. McHardy, A. Zoghbi, G. Rieke, M. Page, A. Hopkins, and N. Loaring. The star formation history of the Universe as revealed by deep radio observations. *MNRAS*, 386:1695–1708, May 2008. doi:10.1111/j.1365-2966.2008.13166.x. → pages 3, 11
- [162] N. Seymour, M. Huynh, T. Dwelly, M. Symeonidis, A. Hopkins, I. M. McHardy, M. J. Page, and G. Rieke. Investigating the far-IR/radio correlation of star-forming Galaxies to $z = 3$. *MNRAS*, 398:1573–1581, Sept. 2009. doi:10.1111/j.1365-2966.2009.15224.x. → pages 208
- [163] R. K. Sheth and G. Tormen. Large-scale bias and the peak background split. *MNRAS*, 308:119–126, Sept. 1999.
doi:10.1046/j.1365-8711.1999.02692.x. → pages 41
- [164] C. Simpson, A. Martínez-Sansigre, S. Rawlings, R. Ivison, M. Akiyama, K. Sekiguchi, T. Takata, Y. Ueda, and M. Watson. Radio imaging of the Subaru/XMM-Newton Deep Field - I. The 100- μ Jy catalogue, optical identifications, and the nature of the faint radio source population. *MNRAS*, 372:741–757, Oct. 2006. doi:10.1111/j.1365-2966.2006.10907.x. → pages 3
- [165] J. Singal, Ł. Stawarz, A. Lawrence, and V. Petrosian. Sources of the radio background considered. *MNRAS*, 409:1172–1182, Dec. 2010.
doi:10.1111/j.1365-2966.2010.17382.x. → pages 11, 19, 53, 97
- [166] S. K. Sirothia, M. Dennefeld, D. J. Saikia, H. Dole, F. Ricquebourg, and J. Roland. 325-MHz observations of the ELAIS-N1 field using the Giant Metrewave Radio Telescope. *MNRAS*, 395:269–281, May 2009.
doi:10.1111/j.1365-2966.2009.14317.x. → pages 11
- [167] V. Smolčić, E. Schinnerer, M. Scovéggio, P. Franzetti, H. Aussel, and M. e. a. Bondi. A New Method to Separate Star-forming from AGN Galaxies at Intermediate Redshift: The Submilljansky Radio Population in the VLA-COSMOS Survey. *ApJL*, 177:14–38, July 2008.
doi:10.1086/588028. → pages 3
- [168] G. F. Smoot. The Cosmic Microwave Background Spectrum. *ArXiv Astrophysics e-prints*, May 1997. → pages 13

- [169] P. Sreekumar, D. L. Bertsch, B. L. Dingus, J. A. Esposito, C. E. Fichtel, and R. C. e. a. Hartman. EGRET Observations of the Extragalactic Gamma-Ray Emission. *ApJ*, 494:523–534, Feb. 1998.
doi:10.1086/305222. → pages 13
- [170] R. Subrahmanyam and R. Cowsik. Is there an Unaccounted for Excess in the Extragalactic Cosmic Radio Background? *ApJ*, 776:42, Oct. 2013.
doi:10.1088/0004-637X/776/1/42. → pages 120
- [171] R. Subrahmanyam, M. J. Kesteven, R. D. Ekers, M. Sinclair, and J. Silk. An Australia Telescope survey for CMB anisotropies. *MNRAS*, 315:808–822, July 2000. doi:10.1046/j.1365-8711.2000.03444.x. → pages 173, 199, 200
- [172] R. Subrahmanyam, R. D. Ekers, L. Saripalli, and E. M. Sadler. ATLBS: the Australia Telescope Low-Brightness Survey. *MNRAS*, 402:2792–2806, Mar. 2010. doi:10.1111/j.1365-2966.2009.16105.x. → pages 4, 12
- [173] Surace and et.al. The SWIRE Data Release 2. *VizieR Online Data Catalog*, 2302:1, Nov. 2012. → pages 166
- [174] P. M. Sutter, B. D. Wandelt, and S. S. Malu. Bayesian Angular Power Spectrum Analysis of Interferometric Data. *ApJl*, 202:9, Sept. 2012.
doi:10.1088/0067-0049/202/1/9. → pages 174
- [175] T. T. Takeuchi and T. T. Ishii. A general formulation of the source confusion statistics and application to infrared galaxy surveys. *ApJ*, 604:40, Mar 2004. doi:10.1086/381882. URL
http://adsabs.harvard.edu/cgi-bin/nph-data_query?bibcode=2004ApJ...604...40T&link_type=ABSTRACT. → pages 51
- [176] T. T. Takeuchi, R. Kawabe, K. Kohno, K. Nakanishi, T. T. Ishii, H. Hirashita, and K. Yoshikawa. Impact of Future Submillimeter and Millimeter Large Facilities on the Studies of Galaxy Formation and Evolution. *PASP*, 113:586–606, May 2001. doi:10.1086/320282. → pages 46
- [177] A. R. Taylor, J. M. Stil, J. K. Grant, T. L. Landecker, R. Kothes, R. I. Reid, A. D. Gray, D. Scott, P. G. Martin, A. I. Boothroyd, G. Joncas, F. J. Lockman, J. English, A. Sajina, and J. R. Bond. Radio Polarimetry of the ELAIS N1 Field: Polarized Compact Sources. *ApJ*, 666:201–211, Sept. 2007. doi:10.1086/519786. → pages 208

- [178] C. M. Trott, R. B. Wayth, and S. J. Tingay. The Impact of Point-source Subtraction Residuals on 21 cm Epoch of Reionization Estimation. *ApJ*, 757:101, Sept. 2012. doi:10.1088/0004-637X/757/1/101. → pages 174
- [179] C. M. Urry and P. Padovani. Unified Schemes for Radio-Loud Active Galactic Nuclei. *PASP*, 107:803, Sept. 1995. doi:10.1086/133630. → pages 2
- [180] T. Venturi, S. Giacintucci, G. Brunetti, R. Cassano, S. Bardelli, D. Dallacasa, and G. Setti. GMRT radio halo survey in galaxy clusters at $z = 0.2\text{--}0.4$. I. The REFLEX sub-sample. *A&A*, 463:937–947, Mar. 2007. doi:10.1051/0004-6361:20065961. → pages 4
- [181] T. Venturi, S. Giacintucci, D. Dallacasa, R. Cassano, G. Brunetti, S. Bardelli, and G. Setti. GMRT radio halo survey in galaxy clusters at $z = 0.2\text{--}0.4$. II. The eBCS clusters and analysis of the complete sample. *A&A*, 484:327–340, June 2008. doi:10.1051/0004-6361:200809622. → pages 4
- [182] T. Vernstrom, D. Scott, and J. V. Wall. Contribution to the diffuse radio background from extragalactic radio sources. *MNRAS*, 415:3641–3648, Aug. 2011. doi:10.1111/j.1365-2966.2011.18990.x. → pages iv, 17, 18, 53
- [183] T. Vernstrom, D. Scott, J. V. Wall, J. J. Condon, W. D. Cotton, E. B. Fomalont, K. I. Kellermann, N. Miller, and R. A. Perley. Deep 3 GHz Number Counts from a P(D) Fluctuation Analysis. *MNRAS*, 404: 2791–2809, Apr. 2014. doi:10.1093/mnras/stu470. → pages v, 5, 8, 97, 107, 158, 159, 171
- [184] T. Vernstrom, R. P. Norris, D. Scott, and J. V. Wall. The deep diffuse extragalactic radio sky at 1.75 GHz. *MNRAS*, 447:2243–2260, Mar. 2015. doi:10.1093/mnras/stu2595. → pages v, 5
- [185] J. V. Wall. The extragalactic radio source background. In S. Bowyer & C. Leinert, editor, *The Galactic and Extragalactic Background Radiation*, volume 139 of *IAU Symposium*, pages 327–332, 1990. → pages 16
- [186] J. V. Wall and D. J. Cooke. Source counts at high spatial densities from pencil beam observations of background fluctuations. *MNRAS*, 171:9–25, Apr. 1975. → pages 95
- [187] G. Weidenspointner, M. Varendorff, R. Diehl, G. G. Lichti, V. Schönfelder, S. C. Kappadath, J. Ryan, H. Bloemen, W. Hermsen, and K. Bennett. The cosmic diffuse gamma-ray background measured with COMPTEL. In R. E.

Schielicke, editor, *Astronomische Gesellschaft Abstract Series*, volume 15 of *Astronomische Gesellschaft Abstract Series*, page 62, 1999. → pages 13

- [188] M. White, J. Carlstrom, M. Dragovan, and S. W. L. Holzapfel. Analyzing data from DASI. *ArXiv Astrophysics e-prints*, Dec. 1999. → pages 174
- [189] M. White, J. E. Carlstrom, M. Dragovan, and W. L. Holzapfel. Interferometric Observation of Cosmic Microwave Background Anisotropies. *ApJ*, 514:12–24, Mar. 1999. doi:10.1086/306911. → pages 174, 181
- [190] R. L. White, R. H. Becker, D. J. Helfand, and M. D. Gregg. A Catalog of 1.4 GHz Radio Sources from the FIRST Survey. *ApJ*, 475:479–+, Feb. 1997. doi:10.1086/303564. → pages 11
- [191] R. J. Wilman, L. Miller, M. J. Jarvis, T. Mauch, F. Levrier, F. B. Abdalla, S. Rawlings, H.-R. Klöckner, D. Obreschkow, D. Olteanu, and S. Young. A semi-empirical simulation of the extragalactic radio continuum sky for next generation radio telescopes. *MNRAS*, 388:1335, Aug 2008. doi:10.1111/j.1365-2966.2008.13486.x. URL http://adsabs.harvard.edu/cgi-bin/nph-data_query?bibcode=2008MNRAS.388.1335W&link_type=ABSTRACT. → pages 5, 41, 49, 50, 66, 94, 101, 106, 185
- [192] A. S. Wilson and E. J. M. Colbert. The difference between radio-loud and radio-quiet active galaxies. *ApJ*, 438:62–71, Jan. 1995. doi:10.1086/175054. → pages 2
- [193] R. A. Windhorst, G. K. Miley, F. N. Owen, R. G. Kron, and D. C. Koo. Sub-millijansky 1.4 GHz source counts and multicolor studies of weak radio galaxy populations. *ApJ*, 289:494–513, Feb. 1985. doi:10.1086/162911. → pages 3, 11
- [194] R. A. Windhorst, E. B. Fomalont, R. B. Partridge, and J. D. Lowenthal. Microjansky source counts and spectral indices at 8.44 GHz. *ApJ*, 405:498–517, Mar. 1993. doi:10.1086/172382. → pages 11
- [195] J. M. Wrobel and S. W. Krause. Counts of serendipitous 6 centimeter sources in E/S0 galaxy fields. *ApJ*, 363:11–20, Nov. 1990. doi:10.1086/169315. → pages 11
- [196] Y. Yang, G. Yang, X. Huang, X. Chen, T. Lu, and H. Zong. Contribution of ultracompact dark matter minihalos to the isotropic radio background.

Phys. Rev. D, 87(8):083519, Apr. 2013.
doi:10.1103/PhysRevD.87.083519. → pages 97

- [197] F. Zandanel, C. Pfrommer, and F. Prada. A phenomenological model for the intracluster medium that matches X-ray and Sunyaev-Zel'dovich observations. *MNRAS*, 438:116–123, Feb. 2014.
doi:10.1093/mnras/stt2196. → pages 122
- [198] F. Zandanel, C. Pfrommer, and F. Prada. On the physics of radio haloes in galaxy clusters: scaling relations and luminosity functions. *MNRAS*, 438:124–144, Feb. 2014. doi:10.1093/mnras/stt2250. → pages xiv, 122, 123, 124
- [199] M. Zannoni, A. Tartari, M. Gervasi, G. Boella, G. Sironi, A. De Lucia, A. Passerini, and F. Cavaliere. TRIS. I. Absolute Measurements of the Sky Brightness Temperature at 0.6, 0.82, and 2.5 GHz. *ApJ*, 688:12–23, Nov. 2008. doi:10.1086/592133. → pages 9

Appendix A

C Catalogue

Table A.1: Discrete VLA C Catalogue

ID	Size Flag	RA (J2000) (arcsec)	Dec (J2000) (arcsec)	S_P ($\mu\text{Jy beam}^{-1}$)	S_T (μJy)	θ_{DM} (arcsec)	θ_{Dm} (arcsec)	ϕ (degrees)	α_{IF}	α_{IM}
000	0	161.60004 (0.01)	59.08947 (0.01)	6724.1 ± 0	8572.8 ± 0	0 ± 0	0 ± 0	0	-1.1	-0.9
001	0	161.41577 (0.01)	58.95854 (0.01)	1026.6 ± 0	2076.7 ± 0	0 ± 0	0 ± 0	0	-0.5	-0.5
002	2	161.51746 (0.03)	59.14099 (0.03)	786.7 ± 10.68	794.2 ± 11.61	0.98 ± 0.04	0.5 ± 0.02	-132	-1.3	-1.4
003	3	161.79787 (0.06)	58.91628 (0.06)	762.7 ± 10.21	789.6 ± 15.05	2.14 ± 0.1	0 ± 0.06	-78	-0.9	-2
004	7	161.20349 (0.07)	59.11372 (0.04)	595.8 ± 15.2	595.8 ± 15.27	0.04 ± 0.02	0.04 ± 0	-66	-0.9	-1.1
005	0	161.6575 (0.01)	58.90627 (0.01)	315.3 ± 0	592.6 ± 0	0 ± 0	0 ± 0	0	-1.1	-1.2
006	7	161.70733 (0.06)	59.16539 (0.05)	574.6 ± 12.36	574.6 ± 12.57	0.04 ± 0.03	0 ± 0	-110	0.2	-0.8
007	7	161.46216 (0.02)	59.14486 (0.01)	567.5 ± 13.45	567.7 ± 13.51	0.18 ± 0.02	0.13 ± 0	-85	0	-0.1
008	7	161.3023 (0.02)	59.04216 (0.01)	545.1 ± 12.5	545.4 ± 12.56	0.22 ± 0.02	0.16 ± 0	8	-1	-1.1
009	0	161.45365 (0.01)	58.9023 (0.01)	323.1 ± 0	499.5 ± 0	0 ± 0	0 ± 0	0	-1.3	-1.2
010	7	161.65738 (0.02)	59.03615 (0.01)	359 ± 8.48	359.2 ± 8.51	0.18 ± 0.02	0.13 ± 0	-14	-0.7	-0.8
011	1	161.67179 (0.09)	58.87049 (0.09)	328.8 ± 8.44	344.8 ± 10.33	1.97 ± 0.11	1.53 ± 0.06	-27	-1.3	-1.8
012	3	161.49455 (0.04)	59.05543 (0.05)	318.1 ± 3.26	325.8 ± 4.62	1.78 ± 0.07	0 ± 0.04	-144	0.7	0.8
013	3	161.63812 (0.03)	58.97086 (0.04)	298.3 ± 3.57	303.5 ± 4.43	1.5 ± 0.06	0 ± 0.03	82	0.1	0.1
014	1	161.40533 (0.08)	59.16266 (0.08)	283.7 ± 5.73	293.3 ± 6.93	1.83 ± 0.09	0.99 ± 0.05	-102	-1.3	-2
015	7	161.53146 (0.03)	58.93388 (0.02)	275.4 ± 6.68	275.4 ± 6.71	0.14 ± 0.02	0.1 ± 0	83	-0.3	-0.4
016	7	161.63635 (0.03)	58.98387 (0.02)	256.6 ± 6.24	256.6 ± 6.26	0.14 ± 0.02	0.1 ± 0	0	-0.6	-0.6
017	1	161.41003 (0.06)	59.12597 (0.06)	223.6 ± 2.82	233.5 ± 4.01	1.94 ± 0.08	1.38 ± 0.05	-121	-1.1	-1.3
018	7	161.72318 (0.07)	59.04985 (0.04)	231.4 ± 5.81	231.4 ± 5.84	0.05 ± 0.02	0.04 ± 0	5	-0.5	-0.6
019	7	161.20922 (0.16)	58.99961 (0.07)	221.9 ± 6.29	221.9 ± 6.4	0.04 ± 0.04	0.04 ± 0.01	75	-0.5	-0.8
020	3	161.76541 (0.15)	58.98573 (0.14)	208 ± 6.33	216.6 ± 10.83	2.32 ± 0.3	0 ± 0.14	-72	-1.1	-1.4
021	7	161.59125 (0.05)	58.94153 (0.03)	216.3 ± 5.36	216.3 ± 5.38	0.1 ± 0.02	0.07 ± 0	29	-1	-1
022	7	161.28422 (0.22)	58.89703 (0.09)	195.3 ± 5.88	195.3 ± 6.05	0.04 ± 0.06	0.04 ± 0.01	90	-0.2	-0.7
023	1	161.51478 (0.1)	59.07335 (0.08)	166.4 ± 2.9	180.8 ± 5.08	3.03 ± 0.16	1.45 ± 0.09	113	-1	-0.9
024	7	161.51956 (0.07)	58.91448 (0.04)	176.6 ± 4.49	176.6 ± 4.51	0.04 ± 0.02	0.04 ± 0	-2	0	0
025	3	161.56405 (0.04)	59.04323 (0.05)	169.5 ± 2.12	172.5 ± 2.6	1.5 ± 0.06	0 ± 0.03	32	-0.8	-0.8
026	7	161.51788 (0.15)	58.88876 (0.06)	167.9 ± 4.7	167.9 ± 4.77	0.04 ± 0.04	0.04 ± 0.01	0	-1.5	-1.6
027	1	161.51926 (0.14)	59.11289 (0.12)	129.8 ± 6.67	164.7 ± 13.21	5.78 ± 0.56	1.93 ± 0.19	20	-1	-1.1
028	2	161.64828 (0.14)	58.89443 (0.15)	146.5 ± 6.25	157 ± 8.89	3 ± 0.27	0.67 ± 0.16	-160	-1.3	-1.4
029	7	161.24861 (0.11)	59.10261 (0.14)	157 ± 5.51	157 ± 5.79	0.08 ± 0.08	0 ± 0.03	8	-0.8	-0.9
030	3	161.29653 (0.16)	59.12014 (0.16)	144.2 ± 6.27	153.3 ± 8.63	2.89 ± 0.26	0 ± 0.15	-2	-1.2	-1.6
031	3	161.63061 (0.28)	58.84882 (0.25)	144.2 ± 9.58	151.6 ± 11.22	2.59 ± 0.26	0 ± 0.09	-42	-1.3	-0.7
032	3	161.82865 (0.27)	59.06107 (0.26)	130.9 ± 9.25	143.8 ± 12.05	3.64 ± 0.34	0 ± 0.18	-91	-1.1	-2.8
033	3	161.48681 (0.11)	58.88851 (0.1)	137 ± 4.16	141.7 ± 5.06	2.11 ± 0.13	0 ± 0.08	-137	-0.2	-0.2
034	7	161.63833 (0.1)	58.96796 (0.05)	139 ± 3.57	139 ± 3.6	0 ± 0.03	0 ± 0	0	0.1	0.3
035	3	161.24953 (0.14)	59.05049 (0.15)	124.6 ± 5.26	132.9 ± 7.44	2.96 ± 0.26	0 ± 0.16	-33	-1	-1.5
036	7	161.68557 (0.14)	59.02094 (0.06)	128.1 ± 3.43	128.1 ± 3.47	0 ± 0.04	0 ± 0.01	0	-0.7	-0.7
037	1	161.81489 (0.32)	58.95545 (0.34)	110 ± 8.27	127.1 ± 11.28	3.84 ± 0.36	2.32 ± 0.2	8	-0.6	-1.2
038	7	161.56662 (0.13)	58.93288 (0.06)	124.9 ± 3.4	124.9 ± 3.44	0.04 ± 0.03	0.04 ± 0.01	-68	-0.9	-1
039	7	161.75069 (0.21)	59.0185 (0.08)	124 ± 3.68	124 ± 3.77	0.04 ± 0.05	0.04 ± 0.01	-78	-1	-1.2
040	7	161.73125 (0.05)	59.05007 (0.1)	123.3 ± 3.84	123.3 ± 3.91	0 ± 0.05	0 ± 0.02	26	-1.4	-1.4
041	3	161.23987 (0.49)	58.8769 (0.53)	105.3 ± 13.17	121 ± 16.66	4.52 ± 0.41	0 ± 0.29	-111	0.1	0
042	7	161.675 (0.24)	59.142 (0.17)	116.8 ± 6.5	116.8 ± 6.63	0.04 ± 0.09	0.04 ± 0.02	21	-0.3	-1.5
043	3	161.8283 (0.3)	59.02103 (0.31)	103.9 ± 7.67	113.7 ± 9.75	3.57 ± 0.33	0 ± 0.17	-124	-1.3	-1
044	1	161.48858 (0.06)	59.01142 (0.05)	107.1 ± 1.51	111.2 ± 1.89	1.63 ± 0.07	1.46 ± 0.04	-123	1.1	1
045	3	161.32472 (1.33)	59.20821 (1.36)	73.5 ± 16.04	110.7 ± 27.79	9.01 ± 1.03	0 ± 0.72	-83	-0.7	1
046	6	161.46615 (0.07)	59.05313 (0.06)	106.5 ± 1.75	106.8 ± 2.16	0.63 ± 0.08	0 ± 0.05	22	-0.8	-0.8
047	1	161.75732 (0.43)	58.89934 (0.47)	90 ± 8.31	106.4 ± 11.43	4.43 ± 0.4	2.11 ± 0.27	-61	-0.7	0
048	1	161.48133 (1.1)	59.15398 (0.96)	53.7 ± 8.23	105.1 ± 22.19	11.71 ± 1.69	3.74 ± 0.73	-347	-0.9	-1.1
049	1	161.87069 (1.32)	59.02892 (1.45)	47.6 ± 10.5	102.1 ± 26.19	10.41 ± 1.14	6.75 ± 1.02	-143	0	0

continued on the next page

C Catalogue continued

ID	Size Flag	RA (J2000) (arcsec)	Dec (J2000) (arcsec)	S_P ($\mu\text{Jy beam}^{-1}$)	S_T (μJy)	θ_{DM} (arcsec)	θ_{Dm} (arcsec)	ϕ (degrees)	α_{IF}	α_{IM}
050	1	161.90153 (0.89)	59.03839 (0.92)	91 ± 16.09	101.4 ± 18.56	3.09 ± 0.39	2.25 ± 0.1	167	-0.8	-3
051	6	161.24209 (0.4)	59.13994 (0.4)	99 ± 9.12	99.1 ± 9.29	0.33 ± 0.14	0.09 ± 0.02	-115	-0.4	-2.3
052	3	161.53633 (0.06)	58.9746 (0.07)	95.7 ± 2.01	97.1 ± 2.2	1.35 ± 0.06	0 ± 0.03	-155	-1	-1
053	3	161.19827 (0.36)	59.01025 (0.38)	81.5 ± 6.66	96.2 ± 10.15	5.03 ± 0.52	0 ± 0.3	-29	-1.4	-1.9
054	7	161.56865 (0.06)	58.98906 (0.07)	93.6 ± 1.99	93.6 ± 2.16	0 ± 0.06	0 ± 0.03	-110	-0.5	-0.5
055	7	161.52557 (0.23)	59.14123 (0.13)	93.4 ± 3.79	93.4 ± 3.89	0 ± 0.07	0 ± 0.01	44	-0.9	-1
056	3	161.21219 (0.25)	59.02494 (0.23)	87.9 ± 5.73	93.3 ± 6.9	2.86 ± 0.27	0 ± 0.11	9	-1.3	-1.8
057	3	161.75083 (0.43)	58.90865 (0.46)	79 ± 6.9	91.9 ± 9.78	4.76 ± 0.46	0 ± 0.29	-58	-0.9	-2.5
058	3	161.8699 (0.74)	58.96016 (0.81)	82.3 ± 13.09	91.1 ± 15.09	3.78 ± 0.35	0 ± 0.2	-46	-1.4	0
059	3	161.11841 (1.17)	58.9597 (1.13)	69.1 ± 13.69	88.8 ± 19.31	6.45 ± 0.68	0 ± 0.48	-105	-0.9	0
060	3	161.49977 (0.25)	58.87312 (0.23)	82.1 ± 5.21	86.8 ± 6.23	2.73 ± 0.26	0 ± 0.11	-328	-0.8	-1.2
061	3	161.227 (0.28)	59.07658 (0.27)	80 ± 5.76	86.4 ± 7.1	3.26 ± 0.31	0 ± 0.14	-78	-1.3	-2.1
062	6	161.51094 (0.95)	58.80735 (0.95)	84.4 ± 15.93	85.5 ± 16.24	1.26 ± 0.3	0.28 ± 0.07	133	-1.3	-1.7
063	3	161.6363 (0.18)	59.03703 (0.2)	69.8 ± 3.93	84 ± 7.89	5.37 ± 0.66	0 ± 0.25	-128	-0.8	-0.9
064	3	161.74172 (0.26)	59.0868 (0.25)	77 ± 5.27	83.6 ± 6.71	3.4 ± 0.32	0 ± 0.16	-108	-1.5	-1.3
065	5	161.58695 (0.48)	58.83747 (0.46)	81 ± 9.09	81.6 ± 9.27	0.84 ± 0.18	0.4 ± 0.04	-5	-1.2	0
066	1	161.37505 (0.33)	58.87336 (0.33)	76.3 ± 5.29	81 ± 6.21	2.49 ± 0.26	1.32 ± 0.08	-141	-0.9	-0.4
067	7	161.51768 (0.18)	59.08031 (0.07)	80.9 ± 2.32	80.9 ± 2.37	0.04 ± 0.05	0.04 ± 0.01	-76	-0.7	-0.8
068	7	161.71913 (0.23)	58.98409 (0.14)	80.8 ± 3.58	80.8 ± 3.67	0 ± 0.08	0 ± 0.01	-71	-1.3	-1.1
069	3	161.54514 (0.23)	58.87913 (0.22)	77.3 ± 4.17	79.4 ± 4.7	1.85 ± 0.2	0 ± 0.05	-116	-0.9	-1.3
070	3	161.40186 (1.18)	59.21808 (1.15)	61.2 ± 12.83	76.9 ± 17.3	6.07 ± 0.64	0 ± 0.41	-51	0	2.7
071	1	161.78873 (1.27)	59.15102 (1.21)	50.2 ± 10.34	75.7 ± 17.59	7.12 ± 0.83	4.17 ± 0.66	-326	1.8	1.1
072	7	161.52165 (0.16)	59.00699 (0.07)	74.6 ± 2.1	74.6 ± 2.13	0.04 ± 0.04	0.04 ± 0.01	-88	-0.6	-0.7
073	7	161.66091 (0.23)	58.93669 (0.15)	74.3 ± 3.6	74.3 ± 3.69	0 ± 0.08	0 ± 0.01	114	-0.9	-1.2
074	7	161.46269 (0.2)	58.94402 (0.08)	73.8 ± 2.18	73.8 ± 2.23	0.04 ± 0.05	0.04 ± 0.01	0	-0.9	-0.9
075	6	161.72239 (0.21)	59.05462 (0.2)	72.9 ± 3.97	73.4 ± 4.6	1 ± 0.23	0 ± 0.1	-114	-1	-1.2
076	1	161.50434 (0.17)	59.08056 (0.18)	60.6 ± 2.59	71.4 ± 4.68	3.74 ± 0.38	2.95 ± 0.21	-112	-0.7	-0.7
077	3	161.68684 (1.28)	59.18806 (1.23)	51.9 ± 10.62	71 ± 16.42	7.46 ± 0.84	0 ± 0.61	-68	0.6	0
078	2	161.81393 (1.38)	59.10923 (1.52)	39.4 ± 8.93	69.9 ± 17.95	11.05 ± 1.23	2.33 ± 0.87	-1039	0.9	0
079	3	161.2602 (1.11)	59.07781 (1.04)	37.5 ± 6.26	68.8 ± 15.08	12.29 ± 1.58	0 ± 0.74	11	-0.8	-1.4
080	1	161.16712 (1.48)	58.93831 (1.62)	32 ± 7.74	68.8 ± 19.93	12.33 ± 1.47	4.89 ± 1.15	-111	0	0
081	6	161.24247 (0.44)	58.91101 (0.45)	68.2 ± 7.11	68.4 ± 7.27	0.64 ± 0.17	0.17 ± 0.03	147	-0.9	-1.7
082	3	161.81576 (0.72)	59.02304 (0.8)	47.6 ± 6.75	68 ± 12.1	8.17 ± 0.94	0 ± 0.56	-126	-0.5	-2.4
083	5	161.78191 (0.8)	58.88492 (0.8)	66.8 ± 11.8	67.6 ± 11.95	1.16 ± 0.22	0.36 ± 0.06	-16	-0.8	0.2
084	1	161.27074 (0.32)	58.99663 (0.35)	54.1 ± 4.24	67.3 ± 6.96	5.04 ± 0.54	2.65 ± 0.31	-83	-1	-1.1
085	1	161.44366 (0.35)	58.97394 (0.32)	41.7 ± 4.24	64.5 ± 9.73	7.79 ± 1.12	3.83 ± 0.44	-110	-1	-0.5
086	3	161.25948 (0.4)	58.91967 (0.46)	59.7 ± 5.4	64.3 ± 6.32	3.19 ± 0.3	0 ± 0.13	-152	-1.2	-0.9
087	6	161.20067 (0.48)	58.93515 (0.5)	63.5 ± 7.54	63.9 ± 7.73	0.87 ± 0.21	0.23 ± 0.04	13	-0.9	0
088	3	161.60997 (0.23)	59.09404 (0.23)	57.5 ± 3.33	63.6 ± 4.82	3.81 ± 0.37	0 ± 0.2	58	-0.6	-0.7
089	7	161.34118 (0.23)	58.95114 (0.16)	63.4 ± 3.24	63.4 ± 3.31	0.04 ± 0.08	0.04 ± 0.01	-90	-1	-1
090	3	161.65261 (0.89)	59.19041 (0.93)	55.5 ± 9.69	62.5 ± 11.23	4.13 ± 0.34	0 ± 0.16	-69	-0.6	-2.1
091	7	161.74212 (0.25)	59.03911 (0.2)	62.4 ± 4.26	62.4 ± 4.34	0.04 ± 0.11	0.04 ± 0.02	-116	-1.3	-1.4
092	7	161.56939 (0.21)	58.9856 (0.08)	61.4 ± 1.82	61.4 ± 1.87	0.04 ± 0.05	0.04 ± 0.01	-70	-0.8	-0.9
093	7	161.48452 (0.22)	59.07862 (0.08)	61.1 ± 1.84	61.1 ± 1.89	0.04 ± 0.06	0.04 ± 0.01	-119	-1	-1.2
094	3	161.83821 (1.32)	59.11249 (1.25)	43.7 ± 9.27	60.8 ± 14.63	7.73 ± 0.9	0 ± 0.64	-153	1.5	-0.8
095	7	161.48963 (0.22)	58.94333 (0.1)	60.7 ± 1.95	60.7 ± 2	0.04 ± 0.06	0.04 ± 0.01	3	-0.9	-0.9
096	3	161.22113 (0.59)	58.9148 (0.68)	55.9 ± 7.79	60.7 ± 8.85	3.38 ± 0.32	0 ± 0.17	-40	-1.9	-1.8
097	2	161.50619 (0.39)	58.86489 (0.43)	56.3 ± 4.76	60.3 ± 5.53	3.01 ± 0.29	0.59 ± 0.11	-76	-1	-1.1
098	7	161.75957 (0.29)	59.04837 (0.27)	59 ± 4.61	59 ± 4.7	0.04 ± 0.12	0.04 ± 0.02	-22	-0.8	-1.6
099	3	161.38196 (0.55)	59.17389 (0.61)	51.6 ± 7.19	58.8 ± 8.81	4.35 ± 0.39	0 ± 0.28	137	-1.5	-2.7

continued on the next page

C Catalogue continued

ID	Size Flag	RA (J2000) (arcsec)	Dec (J2000) (arcsec)	S_P ($\mu\text{Jy beam}^{-1}$)	S_T (μJy)	θ_{DM} (arcsec)	θ_{Dm} (arcsec)	ϕ (degrees)	α_{IF}	α_{IM}
100	3	161.76776 (0.35)	59.04287 (0.38)	53.9 ± 4.18	58.7 ± 5.16	3.46 ± 0.32	0 ± 0.15	-77	-1.7	-2.6
101	7	161.57841 (0.23)	59.08374 (0.12)	58.1 ± 2.27	58.1 ± 2.33	0.04 ± 0.07	0.04 ± 0.01	-66	-1.1	-0.7
102	7	161.656 (0.23)	59.0243 (0.13)	58.1 ± 2.37	58.1 ± 2.42	0.04 ± 0.07	0.04 ± 0.01	43	-1.1	-0.9
103	1	161.76347 (1.09)	59.00092 (1.14)	27.6 ± 4.43	57.1 ± 11.46	10.45 ± 1.16	6.09 ± 0.84	-108	0.2	-0.8
104	3	161.5969 (0.25)	58.99287 (0.28)	47.4 ± 3.15	56.8 ± 5.67	5.28 ± 0.63	0 ± 0.28	-85	-1.1	-0.6
105	2	161.34024 (1.01)	58.84726 (0.98)	47.3 ± 9.29	56.7 ± 11.52	4.67 ± 0.52	2.18 ± 0.41	197	-0.7	-1.7
106	2	161.20502 (0.43)	58.97858 (0.51)	51.9 ± 5.55	56.4 ± 6.41	3.28 ± 0.31	0.9 ± 0.15	-157	-1.4	-1.7
107	1	161.3972 (0.95)	58.91341 (0.96)	31.8 ± 4.54	56.1 ± 10.74	10.03 ± 1.29	3.71 ± 0.69	-11	-0.5	-0.9
108	6	161.55166 (0.57)	59.18944 (0.58)	55.6 ± 7.18	56.1 ± 7.37	1 ± 0.23	0.27 ± 0.05	-20	-1.5	-1.6
109	3	161.5495 (1.09)	59.04117 (0.81)	31.3 ± 4.55	55.7 ± 11.37	11.76 ± 1.79	0 ± 0.55	15	-0.8	0.1
110	3	161.8024 (1.14)	59.13994 (1.11)	45.6 ± 9.7	55.2 ± 12.33	5.49 ± 0.53	0 ± 0.31	-131	-2.2	1.6
111	7	161.23255 (0.33)	59.03521 (0.31)	55.1 ± 4.52	55.1 ± 4.61	0.04 ± 0.13	0.04 ± 0.02	-96	-0.5	-1.3
112	6	161.16756 (0.54)	58.99199 (0.6)	54 ± 7.33	54.5 ± 7.61	1.16 ± 0.28	0.23 ± 0.12	-162	-0.3	-0.7
113	5	161.10803 (0.97)	59.0466 (0.95)	53.2 ± 13.2	54.4 ± 13.32	1.58 ± 0.26	0.57 ± 0.09	126	-0.3	0
114	7	161.82938 (0.97)	58.90006 (0.95)	54.2 ± 13.2	54.2 ± 13.36	0 ± 0.29	0 ± 0.1	-495	-1.7	1.1
115	3	161.19976 (0.58)	59.03774 (0.58)	43.1 ± 5.72	54.1 ± 8.51	6.08 ± 0.66	0 ± 0.42	141	-0.2	-2
116	3	161.66305 (0.43)	58.92278 (0.45)	44.1 ± 3.98	53.6 ± 6.28	5.51 ± 0.6	0 ± 0.34	-101	-0.4	-0.7
117	3	161.18461 (0.91)	59.11179 (0.94)	49.7 ± 9.03	53.6 ± 10.06	3.2 ± 0.4	0 ± 0.09	-187	0.1	0
118	1	161.50816 (0.55)	59.15474 (0.58)	38.1 ± 4.6	53.5 ± 8.16	6.58 ± 0.77	3.38 ± 0.49	-151	-0.9	-0.7
119	6	161.45115 (0.11)	59.08407 (0.16)	52.8 ± 2.18	53.2 ± 2.26	0.98 ± 0.09	0 ± 0.02	-27	-0.6	-0.8
120	3	161.21329 (0.55)	59.05499 (0.54)	43 ± 5.51	53.2 ± 8.03	5.82 ± 0.62	0 ± 0.4	-11	-1.4	-0.6
121	5	161.22603 (0.97)	59.16945 (0.95)	51.8 ± 13.45	53.1 ± 13.59	1.68 ± 0.29	0.61 ± 0.1	217	-0.4	0.5
122	3	161.60274 (0.39)	58.88225 (0.41)	50.3 ± 4	52.9 ± 4.56	2.59 ± 0.27	0 ± 0.08	-22	-0.8	-1.6
123	6	161.75899 (0.61)	59.12894 (0.62)	52 ± 6.9	52.5 ± 7.08	1.04 ± 0.24	0.28 ± 0.05	-206	-1.5	-2.5
124	7	161.45405 (0.1)	59.05934 (0.14)	52.2 ± 1.83	52.2 ± 1.92	0.08 ± 0.08	0 ± 0.03	43	0.7	0.1
125	6	161.18639 (0.48)	59.0484 (0.5)	51.7 ± 6.14	52 ± 6.29	0.87 ± 0.21	0.23 ± 0.04	-100	-1.3	-2.7
126	1	161.51512 (0.17)	59.06098 (0.15)	48.2 ± 2.03	51.9 ± 2.52	2.22 ± 0.18	2.18 ± 0.09	-70	-0.8	-0.8
127	7	161.57547 (0.33)	58.88698 (0.32)	51.8 ± 4.27	51.8 ± 4.35	0.04 ± 0.13	0.04 ± 0.02	54	-1.2	-1.4
128	1	161.23836 (0.51)	58.97982 (0.49)	40.7 ± 4.58	51.8 ± 6.97	5.48 ± 0.57	2.58 ± 0.38	-32	-1.5	-1.8
129	3	161.63725 (0.75)	58.86643 (0.72)	42.9 ± 6.38	51.8 ± 8.61	5.44 ± 0.54	0 ± 0.38	-105	-1.2	-0.4
130	6	161.748 (0.37)	58.95914 (0.36)	50.5 ± 3.24	51.6 ± 3.56	1.66 ± 0.23	0 ± 0.03	-79	-1.3	-1.4
131	7	161.39255 (0.26)	58.90755 (0.24)	51.5 ± 3.84	51.5 ± 3.92	0 ± 0.12	0 ± 0.02	52	-1.1	-1.4
132	2	161.55595 (0.2)	58.9948 (0.21)	45.5 ± 2.34	51.4 ± 3.55	3.71 ± 0.37	1.78 ± 0.2	-88	-1	-1
133	5	161.82867 (0.97)	58.91483 (0.95)	50.1 ± 11.6	50.9 ± 11.7	1.42 ± 0.23	0.51 ± 0.08	137	0.2	-1.4
134	7	161.5366 (0.1)	58.98457 (0.13)	50.8 ± 1.72	50.8 ± 1.81	0.07 ± 0.08	0 ± 0.04	76	0.2	-0.1
135	3	161.57982 (1.03)	59.12595 (1.03)	30.4 ± 4.58	50.6 ± 10.09	10.63 ± 1.36	0 ± 0.66	-11	0.1	-0.2
136	3	161.85609 (1.34)	59.05979 (1.46)	31.4 ± 7.14	50.5 ± 13.41	10.11 ± 1.17	0 ± 0.82	0	1.7	0
137	3	161.28965 (1.33)	59.17729 (1.33)	34 ± 7.41	49.9 ± 12.47	8.6 ± 1	0 ± 0.7	-162	0.4	-1.4
138	7	161.56741 (0.3)	58.89554 (0.28)	49.4 ± 3.91	49.4 ± 3.98	0.04 ± 0.12	0.04 ± 0.02	-196	-1	-1.4
139	7	161.53008 (0.97)	58.82029 (0.95)	49.2 ± 11.13	49.2 ± 11.24	0 ± 0.24	0 ± 0.08	-104	-0.1	2.3
140	5	161.25226 (0.97)	59.18073 (0.95)	47.7 ± 12.38	48.9 ± 12.51	1.68 ± 0.29	0.61 ± 0.1	114	1	0
141	3	161.37517 (0.45)	58.87678 (0.56)	44.1 ± 5.41	48.7 ± 6.39	3.73 ± 0.34	0 ± 0.21	-47	-1.3	-2.1
142	7	161.6262 (0.23)	59.01089 (0.14)	48.6 ± 2.27	48.6 ± 2.32	0.04 ± 0.08	0.04 ± 0.01	-43	-0.8	-0.9
143	7	161.31074 (0.39)	59.12049 (0.39)	48.5 ± 4.37	48.6 ± 4.45	0.24 ± 0.14	0.07 ± 0.02	105	-1.2	-1.5
144	6	161.31497 (0.28)	58.93339 (0.29)	48.2 ± 2.98	48.4 ± 3.22	0.83 ± 0.2	0.23 ± 0.03	-155	-0.7	-1
145	2	161.69769 (0.27)	59.02241 (0.25)	43.6 ± 3.07	48.3 ± 4.01	3.64 ± 0.34	1.04 ± 0.18	-81	-1	-1.3
146	1	161.62003 (1.34)	58.8516 (1.47)	23.7 ± 5.42	47.8 ± 12.74	10.23 ± 1.19	5.87 ± 1.02	-341	-0.5	0
147	3	161.49194 (0.24)	58.91923 (0.22)	45.9 ± 2.57	47.3 ± 2.93	2.02 ± 0.21	0 ± 0.06	25	-1.1	-1.5
148	1	161.78751 (0.83)	58.96706 (0.81)	33.7 ± 5.11	47.3 ± 8.16	6.02 ± 0.63	4.06 ± 0.48	-166	-1.3	-1.9
149	7	161.1185 (0.97)	58.98566 (0.95)	46.5 ± 11.1	46.5 ± 11.23	0 ± 0.27	0 ± 0.1	123	0.7	0

C Catalogue continued

ID	Size Flag	RA (J2000) (arcsec)	Dec (J2000) (arcsec)	S_P ($\mu\text{Jy beam}^{-1}$)	S_T (μJy)	θ_{DM} (arcsec)	θ_{Dm} (arcsec)	ϕ (degrees)	α_{IF}	α_{IM}
150	3	161.78209 (1.06)	58.89437 (1.07)	40.3 ± 8.31	46.2 ± 9.73	4.49 ± 0.35	0 ± 0.14	-95	-1.5	0
151	7	161.59008 (0.25)	59.10528 (0.2)	45.8 ± 3.14	45.8 ± 3.2	0.04 ± 0.11	0.04 ± 0.02	-41	-1.2	-1.3
152	6	161.6991 (0.21)	59.00633 (0.23)	44.5 ± 2.47	45.2 ± 2.67	1.39 ± 0.18	0 ± 0.03	-27	-1	-1.3
153	2	161.67685 (1.19)	58.86352 (1.15)	33.9 ± 6.76	44.4 ± 9.53	6.45 ± 0.68	1.58 ± 0.49	-42	-2.2	-1.5
154	6	161.64941 (0.4)	59.12994 (0.4)	43.9 ± 4.03	44 ± 4.11	0.32 ± 0.14	0.09 ± 0.02	-133	-1.2	-1.2
155	3	161.70846 (0.76)	58.95626 (0.82)	29.5 ± 4.11	43.7 ± 7.86	8.75 ± 1.04	0 ± 0.57	-85	-0.3	-0.8
156	5	161.44859 (0.86)	58.83561 (0.85)	43.1 ± 8.47	43.6 ± 8.54	1.18 ± 0.2	0.39 ± 0.06	0	-0.2	0
157	3	161.81346 (0.9)	59.05462 (0.87)	35.7 ± 5.96	43.3 ± 7.85	5.49 ± 0.52	0 ± 0.36	172	-0.9	-3
158	2	161.80169 (1.26)	58.96797 (1.33)	27.7 ± 5.82	43.2 ± 10.4	9.46 ± 1.01	0.98 ± 0.72	-21	-1.6	-0.6
159	1	161.52063 (0.5)	58.97555 (0.55)	25.1 ± 2.88	43.1 ± 6.92	8.13 ± 1.08	5.35 ± 0.59	154	-0.7	-0.9
160	6	161.32707 (0.4)	58.91749 (0.4)	41.9 ± 3.23	43.1 ± 3.49	1.97 ± 0.25	0 ± 0.05	-21	-1.2	-1.2
161	7	161.32176 (0.35)	58.93153 (0.35)	42.7 ± 3.61	42.7 ± 3.67	0.04 ± 0.13	0.04 ± 0.02	-87	-0.9	-1.4
162	3	161.30063 (0.55)	58.90681 (0.6)	37.2 ± 5.17	42.7 ± 6.42	4.49 ± 0.41	0 ± 0.3	-87	-1	-1.6
163	6	161.70773 (0.49)	58.9054 (0.51)	42.4 ± 5.08	42.6 ± 5.21	0.89 ± 0.21	0.24 ± 0.04	-39	-0.9	0
164	6	161.78663 (0.56)	59.08047 (0.58)	42.2 ± 5.42	42.6 ± 5.56	0.99 ± 0.23	0.26 ± 0.05	-186	-0.6	-2
165	3	161.70346 (1.06)	59.17782 (1.07)	37.1 ± 8.19	42.5 ± 9.56	4.48 ± 0.37	0 ± 0.13	-78	-1.5	-0.9
166	2	161.68411 (0.35)	59.00825 (0.38)	35.7 ± 2.83	42.4 ± 4.15	4.71 ± 0.47	1.76 ± 0.28	-107	-1.1	-1.2
167	7	161.34094 (0.32)	59.10362 (0.31)	42.4 ± 3.48	42.4 ± 3.54	0.04 ± 0.13	0.04 ± 0.02	-220	-1.3	-1
168	6	161.29165 (0.3)	59.05858 (0.3)	41.6 ± 2.52	42.2 ± 2.73	1.38 ± 0.2	0 ± 0.03	-151	-1	-0.7
169	1	161.59312 (0.35)	59.03088 (0.39)	30 ± 2.78	42 ± 5.43	6.3 ± 0.78	3.66 ± 0.42	-98	-0.8	-0.4
170	2	161.82602 (1.02)	59.04092 (0.99)	33.8 ± 6.14	42 ± 8.22	5.84 ± 0.56	0.66 ± 0.39	-52	-1.1	0
171	3	161.30378 (1.02)	59.1831 (1.04)	37.5 ± 8.42	41.8 ± 9.54	3.96 ± 0.33	0 ± 0.11	-136	0.2	0
172	7	161.46292 (0.24)	58.96786 (0.16)	41.6 ± 2.2	41.6 ± 2.25	0.04 ± 0.09	0.04 ± 0.01	-32	-1.1	-0.8
173	6	161.19811 (0.54)	58.98883 (0.56)	41.1 ± 5.21	41.4 ± 5.35	0.98 ± 0.23	0.26 ± 0.05	320	-1.3	-2.2
174	1	161.78772 (1.23)	59.10752 (1.18)	28.6 ± 5.81	41.1 ± 9.22	6.63 ± 0.73	3.79 ± 0.57	-124	-0.6	-1.8
175	2	161.19531 (1.33)	59.03242 (1.47)	22.9 ± 5.1	40.8 ± 9.99	10.65 ± 1.17	3.01 ± 0.85	-73	-1	-1.6
176	3	161.77209 (1.26)	59.12439 (1.2)	30.8 ± 6.24	40.8 ± 9.31	6.98 ± 0.8	0 ± 0.57	26	-0.8	1.5
177	3	161.6725 (0.41)	58.91984 (0.46)	38.3 ± 3.56	40.6 ± 4.04	2.84 ± 0.28	0 ± 0.1	-49	-0.9	-1.2
178	6	161.79083 (0.49)	59.03656 (0.5)	39.5 ± 5.08	40.6 ± 5.2	1.9 ± 0.22	0 ± 0.05	-85	-1.2	-0.5
179	3	161.70469 (0.76)	59.14131 (0.82)	35.7 ± 5.75	39.9 ± 6.71	3.99 ± 0.36	0 ± 0.21	-77	0.6	0
180	3	161.3444 (0.36)	58.93589 (0.36)	37.7 ± 2.74	39.7 ± 3.18	2.63 ± 0.27	0 ± 0.08	23	-1.3	-1.4
181	1	161.31443 (1.23)	58.89098 (1.19)	23.8 ± 4.81	39.6 ± 9.07	7.48 ± 0.83	5.57 ± 0.73	4	0.6	-1.1
182	3	161.47222 (0.29)	58.9216 (0.26)	38.1 ± 2.37	39.4 ± 2.7	2.11 ± 0.23	0 ± 0.06	26	-0.6	-0.3
183	2	161.52012 (0.99)	59.15598 (1.03)	26.1 ± 4.01	39.4 ± 7.27	8.67 ± 0.94	1.7 ± 0.6	-110	-0.2	-1
184	5	161.24929 (0.97)	58.86376 (0.95)	38.1 ± 9.89	39 ± 9.99	1.68 ± 0.29	0.61 ± 0.1	-283	0.6	0
185	7	161.5673 (0.24)	59.04126 (0.17)	38.8 ± 2.14	38.8 ± 2.19	0 ± 0.09	0 ± 0.02	0	-0.9	-0.6
186	5	161.58404 (0.97)	59.20997 (0.95)	37.9 ± 9.83	38.8 ± 9.93	1.68 ± 0.29	0.61 ± 0.1	-196	-0.8	0
187	7	161.54556 (0.27)	58.92119 (0.24)	38.5 ± 2.94	38.5 ± 2.99	0.04 ± 0.12	0.04 ± 0.02	-225	-1	-0.9
188	1	161.49087 (0.79)	58.87295 (0.78)	28.4 ± 4.21	38.4 ± 6.51	6.03 ± 0.63	3.22 ± 0.47	-163	-1.3	-1.4
189	1	161.55591 (0.25)	58.97269 (0.23)	34.9 ± 2.25	38.2 ± 2.82	2.95 ± 0.28	1.87 ± 0.13	-26	-0.8	-1
190	3	161.29307 (1.26)	59.17193 (1.21)	28.7 ± 5.95	38.1 ± 8.9	7.02 ± 0.84	0 ± 0.58	-7	-0.1	0
191	3	161.7298 (1.28)	58.91035 (1.33)	24.8 ± 5.27	38 ± 9.26	9.26 ± 1	0 ± 0.71	-167	-0.7	-1.7
192	3	161.59382 (0.3)	59.05156 (0.31)	32.8 ± 2.34	37.6 ± 3.44	4.49 ± 0.44	0 ± 0.25	-147	-0.6	0.2
193	7	161.71874 (0.39)	59.06186 (0.39)	37.6 ± 3.25	37.6 ± 3.31	0 ± 0.13	0 ± 0.02	20	-0.9	-0.9
194	6	161.30732 (0.99)	59.16646 (1.01)	36.5 ± 6.4	37.4 ± 6.47	1.8 ± 0.21	0 ± 0.06	121	0.4	-1.6
195	3	161.22075 (0.91)	59.10929 (0.93)	35.1 ± 6.13	37.2 ± 6.69	2.79 ± 0.36	0 ± 0.08	-127	-1.2	-1.3
196	7	161.40921 (0.24)	58.97356 (0.2)	37.1 ± 2.38	37.1 ± 2.43	0 ± 0.1	0 ± 0.02	-39	-1	-0.7
197	7	161.61043 (0.25)	59.07496 (0.21)	37 ± 2.63	37 ± 2.68	0.04 ± 0.11	0.04 ± 0.02	0	-0.9	-1.5
198	7	161.64783 (0.25)	59.0402 (0.21)	37 ± 2.59	37 ± 2.64	0 ± 0.11	0 ± 0.02	-136	-1.1	-0.9
199	7	161.39271 (0.24)	59.00327 (0.19)	36.8 ± 2.3	36.8 ± 2.35	0.04 ± 0.1	0.04 ± 0.02	48	-0.9	-0.9

continued on the next page

C Catalogue continued

ID	Size Flag	RA (J2000) (arcsec)	Dec (J2000) (arcsec)	S_P ($\mu\text{Jy beam}^{-1}$)	S_T (μJy)	θ_{DM} (arcsec)	θ_{Dm} (arcsec)	ϕ (degrees)	α_{IF}	α_{IM}
200	7	161.34513 (0.25)	58.9801 (0.22)	36.7 ± 2.72	36.7 ± 2.77	0.04 ± 0.11	0.04 ± 0.02	-67	0	0
201	7	161.33046 (0.94)	59.1752 (0.92)	36.7 ± 7.76	36.7 ± 7.82	0 ± 0.21	0 ± 0.07	-260	0.3	-1.2
202	3	161.65324 (1)	59.13852 (1)	25.9 ± 4.25	35.9 ± 6.98	7.67 ± 0.85	0 ± 0.56	-128	0.8	0.2
203	3	161.68697 (0.53)	59.09032 (0.5)	29.4 ± 3.53	35.7 ± 5.05	5.52 ± 0.57	0 ± 0.37	-107	-0.6	-1.1
204	3	161.59208 (0.31)	59.06554 (0.32)	31.1 ± 2.28	35.2 ± 3.19	4.25 ± 0.4	0 ± 0.24	-124	-0.7	-0.5
205	7	161.39729 (0.35)	58.9217 (0.34)	35.2 ± 2.97	35.2 ± 3.03	0.04 ± 0.13	0.04 ± 0.02	196	0.1	0.1
206	3	161.1786 (1.17)	58.99753 (1.13)	27.2 ± 5.39	34.9 ± 7.57	6.42 ± 0.68	0 ± 0.48	146	-1.2	1.1
207	6	161.73528 (0.41)	59.04312 (0.43)	34.6 ± 3.06	34.8 ± 3.28	0.97 ± 0.26	0.19 ± 0.07	-104	-1.2	-1
208	7	161.57094 (0.25)	59.07898 (0.21)	34.7 ± 2.46	34.7 ± 2.51	0.04 ± 0.11	0.04 ± 0.02	-89	-0.7	-0.8
209	7	161.67581 (0.32)	58.97677 (0.3)	34.6 ± 2.81	34.6 ± 2.86	0.04 ± 0.12	0.04 ± 0.02	-229	-0.5	-0.9
210	5	161.74018 (0.47)	59.07545 (0.46)	34.1 ± 3.79	34.4 ± 3.88	0.84 ± 0.2	0.34 ± 0.04	-79	-1.4	-1.7
211	7	161.48337 (0.87)	59.18824 (0.86)	34.4 ± 6.58	34.4 ± 6.63	0 ± 0.19	0 ± 0.06	0	-2	0
212	7	161.58829 (0.32)	59.10543 (0.31)	34.2 ± 2.8	34.2 ± 2.85	0.04 ± 0.13	0.04 ± 0.02	46	-1.1	-1.2
213	5	161.84311 (0.98)	58.98776 (1)	33.1 ± 7.04	33.8 ± 7.24	1.62 ± 0.4	0.32 ± 0.09	19	-0.4	0
214	3	161.58134 (1.3)	59.02247 (0.96)	18 ± 3.39	33.7 ± 9.87	12.68 ± 2.95	0 ± 0.86	22	-1	-0.7
215	3	161.77873 (0.65)	58.97998 (0.74)	30.7 ± 4.51	33.7 ± 5.18	3.59 ± 0.33	0 ± 0.2	-57	-0.9	-1.1
216	3	161.72791 (1.35)	58.92815 (1.49)	19.7 ± 4.41	33.7 ± 8.8	11.08 ± 1.21	0 ± 0.82	-63	0.4	0.2
217	7	161.56461 (0.24)	59.01726 (0.19)	33.4 ± 2.09	33.4 ± 2.13	0.04 ± 0.1	0.04 ± 0.02	-35	-1.1	-1.1
218	3	161.84412 (1)	59.01978 (1.03)	30.6 ± 6.4	33.4 ± 7.12	3.5 ± 0.34	0 ± 0.1	-45	0	1.7
219	6	161.39836 (0.17)	59.00218 (0.21)	33.1 ± 1.77	33.2 ± 1.84	0.63 ± 0.12	0 ± 0.03	-139	-0.5	-0.3
220	7	161.45356 (0.25)	59.08885 (0.22)	33.2 ± 2.47	33.2 ± 2.52	0.04 ± 0.12	0.04 ± 0.02	-56	-1.1	-1.2
221	6	161.49796 (0.41)	59.13342 (0.41)	32.4 ± 2.7	33.2 ± 2.87	1.78 ± 0.24	0 ± 0.04	176	-1.3	-1.3
222	3	161.49596 (1.03)	58.84511 (1.01)	31.9 ± 5.46	33 ± 5.75	2.13 ± 0.26	0 ± 0.06	9	0.5	0.3
223	6	161.47557 (0.22)	59.01849 (0.2)	32.7 ± 1.74	32.9 ± 1.93	0.83 ± 0.2	0 ± 0.06	-59	-1.1	-1
224	3	161.28809 (1.18)	59.02059 (1.06)	24.8 ± 4.47	32.6 ± 8.79	6.82 ± 1.8	0 ± 0.84	-79	-0.7	-1.5
225	3	161.3889 (1.15)	59.13426 (1.22)	20.5 ± 3.67	32.3 ± 6.93	9.76 ± 1.05	0 ± 0.67	-39	-0.6	-0.7
226	7	161.51748 (0.62)	59.16377 (0.63)	32.2 ± 4.16	32.2 ± 4.28	0 ± 0.24	0 ± 0.05	245	-0.6	0.6
227	7	161.80206 (0.97)	58.92146 (0.95)	32.2 ± 7.51	32.2 ± 7.59	0 ± 0.26	0 ± 0.09	44	-1.2	0.9
228	6	161.29357 (0.42)	59.06874 (0.43)	32 ± 3.16	32.1 ± 3.22	0.51 ± 0.16	0.14 ± 0.03	53	-0.5	-0.8
229	3	161.7992 (1.37)	59.08837 (1.51)	19.1 ± 4.43	32.1 ± 8.75	10.8 ± 1.26	0 ± 0.87	157	-0.3	2.2
230	1	161.44731 (0.43)	58.91716 (0.48)	27.3 ± 2.69	32 ± 3.55	4.14 ± 0.37	2.35 ± 0.25	-18	-1	-0.3
231	3	161.16344 (1.32)	59.02122 (1.26)	22.9 ± 4.87	32 ± 7.74	7.83 ± 0.92	0 ± 0.64	-7	-1.7	-1.9
232	7	161.44181 (0.37)	58.91716 (0.37)	31.9 ± 2.72	31.9 ± 2.77	0 ± 0.13	0 ± 0.02	37	-1.1	-1.2
233	6	161.25486 (0.48)	58.96925 (0.5)	31.7 ± 3.76	31.9 ± 3.85	0.86 ± 0.21	0.23 ± 0.04	75	-0.9	-1.3
234	6	161.62602 (0.52)	59.14134 (0.54)	31.6 ± 3.95	31.9 ± 4.05	0.95 ± 0.22	0.25 ± 0.05	18	-0.4	-0.7
235	3	161.69055 (0.46)	59.0214 (0.48)	26.9 ± 2.64	31.6 ± 3.7	4.94 ± 0.48	0 ± 0.31	62	-0.9	-1.2
236	3	161.3627 (0.8)	59.14891 (0.83)	27.7 ± 4.55	31.6 ± 5.44	4.42 ± 0.37	0 ± 0.25	-150	0.6	-0.5
237	1	161.5749 (1.03)	59.09742 (1.08)	16.5 ± 2.58	31.3 ± 6.15	10.01 ± 1.11	5.1 ± 0.77	-53	-1.9	-1.4
238	3	161.66027 (0.55)	59.06914 (0.58)	23.8 ± 2.84	30.8 ± 4.67	6.59 ± 0.77	0 ± 0.45	3	-1.1	-1.9
239	3	161.60752 (0.75)	59.15613 (0.79)	29 ± 4.44	30.8 ± 4.86	2.87 ± 0.31	0 ± 0.12	-58	-1.5	0
240	7	161.44515 (0.24)	59.02976 (0.2)	30.7 ± 2.06	30.7 ± 2.1	0.04 ± 0.11	0.04 ± 0.02	5	-0.9	-0.7
241	2	161.31261 (0.98)	58.98218 (1.04)	18.8 ± 2.91	30.7 ± 5.77	9.71 ± 1.08	2.18 ± 0.65	153	-1.3	-1.7
242	6	161.77048 (0.63)	59.05762 (0.64)	30.3 ± 4.14	30.6 ± 4.19	1.19 ± 0.17	0 ± 0.04	-163	-1.3	-1.6
243	3	161.62108 (0.43)	59.03595 (0.45)	24.9 ± 2.28	30.5 ± 3.64	5.63 ± 0.62	0 ± 0.35	-65	-1.1	-1.7
244	2	161.53867 (0.66)	58.87701 (0.74)	27.3 ± 4	30.4 ± 4.57	3.52 ± 0.33	1.65 ± 0.2	-132	-1.3	-1.9
245	3	161.78065 (1.07)	59.12698 (1.06)	28.9 ± 6.81	30.4 ± 7.26	2.63 ± 0.29	0 ± 0.12	-21	-0.4	-2.6
246	1	161.60212 (0.53)	59.04128 (0.6)	20.4 ± 2.36	30.3 ± 4.76	7.55 ± 0.95	3.2 ± 0.54	-97	-0.6	-0.8
247	7	161.39821 (0.34)	58.94707 (0.33)	30.2 ± 2.47	30.2 ± 2.51	0 ± 0.13	0 ± 0.02	-157	-0.7	-0.7
248	3	161.16801 (1.06)	59.06238 (1.06)	28.6 ± 6.32	30.2 ± 6.78	2.72 ± 0.31	0 ± 0.1	-63	-2.2	-1.5
249	3	161.54851 (0.35)	58.93854 (0.36)	28.4 ± 2.11	30.1 ± 2.47	2.83 ± 0.28	0 ± 0.1	-141	-1.4	-0.2

continued on the next page

C Catalogue continued

ID	Size Flag	RA (J2000) (arcsec)	Dec (J2000) (arcsec)	S_P ($\mu\text{Jy beam}^{-1}$)	S_T (μJy)	θ_{DM} (arcsec)	θ_{Dm} (arcsec)	ϕ (degrees)	α_{IF}	α_{IM}
250	3	161.43392 (1.33)	59.16595 (1.4)	19.3 ± 4.22	30 ± 7.56	9.48 ± 1.06	0 ± 0.74	-353	-1.6	-2
251	3	161.37057 (0.38)	58.99995 (0.4)	26.2 ± 2.08	29.9 ± 2.9	4.46 ± 0.42	0 ± 0.26	-88	-0.9	-0.8
252	7	161.14888 (0.97)	59.00806 (0.95)	29.8 ± 7.09	29.8 ± 7.17	0 ± 0.27	0 ± 0.1	27	-1.8	0.5
253	6	161.50932 (0.26)	59.08221 (0.25)	29.5 ± 1.77	29.7 ± 1.94	1.02 ± 0.21	0.23 ± 0.04	-105	-0.6	-1
254	3	161.58913 (1.24)	58.8672 (1.19)	22.1 ± 4.46	29.7 ± 6.77	7.2 ± 0.82	0 ± 0.59	-113	0.4	0.3
255	7	161.42138 (0.32)	58.94485 (0.31)	29.6 ± 2.41	29.6 ± 2.46	0.04 ± 0.12	0.04 ± 0.02	178	-0.7	-0.9
256	7	161.61833 (0.26)	58.99861 (0.24)	29.5 ± 2.25	29.5 ± 2.29	0.04 ± 0.12	0.04 ± 0.02	183	-1.4	-1.3
257	7	161.25547 (0.74)	58.93193 (0.74)	29.5 ± 4.44	29.5 ± 4.53	0 ± 0.24	0 ± 0.06	0	-1	-1.2
258	3	161.43603 (1)	59.19768 (1.03)	26.9 ± 6.13	29.5 ± 6.81	3.59 ± 0.31	0 ± 0.11	-74	-0.4	0
259	7	161.56463 (0.26)	58.96943 (0.23)	29.4 ± 2.18	29.4 ± 2.23	0 ± 0.12	0 ± 0.02	-21	-0.2	-0.2
260	3	161.73608 (1.01)	58.90548 (0.99)	28.4 ± 4.83	29.4 ± 5.1	2.21 ± 0.27	0 ± 0.06	-75	0.5	-2.4
261	5	161.14189 (0.97)	58.99295 (0.95)	28.7 ± 7.44	29.4 ± 7.52	1.68 ± 0.29	0.61 ± 0.1	110	-2	0
262	6	161.67606 (0.39)	59.06957 (0.43)	29 ± 2.5	29.3 ± 2.72	1.04 ± 0.28	0.11 ± 0.1	-113	0	-0.2
263	3	161.5259 (0.52)	58.90709 (0.52)	24.5 ± 3.06	29.1 ± 4.13	5.11 ± 0.5	0 ± 0.34	-112	-1.4	-0.9
264	7	161.57773 (0.28)	58.96269 (0.26)	29 ± 2.26	29 ± 2.3	0.04 ± 0.12	0.04 ± 0.02	49	-1.3	-1.2
265	6	161.40164 (0.28)	59.07558 (0.29)	28.9 ± 1.79	29 ± 1.92	0.75 ± 0.19	0.24 ± 0.03	-141	-1	-0.9
266	3	161.62601 (0.44)	58.95055 (0.48)	25.3 ± 2.45	29 ± 3.25	4.49 ± 0.41	0 ± 0.27	-87	-1	-0.4
267	3	161.3959 (1.01)	58.84715 (1.04)	26.2 ± 5.93	29 ± 6.66	3.78 ± 0.32	0 ± 0.11	-40	-0.7	-1.3
268	3	161.56059 (0.4)	59.11049 (0.44)	27.3 ± 2.36	28.9 ± 2.69	2.75 ± 0.28	0 ± 0.09	-141	-0.8	-1.5
269	3	161.70505 (0.42)	59.0243 (0.5)	26.6 ± 2.72	28.9 ± 3.19	3.38 ± 0.32	0 ± 0.16	-97	-0.7	-1.2
270	5	161.8645 (0.97)	58.9939 (0.95)	28.2 ± 7.33	28.9 ± 7.41	1.68 ± 0.29	0.61 ± 0.1	0	-0.7	-1.4
271	7	161.65054 (0.36)	58.96719 (0.36)	28.8 ± 2.47	28.8 ± 2.51	0.04 ± 0.13	0.04 ± 0.02	33	-1.3	-0.8
272	3	161.30313 (0.62)	59.09329 (0.65)	24.7 ± 3.56	28.8 ± 4.51	4.75 ± 0.44	0 ± 0.32	-93	-0.4	0.4
273	6	161.64655 (0.35)	58.98649 (0.38)	28.1 ± 2.22	28.7 ± 2.65	1.58 ± 0.36	0 ± 0.2	-56	-0.4	-0.6
274	1	161.55428 (1.37)	59.05361 (1.35)	11.3 ± 2.09	28.6 ± 6.71	14.59 ± 1.63	5.5 ± 1.04	-84	-1.3	-1.8
275	2	161.63917 (1.34)	59.15769 (1.43)	17.1 ± 3.84	28.6 ± 7.09	9.73 ± 1.13	2.88 ± 0.84	-183	2	0
276	2	161.3621 (0.56)	59.05263 (0.63)	21 ± 2.55	28.5 ± 4.53	7.31 ± 0.89	0.65 ± 0.5	-84	-1.1	-0.7
277	3	161.3137 (0.98)	59.13425 (0.97)	24 ± 4.3	28.5 ± 5.38	5.15 ± 0.44	0 ± 0.28	-139	-0.4	-1.2
278	5	161.27024 (0.99)	59.14054 (1)	27.9 ± 5.9	28.5 ± 6.06	1.55 ± 0.39	0.33 ± 0.08	178	-0.2	-2.7
279	6	161.55459 (0.28)	58.95954 (0.27)	28.1 ± 1.75	28.4 ± 1.92	1.01 ± 0.22	0.21 ± 0.04	-129	-0.9	-0.6
280	6	161.27595 (0.45)	59.00987 (0.46)	28.3 ± 3.03	28.4 ± 3.1	0.69 ± 0.18	0.18 ± 0.03	46	-0.5	-0.6
281	6	161.77664 (0.82)	58.95529 (0.85)	27.7 ± 4.9	28.4 ± 5.11	1.84 ± 0.35	0.17 ± 0.23	-7	-1.7	-0.1
282	5	161.34407 (0.97)	58.84934 (0.95)	27.8 ± 7.21	28.4 ± 7.28	1.68 ± 0.29	0.61 ± 0.1	0	-0.2	0
283	5	161.62153 (0.97)	59.19394 (0.95)	27.6 ± 7.16	28.3 ± 7.24	1.68 ± 0.29	0.61 ± 0.1	0	-0.5	-2.4
284	2	161.67015 (1.13)	59.08956 (1.2)	17.5 ± 2.98	28.1 ± 5.75	9.84 ± 1.05	1.29 ± 0.67	-55	-0.7	-1
285	1	161.27888 (0.98)	58.90751 (0.97)	26.1 ± 4.38	27.8 ± 4.75	2.2 ± 0.26	1.84 ± 0.06	69	0.9	-0.3
286	3	161.34151 (1.04)	59.13127 (1.02)	21 ± 3.78	27.1 ± 5.45	6.5 ± 0.69	0 ± 0.48	-117	0.1	0
287	7	161.82451 (0.97)	58.93968 (0.95)	27 ± 6.58	27 ± 6.66	0 ± 0.29	0 ± 0.1	-231	-0.3	0
288	1	161.41795 (1.76)	59.03304 (1.87)	5.6 ± 1.49	26.9 ± 10.38	20.79 ± 2.66	11.39 ± 3.47	-61	0	-1.2
289	4	161.25366 (1.01)	59.13438 (1.04)	25.7 ± 5.8	26.7 ± 6.01	1.73 ± 0.34	1.44 ± 0.11	-9	-2	-2.9
290	3	161.27993 (0.92)	59.1234 (0.96)	24.1 ± 4.41	26.6 ± 5	3.73 ± 0.37	0 ± 0.11	-113	-0.5	-2.9
291	6	161.32826 (0.41)	58.97667 (0.42)	26.3 ± 2.51	26.4 ± 2.56	0.43 ± 0.15	0.12 ± 0.02	54	-1.1	-1.2
292	3	161.70235 (0.47)	59.07329 (0.53)	25 ± 3.1	26.4 ± 3.4	2.66 ± 0.27	0 ± 0.1	161	-0.5	-0.7
293	1	161.77635 (1.14)	59.01796 (1.1)	18.8 ± 3.67	26.4 ± 5.65	6.44 ± 0.67	3.53 ± 0.52	158	-0.9	-1.9
294	3	161.51187 (1.33)	59.1709 (1.32)	18.1 ± 3.89	26.4 ± 6.51	8.54 ± 0.98	0 ± 0.69	350	0	-1.2
295	7	161.25188 (0.86)	59.10869 (0.86)	26.3 ± 4.98	26.3 ± 5.02	0 ± 0.19	0 ± 0.06	35	-1.3	-1.4
296	6	161.54088 (0.4)	58.92632 (0.4)	26.1 ± 2.41	26.2 ± 2.46	0.33 ± 0.14	0.09 ± 0.02	0	-0.6	-0.7
297	7	161.72878 (0.57)	58.96319 (0.59)	26.1 ± 3.28	26.1 ± 3.37	0 ± 0.24	0 ± 0.05	-171	0.7	-1.1
298	6	161.62206 (0.38)	58.96081 (0.38)	25.6 ± 1.69	26 ± 1.84	1.56 ± 0.23	0 ± 0.03	-16	-1	-1
299	1	161.57454 (1.14)	58.86768 (1.11)	18.4 ± 3.81	26 ± 5.65	5.49 ± 0.52	4.75 ± 0.37	-23	-1.3	-3

continued on the next page

C Catalogue continued

ID	Size Flag	RA (J2000) (arcsec)	Dec (J2000) (arcsec)	S_P ($\mu\text{Jy beam}^{-1}$)	S_T (μJy)	θ_{DM} (arcsec)	θ_{Dm} (arcsec)	ϕ (degrees)	α_{IF}	α_{IM}
300	3	161.58551 (1.09)	59.1835 (1.07)	24.8 ± 5.72	25.8 ± 6.04	2.32 ± 0.3	0 ± 0.12	-53	1.4	1.3
301	6	161.53598 (0.23)	59.00664 (0.23)	25.6 ± 1.5	25.7 ± 1.63	0.9 ± 0.2	0.22 ± 0.04	-16	-1.8	-1.4
302	7	161.56765 (0.34)	59.07496 (0.33)	25.7 ± 2.14	25.7 ± 2.17	0.04 ± 0.13	0.04 ± 0.02	2	-0.9	-0.9
303	7	161.59696 (0.35)	58.96298 (0.35)	25.6 ± 2.16	25.6 ± 2.2	0.04 ± 0.13	0.04 ± 0.02	-1	-0.9	-1.3
304	3	161.55533 (0.45)	59.05588 (0.46)	21.3 ± 1.92	25.6 ± 2.96	5.38 ± 0.57	0 ± 0.33	32	-0.7	-0.7
305	7	161.47587 (0.97)	58.83953 (0.95)	25.6 ± 6.23	25.6 ± 6.3	0 ± 0.29	0 ± 0.1	-119	-2	-1.6
306	7	161.36345 (0.97)	58.85324 (0.95)	25.6 ± 6.23	25.6 ± 6.31	0 ± 0.29	0 ± 0.1	82	1.5	0
307	6	161.60542 (0.44)	58.93987 (0.48)	24.8 ± 2.5	25.5 ± 2.95	1.96 ± 0.42	0 ± 0.28	-101	-0.7	-0.8
308	5	161.16791 (0.97)	59.01641 (0.95)	24.8 ± 5.96	25.3 ± 6.02	1.51 ± 0.24	0.54 ± 0.08	-53	0	0
309	7	161.61245 (0.97)	59.18541 (0.95)	25.3 ± 6.15	25.3 ± 6.23	0 ± 0.29	0 ± 0.1	0	0.6	0.2
310	2	161.46013 (1.03)	58.99394 (1.04)	14 ± 2.19	25.1 ± 4.76	10.64 ± 1.27	3.17 ± 0.72	-102	-0.1	-0.7
311	6	161.26142 (0.57)	58.98061 (0.59)	24.8 ± 3.21	25.1 ± 3.3	1.01 ± 0.24	0.27 ± 0.05	2	-0.7	-1.3
312	3	161.57422 (1.23)	58.85868 (1.18)	19.4 ± 4.06	25.1 ± 5.79	6.6 ± 0.75	0 ± 0.51	158	0.5	1.1
313	3	161.47662 (0.44)	58.92024 (0.44)	24.3 ± 2.37	25 ± 2.56	2.02 ± 0.24	0 ± 0.05	3	-1	-0.8
314	5	161.35855 (0.97)	59.17275 (0.95)	24.4 ± 6	25 ± 6.06	1.56 ± 0.26	0.56 ± 0.09	-341	0.7	0
315	5	161.34345 (1.01)	58.85267 (1.04)	24.4 ± 6.09	25 ± 6.18	1.78 ± 0.32	0.43 ± 0.11	-5	0	-1
316	1	161.32139 (1.04)	59.09125 (1.02)	15.7 ± 2.81	24.9 ± 5.01	6.59 ± 0.71	5.69 ± 0.61	-153	-0.7	-1
317	7	161.48755 (0.28)	59.00011 (0.26)	24.6 ± 1.87	24.6 ± 1.91	0 ± 0.12	0 ± 0.02	-70	-0.4	-1.3
318	7	161.49486 (0.35)	58.95311 (0.34)	24.5 ± 2.06	24.5 ± 2.09	0.04 ± 0.13	0.04 ± 0.02	-32	-0.7	-1
319	7	161.49939 (0.42)	59.10844 (0.43)	24.5 ± 2.39	24.5 ± 2.45	0 ± 0.16	0 ± 0.03	107	-0.9	-0.9
320	5	161.31079 (0.83)	58.90063 (0.83)	24.2 ± 4.52	24.5 ± 4.57	1.17 ± 0.21	0.37 ± 0.06	120	0.7	-0.5
321	6	161.49925 (0.47)	59.12545 (0.49)	24.2 ± 2.75	24.3 ± 2.82	0.8 ± 0.2	0.21 ± 0.04	9	-0.7	-1.3
322	6	161.38101 (0.36)	59.04119 (0.39)	23.9 ± 1.89	24.1 ± 2.12	1.15 ± 0.3	0 ± 0.12	-95	-1.1	-1.2
323	6	161.2135 (0.85)	58.99551 (0.87)	23.8 ± 4.24	24.1 ± 4.36	1.33 ± 0.33	0.28 ± 0.09	-162	-1.6	-2
324	2	161.7154 (1.39)	58.96317 (1.52)	13.5 ± 3.07	24.1 ± 6.29	11.38 ± 1.26	1.82 ± 0.87	-64	-0.3	0.2
325	7	161.37554 (0.37)	58.99689 (0.36)	24 ± 2.03	24 ± 2.07	0 ± 0.13	0 ± 0.02	-36	-0.5	-0.5
326	6	161.62546 (0.44)	59.08828 (0.45)	23.8 ± 2.49	23.9 ± 2.54	0.64 ± 0.17	0.17 ± 0.03	97	-0.7	-0.5
327	5	161.53328 (0.32)	59.00471 (0.34)	22.6 ± 1.73	23.8 ± 2.05	2.12 ± 0.34	1.49 ± 0.18	-211	-1	-0.8
328	7	161.40827 (0.34)	58.99059 (0.32)	23.8 ± 1.98	23.8 ± 2.01	0.04 ± 0.13	0.04 ± 0.02	1	-0.8	-1.1
329	7	161.46468 (0.86)	58.86754 (0.85)	23.7 ± 4.42	23.7 ± 4.46	0 ± 0.2	0 ± 0.06	-162	0.9	-0.7
330	3	161.2479 (0.99)	59.11155 (1.03)	21.5 ± 4.53	23.7 ± 5.07	3.62 ± 0.34	0 ± 0.11	-62	1.1	0
331	5	161.19595 (0.97)	58.94148 (0.95)	23.1 ± 5.94	23.7 ± 6	1.66 ± 0.28	0.61 ± 0.1	97	-1.4	0
332	7	161.49879 (0.39)	58.94224 (0.39)	23.6 ± 2.07	23.6 ± 2.11	0.04 ± 0.13	0.04 ± 0.02	-61	-0.9	0.1
333	3	161.51761 (0.88)	58.89991 (0.86)	18.4 ± 2.85	23.6 ± 4.19	6.36 ± 0.68	0 ± 0.46	-144	-1.1	-1.3
334	1	161.41137 (0.83)	58.91264 (0.82)	17.1 ± 2.76	23.6 ± 4.11	5.2 ± 0.49	4.61 ± 0.39	-2	0	0.5
335	5	161.44783 (0.95)	58.85624 (0.93)	23.3 ± 5.27	23.6 ± 5.31	1.37 ± 0.21	0.48 ± 0.07	46	0.7	0
336	5	161.72903 (0.97)	59.13848 (0.95)	23.1 ± 5.67	23.6 ± 5.72	1.56 ± 0.26	0.56 ± 0.09	-11	-1	0
337	3	161.43383 (1.18)	58.8696 (1.14)	18.9 ± 3.8	23.5 ± 5.09	5.97 ± 0.6	0 ± 0.4	-65	0.9	-0.1
338	5	161.55931 (0.37)	58.98731 (0.41)	21.9 ± 1.75	23.4 ± 2.15	2.39 ± 0.39	1.76 ± 0.24	-122	-0.3	0.3
339	4	161.53709 (0.37)	59.07013 (0.36)	22.6 ± 1.47	23.4 ± 1.64	1.85 ± 0.24	1.16 ± 0.04	-12	-1.6	-1.9
340	2	161.74562 (1.34)	58.95261 (1.47)	13 ± 2.97	23.4 ± 5.72	10.2 ± 1.19	3.86 ± 0.91	-94	-0.2	-0.3
341	3	161.57024 (0.59)	58.91589 (0.62)	20 ± 2.84	23.3 ± 3.59	4.71 ± 0.44	0 ± 0.32	-92	-1.7	-1.6
342	6	161.7197 (0.99)	59.12241 (0.98)	22.6 ± 4.41	23.3 ± 4.6	1.96 ± 0.4	0 ± 0.24	-371	-0.5	0
343	3	161.20287 (1.02)	59.02145 (1.04)	20.6 ± 4	23.3 ± 4.62	4.25 ± 0.32	0 ± 0.12	-3	0.4	-0.2
344	3	161.52148 (0.95)	58.87739 (0.95)	19.9 ± 3.52	23.2 ± 4.27	4.78 ± 0.38	0 ± 0.23	158	-0.9	-0.4
345	3	161.24243 (0.79)	58.99207 (0.85)	21.3 ± 3.49	23.1 ± 3.92	3.39 ± 0.35	0 ± 0.14	-5	-0.4	0.4
346	7	161.63481 (0.71)	58.90329 (0.71)	23 ± 3.25	23 ± 3.33	0 ± 0.25	0 ± 0.06	147	0	-1.1
347	5	161.69639 (0.97)	59.14763 (0.95)	22.6 ± 5.37	23 ± 5.42	1.48 ± 0.24	0.53 ± 0.08	-207	1.1	1.9
348	3	161.48362 (1.02)	58.88467 (0.99)	18.3 ± 3.3	22.9 ± 4.52	6.04 ± 0.6	0 ± 0.42	352	0.4	0.2
349	5	161.82753 (1)	58.96897 (1.03)	22.2 ± 5.56	22.8 ± 5.63	1.75 ± 0.31	0.43 ± 0.11	28	0.6	2.7

continued on the next page

C Catalogue continued

ID	Size Flag	RA (J2000) (arcsec)	Dec (J2000) (arcsec)	S_P ($\mu\text{Jy beam}^{-1}$)	S_T (μJy)	θ_{DM} (arcsec)	θ_{Dm} (arcsec)	ϕ (degrees)	α_{IF}	α_{IM}
350	3	161.17529 (1.06)	59.06072 (1.06)	21.6 ± 5.06	22.8 ± 5.43	2.8 ± 0.28	0 ± 0.12	-150	1.1	0.1
351	6	161.55436 (0.41)	59.08896 (0.41)	22.7 ± 2.13	22.7 ± 2.17	0.39 ± 0.15	0.11 ± 0.02	0	-0.9	-1.4
352	3	161.75433 (1.32)	58.99225 (1.37)	14.9 ± 3.2	22.7 ± 5.61	9.19 ± 1.01	0 ± 0.72	-66	-0.9	0.2
353	5	161.65246 (0.87)	58.88707 (0.86)	22.3 ± 4.49	22.6 ± 4.53	1.18 ± 0.19	0.39 ± 0.06	-238	-0.6	-0.7
354	6	161.38646 (0.93)	58.87634 (0.97)	22.2 ± 3.85	22.6 ± 3.89	1.6 ± 0.19	0 ± 0.05	-22	1.3	-0.9
355	2	161.50623 (1.13)	59.07372 (1.19)	12.3 ± 2.01	22.4 ± 4.3	10.81 ± 1.18	3.34 ± 0.74	60	-0.9	-0.5
356	7	161.52772 (0.35)	59.06101 (0.34)	22.3 ± 1.88	22.3 ± 1.91	0.04 ± 0.13	0.04 ± 0.02	6	-1.2	-0.8
357	3	161.5919 (0.4)	58.98545 (0.47)	20.1 ± 1.81	22.3 ± 2.27	3.84 ± 0.35	0 ± 0.2	-90	-1.7	-1.2
358	3	161.52185 (0.45)	58.97977 (0.47)	18.9 ± 1.77	22.2 ± 2.52	4.94 ± 0.49	0 ± 0.3	68	0.1	0.1
359	7	161.62284 (0.97)	59.18108 (0.95)	22.1 ± 5.39	22.1 ± 5.45	0 ± 0.29	0 ± 0.1	0	-0.1	0
360	3	161.36014 (1.08)	59.08467 (1.13)	14.6 ± 2.48	22 ± 4.47	8.99 ± 0.97	0 ± 0.63	127	-0.3	-1.5
361	6	161.81072 (1.49)	58.96015 (1.62)	19.3 ± 5.09	21.9 ± 6.67	4.34 ± 1.49	0 ± 0.99	-156	-0.1	-0.1
362	5	161.23369 (0.96)	59.09812 (0.94)	21.4 ± 4.91	21.8 ± 4.95	1.4 ± 0.22	0.5 ± 0.08	-295	0.2	-2
363	7	161.56209 (0.34)	59.01121 (0.33)	21.7 ± 1.81	21.7 ± 1.84	0.04 ± 0.13	0.04 ± 0.02	-77	-1.3	-0.8
364	2	161.21019 (1.33)	59.01073 (1.38)	14.2 ± 3.15	21.7 ± 5.53	9.16 ± 1.06	0.44 ± 0.74	-40	-1	-1.7
365	3	161.30888 (0.57)	59.00546 (0.61)	18.8 ± 2.63	21.6 ± 3.29	4.57 ± 0.42	0 ± 0.3	-129	-1	-1.9
366	5	161.24557 (0.83)	59.07666 (0.82)	21.4 ± 3.99	21.6 ± 4.03	1.17 ± 0.21	0.37 ± 0.06	329	-0.2	-1.7
367	7	161.58308 (0.97)	58.84618 (0.95)	21.6 ± 5.26	21.6 ± 5.33	0 ± 0.29	0 ± 0.1	-105	0.9	1.3
368	1	161.49788 (0.45)	59.10342 (0.54)	19 ± 2.27	21.5 ± 2.71	3.26 ± 0.31	2.48 ± 0.16	-63	-1	-1.2
369	3	161.68893 (0.5)	58.98797 (0.62)	19.6 ± 2.6	21.5 ± 3.02	3.63 ± 0.34	0 ± 0.2	144	-1.4	-0.9
370	3	161.29517 (0.87)	59.0985 (0.91)	19.1 ± 3.29	21.5 ± 3.82	4.13 ± 0.34	0 ± 0.17	-67	-0.8	-1.2
371	5	161.70461 (1)	58.90335 (0.99)	21.2 ± 4.06	21.5 ± 4.13	1.24 ± 0.27	0.3 ± 0.06	-265	0.3	0
372	6	161.57813 (0.43)	59.08397 (0.44)	21.3 ± 2.14	21.3 ± 2.19	0.57 ± 0.17	0.15 ± 0.03	45	-1.1	-0.8
373	3	161.2493 (0.97)	59.00864 (0.95)	17.6 ± 3.12	21.1 ± 3.97	5.3 ± 0.47	0 ± 0.31	-84	-1.7	-1.6
374	7	161.41601 (0.74)	59.13902 (0.74)	20.9 ± 3.17	20.9 ± 3.23	0 ± 0.24	0 ± 0.06	116	-0.3	-0.9
375	1	161.66989 (0.96)	59.04002 (0.95)	13.1 ± 2.15	20.9 ± 3.96	6.76 ± 0.75	5.52 ± 0.62	65	-0.9	-0.7
376	7	161.79117 (0.93)	59.00026 (0.91)	20.9 ± 4.34	20.9 ± 4.37	0 ± 0.2	0 ± 0.07	-9	-1	-0.4
377	5	161.71663 (0.97)	58.90095 (0.95)	20.5 ± 4.91	20.9 ± 4.95	1.5 ± 0.24	0.54 ± 0.08	-62	0	1.9
378	3	161.72457 (1.08)	58.91443 (1.08)	18 ± 3.81	20.9 ± 4.53	4.7 ± 0.39	0 ± 0.17	-98	-0.4	0
379	5	161.81116 (1)	58.96067 (1.03)	20.4 ± 5.08	20.9 ± 5.15	1.73 ± 0.31	0.42 ± 0.11	29	-0.1	-1.3
380	3	161.20523 (1.09)	58.95602 (1.08)	17.9 ± 3.92	20.9 ± 4.7	4.84 ± 0.42	0 ± 0.2	-43	0.2	0
381	3	161.25494 (1.04)	59.12692 (1.05)	18.5 ± 4.12	20.9 ± 4.73	4.22 ± 0.34	0 ± 0.11	-98	0.1	-2.5
382	1	161.52398 (0.7)	58.95701 (0.76)	14.1 ± 1.95	20.8 ± 3.57	7.38 ± 0.85	3.32 ± 0.56	349	-1.2	0.4
383	6	161.76485 (1.06)	58.98236 (1.04)	19.7 ± 3.84	20.8 ± 4.51	2.65 ± 0.78	0 ± 0.55	4	0.5	0.1
384	1	161.41973 (0.45)	59.0857 (0.49)	19.1 ± 2.14	20.7 ± 2.42	2.54 ± 0.26	2.05 ± 0.09	14	-0.6	-0.7
385	3	161.2986 (0.65)	58.97163 (0.74)	18.9 ± 2.78	20.7 ± 3.19	3.6 ± 0.33	0 ± 0.2	167	-0.6	-0.4
386	6	161.34436 (0.45)	58.99753 (0.46)	20.5 ± 2.19	20.6 ± 2.24	0.69 ± 0.18	0.18 ± 0.03	-74	-0.8	-0.9
387	7	161.29632 (0.53)	59.03142 (0.55)	20.6 ± 2.53	20.6 ± 2.6	0 ± 0.23	0 ± 0.05	70	-1.5	-0.9
388	3	161.28984 (1.3)	58.97771 (1.4)	12.9 ± 2.79	20.6 ± 5.18	10.03 ± 1.08	0 ± 0.75	-123	1.3	0.1
389	5	161.84099 (1.02)	59.03691 (1.05)	20.1 ± 5.5	20.6 ± 5.57	1.73 ± 0.31	0.82 ± 0.15	-79	0	0
390	3	161.50438 (0.37)	59.03508 (0.38)	19.7 ± 1.39	20.5 ± 1.6	2.35 ± 0.26	0 ± 0.07	162	-1	-0.9
391	3	161.63788 (1.35)	59.00404 (1.26)	14.7 ± 2.68	20.5 ± 5.48	7.73 ± 1.83	0 ± 0.85	51	-1	-0.6
392	2	161.75801 (1.32)	59.07967 (1.3)	13.6 ± 2.93	20.5 ± 4.83	8.23 ± 0.96	2.48 ± 0.7	-102	-0.1	-1.5
393	7	161.52201 (0.35)	59.01421 (0.34)	20.4 ± 1.71	20.4 ± 1.75	0.04 ± 0.13	0.04 ± 0.02	-134	-0.8	-0.9
394	2	161.47917 (0.4)	59.00202 (0.46)	18.1 ± 1.57	20.3 ± 2	3.96 ± 0.36	0.9 ± 0.21	-101	-0.6	-0.5
395	6	161.61273 (0.42)	58.97507 (0.44)	20.1 ± 1.91	20.3 ± 2.03	0.97 ± 0.26	0.19 ± 0.08	-77	-1.3	-0.9
396	2	161.54434 (0.39)	58.98248 (0.4)	19.3 ± 1.45	20.2 ± 1.65	2.27 ± 0.27	0.98 ± 0.07	-51	-1.4	-1.1
397	2	161.41601 (1.07)	59.12362 (1.05)	15 ± 2.72	20.2 ± 4.1	6.91 ± 0.77	1.58 ± 0.55	-126	0.1	1.6
398	3	161.25867 (1.26)	58.93416 (1.2)	15.3 ± 3.16	20.2 ± 4.72	6.98 ± 0.83	0 ± 0.58	61	1.3	0
399	1	161.62433 (0.54)	59.0209 (0.53)	15.3 ± 2.04	20.1 ± 3.02	5.23 ± 0.52	3.66 ± 0.39	-110	-1.1	-0.9

continued on the next page

C Catalogue continued

ID	Size Flag	RA (J2000) (arcsec)	Dec (J2000) (arcsec)	S_P ($\mu\text{Jy beam}^{-1}$)	S_T (μJy)	θ_{DM} (arcsec)	θ_{Dm} (arcsec)	ϕ (degrees)	α_{IF}	α_{IM}
400	3	161.28448 (1.08)	58.90608 (1.07)	17.2 ± 3.79	20 ± 4.49	4.69 ± 0.4	0 ± 0.17	-94	-0.7	0.3
401	2	161.55774 (1.33)	59.15762 (1.38)	12.1 ± 2.69	20 ± 4.8	9.24 ± 1.07	3.24 ± 0.81	163	1.6	0.3
402	5	161.67155 (0.87)	58.90501 (0.86)	19.6 ± 3.88	19.8 ± 3.92	1.18 ± 0.19	0.39 ± 0.06	168	0.7	-0.4
403	7	161.5502 (0.37)	59.01827 (0.37)	19.7 ± 1.7	19.7 ± 1.73	0.04 ± 0.13	0.04 ± 0.02	-115	-0.9	-1
404	6	161.3696 (0.43)	59.03589 (0.44)	19.7 ± 2.02	19.7 ± 2.06	0.6 ± 0.17	0.16 ± 0.03	30	-1.3	-1.1
405	6	161.61663 (0.57)	59.10692 (0.59)	19.5 ± 2.53	19.7 ± 2.6	1.01 ± 0.24	0.27 ± 0.05	-98	-1.2	-0.8
406	3	161.32292 (1.03)	58.91627 (1.03)	16.7 ± 3.14	19.7 ± 3.81	4.92 ± 0.39	0 ± 0.22	83	-2.2	-1.2
407	5	161.64582 (0.43)	58.99005 (0.53)	19.2 ± 2.2	19.6 ± 2.39	1.46 ± 0.34	0.32 ± 0.2	-99	-0.4	-0.6
408	6	161.6283 (0.42)	58.98537 (0.51)	19.2 ± 2.07	19.5 ± 2.25	1.36 ± 0.33	0.12 ± 0.17	-103	-0.4	0
409	2	161.46677 (0.61)	59.00449 (0.69)	14 ± 1.85	19.5 ± 3.26	7.6 ± 0.9	1.01 ± 0.53	-137	-0.3	0.7
410	5	161.77441 (0.83)	59.03001 (0.88)	19.2 ± 3.78	19.4 ± 3.81	1.05 ± 0.2	0.41 ± 0.05	-92	-1.6	-1.2
411	5	161.74297 (1.05)	59.10903 (1.05)	19 ± 4.27	19.3 ± 4.35	1.52 ± 0.35	0.39 ± 0.09	-130	-0.8	-1.8
412	3	161.36932 (1)	59.1495 (1.03)	17.6 ± 3.68	19.3 ± 4.13	3.67 ± 0.34	0 ± 0.11	-33	-1.4	-1.4
413	5	161.82564 (0.97)	58.99903 (0.95)	18.8 ± 4.89	19.3 ± 4.94	1.68 ± 0.29	0.61 ± 0.1	-150	-1.2	-0.9
414	7	161.2303 (0.94)	59.06888 (0.93)	19.2 ± 4.1	19.2 ± 4.13	0 ± 0.21	0 ± 0.07	88	-0.5	1.1
415	7	161.54297 (0.4)	59.04515 (0.4)	19.1 ± 1.71	19.1 ± 1.74	0 ± 0.14	0 ± 0.02	373	-1.5	-1.9
416	3	161.6133 (1.3)	58.90805 (1.41)	15.9 ± 3.42	19 ± 5.09	5.2 ± 1.22	0 ± 0.78	-76	-0.6	-1.4
417	7	161.2236 (0.93)	58.98478 (0.92)	19 ± 3.98	19 ± 4.01	0 ± 0.2	0 ± 0.07	-19	0	-1.2
418	3	161.44709 (1.01)	59.17753 (1.04)	17.3 ± 3.97	18.9 ± 4.37	3.42 ± 0.3	0 ± 0.11	-131	-2.2	-0.4
419	6	161.52608 (0.51)	59.11285 (0.51)	18.7 ± 2.52	18.8 ± 2.57	0.87 ± 0.21	0.28 ± 0.04	-173	-0.5	-0.1
420	5	161.76669 (0.86)	59.02971 (0.85)	18.5 ± 3.63	18.8 ± 3.66	1.18 ± 0.2	0.38 ± 0.06	175	-1.1	-1.4
421	3	161.67811 (1)	59.12516 (1.02)	17.5 ± 3.49	18.8 ± 3.85	3.16 ± 0.39	0 ± 0.09	-168	-0.1	-0.5
422	5	161.28646 (0.97)	59.13491 (0.95)	18.3 ± 4.67	18.8 ± 4.72	1.64 ± 0.28	0.6 ± 0.1	0	-1	-0.9
423	6	161.4259 (0.41)	59.03983 (0.41)	18.7 ± 1.77	18.7 ± 1.8	0.41 ± 0.15	0.11 ± 0.02	-145	-1.2	-0.8
424	3	161.28774 (0.94)	59.05411 (0.92)	15.5 ± 2.69	18.7 ± 3.48	5.43 ± 0.5	0 ± 0.34	-132	-0.1	-0.3
425	3	161.25638 (1.33)	59.06102 (1.34)	12.6 ± 2.74	18.7 ± 4.66	8.75 ± 1	0 ± 0.71	300	0.1	-1.2
426	7	161.63468 (0.97)	59.17182 (0.95)	18.7 ± 4.56	18.7 ± 4.61	0 ± 0.29	0 ± 0.1	-214	0	1.2
427	3	161.35537 (1.21)	58.91647 (1.17)	14 ± 2.8	18.6 ± 4.18	6.98 ± 0.79	0 ± 0.57	30	-1.1	-1.8
428	3	161.37596 (0.76)	59.11027 (0.77)	17.8 ± 2.74	18.5 ± 2.91	2.29 ± 0.25	0 ± 0.08	-327	-0.6	-0.9
429	5	161.19882 (1.01)	58.97069 (1.04)	18 ± 4.4	18.5 ± 4.47	1.77 ± 0.32	0.42 ± 0.11	-53	0	0
430	1	161.52334 (1.13)	59.16164 (1.1)	13.8 ± 2.97	18.5 ± 4.16	5.4 ± 0.52	3.91 ± 0.33	65	1.1	1.8
431	3	161.35593 (0.76)	59.02487 (0.78)	14.1 ± 2	18.4 ± 3.12	6.68 ± 0.75	0 ± 0.48	-140	-1.2	-1.4
432	3	161.45564 (0.75)	59.08113 (0.78)	13.8 ± 1.93	18.3 ± 3.13	6.98 ± 0.8	0 ± 0.51	-56	-0.7	-0.2
433	6	161.56201 (0.44)	58.95961 (0.45)	17.9 ± 1.87	18.1 ± 1.95	0.98 ± 0.23	0.24 ± 0.05	-128	-1.1	-1.5
434	3	161.4235 (0.43)	58.98904 (0.5)	16.9 ± 1.77	18.1 ± 2.03	3.15 ± 0.3	0 ± 0.13	-162	-0.6	-0.1
435	6	161.37869 (0.47)	58.97152 (0.49)	18 ± 2.06	18.1 ± 2.11	0.81 ± 0.2	0.22 ± 0.04	-140	-1.5	-0.5
436	3	161.36009 (0.88)	58.91885 (0.92)	16.1 ± 2.79	18.1 ± 3.24	4.15 ± 0.34	0 ± 0.17	-42	0.1	0.2
437	7	161.17707 (0.97)	58.99335 (0.95)	18.1 ± 4.4	18.1 ± 4.45	0 ± 0.29	0 ± 0.1	-11	-0.6	0.8
438	1	161.38273 (0.8)	59.1139 (0.81)	17.2 ± 2.7	18 ± 2.89	2.24 ± 0.25	1.17 ± 0.08	-71	-0.7	-0.4
439	7	161.69205 (0.77)	59.08791 (0.77)	18 ± 2.89	18 ± 2.94	0 ± 0.23	0 ± 0.06	-223	-1.1	-0.6
440	3	161.71276 (0.77)	58.98534 (0.84)	16.4 ± 2.68	18 ± 3.05	3.62 ± 0.35	0 ± 0.17	42	0	-0.2
441	2	161.73147 (0.88)	59.00447 (0.92)	15.7 ± 2.72	18 ± 3.15	4.08 ± 0.34	1.61 ± 0.17	56	-2.1	-1.8
442	6	161.56819 (0.44)	59.02445 (0.48)	17.3 ± 1.75	17.9 ± 2.06	1.95 ± 0.42	0 ± 0.28	-86	-0.5	-0.7
443	3	161.21044 (1.08)	59.04075 (1.07)	17.1 ± 3.83	17.9 ± 4.07	2.5 ± 0.3	0 ± 0.11	-97	-0.5	-0.9
444	5	161.34465 (0.69)	59.09574 (0.69)	17.6 ± 2.46	17.8 ± 2.53	1.11 ± 0.26	0.3 ± 0.06	-379	-1.4	-1
445	3	161.47227 (0.99)	59.15317 (0.99)	17.4 ± 2.91	17.8 ± 3.02	1.88 ± 0.21	0 ± 0.05	-157	-0.4	0
446	5	161.56174 (0.97)	59.17034 (0.95)	17.3 ± 4.36	17.7 ± 4.4	1.62 ± 0.27	0.59 ± 0.09	0	1.4	1.9
447	6	161.57061 (0.47)	59.07994 (0.49)	17.5 ± 2	17.6 ± 2.05	0.81 ± 0.2	0.22 ± 0.04	-58	-0.9	-0.3
448	3	161.46004 (0.92)	59.13758 (0.95)	15.6 ± 2.75	17.6 ± 3.19	4.22 ± 0.33	0 ± 0.15	5	0.1	-0.4
449	6	161.63357 (0.48)	59.04906 (0.5)	17.4 ± 2.03	17.5 ± 2.08	0.84 ± 0.2	0.22 ± 0.04	-39	-0.7	-0.5

continued on the next page

C Catalogue continued

ID	Size Flag	RA (J2000) (arcsec)	Dec (J2000) (arcsec)	S_P ($\mu\text{Jy beam}^{-1}$)	S_T (μJy)	θ_{DM} (arcsec)	θ_{Dm} (arcsec)	ϕ (degrees)	α_{IF}	α_{IM}
450	6	161.61214 (1.08)	58.90806 (1.07)	16.2 ± 3.1	17.5 ± 3.74	3.29 ± 0.85	0 ± 0.59	82	-0.4	-1.8
451	3	161.28503 (0.89)	58.97295 (0.92)	15.5 ± 2.69	17.5 ± 3.14	4.24 ± 0.33	0 ± 0.17	-150	-0.9	-0.6
452	6	161.49535 (0.48)	59.09193 (0.5)	17.3 ± 2.02	17.4 ± 2.07	0.84 ± 0.2	0.23 ± 0.04	-68	-1.1	-1.3
453	7	161.42651 (0.75)	59.12674 (0.75)	17.4 ± 2.69	17.4 ± 2.74	0 ± 0.23	0 ± 0.06	-213	-0.7	0.7
454	3	161.78729 (1.15)	59.03046 (1.12)	14.2 ± 3.05	17.4 ± 3.94	5.66 ± 0.57	0 ± 0.34	-339	1.4	0.3
455	5	161.73573 (0.8)	59.04365 (0.79)	17.1 ± 3.01	17.3 ± 3.05	1.15 ± 0.22	0.36 ± 0.06	-5	-1.3	-1.8
456	7	161.31432 (0.68)	59.06485 (0.69)	17.2 ± 2.31	17.2 ± 2.38	0 ± 0.26	0 ± 0.06	222	-0.7	-0.4
457	2	161.53366 (1.02)	58.87535 (1.05)	15.4 ± 3.24	17.2 ± 3.69	3.99 ± 0.33	0.47 ± 0.11	-112	0.7	-0.6
458	6	161.62752 (0.44)	58.99341 (0.55)	16.9 ± 2.05	17.1 ± 2.21	1.44 ± 0.34	0.14 ± 0.19	-91	-1.2	-0.2
459	6	161.64311 (0.49)	58.98694 (0.51)	17 ± 2.05	17.1 ± 2.1	0.89 ± 0.21	0.24 ± 0.04	171	-0.6	-0.9
460	3	161.50088 (0.92)	58.91777 (0.89)	13.9 ± 2.31	17.1 ± 3.13	5.76 ± 0.57	0 ± 0.39	-118	-1	-0.6
461	3	161.57685 (1.14)	59.13053 (1.11)	13.5 ± 2.63	17.1 ± 3.64	6.25 ± 0.64	0 ± 0.45	-132	-0.4	0.9
462	3	161.79523 (1)	59.05194 (1.03)	15.5 ± 3.53	17 ± 3.92	3.58 ± 0.31	0 ± 0.11	-43	0.2	1.5
463	6	161.48187 (0.45)	59.06634 (0.46)	16.9 ± 1.8	16.9 ± 1.84	0.68 ± 0.18	0.18 ± 0.03	165	-1.1	-1.2
464	7	161.4149 (0.78)	58.9072 (0.78)	16.9 ± 2.77	16.9 ± 2.81	0 ± 0.22	0 ± 0.06	7	-1.5	-2
465	3	161.72572 (1.04)	59.09067 (1.05)	15 ± 3.06	16.9 ± 3.52	4.16 ± 0.33	0 ± 0.12	-98	1.5	0.9
466	3	161.61484 (1.07)	59.09117 (1.13)	14.6 ± 2.42	16.8 ± 3.6	4.5 ± 1.02	0 ± 0.65	-71	0.4	0.1
467	7	161.41761 (0.85)	58.89762 (0.84)	16.8 ± 3.1	16.8 ± 3.13	0 ± 0.2	0 ± 0.06	-19	-0.8	-0.7
468	3	161.40847 (1.49)	59.00453 (1.58)	8.4 ± 1.92	16.8 ± 4.58	13.78 ± 1.53	0 ± 0.93	-52	-1.1	-0.8
469	5	161.42956 (0.87)	58.88999 (0.86)	16.6 ± 3.32	16.8 ± 3.34	1.18 ± 0.19	0.39 ± 0.06	-126	-0.8	0.4
470	1	161.65009 (0.94)	58.91871 (0.98)	14.8 ± 2.73	16.8 ± 3.17	3.85 ± 0.36	1.68 ± 0.11	-319	-1.5	-0.4
471	3	161.60736 (0.79)	59.02444 (0.86)	14.6 ± 2.17	16.7 ± 3.37	4.54 ± 1.03	0 ± 0.6	-87	-1	-0.7
472	3	161.27935 (1.03)	59.09482 (1.05)	15.6 ± 3.22	16.7 ± 3.53	3.1 ± 0.36	0 ± 0.09	-95	0.6	-0.2
473	3	161.52324 (1.15)	59.15243 (1.12)	13.6 ± 2.84	16.7 ± 3.68	5.66 ± 0.56	0 ± 0.34	135	-0.3	-0.3
474	5	161.25095 (0.97)	58.92837 (0.95)	16.3 ± 4.19	16.7 ± 4.23	1.66 ± 0.28	0.6 ± 0.1	46	2.1	-0.6
475	3	161.30485 (1)	59.08187 (1)	14.2 ± 2.59	16.6 ± 3.13	4.85 ± 0.38	0 ± 0.22	-161	-0.8	-1.7
476	5	161.29075 (0.97)	59.13193 (0.95)	16.2 ± 4.21	16.6 ± 4.25	1.68 ± 0.29	0.61 ± 0.1	-92	-1.7	1
477	5	161.35701 (0.97)	58.86939 (0.95)	16.2 ± 4.22	16.6 ± 4.26	1.68 ± 0.29	0.61 ± 0.1	92	1	0
478	3	161.63311 (1.11)	58.95813 (1.09)	11.9 ± 2.17	16.5 ± 3.49	7.76 ± 0.85	0 ± 0.59	-96	-2	-1.1
479	5	161.21991 (0.97)	59.03821 (0.95)	16.2 ± 3.82	16.5 ± 3.85	1.46 ± 0.23	0.52 ± 0.08	-184	-2	0
480	3	161.48816 (0.43)	59.03145 (0.51)	15.2 ± 1.63	16.4 ± 1.89	3.34 ± 0.31	0 ± 0.15	-2	-0.9	-0.3
481	3	161.47204 (0.61)	59.05175 (0.7)	14.7 ± 2	16.4 ± 3.02	3.98 ± 0.93	0 ± 0.53	30	-1.8	-1.4
482	3	161.60364 (1.1)	58.89603 (1.09)	13.9 ± 2.81	16.4 ± 3.42	4.98 ± 0.42	0 ± 0.23	-65	-0.5	-1.5
483	6	161.38686 (0.47)	59.0407 (0.49)	16.2 ± 1.87	16.3 ± 1.92	0.82 ± 0.2	0.22 ± 0.04	26	-1.6	-1.6
484	7	161.7021 (0.7)	59.01235 (0.71)	16.3 ± 2.28	16.3 ± 2.34	0 ± 0.25	0 ± 0.06	-158	-0.9	-0.8
485	3	161.74325 (0.96)	58.98698 (0.99)	15.1 ± 2.9	16.3 ± 3.23	3.29 ± 0.4	0 ± 0.09	-11	-0.4	-1.8
486	6	161.33588 (0.84)	59.09717 (0.86)	15.9 ± 2.58	16.2 ± 2.61	1.64 ± 0.19	0 ± 0.05	161	-1.8	-1.8
487	5	161.81037 (0.97)	58.97874 (0.95)	15.8 ± 4.09	16.2 ± 4.14	1.68 ± 0.29	0.61 ± 0.1	0	0	1.5
488	5	161.60005 (0.97)	59.14937 (0.95)	15.8 ± 3.66	16.1 ± 3.69	1.42 ± 0.23	0.51 ± 0.08	-188	0.2	-1.4
489	5	161.72223 (0.97)	59.11898 (0.95)	15.6 ± 4.02	16 ± 4.06	1.65 ± 0.28	0.6 ± 0.1	-54	0.2	-1.7
490	7	161.72177 (0.97)	58.91669 (0.95)	15.9 ± 3.86	15.9 ± 3.91	0 ± 0.29	0 ± 0.1	-194	0.7	-0.5
491	3	161.58761 (0.55)	58.97323 (0.63)	14.1 ± 1.95	15.8 ± 2.34	4.07 ± 0.37	0 ± 0.25	-102	-0.8	-1.1
492	3	161.69561 (0.77)	59.0059 (0.84)	14.3 ± 2.34	15.8 ± 2.67	3.67 ± 0.35	0 ± 0.17	24	-1.3	-1.5
493	7	161.39307 (0.97)	58.86676 (0.95)	15.7 ± 3.83	15.7 ± 3.88	0 ± 0.29	0 ± 0.1	0	0.2	0.7
494	6	161.49103 (0.48)	58.95944 (0.5)	15.5 ± 1.81	15.6 ± 1.85	0.84 ± 0.2	0.22 ± 0.04	34	-2.1	-1.8
495	7	161.7355 (0.91)	59.06225 (0.9)	15.6 ± 3.17	15.6 ± 3.19	0 ± 0.19	0 ± 0.06	68	1.2	-0.1
496	3	161.71708 (1.25)	58.9475 (1.2)	11.8 ± 2.45	15.6 ± 3.63	6.92 ± 0.81	0 ± 0.57	-89	-1.4	-1.6
497	5	161.58455 (0.47)	58.99223 (0.45)	15.4 ± 1.67	15.5 ± 1.72	0.83 ± 0.19	0.35 ± 0.04	-116	-0.7	-0.4
498	6	161.58703 (0.5)	58.96436 (0.52)	15.3 ± 1.88	15.5 ± 1.93	0.92 ± 0.22	0.25 ± 0.04	91	-1.7	-0.9
499	5	161.43019 (0.73)	59.11574 (0.73)	15.4 ± 2.35	15.5 ± 2.4	1.13 ± 0.24	0.32 ± 0.06	-31	-1.9	-1.9

continued on the next page

C Catalogue continued

ID	Size Flag	RA (J2000) (arcsec)	Dec (J2000) (arcsec)	S_P ($\mu\text{Jy beam}^{-1}$)	S_T (μJy)	θ_{DM} (arcsec)	θ_{Dm} (arcsec)	ϕ (degrees)	α_{IF}	α_{IM}
500	7	161.51968 (0.97)	59.17279 (0.95)	15.5 ± 3.76	15.5 ± 3.81	0 ± 0.29	0 ± 0.1	0	-0.3	-2.7
501	3	161.67333 (1.35)	59.03777 (1.49)	9.3 ± 2.08	15.4 ± 4.03	10.64 ± 1.18	0 ± 0.81	-132	-1.2	1
502	6	161.71775 (1.09)	58.94039 (1.08)	14.9 ± 3.03	15.4 ± 3.08	2.07 ± 0.27	0 ± 0.09	-183	0.4	-0.4
503	3	161.48467 (0.5)	59.04186 (0.55)	13.2 ± 1.74	15.2 ± 2.2	4.59 ± 0.42	0 ± 0.3	-95	-0.5	-1.7
504	7	161.40923 (0.76)	58.92226 (0.76)	15.2 ± 2.39	15.2 ± 2.43	0 ± 0.23	0 ± 0.06	4	-0.3	-0.6
505	6	161.52002 (0.46)	59.04573 (0.47)	15.1 ± 1.66	15.1 ± 1.7	0.74 ± 0.19	0.2 ± 0.04	26	-1.2	-0.9
506	5	161.5406 (0.85)	58.89724 (0.85)	14.9 ± 2.9	15.1 ± 2.92	1.18 ± 0.2	0.38 ± 0.06	-67	-2	-1.9
507	5	161.63002 (1.03)	59.13877 (1.04)	14.8 ± 3.31	15.1 ± 3.38	1.6 ± 0.37	0.34 ± 0.09	-80	-0.5	-1.2
508	5	161.27275 (1.01)	58.90824 (1.04)	14.6 ± 3.66	15.1 ± 3.71	1.8 ± 0.32	0.68 ± 0.11	-171	-1.3	0
509	3	161.48154 (1.02)	58.86653 (1.05)	13.5 ± 3.04	15.1 ± 3.45	3.99 ± 0.33	0 ± 0.11	-84	0	0.2
510	7	161.54064 (0.66)	59.10318 (0.67)	15 ± 1.98	15 ± 2.04	0 ± 0.25	0 ± 0.05	-2	-1.4	-0.6
511	6	161.29216 (1.04)	58.96862 (1.01)	14.3 ± 2.78	15 ± 3.17	2.53 ± 0.7	0 ± 0.5	-21	-2	0.9
512	3	161.40193 (0.96)	59.12578 (0.98)	13.9 ± 2.63	15 ± 2.92	3.15 ± 0.42	0 ± 0.08	-155	0.1	0.9
513	4	161.64246 (1.04)	59.14063 (1.05)	14.2 ± 3.4	15 ± 3.51	2.1 ± 0.32	1.55 ± 0.11	-47	1.2	0
514	5	161.48985 (0.86)	58.89559 (0.85)	14.7 ± 2.89	14.9 ± 2.92	1.18 ± 0.2	0.39 ± 0.06	101	-0.9	-1.4
515	3	161.71454 (1.02)	59.07411 (1.01)	14.5 ± 2.49	14.9 ± 2.61	2.05 ± 0.24	0 ± 0.06	-352	-0.8	-0.8
516	5	161.31012 (0.97)	58.89721 (0.95)	14.6 ± 3.78	14.9 ± 3.82	1.68 ± 0.29	0.61 ± 0.1	0	-0.1	0.8
517	6	161.58627 (0.9)	59.09665 (0.92)	13.8 ± 2.17	14.8 ± 2.75	3.11 ± 0.82	0 ± 0.53	-93	-1.3	0.3
518	7	161.7077 (0.79)	59.01057 (0.78)	14.8 ± 2.45	14.8 ± 2.49	0 ± 0.22	0 ± 0.06	-20	-0.9	-0.9
519	7	161.22271 (0.97)	58.97851 (0.95)	14.8 ± 3.61	14.8 ± 3.65	0 ± 0.29	0 ± 0.1	153	0.2	-1.5
520	7	161.33187 (0.67)	58.99859 (0.68)	14.7 ± 1.96	14.7 ± 2.02	0 ± 0.26	0 ± 0.06	-9	-0.8	-0.7
521	6	161.76456 (1.43)	58.98585 (1.57)	12.8 ± 3.3	14.7 ± 4.22	4.42 ± 1.36	0 ± 0.92	-64	-1.1	-1.1
522	3	161.72344 (1.15)	58.93581 (1.12)	12 ± 2.58	14.7 ± 3.33	5.66 ± 0.57	0 ± 0.34	362	-0.4	0.5
523	6	161.40262 (0.47)	59.02794 (0.55)	14.3 ± 1.88	14.6 ± 2.05	1.69 ± 0.37	0.1 ± 0.25	-75	-1.6	-1.3
524	7	161.72579 (0.88)	58.99045 (0.87)	14.6 ± 2.81	14.6 ± 2.84	0 ± 0.19	0 ± 0.06	238	-0.8	1.3
525	3	161.5133 (1.47)	59.09542 (1.61)	8 ± 1.88	14.6 ± 4.08	12.23 ± 1.39	0 ± 0.92	-70	-1.9	-1
526	1	161.24356 (1.01)	59.05422 (1.04)	13 ± 2.89	14.6 ± 3.3	3.82 ± 0.32	1.35 ± 0.11	-66	1	0.2
527	3	161.69693 (1.09)	58.91219 (1.07)	14 ± 3.35	14.6 ± 3.54	2.36 ± 0.3	0 ± 0.13	-129	-0.1	-0.9
528	6	161.56662 (0.48)	58.99501 (0.49)	14.5 ± 1.68	14.5 ± 1.72	0.83 ± 0.2	0.22 ± 0.04	-8	-2	-1.5
529	6	161.61656 (0.53)	58.99012 (0.55)	14.4 ± 1.81	14.5 ± 1.86	0.96 ± 0.23	0.26 ± 0.05	-57	-0.7	-0.4
530	6	161.60446 (0.56)	59.07106 (0.66)	14.3 ± 2.08	14.5 ± 2.21	1.55 ± 0.35	0.15 ± 0.22	-4	0.3	-0.8
531	5	161.52862 (0.74)	58.91811 (0.74)	14.3 ± 2.23	14.5 ± 2.27	1.13 ± 0.24	0.32 ± 0.06	59	-0.8	1.5
532	3	161.22349 (1.01)	59.02105 (1.04)	13.3 ± 3.05	14.5 ± 3.36	3.42 ± 0.3	0 ± 0.11	-128	0.1	-0.6
533	5	161.4128 (0.97)	58.87168 (0.95)	14.2 ± 3.67	14.5 ± 3.71	1.68 ± 0.29	0.61 ± 0.1	0	0	1.4
534	5	161.79901 (0.97)	59.03401 (0.95)	14.1 ± 3.66	14.5 ± 3.7	1.68 ± 0.29	0.61 ± 0.1	84	-0.3	-1.2
535	3	161.69863 (0.89)	59.04438 (0.9)	13.7 ± 2.31	14.4 ± 2.5	2.64 ± 0.33	0 ± 0.08	-161	-1.4	-0.6
536	5	161.61792 (0.97)	59.14459 (0.95)	14 ± 3.45	14.3 ± 3.48	1.56 ± 0.26	0.57 ± 0.09	0	0	-1.5
537	3	161.75028 (1.01)	58.98855 (1.04)	12.9 ± 2.77	14.3 ± 3.12	3.78 ± 0.33	0 ± 0.11	44	1.8	0.4
538	5	161.45683 (0.97)	59.16813 (0.95)	13.9 ± 3.62	14.3 ± 3.65	1.68 ± 0.29	0.61 ± 0.1	0	2	-0.6
539	3	161.37687 (1.07)	58.92101 (1.06)	12 ± 2.34	14.2 ± 2.87	5.02 ± 0.42	0 ± 0.24	-141	-1.1	-0.9
540	5	161.44772 (0.96)	58.88671 (0.94)	13.9 ± 3.2	14.2 ± 3.23	1.4 ± 0.22	0.5 ± 0.08	-135	-0.2	0.5
541	5	161.41781 (0.97)	59.14851 (0.95)	14 ± 3.36	14.2 ± 3.39	1.51 ± 0.24	0.54 ± 0.08	222	-0.3	-2
542	3	161.29843 (1.05)	59.1033 (1.05)	13.4 ± 2.97	14.2 ± 3.21	2.93 ± 0.31	0 ± 0.1	-90	0.1	0
543	3	161.27678 (1)	58.94347 (1.03)	12.9 ± 2.88	14.2 ± 3.21	3.67 ± 0.32	0 ± 0.11	-48	-0.5	-0.1
544	3	161.72109 (1.02)	58.98704 (1.04)	12.4 ± 2.4	14.1 ± 2.77	4.27 ± 0.32	0 ± 0.12	-109	-1.8	-0.1
545	5	161.5399 (0.97)	59.15229 (0.95)	13.8 ± 3.31	14.1 ± 3.34	1.5 ± 0.24	0.54 ± 0.08	-20	-0.8	-0.4
546	6	161.40002 (0.59)	59.03137 (0.57)	13.4 ± 1.89	14 ± 2.24	2.58 ± 0.6	0 ± 0.4	-40	-1.6	-2.2
547	5	161.71501 (0.83)	59.02842 (0.82)	13.8 ± 2.58	14 ± 2.61	1.17 ± 0.21	0.37 ± 0.06	-73	-1.3	-1.3
548	3	161.50319 (0.77)	59.10383 (0.83)	12.8 ± 2.05	13.9 ± 2.3	3.29 ± 0.35	0 ± 0.14	-78	-0.6	0.1
549	3	161.38961 (0.86)	59.09488 (0.86)	13.3 ± 2.15	13.9 ± 2.29	2.33 ± 0.27	0 ± 0.07	-26	-1.5	-0.3

continued on the next page

C Catalogue continued

ID	Size Flag	RA (J2000) (arcsec)	Dec (J2000) (arcsec)	S_P ($\mu\text{Jy beam}^{-1}$)	S_T (μJy)	θ_{DM} (arcsec)	θ_{Dm} (arcsec)	ϕ (degrees)	α_{IF}	α_{IM}
550	5	161.73319 (0.91)	59.04285 (0.89)	13.7 ± 2.91	13.9 ± 2.93	1.21 ± 0.18	0.41 ± 0.06	-24	-1.5	-1.5
551	3	161.51579 (0.95)	58.90318 (0.98)	12.9 ± 2.42	13.9 ± 2.71	3.3 ± 0.4	0 ± 0.09	-50	-1.9	-2.7
552	5	161.20322 (0.97)	59.04588 (0.95)	13.6 ± 3.53	13.9 ± 3.57	1.68 ± 0.29	0.61 ± 0.1	0	-0.3	0
553	5	161.43181 (0.81)	59.1185 (0.81)	13.7 ± 2.48	13.8 ± 2.51	1.16 ± 0.21	0.36 ± 0.06	-122	-0.4	-0.4
554	5	161.38533 (0.96)	58.90427 (0.99)	13.5 ± 2.83	13.8 ± 2.91	1.63 ± 0.39	0.35 ± 0.09	-82	-2.1	-0.9
555	6	161.77145 (1.33)	58.98043 (1.4)	12.6 ± 3.15	13.8 ± 3.79	3.6 ± 1.1	0 ± 0.77	68	-0.9	-0.1
556	6	161.57533 (0.46)	59.0255 (0.54)	13.6 ± 1.7	13.7 ± 1.79	1.23 ± 0.3	0.2 ± 0.13	29	-1.4	-1.6
557	6	161.45776 (0.5)	58.97474 (0.52)	13.6 ± 1.67	13.7 ± 1.71	0.93 ± 0.22	0.25 ± 0.04	-29	-1.4	-0.6
558	3	161.46972 (0.59)	59.06162 (0.68)	12.3 ± 1.76	13.7 ± 2.07	3.87 ± 0.35	0 ± 0.23	-53	-2.1	-0.2
559	3	161.395 (0.82)	58.95067 (0.86)	12.2 ± 2.03	13.7 ± 2.37	4.14 ± 0.35	0 ± 0.2	-156	-1.1	0
560	5	161.25345 (0.97)	58.98002 (0.95)	13.4 ± 3.13	13.6 ± 3.16	1.45 ± 0.23	0.52 ± 0.08	171	-1.3	-1.6
561	5	161.6362 (1.1)	59.13907 (1.08)	13.3 ± 3.29	13.6 ± 3.33	1.52 ± 0.29	0.64 ± 0.11	-145	0.2	-0.7
562	5	161.45451 (0.96)	59.1418 (1)	13.2 ± 2.79	13.5 ± 2.86	1.68 ± 0.36	0.42 ± 0.11	-89	1.6	-0.1
563	5	161.49897 (0.94)	59.14258 (0.92)	13.3 ± 2.97	13.5 ± 2.99	1.33 ± 0.21	0.46 ± 0.07	-250	0.5	0.4
564	5	161.76455 (1)	58.98702 (1.03)	13.2 ± 3.11	13.5 ± 3.16	1.71 ± 0.33	0.39 ± 0.11	85	-1	-1.2
565	5	161.64888 (0.96)	59.13959 (1.02)	13.3 ± 3.26	13.5 ± 3.3	1.5 ± 0.29	0.72 ± 0.12	-185	-0.8	-0.7
566	6	161.44801 (0.48)	59.03592 (0.55)	13.1 ± 1.77	13.4 ± 1.93	1.79 ± 0.38	0.07 ± 0.27	-51	-1	-0.5
567	3	161.49657 (0.73)	59.07948 (0.77)	11.7 ± 1.85	13.3 ± 2.23	4.34 ± 0.38	0 ± 0.28	-64	-1.6	-1.4
568	3	161.51676 (1.44)	59.07664 (1.58)	7.4 ± 1.72	13.3 ± 3.65	11.96 ± 1.34	0 ± 0.89	77	-0.2	-1.4
569	2	161.53446 (0.6)	58.98259 (0.69)	11.7 ± 1.68	13.2 ± 1.96	3.78 ± 0.35	1.39 ± 0.23	-13	0.3	-1.1
570	3	161.53017 (0.99)	58.90383 (1.02)	11.8 ± 2.33	13.1 ± 2.64	3.78 ± 0.35	0 ± 0.11	-31	0.4	-1.5
571	5	161.49354 (0.98)	58.8882 (1.02)	12.8 ± 2.81	13.1 ± 2.87	1.67 ± 0.35	0.34 ± 0.1	-85	-0.2	-1.1
572	6	161.62965 (1.03)	59.13064 (1.05)	12.8 ± 2.9	13.1 ± 2.94	1.76 ± 0.28	0 ± 0.12	172	0	0.1
573	5	161.42303 (0.97)	58.88585 (0.95)	12.8 ± 3.18	13.1 ± 3.21	1.59 ± 0.26	0.58 ± 0.09	-233	-0.6	-1
574	5	161.47965 (0.97)	58.87956 (0.95)	12.9 ± 3.21	13.1 ± 3.24	1.59 ± 0.26	0.58 ± 0.09	0	-1.9	-1.2
575	7	161.46141 (0.5)	58.99672 (0.52)	13 ± 1.56	13 ± 1.6	0 ± 0.22	0 ± 0.04	4	0.9	0.9
576	3	161.39297 (0.87)	58.94458 (0.91)	11.6 ± 2.02	13 ± 2.33	4.03 ± 0.35	0 ± 0.16	-145	-1.1	-0.4
577	5	161.68022 (1.01)	59.1025 (1.03)	12.7 ± 2.8	13 ± 2.87	1.6 ± 0.39	0.33 ± 0.08	-326	-0.7	0.2
578	1	161.53557 (0.85)	58.91624 (0.91)	11.9 ± 2.24	12.9 ± 2.51	2.89 ± 0.37	1.61 ± 0.14	-228	0.6	0.6
579	2	161.45633 (1.74)	58.9548 (1.85)	7.3 ± 1.9	12.9 ± 4.3	10.87 ± 2.35	2.33 ± 1.23	-86	-0.2	1.7
580	5	161.4326 (0.93)	59.15674 (1.01)	12.6 ± 3.04	12.9 ± 3.09	1.47 ± 0.29	0.72 ± 0.13	-104	1	-1.7
581	1	161.53404 (1.27)	59.12664 (1.21)	7.7 ± 1.59	12.9 ± 3.01	7.07 ± 0.84	6.06 ± 0.73	299	-1.8	-2
582	3	161.54584 (0.61)	59.05361 (0.68)	11.9 ± 1.64	12.8 ± 1.83	3.12 ± 0.3	0 ± 0.14	-63	-0.9	-0.8
583	3	161.46413 (0.89)	58.92563 (0.89)	12.3 ± 2.02	12.8 ± 2.16	2.35 ± 0.28	0 ± 0.07	-37	-0.4	-0.7
584	3	161.5301 (0.85)	59.10684 (0.91)	11.7 ± 2.04	12.8 ± 2.3	3.42 ± 0.37	0 ± 0.12	-87	-0.7	0.3
585	6	161.27684 (1.07)	59.02611 (1.04)	12.3 ± 2.53	12.8 ± 2.73	2.21 ± 0.55	0 ± 0.38	-134	0	-0.5
586	6	161.5867 (0.77)	59.02942 (0.81)	11.7 ± 1.74	12.7 ± 2.26	3.29 ± 0.83	0 ± 0.52	-13	-0.3	-0.5
587	5	161.58914 (0.68)	59.0744 (0.69)	12.5 ± 1.74	12.7 ± 1.78	1.11 ± 0.26	0.29 ± 0.06	0	-1.4	-1.6
588	5	161.31951 (0.89)	59.08114 (0.88)	12.5 ± 2.6	12.7 ± 2.62	1.19 ± 0.18	0.4 ± 0.06	114	-1.3	-1.7
589	3	161.29349 (1.01)	58.99307 (1)	12.1 ± 2.19	12.7 ± 2.34	2.49 ± 0.33	0 ± 0.07	32	0.2	1.3
590	3	161.63584 (1.04)	59.10951 (1.04)	12 ± 2.43	12.7 ± 2.64	2.84 ± 0.36	0 ± 0.09	-84	-0.2	-0.2
591	7	161.54077 (0.97)	59.1472 (0.95)	12.6 ± 2.97	12.6 ± 3	0 ± 0.27	0 ± 0.09	14	-1.8	-1.2
592	3	161.3342 (1.02)	59.13018 (1.04)	11.7 ± 2.69	12.6 ± 2.94	3.26 ± 0.29	0 ± 0.11	298	-0.1	-1.6
593	5	161.56703 (0.66)	58.95915 (0.67)	12.4 ± 1.69	12.5 ± 1.73	1.09 ± 0.25	0.29 ± 0.05	-22	-0.5	-0.4
594	5	161.50396 (0.9)	59.12228 (0.91)	12.3 ± 2.29	12.5 ± 2.35	1.35 ± 0.34	0.28 ± 0.08	-172	-0.5	-1.5
595	5	161.37082 (0.65)	59.01829 (0.66)	12.3 ± 1.85	12.4 ± 1.88	0.81 ± 0.18	0.38 ± 0.04	-72	-1.2	-1
596	7	161.41743 (0.76)	59.08879 (0.76)	12.4 ± 1.95	12.4 ± 1.99	0 ± 0.23	0 ± 0.06	96	-0.3	0.1
597	3	161.34304 (1.05)	58.92966 (1.05)	11.7 ± 2.47	12.4 ± 2.68	2.9 ± 0.34	0 ± 0.09	-124	-0.8	0.7
598	3	161.26675 (1.16)	59.00184 (1.12)	10.1 ± 2.16	12.4 ± 2.81	5.74 ± 0.58	0 ± 0.36	-90	-0.4	-1.3
599	5	161.38286 (0.65)	59.03491 (0.66)	12.2 ± 1.65	12.3 ± 1.7	1.08 ± 0.25	0.29 ± 0.05	-124	-0.4	0.2

continued on the next page

C Catalogue continued

ID	Size Flag	RA (J2000) (arcsec)	Dec (J2000) (arcsec)	S_P ($\mu\text{Jy beam}^{-1}$)	S_T (μJy)	θ_{DM} (arcsec)	θ_{Dm} (arcsec)	ϕ (degrees)	α_{IF}	α_{IM}
600	3	161.58806 (0.7)	58.98313 (0.77)	11.3 ± 1.69	12.2 ± 1.89	3.24 ± 0.32	0 ± 0.16	-125	-1	-1
601	7	161.46267 (0.71)	58.94951 (0.71)	12.2 ± 1.71	12.2 ± 1.76	0 ± 0.25	0 ± 0.06	121	-1.5	-1.2
602	5	161.64546 (0.89)	59.09572 (0.88)	12 ± 2.49	12.2 ± 2.5	1.19 ± 0.19	0.4 ± 0.06	-50	-0.9	-0.8
603	5	161.42111 (0.97)	59.13197 (0.95)	12 ± 2.77	12.2 ± 2.79	1.42 ± 0.23	0.5 ± 0.08	-147	-1.4	-2.2
604	3	161.37222 (1.17)	58.9402 (1.13)	9.9 ± 1.98	12.2 ± 2.63	5.89 ± 0.58	0 ± 0.39	-312	-0.4	2
605	6	161.30164 (1.26)	59.11454 (1.2)	11.7 ± 2.78	12.2 ± 3.15	2.34 ± 0.83	0.04 ± 0.58	74	0.4	-1
606	3	161.36454 (0.8)	59.02246 (0.86)	10.9 ± 1.8	12.1 ± 2.09	3.96 ± 0.35	0 ± 0.19	128	-0.6	-0.9
607	3	161.49406 (0.92)	59.10009 (0.94)	10.6 ± 1.86	12.1 ± 2.19	4.45 ± 0.33	0 ± 0.18	-121	-0.4	-1.2
608	5	161.55567 (0.91)	58.90834 (0.9)	12 ± 2.55	12.1 ± 2.57	1.22 ± 0.19	0.42 ± 0.06	-5	-0.5	0.3
609	3	161.62366 (0.95)	58.93659 (0.99)	11 ± 2.1	12.1 ± 2.36	3.67 ± 0.36	0 ± 0.1	3	-0.9	-0.5
610	3	161.68823 (1.06)	59.012 (1.05)	10.3 ± 1.96	12.1 ± 2.41	5.01 ± 0.42	0 ± 0.24	1	-0.4	-0.2
611	5	161.24204 (0.97)	59.00957 (0.95)	11.8 ± 2.98	12.1 ± 3.01	1.61 ± 0.27	0.59 ± 0.09	147	-1	1.4
612	3	161.64254 (1.01)	59.12423 (1.04)	11.2 ± 2.56	12.1 ± 2.81	3.39 ± 0.3	0 ± 0.11	10	-0.8	-0.6
613	3	161.67701 (1.01)	58.91836 (1.04)	10.9 ± 2.47	12.1 ± 2.77	3.78 ± 0.32	0 ± 0.11	50	0.8	0.4
614	3	161.71994 (1.03)	59.09356 (1.04)	11.3 ± 2.6	12.1 ± 2.83	3.21 ± 0.29	0 ± 0.11	-136	-1.3	-1.8
615	3	161.50062 (1.01)	59.15588 (1.04)	11 ± 2.48	12.1 ± 2.78	3.78 ± 0.32	0 ± 0.11	-122	0.2	-1.1
616	3	161.41474 (0.91)	58.97559 (0.89)	10 ± 1.7	12 ± 2.18	5.3 ± 0.49	0 ± 0.33	-53	-2.2	-0.7
617	5	161.57043 (1)	58.89952 (1.02)	11.8 ± 2.43	12 ± 2.46	1.32 ± 0.22	0.45 ± 0.07	32	0.2	-0.7
618	7	161.44143 (0.63)	58.97808 (0.65)	11.9 ± 1.56	11.9 ± 1.6	0 ± 0.25	0 ± 0.05	186	-1.7	-1.7
619	6	161.50422 (0.71)	58.94845 (0.75)	11.8 ± 1.82	11.9 ± 1.87	1.1 ± 0.27	0.25 ± 0.11	-204	-0.9	-0.6
620	3	161.56242 (1.04)	59.12632 (1.05)	11.2 ± 2.36	11.9 ± 2.57	3.02 ± 0.36	0 ± 0.09	-80	-1.2	-1.6
621	5	161.27775 (1.02)	58.95318 (1.04)	11.6 ± 2.78	11.9 ± 2.82	1.6 ± 0.32	0.38 ± 0.1	67	0.1	-1.6
622	5	161.77391 (0.97)	59.03535 (0.95)	11.6 ± 3.01	11.9 ± 3.04	1.68 ± 0.29	0.61 ± 0.1	-314	0.8	-0.7
623	3	161.68732 (1.1)	58.91392 (1.08)	11.4 ± 2.75	11.9 ± 2.89	2.26 ± 0.3	0 ± 0.13	-12	0.8	1.3
624	6	161.64257 (0.71)	58.99484 (0.76)	11.8 ± 1.97	11.8 ± 1.99	0.97 ± 0.18	0 ± 0.05	-142	-0.6	-0.3
625	3	161.45466 (0.82)	59.08469 (0.87)	10.7 ± 1.8	11.8 ± 2.06	3.78 ± 0.36	0 ± 0.16	1	-0.6	-0.6
626	5	161.53233 (0.88)	58.9134 (0.87)	11.6 ± 2.38	11.8 ± 2.4	1.19 ± 0.19	0.4 ± 0.06	0	-0.7	0
627	7	161.47566 (0.7)	59.07655 (0.7)	11.7 ± 1.61	11.7 ± 1.66	0 ± 0.25	0 ± 0.06	-143	-1.4	-0.7
628	6	161.59777 (1.32)	59.12774 (1.27)	10.9 ± 2.55	11.7 ± 2.97	3.09 ± 0.9	0 ± 0.65	-15	1.6	-1.1
629	5	161.27181 (0.97)	58.96365 (0.95)	11.5 ± 2.8	11.7 ± 2.82	1.54 ± 0.25	0.56 ± 0.09	0	-0.7	-1.5
630	5	161.25475 (1.1)	58.97968 (1.08)	11.5 ± 2.86	11.7 ± 2.9	1.52 ± 0.29	0.62 ± 0.12	-103	-1.3	-1.6
631	6	161.58841 (1.07)	59.14396 (1.07)	11.4 ± 2.79	11.7 ± 2.83	1.95 ± 0.31	0 ± 0.14	-155	1.1	1.7
632	5	161.30026 (0.97)	58.95454 (0.95)	11.4 ± 2.67	11.6 ± 2.7	1.46 ± 0.23	0.52 ± 0.08	0	0.4	0.8
633	7	161.33686 (0.97)	59.12367 (0.95)	11.6 ± 2.82	11.6 ± 2.85	0 ± 0.29	0 ± 0.1	15	0.1	-1.8
634	3	161.24071 (1.09)	58.98455 (1.07)	11.2 ± 2.69	11.6 ± 2.83	2.3 ± 0.3	0 ± 0.13	-132	-1.9	-1.2
635	5	161.5402 (0.71)	58.9542 (0.72)	11.3 ± 1.68	11.5 ± 1.72	1.12 ± 0.25	0.31 ± 0.06	-36	0	0.4
636	3	161.40328 (1)	58.89862 (1.03)	10.4 ± 2.37	11.4 ± 2.63	3.6 ± 0.31	0 ± 0.11	-140	-0.7	-1.2
637	7	161.59044 (0.69)	59.04088 (0.69)	11.3 ± 1.53	11.3 ± 1.57	0 ± 0.26	0 ± 0.06	92	-1.3	-1
638	3	161.50103 (0.74)	59.02063 (0.77)	9.8 ± 1.55	11.3 ± 1.89	4.48 ± 0.4	0 ± 0.3	-92	-1.4	-1.4
639	5	161.53725 (0.78)	59.09275 (0.78)	11.2 ± 1.89	11.3 ± 1.92	1.15 ± 0.23	0.35 ± 0.06	31	-2	-2.3
640	5	161.3734 (0.84)	58.95119 (0.84)	11.2 ± 2.13	11.3 ± 2.15	1.17 ± 0.2	0.38 ± 0.06	-40	-1.9	-2
641	5	161.30038 (0.97)	58.92716 (0.95)	11 ± 2.86	11.3 ± 2.89	1.68 ± 0.29	0.61 ± 0.1	167	-0.8	0
642	3	161.33119 (1.04)	59.11272 (1.05)	10 ± 2.23	11.3 ± 2.56	4.17 ± 0.34	0 ± 0.11	-134	-0.5	-1.4
643	6	161.51695 (0.61)	58.98242 (0.69)	11 ± 1.67	11.2 ± 1.77	1.61 ± 0.36	0.14 ± 0.24	-79	-0.6	-0.9
644	3	161.47681 (1.19)	58.94982 (1.15)	8.4 ± 1.68	11.2 ± 2.5	6.98 ± 0.78	0 ± 0.57	23	-0.4	-0.9
645	5	161.28203 (0.97)	58.95532 (0.95)	11 ± 2.77	11.2 ± 2.8	1.62 ± 0.27	0.59 ± 0.09	0	-0.9	-1.8
646	7	161.29197 (0.97)	58.95044 (0.95)	11.2 ± 2.68	11.2 ± 2.71	0 ± 0.28	0 ± 0.1	102	-1	-0.8
647	6	161.52233 (0.56)	59.0036 (0.66)	11 ± 1.58	11.1 ± 1.66	1.42 ± 0.33	0.19 ± 0.19	-99	-0.8	0.3
648	7	161.53229 (0.65)	59.04752 (0.66)	11.1 ± 1.46	11.1 ± 1.5	0 ± 0.25	0 ± 0.05	-74	-0.6	-1.1
649	3	161.46035 (0.99)	59.07625 (0.97)	9.2 ± 1.65	11.1 ± 2.12	5.43 ± 0.49	0 ± 0.33	-145	-1.3	-1.1

continued on the next page

C Catalogue continued

ID	Size Flag	RA (J2000) (arcsec)	Dec (J2000) (arcsec)	S_P ($\mu\text{Jy beam}^{-1}$)	S_T (μJy)	θ_{DM} (arcsec)	θ_{Dm} (arcsec)	ϕ (degrees)	α_{IF}	α_{IM}
650	3	161.52394 (1.47)	58.96979 (1.61)	6.1 ± 1.45	11.1 ± 3.14	12.21 ± 1.43	0 ± 0.95	-270	-1.6	2.5
651	7	161.25862 (0.97)	59.06814 (0.95)	11.1 ± 2.71	11.1 ± 2.74	0 ± 0.29	0 ± 0.1	193	1.1	-0.8
652	3	161.46356 (0.99)	59.07979 (0.97)	9.2 ± 1.66	11 ± 2.08	5.2 ± 0.45	0 ± 0.29	-136	-0.7	-2.1
653	5	161.70283 (0.97)	58.9711 (0.95)	10.8 ± 2.5	11 ± 2.52	1.43 ± 0.23	0.51 ± 0.08	-164	-0.1	-0.9
654	5	161.43861 (1.02)	59.1536 (1.04)	10.7 ± 2.68	11 ± 2.72	1.85 ± 0.33	0.44 ± 0.11	-89	-2.1	1
655	3	161.58797 (0.79)	59.04684 (0.83)	10.2 ± 1.64	10.9 ± 1.82	3.14 ± 0.35	0 ± 0.12	-92	-2	-1
656	6	161.69265 (1.01)	59.05962 (1)	10.8 ± 2.09	10.9 ± 2.12	1.27 ± 0.28	0.28 ± 0.06	-127	0.2	-0.1
657	3	161.37838 (1.12)	58.94489 (1.1)	9.1 ± 1.84	10.9 ± 2.3	5.27 ± 0.48	0 ± 0.28	-105	-0.9	-0.4
658	7	161.74537 (0.97)	58.9993 (0.95)	10.9 ± 2.65	10.9 ± 2.68	0 ± 0.29	0 ± 0.1	0	-0.2	-2
659	7	161.51453 (0.8)	59.0898 (0.8)	10.8 ± 1.83	10.8 ± 1.86	0 ± 0.22	0 ± 0.06	-124	-1	0.4
660	2	161.56786 (1.33)	59.08793 (1.4)	6.3 ± 1.41	10.8 ± 2.57	9.46 ± 1.1	3.75 ± 0.85	344	0.4	1.2
661	5	161.40182 (0.73)	59.04904 (0.74)	10.6 ± 1.65	10.7 ± 1.68	1.13 ± 0.24	0.32 ± 0.06	-88	-1.2	-1.6
662	6	161.62993 (0.77)	58.98854 (0.85)	10.5 ± 1.83	10.7 ± 1.9	1.57 ± 0.35	0.23 ± 0.16	-92	0.2	-0.3
663	6	161.59173 (0.74)	58.97244 (0.79)	10.6 ± 1.81	10.7 ± 1.82	1.12 ± 0.19	0 ± 0.05	150	-0.9	0.4
664	1	161.60031 (0.91)	59.05963 (0.96)	8.9 ± 1.61	10.7 ± 2.01	3.76 ± 0.36	3.56 ± 0.13	-81	0.8	-2
665	5	161.3081 (0.97)	58.92683 (0.95)	10.4 ± 2.7	10.7 ± 2.73	1.68 ± 0.29	0.61 ± 0.1	-110	-2.1	0
666	7	161.39443 (0.77)	58.98374 (0.77)	10.6 ± 1.71	10.6 ± 1.74	0 ± 0.23	0 ± 0.06	-85	-1.1	-0.1
667	5	161.62836 (0.76)	59.06098 (0.82)	10.5 ± 2.01	10.6 ± 2.02	1.04 ± 0.19	0.48 ± 0.05	31	0.5	-1
668	6	161.48687 (0.9)	59.10587 (0.93)	10.4 ± 1.96	10.6 ± 2.02	1.74 ± 0.34	0.24 ± 0.15	-122	-1.9	-1.7
669	6	161.61424 (0.91)	59.09356 (0.96)	10.4 ± 2.04	10.6 ± 2.09	1.68 ± 0.36	0.27 ± 0.12	64	-0.3	-0.2
670	7	161.37902 (0.9)	59.08801 (0.89)	10.6 ± 2.14	10.6 ± 2.16	0 ± 0.18	0 ± 0.06	-124	-0.8	-1.2
671	7	161.3037 (0.97)	59.0564 (0.95)	10.6 ± 2.35	10.6 ± 2.37	0 ± 0.23	0 ± 0.08	77	-0.2	0.4
672	3	161.30436 (1.05)	59.06949 (1.06)	9.3 ± 2.05	10.6 ± 2.38	4.4 ± 0.35	0 ± 0.12	-46	-1.2	-0.5
673	3	161.56376 (0.8)	59.04931 (0.83)	9.9 ± 1.57	10.5 ± 1.73	2.87 ± 0.33	0 ± 0.11	-20	-1	-2.2
674	5	161.37597 (0.78)	58.99344 (0.84)	10.3 ± 1.79	10.5 ± 1.86	1.63 ± 0.35	0.34 ± 0.18	-174	-1	-2.2
675	6	161.64198 (0.84)	59.05758 (0.9)	10.3 ± 1.92	10.5 ± 1.99	1.59 ± 0.37	0.26 ± 0.13	22	-1.1	-0.5
676	4	161.71304 (1.08)	59.04614 (1.08)	9.9 ± 2.22	10.5 ± 2.35	1.99 ± 0.38	1.99 ± 0.19	-67	-0.5	-1.2
677	3	161.70078 (1.14)	58.98811 (1.11)	8.7 ± 1.86	10.5 ± 2.37	5.48 ± 0.53	0 ± 0.31	-89	-1.3	-0.6
678	5	161.36988 (0.97)	59.13386 (0.95)	10.2 ± 2.66	10.5 ± 2.68	1.68 ± 0.29	0.61 ± 0.1	-254	0.6	0.1
679	3	161.27196 (1.1)	59.04928 (1.09)	8.9 ± 1.94	10.5 ± 2.35	4.98 ± 0.45	0 ± 0.22	159	-1.7	-1.3
680	3	161.47412 (0.74)	58.99912 (0.79)	9.6 ± 1.48	10.4 ± 1.64	3.13 ± 0.33	0 ± 0.14	-165	0.1	-0.2
681	3	161.4106 (0.92)	58.97993 (0.93)	9.1 ± 1.59	10.4 ± 1.88	4.48 ± 0.34	0 ± 0.19	-130	0.5	0.3
682	5	161.55214 (0.87)	59.10078 (0.86)	10.3 ± 2.05	10.4 ± 2.07	1.18 ± 0.19	0.39 ± 0.06	-106	-0.9	-0.7
683	5	161.62026 (1.04)	58.91939 (1.05)	10.2 ± 2.36	10.4 ± 2.41	1.57 ± 0.34	0.36 ± 0.1	-113	0.7	0.5
684	6	161.63354 (0.81)	59.01189 (0.85)	10.1 ± 1.77	10.3 ± 1.83	1.45 ± 0.36	0.28 ± 0.11	-96	-0.9	-0.4
685	3	161.47128 (1.02)	59.10031 (1.03)	9.1 ± 1.73	10.3 ± 2.01	4.4 ± 0.32	0 ± 0.13	-91	0	-1.1
686	5	161.67755 (0.96)	58.95974 (0.95)	10.1 ± 2.34	10.3 ± 2.36	1.41 ± 0.22	0.5 ± 0.08	136	-0.8	0
687	5	161.32004 (0.97)	59.07288 (0.95)	10.1 ± 2.35	10.3 ± 2.36	1.43 ± 0.23	0.51 ± 0.08	0	-0.6	-1.9
688	7	161.49079 (0.97)	58.90885 (0.95)	10.3 ± 2.31	10.3 ± 2.33	0 ± 0.24	0 ± 0.08	-55	0.9	1
689	3	161.70977 (1.06)	59.06005 (1.07)	9 ± 1.98	10.3 ± 2.31	4.48 ± 0.37	0 ± 0.13	-114	0.8	0.5
690	5	161.3547 (0.83)	58.99743 (0.83)	10.1 ± 1.89	10.2 ± 1.91	1.17 ± 0.21	0.37 ± 0.06	-8	-1	-1.1
691	6	161.32453 (0.96)	59.00152 (0.95)	10.1 ± 1.87	10.2 ± 1.89	1.16 ± 0.25	0.27 ± 0.06	-116	-0.2	-0.7
692	3	161.49263 (1.12)	59.03543 (1.09)	7.7 ± 1.44	10.2 ± 2.18	6.98 ± 0.78	0 ± 0.56	-6	-0.9	-0.7
693	5	161.76352 (1)	58.98528 (1.03)	9.9 ± 2.48	10.2 ± 2.52	1.73 ± 0.31	0.43 ± 0.11	-41	-1.1	0
694	3	161.58198 (0.82)	59.01644 (0.87)	9.1 ± 1.53	10.1 ± 1.76	3.78 ± 0.36	0 ± 0.16	-16	-1.4	0.1
695	5	161.50426 (0.96)	59.12089 (0.94)	9.9 ± 2.27	10.1 ± 2.29	1.39 ± 0.22	0.49 ± 0.07	112	-0.6	-0.9
696	5	161.61039 (0.97)	58.89666 (0.95)	9.8 ± 2.55	10.1 ± 2.57	1.68 ± 0.29	0.61 ± 0.1	0	-0.7	-0.4
697	5	161.51958 (0.94)	58.9187 (0.98)	9.8 ± 2.03	10 ± 2.08	1.67 ± 0.37	0.31 ± 0.1	-77	-0.5	-0.5
698	6	161.70738 (1.43)	59.01543 (1.57)	8.7 ± 2.23	10 ± 2.86	4.51 ± 1.35	0 ± 0.94	70	-0.3	0
699	3	161.45104 (0.91)	59.08152 (0.96)	9 ± 1.64	9.9 ± 1.85	3.59 ± 0.38	0 ± 0.11	-11	-1.7	-1.6

C Catalogue continued

ID	Size Flag	RA (J2000) (arcsec)	Dec (J2000) (arcsec)	S_P ($\mu\text{Jy beam}^{-1}$)	S_T (μJy)	θ_{DM} (arcsec)	θ_{Dm} (arcsec)	ϕ (degrees)	α_{IF}	α_{IM}
700	3	161.62599 (1.41)	58.96725 (1.54)	8.4 ± 2.05	9.9 ± 2.98	5.05 ± 1.29	0 ± 0.86	-19	-1.7	0.5
701	7	161.32979 (0.94)	59.05256 (0.92)	9.9 ± 2.09	9.9 ± 2.11	0 ± 0.21	0 ± 0.07	70	0.9	1.6
702	5	161.55597 (0.97)	58.89361 (0.95)	9.7 ± 2.51	9.9 ± 2.54	1.68 ± 0.29	0.61 ± 0.1	0	-0.8	0
703	6	161.552 (0.73)	58.98306 (0.81)	9.6 ± 1.6	9.8 ± 1.67	1.54 ± 0.34	0.21 ± 0.18	-111	-1.4	-1.8
704	3	161.5002 (0.81)	58.9845 (0.87)	8.8 ± 1.49	9.8 ± 1.7	3.81 ± 0.35	0 ± 0.17	-86	-1.3	-0.7
705	3	161.46299 (0.9)	59.06276 (0.93)	8.6 ± 1.51	9.8 ± 1.76	4.24 ± 0.33	0 ± 0.16	-83	-1.7	-2.9
706	7	161.45136 (0.97)	59.13763 (0.95)	9.8 ± 2.38	9.8 ± 2.41	0 ± 0.29	0 ± 0.1	-230	-1	-2.7
707	6	161.54588 (0.8)	59.05818 (0.83)	9.5 ± 1.55	9.7 ± 1.57	1.56 ± 0.19	0 ± 0.05	-144	-1.9	-1.8
708	3	161.54321 (1.73)	58.96444 (1.83)	7.1 ± 1.83	9.7 ± 3.27	7.47 ± 1.88	0 ± 1.04	10	-1.1	1.2
709	7	161.475 (0.97)	59.11486 (0.95)	9.7 ± 2.13	9.7 ± 2.15	0 ± 0.23	0 ± 0.08	64	-0.5	-1.3
710	7	161.35603 (0.97)	59.08916 (0.95)	9.7 ± 2.19	9.7 ± 2.21	0 ± 0.24	0 ± 0.08	19	-0.1	-1.4
711	6	161.4542 (0.74)	58.97673 (0.78)	9.6 ± 1.68	9.6 ± 1.7	0.42 ± 0.2	0 ± 0.06	-85	0	0
712	5	161.4844 (0.91)	59.10587 (0.9)	9.5 ± 2.03	9.6 ± 2.05	1.24 ± 0.19	0.42 ± 0.06	-120	-1.5	-0.8
713	5	161.53806 (0.94)	58.92539 (0.98)	9.4 ± 1.93	9.6 ± 1.98	1.67 ± 0.37	0.3 ± 0.1	45	-1.4	-1.1
714	6	161.29239 (0.88)	59.05262 (0.99)	9.5 ± 1.9	9.6 ± 1.93	1.04 ± 0.28	0 ± 0.11	283	-0.3	-1
715	6	161.52343 (1.26)	58.8865 (1.2)	9.2 ± 2.2	9.6 ± 2.49	2.34 ± 0.83	0.05 ± 0.58	34	0.5	-0.8
716	5	161.48011 (0.89)	58.93344 (0.88)	9.4 ± 1.96	9.5 ± 1.97	1.19 ± 0.18	0.4 ± 0.06	-57	-0.7	-1.7
717	5	161.59181 (0.78)	59.02486 (0.78)	9.3 ± 1.58	9.4 ± 1.6	1.15 ± 0.22	0.35 ± 0.06	-26	0	0.2
718	3	161.39196 (1)	58.94865 (1.03)	8.6 ± 1.78	9.4 ± 1.98	3.52 ± 0.34	0 ± 0.1	-34	0	-0.3
719	3	161.38886 (1.1)	58.93704 (1.08)	9.1 ± 1.94	9.4 ± 2.05	2.26 ± 0.29	0 ± 0.1	-40	-0.7	-2.1
720	7	161.34793 (0.97)	58.93784 (0.95)	9.4 ± 2.25	9.4 ± 2.27	0 ± 0.27	0 ± 0.1	36	1.2	0.3
721	5	161.5056 (0.75)	59.04715 (0.75)	9.2 ± 1.47	9.3 ± 1.49	1.14 ± 0.24	0.33 ± 0.06	-127	-1.1	-0.8
722	7	161.60505 (0.87)	59.06158 (0.86)	9.3 ± 1.79	9.3 ± 1.8	0 ± 0.19	0 ± 0.06	-105	0.3	-0.3
723	5	161.3451 (0.89)	59.01142 (0.88)	9.2 ± 1.9	9.3 ± 1.92	1.19 ± 0.19	0.4 ± 0.06	-14	-1.4	-2.1
724	5	161.70476 (0.97)	58.99821 (0.95)	9.1 ± 2.23	9.3 ± 2.25	1.54 ± 0.25	0.56 ± 0.09	-18	0.7	-1
725	7	161.27941 (0.97)	59.04987 (0.95)	9.3 ± 2.26	9.3 ± 2.29	0 ± 0.29	0 ± 0.1	0	-0.5	-1.2
726	3	161.49791 (0.84)	58.98922 (0.89)	8.5 ± 1.45	9.2 ± 1.62	3.24 ± 0.37	0 ± 0.12	-104	-0.6	-0.8
727	5	161.38534 (0.82)	59.01414 (0.82)	9.1 ± 1.68	9.2 ± 1.7	1.17 ± 0.21	0.37 ± 0.06	-241	-1.7	-1.8
728	5	161.43169 (0.9)	58.94293 (0.89)	9.1 ± 1.92	9.2 ± 1.93	1.2 ± 0.18	0.41 ± 0.06	-136	-0.3	0.6
729	5	161.33765 (0.84)	59.01465 (0.91)	9.1 ± 2.23	9.2 ± 2.25	1.28 ± 0.24	0.57 ± 0.08	-9	-1.6	0.4
730	5	161.67857 (1.04)	58.98011 (1.05)	9.1 ± 2.02	9.2 ± 2.06	1.52 ± 0.35	0.38 ± 0.09	-134	-0.6	-0.7
731	5	161.36409 (0.97)	58.92167 (0.95)	9 ± 2.34	9.2 ± 2.36	1.68 ± 0.29	0.61 ± 0.1	-9	-0.6	-0.3
732	5	161.27533 (1.06)	58.98571 (1.06)	8.9 ± 2.28	9.1 ± 2.3	1.52 ± 0.29	0.53 ± 0.12	-181	0.5	-0.7
733	5	161.5212 (0.97)	58.88749 (0.95)	8.9 ± 2.31	9.1 ± 2.34	1.68 ± 0.29	0.61 ± 0.1	26	-0.7	-1.5
734	5	161.51817 (0.97)	58.88766 (0.95)	8.9 ± 2.31	9.1 ± 2.33	1.68 ± 0.29	0.61 ± 0.1	0	-1.6	-1.7
735	5	161.51167 (0.86)	58.95118 (0.85)	8.9 ± 1.74	9 ± 1.76	1.18 ± 0.2	0.39 ± 0.06	-46	0.7	0.9
736	5	161.65248 (0.93)	59.04609 (0.91)	8.8 ± 1.93	9 ± 1.94	1.28 ± 0.2	0.44 ± 0.07	-103	-2	-1.5
737	5	161.73007 (0.97)	59.03682 (0.95)	8.7 ± 2.27	9 ± 2.29	1.68 ± 0.29	0.61 ± 0.1	-131	-1.8	-1
738	5	161.26612 (1.08)	58.98869 (1.07)	8.8 ± 2.3	9 ± 2.32	1.54 ± 0.29	0.61 ± 0.13	-299	-0.8	-1.6
739	5	161.25199 (0.97)	59.02089 (0.95)	8.8 ± 2.27	9 ± 2.3	1.68 ± 0.29	0.61 ± 0.1	231	-0.3	-0.8
740	7	161.63177 (0.97)	59.12232 (0.95)	9 ± 2.2	9 ± 2.23	0 ± 0.29	0 ± 0.1	-58	2.2	1.5
741	5	161.52578 (0.84)	59.07064 (0.89)	8.7 ± 1.61	8.9 ± 1.66	1.55 ± 0.37	0.53 ± 0.12	-118	-1.3	0
742	5	161.38249 (0.86)	59.03765 (0.85)	8.8 ± 1.72	8.9 ± 1.74	1.18 ± 0.2	0.38 ± 0.06	72	0	-1.3
743	3	161.61541 (1.35)	59.03981 (1.48)	7.5 ± 1.81	8.8 ± 2.55	4.82 ± 1.19	0 ± 0.81	-102	-1.3	-1.3
744	5	161.60247 (0.93)	58.95191 (0.92)	8.7 ± 1.91	8.8 ± 1.93	1.31 ± 0.2	0.45 ± 0.07	-3	-0.3	-1.1
745	3	161.62386 (0.98)	59.03348 (1.01)	7.9 ± 1.54	8.8 ± 1.74	3.78 ± 0.35	0 ± 0.11	14	0.6	0.5
746	7	161.34532 (0.97)	59.0668 (0.95)	8.8 ± 1.99	8.8 ± 2.01	0 ± 0.24	0 ± 0.08	-21	-1.2	-1.2
747	6	161.63907 (1.14)	59.1018 (1.11)	8.5 ± 2.03	8.8 ± 2.14	2.16 ± 0.54	0 ± 0.33	9	0.5	-0.3
748	3	161.46869 (1.02)	58.9248 (1.04)	7.9 ± 1.73	8.8 ± 1.96	3.93 ± 0.33	0 ± 0.11	-25	-0.2	1.2
749	3	161.61239 (1.03)	59.09625 (1.05)	8.2 ± 1.86	8.8 ± 2.02	3.1 ± 0.3	0 ± 0.11	-46	0.1	-1.1

continued on the next page

C Catalogue continued

ID	Size Flag	RA (J2000) (arcsec)	Dec (J2000) (arcsec)	S_P ($\mu\text{Jy beam}^{-1}$)	S_T (μJy)	θ_{DM} (arcsec)	θ_{Dm} (arcsec)	ϕ (degrees)	α_{IF}	α_{IM}
750	3	161.34775 (1.02)	58.934 (1.04)	8.1 ± 1.86	8.8 ± 2.04	3.34 ± 0.3	0 ± 0.11	35	-0.8	-1.9
751	6	161.48113 (0.8)	59.04994 (0.86)	8.5 ± 1.51	8.7 ± 1.57	1.63 ± 0.35	0.23 ± 0.17	-31	-1.2	-1.3
752	3	161.57076 (1.01)	58.93465 (1.04)	7.9 ± 1.71	8.7 ± 1.92	3.78 ± 0.33	0 ± 0.11	30	-0.9	-1.2
753	3	161.64992 (1.05)	58.94703 (1.06)	7.7 ± 1.7	8.7 ± 1.96	4.33 ± 0.35	0 ± 0.11	-72	-0.7	0
754	5	161.28815 (0.97)	59.07316 (0.95)	8.5 ± 2.21	8.7 ± 2.23	1.68 ± 0.29	0.61 ± 0.1	158	0.5	1.4
755	5	161.45789 (0.79)	59.03339 (0.79)	8.5 ± 1.47	8.6 ± 1.49	1.15 ± 0.22	0.35 ± 0.06	0	0	-1
756	5	161.56114 (0.8)	59.02578 (0.8)	8.5 ± 1.5	8.6 ± 1.52	1.16 ± 0.22	0.36 ± 0.06	0	-0.1	0.3
757	5	161.56236 (0.86)	59.06359 (0.85)	8.5 ± 1.66	8.6 ± 1.67	1.18 ± 0.2	0.38 ± 0.06	-120	-0.7	-0.3
758	5	161.40502 (0.92)	59.06821 (0.96)	8.3 ± 1.64	8.6 ± 1.69	1.68 ± 0.36	1.3 ± 0.12	-50	-1.7	0.7
759	5	161.62989 (1.08)	59.10317 (1.07)	8.4 ± 2.13	8.6 ± 2.16	1.52 ± 0.3	0.59 ± 0.12	182	-0.6	-1.2
760	5	161.41551 (0.97)	59.11579 (0.95)	8.4 ± 2.16	8.6 ± 2.18	1.65 ± 0.28	0.6 ± 0.1	176	1.8	1.6
761	3	161.35519 (1.11)	58.96032 (1.09)	7.2 ± 1.57	8.6 ± 1.93	5.07 ± 0.46	0 ± 0.24	-97	0.6	1.1
762	5	161.55419 (0.97)	58.90613 (0.95)	8.3 ± 2.17	8.6 ± 2.19	1.68 ± 0.29	0.61 ± 0.1	0	-2.1	-1.1
763	5	161.73438 (0.97)	59.02381 (0.95)	8.4 ± 2.18	8.6 ± 2.2	1.68 ± 0.29	0.61 ± 0.1	-1	-0.6	-0.1
764	3	161.48615 (0.9)	58.99069 (0.94)	7.7 ± 1.37	8.5 ± 1.56	3.78 ± 0.36	0 ± 0.12	28	-0.2	1.3
765	5	161.35424 (0.93)	58.99416 (0.92)	8.4 ± 1.84	8.5 ± 1.85	1.3 ± 0.2	0.45 ± 0.07	53	-0.2	-0.9
766	5	161.66792 (0.97)	59.05067 (0.95)	8.3 ± 1.98	8.5 ± 2	1.49 ± 0.24	0.53 ± 0.08	161	0.4	1.8
767	5	161.51048 (0.97)	59.11905 (0.95)	8.3 ± 2.08	8.5 ± 2.1	1.6 ± 0.27	0.58 ± 0.09	-90	0.5	1.2
768	5	161.53275 (1.02)	58.91103 (1.04)	8.3 ± 2.03	8.5 ± 2.06	1.6 ± 0.3	0.39 ± 0.11	-68	0	1.3
769	5	161.72139 (0.97)	59.01302 (0.95)	8.3 ± 2.15	8.5 ± 2.17	1.68 ± 0.29	0.61 ± 0.1	5	-0.9	-0.5
770	5	161.74531 (1.02)	59.02359 (1.05)	8.3 ± 2.07	8.5 ± 2.1	1.86 ± 0.33	0.44 ± 0.11	-88	-0.5	0
771	6	161.43708 (0.86)	59.03747 (0.9)	8.2 ± 1.49	8.4 ± 1.55	1.74 ± 0.35	0.22 ± 0.18	-117	0.3	1
772	7	161.44004 (0.84)	58.99166 (0.84)	8.4 ± 1.54	8.4 ± 1.55	0 ± 0.2	0 ± 0.06	-34	0	-0.6
773	3	161.38822 (1.06)	58.98076 (1.04)	8.1 ± 1.5	8.4 ± 1.58	2.15 ± 0.27	0 ± 0.07	-20	0	-1
774	5	161.69475 (1.08)	59.03195 (1.07)	8.2 ± 2	8.4 ± 2.02	1.49 ± 0.3	0.54 ± 0.11	-39	-0.7	-0.8
775	7	161.59835 (0.88)	59.03477 (0.87)	8.3 ± 1.62	8.3 ± 1.63	0 ± 0.19	0 ± 0.06	-12	0.7	0
776	5	161.50409 (0.95)	58.93542 (0.93)	8.2 ± 1.86	8.3 ± 1.87	1.37 ± 0.21	0.48 ± 0.07	-54	0	-1.8
777	6	161.66119 (1.1)	59.08641 (1.08)	8.1 ± 1.96	8.3 ± 1.99	2.1 ± 0.3	0 ± 0.14	-111	-1.1	2
778	7	161.3608 (0.95)	59.03029 (0.93)	8.2 ± 1.75	8.2 ± 1.76	0 ± 0.21	0 ± 0.07	410	-0.7	0.3
779	5	161.35231 (0.97)	58.97055 (0.95)	8 ± 1.91	8.2 ± 1.93	1.49 ± 0.24	0.53 ± 0.08	0	-1.2	-1.1
780	7	161.66206 (0.97)	58.9339 (0.95)	8.2 ± 1.99	8.2 ± 2.02	0 ± 0.29	0 ± 0.1	-85	-0.8	-1.6
781	7	161.63211 (0.97)	59.11257 (0.95)	8.2 ± 1.98	8.2 ± 2.01	0 ± 0.29	0 ± 0.1	-585	2	-1
782	6	161.52861 (0.81)	59.00983 (0.87)	8 ± 1.43	8.1 ± 1.48	1.56 ± 0.36	0.25 ± 0.14	-92	-1.4	-0.2
783	3	161.66316 (1.06)	58.97631 (1.06)	7.6 ± 1.77	8.1 ± 1.9	2.79 ± 0.29	0 ± 0.12	199	-0.1	0.5
784	5	161.71768 (0.97)	59.04569 (0.95)	7.9 ± 2.05	8.1 ± 2.08	1.68 ± 0.29	0.61 ± 0.1	0	2.1	-0.4
785	7	161.71288 (0.97)	58.97661 (0.95)	8.1 ± 1.98	8.1 ± 2	0 ± 0.29	0 ± 0.1	-146	-0.2	-1.4
786	5	161.50255 (0.86)	58.97301 (0.85)	7.9 ± 1.56	8 ± 1.57	1.18 ± 0.2	0.39 ± 0.06	0	-1.5	-1
787	5	161.44483 (0.9)	59.06671 (0.89)	7.9 ± 1.64	8 ± 1.65	1.19 ± 0.18	0.4 ± 0.06	110	-2.1	0
788	5	161.62375 (0.95)	58.97306 (0.94)	7.9 ± 1.79	8 ± 1.81	1.38 ± 0.22	0.49 ± 0.07	-37	-2.1	-0.3
789	5	161.50869 (1.04)	59.10954 (1.05)	7.8 ± 1.79	8 ± 1.82	1.89 ± 0.33	0.39 ± 0.12	-108	-0.9	-1.2
790	6	161.51785 (1.26)	59.11052 (1.2)	7.6 ± 1.77	8 ± 2.01	2.4 ± 0.81	0 ± 0.58	-63	-1.3	-1.3
791	7	161.36299 (0.97)	58.93734 (0.95)	8 ± 1.94	8 ± 1.96	0 ± 0.29	0 ± 0.1	-119	-0.5	0.4
792	5	161.58507 (0.87)	59.00356 (0.86)	7.8 ± 1.57	7.9 ± 1.58	1.18 ± 0.19	0.39 ± 0.06	0	-1.5	0.6
793	5	161.4759 (0.89)	58.96248 (0.88)	7.8 ± 1.63	7.9 ± 1.64	1.19 ± 0.18	0.4 ± 0.06	-123	-1.8	0.1
794	5	161.46898 (0.89)	58.96485 (0.88)	7.8 ± 1.62	7.9 ± 1.63	1.19 ± 0.18	0.4 ± 0.06	0	-1.9	-2
795	5	161.57292 (0.9)	59.05937 (0.89)	7.8 ± 1.64	7.9 ± 1.65	1.19 ± 0.18	0.4 ± 0.06	-63	-0.8	0.2
796	3	161.59079 (1.03)	59.05779 (1.04)	7.4 ± 1.53	7.9 ± 1.67	3.01 ± 0.37	0 ± 0.09	176	0	0.3
797	3	161.60696 (1.04)	59.03202 (1.06)	7 ± 1.41	7.9 ± 1.62	4.26 ± 0.33	0 ± 0.12	-95	-0.4	0.4
798	5	161.62592 (0.97)	59.09845 (0.95)	7.7 ± 1.99	7.9 ± 2.01	1.68 ± 0.29	0.61 ± 0.1	-136	-0.4	-1.5
799	5	161.61673 (0.95)	58.98135 (0.99)	7.6 ± 1.6	7.8 ± 1.64	1.67 ± 0.36	0.32 ± 0.1	-16	-1.7	-2.2

continued on the next page

C Catalogue continued

ID	Size Flag	RA (J2000) (arcsec)	Dec (J2000) (arcsec)	S_P ($\mu\text{Jy beam}^{-1}$)	S_T (μJy)	θ_{DM} (arcsec)	θ_{Dm} (arcsec)	ϕ (degrees)	α_{IF}	α_{IM}
800	5	161.65057 (0.99)	59.02086 (1.02)	7.6 ± 1.66	7.8 ± 1.7	1.67 ± 0.36	0.34 ± 0.1	-90	-1.6	-1.2
801	5	161.68309 (1.02)	59.06557 (1.04)	7.6 ± 1.89	7.8 ± 1.92	1.83 ± 0.32	0.44 ± 0.11	-82	2.2	1.4
802	5	161.50308 (0.97)	58.90764 (0.95)	7.6 ± 1.96	7.8 ± 1.98	1.68 ± 0.29	0.61 ± 0.1	0	-0.1	-0.1
803	7	161.28163 (0.97)	59.00181 (0.95)	7.8 ± 1.9	7.8 ± 1.92	0 ± 0.29	0 ± 0.1	17	0.5	-0.2
804	3	161.55503 (1.01)	58.96837 (1.04)	7.1 ± 1.46	7.7 ± 1.61	3.29 ± 0.36	0 ± 0.1	-155	-1.9	0
805	5	161.33684 (0.97)	58.96792 (0.95)	7.5 ± 1.92	7.7 ± 1.94	1.66 ± 0.28	0.61 ± 0.1	-35	-0.5	0
806	5	161.47714 (1.01)	58.91596 (1.04)	7.5 ± 1.86	7.7 ± 1.89	1.66 ± 0.3	0.41 ± 0.11	-105	-0.2	0.6
807	5	161.54571 (0.97)	59.09616 (0.95)	7.4 ± 1.79	7.6 ± 1.81	1.52 ± 0.25	0.55 ± 0.09	35	-1.4	-2.3
808	5	161.39206 (0.97)	58.93109 (0.95)	7.4 ± 1.93	7.6 ± 1.95	1.68 ± 0.29	0.61 ± 0.1	0	-1.1	0.3
809	5	161.68192 (0.97)	59.06394 (0.95)	7.4 ± 1.93	7.6 ± 1.95	1.68 ± 0.29	0.61 ± 0.1	223	-0.9	0
810	5	161.28656 (0.97)	59.0158 (0.95)	7.4 ± 1.92	7.6 ± 1.94	1.68 ± 0.29	0.61 ± 0.1	0	-1	-1.8
811	5	161.45672 (0.87)	59.00928 (0.86)	7.4 ± 1.46	7.5 ± 1.47	1.18 ± 0.19	0.39 ± 0.06	0	-2	-1.5
812	5	161.58025 (0.98)	59.05434 (0.98)	7.4 ± 1.45	7.5 ± 1.48	1.35 ± 0.33	0.29 ± 0.06	-70	-0.3	-0.3
813	2	161.38884 (1.11)	59.03459 (1.09)	6.6 ± 1.45	7.5 ± 1.67	3.8 ± 0.45	2.06 ± 0.29	-155	-1.7	-2.1
814	5	161.60931 (0.97)	58.96512 (0.95)	7.4 ± 1.74	7.5 ± 1.76	1.47 ± 0.24	0.52 ± 0.08	-35	0	0.6
815	5	161.54503 (1.07)	58.93215 (1.07)	7.3 ± 1.76	7.5 ± 1.78	1.5 ± 0.27	0.63 ± 0.11	12	-1.4	-1.2
816	5	161.65675 (0.97)	59.00407 (0.95)	7.4 ± 1.78	7.5 ± 1.8	1.52 ± 0.25	0.55 ± 0.09	17	-0.6	1.1
817	5	161.65704 (0.97)	59.08994 (0.95)	7.4 ± 1.91	7.5 ± 1.93	1.68 ± 0.29	0.61 ± 0.1	0	-0.8	0
818	5	161.55163 (0.87)	59.00747 (0.86)	7.3 ± 1.47	7.4 ± 1.49	1.18 ± 0.19	0.39 ± 0.06	0	-2.2	-0.5
819	5	161.43863 (0.88)	59.01786 (0.87)	7.3 ± 1.49	7.4 ± 1.5	1.19 ± 0.19	0.39 ± 0.06	0	-1.8	-1.1
820	7	161.46511 (0.88)	59.01528 (0.87)	7.4 ± 1.44	7.4 ± 1.45	0 ± 0.19	0 ± 0.06	32	-2	0.4
821	7	161.59968 (0.96)	58.98421 (0.94)	7.4 ± 1.61	7.4 ± 1.62	0 ± 0.22	0 ± 0.08	-89	-1.1	-1.8
822	5	161.54231 (1.05)	58.91225 (1.05)	7.2 ± 1.81	7.4 ± 1.83	1.52 ± 0.28	0.43 ± 0.11	-36	0	0.3
823	5	161.64821 (0.97)	59.08035 (0.95)	7.1 ± 1.84	7.3 ± 1.86	1.68 ± 0.29	0.61 ± 0.1	0	-0.8	-0.4
824	5	161.47764 (0.97)	59.12098 (0.95)	7.2 ± 1.86	7.3 ± 1.88	1.68 ± 0.29	0.61 ± 0.1	0	-1.1	1.2
825	6	161.6289 (1.31)	58.97508 (1.25)	6.8 ± 1.59	7.2 ± 1.83	2.85 ± 0.87	0 ± 0.62	5	0.4	-0.3
826	5	161.38096 (0.97)	59.0646 (0.95)	7 ± 1.71	7.1 ± 1.72	1.55 ± 0.26	0.56 ± 0.09	0	-0.1	0.8
827	5	161.60397 (0.97)	58.93382 (0.95)	6.9 ± 1.8	7.1 ± 1.82	1.68 ± 0.29	0.61 ± 0.1	0	1	1.3
828	5	161.42834 (0.93)	58.91254 (1.01)	6.9 ± 1.68	7.1 ± 1.71	1.48 ± 0.3	0.73 ± 0.13	-4	-1.9	-0.6
829	7	161.40583 (0.97)	59.05603 (0.95)	7 ± 1.58	7 ± 1.6	0 ± 0.24	0 ± 0.08	28	0	-0.2
830	3	161.35943 (1.08)	58.97909 (1.08)	6 ± 1.32	7 ± 1.57	4.77 ± 0.41	0 ± 0.18	-72	-1.8	0
831	5	161.54121 (0.97)	59.11824 (0.95)	6.8 ± 1.77	7 ± 1.79	1.68 ± 0.29	0.61 ± 0.1	-49	1.1	-2.8
832	5	161.42702 (0.93)	59.02951 (0.92)	6.8 ± 1.49	6.9 ± 1.5	1.3 ± 0.2	0.45 ± 0.07	0	-0.5	-0.8
833	5	161.63323 (0.97)	59.05948 (0.95)	6.7 ± 1.7	6.9 ± 1.71	1.62 ± 0.27	0.59 ± 0.1	36	1	-0.5
834	5	161.46065 (0.97)	59.10803 (0.95)	6.8 ± 1.75	6.9 ± 1.77	1.68 ± 0.29	0.61 ± 0.1	0	-2.1	-0.1
835	5	161.48848 (0.97)	59.11611 (0.95)	6.7 ± 1.75	6.9 ± 1.76	1.68 ± 0.29	0.61 ± 0.1	0	0.1	-0.6
836	5	161.61036 (0.97)	59.07505 (0.95)	6.7 ± 1.7	6.8 ± 1.71	1.63 ± 0.27	0.59 ± 0.1	-24	-0.9	-1.4
837	5	161.34441 (0.97)	59.04333 (0.95)	6.6 ± 1.71	6.8 ± 1.73	1.66 ± 0.28	0.61 ± 0.1	88	-1.6	0.2
838	7	161.36656 (0.97)	59.05698 (0.95)	6.8 ± 1.64	6.8 ± 1.66	0 ± 0.28	0 ± 0.1	-6	-1.1	0.4
839	5	161.46885 (0.97)	59.10574 (0.95)	6.7 ± 1.73	6.8 ± 1.75	1.68 ± 0.29	0.61 ± 0.1	0	-0.4	-0.9
840	5	161.56109 (0.86)	58.98501 (0.96)	6.6 ± 1.52	6.7 ± 1.53	1.21 ± 0.24	0.54 ± 0.08	-94	-1.6	-0.6
841	5	161.41074 (0.99)	59.01624 (1.02)	6.5 ± 1.38	6.7 ± 1.41	1.74 ± 0.34	0.33 ± 0.11	-328	-0.3	0.9
842	5	161.39689 (0.97)	58.9727 (0.95)	6.6 ± 1.61	6.7 ± 1.62	1.55 ± 0.25	0.56 ± 0.09	2	-0.2	-0.9
843	5	161.67038 (0.86)	59.0164 (0.97)	6.6 ± 1.35	6.7 ± 1.37	1.32 ± 0.28	0.58 ± 0.1	-28	0	-0.9
844	5	161.45242 (0.96)	59.03649 (1)	6.3 ± 1.33	6.6 ± 1.36	1.7 ± 0.35	1.18 ± 0.11	-19	-0.6	0.8
845	7	161.48895 (0.96)	58.98182 (0.94)	6.6 ± 1.43	6.6 ± 1.45	0 ± 0.22	0 ± 0.08	-254	-1.3	1.6
846	5	161.5731 (0.97)	59.06531 (0.95)	6.5 ± 1.56	6.6 ± 1.57	1.51 ± 0.25	0.54 ± 0.09	-45	-0.2	-1.1
847	5	161.37608 (0.97)	59.07779 (0.95)	6.4 ± 1.66	6.6 ± 1.68	1.68 ± 0.29	0.61 ± 0.1	0	-1.1	-1.5
848	5	161.48633 (0.95)	59.11089 (0.95)	6.5 ± 1.6	6.6 ± 1.61	1.58 ± 0.28	0.61 ± 0.1	-173	-1.4	-0.3
849	1	161.4565 (1.07)	59.06203 (1.07)	5.8 ± 1.33	6.5 ± 1.53	3.6 ± 0.36	1.99 ± 0.17	-238	-1.1	-2

C Catalogue continued

ID	Size Flag	RA (J2000) (arcsec)	Dec (J2000) (arcsec)	S_P ($\mu\text{Jy beam}^{-1}$)	S_T (μJy)	θ_{DM} (arcsec)	θ_{Dm} (arcsec)	ϕ (degrees)	α_{IF}	α_{IM}
850	5	161.58692 (0.97)	59.09591 (0.95)	6.3 ± 1.64	6.5 ± 1.65	1.68 ± 0.29	0.61 ± 0.1	626	-0.8	0.1
851	6	161.45444 (1.26)	59.05628 (1.21)	6.1 ± 1.39	6.4 ± 1.59	2.57 ± 0.82	0 ± 0.59	-81	-0.9	-1.3
852	3	161.49039 (1)	59.00236 (1.03)	5.8 ± 1.22	6.4 ± 1.38	3.73 ± 0.33	0 ± 0.11	-97	-1.6	0.3
853	5	161.36635 (1.03)	59.0324 (1.05)	6.3 ± 1.51	6.4 ± 1.54	1.57 ± 0.31	0.38 ± 0.1	-86	-0.4	-0.1
854	5	161.38667 (0.97)	59.06676 (0.95)	6.3 ± 1.62	6.4 ± 1.63	1.66 ± 0.28	0.61 ± 0.1	20	0	0.6
855	5	161.60041 (1)	58.94066 (1.03)	6.3 ± 1.57	6.4 ± 1.59	1.73 ± 0.31	0.43 ± 0.11	-90	-1.4	-0.3
856	5	161.53351 (0.97)	59.10305 (0.95)	6.2 ± 1.61	6.4 ± 1.63	1.68 ± 0.29	0.61 ± 0.1	0	0.5	0.1
857	5	161.44773 (0.97)	58.92795 (0.95)	6.2 ± 1.62	6.4 ± 1.63	1.68 ± 0.29	0.61 ± 0.1	274	-0.1	-0.3
858	5	161.50248 (0.97)	58.96052 (0.95)	6.1 ± 1.5	6.3 ± 1.51	1.54 ± 0.25	0.56 ± 0.09	40	0	0
859	3	161.60189 (1.03)	59.04428 (1.05)	5.9 ± 1.36	6.3 ± 1.48	3.17 ± 0.29	0 ± 0.11	-123	0.3	-0.7
860	5	161.58507 (1)	58.94303 (1.03)	6.2 ± 1.54	6.3 ± 1.56	1.72 ± 0.31	0.42 ± 0.11	-90	-0.9	-1.6
861	1	161.46225 (1)	59.05865 (1.03)	5.2 ± 1.18	6.3 ± 1.45	3.67 ± 0.31	3.67 ± 0.12	-18	-1.9	0.2
862	5	161.66684 (1)	59.0385 (1.03)	6.2 ± 1.54	6.3 ± 1.56	1.73 ± 0.31	0.48 ± 0.11	-90	-0.8	-1.8
863	5	161.50312 (0.95)	59.00642 (0.93)	6.1 ± 1.37	6.2 ± 1.38	1.37 ± 0.21	0.48 ± 0.07	-32	1.2	-1.5
864	7	161.45741 (0.97)	59.02477 (0.95)	6.2 ± 1.38	6.2 ± 1.39	0 ± 0.23	0 ± 0.08	76	-0.4	-0.5
865	6	161.44333 (1.4)	58.98251 (1.55)	5.4 ± 1.38	6.2 ± 1.75	4.35 ± 1.3	0 ± 0.89	-90	0	-1
866	5	161.36874 (0.97)	59.01388 (0.95)	6.1 ± 1.54	6.2 ± 1.55	1.63 ± 0.27	0.6 ± 0.1	8	-1.5	-1.5
867	5	161.47098 (0.98)	59.02183 (1.01)	6 ± 1.3	6.1 ± 1.33	1.63 ± 0.38	0.36 ± 0.1	0	-1.4	-0.8
868	5	161.42481 (0.97)	59.07434 (0.95)	6 ± 1.53	6.1 ± 1.55	1.66 ± 0.28	0.61 ± 0.1	-242	-0.5	-2.2
869	3	161.54152 (1.1)	59.07204 (1.08)	5.9 ± 1.42	6.1 ± 1.49	2.24 ± 0.3	0 ± 0.13	-176	-0.6	0.2
870	5	161.38212 (0.97)	58.96669 (0.95)	6 ± 1.55	6.1 ± 1.56	1.68 ± 0.29	0.61 ± 0.1	0	-0.8	-1.4
871	5	161.63274 (1)	59.06309 (1.03)	5.9 ± 1.48	6.1 ± 1.5	1.73 ± 0.31	1.14 ± 0.11	39	2	1.1
872	5	161.65235 (0.97)	59.0291 (0.95)	6 ± 1.55	6.1 ± 1.56	1.68 ± 0.29	0.61 ± 0.1	0	-1.7	-1.3
873	6	161.57314 (0.83)	58.95116 (0.97)	6.1 ± 1.08	6.1 ± 1.1	0.74 ± 0.28	0 ± 0.11	-8	-0.3	-0.1
874	5	161.34456 (0.97)	59.01665 (0.95)	5.9 ± 1.53	6.1 ± 1.55	1.68 ± 0.29	0.61 ± 0.1	7	-1.3	2
875	5	161.37539 (0.97)	59.06659 (0.95)	5.9 ± 1.53	6.1 ± 1.55	1.68 ± 0.29	0.61 ± 0.1	0	0	1.5
876	5	161.52546 (0.97)	59.0998 (0.95)	6 ± 1.55	6.1 ± 1.57	1.68 ± 0.29	0.61 ± 0.1	491	0	-0.7
877	3	161.55618 (1)	58.99773 (1.03)	5.4 ± 1.22	6 ± 1.36	3.67 ± 0.32	0 ± 0.11	-49	-0.7	0.3
878	3	161.59337 (1.02)	58.97442 (1.04)	5.6 ± 1.28	6 ± 1.41	3.33 ± 0.29	0 ± 0.11	-121	-0.2	-1.2
879	5	161.57579 (1)	58.93094 (1.03)	5.9 ± 1.47	6 ± 1.49	1.72 ± 0.31	0.42 ± 0.11	-95	-0.5	1.2
880	5	161.47465 (1)	59.04927 (1.03)	5.7 ± 1.3	5.9 ± 1.32	1.72 ± 0.34	0.37 ± 0.11	-109	-1.7	-0.4
881	5	161.47006 (0.97)	59.05555 (0.95)	5.8 ± 1.4	5.9 ± 1.42	1.54 ± 0.25	0.56 ± 0.09	44	-0.9	-0.6
882	5	161.54724 (0.97)	58.98241 (0.95)	5.8 ± 1.4	5.9 ± 1.42	1.54 ± 0.25	0.56 ± 0.09	43	-1.7	1.7
883	5	161.44425 (0.97)	59.07239 (0.95)	5.8 ± 1.48	5.9 ± 1.49	1.65 ± 0.28	0.6 ± 0.1	0	0	-1
884	5	161.4265 (1.09)	59.01627 (1.07)	5.7 ± 1.32	5.8 ± 1.34	1.45 ± 0.3	0.51 ± 0.1	-8	0	-1.4
885	5	161.55258 (1)	58.99056 (1.03)	5.7 ± 1.31	5.8 ± 1.33	1.7 ± 0.34	0.37 ± 0.11	-88	-2.1	-0.5
886	3	161.48397 (1.01)	58.99792 (1.04)	5.4 ± 1.2	5.8 ± 1.32	3.4 ± 0.31	0 ± 0.11	-129	-0.2	0.4
887	5	161.50369 (0.97)	59.09076 (0.95)	5.7 ± 1.48	5.8 ± 1.5	1.68 ± 0.29	0.61 ± 0.1	0	0.1	0.9
888	5	161.58663 (0.97)	59.08375 (0.95)	5.6 ± 1.46	5.8 ± 1.48	1.68 ± 0.29	0.61 ± 0.1	0	1.4	1.3
889	5	161.63528 (0.97)	59.06528 (0.95)	5.6 ± 1.46	5.8 ± 1.48	1.68 ± 0.29	0.61 ± 0.1	0	-0.4	1.3
890	5	161.54881 (1.1)	59.03371 (1.08)	5.6 ± 1.29	5.7 ± 1.31	1.44 ± 0.29	0.53 ± 0.1	-113	-0.4	-0.3
891	5	161.55513 (1.05)	58.98567 (1.05)	5.6 ± 1.33	5.7 ± 1.36	1.55 ± 0.32	0.39 ± 0.1	-13	0.6	0.7
892	6	161.52506 (1.32)	58.98192 (1.3)	5.3 ± 1.26	5.7 ± 1.47	3.2 ± 0.95	0 ± 0.67	388	0	1.1
893	5	161.66521 (1)	59.03406 (1.03)	5.6 ± 1.39	5.7 ± 1.41	1.72 ± 0.31	0.44 ± 0.11	-90	-0.6	-0.8
894	5	161.41668 (0.97)	59.02476 (0.95)	5.4 ± 1.37	5.6 ± 1.38	1.62 ± 0.27	0.59 ± 0.09	-90	-0.8	-1.7
895	5	161.43729 (0.97)	58.95997 (0.95)	5.4 ± 1.41	5.6 ± 1.42	1.68 ± 0.29	0.61 ± 0.1	0	0	-1.3
896	7	161.59335 (0.97)	59.06879 (0.95)	5.6 ± 1.37	5.6 ± 1.39	0 ± 0.29	0 ± 0.1	0	0	0
897	5	161.38162 (0.97)	59.06668 (0.95)	5.5 ± 1.41	5.6 ± 1.43	1.68 ± 0.29	0.61 ± 0.1	0	2.1	0
898	5	161.50676 (1)	58.94283 (1.03)	5.3 ± 1.33	5.5 ± 1.35	1.7 ± 0.31	0.42 ± 0.11	-75	-1.3	-0.5
899	3	161.46163 (1)	59.06319 (1.03)	5 ± 1.13	5.5 ± 1.27	3.68 ± 0.31	0.22 ± 0.11	-90	-1.4	-1.2

C Catalogue continued

ID	Size Flag	RA (J2000) (arcsec)	Dec (J2000) (arcsec)	S_P ($\mu\text{Jy beam}^{-1}$)	S_T (μJy)	θ_{DM} (arcsec)	θ_{Dm} (arcsec)	ϕ (degrees)	α_{IF}	α_{IM}
900	5	161.59946 (0.97)	59.0747 (0.95)	5.4 ± 1.39	5.5 ± 1.41	1.68 ± 0.29	0.61 ± 0.1	0	-0.5	0.2
901	5	161.50485 (0.97)	58.99817 (0.95)	5.3 ± 1.3	5.4 ± 1.31	1.57 ± 0.26	0.57 ± 0.09	-62	0	-0.9
902	5	161.47498 (0.97)	59.04262 (0.95)	5.3 ± 1.32	5.4 ± 1.33	1.59 ± 0.26	0.58 ± 0.09	-29	-0.2	0.5
903	5	161.52523 (0.97)	59.0555 (0.95)	5.2 ± 1.34	5.4 ± 1.35	1.64 ± 0.28	0.6 ± 0.1	137	-1.4	-2.1
904	3	161.44913 (1.04)	59.01834 (1.05)	5 ± 1.16	5.4 ± 1.25	3.08 ± 0.28	0 ± 0.11	-118	1.1	1
905	5	161.52729 (0.97)	59.08034 (0.95)	5.3 ± 1.38	5.4 ± 1.39	1.68 ± 0.29	0.61 ± 0.1	0	-0.5	0.6
906	5	161.39783 (1)	59.06307 (1.03)	5.3 ± 1.32	5.4 ± 1.33	1.76 ± 0.32	0.43 ± 0.11	-101	-0.3	-0.7
907	5	161.53159 (0.97)	58.99178 (0.95)	5.2 ± 1.31	5.3 ± 1.32	1.61 ± 0.27	0.59 ± 0.09	-41	0	-1.3
908	5	161.41748 (0.97)	59.06323 (0.95)	5.2 ± 1.35	5.3 ± 1.37	1.68 ± 0.29	0.61 ± 0.1	0	0.6	-1.4
909	3	161.54721 (0.01)	58.96701 (0.01)	4.8 ± 1.09	5.3 ± 1.23	3.78 ± 0.32	0 ± 0.11	16	-2.1	-1.4
910	5	161.44124 (0.97)	59.00372 (0.95)	5.1 ± 1.3	5.2 ± 1.31	1.65 ± 0.28	0.6 ± 0.1	15	-2.1	-0.9
911	5	161.43143 (1.03)	59.03707 (1.05)	5.1 ± 1.26	5.2 ± 1.28	1.56 ± 0.29	0.42 ± 0.11	-142	0	-0.6
912	5	161.49459 (0.97)	59.06628 (0.95)	5.1 ± 1.31	5.2 ± 1.33	1.68 ± 0.29	0.61 ± 0.1	0	0	-1.1
913	5	161.53844 (1)	58.96281 (1.03)	5 ± 1.25	5.2 ± 1.27	1.73 ± 0.31	0.43 ± 0.11	35	-0.6	-1
914	5	161.63492 (1.01)	59.01534 (1.04)	5.1 ± 1.26	5.2 ± 1.28	1.64 ± 0.3	0.41 ± 0.11	-99	-0.5	-1.2
915	5	161.48242 (0.97)	59.08825 (0.95)	5.1 ± 1.33	5.2 ± 1.34	1.68 ± 0.29	0.61 ± 0.1	-74	-1.6	-3
916	5	161.49218 (1)	58.93883 (1.03)	5.1 ± 1.27	5.2 ± 1.28	1.71 ± 0.31	0.42 ± 0.11	-83	-1.8	-0.9
917	3	161.48741 (1.02)	58.97797 (1.05)	4.5 ± 1.01	5.1 ± 1.15	3.99 ± 0.33	0 ± 0.11	-98	-2.2	0.7
918	7	161.48314 (0.97)	58.95616 (0.95)	5 ± 1.23	5 ± 1.24	0 ± 0.29	0 ± 0.1	0	-1.5	-2.2
919	5	161.601 (0.97)	59.00383 (0.95)	4.8 ± 1.24	4.9 ± 1.26	1.68 ± 0.29	0.61 ± 0.1	108	0	-1.5
920	5	161.6219 (1.04)	58.99472 (1.05)	4.8 ± 1.2	4.9 ± 1.22	1.53 ± 0.28	0.38 ± 0.11	-96	0	0.4
921	7	161.48659 (0.97)	58.9869 (0.95)	4.8 ± 1.17	4.8 ± 1.19	0 ± 0.29	0 ± 0.1	29	0.5	-0.6
922	5	161.45244 (1)	59.05024 (1.03)	4.6 ± 1.14	4.7 ± 1.15	1.67 ± 0.3	0.42 ± 0.11	-84	0	0
923	5	161.57834 (0.97)	59.01143 (0.95)	4.6 ± 1.19	4.7 ± 1.2	1.68 ± 0.29	0.61 ± 0.1	0	-1.2	-0.3
924	5	161.56744 (0.97)	59.03607 (0.95)	4.5 ± 1.18	4.7 ± 1.19	1.68 ± 0.29	0.61 ± 0.1	29	-1.8	-0.4
925	5	161.42363 (0.97)	59.03542 (0.95)	4.6 ± 1.18	4.7 ± 1.2	1.68 ± 0.29	0.61 ± 0.1	0	0.2	0.2
926	5	161.54588 (0.97)	58.97737 (0.95)	4.6 ± 1.19	4.7 ± 1.2	1.68 ± 0.29	0.61 ± 0.1	0	-0.7	1.7
927	5	161.41484 (0.97)	59.0375 (0.95)	4.6 ± 1.2	4.7 ± 1.21	1.68 ± 0.29	0.61 ± 0.1	0	-1.6	-0.1
928	5	161.5216 (0.97)	58.99233 (0.95)	4.4 ± 1.14	4.5 ± 1.15	1.68 ± 0.29	0.61 ± 0.1	0	0	-2
929	5	161.5123 (1.01)	59.04032 (1.04)	4 ± 1.1	4.2 ± 1.11	1.71 ± 0.31	0.82 ± 0.15	-81	-1.6	0.4
930	5	161.51888 (1)	59.00055 (1.03)	4 ± 1	4.1 ± 1.01	1.7 ± 0.31	0.42 ± 0.11	-93	-1.1	-0.3
931	5	161.50384 (1)	59.04229 (1.03)	4 ± 0.99	4.1 ± 1	1.75 ± 0.31	0.43 ± 0.11	-80	-1.6	0

Appendix B

CB Catalogue

Table B.1: Discrete VLA CB Catalogue

ID	Size Flag	RA (J2000) (arcsec)	Dec (J2000) (arcsec)	S_P ($\mu\text{Jy beam}^{-1}$)	S_T (μJy)	θ_{DM} (arcsec)	θ_{Dm} (arcsec)	ϕ (degrees)	α_{IF}	α_{IM}
000	0	161.60004 (0)	59.08947 (0)	4956 \pm 8937.95	8447 \pm 8572.76	765.84 \pm	25.85 \pm		-1	-0.7
001	0	161.41577 (0)	58.95854 (0)	644.6 \pm 2078.88	1870 \pm 2076.71	1118.13 \pm	37.86 \pm		-0.3	-0.3
002	7	161.79796 (0.01)	58.91626 (0.02)	859.7 \pm 20.14	859.7 \pm 20.31	0 \pm 0.01	0 \pm 0.01	-3	-0.9	-2
003	2	161.51745 (0.01)	59.14101 (0.01)	779.4 \pm 13.31	790 \pm 15.2	0.4 \pm 0.02	0.22 \pm 0.01	-111	-1.3	-1.4
004	3	161.70731 (0.02)	59.16544 (0.02)	649.3 \pm 12.74	663 \pm 15.8	0.57 \pm 0.04	0.01 \pm 0.01	-53	0.1	-0.8
005	6	161.20335 (0.02)	59.11376 (0.02)	555.2 \pm 14.51	558 \pm 15.42	0.28 \pm 0.02	0 \pm 0.01	4	-0.6	-1.1
006	7	161.30223 (0.01)	59.04216 (0.01)	545.6 \pm 11.09	545.6 \pm 11.29	0 \pm 0.01	0 \pm 0.01	6	-1.1	-1.1
007	6	161.46216 (0.01)	59.14488 (0.01)	540.1 \pm 10.73	542.7 \pm 11.43	0.27 \pm 0.02	0 \pm 0.01	22	-0.2	-0.1
008	0	161.6575 (0)	58.90627 (0)	176.2 \pm 600.56	500.1 \pm 592.61	227.18 \pm	7.21 \pm		-0.5	-0.2
009	0	161.45365 (0)	58.9023 (0)	239.9 \pm 498.89	446.1 \pm 499.49	361.85 \pm	11.97 \pm		-0.4	-0.5
010	6	161.65734 (0.01)	59.03617 (0.01)	365.4 \pm 7.05	367.2 \pm 7.65	0.27 \pm 0.02	0 \pm 0.01	-86	-0.8	-0.8
011	3	161.49451 (0.01)	59.05543 (0.01)	327.1 \pm 5.98	330.2 \pm 6.64	0.35 \pm 0.02	0.14 \pm 0.01	-63	0.7	0.8
012	2	161.67188 (0.04)	58.8704 (0.05)	267.2 \pm 8.81	306.9 \pm 21.39	1.53 \pm 0.17	0.26 \pm 0.08	-18	-1.5	-1.7
013	2	161.40534 (0.03)	59.16268 (0.05)	237.5 \pm 6.5	297.7 \pm 16.51	2.01 \pm 0.14	0.42 \pm 0.07	-119	-1.2	-2
014	1	161.63816 (0.01)	58.97085 (0.01)	241.7 \pm 2.04	282.5 \pm 4.49	1.42 \pm 0.04	0.77 \pm 0.01	-82	0.1	0.1
015	3	161.53149 (0.01)	58.93385 (0.01)	269.5 \pm 5.05	274.7 \pm 5.99	0.53 \pm 0.03	0.11 \pm 0.01	-104	-0.4	-0.3
016	6	161.63641 (0.01)	58.98384 (0.02)	252.8 \pm 5.28	253.5 \pm 5.59	0.21 \pm 0.02	0 \pm 0.01	-85	-0.6	-0.6
017	3	161.72327 (0.02)	59.04986 (0.02)	215.5 \pm 3.87	224.8 \pm 5.25	0.82 \pm 0.04	0 \pm 0.01	-46	-0.6	-0.6
018	1	161.76558 (0.04)	58.98569 (0.04)	144.9 \pm 5.38	220.6 \pm 16.32	2.72 \pm 0.19	1.14 \pm 0.13	-63	-1.2	-1.3
019	7	161.28425 (0.03)	58.897 (0.04)	220.2 \pm 8.15	220.2 \pm 9.39	0 \pm 0.06	0 \pm 0.02	-82	0	-0.7
020	1	161.40993 (0.02)	59.12602 (0.02)	210.3 \pm 4.19	219.6 \pm 5.46	0.68 \pm 0.04	0.45 \pm 0.01	-39	-1.2	-1.3
021	1	161.59129 (0.01)	58.9415 (0.02)	209.8 \pm 4.02	217.8 \pm 4.9	0.56 \pm 0.03	0.51 \pm 0.01	-93	-0.9	-1
022	1	161.51795 (0.02)	58.88871 (0.02)	204.1 \pm 4.68	214.3 \pm 6.61	0.79 \pm 0.06	0.38 \pm 0.02	-62	-1.2	-1.6
023	7	161.20904 (0.03)	58.99958 (0.03)	202 \pm 8.46	202 \pm 8.53	0 \pm 0.01	0 \pm 0.01	-14	-0.8	-0.8
024	2	161.51482 (0.03)	59.07333 (0.03)	103 \pm 1.23	186.3 \pm 4.42	4.07 \pm 0.08	0.42 \pm 0.04	-48	-0.9	-0.9
025	7	161.51961 (0.01)	58.91443 (0.02)	178.7 \pm 4.5	178.7 \pm 4.53	0 \pm 0.01	0 \pm 0.01	4	-0.1	0
026	1	161.56404 (0.01)	59.04326 (0.01)	164.2 \pm 2.98	170.5 \pm 3.8	0.67 \pm 0.03	0.37 \pm 0.01	-6	-0.9	-0.8
027	3	161.90875 (0.3)	59.06516 (0.29)	146.6 \pm 23.21	165.3 \pm 32.02	1.43 \pm 0.32	0 \pm 0.11	64	0.4	0
028	2	161.63069 (0.11)	58.84878 (0.12)	128.9 \pm 8.85	161.1 \pm 18.87	2.05 \pm 0.29	0.2 \pm 0.12	-91	-1.4	-0.7
029	1	161.64838 (0.09)	58.89449 (0.1)	95.4 \pm 5.77	159 \pm 18.71	3.23 \pm 0.36	1.12 \pm 0.16	8	-1	-1.4
030	2	161.48677 (0.04)	58.88855 (0.05)	131 \pm 4.26	146.9 \pm 8.54	1.36 \pm 0.13	0.28 \pm 0.06	11	0	-0.2
031	3	161.24844 (0.05)	59.10257 (0.06)	137.6 \pm 6.19	146.8 \pm 9.38	1.03 \pm 0.12	0 \pm 0.05	39	-1.3	-1
032	1	161.82868 (0.12)	59.06113 (0.13)	107.9 \pm 7.28	139.7 \pm 15.8	1.93 \pm 0.27	0.97 \pm 0.12	-55	-1.1	-2.8
033	2	161.2964 (0.05)	59.12008 (0.06)	127.4 \pm 5.37	135.2 \pm 8.02	0.95 \pm 0.11	0.2 \pm 0.04	-62	-1.2	-1.6
034	1	161.63837 (0.02)	58.96796 (0.03)	127.7 \pm 3.07	133.8 \pm 4.19	0.7 \pm 0.05	0.49 \pm 0.02	-132	0.6	0.3
035	6	161.68565 (0.03)	59.021 (0.03)	129.4 \pm 3.3	131.9 \pm 4.41	0.54 \pm 0.06	0.06 \pm 0.02	-58	-0.7	-0.7
036	1	161.4075 (0.65)	59.20686 (0.62)	39.3 \pm 10.14	131.6 \pm 47.56	5.01 \pm 1.02	3.48 \pm 0.8	-216	1.6	0
037	1	161.51923 (0.03)	59.11311 (0.04)	107.6 \pm 3.03	130.8 \pm 6.59	1.35 \pm 0.12	1.2 \pm 0.05	32	-1	-1.1
038	2	161.87051 (0.42)	58.9152 (0.41)	104.6 \pm 22.93	128.8 \pm 33.23	1.81 \pm 0.46	0.67 \pm 0.15	50	-1.3	0
039	6	161.75085 (0.04)	59.01858 (0.04)	125.4 \pm 4.26	128.1 \pm 5.46	0.58 \pm 0.07	0 \pm 0.02	-31	-1	-1.1
040	7	161.56658 (0.02)	58.93288 (0.03)	125.6 \pm 4.26	125.6 \pm 4.3	0 \pm 0.01	0 \pm 0.01	36	-0.9	-1
041	2	161.41807 (0.62)	58.81823 (0.6)	58.5 \pm 13.53	124.2 \pm 38.55	4.54 \pm 0.94	1.26 \pm 0.49	-154	1	0
042	7	161.73145 (0.03)	59.05004 (0.04)	121.9 \pm 4.4	121.9 \pm 5.12	0 \pm 0.06	0 \pm 0.02	7	-1	-1.4
043	7	161.81524 (0.06)	58.95548 (0.08)	118.8 \pm 8.32	118.8 \pm 8.36	0 \pm 0.02	0 \pm 0.01	-38	0	-1.2
044	2	161.67519 (0.07)	59.14194 (0.08)	105.1 \pm 5.74	118 \pm 9.18	1.27 \pm 0.16	0.55 \pm 0.06	-90	1.2	-1.5
045	3	161.82799 (0.16)	59.02094 (0.16)	82.6 \pm 7.05	114.1 \pm 17.55	2.62 \pm 0.44	0 \pm 0.15	-127	-0.7	-1
046	3	161.48863 (0.02)	59.01139 (0.02)	110.8 \pm 2.18	113 \pm 2.65	0.54 \pm 0.03	0 \pm 0.01	-76	0.9	1
047	2	161.08942 (0.57)	59.01577 (0.56)	64.5 \pm 16.18	109.3 \pm 36.47	3.71 \pm 0.8	0.38 \pm 0.4	-36	0	0
048	1	161.64275 (0.47)	59.21661 (0.46)	70.5 \pm 17.77	108.9 \pm 34.5	2.38 \pm 0.63	1.65 \pm 0.27	-58	0	0

continued on the next page

CB Catalogue continued

ID	Size Flag	RA (J2000) (arcsec)	Dec (J2000) (arcsec)	S_P ($\mu\text{Jy beam}^{-1}$)	S_T (μJy)	θ_{DM} (arcsec)	θ_{Dm} (arcsec)	ϕ (degrees)	α_{IF}	α_{IM}
049	1	161.21188 (0.09)	59.02493 (0.11)	74.4 \pm 4.95	108 \pm 12.37	2.05 \pm 0.28	1.63 \pm 0.14	-77	-0.8	-1.7
050	1	161.46614 (0.02)	59.05314 (0.03)	98.1 \pm 2.07	107.4 \pm 3.46	1.06 \pm 0.07	0.57 \pm 0.03	10	-0.9	-0.8
051	3	161.65204 (0.27)	59.19055 (0.26)	79.8 \pm 10.63	104 \pm 19.77	2.3 \pm 0.43	0 \pm 0.17	-115	-0.5	0
052	2	161.86991 (0.39)	59.02922 (0.38)	63.6 \pm 10.9	102.1 \pm 23.41	2.98 \pm 0.61	1.2 \pm 0.28	-45	-1	0
053	1	161.75729 (0.41)	58.89916 (0.4)	49.2 \pm 7.7	97 \pm 25.43	4 \pm 0.91	1.37 \pm 0.3	-12	0.4	0
054	3	161.23985 (0.4)	58.87673 (0.39)	66.9 \pm 11.84	95.8 \pm 23.67	2.82 \pm 0.58	0 \pm 0.25	-96	-0.9	0
055	7	161.53636 (0.02)	58.97453 (0.03)	93.6 \pm 3.2	93.6 \pm 3.23	0 \pm 0.01	0 \pm 0.01	-12	-0.9	-1
056	1	161.87728 (0.48)	58.95796 (0.47)	55.5 \pm 13.39	91.6 \pm 28.08	2.51 \pm 0.62	1.91 \pm 0.3	-2	0	0
057	4	161.5871 (0.14)	58.83743 (0.14)	87.6 \pm 8.75	91.2 \pm 10.2	0.66 \pm 0.16	0.44 \pm 0.02	37	-1.3	0
058	3	161.90179 (0.44)	59.0381 (0.43)	73.3 \pm 16.3	90.9 \pm 24.81	2.01 \pm 0.49	0 \pm 0.18	-119	-1	0
059	3	161.52542 (0.06)	59.1412 (0.07)	81 \pm 3.92	90.5 \pm 6.9	1.37 \pm 0.16	0 \pm 0.07	-87	-0.9	-1
060	3	161.71928 (0.05)	58.98408 (0.06)	80.1 \pm 3.58	86 \pm 5.58	1.08 \pm 0.13	0 \pm 0.05	121	-0.9	-1.1
061	2	161.7224 (0.06)	59.05467 (0.07)	79.1 \pm 3.69	85.8 \pm 5.78	1.11 \pm 0.13	0.31 \pm 0.05	-112	-1.3	-1.2
062	2	161.13379 (0.56)	59.08284 (0.56)	46 \pm 11.46	84.2 \pm 25.56	3.55 \pm 0.78	1.39 \pm 0.42	-55	-1	0
063	3	161.56846 (0.03)	58.98901 (0.03)	81.3 \pm 2.3	83.6 \pm 3.12	0.67 \pm 0.07	0 \pm 0.02	2	-0.3	-0.5
064	7	161.4997 (0.06)	58.87315 (0.07)	83.4 \pm 5.13	83.4 \pm 5.34	0 \pm 0.05	0 \pm 0.01	-125	-1.4	-1.3
065	2	161.1986 (0.11)	59.01016 (0.11)	73.7 \pm 4.75	83.4 \pm 7.7	1.4 \pm 0.19	0.33 \pm 0.08	-119	-0.5	-1.8
066	7	161.24189 (0.11)	59.14006 (0.12)	82.7 \pm 8.94	82.8 \pm 9.21	0.09 \pm 0.07	0 \pm 0.01	3	0.2	-2
067	2	161.4627 (0.04)	58.94398 (0.04)	77.3 \pm 2.47	81.1 \pm 3.63	0.78 \pm 0.09	0.37 \pm 0.03	-53	-0.7	-0.9
068	3	161.14075 (0.68)	58.99297 (0.64)	35.9 \pm 8.73	79.9 \pm 28.5	5.48 \pm 1.18	0 \pm 0.48	-36	-1.3	0
069	2	161.51138 (0.43)	58.80702 (0.42)	65.2 \pm 16.29	78.4 \pm 23.55	1.8 \pm 0.52	0.32 \pm 0.16	-105	-0.6	-0.6
070	5	161.27694 (0.23)	58.83727 (0.24)	75.9 \pm 19.75	76.7 \pm 20.54	0.31 \pm 0.19	0.24 \pm 0.07	14	0	0
071	7	161.75122 (0.09)	58.90851 (0.11)	76.3 \pm 6.41	76.3 \pm 6.46	0 \pm 0.03	0 \pm 0.01	-2	-0.5	-2.5
072	3	161.782 (0.63)	58.89426 (0.6)	38.9 \pm 9.36	76 \pm 25.95	4.62 \pm 0.94	0 \pm 0.46	-158	0.9	0
073	2	161.83879 (0.53)	58.91796 (0.53)	45.2 \pm 11.25	74.3 \pm 23.04	3.19 \pm 0.76	1.07 \pm 0.35	-156	-1.4	0
074	3	161.28162 (0.62)	58.86038 (0.6)	38.5 \pm 9.68	74.1 \pm 25.84	4.53 \pm 0.89	0 \pm 0.47	15	1.4	0
075	3	161.62001 (0.87)	58.85111 (0.81)	25.5 \pm 7.17	74.1 \pm 30.82	7.5 \pm 1.83	0 \pm 0.56	-79	0.8	0
076	1	161.44931 (0.41)	58.83588 (0.4)	47.8 \pm 8.97	73.2 \pm 18.48	2.67 \pm 0.55	1.25 \pm 0.27	-71	-0.3	0
077	2	161.13923 (0.46)	58.92525 (0.45)	54 \pm 13.65	73 \pm 22.12	2.26 \pm 0.61	0.81 \pm 0.23	-157	-1.9	0
078	3	161.51779 (0.04)	59.08037 (0.04)	70.7 \pm 2.28	72.7 \pm 3.15	0.66 \pm 0.08	0 \pm 0.02	-160	-1.1	-0.9
079	3	161.54534 (0.07)	58.8791 (0.08)	67.3 \pm 4.1	71.1 \pm 5.4	0.93 \pm 0.13	0 \pm 0.04	-70	-0.2	-1.3
080	3	161.5783 (0.04)	59.08384 (0.05)	66.9 \pm 2.34	70.8 \pm 3.78	0.95 \pm 0.11	0 \pm 0.04	-63	-0.6	-0.7
081	2	161.22711 (0.17)	59.07662 (0.16)	56.4 \pm 4.62	70.7 \pm 9.31	2.06 \pm 0.32	0.2 \pm 0.13	-90	-1.4	-2.1
082	6	161.48799 (0.38)	58.80385 (0.37)	66 \pm 16.6	70.6 \pm 19.74	1.05 \pm 0.42	0 \pm 0.14	122	0	-0.4
083	6	161.66086 (0.05)	58.93669 (0.06)	68.9 \pm 3.54	70.1 \pm 4.01	0.51 \pm 0.07	0 \pm 0.01	-63	-1.2	-1.2
084	1	161.74226 (0.07)	59.03917 (0.09)	60.2 \pm 3.53	69.9 \pm 5.97	1.34 \pm 0.17	0.82 \pm 0.07	12	-0.4	-1.3
085	3	161.53147 (0.45)	58.80977 (0.44)	54.7 \pm 13.85	69.3 \pm 21.73	2.14 \pm 0.59	0 \pm 0.21	-92	0	0
086	3	161.24886 (0.07)	59.05075 (0.08)	64.3 \pm 3.84	69.2 \pm 5.47	1.09 \pm 0.14	0 \pm 0.05	-124	-1.6	-1.4
087	3	161.63671 (0.05)	59.03725 (0.06)	58.5 \pm 2.42	68.9 \pm 5.52	1.72 \pm 0.19	0 \pm 0.09	-95	-0.9	-0.8
088	2	161.61903 (0.67)	59.18548 (0.63)	28.1 \pm 7.19	68.5 \pm 22.97	5.31 \pm 1.11	1.4 \pm 0.56	-54	2.1	0
089	3	161.89269 (0.48)	58.97984 (0.47)	50.1 \pm 12.58	68.3 \pm 21.8	2.54 \pm 0.65	0 \pm 0.25	-350	-1.2	0
090	1	161.50635 (0.34)	58.86472 (0.33)	32.9 \pm 4.63	68 \pm 15.77	3.47 \pm 0.72	2.22 \pm 0.3	-86	-0.8	-1.2
091	2	161.86249 (0.43)	58.92955 (0.42)	52.3 \pm 13.35	67.1 \pm 19.63	1.86 \pm 0.55	0.99 \pm 0.18	-62	-1.5	0
092	7	161.52157 (0.02)	59.00702 (0.03)	66.9 \pm 2.76	66.9 \pm 2.79	0 \pm 0.01	0 \pm 0.01	-3	-0.8	-0.7
093	3	161.34127 (0.06)	58.95113 (0.07)	63 \pm 3.06	66.7 \pm 4.33	0.95 \pm 0.12	0 \pm 0.04	-37	-1	-1.1
094	1	161.36242 (0.57)	59.14937 (0.55)	23.1 \pm 4.44	66.7 \pm 20.55	4.95 \pm 1.11	2.69 \pm 0.54	-19	-0.5	-1.1
095	7	161.11867 (0.2)	58.98544 (0.21)	66.4 \pm 12.4	66.4 \pm 12.77	0 \pm 0.12	0 \pm 0.02	-12	1.4	0
096	7	161.48435 (0.03)	59.07867 (0.04)	66.3 \pm 2.35	66.3 \pm 2.87	0 \pm 0.07	0 \pm 0.02	-71	-1.1	-1.2
097	3	161.74184 (0.09)	59.08687 (0.09)	63.3 \pm 4.05	66.2 \pm 5.07	0.84 \pm 0.12	0 \pm 0.03	-39	-0.7	-1.4
098	1	161.70787 (0.42)	58.90566 (0.41)	29.9 \pm 4.95	66 \pm 17.22	3.7 \pm 0.8	2.36 \pm 0.37	-93	-0.8	-2.6

CB Catalogue continued

ID	Size Flag	RA (J2000) (arcsec)	Dec (J2000) (arcsec)	S_P ($\mu\text{Jy beam}^{-1}$)	S_T (μJy)	θ_{DM} (arcsec)	θ_{Dm} (arcsec)	ϕ (degrees)	α_{IF}	α_{IM}
099	3	161.60743 (0.45)	58.81865 (0.43)	52.9 \pm 13.45	65.8 \pm 20.51	2.03 \pm 0.57	0 \pm 0.19	-65	2.2	-0.6
100	4	161.37477 (0.12)	58.8732 (0.12)	61.7 \pm 4.66	65.6 \pm 5.59	0.79 \pm 0.13	0.59 \pm 0.02	-76	-1.3	-0.3
101	1	161.81823 (0.67)	59.02337 (0.63)	19.4 \pm 5.04	64.1 \pm 23.57	5.28 \pm 1.1	3.16 \pm 0.77	-37	-0.8	0
102	7	161.50425 (0.03)	59.08072 (0.03)	63.3 \pm 2.87	63.3 \pm 2.92	0 \pm 0.02	0 \pm 0.01	4	-0.7	-0.7
103	2	161.75987 (0.09)	59.04819 (0.1)	58.1 \pm 3.7	62.9 \pm 5.23	1.12 \pm 0.15	0.26 \pm 0.05	-55	-1.1	-1.4
104	3	161.18455 (0.54)	59.12738 (0.53)	40.6 \pm 10.12	62.6 \pm 20.64	3.22 \pm 0.76	0 \pm 0.33	-137	0.2	0
105	7	161.78236 (0.21)	58.88471 (0.22)	62.3 \pm 11.43	62.3 \pm 11.78	0 \pm 0.13	0 \pm 0.02	52	-1.4	0.3
106	3	161.39247 (0.08)	58.9074 (0.09)	54.9 \pm 3.28	62 \pm 5.54	1.44 \pm 0.19	0 \pm 0.08	-74	-0.8	-1.4
107	7	161.48955 (0.03)	58.94327 (0.04)	61.9 \pm 3.02	61.9 \pm 3.05	0 \pm 0.02	0 \pm 0.01	7	-0.9	-0.9
108	2	161.65577 (0.05)	59.02447 (0.06)	57.4 \pm 2.48	61.3 \pm 3.74	0.98 \pm 0.12	0.28 \pm 0.04	-43	-0.9	-0.9
109	2	161.61247 (0.52)	59.18537 (0.51)	37 \pm 7.89	61.2 \pm 18.23	3.56 \pm 0.77	0.45 \pm 0.35	-36	-1.2	0.2
110	7	161.74793 (0.07)	58.95918 (0.08)	60.9 \pm 4.35	60.9 \pm 4.37	0 \pm 0.02	0 \pm 0.01	6	-0.6	-1.5
111	7	161.56958 (0.03)	58.98549 (0.03)	60.1 \pm 2.75	60.1 \pm 2.78	0 \pm 0.02	0 \pm 0.01	-6	-0.8	-0.9
112	6	161.53656 (0.04)	58.98454 (0.04)	58.6 \pm 1.95	58.9 \pm 2.64	0.26 \pm 0.08	0.01 \pm 0.02	10	-0.5	-0.1
113	1	161.23811 (0.57)	58.98003 (0.55)	20.1 \pm 3.79	58 \pm 17.76	5.04 \pm 1.13	2.62 \pm 0.53	-53	-1.6	-1.5
114	1	161.78693 (0.22)	59.08057 (0.2)	45.3 \pm 5.61	57.9 \pm 9.64	1.81 \pm 0.33	1.04 \pm 0.15	21	-0.6	-2.1
115	1	161.51499 (0.14)	59.06115 (0.14)	25.9 \pm 1.93	57 \pm 7.93	3.88 \pm 0.47	2.18 \pm 0.22	-55	-0.7	-0.8
116	5	161.41738 (0.48)	58.82083 (0.47)	48.3 \pm 12.9	55.6 \pm 17.07	1.56 \pm 0.59	0.18 \pm 0.24	9	0	0
117	6	161.83644 (0.38)	59.12083 (0.37)	51.7 \pm 12.55	55.6 \pm 15	1.09 \pm 0.42	0 \pm 0.13	-47	-1.1	-2.6
118	3	161.6498 (0.22)	59.13013 (0.21)	35.5 \pm 4.17	55 \pm 10.94	3.24 \pm 0.6	0 \pm 0.21	-102	-0.1	-1.2
119	2	161.45117 (0.06)	59.08406 (0.07)	47.4 \pm 2.33	54.9 \pm 4.45	1.53 \pm 0.18	0.44 \pm 0.08	21	-0.9	-0.8
120	3	161.60981 (0.06)	59.09399 (0.07)	52.2 \pm 2.73	54.9 \pm 3.7	0.91 \pm 0.12	0 \pm 0.04	-10	-1	-0.8
121	3	161.7286 (0.72)	59.13844 (0.68)	23.2 \pm 5.9	54.7 \pm 20.41	5.89 \pm 1.3	0 \pm 0.51	-66	-0.4	0
122	1	161.27066 (0.08)	58.99669 (0.08)	49.5 \pm 3.07	53.4 \pm 4.17	0.98 \pm 0.13	0.49 \pm 0.04	-101	-1	-1.2
123	2	161.61021 (0.07)	59.07518 (0.08)	45.9 \pm 2.42	53.3 \pm 4.6	1.58 \pm 0.19	0.33 \pm 0.09	-63	-0.8	-1.4
124	6	161.24266 (0.29)	58.91104 (0.27)	46.1 \pm 6.52	53 \pm 10.62	1.55 \pm 0.46	0 \pm 0.19	-62	-1.2	-1.7
125	3	161.79083 (0.17)	59.03648 (0.16)	46.3 \pm 4.58	52.5 \pm 6.87	1.47 \pm 0.24	0 \pm 0.1	29	0.2	-0.7
126	1	161.25072 (0.13)	59.05022 (0.13)	44.8 \pm 3.03	52.3 \pm 4.8	1.27 \pm 0.17	0.97 \pm 0.07	-24	0	-0.7
127	1	161.59016 (0.07)	59.10523 (0.08)	46.7 \pm 2.68	51 \pm 3.78	1 \pm 0.13	0.63 \pm 0.04	26	-1	-1.3
128	1	161.19551 (0.42)	59.03256 (0.41)	29.6 \pm 5.39	50.8 \pm 13.19	3.08 \pm 0.64	1.53 \pm 0.32	-102	1.3	-1.8
129	1	161.81508 (0.47)	59.02282 (0.46)	28.1 \pm 5.95	50.8 \pm 14.61	3.07 \pm 0.66	1.86 \pm 0.37	32	0.2	-1.8
130	6	161.38137 (0.24)	59.17424 (0.23)	45.8 \pm 6.02	49.6 \pm 7.47	1.14 \pm 0.25	0 \pm 0.08	1	-0.1	-2.3
131	2	161.22034 (0.52)	59.10943 (0.52)	28.4 \pm 6.55	49 \pm 13.66	3.16 \pm 0.71	1.44 \pm 0.37	-49	-1	0
132	1	161.31514 (0.15)	58.93339 (0.15)	39.1 \pm 2.8	48.7 \pm 5.37	1.7 \pm 0.24	0.95 \pm 0.11	-36	-0.8	-1
133	6	161.34449 (0.07)	58.93595 (0.08)	46.9 \pm 2.9	48.3 \pm 3.35	0.67 \pm 0.1	0 \pm 0.01	-39	-1	-1.5
134	3	161.12457 (0.46)	59.04386 (0.45)	37.8 \pm 9.56	48.3 \pm 15.16	2.19 \pm 0.6	0 \pm 0.21	-84	0	0
135	1	161.25436 (0.29)	58.96915 (0.28)	26.9 \pm 3.63	48.2 \pm 10.27	2.97 \pm 0.58	1.91 \pm 0.27	3	-0.7	-2
136	1	161.83256 (0.46)	59.09136 (0.45)	32.1 \pm 8.11	48 \pm 15.14	2.27 \pm 0.61	1.58 \pm 0.25	-75	1	0
137	1	161.25953 (0.27)	58.91965 (0.26)	35.9 \pm 5.01	47.8 \pm 8.55	1.66 \pm 0.32	1.51 \pm 0.15	-2	-0.2	-0.9
138	3	161.62621 (0.06)	59.01081 (0.07)	42.8 \pm 2.19	47.6 \pm 3.72	1.34 \pm 0.16	0 \pm 0.07	-130	-1.1	-0.8
139	6	161.37503 (0.16)	58.87684 (0.15)	44.8 \pm 4.74	47.6 \pm 5.81	0.99 \pm 0.2	0 \pm 0.05	-44	-0.7	-2.1
140	7	161.56725 (0.09)	58.8954 (0.1)	46.8 \pm 3.09	46.8 \pm 3.52	0 \pm 0.1	0 \pm 0.01	-10	-1	-1.4
141	7	161.22076 (0.17)	58.91491 (0.18)	46.7 \pm 7.55	46.7 \pm 7.81	0 \pm 0.12	0 \pm 0.01	23	-1	-1.3
142	3	161.57084 (0.09)	59.07968 (0.1)	35.4 \pm 2.4	46.6 \pm 5.68	2.36 \pm 0.32	0 \pm 0.13	-44	0.1	-0.1
143	2	161.34087 (0.69)	59.16109 (0.64)	19.1 \pm 4.99	46.6 \pm 16.33	5.52 \pm 1.17	1.18 \pm 0.56	-138	0	0
144	2	161.46271 (0.06)	58.96782 (0.07)	42.6 \pm 2.07	46.5 \pm 3.18	1.11 \pm 0.14	0.41 \pm 0.05	-51	-0.7	-0.8
145	2	161.14953 (0.59)	59.0091 (0.58)	26 \pm 6.55	46.4 \pm 15.54	3.95 \pm 0.81	0.55 \pm 0.43	-158	-1.8	1.3
146	6	161.20099 (0.22)	58.93509 (0.22)	45.5 \pm 6.74	46.2 \pm 7.58	0.49 \pm 0.21	0 \pm 0.03	3	-0.5	0
147	1	161.49202 (0.14)	58.91922 (0.14)	32.2 \pm 2.37	46.1 \pm 5.82	2.16 \pm 0.32	1.43 \pm 0.14	4	-1.4	-1.5
148	7	161.60257 (0.1)	58.88225 (0.11)	45.9 \pm 4.27	46 \pm 4.38	0.12 \pm 0.06	0 \pm 0.01	-63	-1.1	-1.3

CB Catalogue continued

ID	Size Flag	RA (J2000) (arcsec)	Dec (J2000) (arcsec)	S_P ($\mu\text{Jy beam}^{-1}$)	S_T (μJy)	θ_{DM} (arcsec)	θ_{Dm} (arcsec)	ϕ (degrees)	α_{IF}	α_{IM}
149	1	161.63463 (0.68)	58.90333 (0.64)	14 ± 3.26	45.3 ± 15.72	5.45 ± 1.18	2.91 ± 0.68	-124	-1.6	-1.3
150	3	161.69653 (0.63)	59.14698 (0.61)	22.3 ± 5.37	44.4 ± 15.2	4.72 ± 0.97	0 ± 0.46	-123	0.8	-0.5
151	3	161.25187 (0.61)	59.10872 (0.59)	22.6 ± 4.84	44.2 ± 14.24	4.62 ± 0.99	0 ± 0.42	-106	-1.6	-1.4
152	3	161.76756 (0.15)	59.04314 (0.15)	40.2 ± 3.78	43.9 ± 5.2	1.2 ± 0.2	0 ± 0.07	-118	-0.7	-2
153	7	161.66308 (0.08)	58.92273 (0.1)	43.8 ± 3.25	43.8 ± 3.26	0 ± 0.02	0 ± 0.01	17	-0.4	-0.8
154	3	161.75926 (0.34)	59.12912 (0.33)	38.4 ± 6.96	43.4 ± 9.49	1.45 ± 0.36	0 ± 0.11	18	-1.7	-2.8
155	1	161.44173 (0.41)	58.91715 (0.41)	15.4 ± 2.48	43 ± 11.2	3.81 ± 0.84	3.57 ± 0.45	-17	-0.7	-1
156	3	161.23407 (0.5)	59.14402 (0.49)	30.6 ± 7.64	42.9 ± 13.8	2.7 ± 0.68	0 ± 0.27	18	0	0
157	7	161.45402 (0.04)	59.05933 (0.05)	42.8 ± 2.47	42.8 ± 2.48	0 ± 0.02	0 ± 0.01	-12	-0.8	0.1
158	3	161.54065 (0.07)	58.92624 (0.08)	41 ± 2.44	42.7 ± 3.04	0.79 ± 0.11	0 ± 0.03	-136	-0.7	-0.8
159	3	161.14336 (0.47)	59.05013 (0.46)	32.5 ± 8.18	42.7 ± 13.47	2.34 ± 0.62	0 ± 0.23	-49	0	0
160	1	161.55578 (0.06)	58.9727 (0.07)	38.4 ± 2.01	42.6 ± 3.07	1.09 ± 0.14	0.68 ± 0.05	-134	-0.9	-1
161	6	161.56745 (0.05)	59.04119 (0.06)	42.3 ± 1.98	42.5 ± 2.54	0.27 ± 0.1	0 ± 0.03	-13	-0.6	-0.6
162	6	161.50786 (0.11)	59.15468 (0.12)	42.2 ± 3.7	42.5 ± 3.92	0.34 ± 0.08	0 ± 0.01	-3	-0.6	-0.8
163	1	161.20474 (0.42)	58.97861 (0.41)	27.1 ± 5.27	42.5 ± 10.97	2.63 ± 0.55	1.46 ± 0.28	-53	-0.9	-1.5
164	1	161.64786 (0.07)	59.04012 (0.09)	36.4 ± 2.16	42.2 ± 3.57	1.3 ± 0.17	0.86 ± 0.07	-57	-1	-0.9
165	3	161.29149 (0.13)	59.05858 (0.13)	38.5 ± 2.62	42.1 ± 4.92	1.23 ± 0.26	0 ± 0.11	-12	-0.2	-0.7
166	2	161.57522 (0.4)	58.88714 (0.39)	23.2 ± 3.61	42.1 ± 10.21	3.8 ± 0.84	1.01 ± 0.28	-126	-1.6	-1.7
167	1	161.73573 (0.43)	58.90558 (0.42)	29.1 ± 5.95	42 ± 10.96	2.39 ± 0.51	1.19 ± 0.24	-144	1	-2.6
168	1	161.69915 (0.13)	59.00629 (0.14)	33.4 ± 2.23	41.8 ± 4.55	1.8 ± 0.25	0.86 ± 0.12	-133	-1.1	-1.3
169	5	161.55611 (0.06)	58.99478 (0.07)	39.2 ± 1.94	41.7 ± 3.23	0.95 ± 0.17	0.31 ± 0.07	-79	-0.8	-1
170	1	161.54932 (0.12)	59.04057 (0.13)	25.4 ± 2.13	41.5 ± 6.52	3.04 ± 0.48	1.23 ± 0.18	-26	-0.9	-0.7
171	2	161.48346 (0.45)	59.18833 (0.44)	30.8 ± 6.72	41.3 ± 11.38	2.43 ± 0.54	0.21 ± 0.23	-50	0.7	0
172	7	161.2156 (0.23)	59.15175 (0.24)	41.3 ± 11.23	41.3 ± 11.68	0 ± 0.2	0 ± 0.07	37	0	0
173	3	161.34088 (0.16)	59.10362 (0.16)	34.6 ± 2.66	41.2 ± 4.86	1.78 ± 0.26	0 ± 0.11	28	-0.5	-1
174	3	161.19806 (0.3)	58.98881 (0.29)	34.4 ± 5.09	41 ± 7.81	1.79 ± 0.35	0 ± 0.14	-20	-0.9	-2.1
175	6	161.55165 (0.29)	59.18943 (0.28)	39.5 ± 6.9	41 ± 8.14	0.75 ± 0.29	0.13 ± 0.06	-3	-0.7	-1.6
176	3	161.81374 (0.45)	59.11714 (0.44)	32.6 ± 8.27	41 ± 12.82	2.1 ± 0.58	0 ± 0.2	-5	0	0
177	3	161.71871 (0.14)	59.06209 (0.14)	35.9 ± 2.68	40.7 ± 4.28	1.46 ± 0.21	0 ± 0.09	-96	-0.6	-1
178	6	161.1871 (0.35)	59.04804 (0.34)	35.4 ± 5.79	40.7 ± 9.09	1.57 ± 0.5	0 ± 0.21	-30	-1.5	-2.9
179	3	161.32163 (0.2)	58.93123 (0.19)	31.7 ± 3.34	40.6 ± 6.46	2.2 ± 0.37	0 ± 0.15	-83	-0.7	-1
180	1	161.6727 (0.22)	58.91971 (0.21)	28.7 ± 3.54	40.3 ± 6.93	2.02 ± 0.36	1.46 ± 0.17	-110	-0.4	-1.2
181	2	161.30997 (0.57)	58.90048 (0.56)	20.6 ± 4.49	40.1 ± 11.58	3.96 ± 0.85	1.34 ± 0.43	-103	-0.7	-0.1
182	2	161.62608 (0.78)	59.14141 (0.73)	14 ± 3.62	40.1 ± 14.39	6.55 ± 1.52	1.31 ± 0.59	-102	-0.4	-0.8
183	1	161.81355 (0.57)	59.05448 (0.56)	20.2 ± 5.07	40 ± 13.41	3.61 ± 0.79	1.82 ± 0.46	-73	0.9	-3
184	6	161.6977 (0.07)	59.02247 (0.08)	39.1 ± 2.56	39.7 ± 2.76	0.46 ± 0.07	0 ± 0.01	-35	-1	-1.3
185	3	161.33074 (0.46)	59.17521 (0.45)	30.6 ± 7.43	39.7 ± 12.03	2.26 ± 0.58	0 ± 0.22	-87	-0.3	-0.6
186	3	161.73046 (0.53)	58.91027 (0.52)	24.3 ± 5.31	39.6 ± 12.11	3.55 ± 0.77	0 ± 0.35	-5	-1	-2.6
187	2	161.47227 (0.09)	58.92153 (0.1)	36.1 ± 2.29	39.4 ± 3.28	1.15 ± 0.15	0.32 ± 0.05	-69	0.3	-0.3
188	2	161.44463 (0.21)	58.97377 (0.22)	19.9 ± 1.71	39.2 ± 5.99	4.47 ± 0.57	0.67 ± 0.21	-131	-0.8	-1
189	7	161.76327 (0.1)	58.98609 (0.12)	39.1 ± 4.15	39.1 ± 4.24	0 ± 0.06	0 ± 0.01	-64	-1.2	-1.2
190	1	161.67585 (0.16)	58.97691 (0.16)	28.7 ± 2.18	38.8 ± 4.83	2 ± 0.3	1.21 ± 0.14	21	-0.1	-0.9
191	7	161.23209 (0.1)	59.0352 (0.11)	38.8 ± 4.13	38.8 ± 4.21	0 ± 0.06	0 ± 0.01	40	-1.2	-1.3
192	2	161.19912 (0.46)	59.03784 (0.45)	24.7 ± 5.3	38.7 ± 10.38	2.9 ± 0.62	1.11 ± 0.32	-110	-0.6	-2.5
193	1	161.5216 (0.61)	59.15631 (0.59)	14.4 ± 3.46	38.6 ± 13	4.32 ± 0.87	2.86 ± 0.65	-135	1.1	-0.6
194	5	161.52014 (0.35)	59.21248 (0.34)	36.4 ± 9.63	38.6 ± 11.03	0.93 ± 0.39	0.26 ± 0.13	-150	0	0
195	3	161.55353 (0.59)	58.84587 (0.58)	22 ± 5.55	38.6 ± 13.12	3.95 ± 0.81	0 ± 0.42	-14	0	0
196	2	161.65062 (0.12)	58.96734 (0.12)	31.7 ± 2.05	38.1 ± 3.79	1.67 ± 0.23	0.66 ± 0.1	-137	-0.2	-0.7
197	6	161.59592 (0.06)	58.99294 (0.07)	37.4 ± 2.09	38 ± 2.32	0.49 ± 0.07	0 ± 0.01	-81	-0.6	-1
198	3	161.34506 (0.08)	58.9802 (0.08)	35.8 ± 2.21	38 ± 2.97	0.99 ± 0.13	0 ± 0.04	-131	0.7	0

CB Catalogue continued

ID	Size Flag	RA (J2000) (arcsec)	Dec (J2000) (arcsec)	S_P ($\mu\text{Jy beam}^{-1}$)	S_T (μJy)	θ_{DM} (arcsec)	θ_{Dm} (arcsec)	ϕ (degrees)	α_{IF}	α_{IM}
199	6	161.31089 (0.19)	59.12072 (0.18)	36 ± 4.08	38 ± 5.74	0.92 ± 0.29	0 ± 0.12	-6	-1.3	-1.6
200	7	161.7405 (0.1)	59.07544 (0.11)	37.6 ± 4	37.6 ± 4.08	0 ± 0.06	0 ± 0.01	8	-1	-1.5
201	2	161.1676 (0.5)	58.99155 (0.5)	24.5 ± 6.05	37.6 ± 11.31	2.8 ± 0.69	1.07 ± 0.3	-30	-0.9	-1.5
202	2	161.31441 (0.62)	59.13515 (0.6)	18.4 ± 4.28	37.4 ± 11.77	4.4 ± 0.9	1.1 ± 0.48	-83	0.1	-1.3
203	1	161.47559 (0.08)	59.01836 (0.1)	27.1 ± 1.72	37.3 ± 4.1	2.01 ± 0.27	1.34 ± 0.13	-55	-0.8	-1.1
204	3	161.64633 (0.18)	58.99017 (0.18)	24.7 ± 2.21	37.3 ± 6.36	3.1 ± 0.53	0 ± 0.18	-98	-0.9	-0.5
205	2	161.49119 (0.51)	58.87385 (0.5)	20.7 ± 4.02	37.2 ± 10.84	4.02 ± 0.88	0.47 ± 0.36	-124	1	-0.5
206	1	161.77686 (0.6)	58.95512 (0.58)	16.8 ± 4.26	37.2 ± 12.8	4.17 ± 0.83	1.91 ± 0.55	-82	0.1	-0.1
207	4	161.54575 (0.09)	58.92124 (0.09)	35 ± 2.28	36.6 ± 2.69	0.73 ± 0.11	0.38 ± 0.02	-47	-0.5	-0.8
208	1	161.45359 (0.1)	59.08888 (0.11)	30.1 ± 1.9	36.4 ± 3.43	1.48 ± 0.2	1.01 ± 0.09	-4	-1.1	-1.1
209	1	161.72279 (0.57)	59.11911 (0.57)	15.3 ± 3.84	36.3 ± 12.21	3.72 ± 0.8	2.74 ± 0.56	-126	0	0
210	7	161.44546 (0.05)	59.02973 (0.06)	36 ± 2.2	36 ± 2.22	0 ± 0.02	0 ± 0.01	10	-1	-0.7
211	1	161.60176 (0.93)	59.04128 (0.79)	6.5 ± 1.77	35.9 ± 14.22	9.01 ± 2.07	3.47 ± 0.83	-229	-1.5	-1
212	2	161.32698 (0.22)	58.91737 (0.2)	28.9 ± 3.59	35.4 ± 5.76	1.8 ± 0.33	0.6 ± 0.14	-63	-0.7	-1.2
213	2	161.40934 (0.1)	58.97351 (0.11)	28.6 ± 1.8	35.1 ± 3.58	1.79 ± 0.24	0.65 ± 0.11	17	-0.6	-0.7
214	3	161.68459 (0.59)	58.88059 (0.58)	19.9 ± 5.02	34.9 ± 11.89	3.97 ± 0.82	0 ± 0.42	-30	1.9	-1.6
215	6	161.6183 (0.07)	58.99849 (0.08)	34.2 ± 2	34.7 ± 2.66	0.47 ± 0.13	0 ± 0.04	-25	-1.3	-1.3
216	1	161.65148 (0.67)	58.91868 (0.63)	11.3 ± 2.83	34.5 ± 12.43	5.25 ± 1.1	2.78 ± 0.7	-147	-1.6	-0.9
217	3	161.39273 (0.08)	59.0034 (0.09)	31.6 ± 1.87	34.2 ± 3.48	1.13 ± 0.22	0 ± 0.1	20	-0.6	-0.9
218	2	161.48168 (0.72)	59.15423 (0.67)	12 ± 3.16	33.8 ± 11.27	5.84 ± 1.27	1.82 ± 0.63	-44	-0.2	-0.9
219	1	161.75423 (0.51)	58.99203 (0.5)	15.2 ± 3.47	33.6 ± 10.27	3.1 ± 0.69	2.96 ± 0.47	4	-1.1	-0.2
220	3	161.46426 (0.59)	58.86758 (0.58)	18.8 ± 4.26	33.4 ± 10.7	4.02 ± 0.85	0 ± 0.4	-30	-0.8	-0.4
221	2	161.53387 (0.62)	58.87559 (0.6)	15.5 ± 3.64	33.4 ± 10.14	4.42 ± 0.9	1.48 ± 0.51	14	-1.4	-0.5
222	6	161.16747 (0.34)	58.93873 (0.33)	32.3 ± 8.04	33.2 ± 9.29	0.65 ± 0.38	0 ± 0.12	-126	-1.4	0
223	3	161.80362 (0.48)	59.10063 (0.47)	24.6 ± 6.18	33.2 ± 10.56	2.48 ± 0.64	0 ± 0.25	-125	0	0
224	3	161.70505 (0.47)	59.15939 (0.46)	25.1 ± 6.34	33 ± 10.44	2.34 ± 0.62	0 ± 0.23	-21	0	0
225	1	161.4981 (0.25)	59.1333 (0.24)	22.6 ± 2.92	32.6 ± 6.17	2.42 ± 0.45	1.11 ± 0.19	-113	-0.3	-1.1
226	3	161.16723 (0.46)	59.06261 (0.45)	25.1 ± 6.34	32.5 ± 10.22	2.25 ± 0.61	0.14 ± 0.22	-127	0.5	0
227	3	161.44676 (0.15)	58.91713 (0.15)	28.1 ± 2.27	32.3 ± 3.71	1.56 ± 0.23	0 ± 0.1	-313	-0.2	-0.5
228	1	161.39735 (0.14)	58.92165 (0.14)	28.5 ± 2.45	32.2 ± 3.42	1.06 ± 0.17	0.92 ± 0.06	-99	0.1	0
229	1	161.57794 (0.15)	58.96255 (0.15)	22.7 ± 1.61	32.1 ± 3.73	1.9 ± 0.27	1.63 ± 0.14	-83	-0.5	-1.2
230	7	161.70505 (0.09)	59.02431 (0.1)	31.9 ± 2.41	31.9 ± 2.41	0 ± 0.02	0 ± 0.01	-11	-1.3	-1.2
231	3	161.26109 (0.26)	58.98067 (0.24)	25.3 ± 3.32	31.8 ± 5.74	2.07 ± 0.38	0.15 ± 0.16	-45	-0.4	-1.1
232	1	161.55409 (0.17)	59.089 (0.17)	23.2 ± 1.92	31.7 ± 4.3	2.14 ± 0.33	1.13 ± 0.14	-88	-0.9	-1.3
233	3	161.22131 (0.53)	59.09477 (0.52)	21.1 ± 5.11	31.7 ± 10.2	3.09 ± 0.73	0 ± 0.32	-97	0	0
234	6	161.36358 (0.35)	58.85291 (0.34)	30.5 ± 7.03	31.6 ± 8.21	0.73 ± 0.37	0 ± 0.11	6	0	0
235	1	161.47633 (0.36)	58.92045 (0.35)	15.2 ± 2.24	31.5 ± 7.23	3.16 ± 0.64	2.54 ± 0.33	-86	-1.2	-0.9
236	3	161.82578 (0.52)	59.0406 (0.51)	21.2 ± 5.26	31.5 ± 10.33	3.03 ± 0.74	0 ± 0.31	-115	-0.1	0
237	1	161.44772 (0.69)	59.12907 (0.65)	9.1 ± 2.38	31.4 ± 11.73	5.56 ± 1.19	3.18 ± 0.78	-13	0	0
238	3	161.73537 (0.26)	59.04306 (0.24)	24.3 ± 3.16	31.3 ± 5.79	2.24 ± 0.41	0 ± 0.17	-125	-1.2	-0.9
239	1	161.30047 (0.49)	58.90675 (0.48)	18.4 ± 4.31	31.3 ± 9.41	2.65 ± 0.63	1.93 ± 0.32	-118	-1.6	-1.6
240	1	161.41121 (0.36)	58.91248 (0.36)	17.8 ± 2.71	31.1 ± 7.24	3.12 ± 0.63	1.59 ± 0.28	8	0.6	0.4
241	1	161.70856 (0.23)	58.95617 (0.22)	24.4 ± 3.12	31 ± 5.31	1.84 ± 0.34	0.94 ± 0.15	18	-0.9	-0.8
242	1	161.36309 (0.69)	59.05273 (0.65)	7.1 ± 1.79	30.8 ± 11.28	5.6 ± 1.21	4.5 ± 0.96	-97	-0.8	-1.4
243	1	161.56482 (0.08)	59.01735 (0.09)	26.9 ± 1.64	30.7 ± 2.55	1.2 ± 0.16	0.82 ± 0.06	-46	-0.9	-1.1
244	2	161.62493 (0.14)	59.08833 (0.14)	27.3 ± 2.04	30.7 ± 3.04	1.3 ± 0.19	0.53 ± 0.07	31	-0.6	-0.2
245	6	161.40158 (0.07)	59.07563 (0.09)	30.4 ± 2.09	30.5 ± 2.16	0.25 ± 0.05	0 ± 0.01	-10	-1.5	-0.9
246	3	161.4892 (0.44)	58.83803 (0.43)	24.8 ± 6.31	30.5 ± 9.5	1.97 ± 0.56	0 ± 0.19	-14	0	0
247	1	161.70268 (0.35)	59.07288 (0.33)	18.8 ± 2.85	30.4 ± 6.6	2.61 ± 0.51	1.7 ± 0.25	-25	-1.5	-0.9
248	3	161.29336 (0.2)	59.06878 (0.19)	25 ± 2.97	30.1 ± 4.87	1.84 ± 0.33	0 ± 0.14	-101	-1.4	-0.8

CB Catalogue continued

ID	Size Flag	RA (J2000) (arcsec)	Dec (J2000) (arcsec)	S_P ($\mu\text{Jy beam}^{-1}$)	S_T (μJy)	θ_{DM} (arcsec)	θ_{Dm} (arcsec)	ϕ (degrees)	α_{IF}	α_{IM}
249	7	161.78769 (0.25)	58.96699 (0.24)	30.1 ± 4.72	30.1 ± 5.44	0 ± 0.25	0 ± 0.04	-11	0.2	-1.2
250	1	161.7785 (0.43)	59.10649 (0.42)	22.5 ± 5.66	30 ± 9.12	1.8 ± 0.53	1.36 ± 0.18	110	0.9	0
251	3	161.58645 (0.46)	59.18523 (0.45)	23 ± 5.81	29.9 ± 9.45	2.29 ± 0.61	0 ± 0.22	-27	0	0
252	6	161.56751 (0.11)	59.0749 (0.12)	27.5 ± 1.78	29.8 ± 3.18	1.14 ± 0.24	0 ± 0.11	-8	-0.9	-0.9
253	1	161.55465 (0.11)	58.95961 (0.12)	25.8 ± 1.67	29.8 ± 2.75	1.37 ± 0.18	0.75 ± 0.08	-31	-0.8	-0.5
254	3	161.42133 (0.15)	58.94478 (0.15)	25 ± 1.77	29.8 ± 3.38	1.8 ± 0.26	0 ± 0.11	-127	-0.6	-0.9
255	3	161.50919 (0.11)	59.08225 (0.12)	26.1 ± 1.69	29.7 ± 2.85	1.49 ± 0.2	0 ± 0.08	-53	-1.1	-1
256	3	161.53911 (0.63)	58.87723 (0.61)	14.9 ± 3.56	29.6 ± 10.11	4.71 ± 0.97	0 ± 0.46	10	0.8	-0.8
257	1	161.59681 (0.15)	58.96275 (0.15)	23.6 ± 1.62	29.3 ± 3.22	1.78 ± 0.25	0.81 ± 0.11	28	-0.9	-1.5
258	1	161.40183 (0.32)	59.02795 (0.32)	13.1 ± 1.77	29.3 ± 7.19	4.43 ± 0.96	1.75 ± 0.29	-50	-0.9	-1
259	2	161.43436 (0.46)	58.85102 (0.44)	22.1 ± 5.57	29.1 ± 8.82	2.17 ± 0.59	0.72 ± 0.22	-4	-1.1	0
260	7	161.21352 (0.17)	59.05423 (0.18)	29 ± 4.73	29 ± 4.89	0 ± 0.12	0 ± 0.01	-14	0	-1
261	1	161.59301 (0.09)	59.0511 (0.09)	26.9 ± 1.73	28.9 ± 2.23	0.86 ± 0.12	0.62 ± 0.03	-152	-0.6	-0.6
262	1	161.561 (0.19)	59.11049 (0.18)	21.7 ± 2.38	28.8 ± 4.29	1.7 ± 0.29	1.46 ± 0.14	-125	-0.8	-1.4
263	1	161.51842 (0.18)	59.11117 (0.18)	21.8 ± 2.28	28.7 ± 4.12	1.7 ± 0.28	1.41 ± 0.13	-63	0.1	-0.9
264	7	161.67632 (0.09)	59.06968 (0.11)	28.6 ± 2.56	28.6 ± 2.58	0 ± 0.04	0 ± 0.01	20	-0.3	-0.2
265	7	161.21309 (0.17)	58.99515 (0.18)	28.6 ± 4.53	28.6 ± 4.69	0 ± 0.12	0 ± 0.01	49	0.1	-1.9
266	1	161.53714 (0.41)	59.07027 (0.41)	12 ± 1.77	28.5 ± 7.66	4.82 ± 1.12	1.7 ± 0.32	5	-1.1	-1.8
267	1	161.45827 (0.8)	58.9938 (0.74)	5.5 ± 1.43	28.5 ± 11.15	6.68 ± 1.56	4.7 ± 1.06	72	-1.4	-1
268	3	161.36028 (0.49)	59.16898 (0.48)	20.5 ± 5.12	28.5 ± 9.16	2.66 ± 0.68	0 ± 0.27	11	0	0
269	2	161.56492 (0.1)	58.96938 (0.11)	25.9 ± 1.67	28.4 ± 2.46	1.21 ± 0.16	0.21 ± 0.06	-21	-0.1	-0.2
270	3	161.52429 (0.2)	58.95671 (0.2)	19 ± 1.97	28.3 ± 5.45	3.04 ± 0.6	0 ± 0.2	-10	0	-0.1
271	7	161.70578 (0.21)	59.14137 (0.22)	28.3 ± 5.38	28.3 ± 5.53	0 ± 0.13	0 ± 0.02	-3	-0.8	0
272	1	161.2252 (0.57)	59.03103 (0.56)	13.6 ± 3.42	27.7 ± 9.29	3.69 ± 0.8	1.88 ± 0.47	-111	0.8	-1.9
273	3	161.7458 (0.66)	58.95279 (0.63)	13 ± 3.36	27.7 ± 10.1	5.18 ± 1.07	0 ± 0.5	8	1.4	1.1
274	3	161.55528 (0.15)	59.05594 (0.15)	22 ± 1.81	27.5 ± 4.18	2.05 ± 0.4	0 ± 0.15	-100	-1.4	-0.7
275	6	161.25539 (0.35)	58.93199 (0.34)	25.7 ± 4.64	27.5 ± 6.1	1.07 ± 0.4	0 ± 0.15	28	-0.6	-1.2
276	1	161.52204 (0.16)	59.01419 (0.16)	18.3 ± 1.5	27.4 ± 3.89	2.34 ± 0.37	1.49 ± 0.16	-121	-1.2	-0.9
277	1	161.55217 (0.72)	59.10113 (0.67)	7.5 ± 1.93	27.4 ± 10.27	5.84 ± 1.28	3.29 ± 0.8	30	0.5	0.6
278	7	161.32793 (0.12)	58.97676 (0.12)	27.3 ± 2.07	27.3 ± 2.43	0 ± 0.13	0 ± 0.02	-157	-0.5	-1.2
279	6	161.38084 (0.08)	59.04112 (0.09)	26.9 ± 1.84	27.2 ± 1.94	0.37 ± 0.06	0 ± 0.01	-65	-1.1	-1.3
280	3	161.71595 (0.51)	59.13136 (0.5)	18.8 ± 4.64	27.2 ± 8.74	2.86 ± 0.71	0 ± 0.29	9	-0.3	0
281	6	161.73233 (0.43)	59.14139 (0.42)	22.8 ± 5.83	27.1 ± 7.44	1.78 ± 0.53	0 ± 0.16	9	0	0
282	6	161.56235 (0.4)	59.18497 (0.39)	24.1 ± 5.94	26.9 ± 7.25	1.35 ± 0.45	0 ± 0.14	-30	1.8	0
283	2	161.77808 (0.39)	58.97987 (0.38)	22 ± 4.25	26.8 ± 6.36	1.91 ± 0.42	0.19 ± 0.16	-115	1.4	-1.2
284	3	161.74843 (0.51)	59.11938 (0.51)	18.3 ± 4.55	26.7 ± 8.71	2.93 ± 0.73	0 ± 0.3	-22	0	0
285	7	161.76232 (0.14)	59.00071 (0.15)	26.6 ± 3.82	26.6 ± 3.95	0 ± 0.1	0 ± 0.01	-8	-0.3	-0.6
286	1	161.58444 (0.2)	58.99224 (0.2)	16.4 ± 1.81	26.5 ± 4.66	2.57 ± 0.46	1.72 ± 0.2	33	-1.2	-0.3
287	3	161.27649 (0.65)	58.94375 (0.62)	12.9 ± 3.25	26.5 ± 9.43	4.95 ± 1.01	0 ± 0.49	-65	-1.1	-1.5
288	7	161.52199 (0.06)	58.97979 (0.08)	26.3 ± 1.85	26.3 ± 1.85	0 ± 0.02	0 ± 0.01	-6	-0.6	-0.1
289	6	161.77072 (0.31)	59.05784 (0.3)	24.1 ± 4.03	26.3 ± 4.95	1.18 ± 0.31	0 ± 0.09	-146	-0.9	-2.2
290	1	161.6422 (0.76)	59.05779 (0.71)	6.6 ± 1.76	26.3 ± 10.25	6.26 ± 1.42	3.44 ± 0.86	-21	-0.1	-0.1
291	2	161.37576 (0.17)	58.99686 (0.17)	20.9 ± 1.76	26.2 ± 3.35	1.95 ± 0.3	0.58 ± 0.13	-74	-1	-0.5
292	3	161.30284 (0.24)	59.09315 (0.23)	23.4 ± 3.09	26.1 ± 4.29	1.36 ± 0.28	0 ± 0.1	-21	0.1	-0.2
293	5	161.6718 (0.47)	58.87134 (0.46)	22.7 ± 6.14	26 ± 8.02	1.52 ± 0.58	0.2 ± 0.23	-92	-0.3	-2
294	1	161.60589 (0.17)	58.93976 (0.17)	21.3 ± 2.24	25.9 ± 3.53	1.43 ± 0.25	1.09 ± 0.1	-52	-1.5	-0.7
295	1	161.55575 (0.5)	58.90845 (0.5)	12.5 ± 2.73	25.9 ± 7.78	3.3 ± 0.71	2.42 ± 0.44	-28	0.1	0.1
296	1	161.56144 (0.57)	59.12634 (0.56)	10.5 ± 2.49	25.8 ± 8.4	3.7 ± 0.8	2.97 ± 0.56	309	-0.6	-1.9
297	2	161.29448 (0.48)	59.09861 (0.47)	16.9 ± 3.71	25.7 ± 7.42	3.03 ± 0.65	0.58 ± 0.32	-29	0.8	-1.4
298	7	161.39827 (0.09)	58.9471 (0.1)	25.6 ± 2.06	25.6 ± 2.08	0 ± 0.02	0 ± 0.01	49	-0.8	-0.7

258

continued on the next page

CB Catalogue continued

ID	Size Flag	RA (J2000) (arcsec)	Dec (J2000) (arcsec)	S_P ($\mu\text{Jy beam}^{-1}$)	S_T (μJy)	θ_{DM} (arcsec)	θ_{Dm} (arcsec)	ϕ (degrees)	α_{IF}	α_{IM}
299	7	161.49875 (0.09)	59.10857 (0.11)	25.6 ± 2.22	25.6 ± 2.25	0 ± 0.03	0 ± 0.01	-94	-1.4	-0.9
300	3	161.49555 (0.18)	59.09199 (0.17)	20.9 ± 1.92	25.6 ± 3.52	1.94 ± 0.31	0 ± 0.13	-134	-0.7	-1.3
301	3	161.39052 (0.44)	59.1759 (0.43)	20.7 ± 5.27	25.6 ± 7.99	2 ± 0.57	0 ± 0.19	-134	1.2	0
302	1	161.65986 (0.53)	59.06983 (0.52)	11.5 ± 2.27	25.5 ± 7.65	4.13 ± 0.91	1.94 ± 0.45	-109	-0.6	-1.3
303	1	161.63341 (0.58)	59.01177 (0.56)	9.5 ± 1.8	25.4 ± 7.85	5.19 ± 1.17	2.08 ± 0.49	-113	-1.6	-0.4
304	1	161.3443 (0.2)	58.99766 (0.19)	18.8 ± 2.09	25.2 ± 3.94	1.92 ± 0.33	1.24 ± 0.15	-81	-1	-1.2
305	7	161.57934 (0.11)	59.12646 (0.12)	25.1 ± 3.11	25.1 ± 3.19	0 ± 0.08	0 ± 0.01	-13	0.1	0
306	2	161.53199 (0.65)	58.89065 (0.62)	11.1 ± 2.83	24.9 ± 8.42	4.99 ± 1.02	1.16 ± 0.53	-91	0.7	-0.4
307	3	161.52044 (0.11)	58.97559 (0.11)	22.9 ± 1.5	24.7 ± 2.11	1.12 ± 0.15	0 ± 0.05	26	-1.3	-1
308	3	161.49505 (0.2)	58.95292 (0.19)	18.2 ± 1.94	24.6 ± 4.16	2.48 ± 0.43	0 ± 0.17	-83	-0.8	-0.8
309	3	161.39729 (0.22)	58.91195 (0.21)	22 ± 2.78	24.5 ± 3.86	1.33 ± 0.27	0 ± 0.09	-138	-0.7	-0.8
310	7	161.3983 (0.08)	59.00224 (0.1)	24.3 ± 1.7	24.3 ± 1.76	0 ± 0.05	0 ± 0.01	-69	-0.8	-0.4
311	3	161.44761 (0.6)	59.15636 (0.58)	13.5 ± 3.41	24.3 ± 8.34	4.12 ± 0.83	0 ± 0.44	-44	2	0
312	3	161.50481 (0.12)	59.03511 (0.12)	21 ± 1.38	24.2 ± 2.39	1.55 ± 0.21	0 ± 0.09	-12	-1.3	-1.1
313	3	161.63355 (0.76)	59.04908 (0.72)	8.9 ± 1.85	24.2 ± 8.28	6.95 ± 1.6	0 ± 0.46	-320	0.2	-0.5
314	2	161.51491 (0.5)	58.90313 (0.49)	14 ± 2.77	24.1 ± 6.88	3.72 ± 0.81	0.58 ± 0.34	-60	-0.9	-1
315	3	161.49869 (0.16)	58.94216 (0.15)	21 ± 1.82	23.9 ± 2.81	1.47 ± 0.23	0 ± 0.09	-53	0.7	-0.1
316	3	161.57049 (0.23)	58.91582 (0.22)	20.2 ± 2.58	23.9 ± 4.04	1.75 ± 0.32	0 ± 0.13	-22	-0.9	-1.7
317	2	161.49927 (0.25)	59.1254 (0.24)	19.6 ± 2.59	23.8 ± 4.02	1.74 ± 0.33	0.67 ± 0.14	1	-1.3	-1.3
318	6	161.63442 (0.41)	59.17177 (0.4)	20.7 ± 5.27	23.8 ± 6.57	1.56 ± 0.5	0 ± 0.15	-88	-0.9	1.2
319	6	161.39758 (0.26)	58.91408 (0.25)	20.8 ± 2.84	23.7 ± 4.56	1.51 ± 0.44	0 ± 0.18	16	-0.5	-0.5
320	3	161.31279 (0.5)	59.13314 (0.49)	16.7 ± 4.07	23.7 ± 7.52	2.78 ± 0.68	0 ± 0.28	-128	0	-0.9
321	3	161.64725 (0.19)	58.98642 (0.18)	19.8 ± 2.04	23.6 ± 3.43	1.8 ± 0.3	0 ± 0.13	-14	-0.7	-0.5
322	1	161.40933 (0.34)	58.92263 (0.33)	15.7 ± 2.47	23.6 ± 5.02	2.29 ± 0.45	1.58 ± 0.22	17	-0.8	-0.9
323	2	161.68697 (0.35)	59.09038 (0.34)	18 ± 2.98	23.6 ± 4.89	2.1 ± 0.42	0.82 ± 0.18	-138	-0.5	-1.1
324	1	161.41983 (0.17)	59.0857 (0.16)	19.5 ± 1.98	23.5 ± 3.09	1.37 ± 0.24	1.12 ± 0.09	9	-0.3	-0.7
325	3	161.4174 (0.38)	58.89758 (0.37)	18.1 ± 3.23	23.5 ± 5.44	2.26 ± 0.47	0 ± 0.19	-63	-0.6	-0.5
326	1	161.70213 (0.54)	59.01258 (0.53)	11.3 ± 2.41	23.5 ± 7.21	3.79 ± 0.82	1.95 ± 0.45	-20	0.1	-0.9
327	3	161.27557 (0.25)	59.00993 (0.24)	20.4 ± 2.73	23.4 ± 4	1.55 ± 0.3	0 ± 0.12	-71	-0.6	-0.5
328	3	161.57097 (0.6)	58.89945 (0.59)	12.7 ± 2.84	23.3 ± 7.53	4.24 ± 0.89	0 ± 0.42	-118	0.2	-0.4
329	1	161.61272 (0.2)	58.97512 (0.19)	17.8 ± 1.93	23.2 ± 3.56	1.92 ± 0.32	1.05 ± 0.15	8	0.9	-0.9
330	6	161.81627 (0.37)	58.97221 (0.37)	21.8 ± 5.48	23.2 ± 6.5	1.02 ± 0.42	0 ± 0.13	-2	1.7	0.5
331	7	161.69082 (0.1)	59.02143 (0.12)	23.1 ± 2.52	23.1 ± 2.58	0 ± 0.06	0 ± 0.01	22	-1.3	-1.2
332	1	161.56201 (0.13)	59.01116 (0.13)	19.4 ± 1.32	23 ± 2.19	1.36 ± 0.19	1.02 ± 0.08	8	-0.8	-0.8
333	3	161.55362 (0.58)	59.15834 (0.57)	13.5 ± 3.4	23 ± 7.75	3.77 ± 0.8	0 ± 0.4	7	1.8	0.1
334	2	161.31448 (0.44)	59.06509 (0.43)	13.8 ± 2.67	22.7 ± 5.71	3.1 ± 0.65	1.22 ± 0.32	-129	0	-1.2
335	1	161.73628 (0.43)	59.06209 (0.42)	15.8 ± 3.29	22.7 ± 5.92	2.24 ± 0.49	1.33 ± 0.23	-119	0.8	-0.1
336	3	161.35514 (0.19)	59.02451 (0.18)	18.9 ± 1.94	22.6 ± 3.28	1.81 ± 0.3	0 ± 0.13	-130	-0.5	-1.2
337	1	161.36945 (0.21)	59.03592 (0.2)	16.9 ± 1.93	22.6 ± 3.67	2.02 ± 0.35	1.11 ± 0.16	8	-0.8	-1.2
338	3	161.55008 (0.14)	59.04256 (0.14)	19.8 ± 1.34	22.5 ± 2.21	1.48 ± 0.2	0 ± 0.08	-92	-0.5	-0.2
339	1	161.56865 (0.45)	59.02429 (0.44)	9.5 ± 1.58	22.5 ± 6.22	4.25 ± 0.98	2.2 ± 0.38	-53	-0.6	-0.8
340	1	161.40847 (0.16)	58.99038 (0.16)	17.7 ± 1.65	22.4 ± 2.78	1.46 ± 0.24	1.35 ± 0.1	-124	-0.9	-1
341	1	161.47933 (0.27)	59.00197 (0.26)	11.7 ± 1.55	22.3 ± 4.75	3.09 ± 0.6	2.15 ± 0.28	-114	-0.1	-0.4
342	2	161.52571 (0.37)	58.90723 (0.36)	15.8 ± 2.66	22.3 ± 4.89	2.48 ± 0.5	0.9 ± 0.22	27	0.5	-1
343	3	161.59263 (0.16)	58.98537 (0.15)	19.3 ± 1.61	22.2 ± 2.62	1.57 ± 0.24	0 ± 0.1	15	0.1	-0.7
344	3	161.3124 (0.61)	58.98168 (0.58)	11 ± 2.29	22.2 ± 7.1	4.82 ± 1.05	0 ± 0.42	-73	0.5	-0.6
345	3	161.62811 (0.19)	58.98532 (0.18)	18.4 ± 1.93	22.1 ± 3.26	1.83 ± 0.31	0 ± 0.13	-57	-0.1	-0.1
346	6	161.5935 (0.1)	59.03106 (0.11)	21.7 ± 1.52	22 ± 1.64	0.48 ± 0.08	0 ± 0.01	-176	-1	-0.5
347	7	161.62094 (0.09)	59.0361 (0.1)	22 ± 1.74	22 ± 1.75	0 ± 0.02	0 ± 0.01	0	-1.5	-1.7
348	6	161.22336 (0.37)	58.98506 (0.36)	19.8 ± 3.98	21.9 ± 4.87	1.31 ± 0.37	0 ± 0.11	-24	-1.6	-1.5

CB Catalogue continued

ID	Size Flag	RA (J2000) (arcsec)	Dec (J2000) (arcsec)	S_P ($\mu\text{Jy beam}^{-1}$)	S_T (μJy)	θ_{DM} (arcsec)	θ_{Dm} (arcsec)	ϕ (degrees)	α_{IF}	α_{IM}
349	7	161.54023 (0.09)	58.95438 (0.1)	21.8 ± 1.77	21.8 ± 1.78	0 ± 0.02	0 ± 0.01	57	-0.3	0.5
350	2	161.46761 (0.66)	59.12378 (0.63)	8.4 ± 2.17	21.8 ± 6.9	5.17 ± 1.07	1.91 ± 0.61	-65	0.5	-0.6
351	3	161.28796 (0.63)	59.07409 (0.6)	11 ± 2.72	21.5 ± 7.44	4.61 ± 0.92	0 ± 0.47	-12	1	1.3
352	7	161.49521 (0.23)	58.84524 (0.24)	21.5 ± 5.85	21.5 ± 6.09	0 ± 0.2	0 ± 0.07	24	-0.9	-0.4
353	3	161.61483 (0.5)	59.0935 (0.49)	12.2 ± 2.3	21.4 ± 6.21	3.99 ± 0.88	0 ± 0.34	-87	0	-0.5
354	3	161.29903 (0.46)	58.97195 (0.45)	14 ± 2.83	21.4 ± 6.03	3.19 ± 0.68	0 ± 0.3	-51	-1.1	-0.2
355	7	161.61659 (0.12)	59.10688 (0.13)	21.3 ± 2.79	21.3 ± 2.87	0 ± 0.09	0 ± 0.01	38	-0.7	-0.8
356	6	161.68448 (0.16)	59.00859 (0.15)	20.1 ± 2.2	21.2 ± 2.66	0.94 ± 0.2	0 ± 0.05	-137	-1	-1.3
357	1	161.29671 (0.34)	59.03124 (0.33)	15.5 ± 2.48	21.1 ± 4.44	2.12 ± 0.42	1.09 ± 0.19	-142	-0.5	-0.8
358	1	161.25468 (0.56)	58.97998 (0.55)	11.2 ± 2.81	21.1 ± 7.04	3.52 ± 0.78	1.61 ± 0.43	-97	-1.4	-1.5
359	2	161.5813 (0.15)	59.02242 (0.15)	18.3 ± 1.49	21 ± 2.35	1.48 ± 0.22	0.43 ± 0.09	-125	-0.4	-0.7
360	3	161.19304 (0.45)	59.03578 (0.44)	16.8 ± 4.26	21 ± 6.57	2.07 ± 0.58	0 ± 0.2	-129	0.7	0
361	3	161.48744 (0.13)	59.00006 (0.13)	19 ± 1.29	20.9 ± 1.91	1.25 ± 0.17	0 ± 0.06	-100	-1.3	-1.3
362	3	161.57368 (0.2)	59.09812 (0.19)	17.9 ± 2.17	20.8 ± 3.28	1.6 ± 0.29	0 ± 0.12	-114	-0.3	-0.2
363	7	161.60317 (0.22)	58.89628 (0.22)	20.8 ± 3.3	20.8 ± 3.6	0 ± 0.19	0 ± 0.03	8	1.3	-1.1
364	3	161.38926 (0.54)	59.13385 (0.53)	13.4 ± 3.15	20.8 ± 6.57	3.27 ± 0.74	0 ± 0.33	-83	-0.4	-0.6
365	3	161.54913 (0.25)	58.93888 (0.24)	15.9 ± 2.06	20.6 ± 3.83	2.28 ± 0.42	0 ± 0.17	-100	-0.2	-1.1
366	3	161.37898 (0.27)	58.97188 (0.26)	14.9 ± 1.98	20.6 ± 4.11	2.63 ± 0.5	0 ± 0.2	-54	-1.6	-0.3
367	2	161.72834 (0.45)	58.93978 (0.44)	16.1 ± 3.66	20.6 ± 5.74	2.13 ± 0.52	0.38 ± 0.2	-89	0.7	0
368	3	161.37166 (0.19)	58.99989 (0.18)	17.2 ± 1.87	20.5 ± 3.06	1.77 ± 0.3	0 ± 0.13	22	-0.8	-0.9
369	1	161.43027 (0.43)	59.11635 (0.42)	12.6 ± 2.57	20.5 ± 5.42	2.57 ± 0.55	1.73 ± 0.29	19	-0.5	-1.1
370	3	161.2522 (0.53)	59.02108 (0.53)	13.3 ± 3.1	20.5 ± 6.4	3.21 ± 0.72	0 ± 0.33	-57	-0.3	-1.1
371	2	161.3048 (0.61)	59.08197 (0.59)	10 ± 2.53	20.5 ± 6.67	4.38 ± 0.85	1.18 ± 0.52	-35	0	-1.7
372	3	161.63563 (0.28)	59.00333 (0.27)	14.4 ± 1.96	20.4 ± 5.08	2.77 ± 0.75	0 ± 0.23	-105	0	0.4
373	1	161.69017 (0.29)	58.98763 (0.28)	16.1 ± 2.35	20.4 ± 3.82	1.75 ± 0.35	1.04 ± 0.15	-13	0.3	-1.2
374	7	161.72844 (0.18)	58.96339 (0.18)	20.3 ± 3.33	20.3 ± 3.44	0 ± 0.12	0 ± 0.01	17	-0.6	-0.8
375	3	161.67472 (0.57)	58.91585 (0.56)	12.3 ± 3.07	20.3 ± 6.8	3.62 ± 0.79	0 ± 0.38	-109	1.5	2
376	3	161.56753 (0.43)	59.16358 (0.42)	16.6 ± 4.1	20 ± 5.98	1.84 ± 0.52	0 ± 0.17	2	1.6	-0.3
377	2	161.49725 (0.56)	59.14225 (0.55)	11.1 ± 2.75	19.9 ± 6.07	3.51 ± 0.78	1.28 ± 0.4	-142	0	-0.5
378	2	161.59933 (0.25)	58.99295 (0.24)	13.8 ± 1.78	19.8 ± 3.92	2.76 ± 0.52	0.51 ± 0.21	-56	-1.6	-0.5
379	1	161.58376 (0.47)	59.1366 (0.46)	13.2 ± 3.05	19.8 ± 5.78	2.41 ± 0.58	1.43 ± 0.26	3	0.4	1.3
380	3	161.33192 (0.32)	58.99853 (0.31)	14.5 ± 2.04	19.7 ± 4.03	2.53 ± 0.49	0 ± 0.2	-78	-0.4	-0.8
381	7	161.38368 (0.23)	59.17303 (0.24)	19.7 ± 5.36	19.7 ± 5.57	0 ± 0.2	0 ± 0.07	1	0.6	-1.4
382	3	161.58957 (0.33)	59.07453 (0.32)	13.2 ± 1.84	19.6 ± 4.27	3.01 ± 0.59	0 ± 0.23	-99	-1	-1.5
383	2	161.62832 (0.45)	59.06111 (0.45)	11 ± 2.03	19.6 ± 5.04	3.59 ± 0.77	1.16 ± 0.33	-107	-0.7	-1
384	2	161.58681 (0.49)	59.08407 (0.48)	10.8 ± 2.01	19.6 ± 5.41	3.92 ± 0.86	0.8 ± 0.34	-107	-0.3	1.1
385	7	161.53278 (0.09)	59.00418 (0.1)	19.5 ± 1.4	19.5 ± 1.45	0 ± 0.05	0 ± 0.01	-68	-1.7	-1.1
386	1	161.62472 (0.66)	59.02078 (0.63)	6 ± 1.54	19.5 ± 7.1	5.13 ± 1.05	3.23 ± 0.77	-134	0	-1.1
387	6	161.42611 (0.14)	59.03969 (0.14)	18.9 ± 1.46	19.4 ± 2.06	0.67 ± 0.2	0 ± 0.08	-18	-0.3	-0.9
388	2	161.3899 (0.56)	59.09488 (0.55)	10.5 ± 2.18	19.4 ± 5.94	4.16 ± 0.9	0.52 ± 0.4	-115	0.1	-0.3
389	1	161.31992 (0.55)	59.08074 (0.54)	10.3 ± 2.47	19.4 ± 6.21	3.36 ± 0.75	1.76 ± 0.41	2	-0.5	-1.6
390	7	161.69194 (0.17)	59.08804 (0.18)	19.3 ± 3.05	19.3 ± 3.16	0 ± 0.12	0 ± 0.01	12	-0.7	-0.2
391	1	161.38673 (0.32)	59.0407 (0.31)	12.4 ± 1.73	19.2 ± 4.02	2.75 ± 0.53	1.21 ± 0.23	-76	-1.4	-1.1
392	2	161.47272 (0.47)	59.15322 (0.46)	13.9 ± 3.35	19.2 ± 5.56	2.35 ± 0.59	0.92 ± 0.24	-138	-0.2	0.3
393	3	161.61781 (0.47)	59.14477 (0.46)	14.7 ± 3.56	19.2 ± 5.84	2.32 ± 0.59	0 ± 0.22	-32	-0.1	-1
394	6	161.56177 (0.15)	58.95976 (0.15)	17.9 ± 1.75	19.1 ± 2.16	1.01 ± 0.19	0 ± 0.05	-2	-1	-1.4
395	1	161.49067 (0.17)	58.95997 (0.17)	16.4 ± 1.71	19.1 ± 2.58	1.41 ± 0.24	0.76 ± 0.1	-61	-0.7	-0.5
396	3	161.58775 (0.18)	58.96408 (0.17)	16.9 ± 1.85	19.1 ± 2.73	1.47 ± 0.26	0 ± 0.1	-51	-0.9	-1.2
397	6	161.28546 (0.32)	59.08419 (0.31)	17.7 ± 3.19	19.1 ± 3.87	1.13 ± 0.33	0 ± 0.09	-28	0.7	0.9
398	3	161.3145 (0.45)	59.13771 (0.44)	15.3 ± 3.89	19.1 ± 5.97	2.05 ± 0.57	0 ± 0.19	11	0.8	0

CB Catalogue continued

ID	Size Flag	RA (J2000) (arcsec)	Dec (J2000) (arcsec)	S_P ($\mu\text{Jy beam}^{-1}$)	S_T (μJy)	θ_{DM} (arcsec)	θ_{Dm} (arcsec)	ϕ (degrees)	α_{IF}	α_{IM}
399	7	161.53175 (0.14)	58.91096 (0.15)	19 ± 2.67	19 ± 2.76	0 ± 0.1	0 ± 0.01	-20	-0.6	1.6
400	1	161.46575 (0.42)	59.06271 (0.41)	9.8 ± 1.69	19 ± 4.97	3.5 ± 0.75	1.84 ± 0.34	19	-1.5	-1.3
401	2	161.66923 (0.57)	59.08995 (0.57)	9.8 ± 2.4	19 ± 5.65	3.74 ± 0.8	1.56 ± 0.45	-105	-0.3	-1
402	1	161.41803 (0.62)	59.03421 (0.6)	5.8 ± 1.43	19 ± 6.55	4.56 ± 0.91	3.75 ± 0.79	-5	-1	-0.6
403	3	161.7174 (0.49)	58.94729 (0.48)	13.6 ± 3.2	18.9 ± 5.74	2.67 ± 0.63	0 ± 0.27	26	-0.8	-1.4
404	3	161.54056 (0.26)	59.10317 (0.25)	15.6 ± 2.12	18.8 ± 3.37	1.83 ± 0.35	0 ± 0.14	-139	1.6	-0.5
405	7	161.59212 (0.1)	59.06574 (0.11)	18.7 ± 1.97	18.7 ± 2.01	0 ± 0.06	0 ± 0.01	-9	-0.8	-0.7
406	7	161.49803 (0.11)	59.10351 (0.12)	18.7 ± 2.29	18.7 ± 2.35	0 ± 0.08	0 ± 0.01	-6	-1.4	-1.2
407	3	161.69876 (0.36)	59.04477 (0.35)	14.8 ± 2.51	18.7 ± 4.13	2.13 ± 0.43	0 ± 0.18	-111	-0.2	-1.2
408	3	161.7802 (0.47)	58.9959 (0.46)	14.3 ± 3.6	18.7 ± 5.93	2.34 ± 0.62	0 ± 0.23	30	1.1	0
409	1	161.40075 (0.55)	59.03083 (0.55)	7.4 ± 1.62	18.6 ± 5.77	3.82 ± 0.82	2.92 ± 0.54	6	-0.5	-0.5
410	3	161.52775 (0.15)	59.06112 (0.15)	17.1 ± 1.57	18.5 ± 2.12	1.13 ± 0.19	0 ± 0.06	-101	-0.9	-0.8
411	2	161.44817 (0.54)	58.88663 (0.54)	11.3 ± 2.82	18.5 ± 5.9	3.32 ± 0.77	0.84 ± 0.36	-7	1.9	0.8
412	3	161.61625 (0.26)	58.99011 (0.25)	13.9 ± 1.89	18.4 ± 4.4	2.38 ± 0.65	0 ± 0.22	-5	-0.3	-0.7
413	6	161.6481 (0.23)	58.89339 (0.23)	18.3 ± 3.95	18.4 ± 4.09	0.2 ± 0.15	0.15 ± 0.04	0	-0.2	-1.9
414	6	161.27887 (0.38)	58.90767 (0.37)	17.1 ± 4.31	18.4 ± 5.15	1.09 ± 0.43	0 ± 0.14	5	-0.7	-0.3
415	2	161.37513 (0.61)	58.92079 (0.59)	9 ± 2.27	18.4 ± 5.93	4.32 ± 0.84	1.27 ± 0.51	-28	-0.9	-2.8
416	2	161.62235 (0.3)	58.9609 (0.29)	14 ± 1.98	18.1 ± 3.38	2.08 ± 0.4	0.72 ± 0.17	-69	-0.4	-1.1
417	3	161.36027 (0.51)	59.05295 (0.5)	10.3 ± 1.98	18.1 ± 5.32	4 ± 0.88	0 ± 0.35	-64	0	0.2
418	3	161.53498 (0.17)	59.00611 (0.17)	15.5 ± 1.49	18 ± 2.37	1.61 ± 0.26	0 ± 0.11	-126	-1.3	-1.2
419	7	161.51758 (0.23)	59.16405 (0.24)	17.9 ± 4.13	17.9 ± 4.27	0 ± 0.16	0 ± 0.05	-24	0.1	0.1
420	3	161.59968 (0.47)	59.14964 (0.46)	13.6 ± 3.43	17.8 ± 5.61	2.31 ± 0.61	0 ± 0.22	-26	0.7	-0.1
421	3	161.42941 (0.55)	58.89004 (0.54)	11.3 ± 2.81	17.8 ± 5.9	3.36 ± 0.77	0 ± 0.35	-126	-0.1	0.8
422	4	161.6121 (0.28)	59.09575 (0.27)	14.8 ± 2.2	17.7 ± 2.98	1.28 ± 0.29	1.13 ± 0.1	-65	-0.5	-0.5
423	2	161.38787 (0.71)	58.93716 (0.67)	7.3 ± 1.92	17.6 ± 6.49	5.76 ± 1.25	0.74 ± 0.54	20	-1.5	-1.6
424	6	161.63573 (0.27)	59.1093 (0.27)	17.3 ± 2.65	17.5 ± 3.24	0.46 ± 0.28	0 ± 0.09	96	-0.4	-0.1
425	2	161.3082 (0.31)	59.00514 (0.3)	14.6 ± 2.3	17.5 ± 3.38	1.68 ± 0.35	0.59 ± 0.14	-130	-1.2	-1.5
426	3	161.38515 (0.42)	58.90439 (0.41)	14.4 ± 3.05	17.5 ± 4.55	1.93 ± 0.46	0 ± 0.16	18	0.6	-1
427	3	161.28729 (0.51)	58.94804 (0.5)	12.2 ± 2.95	17.5 ± 5.54	2.84 ± 0.69	0 ± 0.29	-33	-0.4	-2.1
428	6	161.6841 (0.24)	59.00744 (0.23)	16 ± 2.11	17.4 ± 2.63	1.16 ± 0.26	0 ± 0.08	-34	-0.6	-1.2
429	3	161.39322 (0.33)	58.94474 (0.31)	13.9 ± 2.13	17.4 ± 3.52	2.06 ± 0.41	0 ± 0.17	-124	-0.7	-0.3
430	3	161.54016 (0.47)	59.1527 (0.46)	13.3 ± 3.27	17.4 ± 5.41	2.35 ± 0.61	0 ± 0.23	8	1.2	-0.8
431	3	161.26564 (0.51)	59.08338 (0.5)	12.2 ± 3.03	17.4 ± 5.64	2.82 ± 0.71	0 ± 0.29	-108	2	1.5
432	3	161.51706 (0.49)	58.89977 (0.49)	13.4 ± 2.91	17.3 ± 5.69	2.26 ± 0.77	0 ± 0.33	-78	-1	-0.6
433	1	161.54405 (0.25)	58.98254 (0.24)	12.6 ± 1.62	17.2 ± 3.08	2.07 ± 0.38	1.22 ± 0.17	-29	-0.2	-1.1
434	1	161.58934 (0.45)	58.97354 (0.44)	9.7 ± 1.84	17.2 ± 4.7	3.36 ± 0.71	1.41 ± 0.34	-122	0.2	-0.6
435	3	161.32206 (0.58)	59.09244 (0.57)	9.9 ± 2.49	17.2 ± 5.83	3.9 ± 0.81	0 ± 0.42	-127	1.6	-1.3
436	5	161.50933 (0.23)	59.17176 (0.24)	17 ± 4.57	17.2 ± 4.76	0.33 ± 0.2	0.25 ± 0.07	0	0	0
437	7	161.64345 (0.11)	58.98721 (0.12)	17 ± 2.15	17 ± 2.21	0 ± 0.08	0 ± 0.01	38	-1	-1
438	3	161.53655 (0.24)	59.09301 (0.23)	14.8 ± 1.94	17 ± 2.84	1.55 ± 0.3	0.1 ± 0.12	-120	-0.9	-1.3
439	3	161.28696 (0.37)	59.02114 (0.36)	14.1 ± 2.57	17 ± 3.82	1.84 ± 0.4	0 ± 0.15	-29	-1.3	-1
440	1	161.67097 (0.54)	59.02552 (0.53)	9.2 ± 2.07	17 ± 5.26	3.46 ± 0.76	1.56 ± 0.4	-139	1.1	0.8
441	2	161.36066 (0.65)	59.08451 (0.62)	8 ± 2.05	17 ± 5.99	4.99 ± 1.02	0.65 ± 0.51	-61	0.3	0
442	7	161.63734 (0.23)	59.1577 (0.24)	17 ± 4.61	17 ± 4.79	0 ± 0.2	0 ± 0.07	-17	0.7	0.7
443	2	161.52248 (0.19)	59.00361 (0.19)	13.7 ± 1.53	16.9 ± 2.52	1.79 ± 0.31	0.74 ± 0.13	-36	-2.1	0.3
444	3	161.6044 (0.29)	59.07111 (0.28)	13.6 ± 1.89	16.9 ± 3.18	2.03 ± 0.39	0 ± 0.16	-143	0	-0.7
445	1	161.54925 (0.63)	59.01783 (0.6)	6.5 ± 1.43	16.8 ± 5.51	4.89 ± 1.05	2.12 ± 0.55	-101	-1.3	-0.9
446	3	161.63575 (0.7)	58.95407 (0.65)	7.4 ± 1.93	16.8 ± 6.3	5.63 ± 1.21	0 ± 0.52	-3	-1.5	0
447	2	161.47938 (0.67)	58.93377 (0.63)	6.6 ± 1.7	16.8 ± 5.43	5.24 ± 1.09	1.76 ± 0.6	3	0.2	-0.1
448	3	161.56673 (0.17)	58.99486 (0.17)	14.9 ± 1.59	16.7 ± 2.28	1.38 ± 0.24	0 ± 0.09	-75	-1.3	-1.4

CB Catalogue continued

ID	Size Flag	RA (J2000) (arcsec)	Dec (J2000) (arcsec)	S_P ($\mu\text{Jy beam}^{-1}$)	S_T (μJy)	θ_{DM} (arcsec)	θ_{Dm} (arcsec)	ϕ (degrees)	α_{IF}	α_{IM}
449	3	161.376 (0.38)	59.11015 (0.37)	13.8 ± 2.64	16.7 ± 3.91	1.87 ± 0.41	0 ± 0.15	-83	-0.8	-0.9
450	1	161.27683 (0.51)	59.02632 (0.5)	10 ± 2.45	16.7 ± 5.35	2.91 ± 0.71	1.53 ± 0.34	-145	0	-0.4
451	1	161.60071 (0.54)	59.0755 (0.53)	7 ± 1.72	16.7 ± 5.42	3.23 ± 0.75	3.23 ± 0.51	-3	0	0
452	1	161.68745 (0.58)	58.98859 (0.57)	7.8 ± 1.95	16.7 ± 5.64	3.83 ± 0.81	2.07 ± 0.51	-68	0.7	0.3
453	1	161.47005 (0.26)	59.06138 (0.25)	12.3 ± 1.64	16.6 ± 2.98	1.95 ± 0.36	1.25 ± 0.17	-20	-0.6	-0.2
454	6	161.48966 (0.35)	58.89542 (0.34)	14.9 ± 2.85	16.4 ± 3.48	1.25 ± 0.35	0 ± 0.1	-63	-0.1	-1.5
455	3	161.53571 (0.16)	59.00685 (0.15)	15 ± 1.48	16.3 ± 2.02	1.2 ± 0.21	0 ± 0.07	-83	-1	-1.7
456	3	161.75761 (0.45)	59.00385 (0.44)	12.9 ± 3.14	16.3 ± 4.91	2.13 ± 0.56	0 ± 0.2	-34	-1.7	-0.8
457	3	161.62634 (0.44)	58.88692 (0.43)	13.1 ± 3.34	16.3 ± 5.07	2.01 ± 0.57	0 ± 0.19	11	0	0.7
458	3	161.55091 (0.17)	59.01885 (0.16)	14.5 ± 1.52	16.2 ± 2.17	1.35 ± 0.24	0 ± 0.09	-158	-1.1	-0.8
459	6	161.25014 (0.35)	59.00891 (0.34)	15.3 ± 3.09	16.2 ± 3.69	0.96 ± 0.35	0 ± 0.09	-133	-0.2	-1.8
460	3	161.46722 (0.32)	59.00521 (0.31)	10.7 ± 1.48	16.1 ± 3.52	3.08 ± 0.61	0 ± 0.23	-125	-1.7	-0.4
461	6	161.45897 (0.32)	59.13736 (0.31)	15.8 ± 2.92	16.1 ± 3.5	0.54 ± 0.32	0 ± 0.09	15	-0.1	-0.8
462	7	161.23121 (0.23)	59.09096 (0.24)	16.1 ± 4.38	16.1 ± 4.55	0 ± 0.2	0 ± 0.07	23	0	0
463	3	161.66001 (0.42)	59.06803 (0.41)	11.8 ± 2.35	16 ± 4.15	2.52 ± 0.53	0 ± 0.23	7	-1.3	-1.6
464	2	161.58116 (0.56)	58.91686 (0.56)	9 ± 2.22	16 ± 4.96	3.58 ± 0.78	1.16 ± 0.41	-96	-0.1	1.1
465	1	161.72971 (0.49)	59.03623 (0.48)	9.9 ± 2.47	16 ± 5.13	2.6 ± 0.67	1.72 ± 0.31	44	1.3	0
466	6	161.62972 (0.28)	59.10246 (0.28)	15.6 ± 2.46	15.9 ± 3.03	0.55 ± 0.3	0 ± 0.09	10	-0.8	-2
467	3	161.62944 (0.49)	59.13099 (0.48)	11.5 ± 2.88	15.9 ± 5.11	2.64 ± 0.67	0 ± 0.26	-101	-0.6	0
468	3	161.42396 (0.31)	58.98933 (0.3)	11.4 ± 1.59	15.8 ± 3.24	2.62 ± 0.5	0 ± 0.2	-101	-1.1	-0.6
469	2	161.42806 (0.44)	58.92895 (0.43)	10.9 ± 2.29	15.8 ± 4.05	2.54 ± 0.55	0.99 ± 0.26	-69	-1	-0.6
470	2	161.46845 (0.47)	58.92467 (0.47)	10.2 ± 2.26	15.8 ± 4.29	2.81 ± 0.62	1.15 ± 0.31	-74	-0.8	1.1
471	3	161.57354 (0.49)	59.13988 (0.48)	11.5 ± 2.86	15.8 ± 5	2.58 ± 0.65	0 ± 0.26	18	0	0
472	2	161.71349 (0.58)	59.03082 (0.57)	8.9 ± 2.23	15.8 ± 5.16	3.82 ± 0.8	0.78 ± 0.42	29	1.3	0
473	1	161.57568 (0.31)	59.02556 (0.3)	10.9 ± 1.53	15.7 ± 3.12	2.36 ± 0.45	1.2 ± 0.2	-98	-1.3	-1.6
474	1	161.37108 (0.5)	59.01814 (0.49)	8.6 ± 1.85	15.7 ± 4.68	3.36 ± 0.72	1.6 ± 0.39	-24	-0.8	-1
475	1	161.73455 (0.46)	59.02421 (0.45)	10.8 ± 2.65	15.7 ± 4.8	2.28 ± 0.59	1.37 ± 0.25	-140	0.6	-0.4
476	3	161.45382 (0.51)	58.9367 (0.51)	9.6 ± 2.06	15.5 ± 4.67	3.49 ± 0.75	0 ± 0.34	3	-0.1	0.6
477	7	161.47955 (0.23)	58.87957 (0.24)	15.5 ± 3.53	15.5 ± 3.65	0 ± 0.16	0 ± 0.04	85	0	-1.2
478	5	161.60905 (0.23)	59.15575 (0.24)	15.3 ± 4.11	15.5 ± 4.28	0.33 ± 0.2	0.25 ± 0.07	-9	-0.8	0
479	2	161.56051 (0.36)	58.98537 (0.35)	10.3 ± 1.6	15.3 ± 3.37	2.82 ± 0.56	0.77 ± 0.24	-59	-0.4	-0.5
480	7	161.24118 (0.23)	58.99115 (0.23)	15.3 ± 3.41	15.3 ± 3.53	0 ± 0.15	0 ± 0.04	-109	-1.2	0.1
481	7	161.3039 (0.18)	59.0568 (0.19)	15.2 ± 2.57	15.2 ± 2.65	0 ± 0.12	0 ± 0.01	-43	0.6	-0.7
482	3	161.59069 (0.22)	59.0412 (0.21)	13.1 ± 1.67	15.1 ± 2.46	1.55 ± 0.29	0 ± 0.11	-24	-1.4	-1.3
483	2	161.55218 (0.36)	59.05385 (0.34)	10.2 ± 1.62	15.1 ± 3.15	2.58 ± 0.51	1.1 ± 0.23	-77	0	-0.4
484	3	161.67326 (0.42)	58.92426 (0.41)	12.8 ± 3	15.1 ± 4.26	1.73 ± 0.48	0 ± 0.15	0	-0.1	1.6
485	5	161.76589 (0.23)	58.98564 (0.24)	15 ± 3.67	15.1 ± 3.81	0.28 ± 0.18	0.21 ± 0.06	0	-1.2	-1.3
486	5	161.76646 (0.39)	59.02945 (0.38)	13.2 ± 3.26	15 ± 3.93	1.18 ± 0.43	0.83 ± 0.14	-94	-0.6	0
487	3	161.58818 (0.22)	58.98296 (0.22)	13.1 ± 1.68	14.8 ± 2.38	1.43 ± 0.28	0 ± 0.1	26	-0.6	-1.1
488	2	161.44179 (0.31)	58.97303 (0.3)	11.3 ± 1.62	14.8 ± 2.83	2.17 ± 0.42	0.7 ± 0.18	-16	-2.2	-0.4
489	3	161.38268 (0.47)	59.11372 (0.46)	11.1 ± 2.58	14.8 ± 4.33	2.4 ± 0.58	0 ± 0.23	-120	-1	-0.3
490	6	161.46257 (0.17)	58.94924 (0.17)	14.5 ± 1.73	14.7 ± 1.98	0.44 ± 0.18	0 ± 0.02	-70	-0.1	-1.1
491	3	161.47586 (0.5)	59.07688 (0.49)	8.8 ± 1.78	14.7 ± 4.29	3.65 ± 0.79	0 ± 0.34	-139	-0.5	-0.3
492	7	161.41576 (0.22)	59.13901 (0.23)	14.7 ± 3.14	14.7 ± 3.24	0 ± 0.15	0 ± 0.03	-2	0.1	-1.1
493	1	161.40176 (0.57)	59.04945 (0.56)	7.4 ± 1.66	14.7 ± 4.66	3.84 ± 0.82	1.63 ± 0.44	-56	-1.2	-1.9
494	3	161.711 (0.53)	58.99416 (0.52)	9.7 ± 2.35	14.7 ± 4.73	3.14 ± 0.74	0 ± 0.32	2	1	0.7
495	6	161.56706 (0.14)	58.95898 (0.15)	14.5 ± 1.83	14.6 ± 1.96	0.29 ± 0.13	0 ± 0.01	9	-0.3	-0.3
496	2	161.46225 (0.26)	59.06303 (0.25)	12.1 ± 1.64	14.6 ± 2.51	1.72 ± 0.33	0.64 ± 0.14	-83	-0.6	-0.8
497	7	161.63941 (0.14)	59.0045 (0.15)	14.5 ± 1.98	14.5 ± 2.05	0 ± 0.1	0 ± 0.01	46	-0.9	-0.4
498	5	161.67839 (0.33)	59.12512 (0.33)	13.7 ± 3.46	14.4 ± 3.96	0.87 ± 0.37	0.23 ± 0.11	-25	-0.9	-0.1

CB Catalogue continued

ID	Size Flag	RA (J2000) (arcsec)	Dec (J2000) (arcsec)	S_P ($\mu\text{Jy beam}^{-1}$)	S_T (μJy)	θ_{DM} (arcsec)	θ_{Dm} (arcsec)	ϕ (degrees)	α_{IF}	α_{IM}
499	3	161.43159 (0.33)	58.94295 (0.32)	12 ± 1.98	14.3 ± 2.96	1.78 ± 0.37	0 ± 0.14	-145	0.8	0.6
500	4	161.47065 (0.3)	59.10036 (0.29)	12.3 ± 1.98	14.3 ± 2.61	1.19 ± 0.31	1.03 ± 0.1	-31	-0.9	-1.2
501	2	161.5851 (0.66)	58.96556 (0.62)	6.8 ± 1.65	14.3 ± 4.99	5.06 ± 1.06	0.24 ± 0.48	-99	-0.3	-0.8
502	2	161.59148 (0.32)	59.0248 (0.31)	10.8 ± 1.6	14.2 ± 2.8	2.21 ± 0.43	0.63 ± 0.18	-102	-1	0.1
503	2	161.62346 (0.59)	58.97323 (0.58)	7.6 ± 1.78	14.2 ± 4.45	4.03 ± 0.84	0.9 ± 0.43	-131	-1.5	-0.3
504	3	161.52425 (0.43)	58.90659 (0.41)	11.6 ± 2.5	14.1 ± 3.73	1.93 ± 0.47	0 ± 0.16	-29	-1.3	-1.3
505	1	161.53449 (0.58)	58.9827 (0.57)	6.6 ± 1.49	14.1 ± 4.5	4 ± 0.85	1.85 ± 0.48	-48	-2.1	-1.1
506	2	161.61519 (0.63)	59.09093 (0.61)	7.2 ± 1.83	14.1 ± 4.96	4.63 ± 0.91	0.24 ± 0.48	19	-0.7	0.2
507	6	161.5258 (0.33)	59.11299 (0.32)	12.5 ± 2.22	14 ± 2.76	1.35 ± 0.34	0 ± 0.11	-102	-0.4	-0.5
508	2	161.68121 (0.4)	59.00807 (0.39)	11 ± 2.17	13.9 ± 3.34	2.02 ± 0.44	0.59 ± 0.17	12	-1.1	-0.7
509	5	161.25959 (0.23)	59.0773 (0.24)	13.7 ± 3.5	13.9 ± 3.64	0.3 ± 0.19	0.23 ± 0.07	90	-0.6	-1
510	7	161.49417 (0.16)	59.10013 (0.17)	13.8 ± 2.07	13.8 ± 2.15	0 ± 0.11	0 ± 0.01	40	0.3	-1.2
511	3	161.7148 (0.48)	59.02836 (0.47)	10.2 ± 2.43	13.8 ± 4.19	2.51 ± 0.61	0 ± 0.25	-112	-0.7	-1.1
512	3	161.63912 (0.5)	59.10197 (0.49)	9.8 ± 2.38	13.8 ± 4.33	2.72 ± 0.66	0 ± 0.27	-97	1	0.2
513	6	161.41532 (0.33)	58.90707 (0.32)	13.5 ± 2.72	13.7 ± 3.19	0.51 ± 0.33	0 ± 0.08	10	0	-2
514	3	161.45594 (0.48)	59.08116 (0.47)	9 ± 1.91	13.7 ± 3.99	3.19 ± 0.68	0 ± 0.32	28	0.1	0.2
515	2	161.41446 (0.57)	58.97545 (0.56)	7.6 ± 1.66	13.7 ± 4.23	3.98 ± 0.85	0.57 ± 0.4	-5	-1.6	-1.3
516	1	161.69492 (0.51)	59.00573 (0.51)	8.3 ± 2.05	13.7 ± 4.44	2.93 ± 0.72	1.45 ± 0.34	-108	-0.7	-0.9
517	6	161.50162 (0.34)	58.91792 (0.33)	12.2 ± 2.24	13.6 ± 2.77	1.34 ± 0.35	0 ± 0.11	-134	0	-0.9
518	3	161.45279 (0.46)	58.90485 (0.45)	10.5 ± 2.51	13.6 ± 4.03	2.23 ± 0.57	0 ± 0.21	-54	-1.2	-1.2
519	4	161.328 (0.43)	58.92549 (0.41)	10.2 ± 2.6	13.6 ± 3.75	1.74 ± 0.53	1.47 ± 0.18	-119	-1.6	0
520	3	161.48188 (0.39)	59.0665 (0.38)	9.6 ± 1.71	13.4 ± 3.28	2.7 ± 0.55	0 ± 0.24	28	-0.9	-1.3
521	2	161.44683 (0.39)	59.03602 (0.38)	9.2 ± 1.6	13.3 ± 3.21	2.81 ± 0.57	0.46 ± 0.25	-109	0	-0.3
522	3	161.60716 (0.51)	59.02423 (0.5)	8.1 ± 1.72	13.3 ± 3.96	3.54 ± 0.76	0 ± 0.34	-118	0	-0.7
523	7	161.29821 (0.23)	59.10342 (0.24)	13.3 ± 3.39	13.3 ± 3.52	0 ± 0.18	0 ± 0.06	-2	-1.4	-0.3
524	6	161.34118 (0.37)	59.13114 (0.36)	12.6 ± 3.16	13.3 ± 3.73	0.98 ± 0.41	0 ± 0.13	-15	-1.8	-0.1
525	2	161.46097 (0.27)	58.99694 (0.26)	10.9 ± 1.51	13.2 ± 2.33	1.75 ± 0.34	0.54 ± 0.14	-68	-1.9	-0.3
526	6	161.36515 (0.23)	59.02203 (0.22)	12.7 ± 1.65	13.2 ± 1.95	0.8 ± 0.22	0 ± 0.04	5	-1.4	-1.2
527	1	161.50404 (0.52)	58.94845 (0.52)	7 ± 1.68	13.2 ± 4.18	3.05 ± 0.72	2.1 ± 0.39	-44	-0.2	-0.4
528	1	161.51738 (0.41)	58.9824 (0.41)	8.5 ± 1.62	13.1 ± 3.37	2.71 ± 0.56	1.28 ± 0.27	-109	0	-0.7
529	3	161.67786 (0.52)	58.98026 (0.52)	8.7 ± 2.1	13 ± 4.17	3.07 ± 0.72	0 ± 0.31	-105	-0.6	-1
530	6	161.4579 (0.22)	58.97473 (0.21)	12.4 ± 1.63	12.9 ± 2.16	0.81 ± 0.3	0 ± 0.12	6	-0.7	-0.6
531	3	161.51433 (0.38)	59.08929 (0.37)	10.3 ± 1.88	12.9 ± 3.01	2.1 ± 0.44	0 ± 0.18	-12	-0.6	0.1
532	7	161.70831 (0.21)	59.0108 (0.22)	12.9 ± 2.36	12.9 ± 2.44	0 ± 0.13	0 ± 0.02	30	-1.4	-1.3
533	3	161.62764 (0.3)	58.99346 (0.29)	11.3 ± 1.79	12.8 ± 2.48	1.45 ± 0.32	0 ± 0.11	-136	-0.4	-0.2
534	4	161.63445 (0.31)	59.03601 (0.31)	10.7 ± 1.81	12.8 ± 2.43	1.28 ± 0.32	1.18 ± 0.11	-88	-0.1	0.3
535	2	161.44761 (0.57)	59.10527 (0.57)	7 ± 1.77	12.8 ± 4.06	3.74 ± 0.8	1.11 ± 0.43	-63	1.6	2.1
536	3	161.58613 (0.52)	58.97308 (0.52)	8 ± 1.76	12.7 ± 3.88	3.42 ± 0.74	0 ± 0.34	-43	-1.9	-0.9
537	7	161.25143 (0.23)	59.07555 (0.24)	12.7 ± 3.45	12.7 ± 3.58	0 ± 0.2	0 ± 0.07	-26	0	1.4
538	1	161.53249 (0.28)	59.0472 (0.27)	10.3 ± 1.49	12.6 ± 2.28	1.5 ± 0.31	1.09 ± 0.12	-43	-1.2	-0.5
539	3	161.44119 (0.56)	58.97811 (0.55)	7.3 ± 1.59	12.6 ± 3.92	3.86 ± 0.83	0 ± 0.38	-87	-0.6	-1.6
540	1	161.33998 (0.46)	58.94975 (0.45)	8.9 ± 2.21	12.6 ± 3.9	2.24 ± 0.59	1.27 ± 0.24	-120	1.5	0
541	7	161.47128 (0.18)	59.05154 (0.17)	12.5 ± 1.5	12.5 ± 1.81	0 ± 0.21	0 ± 0.05	-23	-0.5	-1.1
542	3	161.36556 (0.47)	59.05699 (0.46)	8.9 ± 1.98	12.4 ± 3.57	2.66 ± 0.59	0 ± 0.26	-116	-0.1	-0.4
543	7	161.31226 (0.23)	59.10468 (0.24)	12.4 ± 3.17	12.4 ± 3.29	0 ± 0.19	0 ± 0.06	163	1	-0.9
544	1	161.44258 (0.36)	58.97462 (0.35)	9 ± 1.63	12.3 ± 2.74	1.81 ± 0.39	1.54 ± 0.16	-12	0	-1.4
545	5	161.52957 (0.35)	59.10704 (0.34)	10.8 ± 2.07	12.3 ± 2.54	1.27 ± 0.36	0.74 ± 0.11	-107	-0.9	-0.3
546	3	161.59961 (0.58)	58.98418 (0.57)	7.2 ± 1.64	12.3 ± 3.91	3.8 ± 0.81	0 ± 0.38	-100	-1.7	-1.6
547	6	161.57703 (0.36)	59.13003 (0.35)	11.7 ± 2.67	12.3 ± 3.14	0.86 ± 0.37	0 ± 0.11	-165	-0.4	-0.6
548	2	161.3451 (0.45)	59.0958 (0.44)	9.6 ± 2.37	12.3 ± 3.72	2.14 ± 0.57	0.47 ± 0.21	-47	-1	-1

CB Catalogue continued

ID	Size Flag	RA (J2000) (arcsec)	Dec (J2000) (arcsec)	S_P ($\mu\text{Jy beam}^{-1}$)	S_T (μJy)	θ_{DM} (arcsec)	θ_{Dm} (arcsec)	ϕ (degrees)	α_{IF}	α_{IM}
549	6	161.2786 (0.42)	58.96354 (0.41)	10.4 ± 2.66	12.3 ± 3.37	1.73 ± 0.53	0 ± 0.16	-46	-2	-1.5
550	3	161.45497 (0.48)	59.08474 (0.48)	8.4 ± 1.89	12.2 ± 3.59	2.86 ± 0.64	0 ± 0.29	-79	-0.7	-0.6
551	3	161.4604 (0.3)	59.07613 (0.29)	10.7 ± 1.71	12.1 ± 2.35	1.41 ± 0.32	0 ± 0.11	-17	-1.1	-0.9
552	3	161.49704 (0.49)	59.07941 (0.48)	8.2 ± 1.83	12.1 ± 3.6	3 ± 0.66	0 ± 0.31	-57	-1.1	-0.6
553	3	161.36067 (0.42)	59.03003 (0.41)	9.2 ± 1.88	12 ± 3.11	2.32 ± 0.5	0 ± 0.21	14	-0.5	-0.5
554	1	161.35385 (0.52)	58.98611 (0.51)	7 ± 1.72	11.9 ± 3.86	2.98 ± 0.73	1.59 ± 0.35	-157	-0.4	1.4
555	3	161.48568 (0.48)	58.99084 (0.47)	7.6 ± 1.58	11.8 ± 3.4	3.26 ± 0.7	0 ± 0.32	-71	-1.1	0.3
556	7	161.58023 (0.23)	59.12426 (0.23)	11.8 ± 2.63	11.8 ± 2.71	0 ± 0.15	0 ± 0.04	44	-0.4	0.2
557	1	161.64377 (0.5)	58.9948 (0.49)	7.2 ± 1.74	11.7 ± 3.67	2.75 ± 0.67	1.55 ± 0.32	13	-1.6	-1.2
558	2	161.62124 (0.6)	59.03782 (0.59)	5.7 ± 1.45	11.7 ± 3.73	4.23 ± 0.84	1.35 ± 0.51	-140	0.8	-0.1
559	3	161.65783 (0.56)	59.02358 (0.56)	7 ± 1.74	11.6 ± 3.84	3.59 ± 0.79	0 ± 0.38	18	-0.3	-1.2
560	7	161.48358 (0.23)	58.88648 (0.24)	11.6 ± 3.12	11.6 ± 3.25	0 ± 0.2	0 ± 0.07	-21	-1.1	0.4
561	2	161.40346 (0.53)	59.09303 (0.52)	6.8 ± 1.68	11.6 ± 3.46	3.17 ± 0.75	1.41 ± 0.37	-20	1.9	-0.4
562	6	161.39399 (0.31)	58.98348 (0.3)	10.4 ± 1.72	11.5 ± 2.14	1.31 ± 0.32	0 ± 0.1	-39	1.1	0.7
563	3	161.51959 (0.29)	59.04592 (0.28)	9.9 ± 1.49	11.4 ± 2.13	1.55 ± 0.32	0 ± 0.12	-46	-1.8	-0.8
564	3	161.5716 (0.41)	58.93494 (0.39)	9.6 ± 2.02	11.4 ± 2.86	1.72 ± 0.43	0 ± 0.14	-46	-0.1	-0.9
565	6	161.48861 (0.19)	59.03144 (0.19)	11 ± 1.35	11.3 ± 1.57	0.65 ± 0.2	0 ± 0.03	57	-1.3	-1
566	1	161.5516 (0.33)	59.0076 (0.32)	9 ± 1.5	11.3 ± 2.33	1.71 ± 0.36	0.99 ± 0.14	15	-1.6	-0.5
567	3	161.58042 (0.4)	59.05441 (0.38)	8.9 ± 1.7	11.3 ± 2.72	2.15 ± 0.46	0 ± 0.19	-102	-1.3	-1
568	4	161.69158 (0.4)	59.04428 (0.39)	9.4 ± 2.2	11.3 ± 2.87	1.42 ± 0.44	0.99 ± 0.14	-3	0	-0.1
569	7	161.71528 (0.23)	58.96304 (0.24)	11.3 ± 2.88	11.3 ± 2.99	0 ± 0.18	0 ± 0.06	-1	0.1	0.1
570	3	161.45121 (0.45)	59.08154 (0.44)	8.4 ± 1.82	11.2 ± 3.09	2.44 ± 0.54	0 ± 0.23	-130	0.4	-1.6
571	5	161.2719 (0.23)	58.97744 (0.24)	11.1 ± 2.88	11.2 ± 2.99	0.31 ± 0.19	0.24 ± 0.07	90	-0.7	-0.6
572	6	161.59106 (0.21)	59.06497 (0.21)	11.1 ± 1.76	11.1 ± 1.9	0.3 ± 0.18	0 ± 0.03	-1	-1.1	-0.5
573	3	161.65199 (0.5)	59.04609 (0.49)	7.7 ± 1.86	11 ± 3.41	2.75 ± 0.66	0 ± 0.28	18	-1.1	-1.6
574	6	161.66197 (0.4)	58.93352 (0.39)	9.8 ± 2.48	11 ± 3.03	1.36 ± 0.47	0 ± 0.15	8	0	-2.1
575	3	161.68296 (0.46)	59.06551 (0.45)	8.6 ± 2.16	11 ± 3.45	2.21 ± 0.6	0 ± 0.21	21	-1	1.6
576	3	161.68678 (0.47)	59.0136 (0.46)	8.2 ± 2.01	10.9 ± 3.37	2.4 ± 0.61	0 ± 0.24	-90	0.5	1.4
577	6	161.39497 (0.33)	58.95051 (0.32)	10.2 ± 1.96	10.7 ± 2.33	0.89 ± 0.33	0 ± 0.08	5	-1.8	0
578	3	161.63376 (0.44)	58.95797 (0.43)	8.7 ± 2.01	10.7 ± 3.01	1.97 ± 0.5	0 ± 0.17	-62	1.1	0.1
579	3	161.57276 (0.53)	58.95081 (0.53)	7 ± 1.7	10.7 ± 3.47	3.21 ± 0.75	0 ± 0.33	-86	-0.6	-0.1
580	1	161.41652 (0.55)	59.02486 (0.54)	5.8 ± 1.42	10.7 ± 3.49	3.34 ± 0.76	1.68 ± 0.41	-33	-1.7	-1.8
581	3	161.63316 (0.5)	58.94679 (0.49)	7.5 ± 1.88	10.7 ± 3.47	2.78 ± 0.7	0 ± 0.28	-81	0.2	0.3
582	3	161.36883 (0.6)	59.01399 (0.59)	5.8 ± 1.47	10.7 ± 3.68	4.23 ± 0.83	0 ± 0.46	-126	0	-1.9
583	6	161.35497 (0.23)	58.99719 (0.23)	10.5 ± 1.86	10.6 ± 2.01	0.28 ± 0.19	0 ± 0.03	123	-1.8	-0.7
584	2	161.44487 (0.47)	59.06712 (0.46)	7.4 ± 1.66	10.6 ± 2.88	2.49 ± 0.57	1 ± 0.26	-84	-0.9	-1.7
585	3	161.68568 (0.49)	59.03189 (0.48)	7.7 ± 1.92	10.6 ± 3.38	2.6 ± 0.66	0 ± 0.26	-119	-1.9	1.2
586	1	161.48114 (0.57)	59.04994 (0.56)	5.2 ± 1.31	10.6 ± 3.58	3.7 ± 0.8	1.91 ± 0.48	-57	0	-1.3
587	7	161.60472 (0.19)	59.06164 (0.2)	10.5 ± 1.8	10.5 ± 1.86	0 ± 0.12	0 ± 0.02	100	-1.1	-0.8
588	2	161.5784 (0.5)	59.01105 (0.49)	6.9 ± 1.58	10.5 ± 3.06	2.93 ± 0.66	0.72 ± 0.31	-60	0.2	0.4
589	6	161.5082 (0.39)	59.10939 (0.38)	9.5 ± 2.05	10.5 ± 2.51	1.33 ± 0.4	0 ± 0.12	-111	1.6	-0.3
590	7	161.27156 (0.25)	59.04908 (0.25)	10.5 ± 2.75	10.5 ± 2.91	0.15 ± 0.23	0 ± 0.08	-100	-1.9	0
591	2	161.50033 (0.61)	59.05563 (0.59)	5 ± 1.26	10.5 ± 3.29	4.28 ± 0.84	1.5 ± 0.53	-140	-1.1	-1.1
592	3	161.55618 (0.58)	58.98519 (0.57)	6.1 ± 1.45	10.4 ± 3.39	3.79 ± 0.81	0 ± 0.39	15	0.5	1.5
593	7	161.54059 (0.23)	58.89721 (0.24)	10.4 ± 2.78	10.4 ± 2.88	0 ± 0.2	0 ± 0.07	-12	-0.5	-2.3
594	6	161.43301 (0.51)	59.13768 (0.5)	8.8 ± 2.67	10.4 ± 3.62	1.7 ± 0.71	0.14 ± 0.29	-113	1.2	1.7
595	2	161.51106 (0.57)	58.96003 (0.56)	5.5 ± 1.37	10.3 ± 3.14	3.66 ± 0.79	1.42 ± 0.44	-87	-1.3	0
596	3	161.50462 (0.46)	58.93546 (0.45)	7.9 ± 1.85	10.2 ± 2.97	2.22 ± 0.55	0 ± 0.21	-72	-0.7	-2.1
597	3	161.45423 (0.59)	59.05621 (0.58)	5.7 ± 1.42	10.2 ± 3.44	4.05 ± 0.83	0 ± 0.43	-128	-1.5	-1.3
598	6	161.5565 (0.29)	59.05346 (0.29)	9.4 ± 1.56	10.1 ± 1.88	1.02 ± 0.3	0 ± 0.08	-70	-1.3	-0.7

CB Catalogue continued

ID	Size Flag	RA (J2000) (arcsec)	Dec (J2000) (arcsec)	S_P ($\mu\text{Jy beam}^{-1}$)	S_T (μJy)	θ_{DM} (arcsec)	θ_{Dm} (arcsec)	ϕ (degrees)	α_{IF}	α_{IM}
599	3	161.56419 (0.41)	59.04217 (0.4)	7.9 ± 1.58	10.1 ± 2.53	2.19 ± 0.47	0 ± 0.19	-82	0	-0.5
600	2	161.57305 (0.47)	59.05933 (0.46)	7.2 ± 1.63	10.1 ± 2.77	2.42 ± 0.57	0.93 ± 0.25	23	-0.5	0.2
601	7	161.48534 (0.16)	59.04183 (0.17)	10 ± 1.54	10 ± 1.6	0 ± 0.11	0 ± 0.01	-16	-0.9	-1.5
602	6	161.55202 (0.26)	58.98304 (0.25)	10 ± 1.49	10 ± 1.78	0.2 ± 0.26	0 ± 0.06	-8	-1.3	-1.8
603	3	161.62928 (0.43)	58.97514 (0.42)	8.3 ± 1.84	10 ± 2.71	1.89 ± 0.48	0 ± 0.16	143	-1.2	-0.6
604	3	161.38463 (0.48)	58.98104 (0.47)	7.4 ± 1.72	9.9 ± 2.92	2.44 ± 0.59	0 ± 0.24	26	-1.5	-0.5
605	7	161.62623 (0.23)	59.09854 (0.24)	9.9 ± 2.34	9.9 ± 2.42	0 ± 0.17	0 ± 0.05	-9	-1.2	-1.1
606	3	161.66842 (0.45)	59.0506 (0.44)	7.9 ± 1.96	9.9 ± 3.02	2.08 ± 0.56	0 ± 0.2	-86	-0.2	0.9
607	2	161.52868 (0.56)	58.97008 (0.55)	5.7 ± 1.41	9.9 ± 3.09	3.52 ± 0.78	1.07 ± 0.4	15	-1	-1.3
608	3	161.38187 (0.58)	59.03434 (0.57)	5.8 ± 1.45	9.9 ± 3.36	3.86 ± 0.81	0 ± 0.41	-59	-1.2	-1.1
609	3	161.44016 (0.42)	58.9915 (0.4)	7.7 ± 1.56	9.8 ± 2.48	2.17 ± 0.47	0 ± 0.19	-26	-1.1	-0.5
610	3	161.41728 (0.52)	59.06362 (0.52)	6.5 ± 1.59	9.8 ± 3.15	3.08 ± 0.73	0 ± 0.32	-41	0	-1.3
611	6	161.72135 (0.4)	59.01273 (0.39)	8.8 ± 2.22	9.8 ± 2.72	1.36 ± 0.47	0 ± 0.15	-102	-1.3	-0.4
612	6	161.49156 (0.39)	58.91733 (0.38)	8.9 ± 2.11	9.7 ± 2.54	1.18 ± 0.42	0 ± 0.13	-146	0	-0.1
613	5	161.34337 (0.23)	58.92963 (0.24)	9.5 ± 2.56	9.7 ± 2.67	0.33 ± 0.2	0.25 ± 0.07	90	1.4	0.4
614	7	161.5986 (0.23)	59.12791 (0.24)	9.7 ± 2.61	9.7 ± 2.73	0.05 ± 0.21	0 ± 0.08	13	-0.2	-0.7
615	5	161.62791 (0.41)	59.02132 (0.4)	8.2 ± 1.78	9.6 ± 2.35	1.29 ± 0.47	0.92 ± 0.2	-117	-0.1	-0.4
616	1	161.4168 (0.45)	59.08915 (0.43)	6.5 ± 1.65	9.6 ± 2.99	2.03 ± 0.57	1.78 ± 0.23	-13	-1.3	-1
617	3	161.56201 (0.49)	59.08632 (0.48)	6.9 ± 1.7	9.5 ± 2.98	2.59 ± 0.65	0 ± 0.26	-132	-0.5	1.7
618	2	161.58768 (0.54)	59.04675 (0.53)	5.7 ± 1.41	9.5 ± 2.94	3.27 ± 0.76	1.13 ± 0.37	-138	0.3	0
619	5	161.53461 (0.35)	59.12942 (0.34)	8.8 ± 2.33	9.3 ± 2.66	0.92 ± 0.38	0.26 ± 0.12	-34	-0.7	0.4
620	3	161.56842 (0.6)	59.02952 (0.58)	5.1 ± 1.29	9.3 ± 3.18	4.15 ± 0.83	0 ± 0.45	-211	-0.5	-0.2
621	7	161.41165 (0.2)	58.98053 (0.21)	9.2 ± 1.63	9.2 ± 1.69	0 ± 0.12	0 ± 0.02	-53	0	-1.3
622	6	161.37737 (0.36)	58.99354 (0.35)	8.4 ± 1.7	9.2 ± 2.07	1.21 ± 0.37	0 ± 0.11	-131	-1.5	-0.8
623	3	161.52598 (0.42)	59.07069 (0.41)	7.6 ± 1.61	9.2 ± 2.37	1.88 ± 0.45	0 ± 0.16	1	1.1	-0.7
624	7	161.58579 (0.23)	59.09693 (0.23)	9.2 ± 2.06	9.2 ± 2.13	0 ± 0.16	0 ± 0.04	16	-1.2	0.2
625	7	161.69724 (0.23)	59.06407 (0.24)	9.2 ± 2.48	9.2 ± 2.57	0 ± 0.2	0 ± 0.07	39	2.2	0
626	6	161.50517 (0.31)	59.04697 (0.3)	8.5 ± 1.47	9.1 ± 1.78	1.05 ± 0.31	0 ± 0.08	-136	0	-0.6
627	3	161.58454 (0.45)	59.00327 (0.44)	7.1 ± 1.56	9.1 ± 2.52	2.25 ± 0.52	0 ± 0.21	-105	-1.3	-1
628	5	161.3732 (0.44)	58.95249 (0.43)	8.3 ± 2.06	9.1 ± 2.58	1.25 ± 0.49	0.2 ± 0.17	-79	0.1	-1.3
629	3	161.35798 (0.46)	58.97927 (0.45)	7 ± 1.76	9.1 ± 2.82	2.23 ± 0.59	0 ± 0.22	-40	-1	-0.5
630	6	161.47393 (0.33)	58.99929 (0.33)	8.1 ± 1.45	9 ± 1.8	1.35 ± 0.34	0 ± 0.11	-72	-0.2	0
631	7	161.45494 (0.2)	58.97706 (0.2)	9 ± 1.57	9 ± 1.62	0 ± 0.12	0 ± 0.02	-33	-1.2	-1.8
632	7	161.34498 (0.22)	59.01155 (0.23)	9 ± 1.85	9 ± 1.91	0 ± 0.14	0 ± 0.03	-28	-0.8	-2
633	3	161.60907 (0.49)	58.96503 (0.48)	6.6 ± 1.64	9 ± 2.88	2.58 ± 0.66	0 ± 0.26	-86	-0.8	-0.7
634	3	161.50636 (0.44)	59.06226 (0.42)	7.1 ± 1.55	8.9 ± 2.39	2.08 ± 0.49	0 ± 0.18	-121	0.6	-0.3
635	7	161.70488 (0.23)	58.9982 (0.24)	8.9 ± 2.36	8.9 ± 2.45	0 ± 0.19	0 ± 0.07	44	-1.4	-1.3
636	1	161.474 (0.5)	58.98463 (0.49)	5.2 ± 1.3	8.9 ± 2.86	2.73 ± 0.69	1.87 ± 0.33	-54	-0.6	0
637	3	161.45991 (0.45)	59.1081 (0.44)	7.2 ± 1.82	8.9 ± 2.79	2.05 ± 0.57	0 ± 0.19	-79	0.4	0.8
638	2	161.45678 (0.48)	59.00949 (0.47)	6.2 ± 1.42	8.8 ± 2.45	2.47 ± 0.59	1 ± 0.26	-56	-1.7	-2.2
639	3	161.43802 (0.59)	59.01821 (0.58)	4.9 ± 1.24	8.7 ± 2.97	4.01 ± 0.82	0 ± 0.43	-8	-1.8	-1.6
640	2	161.51342 (0.52)	59.04004 (0.51)	5.6 ± 1.36	8.5 ± 2.68	3.03 ± 0.72	0.57 ± 0.32	-48	-1.5	-2
641	2	161.6005 (0.52)	59.00348 (0.51)	5.3 ± 1.32	8.5 ± 2.62	3.03 ± 0.74	1.09 ± 0.33	-118	-1.9	-2.5
642	3	161.47846 (0.53)	58.95168 (0.52)	5.6 ± 1.4	8.5 ± 2.8	3.11 ± 0.75	0 ± 0.32	-133	1.2	-0.7
643	6	161.55377 (0.45)	58.99496 (0.44)	7.1 ± 1.63	8.4 ± 2.36	1.76 ± 0.6	0 ± 0.28	6	-1.1	-1.2
644	3	161.53159 (0.49)	58.99183 (0.48)	6.1 ± 1.43	8.4 ± 2.54	2.61 ± 0.62	0 ± 0.26	9	-1.6	-1
645	3	161.57127 (0.55)	58.98898 (0.54)	5.3 ± 1.32	8.4 ± 2.79	3.39 ± 0.77	0 ± 0.35	1	0	-0.7
646	3	161.57191 (0.52)	59.06544 (0.52)	5.6 ± 1.39	8.4 ± 2.76	3.07 ± 0.75	0 ± 0.32	-88	-1.4	-0.7
647	5	161.39488 (0.42)	58.9141 (0.41)	7.5 ± 2.25	8.4 ± 2.68	1.28 ± 0.5	0.36 ± 0.15	-125	-1.3	-1.7
648	6	161.52861 (0.32)	59.00978 (0.31)	7.8 ± 1.42	8.3 ± 1.71	0.98 ± 0.32	0 ± 0.08	-52	-1	-0.3

CB Catalogue continued

ID	Size Flag	RA (J2000) (arcsec)	Dec (J2000) (arcsec)	S_P ($\mu\text{Jy beam}^{-1}$)	S_T (μJy)	θ_{DM} (arcsec)	θ_{Dm} (arcsec)	ϕ (degrees)	α_{IF}	α_{IM}
649	7	161.62156 (0.22)	59.02679 (0.22)	8.3 ± 1.64	8.3 ± 1.68	0 ± 0.13	0 ± 0.02	86	-0.6	0.1
650	7	161.62878 (0.23)	59.07424 (0.24)	8.3 ± 2	8.3 ± 2.07	0 ± 0.17	0 ± 0.05	0	0	0
651	5	161.63497 (0.41)	59.01553 (0.4)	7 ± 1.66	8.3 ± 2.07	1.56 ± 0.47	0.71 ± 0.15	-71	-0.5	-2.2
652	3	161.36748 (0.48)	59.00473 (0.47)	6.1 ± 1.54	8.3 ± 2.63	2.48 ± 0.64	0 ± 0.25	-52	0.8	0.6
653	7	161.48734 (0.23)	59.10571 (0.24)	8.1 ± 2.02	8.1 ± 2.09	0 ± 0.18	0 ± 0.06	-81	0.1	-0.4
654	3	161.35989 (0.45)	59.02597 (0.44)	6.5 ± 1.63	8.1 ± 2.51	2.07 ± 0.57	0 ± 0.2	-146	-0.2	0.2
655	3	161.60096 (0.5)	59.05527 (0.49)	5.7 ± 1.42	8 ± 2.56	2.7 ± 0.68	0 ± 0.27	-53	0	-2.1
656	3	161.45053 (0.5)	59.07729 (0.49)	5.6 ± 1.41	8 ± 2.59	2.78 ± 0.7	0 ± 0.28	-74	-1.4	-0.2
657	6	161.54646 (0.33)	59.05361 (0.32)	7.6 ± 1.51	7.9 ± 1.79	0.82 ± 0.34	0 ± 0.08	-91	-1.7	-0.9
658	7	161.65647 (0.23)	59.00396 (0.24)	7.9 ± 1.9	7.9 ± 1.97	0 ± 0.17	0 ± 0.05	21	-0.7	0.7
659	3	161.47529 (0.43)	58.96233 (0.42)	6.6 ± 1.55	7.9 ± 2.27	1.86 ± 0.5	0 ± 0.16	-325	-0.9	-0.4
660	5	161.30267 (0.48)	59.04022 (0.47)	6.8 ± 2.07	7.9 ± 2.69	1.61 ± 0.65	0.23 ± 0.25	-39	-1.2	-0.2
661	3	161.54373 (0.45)	59.04503 (0.44)	6.3 ± 1.45	7.8 ± 2.22	2.04 ± 0.52	0 ± 0.18	-37	-0.8	-1.6
662	2	161.50354 (0.46)	59.00598 (0.45)	5.8 ± 1.37	7.8 ± 2.19	2.22 ± 0.56	0.86 ± 0.22	-7	-0.5	1.3
663	5	161.48847 (0.32)	59.11597 (0.32)	7.5 ± 1.95	7.8 ± 2.2	0.83 ± 0.35	0.25 ± 0.12	125	0	-0.7
664	3	161.5923 (0.47)	59.03033 (0.45)	5.9 ± 1.45	7.7 ± 2.37	2.3 ± 0.6	0 ± 0.22	-17	-0.7	-1.1
665	5	161.34563 (0.33)	59.07484 (0.32)	7.3 ± 1.9	7.7 ± 2.15	0.88 ± 0.36	0.25 ± 0.12	-42	1.2	0
666	7	161.42644 (0.21)	59.0164 (0.22)	7.6 ± 1.45	7.6 ± 1.49	0 ± 0.13	0 ± 0.02	-19	-1.3	-1.3
667	7	161.43728 (0.23)	58.95984 (0.23)	7.6 ± 1.69	7.6 ± 1.75	0 ± 0.15	0 ± 0.04	-42	-1.7	-1
668	3	161.50291 (0.51)	59.02087 (0.5)	5.3 ± 1.29	7.6 ± 2.42	2.83 ± 0.69	0 ± 0.29	-112	-1.4	-0.9
669	7	161.46634 (0.21)	59.01508 (0.21)	7.5 ± 1.41	7.5 ± 1.45	0 ± 0.12	0 ± 0.02	-49	-0.6	0.4
670	3	161.58682 (0.44)	59.02893 (0.43)	6 ± 1.45	7.4 ± 2.2	2 ± 0.54	0 ± 0.18	17	-1.4	-1.1
671	7	161.5075 (0.23)	58.92274 (0.24)	7.4 ± 2.02	7.4 ± 2.1	0 ± 0.2	0 ± 0.07	-61	1.5	1.2
672	7	161.46153 (0.21)	58.99393 (0.22)	7.2 ± 1.41	7.2 ± 1.45	0 ± 0.13	0 ± 0.02	-11	-1.6	-0.6
673	5	161.38166 (0.35)	58.96652 (0.34)	6.9 ± 1.73	7.2 ± 1.98	0.85 ± 0.37	0.23 ± 0.11	0	0	0
674	2	161.44439 (0.46)	58.97612 (0.45)	5.4 ± 1.37	7.2 ± 2.18	2.19 ± 0.6	0.79 ± 0.22	-123	0	1.2
675	3	161.59391 (0.44)	58.97423 (0.43)	5.8 ± 1.48	7.2 ± 2.23	1.97 ± 0.56	0 ± 0.19	-4	0	-1.3
676	6	161.40616 (0.41)	59.05556 (0.4)	6.1 ± 1.54	7 ± 1.91	1.52 ± 0.48	0 ± 0.15	-155	-2.2	-0.9
677	7	161.49157 (0.23)	58.95791 (0.24)	6.9 ± 1.64	6.9 ± 1.69	0 ± 0.17	0 ± 0.05	-5	-1.3	-1.4
678	6	161.54347 (0.4)	59.06701 (0.39)	6.1 ± 1.49	6.9 ± 1.84	1.45 ± 0.47	0 ± 0.14	9	-0.2	-1.2
679	5	161.5449 (0.37)	59.05785 (0.36)	6.2 ± 1.46	6.8 ± 1.73	0.94 ± 0.39	0.74 ± 0.12	76	-0.1	-0.9
680	5	161.50674 (0.39)	59.07986 (0.38)	6.2 ± 1.6	6.7 ± 1.88	0.95 ± 0.42	0.6 ± 0.13	-86	0.8	0.3
681	3	161.44397 (0.45)	58.98249 (0.44)	5.3 ± 1.36	6.7 ± 2.09	2.07 ± 0.58	0 ± 0.2	-72	-0.6	-1
682	6	161.50265 (0.39)	58.97286 (0.38)	6 ± 1.43	6.6 ± 1.74	1.26 ± 0.43	0 ± 0.13	-85	-0.1	-0.7
683	7	161.45702 (0.23)	59.02492 (0.23)	6.4 ± 1.43	6.4 ± 1.47	0 ± 0.15	0 ± 0.04	-50	-1.3	-0.3
684	5	161.45557 (0.23)	58.95469 (0.24)	6.3 ± 1.67	6.4 ± 1.74	0.32 ± 0.2	0.24 ± 0.07	90	-1.4	1
685	7	161.47746 (0.23)	58.95001 (0.24)	6.3 ± 1.69	6.3 ± 1.75	0 ± 0.2	0 ± 0.07	111	-1.5	-1.9
686	7	161.60792 (0.23)	59.0319 (0.24)	6.2 ± 1.61	6.2 ± 1.67	0 ± 0.19	0 ± 0.06	-68	1.2	0.9
687	7	161.51737 (0.23)	59.07635 (0.24)	6.2 ± 1.62	6.2 ± 1.69	0 ± 0.19	0 ± 0.07	3	0	-1.5
688	5	161.46491 (0.33)	58.94886 (0.32)	5.9 ± 1.55	6.2 ± 1.75	0.87 ± 0.36	0.25 ± 0.12	-87	1.3	-0.8
689	6	161.50726 (0.32)	59.07397 (0.31)	5.9 ± 1.48	6.1 ± 1.68	0.55 ± 0.35	0 ± 0.11	7	-1.3	-0.7
690	3	161.46715 (0.44)	59.03585 (0.43)	5 ± 1.26	6.1 ± 1.9	1.99 ± 0.56	0 ± 0.19	-14	-0.2	-1.4
691	3	161.55215 (0.44)	58.99043 (0.43)	5 ± 1.26	6.1 ± 1.91	2 ± 0.57	0 ± 0.19	-30	-1.1	-0.8
692	6	161.47264 (0.51)	59.05251 (0.5)	5 ± 1.43	6 ± 1.99	1.75 ± 0.69	0.09 ± 0.3	-86	-1.3	-1.8
693	6	161.45765 (0.42)	59.03342 (0.41)	5.1 ± 1.3	6 ± 1.64	1.67 ± 0.52	0 ± 0.16	-80	-1	-0.1
694	3	161.49726 (0.44)	58.9893 (0.43)	4.8 ± 1.23	6 ± 1.87	2.02 ± 0.57	0 ± 0.19	15	0	-1.2
695	7	161.39933 (0.23)	59.02911 (0.24)	5.9 ± 1.56	5.9 ± 1.62	0 ± 0.19	0 ± 0.07	63	0	1.7
696	6	161.56133 (0.42)	59.02568 (0.41)	5.1 ± 1.3	5.9 ± 1.64	1.68 ± 0.52	0 ± 0.16	19	-0.6	0.5
697	7	161.49247 (0.23)	59.03573 (0.24)	5.5 ± 1.41	5.5 ± 1.46	0 ± 0.19	0 ± 0.06	57	-0.9	-0.1
698	5	161.52377 (0.23)	58.97579 (0.24)	5.4 ± 1.44	5.4 ± 1.5	0.33 ± 0.2	0.25 ± 0.07	113	-0.7	-0.3

CB Catalogue continued

ID	Size Flag	RA (J2000) (arcsec)	Dec (J2000) (arcsec)	S_P ($\mu\text{Jy beam}^{-1}$)	S_T (μJy)	θ_{DM} (arcsec)	θ_{Dm} (arcsec)	ϕ (degrees)	α_{IF}	α_{IM}
699	7	161.42078 (0.23)	59.03622 (0.24)	5.3 ± 1.44	5.3 ± 1.5	0 ± 0.2	0 ± 0.07	-104	-0.3	0
700	7	161.4839 (0.23)	58.9978 (0.24)	5.2 ± 1.39	5.2 ± 1.45	0 ± 0.2	0 ± 0.07	-16	0	0.9
701	7	161.49622 (0.23)	59.05625 (0.24)	5.2 ± 1.4	5.2 ± 1.46	0 ± 0.2	0 ± 0.07	90	0.7	0.8
702	5	161.53728 (0.34)	59.05798 (0.33)	4.9 ± 1.27	5.2 ± 1.46	0.92 ± 0.38	0.25 ± 0.12	5	-1.1	0.7
703	5	161.54129 (0.23)	59.0243 (0.24)	5 ± 1.34	5.1 ± 1.39	0.33 ± 0.2	0.25 ± 0.07	0	-2.2	-0.2
704	7	161.48688 (0.23)	58.97815 (0.24)	5.1 ± 1.39	5.1 ± 1.44	0 ± 0.2	0 ± 0.07	-2	0.4	0.1
705	6	161.54901 (0.59)	59.03387 (0.58)	4.1 ± 1.21	5.1 ± 1.83	2.15 ± 0.82	0 ± 0.44	-86	-0.9	-0.4
706	5	161.48597 (0.23)	59.01097 (0.24)	4.9 ± 1.32	5 ± 1.37	0.33 ± 0.2	0.25 ± 0.07	90	0.2	-0.3